Strål
säkerhets
myndigheten
Swedish Radiation Safety Authority

2017:31

# SSM's external experts' review of SKB's safety assessment SR-PSU – rock engineering and concrete barriers

## Main review phase

**Report number:** 2017:31 **ISSN:** 2000-0456
Available at www.stralsakerhetsmyndigheten.se

## SSM perspective

### Background

The Swedish Radiation Safety Authority (SSM) received an application for the expansion of SKB's final repository for low and intermediate level waste at Forsmark (SFR) on the 19 December 2014. SSM is tasked with the review of the application and will issue a statement to the government who will decide on the matter. An important part of the application is SKB's assessment of the long-term safety of the repository, which is documented in the safety analysis named SR-PSU.

Present report compiles results from SSM's external experts' reviews of SR-PSU during the main review phase. The general objective of these reviews has been to give support to SSM's assessment of the license application. More specifically, the instructions to the external experts have been to make an in depth assessment of the specific issues defined for the different disciplines.

### Project information

Contact person SSM: Georg Lindgren

Contact persons and registration numbers for the different expert review contributions are given in the report

### Table of Contents

Strål
säkerhets
myndigheten
Swedish Radiation Safety Authority

2017:31

# SSM's external experts' review of SKB's safety assessment SR-PSU – rock engineering and concrete barriers

## Main review phase

**Date:** November 2017
**Report number:** 2017:31 **ISSN:** 2000-0456
Available at www.stralsakerhetsmyndigheten.se

This report concerns a study which has been conducted for the Swedish Radiation Safety Authority, SSM. The conclusions and viewpoints presented in the report are those of the author/authors and do not necessarily coincide with those of the SSM.

**Authors:** Erik Eberhardt, Mark Diederichs[1)]
[1)]Fisher Rock Engineering LLC, Radford, VA, USA

# Review of the evolution of the mechanical stability and hydraulic conductivity around the rock vaults of SFR

**Activity number:** 3030014-1026
**Registration number:** SSM2016-4329
**Contact person at SSM:** Flavio Lanaro

# Abstract

This Report presents the results from a detailed review of the evolution of the mechanical stability and associated hydraulic conductivity around the rock vaults of SKB's Final Repository for Short-Lived Radioactive Waste (SFR) at Forsmark.

The review first examines the relevant parts of SKB's license application and related analyses concerning the long-term mechanical stability and hydraulic conductivity of the rock mass around the SFR rock vaults. This is discussed in parallel with the findings of SSM's initial review. A detailed analysis is then presented using the 2-D distinct-element code UDEC to investigate the expected deterioration of the mechanical properties of the intact rock and rock fractures over time, and its effects on the stability of the SFR rock vaults, which in turn may result in changes in the hydraulic conductivity of the near-field rock mass. Both the existing SFR 1 rock vault layout and the proposed SFR 3 rock vault layout were analysed, and each layout was analysed using four Discrete Fracture Network (DFN) realizations to account for spatial variability in the location, intersection and dip angles of critical fractures. Each analysis was carried out for the reference times of 1000, 10,000, 20,000 and 50,000 years, with the latter time periods including simulations of permafrost and permafrost melting, and glacial loading and unloading.

It was found that the SKB analysis, reported in SKB R-13-53, was overly conservative in how the strength degradation procedure was implemented (i.e., fracture friction angles were reduced uniformly as a function of distances from the excavation boundary), and that friction angles as low as 5.7 degrees were required to simulate large-scale collapse. This compares to the lowest values we could find in the literature of 8 degrees. SKB R-13-53 found that the height of the loosened rock would not reach the seabed, from which the SKB Safety Analysis for SFR (SKB TR-14-01) concludes that there should be no risk of a direct connection between the rock vaults and the seabed.

The UDEC analysis presented in this Report reaches a similar conclusion. The UDEC models employ a time-dependent strength degradation procedure based on extrapolated data from long-term testing of granitic rock, and implemented using functions that account for dependencies on the driving differential stress (or shear stress in the case of fractures) and the confinement (or normal stress). In contrast to the analysis reported in SKB R-13-53, our analysis considers both strength degradation of the intact blocks and along the fractures. However, it is also conservative as it assumes full fracture persistence and assumes 2-D plane strain conditions for block stability and movement.

The UDEC results for SFR 1 suggest that over the full time and climate based scenarios modelled, that instabilities will likely not evolve beyond minor roof failures (isolated wedges) and limited, localized spalling and structural shear. The latter (i.e., structural shear and dilation of fractures), may however evolve to include a 40% increase in the cumulative fracture apertures in the near-field surrounding the rock vaults, and up to a 300% increase within a 1 m zone of the individual rock vaults. Assuming a cubic law relationship for fracture permeability, this approximates as a 2.7 (40%) to 64 (300%) times increase, respectively, of the rock mass permeability. For the SFR 3 case, the combination of greater depth and increased number of larger non-backfilled excavations (3 of 4 excavations backfilled in SFR-1 versus only 2 of 6 in SFR-3), resulted in a significant increase in rock mass damage above and around the excavations. For the permafrost and permafrost melting scenario, several instabilities were seen to initiate involving block movements enabled by the removal of the permafrost-enhanced fracture strength (i.e., cohesive ice) together with the normal stresses acting on the fractures relaxing

in response to ice pressures returning to their hydrostatic levels upon melting. However, only one of these DFN realizations evolved into a partial collapse, with a stable arch subsequently re-establishing. Ultimately, failure in this case was due to the combination of fracture orientations and intersections specific to the DFN realization as the same failure did not develop in the other three DFN realizations. For the glacial loading and unloading scenario, significant rock mass spalling and block failures were observed for the SFR 3 models, most notably in the non-backfilled BLA-type rock vaults. During the start of glacial loading, there is a phase of stress relaxation (due to crustal flexure) followed by horizontal and vertical compression. This cycle creates significant rock mass damage and the stress conditions for accelerated time-dependent strength degradation. Subsequent glacial unloading, restoration of the pre-glacial stress state and permafrost melting then allows this damaged rock to destabilize further, creating more significant failures and limited collapse. In the worst cases, spalling and failure extends up to 20 m above the roof, although runaway collapse beyond the upper bounding deformation zones does not occur. The effects of this increased block instability on the cumulative fracture aperture and fracture permeability of the near-field rock mass around the SFR 3 rock vaults was similar to that in SFR 1. However, for the SFR 3 case, the EDZ was seen to evolve more deeply and extend across the full width of the rock vaults, especially above the non-backfilled BLA-type rock vaults. In several cases, the EDZ interacts with intersecting sub-vertical fractures and propagates several metres upwards towards the overlying deformation zone, amplifying the extent of the EDZ during glacial loading and unloading. Based on relationships in the published literature, this could drive the local intact rock permeability up to 2 to 3 orders of magnitude higher within these damage zones.

# Contents

# 1. Introduction

This Report presents the findings of a detailed review of the evolution of the mechanical stability and associated hydraulic conductivity around the rock vaults of SKB's Final Repository for Short-Lived Radioactive Waste (SFR) at Forsmark. This follows SSM's initial review phase completed in 2016 regarding SKB's application to expand the SFR. SKB's analysis of the long-term safety for the extension is documented in the safety assessment named SR-PSU (SKB TR-14-01). The initial SSM review included three reports covering different aspects of the SKB assessment. These examined:

- the hydrogeological and chemical aspects (SSM 2016:08)
- the radionuclide transport, dose assessment, and safety analysis methodology (SSM 2016:09)
- the engineered barriers, engineering geology and chemical inventory (SSM 2016:12)

SSM is now conducting their main review phase and this Report describes the findings of an in-depth analysis that builds on the following objective:

> *To evaluate SKB's understanding of the evolution of the mechanical stability and hydraulic conductivity of the rock mass around the rock caverns after closure with respect to its implications on the long-term safety of the SFR repository.*

This recognizes that the stability of the rock vaults and associated changes in the hydraulic conductivity of the rock mass are important factors for achieving the safety requirement of limiting the groundwater flow into the rock vaults containing the waste.

The review reported here first examines the relevant parts of SKB's license application and related analyses concerning the long-term mechanical stability and hydraulic conductivity of the rock mass around the SFR vaults. This is discussed in parallel with the findings of SSM's initial review. Next, a series of scoping calculations are reported that investigate the expected deterioration of the mechanical properties of the rock and rock fractures over the long time periods involved, and its effects on the stability of the rock vaults, which in turn may result in changes in the hydraulic conductivity of the rock mass in the near-field of the SFR rooms. The consequence of such changes on the localisation of groundwater flow is of concern to SSM. To address these concerns, the analyses were directed to address several specific questions posed by SSM, which focus on:

- The appropriateness and uncertainty of the degraded and residual mechanical properties of the rock fractures as assumed in SKB R-13-53. This includes estimates of the points in time when the degraded and residual values of the mechanical properties of the rock fractures assumed in SKB R-13-53 could be reached after closure of the repository.
- The initial stability of the pillars between the rock vaults, and its evolution due to loads and degradation of the rock mass properties at different points

in time, specifically at 1000, 10,000, 20,000 and 50,000 years after closure of the repository, with the simulation of permafrost and permafrost melting at Year 20,000 and glacial loading and unloading at Year 50,000. This will be carried out through a series of advanced 2-D numerical models employing a hydro-mechanical coupling to account for the influence of pore pressures on the effective stresses. The treatment of fluid flow is outside the scope of the analyses and not considered. Results will be used to estimate changes in the hydraulic conductivity of the near-field rock mass surrounding the vaults arising from the strength degradation and any modelled instabilities.

- The effect of the supporting function of rock reinforcements in the rock vaults and their deterioration after closure of the repository.

This Report concludes with recommendations on the suitability of the rock vault design proposed by SKB, based on scoping calculations that study the potential of significant risk of instability after closure of the repository. Where necessary, suggestions for requests of complementary information to SKB and its extension are provided.

# 2. Review of Relevant SKB Analyses

## 2.1. SKB TR-14-01 and R-13-53

SKB TR-14-01 presents the main reporting of the long-term safety assessment, SR-PSU, for the SFR repository for short-lived low- and intermediate-level radioactive wastes located in Forsmark. The assessment is based on plans to extend the existing facility, SFR 1, to include additional rock vaults for decommissioning waste as part of a SFR 3 (Figure 1). The review presented here only pertains to the sections of SKB TR-14-01 and associated documents concerning the long-term mechanical stability and hydraulic conductivity of the rock mass around the SFR 1 and 3 vaults.

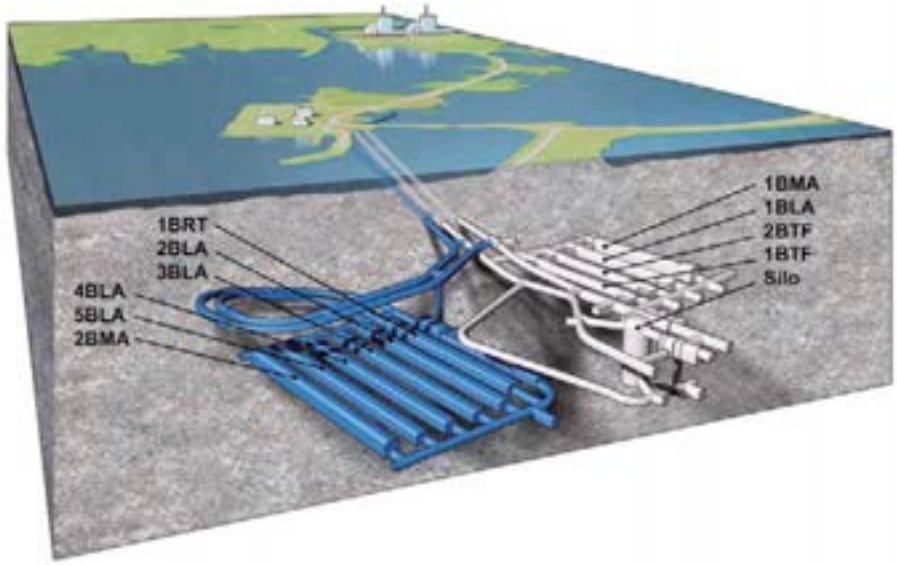


**Figure 1:** The existing SFR facility at Forsmark, SFR 1 (light grey), and extension, SFR 3 (blue), with access tunnels. From SKB TR-14-01.

The safety assessment SR-PSU builds on the assessment for SFR 1 (SKB R-08-130), and evaluates the safety of the repository over a period of 100,000 years. SKB R-13-53 (referenced as Mas Ivars et al., 2014) is cited as the basis for the assessment of long-term mechanical stability of the SFR 1 and 3 vaults. This report is similarly referenced in the Geosphere process report, SKB TR-14-05, which serves as the supporting document for SKB TR-14-01 with respect to describing the influence of geosphere processes on the long-term safety of the repository.

In SKB R-13-53, the commercial 3-D distinct-element program 3DEC was used to model the 1BMA and 1BLA vaults (3DEC is the 3-D version of the 2-D program UDEC used in the present Report, as described in later sections). Two objectives are cited for SKB R-13-53: i) to analyse if there is a risk of loosening of the rock mass through displacements into the vaults that can lead to collapse up to the surface and breaching of the sea bed; and ii) if there is a risk of instability in the pillars between the vaults. The analyses are conducted without considering the influence of groundwater and water pressures in the fractures.

The analysis in SKB R-13-53 first assesses the question of excavation and pillar stability by analyzing eight different Discrete Fracture Network (DFN) realizations

based on the average orientations of the different joint sets and their standard deviations mapped during construction of SFR 1 (taken from SKB SFR-87-03). A different fracture random generator is used for each DFN case. All discontinuities are modelled as being perfectly planar, infinite structures, which is correctly considered to be conservative. The blocks were modelled as being deformable employing a Mohr-Coulomb elasto-plastic constitutive model and the discontinuities were modelled employing a Coulomb slip model. The presence of two distinct deformation zones was also modelled. Representative material properties for the intact rock and discontinuities were based on those reported in SKB R-07-06, which in turn are based on the modelling of the Singö deformation zone. The Singö is a regional deformation zone with a length of 30 km and width between 53 and 200 m (SKB R-07-45, p. 160). A review of SKB R-07-06 indicates that these values are not based on site specific testing but involve estimates derived from values taken from the literature and empirical relationships. The set of values used in SKB R-13-53 are those reported as transition values between those for the host rock and core of the Singö deformation zone (Figure 2). The in situ stress state was based on values reported in a preliminary report for a proposed final repository for spent nuclear fuel at Forsmark (SKB R-02-32).

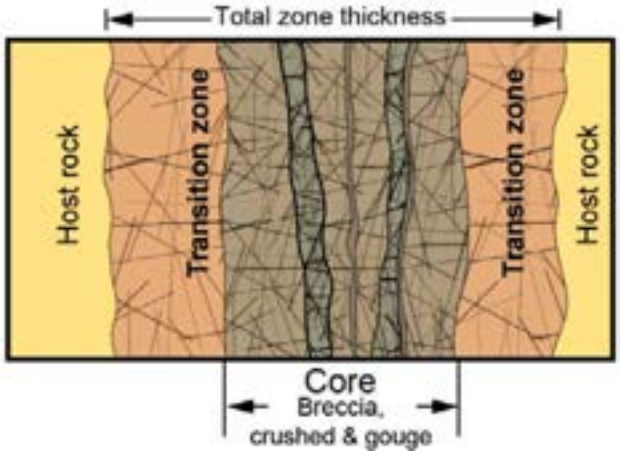


**Figure 2:** Schematic illustration of the transition zone associated with brittle deformation zones observed at Forsmark such as the Singö deformation zone. From SKB R-14-17.

The results of this analysis indicate that the excavations are stable, even without rock reinforcement and with fracture properties for the worst case scenario of zero cohesion and 15 degree friction angle. The authors note that in addition to the modelling of eight different DFN realizations, the models encompass 100 meters of length of each vault, thus incorporating with good certainty the most adverse block configurations possible. For block instabilities to arise, unreasonably low residual friction angles between 5.7 and 8.7 degrees are required. The authors compare this to the absolute lowest value of 8 degrees they could find through a literature review they conducted.

SKB TR-14-01 reports the findings based on the lower friction angle value of 5.7 degrees, and its subsequent use in a rigid block analysis performed in SKB R-13-53 to model the collapse of blocks into the 1BLA and 1BMA rock vaults. The results of this analysis suggest that in the event of collapse due to long-term strength degradation (leading to fracture strengths of zero cohesion and friction angles of 5.7 degrees), the height of the loosed rock would reach 34 m above the roof of the vaults

and then form a stable arch. This would leave approximately 26 m of cover between the collapse and seabed, from which SKB TR-14-01 draws the conclusion that there should be no risk of a direct connection between the vaults and the seabed.

Notably, the analysis in SKB R-13-53 does not consider the effects of permafrost or glacial loading. The Geosphere report (SKB TR-14-05, p. 84) suggests that the expected thermo-mechanical effects on groundwater flow modelling during the periglacial and glacial periods are insignificant, but this statement does not include mechanical stability. The climate cases for the SR-PSU safety assessment (SKB TR-13-05) indicates that permafrost is expected to develop at Forsmark in three of the four climate cases considered. However, only one of these, the Weichselian glacial cycle, includes significant permafrost within the 50,000 year time interval considered for the independent stability analyses presented later in this Report. A permafrost depth of 75-100 m between 25,000 and 35,000 years from present is indicated (Figure 3). These depths would reach the SFR 1 repository level, but not the SFR 3 extension. The Weichselian climate case predicts the maximum depth of permafrost extending to approximately 200-250 m after 50,000 years, which would reach the SFR 3 extension. An exception regarding the other climate cases is raised for the "early periglacial climate case". SKB TR-13-04 (p. 65) concludes that based on the assumptions made for the permafrost modelling, frozen ground down to the SFR 1 depth (and approaching the SFR 3 depth) cannot be excluded at 17,000 years.

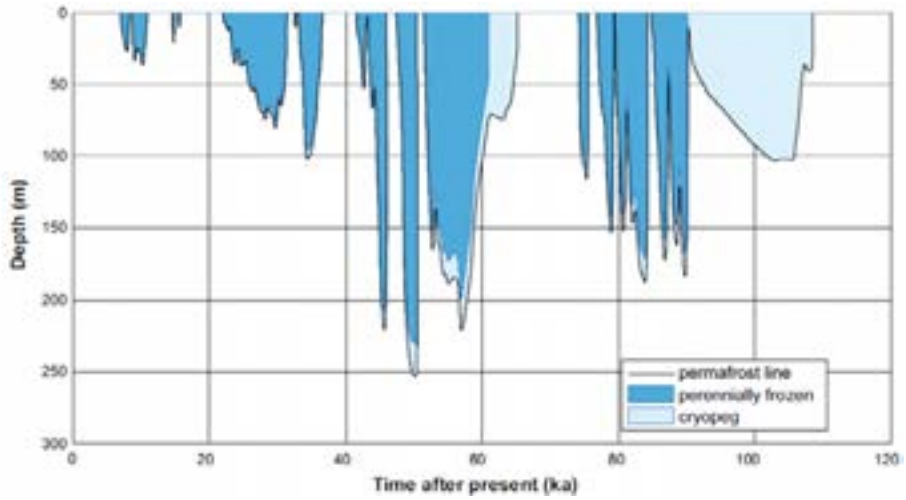


**Figure 3:** Modelled permafrost and perennially frozen ground depths at Forsmark for the SKB Weichselian glacial cycle climate case. From SKB TR-13-05.

SKB TR-14-01 (p. 19) suggests that the current Holocene interglacial will be considerably longer than previous interglacials and that the onset of the next glaciation will not occur in the next 50,000 years, or perhaps not even in the next 100,000 years. The glacial climate domain is therefore not included in the reference evolution. The Climate report (SKB TR-13-05, p. 175-178) does include one climate case, the Weichselian glacial cycle, that includes the Forsmark area being covered by glacial ice in the next 100,000 years. Reference is made to a maximum ice-sheet thickness over Forsmark of approximately 2000 m after 60,000 years from present and 2900 m at around 100,000 years (Figure 4). SKB TR-13-05 explains that any scenario involving glacial ice above the SFR repository, and the associated increase in groundwater flux, is covered by cases in the safety assessments in SR-PSU that assume complete degradation of the concrete containment structures and no

geosphere retention. SKB TR-14-01 reports that loss of barrier function and/or high water flow in the repository is considered to be a low likelihood to residual scenario (i.e., sequences of events illustrating the significance of individual barriers and barrier functions), which when combined, exceed SSM risk criteria (regulation SSMFS 2008:37) for peak dose exposure limits for groups but are less than limits for individual exposure.

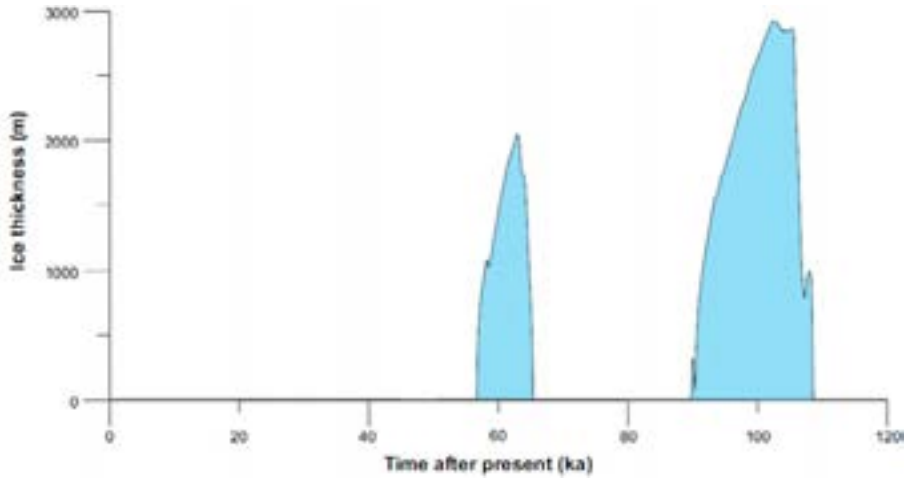


**Figure 4:** Modelled ice-sheet thickness at the Forsmark site for the SKB Weichselian glacial cycle climate case. From SKB TR-13-05.

### 2.1.1. Authors' Review Considerations

A note regarding the conclusions in SKB R-13-53 suggesting that any potential failure of the rock vaults will be limited and should be of no risk in directly connecting the vaults and the seabed, this assumes that unravelling will not occur along the steeply dipping deformation zone that intersects the roof of 1BMA. Caving along such features has been seen to form collapse structures above shallow tunnels that reach surface (e.g., Nilsen, 1994). However, as demonstrated in SKB R-13-53, the bulking of the failed material often arrests void migration. SKB TR-14-01 (p. 147) also refers to "no risk" of breach of the seabed, but at least in the assessment presented regarding the mechanical evolution, only discusses the likelihood of the event occurring but not the consequences of a direct conduit between the sea floor and rock vaults. It is therefore not clear if the assessment of risk properly considers both the likelihood and consequences.

Concerning the effects of a glacial cycle (including permafrost) on the repository safety, the independent analysis conducted for this Report will be carried out from construction of the repository up to and including a nominal 66,000 year case. This includes simulations that account for both the loading and unloading effects related to permafrost and glaciation. For the permafrost assumption, this will consider the early periglacial case in SKB TR-13-05, in which permafrost down to the repository level is considered a possibility between 17,500 and 20,500 years from present. Permafrost melting is assumed to occur within 1000 years. For the glacial cycle assumption, the peak glaciation at 60,000 years from the Weichselian climate case will be used for this. Glacially induced stresses will be applied following the logic outlined in SKB TR-09-15 with some modifications to account for near-field conditions in the upper few hundred metres of the crust. Deglaciation based on this climate case is assumed to occur within 2500 years.

## 2.2. SSM Initial Review

SSM's initial review phase included several external expert reviews of SKB's safety assessment in SR-PSU, as previously noted. Of specific relevance to the detailed analysis reported here are the reviews of the hydrogeological and engineering geology models.

The review of the hydrogeological models discussed in SSM 2016:08 includes an examination of the structural geological model and treatment of deformation zones and natural fractures (derived from SKB TR-11-04) used as the basis for the hydrogeological models used for the SR-PSU safety assessment (SKB TR-14-01). The review points to the quantitative treatment of the fracture mapping data obtained during construction of SFR 1 (reported in SKB SFR 87-03, and cited as Christiansson & Bolvede, 1987), as being limited and including size bias (SSM 2016:08, Part 1, p. 22). The same data is used to generate the DFNs used in SKB R-13-53 and the analyses conducted for this review. However, because both of these assume the conservative case of fully persistent discontinuities (relative to the mechanical stability of the excavated rock vaults), the issue of size bias is not applicable here. SSM 2016:08 Parts 1 and 2 also both point to a lack of consideration given to the treatment of heterogeneity as a function of depth and structural domains. This same point is raised in SSM 2016:12, Part 3, regarding the site description of the SFR area used in the SKB TR-14-01 safety assessment. SKB R-13-53 reports the presence of three joint sets mapped in the excavation roof and walls of SFR 1, and reports the orientations with standard deviations and average spacings for each of these sets. These are uniformly applied through the model domains in the stability analyses conducted (both in SKB R-13-53 and here), and is acknowledged here as a key uncertainty. SSM 2016:08 provides further suggestions regarding parametrization of the hydraulic domains and flow connectivity of transmissive fractures. Although these are important considerations, the scope of the independent analyses presented in this Report is limited to the consideration of pore pressures and effective stresses, but not flow.

SSM 2016:12, Part 3, which reviews the engineering geology aspects of SR-PSU, provides several important comments relevant to the stability of the rock vaults. First, it is noted that no new data was collected regarding the rock mass properties and characteristics specific to SFR 3 (SSM 2016:12, Part 3, p. 13). Instead, the data used pertains to old data collected during construction of SFR 1. This same data was used in the stability analyses reported in SKB R-13-53, and by default, in the stability analyses presented in this Report. A related oversight identified in SSM 2016:12, Part 3 (p. 48), is that the in situ stress input used for the long-term stability analysis in SKB R-13-53 appears to be based on an older interpretation of the in situ stress measurement data reported in SKB R-02-32. The estimated trends for the SFR 1 were later updated in SKB TR-11-04. The SKB TR-11-04 stress field was used for the independent analyses carried out as part of this Report, and is discussed in more detail in the description of the numerical models developed.

Second, it is noted that the stability analyses in SKB R-13-53 is limited to two rock vaults, 1BMA and 1BLA, in the existing SFR 1 (SSM 2016:12, Part 3, p. 13, 47-48); no analyses are provided specific to SFR 3. Accordingly, the independent stability analyses presented in this Report includes the consideration of all five rock vaults in SFR 1, as well as a comparative analysis that includes all six rock vaults associated with the planned layout of SFR 3. Reference is also made in SSM 2016:12, Part 3 to the need for a renewed stability analysis of the existing silo in SFR 1 given its importance to the long-term safety of the completed SFR and its large size. Because

the scope of the analyses requested as part of this review was limited to two-dimensional modelling, the long-term stability of the silo is also not considered here.

Another important comment was that no attempt at using monitoring data collected during construction of SFR 1 was made to calibrate the stability analyses reported in SKB R-13-53. SSM 2016:12, Part 3 (p. 14) correctly notes that such data is routinely collected in tunnel construction and SKB should be in a good position to use/provide monitoring data to calibrate and validate the numerical results. Reporting of the experiences during construction of SFR 1 is provided in SKB R-07-10 and R-14-17. SKB R-07-10 (p. 75-76) describes the deformation monitoring conducted during construction, which involved the use of extensometers and focussed on the Singö deformation zone and the silo. These report total deformation values on the order of 1 mm. No deformation data is reported in association with the construction and performance of the rock vaults. SKB R-07-10 (p. 79) concludes with the observation that no stability or other rock engineering problems had been identified after the commissioning of the SFR. The only exception was in relation to the Forsmark Plant and the discharge tunnel for cooling water from Reactor #3 ("Forsmark 3 tunnel"), which experienced a rock fall within the Singö deformation zone across a 10-20 m section of the tunnel (Figure 5).

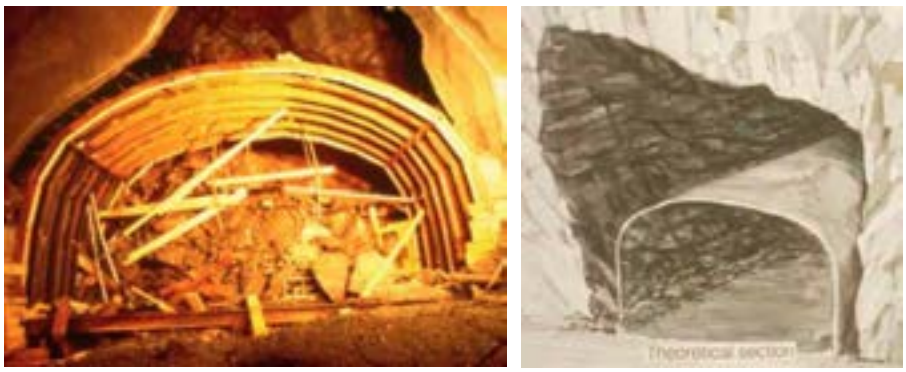

**Figure 5:** Photo and sketch of the overbreak experienced above the Forsmark 3 tunnel after intersecting the Singö deformation zone. From SKB R-07-10.

SSM 2016:12, Part 3 (p. 14-15) also notes that the stability analysis reported in SKB R-13-53 was conducted without consideration of pore pressures within the existing natural fractures and their effect on the effective normal stresses and deterioration of frictional strength properties of the fractures. SSM 2016:12, Part 3 emphasizes that analyses of the rock mass response to excavation and strength degradation over time should include an accounting of the ground water pressures around the rock caverns. It is noted here that the lower bound friction angles assumed in SKB R-13-53 are exceptionally low regardless of the absence of pore pressures in the analyses. A discussion of these properties as well as the inclusion of pore pressures in the independent analyses conducted in this Report, is presented in later sections of the report. SSM 2016:12, Part 3 also discusses the absence of earthquake loading in the SKB stability analyses and recommends this be undertaken. Earthquake loading wasn't included in the scope of the independent analyses performed here.

In summarizing the suggested topics for more detailed review, SSM 2016:12, Part 3 (pp. 59-64) suggests in order of priority:

- Long-term stability of SFR rock vaults and the impact of climate changes and future glaciations.
- Effect of earthquakes on nearby faults and the stability of SFR caverns.
- Systematic methodology for rock mass property determination.
- Effect of rock support degradation on the long-term performance of SFR.
- Suitability of the location of the SFR extension.

The independent analyses presented in the next section addresses several of these. Included is consideration of the impact of climate change and future glaciations in the form of simulated permafrost to the repository depth and glacial loading, followed by glacial unloading and permafrost melting, as indicated in Figure 3 and Figure 4. The effect of rock support degradation over time and evaluation of the SFR 3 layout is also included. Not considered within the scope of the present review assignment was the effect of earthquakes and systematic determination of rock mass properties. Because the natural fractures present in the rock were modelled in the near-field explicitly at a 1:1 spacing in this Report, the use of intact rock properties was assumed to be acceptable. However, as previously noted, the effects of size bias in the fracture mapping data limiting the consideration of smaller fractures in the DFNs embedded in the analyses may warrant some scaling of the intact rock properties used to account for the weakening effects of smaller fractures.

# 3. Independent Scoping Analyses

## 3.1. Requirements and Allowances

The requirements and allowances for the numerical analyses as specified by SSM for this review assignment are summarized below. Included with these are details describing the actions taken, and any deviations from the allowances provided where it was decided that the models could be improved.

- *Specification*: 2-D model scoping calculations of the mechanical stability and hydraulic conductivity of the rock mass around the rock vaults should be done considering one typical section of the existing SFR 1 (e.g. the rock pillar between 1BMA and 1BLA) and one typical section of the SFR 3 extension. The advantage of a symmetrical section could be exploited.

  *Action*: Because the 2-D models are not overly demanding with respect to computational requirements, it was decided that the SFR 1 models should include the rock vaults adjacent to 1BMA and 1BLA (i.e., 1BTF and 2BTF). Symmetry for model simplification was not necessary. Similarly, the models for the SFR 3 extension were developed to include the full rock vault layout (i.e., 2BMA, 5BLA, 4BLA, 3BLA, 2BLA and1BRT).

- *Specification*: The modelling of rock reinforcements of the rock vaults is not required.

  *Action*: Rock reinforcements were not explicitly modelled in the analyses. However, their influence on limiting block movements during excavation of the rock vaults was implicitly included. This was deemed necessary given the conservative joint friction values adopted. It was assumed that any rock reinforcement (shotcrete, rockbolts, etc.) would be fully degraded and non-functioning after 100 years. Thus, the stabilizing influence of reinforcement added during excavation of the rock vaults was subsequently removed at Year 100 in the models.

- *Specification*: 2-D modelling should be carried out with a numerical code that can explicitly describe Discrete Fracture Networks (DFN) and rock fracture deformability. The adopted numerical code for the calculations must be chosen among available codes that have been extensively validated, verified, well documented and quality assured.

  *Action*: The 2-D distinct-element code UDEC v. 6.00.322 (Itasca, 2016) was used for this assignment. The code meets the requirements specified, as described in detail in subsequent sections of this Report.

- *Specification*: Input parameters for the rock and fractures should be compatible with assumptions in SKB R-13-53, and considering the review comments from SSM's initial review phase contained in SSM Report 2016:12, Part 3.

  *Action*: Unless otherwise noted, input parameters were based on those reported in SKB R-13-53. Where incompatibilities have been identified in SSM 2016:12 Part 3, for example reporting that outdated data for the in situ stress input was used in the stability analyses reported in SKB R-13-53, the relevant input parameters were vetted accordingly. Where required input parameters not specified in SKB R-13-53 or provided as singular values where a range might be more appropriate to bound the uncertainty, values were based on those reported in SKB TR-14-01 (e.g. rock mass density) or

in SKB R-07-31 (referenced as Glamheden et al, 2007), where a more thorough treatment of the site characteristics are reported. The input parameters used in the analyses together with explanations as to their sources are discussed in detail in the description of the model development.

- *Specification*: The effect of groundwater pressure on the stability of the rock caverns should be explicitly evaluated (as suggested in SSM Report 2016:12, Part 3, sec. 3.9.5). However, no groundwater flow calculations are required. The regional flow at Forsmark occurs mainly parallel to the long axis of the rock caverns. A comment about the relation between the hydraulic conductivity of the undisturbed rock mass to its value after excavation of the vaults should be provided.

  *Action*: It was assumed that the near-field groundwater flow is parallel to the rock vaults, and therefore perpendicular to the 2-D section modelled. As such, the total pore pressure head was treated as static with pore pressures equal to pressure head equal to sea level. Effective stresses were used for matrix and water pressures applied to joints, but these were not fully coupled given the time frames considered where excess over/under pressures would dissipate quickly (relative to 1000 or 10,000 years). In the short-term construction phase, it can be assumed that mean apertures of at least one joint set will increase towards the excavation boundary leading to a short-term state that is more stable (higher effective normal pressure) than the longer term saturated state. Thus, the saturated state was considered to be critical.

- *Specification*: The reference points in times (1000, 10,000, 20,000 and 50,000 years) should highlight the deterioration of the rock and fracture properties and the changes of the loading conditions (e.g., permafrost at Year 20,000, and glacial loading at Year 50,000).

  *Action*: The reference times were modelled as specified, with the 20,000 year model simulating the effects of permafrost, and the 50,000 year model simulating glacial loading. These were considered via two separate scenarios. The first modelled permafrost at Year 20,000 followed by permafrost melting at Year 21,000. Separately, the Year 20,000 permafrost model was extended to consider glacial loading at Year 50,000 followed by glacial unloading and then permafrost melting. Rock and joint strength degradation rates were based on existing data-driven models for granitic rock accounting for such time-dependent factors as subcritical crack growth. It was assumed that due to the already conservative frictional values adopted in SKB R-13-53 that friction will not modify over the specified time periods but that cohesion from joint asperities will degrade at the same rates as those extrapolated from published long-term tests on intact granite. Permafrost has the effect of increasing joint cohesion but also joint aperture. The rates of freezing advance in permafrost at depth are assumed to be low such that excess pore pressure can dissipate and fracture expansion is limited although the impact of a 10% pressure increase in the fractures was explored (to correspond to expansion during static freezing). In the latter time period, this expansion was combined with elevated pore pressure assumptions due to glaciation. Glacial loading was simulated using current models of vertical boundary load increase and associated Poisson ratio effects as well as increments of load from crustal flexure. These will be based on the peak glaciation at 60,000 years from the Weichselian climate case described in SKB TR-09-15.

- *Specifications*: Quantify loads on the concrete barriers of the repository if stability of the rock vaults change over time.

  *Action*: The UDEC model was developed to include the concrete barriers and backfill as described in SKB R-13-53 and TR-14-01. History points were included to track the stresses that develop in these.

## 3.2. Numerical Method and Software Used

Selection of the numerical modelling software used was restricted to commercially available codes that have been extensively validated, verified, well documented and quality assured. Preference was given to a numerical method and program capable of explicitly modelling a Discrete Fracture Network (DFN) and associated rock fracture deformability. Based on these, the 2-D distinct-element code UDEC (version 6.0) was selected. UDEC is developed and distributed by Itasca International (Itasca, 2016), and has been extensively used in the rock engineering community and features prominently in the published scientific and technical literature. The analyses in SKB R-13-53 was performed using 3DEC, the 3-D version of UDEC. The capabilities of UDEC and its verification are fully documented in its user manual (Itasca, 2016). These are summarized below.

UDEC models a rock mass as an assemblage of discrete, deformable blocks defined by a DFN model. Discontinuities are generated as interconnected planar features. The relative movement along these contacts is governed by linear or non-linear force-displacement relations for movement in both shear and normal directions. Numerical contacts are comprised of corner-to-corner, edge-to-corner, and edge-to-edge contacts. The contact forces and displacements between blocks are calculated based on the applied loads and interactions that develop between the deformable blocks. The calculations performed alternate between the application of a force displacement law at all block contacts and Newton's second law, which gives motion to the blocks in response to the acting forces. Thus, the method accounts for complex non-linear interaction between blocks (i.e. slip and/or opening/closing along discontinuities) together with the deformation and yielding of the joint-bounded blocks (Figure 6).

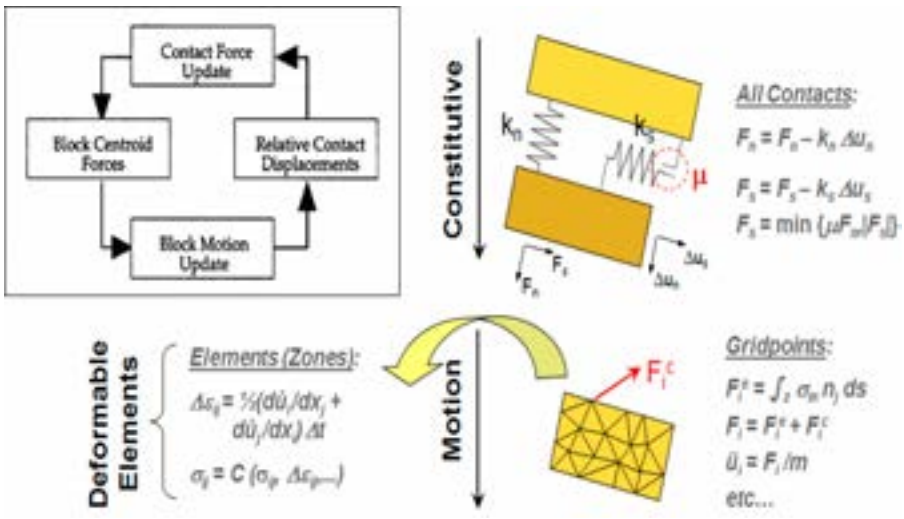


**Figure 6:** Overview of the formulation used in the distinct-element code UDEC.

The effects of groundwater and pore pressure changes can also be modelled with UDEC. The formulation separates pore pressure changes acting along a discontinuity from those in the block; the blocks bounded by the discontinuities are assumed to be impermeable from a flow point of view but can be subject to assigned pore pressures for effective stress calculations. Fracture flow is controlled by the joint aperture based on a cubic law relationship (see Priest, 1993). The hydro-mechanical coupling thus relates mechanical deformation occurring in the form of normal joint displacements to joint aperture (i.e. joint closure or opening), which in turn changes the joint hydraulic conductivity and the subsequent distribution of joint water pressures; conversely, changing joint water pressures result in a corresponding change in mechanical aperture, as well as in the effective stresses acting along a joint thereby creating the potential for slip (Olsson and Barton, 2001).

For the analyses performed in this Report, it is specified that the hydraulic flow is aligned parallel to the cavern axes. In this case there is no fracture flow (long term) within the 2-D UDEC section at steady state conditions, and thus the analyses performed only consider static pore pressures with respect to their influence on the effective stresses. It is noted that because local excess pore pressures will be dissipated, a fully coupled hydro-mechanical analysis is not required in this case. Not considered therefore are aperture change due to short- and long-term deformations, which would result in altered fracture conductivity in the model and thus changes in bulk permeability, both in and perpendicular to the 2-D section.

## 3.3. UDEC Model Development

### 3.3.1. Model Geometry for SFR 1 and 3

Two sets of UDEC analyses were carried out: one based on the layout and initial state for the existing SFR 1, and one based on the layout and initial state for the planned SFR 3 extension (Figure 7). The models adopt a 2-D plane strain assumption. Each SFR 1 rock vault is approximately 160 m long, and the SFR 3 vaults are planned to be approximately 275 m long. Given their lengths relative to their heights and widths, a 2-D plain strain assumption is assumed to be reasonably valid for the purpose of the scoping calculations being performed here.

The layout of the SFR 1 rock vaults (i.e., which vault type is next to which) were modelled based on the descriptions provided in SKB TR-14-01 (Figure 7). For completeness, the UDEC analyses included all four adjacent rock vaults of the SFR 1 facility (1BTF, 2BTF, 1BLA, 1BMA). This differs from the 3DEC analysis reported in SKB R-13-53, which was limited to the adjacent 1BLA and 1BMA vaults. The 1BLA and 1BMA vaults in the existing SFR 1 facility are neighboured by two additional smaller vaults, 1- and 2BTF (Figure 8). The depth of the SFR 1 is reported in SKB TR-14-01 as being below the Baltic Sea with approx. 60 m of rock cover, which for the purpose of the UDEC models is assumed to be measured from the top of the 1BMA vault. This assumption is based on the dimensions reported in SKB R-13-53 for the 3DEC models.

Values for the depth of SFR 1 relative to sea level reported in SKB TR-14-01 are similar to those for the rock cover suggesting that the depth of water is negligible. Although it is not explicitly stated, the depth of water above the repository is shown in Figure 4-3 in SKB TR-14-01 as ranging between 0 and 3m. The UDEC models were developed assuming the height of the water column above the seabed overlying the SFR 1 and 3 is negligible.

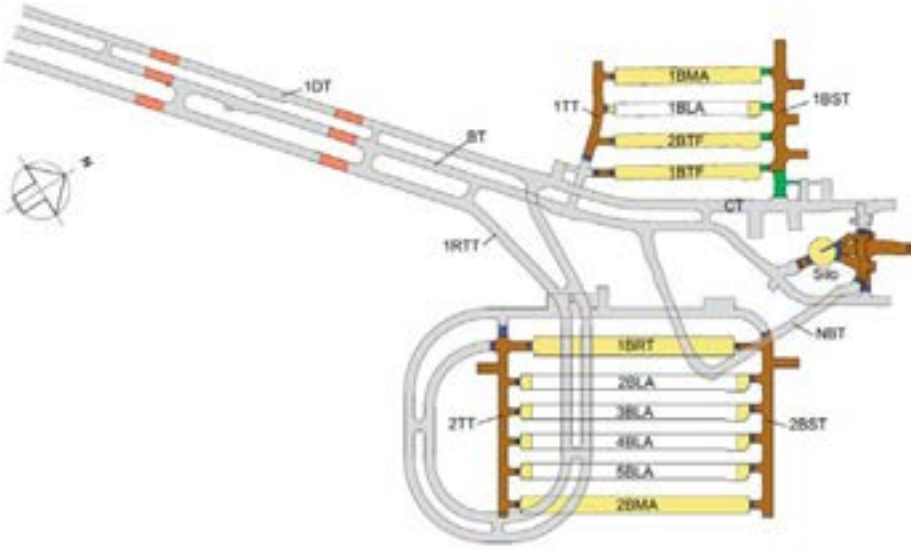


**Figure 7:** Layout of the rock vaults for the existing SFR 1 facility (1BTF, 2BTF, 1BLA, 1BMA), and for the SFR 3 extension (2BMA, 5BLA, 4BLA, 3BLA, 2BLA,1BRT). From SKB TR-14-01.

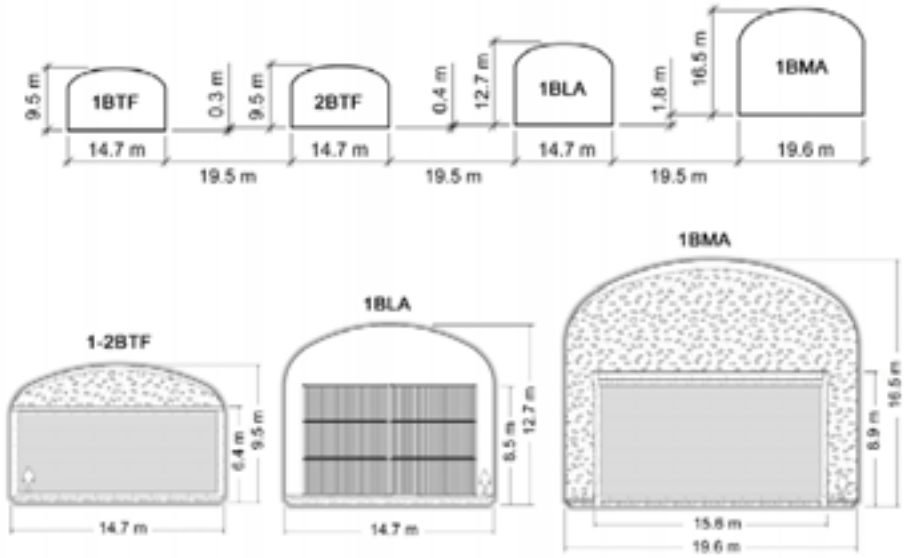


**Figure 8:** (Top) Vertical section through the existing SFR 1 rock vaults showing pillar dimensions, and (bottom) detailed dimensions of the 1-2BTF, 1BLA and 1BMA vaults. From SKB TR-14-01 and R-13-53.

The UDEC model geometry for the SFR 3 extension includes six adjacent vaults as shown in Figure 7 and Figure 9 (2BMA, 5BLA, 4BLA, 3BLA, 2BLA, 1BRT). The 2-D profiles provided in SKB TR-14-01 were used, maintaining the minor differences in dimensions compared to the rock vaults of SFR 1 (Figure 8). These follow the dimensions according to Layout 2.0 (as reported in SKB TR-14-01), whereas SKB TR-14-01 (p. 84) reports that the dimensions of Layout 1.5 were used in the modelling for the SR-PSU long-term safety assessment. The main difference between these, relevant to the 2-D UDEC models developed, is that 2BMA in Layout 2.0 is 0.4 m shorter and 0.6 m wider. Not provided in any of the drawings in

SKB TR-14-01, or any of the associated reports, are the planned spacings between the adjacent rock vaults in SFR 3. SKB R-14-17 (p. 58) reports that the width of the pillars separating the SFR 3 rock vaults will range from a width to height ratio of 0.75 to 1. This range was adopted for the SFR 3 spacings used in the UDEC models as represented in Figure 9. The depth of the SFR 3 extension is reported in SKB TR-14-01 (p. 83) as involving 120 m of rock cover. Based on the description of design constraints for SFR 3 (SKB R-14-17), the depth of the rock vaults was modelled so that the roof of the highest cavern in the repository is set at around -120 m.

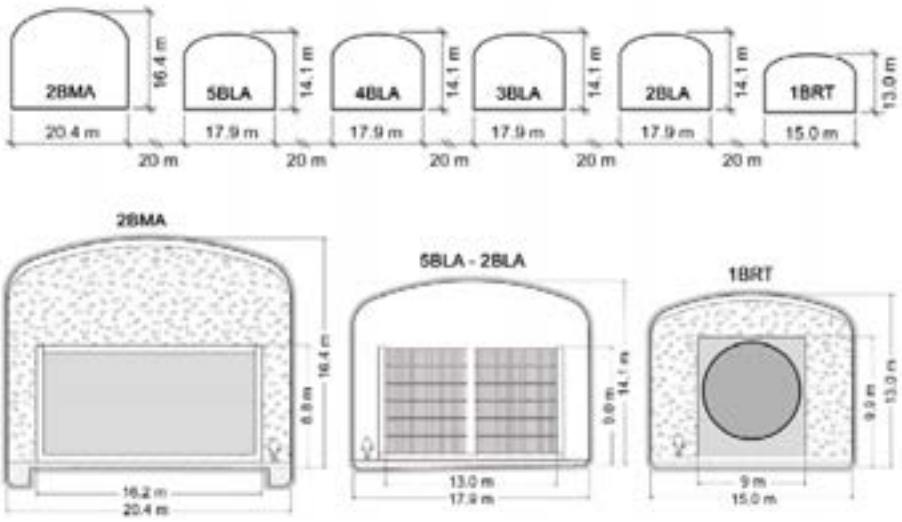


**Figure 9:** (Top) Constructed vertical section through the planned SFR 3 rock vaults assuming 20 m pillar widths, and (bottom) detailed dimensions of the 2BMA, 5-2BLA and 1BRT vaults from SKB TR-14-01.

The external dimensions of the 3DEC model of SFR 1 in SKB R-13-53 is a block that is 240 m long, 140 m wide and 100 m high. For the purpose of the UDEC analyses performed here, these boundaries were viewed as being closer to the modelled rooms than would normally be recommended, and necessitated due to the more intensive computing requirements of 3DEC. For the UDEC models, we assume external boundaries that extend at least 240 m laterally and 220 m vertically from the outer walls and floors of the outer rock vaults in each sequence. For SFR 1, this results in a block that is 600 m wide and 300 m high, and for SFR 3, a block that is 680 m wide and 360 m high.

### 3.3.2. Geology and Deformation Zones

The geology of the SFR is described in SKB TR-14-01 as involving four domains: RFR01 to RFR04. For the most part, the SFR is situated in RFR02 (Figure 10), which is described as being heterogeneous and consisting of fine- to medium-grained metagranite-granodiorite. The domain also contains 24% pegmatite and pegamitic granite.

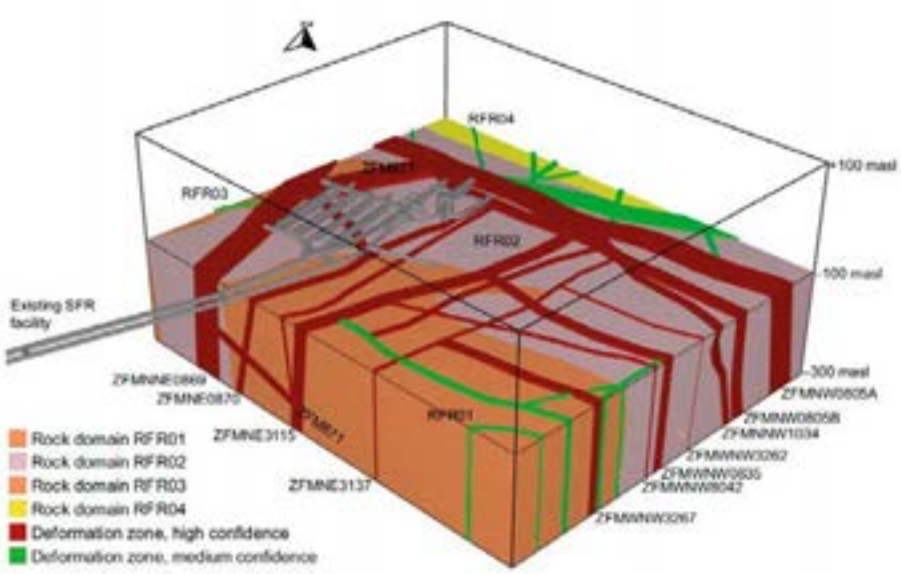


**Figure 10:** Rock domains and deformation zones of the SFR facility. From SKB TR-14-01.

Two one-metre thick deformation zones cross the SFR 1 in the proximity of the 1BLA and 1BMA vaults. The first dips at 27 degrees in the direction of 161 degrees. The second dips at 70 degrees in the direction 25 degrees. Figure 11a shows the orientation of these deformation zones relative to the orientation of the rock vaults, which are oriented at N30°E. In 2-D, it is not possible to directly model the role these deformation zones play with respect to the 3-D block kinematics. Notably, the orientation of the steeper deformation zone (‘2’ in Figure 11b) is sub-parallel to the 2-D section. Thus, relative to the 2-D modelled plane, this feature is treated implicitly as accommodating block release in the out-of-plane direction (i.e., 2-D plane-strain block movements modelled in UDEC, in projecting to 3-D reality, are assumed to release along either the steeply dipping deformation zone or similarly oriented joints sub-parallel to the 2-D plane modelled). With respect to the shallower dipping deformation zone (‘1’ in Figure 11b), its location relative to the rock vaults in a 2-D representation varies along the out-of-plane direction. In the middle of the vault, along its long axis, the deformation zone is approximately 20 m above the roof (blue line in Figure 11b). This separation distance then either increases moving towards one end of the vault, or decreases towards the other end, resulting in the deformation zone transecting the rock vaults and then dipping below the floor in the 2-D plane of representation. To model this, four different 2-D section scenarios were considered (Figure 12):

i) Fault 20 m above the roof of the 1BMA vault
ii) Fault 5 m above the roof of the 1BMA vault
iii) Fault transecting through the 1BMA vault
iv) Fault 5 m below the floor of the 1BMA vault

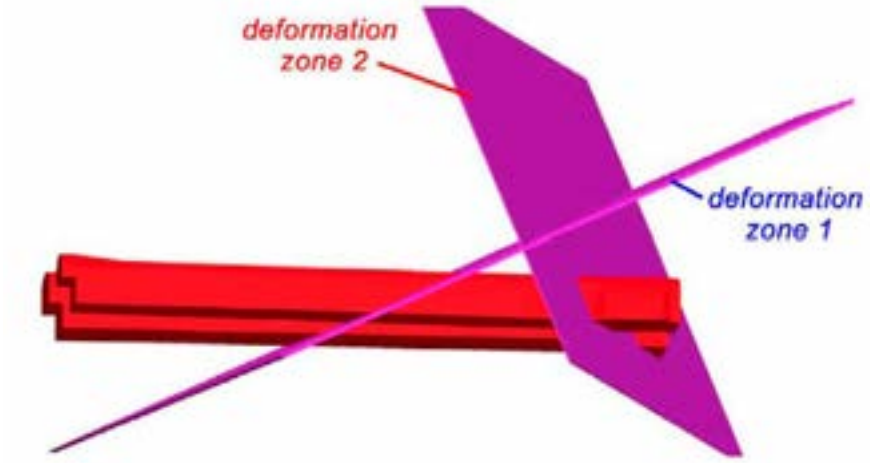


a)

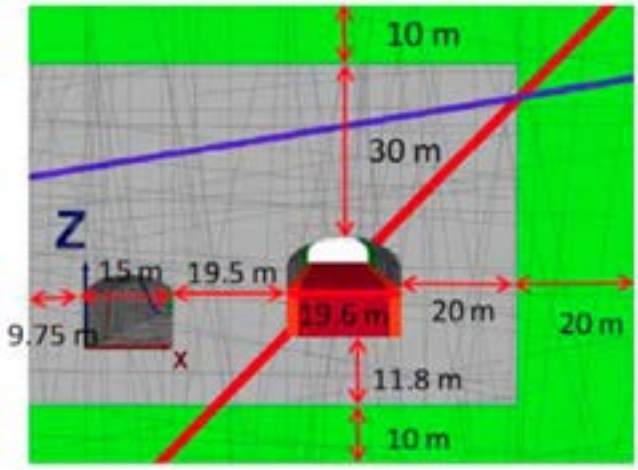


b)

**Figure 11:** a) 3-D illustration of deformation zones relative to the BLA and BMA rock vaults. b) Corresponding projected intersections of the deformation zones with the 2-D section through the centre of the long axis of the BLA and BMA rock vaults. From SKB R-13-53.

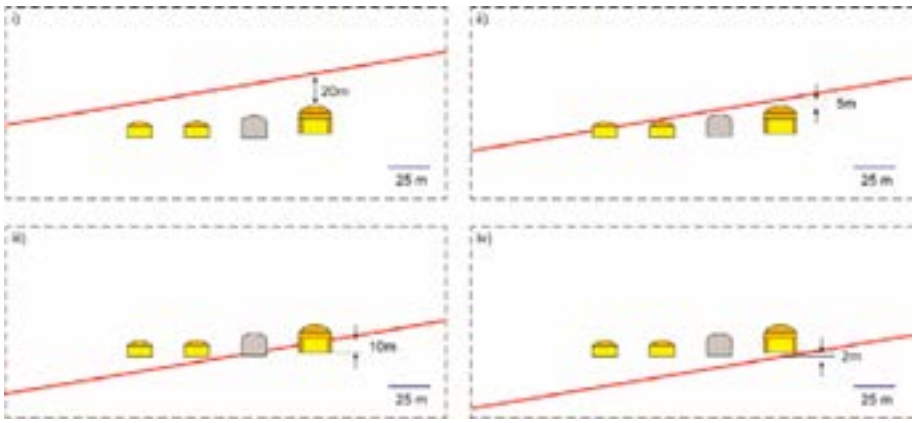

**Figure 12:** Deformation zone intersection scenarios in modelled 2-D plane for SFR 1, relative to the 1BMA rock vault.

The presence and locations of deformation zones intersecting the rock volume for the SFR 3 extension are not explicitly provided in SKB TR-14-01 or any of the associated reports. However, the design constraints provided in the Site Engineering Report (SKB R-14-17, p. 58) indicates that borehole investigations suggest that two sub-horizontal structures, SBA1 and SBA2, might be encountered. The SBA structures refer to "shallow bedrock aquifer" fractures that are interpreted to be highly transmissive, sub-horizontal sheet joints (SKB TR-11-4, p. 131). SKB R-14-17 (p. 58) notes that the suggested lowering of the SFR 3 extension to a depth that is 60 m below SFR 1 is to avoid these two structures. At a depth of -120 m, the SFR 3 repository would be below SBA1 and SBA2, and above another similar structure SBA6 (Figure 13). SKB TR-11-04 (pp. 159-160) notes that these features lack interpreted orientations, and stereonets show them dipping sub-horizontally in various directions. To model this scenario, persistent sheet joint structures were included above and below the modelled SFR 3 rock vaults based on the elevations for SBA2 and SBA6 reported in SKB R-14-17 (Figure 13). Given the absence of a specific orientation, a NW dip direction was chosen to represent a more adverse condition favouring a predisposition towards larger scale failure by maximizing the distance between the roof of the 2BMA rock vault and overlying SBA2, while maintaining the positioning of one fracture zone above and one below the SFR 3 extension. This is shown in Figure 14. In contrast to the SFR 1 case, where the sensitivity of the UDEC results to the location of the deformation zone was tested, the locations of the SBA fractures in the SFR 3 models were kept constant to respect the borehole data constraints.

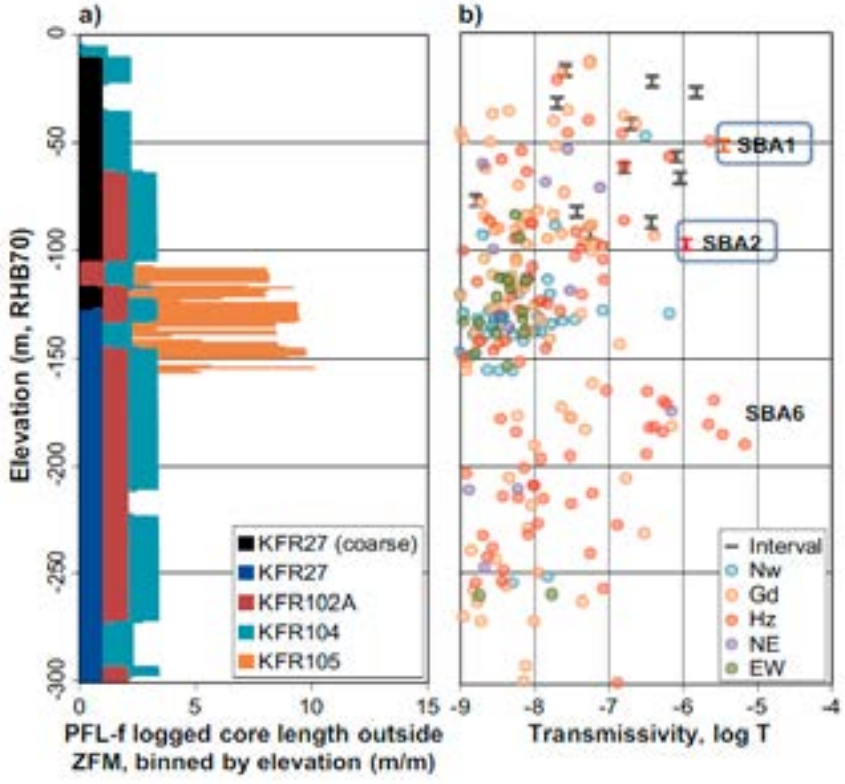


**Figure 13:** Borehole data indicating the presence of the SBA fracture zones that the proposed siting of the SFR 3 extension will try to avoid. From SKB R-14-17.

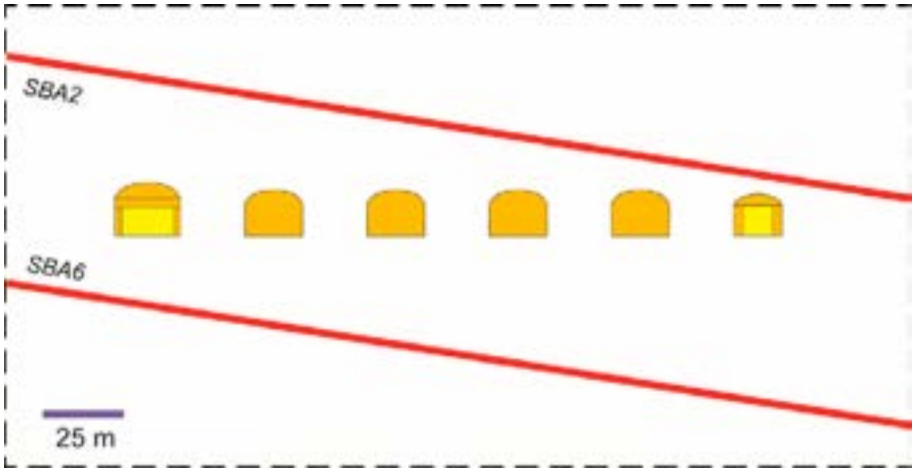


**Figure 14:** Assumed locations of the SBA2 and SBA6 fractures zones relative to their intersections with the modelled 2-D plane for SFR 3.

### 3.3.3. Discrete Fracture Network (DFN)

SKB R-13-53 describes three main fracture sets that were mapped in 1BMA during construction of SFR 1 Figure 15a. These are reported relative to the longitudinal axis of the rock vaults, and are listed in Table 1 and depicted in Figure 15b. Two of these are perpendicular relative to the 2-D UDEC section, dipping sub-vertically and sub-horizontally (marked with red arrows in Table 1 and Figure 15b). These were explicitly included in the analyses assuming a uniform probability distribution. The third fracture set is parallel to the 2-D UDEC section. This set was not modelled, but implicitly represents a vertical release plane in the third dimension.

**Table 1:** Fracture sets mapped during construction of SFR 1, as reported in SKB R-13-53. Fractures explicitly modelled in the 2-D UDEC analyses in this Review, are marked with red arrows.

| | Strike relative to longitudinal axis of rock caverns [degrees] | Dip [degrees] | Average Spacing [m] |
|---|---|---|---|
| → | 13 ± 20 | 90 ± 5 | 2 |
| | 97 ± 27 | 90 ± 14 | 2 |
| → | 0 ± 180 | 0 ± 17 | 3 |

SKB R-14-17 (p. 59) reports that in general, the rock mass hydraulic and mechanical conditions in the planned SFR 3 repository area are judged to be comparable to those in the existing SFR 1 area. Accordingly, the same DFN inputs were used for both the SFR 1 and SFR 3 UDEC model geometries.

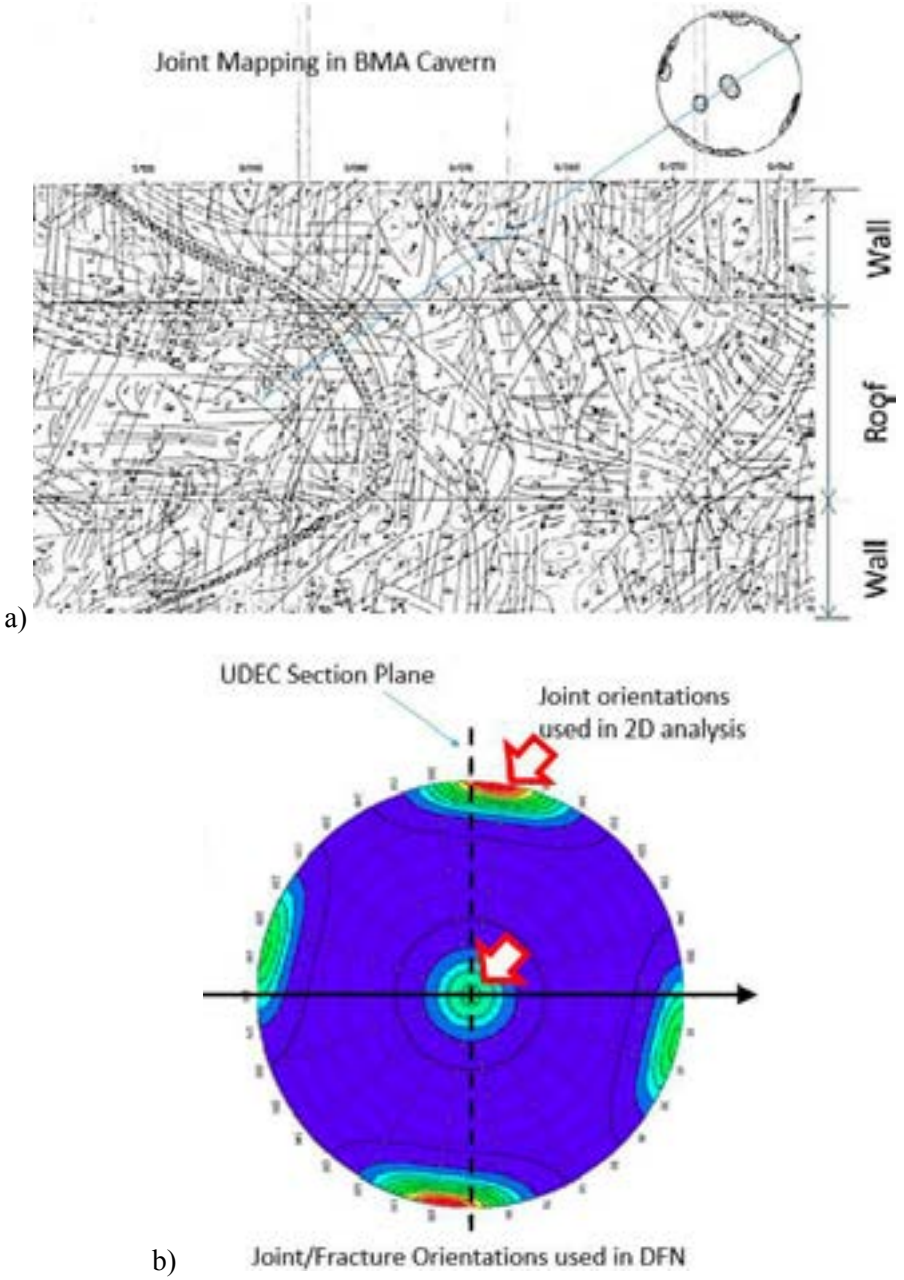


**Figure 15:** a) Fracture mapping of the 1BMA rock vault recorded during construction of SFR 1 (as per SKB R-13-53). b) Stereonet of fracture orientations used for the DFN input (note that the zero-degree datum is rotated here to align with the cavern axis). Fractures used for the 2-D UDEC analyses in this Report are marked with red arrows.

For the two joint sets in the modelled plane, the same dip angles and standard deviations were used as reported in SKB R-13-53. The joint spacings are modelled in the far-field as being twice the average reported in SKB R-13-53. This is done to reduce the number of numerical errors that arise from odd shaped blocks formed by intersecting joints relative to the size of elements that would be required to mesh these blocks. This allows computational efficiencies to be gained in the far-field where larger elements can be used allowing a denser joint network and a finer block meshing to be used for the near-field. The near-field boundary extends 40 m in the x-direction from the outer walls of the outer rock vaults, and in the y-direction from

the ground surface (zero elevation) down to 25 m below the floors of the rock vaults. A 1:1 joint spacing was used for the near-field using the average spacing reported in SKB R-13-53. The UDEC geometry for the SFR 1 case is shown in Figure 16. The UDEC geometry for the SFR 3 case is shown in Figure 17.

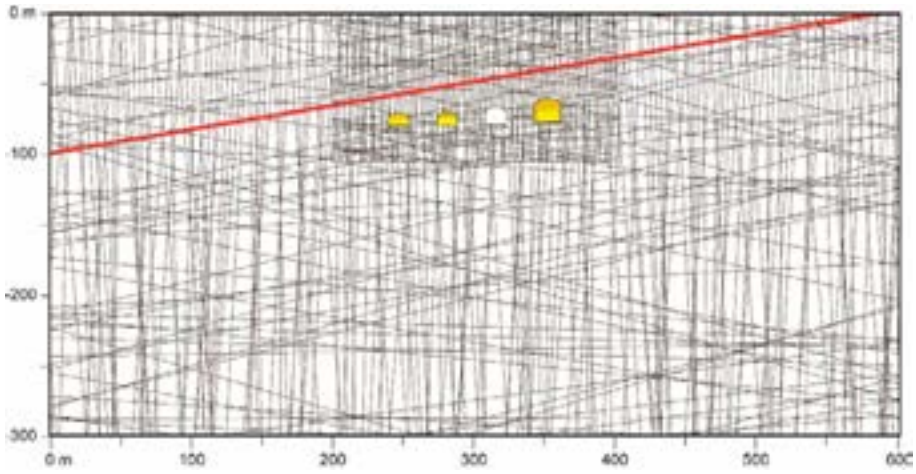


**Figure 16:** UDEC geometry showing the full model with embedded DFN for the existing SFR 1 case. The modelled deformation zone is highlighted in red.

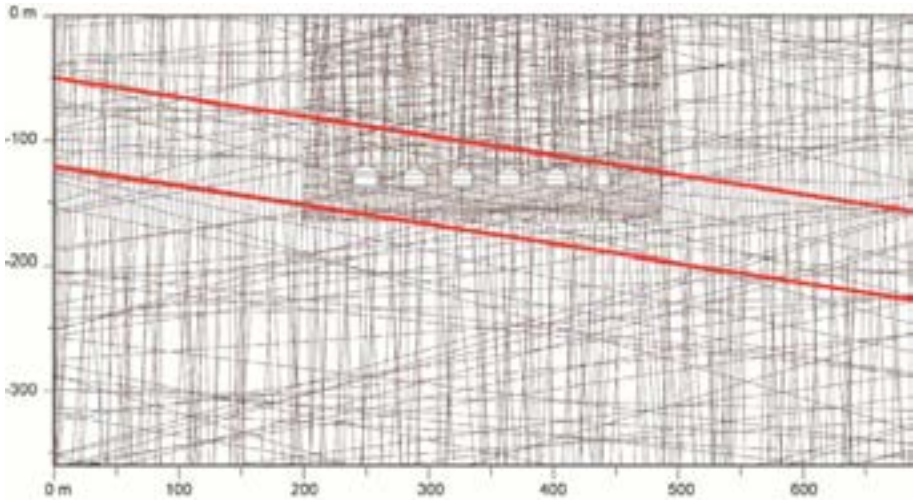


**Figure 17:** UDEC geometry showing the full model with embedded DFN for the SFR 3 extension case. The modelled SBA fracture zones are highlighted in red.

Four different DFN realizations were modelled for the SFR 1 case in which the position of the deformation zone was varied (as previously discussed and shown in Figure 12). Each model was seeded with the same DFN inputs (Table 1) but with a different start point resulting in a different DFN that fit to the same statistical input. The four DFNs modelled for SFR 1 case are shown in Figure 18. For the SFR 3 extended case, a similar procedure was used except the position of the upper and lower bounding fracture zones was not varied. Four different DFN realizations were modelled drawing from the same statistical distribution of fracture dip angles for the two joint sets modelled. The four DFNs modelled for SFR 3 case are shown in Figure 19.

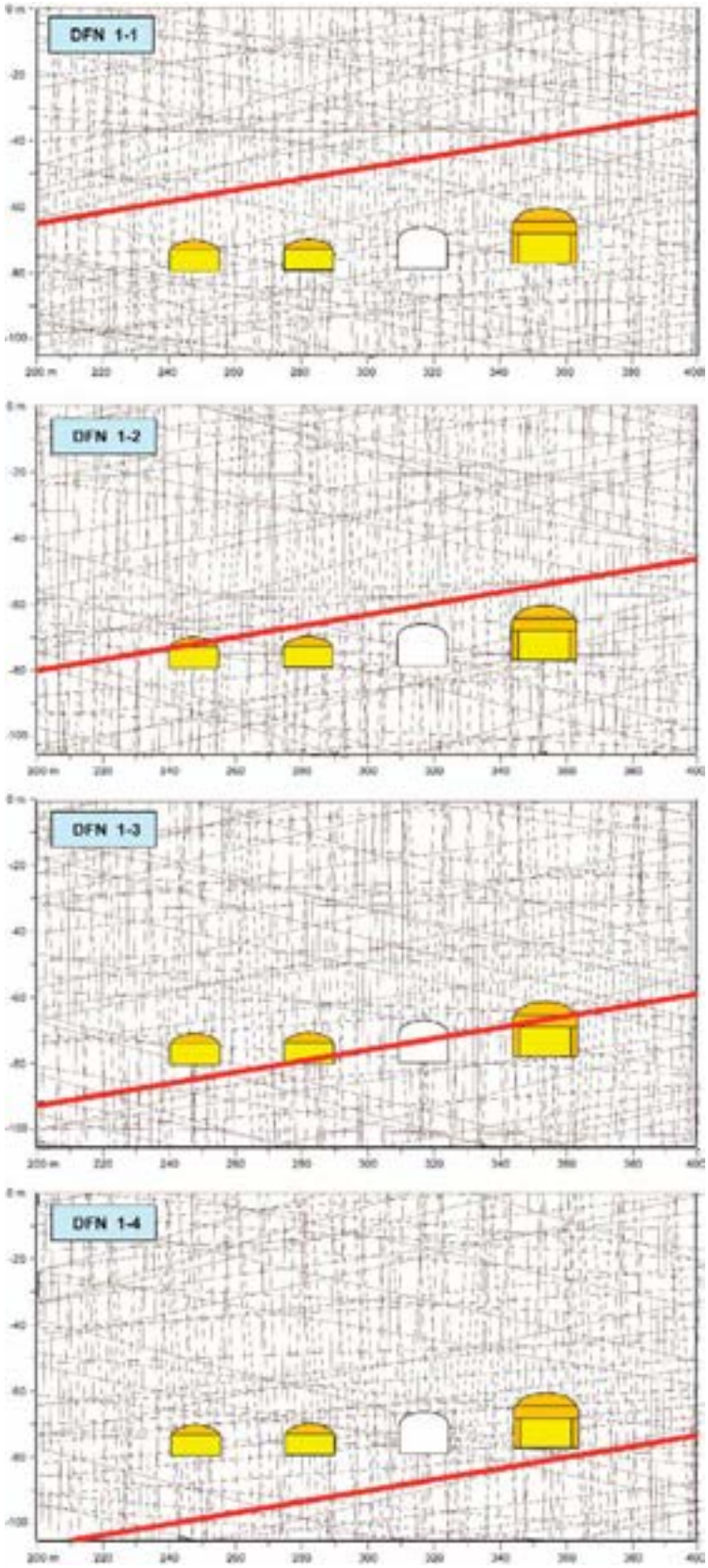


**Figure 18:** Close-up details of the four UDEC-DFN realizations modelled for the existing SFR 1 case. The models differ in the position of the deformation zone (highlighted in red) and the detailed DFN, but are drawn from the same statistical DFN input as reported in Table 1.

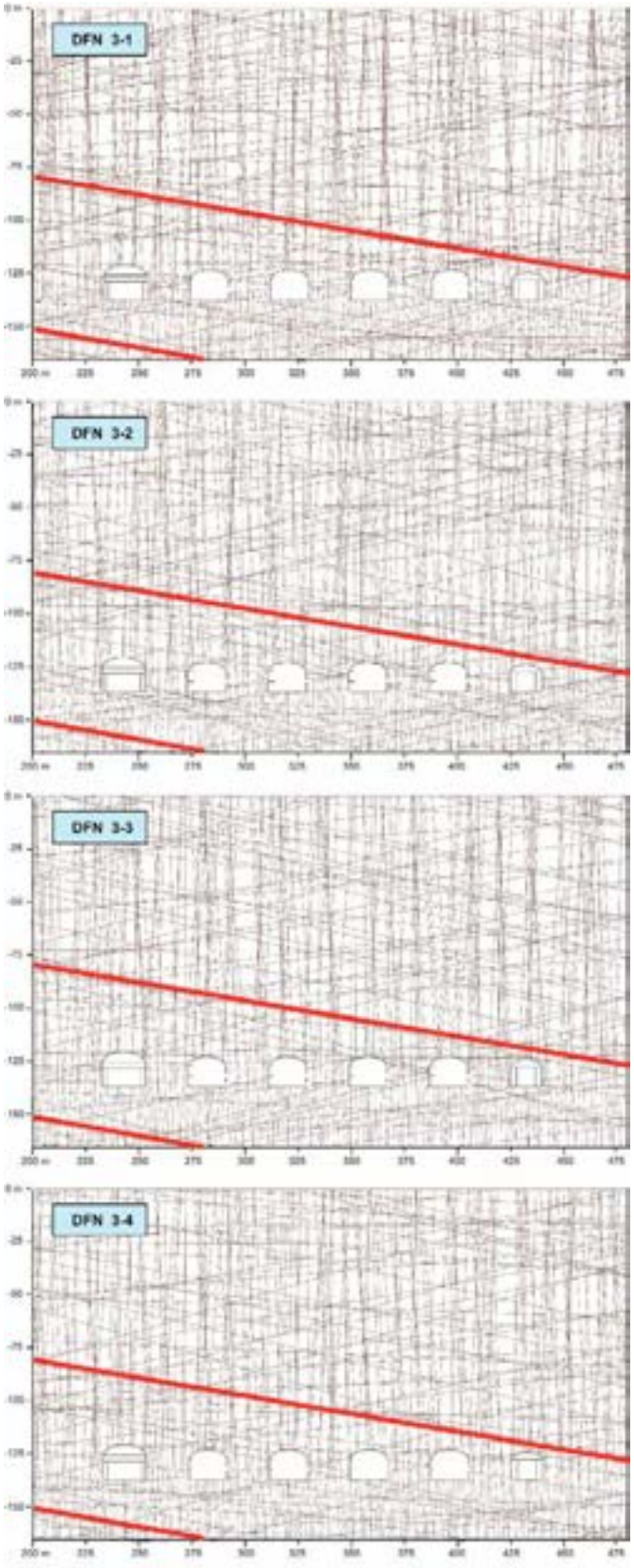


**Figure 19:** Close-up details of the four UDEC-DFN realizations modelled for the SFR 3 extension case. The detailed DFN for each differs, but is derived from the same statistical DFN input as reported in Table 1.

### 3.3.4. Model Discretization and Meshing

Where the DFN block shape allowed it, quadrilateral elements were used. This improves the plastic flow calculations with respect to the modelling of yielding of the intact blocks. For three-sided blocks, triangular elements were used. The discretization of the joint bounded blocks involves 4 m element edge lengths for blocks located around the outer model periphery. These narrow to 2 m where the far-field adjoins the near-field. The discretization of the blocks in the near-field uses a 0.5 m element edge length. This reduces to 0.25 m within 20 m of the rock vaults. Thus, the maximum element size adjacent to the excavations was set to 0.25 m (Figure 20). This represents the resolution to which the depth of EDZ around the rock vaults can be modelled.

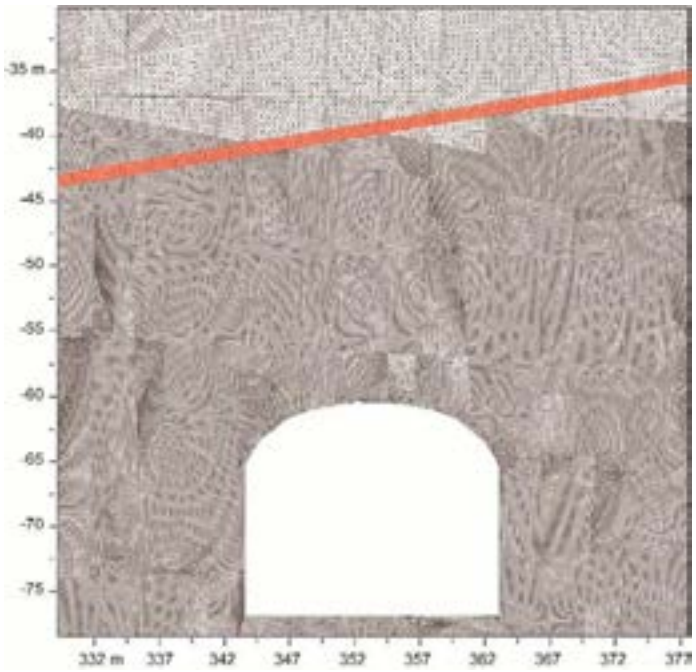


**Figure 20:** Plot of mesh with maximum 0.25 m elements relative to 1BMA vault. The modelled deformation zone is highlighted in red.

### 3.3.5. Rock Mass and Discontinuity Properties

The UDEC models adopt a 1:1 representation of the joint spacing reported in SKB R-13-53. Accordingly, the blocks between the joints were assigned the same intact block properties provided in SKB R-13-53 (p. 13). These properties are described as the "rock mass properties between fractures". Similar to the 3DEC analyses reported in SKB R-13-53 (p. 17), a Mohr-Coulomb elasto-plastic constitutive model was used to model stress-induced damage (i.e., EDZ) of the intact blocks. Reference is made to SKB R-07-06 as the source of the elastic and Mohr-Coulomb input properties. The values provided in SKB R-13-53 correspond to those described in SKB R-07-06 (p. 43) as relating to the transition zone between the stronger host rock and weaker core of a brittle deformation zone (Figure 2). SKB R-07-06 (p. 43) notes that there are no tests available from the intact rock, nor from the fractures, in the transition zone, and that the properties provided are based on values given in the literature and empirical experiences. However, SKB R-06-38 is cited as an additional source, which reports the site descriptive modelling for the Forsmark site, and this Report provides very similar values that are described as being based on

laboratory testing of borehole samples of granite to granodiorite. Added to the Mohr-Coulomb properties was a Biot's constant for treatment of effective stresses within the intact blocks (i.e., modelling of yielding and stress-induced damage in the intact blocks was based on the effective stresses). A value of 0.9 was assumed based on laboratory testing results for intact granite reported by Zangerl (2003). The input properties were applied homogeneously throughout the model with the only differentiation being between the host rock and deformation/SBA fracture zones (highlighted in red in the previous figures). Properties for the deformation and SBA fracture zones were based on values reported in SKB R-13-53, which notes that these are derived from a back analysis of the "Singö-zone" as conducted for SKB R-07-06. As previously noted, the Singö is a regional deformation zone with a width between 53 and 200 m, which contrasts with the 1-2 m width of the deformation zones intersecting the rock vaults in the SFR 1 model.

The intact block properties used in the UDEC models, for both the SFR 1 and SFR 3 cases, are provided in Table 2. As previously noted, SKB R-14-17 (p. 59) reports that the rock mass hydraulic and mechanical conditions in the extended repository area, SFR 3, are judged to be comparable with the conditions of the existing SFR.

**Table 2:** Input properties used for both the SFR 1 and SFR 3 UDEC models, based on values reported in SKB R-13-53 and derived from SKB R-07-06 and SKB R-06-38 for granite to granodiorite in the transition zone between the undamaged host rock and core of a deformation zone.

| | Rock Mass Between Fractures | Deformation/Fracture Zones |
|---|---|---|
| Modulus of deformation | 60 GPa | 16 GPa |
| Poisson's ratio | 0.23 | 0.43 |
| Internal friction angle | 40° | 51° |
| Cohesion | 23 MPa | 2 MPa |
| Tensile strength | 6.8 MPa | 0.1 MPa |
| Dilation angle | 15° | 15° |
| Biot coefficient | 0.9 | 0.9 |

SKB R-13-53 also provides properties for the fractures comprising the DFN based on the same back analysis reported in SKB R-07-06. However, the base friction angle value reported (before strength degradation is applied) is lower than would typically be expected for crystalline rocks at 25 degrees. Consulting SKB R-07-06 (p. 43), it can be seen that the fracture properties used are those for fractures in the transition zone between the host rock and core of the deformation zone (i.e., tectonically disturbed). SKB R-13-53 also references a more detailed data presentation in SKB R-07-31 (referenced as Glamheden et al. 2007). This report was also consulted and it was noted that the peak friction values used for the fractures in SKB R-13-53 represent the minimum values indicated by SKB R-07-31 (p. 57). Mean values are reported to be 34 degrees based on a series of tilt tests. Similar values are reported in SKB R-06-38, which includes data from direct shear testing of fractures. The maximum friction angle based on this data is given as 40 degrees.

This higher value was applied to the initial state modelled in UDEC. It was judged that starting with the initial friction values used in SKB R-13-53 resulted in unrealistically low values when strength degradation over time was subsequently

considered. Instead, the SKB R-13-53 fracture properties were adopted as representing the degraded values 50 years after construction of the repository (this is discussed in more detail in the description of the strength degradation procedure applied). The rock vaults are largely sited in the host rock, and although these are in proximity to one or more deformation/fracture zones, the latter are explicitly modelled in UDEC, thus accounting for their influence on the rock mass response. Consideration was also given to the 2-D treatment of the stability analysis limited by UDEC, which conservatively assumes kinematic feasibility based on the intersection of fully persistent fractures in the 2-D plane of the analysis. In reality, the formation of a wedge above the rock faults would require the intersection of fractures in three dimensions, and involving fractures that are generally limited in persistence. Accordingly, higher values than those reported in SKB R-13-53 for the fracture shear strength properties were judged to be more appropriate.

The fracture properties used in the UDEC models, for both the SFR 1 and SFR 3 cases, and a comparison to the values used in the 3DEC analyses reported in SKB R-13-53 are provided in Table 3.

**Table 3:** Properties of rock fractures used for modelling the initial state of the repository, comparing those used in the analysis reported in SKB R-13-53, and those assumed for the UDEC analysis reported here.

| | 3DEC Analysis (R-13-53) | UDEC Analysis (this Report) |
|---|---|---|
| Fracture friction angle | 25° | 40° |
| Fracture cohesion | 0.05 MPa | 0.10 MPa |
| Fracture tensile strength | 0 MPa | 0 MPa |
| Fracture dilation angle | 0° | 5° |
| Fracture normal stiffness | 80 GPa/m | 80 GPa/m |
| Fracture shear stiffness | 2 GPa/m | 2 GPa/m |

The fracture properties were assigned in the UDEC models using a Coulomb slip model for the modelled fractures. Normal and shear fracture stiffness values were based on those provided in SKB R-13-53. These correspond to the minimum values reported in SKB R-07-06 and SKB R-07-31. It is unclear whether this assumption is conservative. In addition, the use of zero dilation in SKB R-13-53 for the joints may be conservative for stability but it is likely not conservative for hydraulic parameter evolution. Hydraulic properties for the fractures were not evaluated or assigned as the UDEC models were run with a defined fracture pore pressure distribution for the purpose of allowing for effective stress calculations, but not for fracture flow.

### 3.3.6. In Situ Stress and Boundary Conditions

As noted in SSM 2016:12, Part 3 (p. 48), an incompatibility appears in the in situ stress values used for the long-term stability analysis in SKB R-13-53. The values used are cited as having been based on in situ stress measurements carried out in 2002 as reported in SKB R-02-32. The estimate of the in situ stress state based on this data was subsequently updated in SKB TR-11-04, as shown in Table 4. However, it can be noted that a significant degree of variability and uncertainty exists in the measured stress values these estimated trends are based on. This is shown for the major (horizontal) principal stress data in Figure 21.

**Table 4:** In situ stress boundary conditions assumed for the 3DEC analysis in SKB R-13-53 (based on data provided in SKB R-02-32), and updated stress state reported for the SFR descriptive model in SKB TR-11-04. The depth z is given in meters.

| | 3DEC Analysis (SKB R-13-53) | SFR Descriptive Model (SKB TR-11-04) |
|---|---|---|
| Major horizontal stress, MPa (orientation) | 4.8 + 0.095z (120°) | 5 + 0.07z (142°) |
| Minor horizontal stress, MPa | 1.4 + 0.028z | 0.07z |

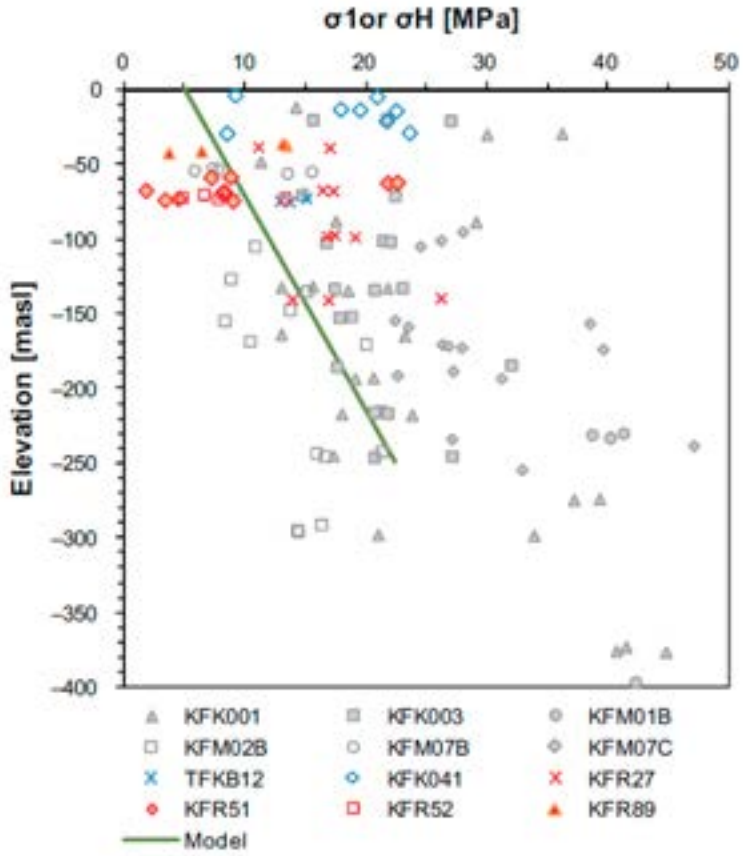


**Figure 21:** Major principal stress (horizontal) from in situ stress measurements. Red symbols indicate data points corresponding to the SFR 1 local volume, while the white and blue symbols represent data from other locations at Forsmark. The line indicates the descriptive model for σ1 at SFR (as given in Table 4). From SKB TR-11-04.

Additional reference was made to SKB R-07-31 where stresses were analysed using a stratified modulus approach in simulation. The numerical analyses in SKB R-07-31 were not used here but the mean measured maximum horizontal stress taken at several intervals was examined as shown in Figure 22. The gradient used in the UDEC analysis for this Report uses an adjusted maximum stress gradient of 5MPa + 0.0866D, with D in metres and the result in MPa. It should be noted that similar to the stress measurement data in Figure 21, the discontinuum nature of the UDEC analysis in this Report also results in stress heterogeneity within the model during stress initialization arising from localized interactions with the embedded DFN. The modelled initial stress states for the SFR 1 and 3 cases are provided in Appendix 3.

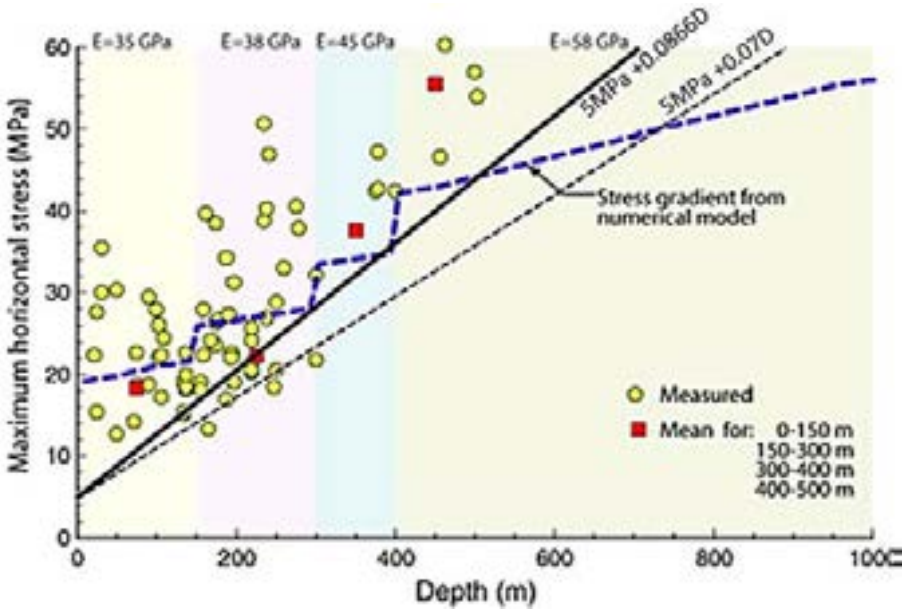


**Figure 22:** Major principal stress (horizontal) from in situ stress measurements. Red symbols indicate average values for the depth ranges given. Data and modelling results given by SKB-R-07-31, which are based on an equivalent rock mass deformation modulus (rock blocks and fractures) and not that for intact rock.

The Site Engineering Report SKB R-14-17 (p. 59) indicates that the alignment of the SFR 3 caverns is consistent with the alignment of the existing SFR 1 facility. As such, the same in situ stress state was assumed for both sets of models, with the exception that the SFR 3 rock vaults are 60 m deeper.

The boundary conditions assigned to the external boundaries of the model were velocity boundaries. Horizontal velocities were fixed in the x-direction but free in the y-direction for the lateral boundaries, whereas the bottom of the model was fixed in the y-direction and free in the x-direction. The top of the model was treated as a free surface.

### 3.3.7. Groundwater Conditions

Groundwater flow at Forsmark is reported to be mainly parallel to the rock vaults, and therefore along the out-of-plane direction to the 2-D section modelled in UDEC. As such, the modelling of groundwater flow was specified by SSM to be outside the scope of the analysis presented in this Report. The total pore pressure head was therefore treated as being static with pore pressure equal to pressure head equal to sea level. This was applied as a linear vertical gradient (Pw = 0.010z, with depth z in meters and pressure Pw in MPa). Pore pressures were accounted for both with respect to those acting along the fractures comprising the DFN, as well as the intact blocks between (Figure 23).

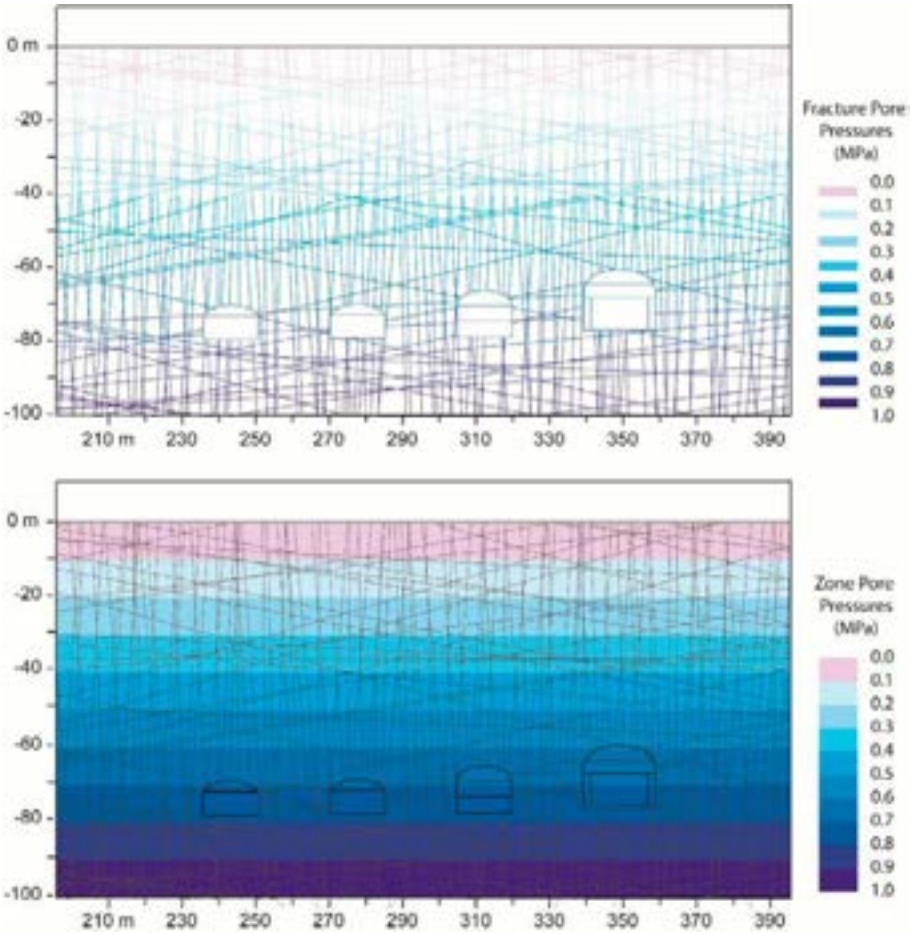


**Figure 23:** Initialized pore pressures in the UDEC models assuming hydrostatic conditions, as assigned to the fracture contacts (above) and intact block zones (lower).

The short-term effect of pore pressure drainage around the rock vaults after excavation and during operations, and re-saturation after closure of the repository was assumed to be negligible relative to the time intervals being modelled (1000 to 50,000 years). For this reason, it was assumed that the rock vaults will fill with water soon after closure, with pore pressures returning to their initial hydrostatic values. The sensitivity of this assumption to the results was tested by running the SFR 1 case as a fully coupled hydro-mechanical model assuming steady state flow conditions. Figure 24 shows the difference in the fracture pore pressures around the 1BMA vault for the no-flow assumption compared to that assuming steady state flow and accounting for drainage into the rock vaults. It can be seen that although the near-field fracture pore pressures are reduced because of tunnel drainage, the degree of drainage is limited by the constant head condition (i.e., sea level at the top of the model) combined with the connectivity of the fracture network. As a result, the near-field fracture pore pressures are comparable to what would be expected where constant seepage into the rock vaults is experienced. The corresponding displacements based on a history point 0.5 m above the roof of each modelled rock vault is included. These effectively show little to no difference between the no-flow and steady state drained conditions (<1 mm). This is because of a combination of the compressive arching effect that develops in the roofs of the rock vaults (due to the high horizontal in situ stresses), reinforcement provided by the simulation of rock bolting, and sufficient fracture shear strengths, relative to any adverse influence the

undrained fixed pore pressures might have on the effective stresses in the short term. Later modelling of the effects of strength degradation over time would coincide with post-closure pore pressures, which as previously noted, would return to the initial hydrostatic state as assumed in the non-drained case.

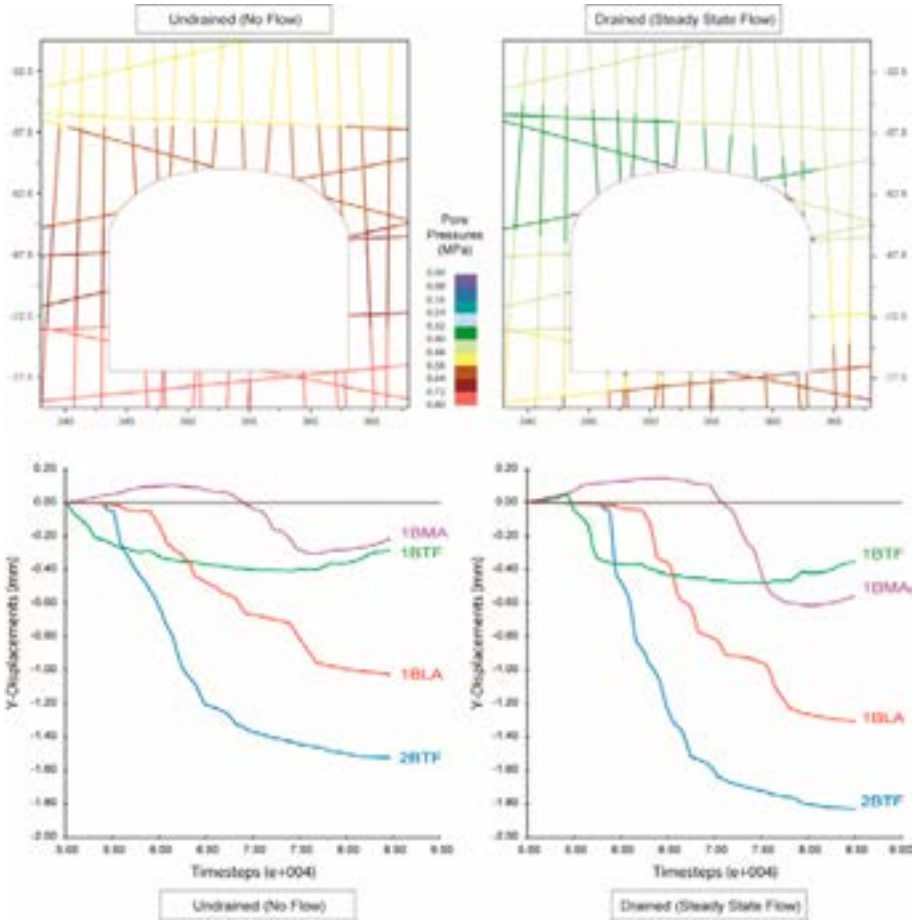


**Figure 24:** (Upper) Comparison of modelled pore pressure distribution for rock vault 1BMA between assumptions of fixed pore pressures (i.e., no flow/undrained tunnel) and drained pore pressures (i.e., steady state flow). (Lower) Corresponding convergence displacement histories for points 0.5 m above the roof of each rock vault in the SFR 1 layout at simulated closure (backfilling) for the undrained and drained UDEC model scenarios.

### 3.3.8. Rock Reinforcement and Backfill Material

Excavation of the rock vaults in the UDEC models incorporated sequencing involving a top heading and lower benches (e.g., Figure 25). This approximated the sequencing reported in SKB R-07-10 (p. 47), with the largest rock caverns being excavated with one top heading and two benches, and the smaller rock vaults being excavated with one top heading and one bench. Reference was made to the excavation of the SFR 1 operation tunnel using contour blasting with a designed blast damage limit of 0.3 m (SKB R-07-10, p. 49), and presumably similar blasting practices were carried out for the rock vaults. This thin skin of blast damage was considered in the UDEC models together with the temporary effects of rock reinforcement (described below).

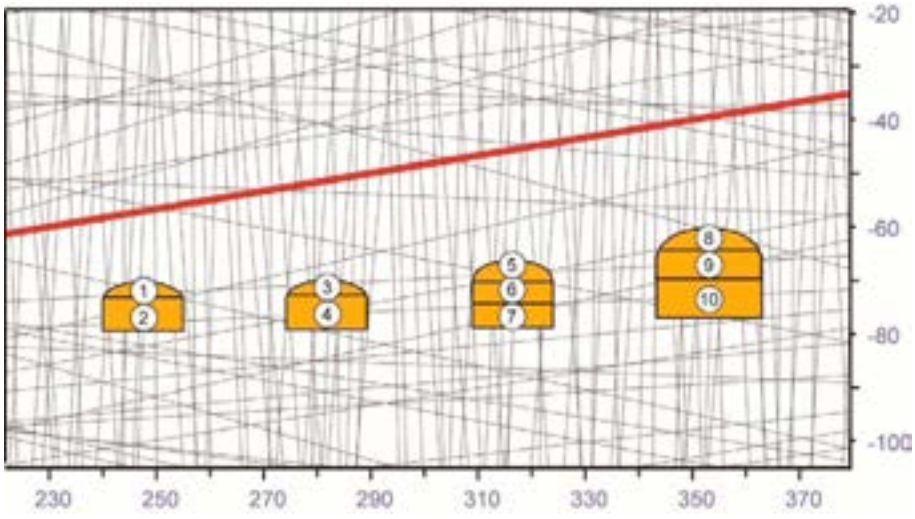


**Figure 25:** Excavation sequencing modelled for the SFR 1 layout, following a top heading and lower bench sequence.

SKB R-07-10 (p. 47-48) reports that scaling was then carried out after excavation to remove loose blocks. Similarly, in the UDEC models after excavation, any small, loose blocks forming on the boundary of the rock vaults were "scaled" by deleting them from the UDEC model. During later simulation of the backfilling phase, these deleted blocks were replaced by backfill.

SKB R-14-17 (p. 62) reports that in some areas spot bolting was used to provide support during construction of the SFR 1 access tunnels. In describing the different types of rock vaults, SKB TR-14-01 (p. 85-100), makes reference to the walls and roof of the existing SFR 1 and planned SFR 3 rock vaults being lined with shotcrete. SKB R-07-10 also makes reference to rock bolting operations during construction of SFR 1, showing photos and listing details of the bolting equipment (p. 47-51) and describing the support types used. These primarily involved grouted dowels and shotcreting, with heavier support in the form of shotcrete arches containing reinforcing bars and mesh being used in tunnel sections passing through the Singö deformation zone (SKB R-07-10, p. 54). Although the scope of the UDEC analyses specifies that the modelling of rock reinforcement is not required, the orientations, spacing and persistence of the fractures defined in the 2-D DFN are such that block movements and small wedge failures will develop in the UDEC models if left without reinforcement (and before backfill is placed). This was seen in preliminary testing of the SFR 1 UDEC models.

Accordingly, the supporting influence of rock reinforcement in limiting block movements was treated implicitly in the UDEC models, together with the marginal strength reduction expected due to blast damage extending 0.3 m into the rock. The benefit of reinforcement was simulated by applying a net increase of 50 kPa of fracture cohesion extending 2 m around the periphery of the roof and walls of the rock vaults. This represents either a thin layer of shotcrete or pattern bolting, and the benefit these would provide in helping to constrain the opening of fractures at the excavation surface. Fracture friction angles in this zone were increased by 5 degrees to simulate the preservation of asperity interlocking permitted through the addition of shotcrete and/or rock bolting. These increases in strength were added for only the first 100 years of simulated time, and then were removed. This return assumes that any reinforcement added, whether shotcrete or rock bolting, will be fully degraded

after 100 years. Both would be in direct contact with a higher groundwater flow around the periphery of the excavations (i.e., a more aggressive environment), accelerating any deterioration of the shotcrete or corrosion of any rock bolts.

Backfill was added to the excavated rock vaults, where applicable, before modelling the first 100 years. This was simulated following the descriptions of the closure plans for the different rock vault types provided in SKB TR-14-01 (see Figure 8 and Figure 9 for backfilling pertaining to SFR 1 and SFR 3, respectively). For 1- and 2BTF and 1BRT, the presence of concrete tanks overlain with backfill to the excavation roof was simulated. For 1- and 2BMA, a reinforced concrete enclosure surrounded by backfill was simulated. The backfill type in SKB TR-14-01 (p. 83) is described as macadam, involving crushed rock sieved in fractions of 2–65 mm. Macadam has no or very little fine material (grain size < 2 mm). Input properties for the concrete and backfill were taken from those provided in SKB R-13-53, with the latter being described as being equivalent to the properties for sand. This lists the deformation modulus as being 6 MPa, which was judged to be too low and resulted in block overlap errors during preliminary modelling in UDEC. Instead a higher deformation modulus of 300 MPa for crushed rock was used based on values reported in the literature (e.g., Xiao et al., 2014). The UDEC model input properties used for simulating backfill are provided in Table 5.

**Table 5:** Input properties for concrete and macadam backfill used to simulate closure of the UDEC modelled rock vaults. Properties are based on those provided in SKB R-13-53, with the exception of the deformation modulus of the macadam which was based on typical values in the published literature for crushed rock.

| | Concrete structures | Macadam backfill |
|---|---|---|
| Density | 2400 kg/m$^3$ | 1900 kg/m$^3$ |
| Modulus of deformation | 17 GPa | 0.30 GPa |
| Poisson's ratio | 0.15 | 0.3 |

## 3.4. Modelling Procedure for Long-Term Behaviour

### 3.4.1. Long-Term Strength Degradation Formulation

There have been a number of studies investigating "time to failure" of brittle rocks as a function of the driving stress ratio. These account for long-term strength degradation, including such processes as sub-critical crack growth. The procedure adopted for the UDEC analysis carried out in this Report follows that of Damjanac and Fairhurst (2010).

For uniaxial conditions, the driving stress ratio is simply the axial applied (sustained) stress divided by the known UCS of the rock. Based on NWMO DGR-TR-2011-17 and NWMO-TR-2015-27 the following assumptions are made for granitic rocks over time. The standard data set for granitic rocks is based on Schmidtke and Lajtai (1985) and Lau et al. (2000), as shown in Figure 26. The crack initiation threshold, CI, is considered to be a lower bound for strength degradation. In other words, stress levels below CI result in no strength reduction over time. The value of CI depends on the rock in question and varies from 0.3 to 0.6 (i.e., 30 to 60% of the UCS). Damjanac and Fairhurst (2010) cite a CI threshold of 0.4 for granite in their work, and the same value is assumed for this analysis as a

conservative lower bound. For degradation of fracture asperities this threshold is taken as 30% of the nominal peak shear strength. Failure is instantaneous for stress levels at the UCS of the rock (or at the confined strength defined by the yield function for the rock). For increasing differential stress levels between the CI threshold and the yield function, the strength degradation rate increases (i.e., time to failure decreases). In Figure 26, the driving stress ratio, DSR, is defined as $\sigma/\sigma_c$ with:

$$\sigma = \sigma_1 - p_c \quad (1)$$

$$\sigma_c = \sigma_f - p_c \quad (2)$$

where: $\sigma$ is the differential stress, $\sigma_c$ is the differential stress at failure, $\sigma_1$ is the applied axial stress, $\sigma_f$ is the applied stress at failure, and $p_c$ is the applied confining stress.

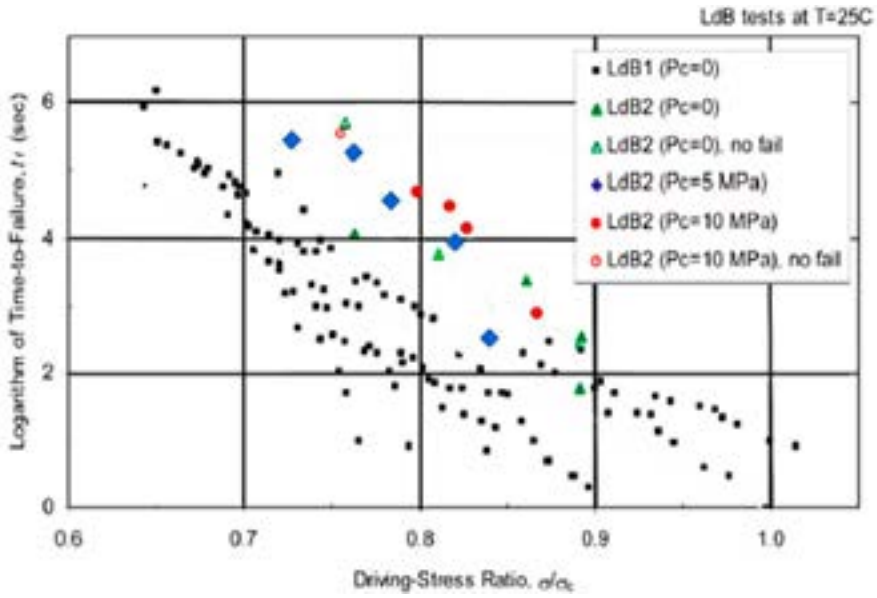


**Figure 26:** Time to failure data for Lac du Bonnet granite based on Schmidtke and Lajtai (1985) and Lau et al. (2000).

The data represents time to failure when a sample is held at a given differential stress at a given confinement. The data can be interpreted to indicate the time it takes for the strength (maximum allowable differential pressure) to drop to the applied stress level. There are three sets of "failed" data at 0, 5 and 10 MPa of confinement.

As previously noted, the minimum strength decay for intact rock under unconfined conditions is taken as approximately 40% of the UCS (CI = 0.4). For existing fractures, this threshold is taken as 30% of the nominal peak cohesion. This is shown in Figure 27, which is reproduced from NWMO-TR-2015-27. Simplifications must be made here to convert this time to failure information into a useable strength decay relationship. In NWMO DGR-TR-2011-17, a Particle Flow Code (PFC) analogue is used to synthesize a damage relationship and thereby define strength degradation rates for modelling. It is not felt that this is warranted here and is not reproducible for the rocks at SFR 1 and 3. The basic premise represented in these figures is valid, however, and will be adopted here.

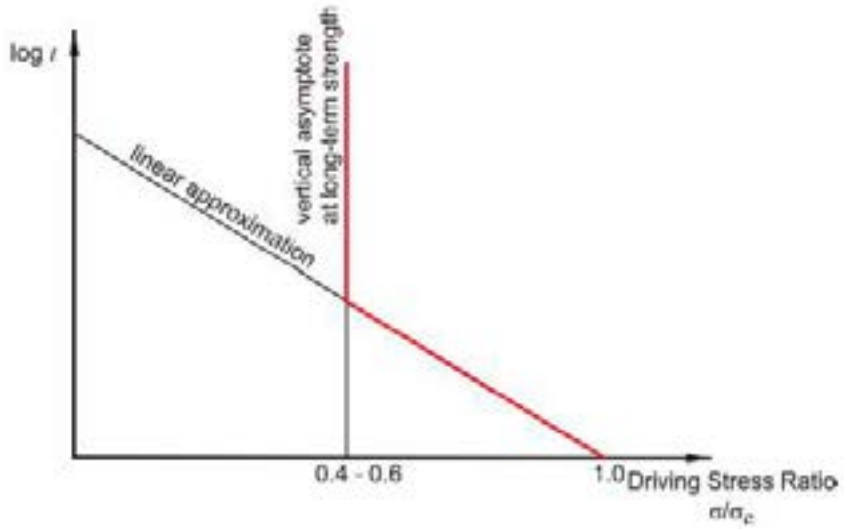


**Figure 27:** Concept of strength degradation with a lower bound. From NWMO-TR-2015-27.

Degradation as a Function of Time and Confinement

The data used in Figure 26 is primarily weighted towards data for unconfined compression, and only limited data for confined testing is included. Nevertheless, it is possible to derive a best-fit relationship for strength decay as a function of time and confinement. Best-fit lines are added to the data in Figure 26, with the results shown in Figure 28. These initial and generalized fits are based on the assumption (required by the limits of the dataset) that the level of applied stress does not impact the rate of strength decay.

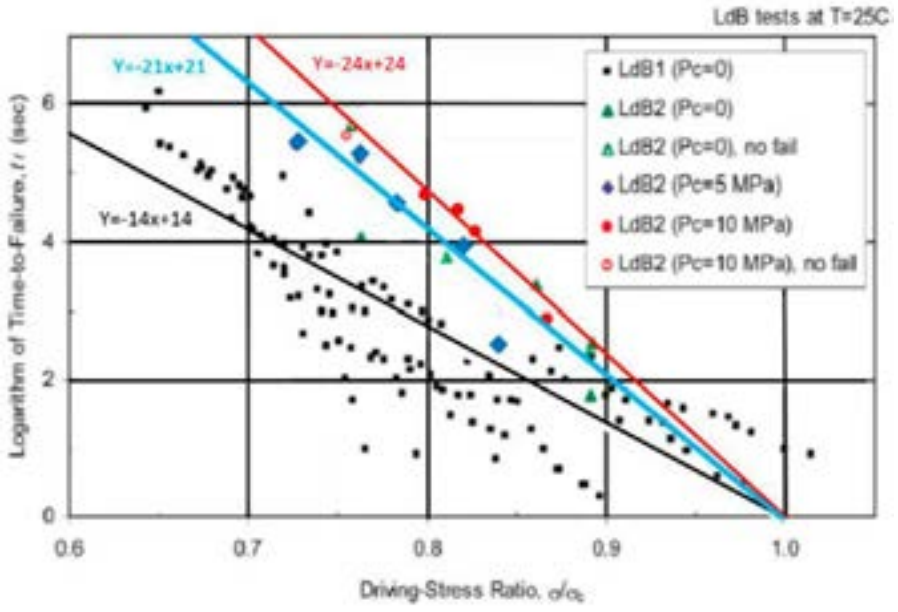


**Figure 28:** Basic best fit curves for three confining stresses (simplified approach).

From the three time-to-failure lines in Figure 28, the following relationship can be derived:

$$\sigma_t = D\sigma_c \tag{3}$$

where: $\sigma_t$ is the strength at time $t$, and $D$ is a strength degradation factor that utilizes the CI/UCS crack damage threshold ratio for rock (typically 40% as a lower bound):

$$D = MAX\left[\frac{log\ t(seconds) - B}{-B}, 0.4\right] \tag{4}$$

For fractures, 0.3 or 30% is used as a lower bound in the above expression.

A lower limit of degradation $D$=0.4 is used for intact rock cohesion in accordance with current views on lower bound uniaxial strength and consistent with assumptions used in NWMO-TR-2015-27. Lower values have been cited (down to 1/3) based on some lab data although this is likely to be overly conservative even for this application. In the equation above:

$$B = 14 + 3.2\sqrt{\sigma_3} \tag{5}$$

where: $\sigma_3$ is the minimum (confining) stress in the intact rock blocks or the normal stress acting on the fractures. From this reasoning, the strength decay curves (degradation as a function of time and confining stress) in Figure 29 are obtained. Note that time is the independent variable in this plot and thus the axes are reversed relative to Figure 28.

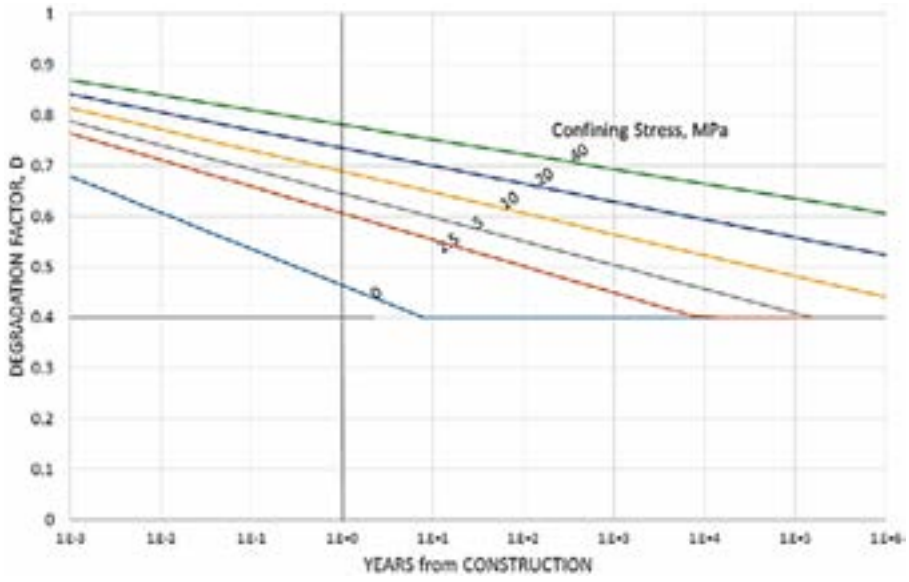


**Figure 29:** Degradation function based on simplified approach. Strengths are deemed to converge at D=1 at a time of 1 second (off chart); note that years are plotted here although function is in terms of seconds. Note that D=0.4 represents the lower limit of degradation below which strength decay and failure does not occur.

For uniaxial strength and loading conditions (i.e., the immediate tunnel boundary), this degradation function means that strength has degraded to 60% of UCS within several days (0.01 years) and to approximately 45% in one year. This is in accordance with accepted design assumptions in brittle rock (Martin, 1997; Diederichs et al., 2004; Diederichs, 2007).

Degradation as a Function of Driving Stress Ratio

The above formulation does not consider the relationship between applied stress and strength decay rate. It seems reasonable that creep and strength degradation rates should increase with stress levels closer to the yield limit and should approach zero near the lower bound stress limit (CI in the case of brittle rocks).

To account for the influence of the applied stress on the rate of strength degradation, the following approach can be used in which parameter A is introduced to account for confining stress and the equation for B is rewritten in terms of the Driving Stress Ratio, DSR:

$$A = m * e^{n\sigma_3} \quad (6)$$

$$B = C + A(1 - DSR) \quad (7)$$

where: $C$, $m$ and $n$ are fit parameters. Confining Stress, $\sigma_3$, is in MPa.

It can be assumed that the yield points in Figure 26 indicate the time for strength to degrade to the indicated driving stress ratio, which represents the sustained boundary condition. The dataset is limited, however, and so in order to capture useable trends, a series of rate lines can be derived as in Figure 30 (coloured lines) where the rate line for a given driving stress passes just under (to be conservative) the lower range of the yield points near that specified driving stress ratio. The result is that each rate line is valid only for a limited range of driving stresses associated with it. Connecting the points where each local rate line intersects the vertical grid line associated with the same driving stress ratio (coloured X's in Figure 30), a dashed black line is obtained which represents the time to failure for a given sustained driving stress ratio. These are calculated for three different confining stresses in Figure 30. The same coloured rate lines and dashed time-to-failure curves are then used in subsequent figures.

Although a rigorous statistical fit is not possible with the data that exists today (and is unlikely to exist in the near future due to the challenges of this form of testing) a conservative best approximate fit can be found using m=3 and n=0.1. These variables can be adjusted if less conservative curves are desired. The resulting strength decay curves (as a function of time, driving ratio and confinement) are provided in Figure 31. Again, it should be noted that the axes are reversed in these plots relative to the time-to-failure plots. The objective here is to transform the time-to-failure plots (Figure 30), where time is the dependent variable, into a strength degradation with time plot (Figure 31) where time is the independent variable.

The coloured solid lines in Figure 31 are decay rate curves for different driving stress ratios. Combining the dashed lines in the above figure (time to failure at the specified driving stress), the final figure (Figure 32) is obtained representing time to failure (at a sustained confining stress and driving ratio).

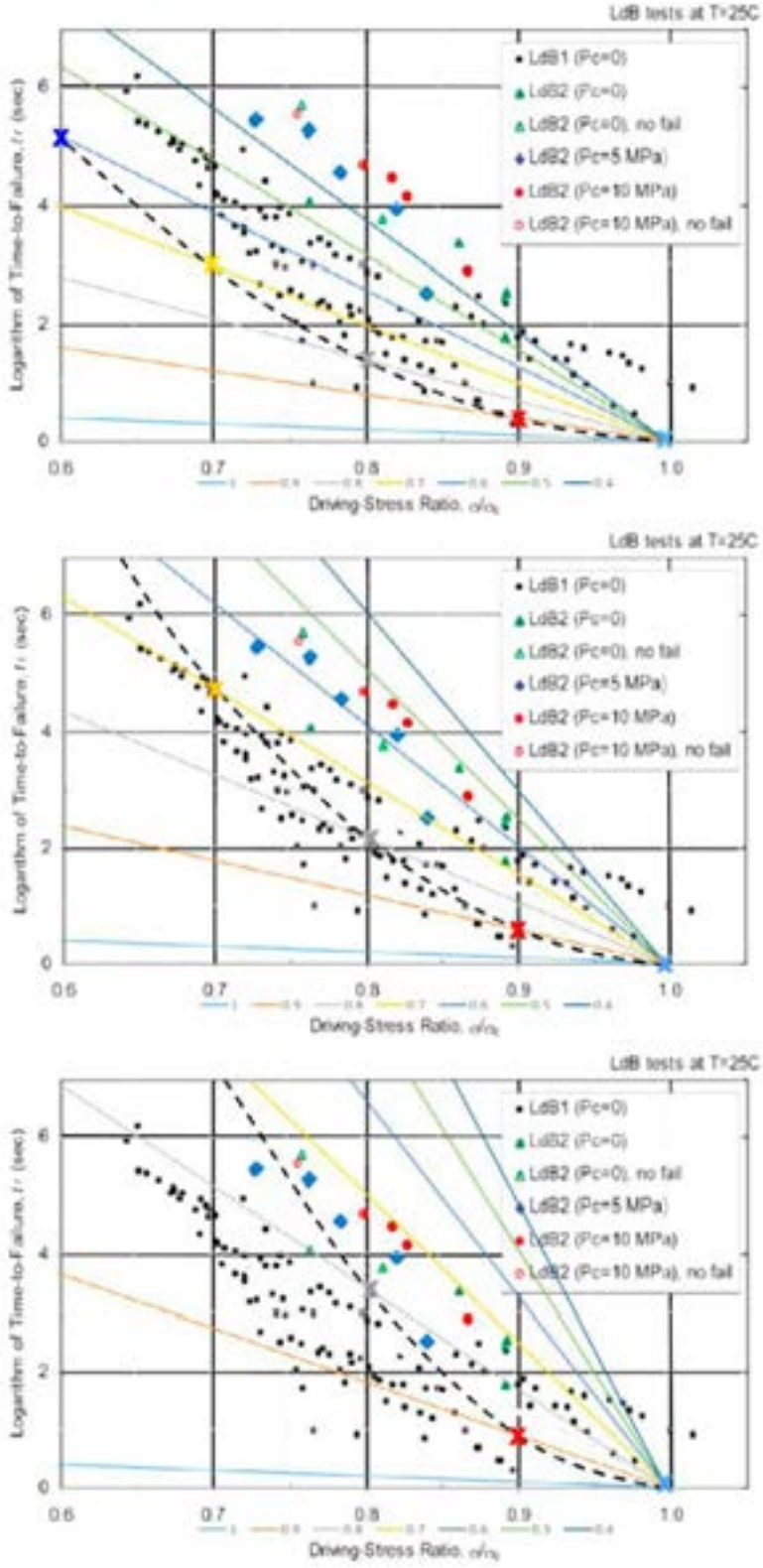


**Figure 30:** Best fit functions for confining stresses, from top to bottom, of 0, 5, and 10 MPa, using best fit parameters such that $\boldsymbol{A = 30\,x\,e^{0.1\sigma_3}}$ and $\boldsymbol{B = 1 + A(1 - DSR)}$. The coloured X's mark the points where each local rate line (coloured lines) intersect the vertical grid line associated with the same driving stress ratio. The dashed black line that connects these points represents the time to failure for a given sustained driving stress ratio.

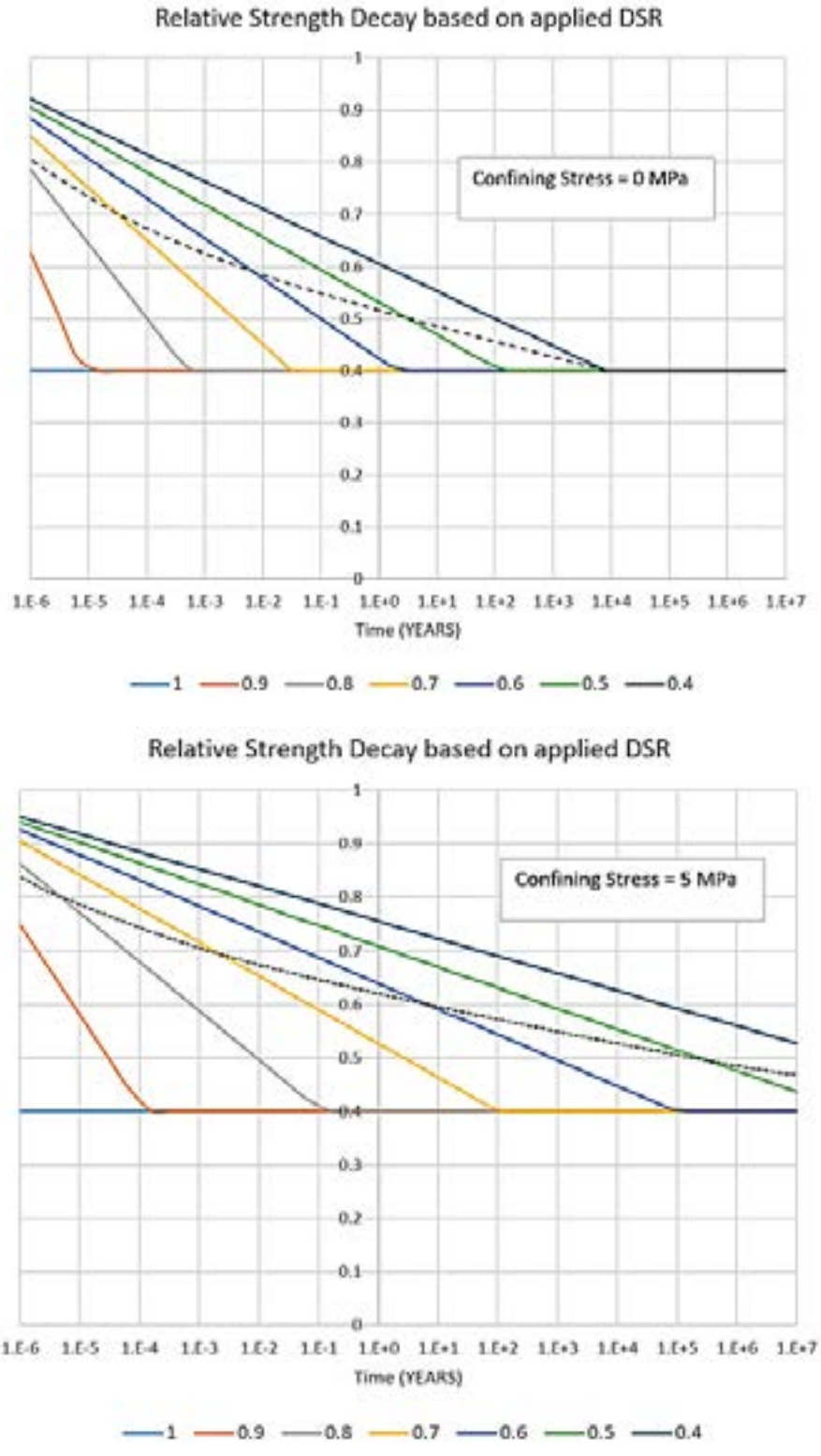


**Figure 31:** Strength decay curves (advanced function) for confining stresses of 0 MPa (upper) and 5 MPa (lowers), using best fit parameters such that $\boldsymbol{A = 30\ x\ e^{0.1\sigma_3}}$ and $\boldsymbol{B = 1 + A(1 - DSR)}$. The coloured lines are the driving stress ratio rate lines derived from Figure 30, and the black dashed lines are the corresponding time-to-failure curves. Note that D=0.4 represents the lower limit of degradation below which strength decay and failure does not occur.

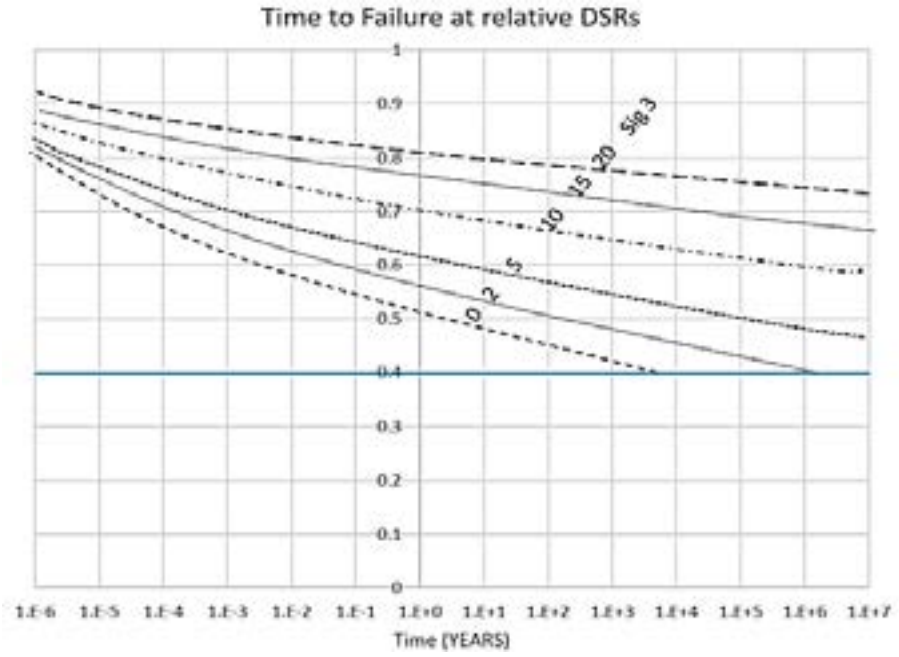


**Figure 32:** Time to failure curves (advanced function) for different confining stresses (Sig 3) using best fit parameters such that $\boldsymbol{A = 30\ x\ e^{0.1\sigma_3}}$ and $\boldsymbol{B = 1 + A(1 - DSR)}$. Time to failure is obtained by matching the confinement curve to the DSR of interest. For example, the horizontal grid line associated with DSR 0.6 crossing the 10MPa confinement curve gives a ToF of 1E+6 years. Note that D=0.4 represents the lower limit of degradation below which strength decay and failure does not occur.

### 3.4.2. Long-Term Strength Degradation Implementation

Long-term strength degradation was modelled in UDEC starting at the point following simulation of backfilling and closure of the rock vaults. This was done by applying the strength degradation factor D, described in the previous section, to the initial "base" strength parameters reported in Table 2 and Table 3, for the time intervals being modelled. The same D factor was applied to both the intact rock and fractures in the absence of any long-term strength degradation data for fractures (the authors are not aware of any).

Using the best fit parameters determined in Figure 30 for equations (6) and (7):

$$A = 30\ x\ e^{01\sigma_3} \tag{8}$$

$$B = 1 + A(1 - DSR) \tag{9}$$

the corresponding degradation relationships for the different UDEC base properties were derived and applied as shown in Table 6. For cohesion, the degradation rate was applied equally to both the intact blocks and fractures. However, the degradation of friction was applied only to the fractures, with the fracture dilation angles being maintained as a function of the friction angles. The friction angle for the intact blocks was assumed to remain constant. This is in accordance with pre-peak brittle fracture damage models for intact rock, which assume that strength degradation is driven by cohesion loss more so than friction mobilization (e.g., Diederichs, 2007; Eberhardt et al., 2016).

**Table 6:** Degradation functions derived and applied in UDEC to simulate long-term strength degradation of the intact blocks and fractures.

| | Intact Blocks | Fractures |
|---|---|---|
| Compressive strength | $\sigma_{ct} = D_t(\sigma_{co})$ | n/a |
| Cohesion | $C_o = \frac{\sigma_{co}\left(1 - sin(\emptyset_o)\right)}{2cos(\emptyset_o)}$<br>$C_t = D_t(C_o)$ | $C_t = D_t(C_o)$ |
| Friction angle | $\emptyset_t = \emptyset_o$ | $\emptyset_t = D_t(\emptyset_o)$ |
| Tensile strength | $T_t = D_t T_o$ | $T_t = D_t T_o$ |

This procedure contrasts with that implemented for the 3DEC analysis reported in SKB R-13-53, where strength degradation was applied uniformly across a specified zone defined by an initial radius extending 0.5 m from the excavation boundary (Figure 33a). The reduction factor was applied to both the fracture cohesion and friction angle, whereas the properties of the intact rock blocks were assumed to remain constant. For each time interval modelled, the radius of the strength degradation zone was increased by 0.5 m, to which an exponentially decreasing reduction factor was subsequently applied (SKB R-13-53; p. 18-19).

In contrast, the strength degradation procedure implemented for the UDEC modelling conducted for this Report varied both with time and as a function of the driving stress and confining stress. For the fractures, the modelled normal stress on the joint plane was used in place of the minimum principal stress, $\sigma_3$, in equation (8). The shear stress capacity at this normal stress and the modelled shear stress on the plane were used to calculate the driving stress ratio, DSR, in equation (9). Accordingly, strength degradation only occurs for those block elements and fracture contacts where the driving stress exceeded the damage initiation threshold (D=0.4). This resulted in a more heterogeneous distribution of reduced fracture strengths for each modelled time interval (Figure 33b).

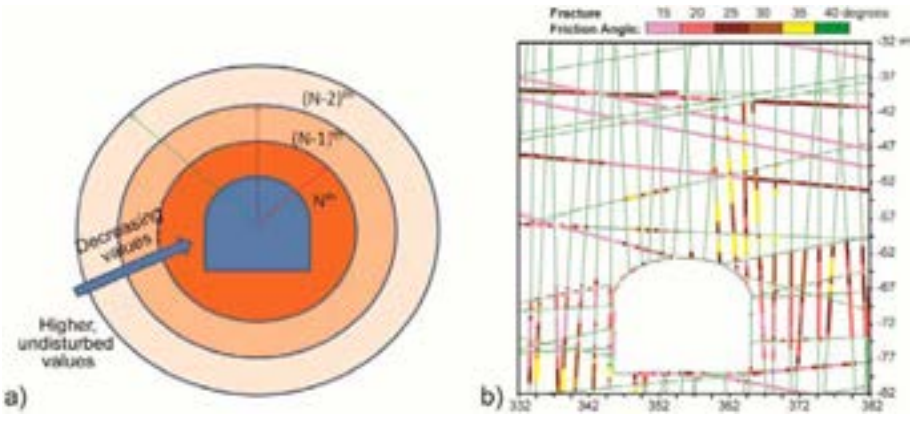


**Figure 33:** a) Strength degradation procedures implemented in the 3DEC modelling reported in SKB R-13-53, based on uniformly applying reduction factors to the fracture cohesion and friction angles within a given zone. With each time increment, zones were added in 0.5 m increments, to which exponentially decreasing reduction factors were applied. b) Distribution of fracture friction angles resulting from strength degradation procedure implemented in this Report, where strength degradation is dependent on both time and the driving stress and confining stress distributions. This results in a more heterogeneous distribution of reduced strengths.

Comparing this procedure and the resulting values to SKB R-13-53, the latter assumed conservative residual fracture strength parameters and used these as input in later models. In the UDEC analysis performed here, it is assumed that the fracture parameters in SKB R-13-53 are for 50 years after the beginning of repository construction. Furthermore, assuming an average 2.5 MPa normal stress on fractures before any disturbance, the 50-year strength parameter can be projected to the original values before excavation had started. Interpolating between the values in the plots in Figure 31 for a confining pressure of 2.5 MPa and a driving stress ratio DSR of 0.4, a degradation factor $D_t$ of 0.62 can be extracted at 50 years from the beginning of the construction. The inverse of this factor can be used to obtain the starting parameters at model time zero. Using this degradation factor the fracture strength parameters before any disturbance to the rock mass is given in Table 7. This increase in initial strength parameters, relative to the analysis in SKB R-13-53, will not be of concern in terms of conservative considerations since they decay in 50 years to the reported values in R-13-53 and continue to decay to lower values over time.

**Table 7:** Initial strength parameters adopted for the UDEC models, and the targeted values 50 years after repository construction to correspond with those reported in SKB R-13-53.

| | Initial values | 50 Years from construction (from SKB R-13-53) |
|---|---|---|
| Fracture cohesion | 0.1 MPa | 0.05 MPa |
| Fracture friction angle | 40 degrees | 25 degrees |

The UDEC modelling therefore proceeded with solving for the initial conditions using the pre-disturbance fracture strength parameters given in Table 7. Upon start excavation of the rock vaults, degradation begins to take effect. However, degradation does not proceed as the model cycles. Instead, certain time points are selected over the long-term life cycle of the repository, for which the associated degradation factors $D_t$ are calculated according to the degradation equations presented in Table 6. These time points are 10, 20, 50, 100, 200, 500, 1000, 2000, 5000, 10000, 20000, and 50000 years from the beginning of construction. During the first 10 years from the beginning of the construction, all vaults will be excavated. Excavation coincides with the simulation of rock support (shotcrete and grouted dowels) being added, as previously described. Backfilling is then simulated and strength degradation started. This coincides with the degradation of the rock support.

It is important to note here that the degradation simulated is purely of a stress-induced nature. The applied strength reductions relate to the effect of stress levels in the intact rock and those acting on the joints that exceed a damage threshold, thereby causing micro-damage to accumulate and propagate, reducing the ultimate strength of the intact rock or fracture. Strength degradation related to purely chemical processes, for example resulting from the interaction of intact rock or joint wall rock with sea water or air is not simulated here.

## 3.5. Modelling of Permafrost (Year 20,000)

According to SKB TR-13-05 (Climate and climate-related issues for the safety assessment SR-PSU), the depth of permafrost is expected to reach up to 100 m below surface, and cannot be excluded to a depth of 150 m (SKB TR-14-01; p. 211),

for the time period of 20,000 to 40,000 years in the Weichselian glacial cycle climate case (see Fig. 4-13 in SKB TR-13-05, reproduced here in Figure 3). However, this same figure shows the evolution of permafrost reaching maximum depths of 200 to 250 m below surface at a time that coincides with the start of glaciation between 45,000 and 60,000 years (see Figure 3 and Figure 4). Accordingly, the UDEC simulations carried out for this study consider both the SFR 1 between 60 and 80 m depth and SFR 3 between 120 and 140 m depth as within the permafrost zone starting at 20,000 years after construction of the rock vaults. The effect of permafrost is only considered in the fractures between the modelled rock mass blocks, while the intact rock blocks remain unaffected. Two subsequent scenarios are then modelled: one where permafrost melts after 1000 years (referenced as Year 21,000), and one where permafrost remains in effect for the period extending to the final step in this review involving glaciation at 50,000 years.

There is little guidance in the literature for accounting for ice formation in deep fractures; most of the work in the literature refers to shallow near-surface fissures and seasonal freezing. For this review, the simulation of permafrost in the fractures (i.e., block contacts) is done by finding all contacts within 200 m depth from the surface and increasing the pore pressures in the associated domains of those contacts by 10% of their original values. The logic behind this value is that, unlike many bench studies on shallow depth frost jacking, the downward migrating permafrost front at depth will move very slowly, freezing into an open “reservoir” of fracture-based groundwater. Most of the expansion of ice occurs before solidification (between 5 and 0 degrees) and so there will be a release of pressure during freezing into the unfrozen zone. In addition, the fractures in our model (mostly subvertical) will be constrained laterally and will resist the volumetric heave encountered in near surface horizontal fractures. Residual pressure increases due to expansion in trapped pores and smaller non-persistent cracks should be equivalent to the restrained expansion of 10%.

Furthermore, since permafrost has a positive influence on the discontinuity strength, contact cohesive and tensile strengths are increased by 0.5 and 0.25 MPa, respectively, as per the recommendations of Davis et al. (2000). The fracture conductivity in the frozen zone (as well as matrix permeability) is assumed to be zero during the permafrost phase (as per Jung et al. 2011). As a result, pore pressure increases during the final glacial stage do not affect the frozen ground zone. The subsequent simulation of permafrost melting is modelled by simply removing the contact strengths and pressures added.

## 3.6. Modelling of Glacial Loading (Year 50,000)

According to the Weichselian glacial cycle climate case reported in SKB TR-13-05 (see Figure 4-10 in SKB TR-13-05, reproduced here in Figure 4), there are two periods of glaciation expected over the next 120,000 years. However, since the scope for this review focusses on simulation up to 50,000 years, only the first of these glaciation cycles is considered. Glacial loading was simulated by applying current models of vertical boundary load increase and associated Poisson’s ratio effects to the UDEC models, as well as increments of load from crustal flexure. Assumptions were based on SKB TR-09-15 (Stress evolution and fault stability during the Weichselian glacial cycle).

The thickness of the ice sheets at the first glacial cycle in the Weichselian climate case reaches approximately 2000 m (Figure 4). Therefore, a maximum of 20 MPa vertical boundary stress is applied at the top surface of the UDEC model for the 50,000 year case. Furthermore, the stress histories for glacial loading reported in

SKB TR-09-15 (reproduced here in Figure 34) show that both maximum and minimum horizontal stresses likewise experience significant increases (5-9 MPa) at the same time. However, this is first preceded by a noticeable reduction (~5 MPa) in minimum horizontal stress (Figure 34) due to crustal flexure upon ice advance.

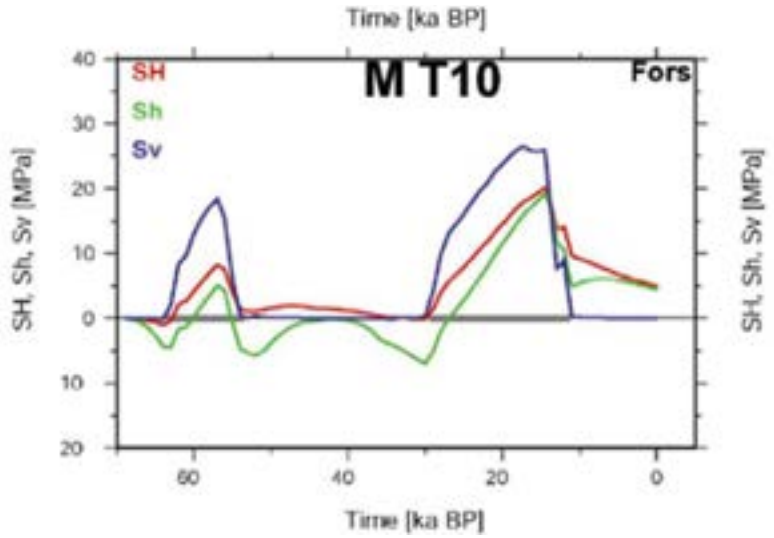


**Figure 34:** Temporal evolution of the induced maximum horizontal (SH), minimum horizontal (Sh), and vertical (Sv) stress at 500 m depth at Forsmark during glaciation (SKB TR-09-15).

Accordingly, a horizontal stress decrease was first required in the UDEC model before imposing a stress increase. This corresponds to conditions just before and at the peak of glaciation, respectively. It is important to note here that the stresses in Figure 34 are based on a model with stiffness layering on the order of kilometres. The softening of the disturbed upper few hundred metres is not considered. The initial stress state simulations shown by the blue dashed line in Figure 22 assume that the rock mass modulus in the upper 200 to 300 m is half of the stiffness below 500 m. This assumption is necessary to match the tectonic influence on horizontal stress.

This same logic can be applied here for simulating glaciation in the UDEC models. In crustal flexure, a thin skin of softer material on top of the crust will result in lower stress change due to glaciation. Assuming a 50% reduction in shallow modulus, the modelled stress changes in Figure 34 can be halved at the repository horizon.

Care is needed to impose this stress change as a boundary condition in the UDEC model. First, it was necessary to establish the corresponding initial stress reduction due to glacial advance) for the repository depth (i.e., 75 m in the case of SFR 1) based on the stress magnitudes provided in Figure 34 for 500 m depth. Here the 5 MPa stress decrease at 500 m depth reduces to 1 MPa at 75 m depth assuming a linear stress gradient (see orange line in Figure 35). This 1 MPa decrease equates to almost 10% of the in situ horizontal stress at this level (10 MPa). The linear trend extends to the surface with values as small as 0.3 MPa, implying that the stresses at the surface would remain almost the same as their original values. Similarly, in terms of horizontal stress increase during glacial loading, the 10 MPa stress increase at 500 m depth linearly reduces to 5 MPa at 75 m depth (see blue line in Figure 35). This corresponds to a 50% increase in horizontal stress at this depth. In this case, the horizontal stress increases by 4.1 MPa at the surface (Figure 35).

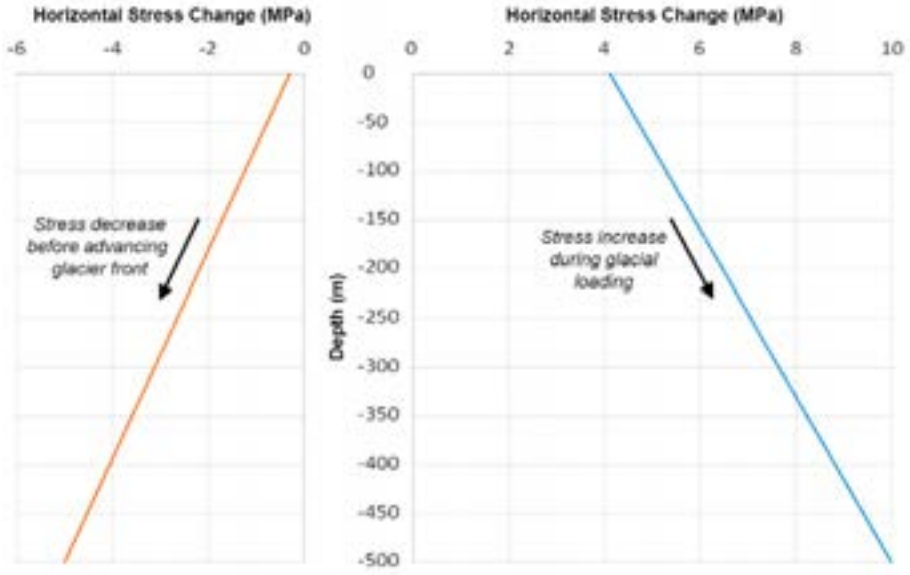


**Figure 35:** Horizontal stress decrease as glacial front approaches (orange curve) and increase during (blue curve) glaciation for different depths for implementation in the UDEC model. Note that compression is positive in this figure

Second, it was necessary to determine the boundary condition to be applied to the UDEC model to obtain the required horizontal stress magnitudes for glacial advance and loading at the repository depth. These were imposed using a horizontal displacement boundary condition applied to the left boundary of the UDEC model. To establish the appropriate displacement rate, the UDEC model was solved without the presence of the repository excavations and tested for different displacement rates to fulfil two main objectives: 1) to reduce the induced unbalanced force because of the new boundary condition, and 2) to reduce the time step required to obtain the horizontal stress change of interest. For each trial, the horizontal stresses were recorded along a vertical profile extending from the surface to the bottom of the model through its middle and compared to the desired horizontal stress states.

For simulating the decrease in horizontal stress expected with glacial advance, the UDEC model was stretched with a constant velocity of -1 mm/s applied to the left boundary. The number of solution cycles was then determined that resulted in the required horizontal stress decrease of 1 MPa for the depth of 75 m. The same procedure was followed to determine the number of cycles at the same velocity but in compression with a constant velocity of +1 mm/s to arrive at the horizontal stress increase of 5 MPa at 75 m depth to simulate glacial loading. The horizontal stress gradients modelled during this exercise for the desired horizontal stress values at the SFR 1 repository depth of 75 m are shown in Figure 36. Once the required stress magnitudes were established, the left boundary condition was returned to zero displacement and the model cycled to reduce the unbalanced force in the model.

A similar process was followed for the SFR 3 models. The periods of horizontal stress relaxation followed by compression are modelled as part of the 50,000 year case (i.e., the Year 50,000 model includes both relaxation to simulate the approaching glacial front followed by compression in the horizontal direction as part of the simulation of glacial loading).

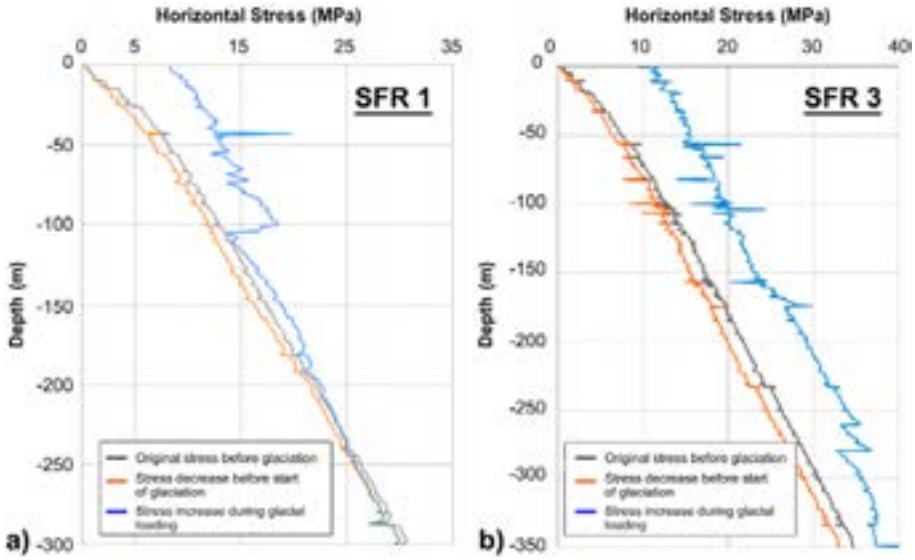


**Figure 36:** Horizontal stress gradients for the UDEC test models to determine the applied boundary conditions required to simulate the appropriate horizontal stress decrease and increase due to glacial advance and loading, respectively, for a) SFR 1 and b) SFR 3. Note that the stress jump during glacial loading at 100 m for the SFR 1 case and more subtly at 170 m for the SFR 3 case is a modelling artefact due to the transition from the finer near-field DFN to the courser far-field DFN (see Figure 16 and Figure 17).

After determining the number of cycles required for each DFN realization to impose the desired horizontal stress changes (i.e., decrease due to glacial advance and increase due to glacial loading), these were then applied with the established boundary condition displacement rates to the UDEC models. Specifically, these were added to the permafrost case for Year 20,000 after first extending the model to account for strength degradation up to Year 50,000. Note that for this modelling exercise, permafrost preceding glaciation is assumed to act to inhibit the influence of any increase in glacial water table on effective stress within the permafrost zone. Glacial loading was then simulated at Year 50,000. Based on the Weichselian glacial cycle climate case (SKB TR-13-05; see also Figure 4), the glacial cycle was then concluded by simulating glacial unloading finishing at Year 65,000, followed by permafrost melting finishing at Year 66,000.

# 4. Analysis Results

## 4.1. Stability

Stability was evaluated by comparing the UDEC results for the block displacements and shear slip along fractures. History points were used to track displacements above each rock vault, similar to those that would be recorded using a multipoint extensometer. Also considered were the plastic yield indicators for the intact blocks, which was used as a proxy for stress-induced damage (i.e., EDZ). These different outputs were examined for each of the key time intervals modelled: i) Year 50, which encompasses rock vault construction and backfilling, ii) Year 1000, iii) Year 10,000, iv) Year 20,000 with permafrost followed by permafrost melting in Year 21,000, and v) Year 50,000 with glacial loading followed by glacial unloading and permafrost melting ending in Year 66,000. Each of the time intervals include the application of the strength degradation algorithm reported in the previous sections.

### 4.1.1. Year 50 - Construction and Backfilling

Existing SFR 1 Repository Case

The UDEC results for the SFR 1 case show that the rock vaults are stable after excavation and subsequent backfilling for each of the four DFN realizations modelled. This agrees with the experiences of the constructed SFR 1 for which there were no stability issues reported related to the rock vaults (SKB R-07-10). The maximum modelled displacements are less than 1 cm (Figure 37), and these are largely derived from localized slip along persistent fractures that intersect the excavations (Figure 38). Note that the figures shown here are for the DFN showing the largest displacements, which in this case is DFN 1-1 (Figure 18). The plots for all DFN realizations for the SFR 1 case are provided in Appendix 2.

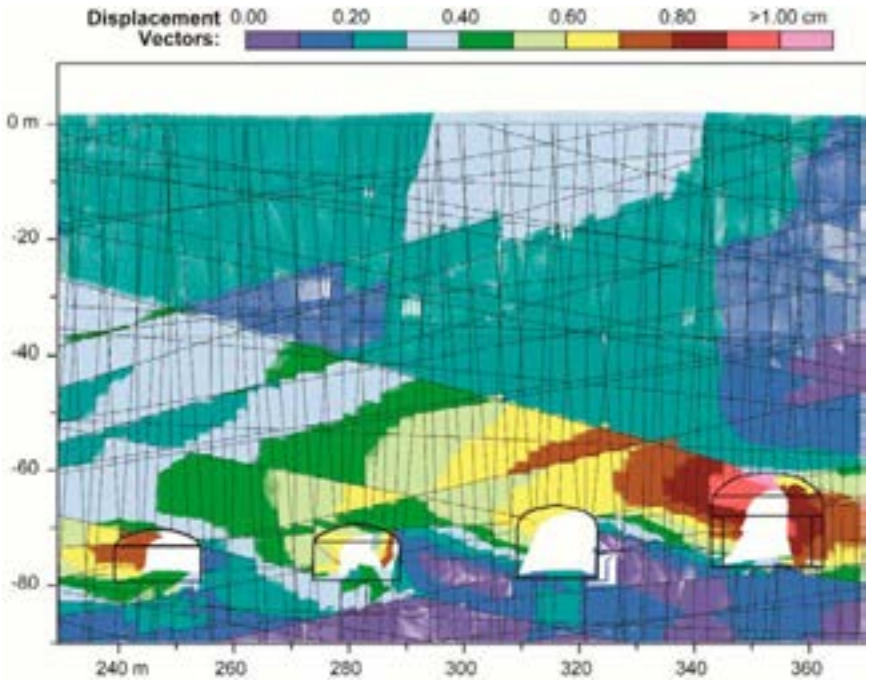


**Figure 37:** Displacement vectors for DFN 1-1 for the SFR 1 case, after excavation and backfilling.

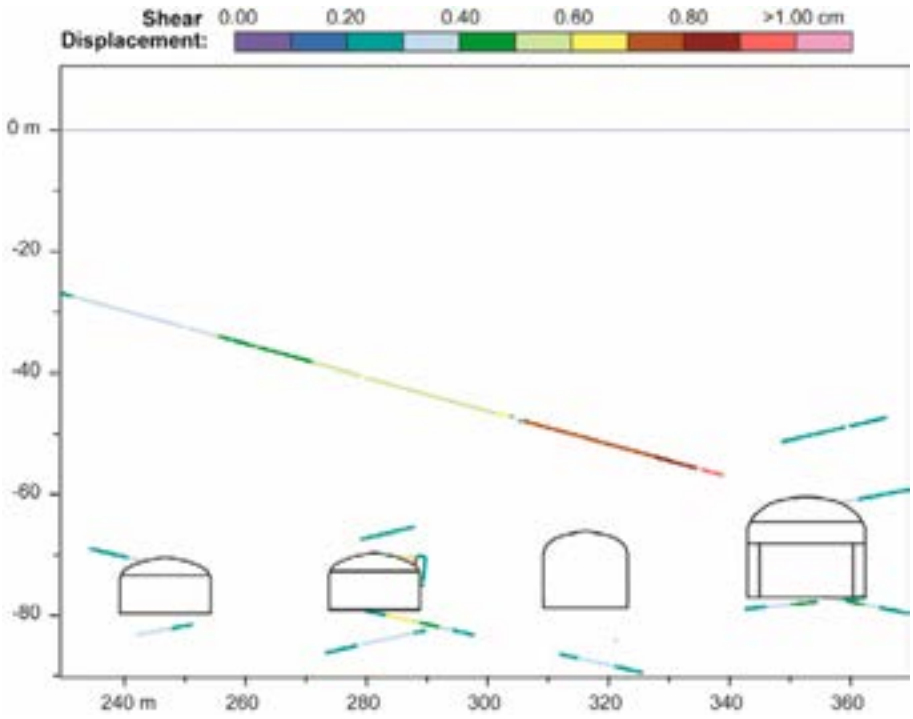


**Figure 38:** Shear displacements along fractures for DFN 1-1 for the SFR 1 case, after excavation and backfilling.

Outside of the localized slip along adversely dipping persistent structures, the modelled extensometer histories in the roof of each rock vault shows a generalized response of a millimetre or less of vertical convergence (Figure 39). Figure 40 provides the corresponding vertical displacement contours. These values are comparable to the SFR 1 construction experiences where extensometer measurements over a 10-year period (1997-2006) report deformations on the order of tenths of a millimetre (see Tables 8-1 and 8-2 in SKB R-07-10). It should be noted that the reported measurements are limited to those for the silo (see Figure 1) and the Singö deformation zone intersecting the SFR 1 access tunnel, neither of which are modelled here. Nevertheless, they represent measured deformations representative of the SFR 1 rock mass and stress conditions and provide an important measure of validation of the UDEC models.

With respect to plastic yielding and spalling of the intact blocks, the UDEC results indicate that the intact rock strength relative to the SFR 1 depth and in situ stress state is sufficient to limit spalling and stress-induced damage (Figure 41a). Some localized damage is observed due to geometrical effects relative to the high horizontal stresses especially where the arch of the top heading meets the walls of the 1BMA and 1BLA rock vaults. This effect increases when the overlying flat dipping deformation zone is in closer proximity to the rock vault excavations (Figure 41b). However, these effects are minor and suggest only superficial spalling at the corners. Thus, the modelled yield state and plasticity indicators are in agreement with the modelled deformations, as well as the construction observations and current operating state, and together indicate that the SFR 1 excavations after excavation and backfilling are stable.

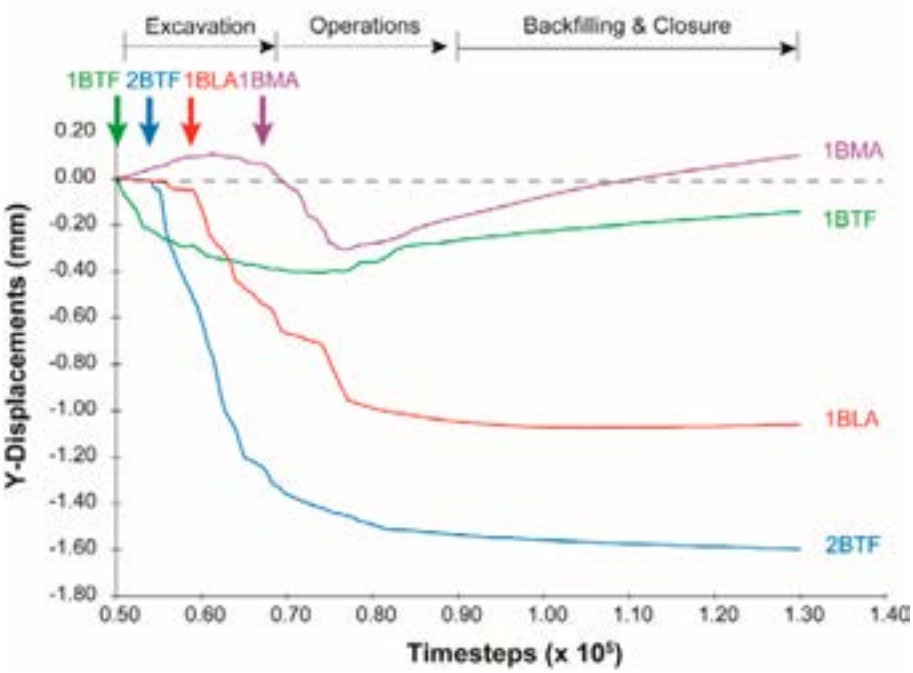


**Figure 39:** Vertical displacement histories for DFN 1-1 for the SFR 1 case for monitoring points 0.5 m above the roof of each rock vault excavation. Negative displacements are downwards.

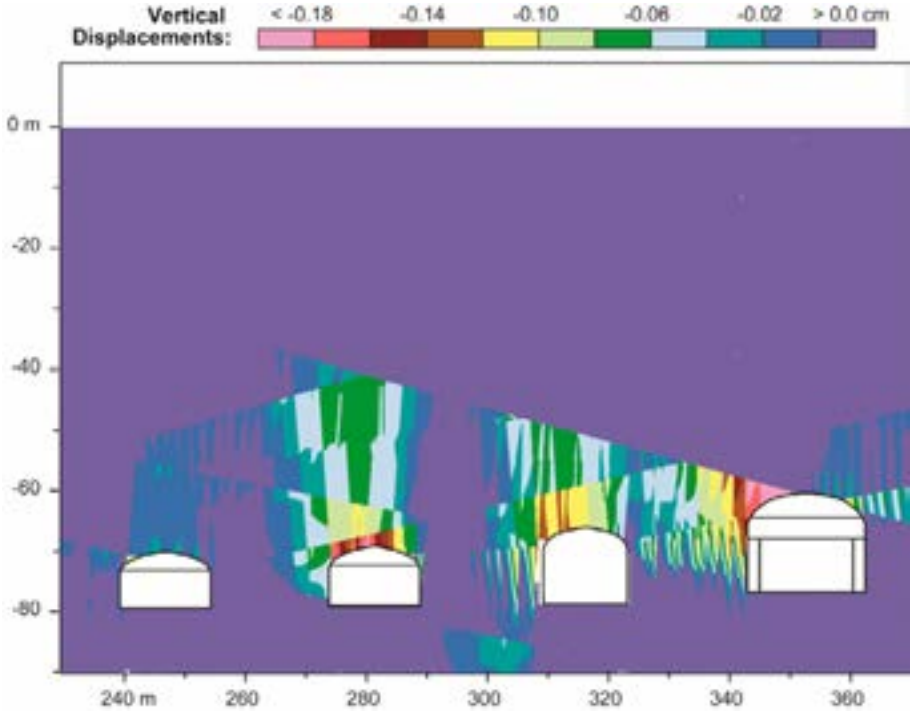


**Figure 40:** Vertical displacement contours for DFN 1-1 for the SFR 1 case, after excavation and backfilling. Negative displacements are downwards.

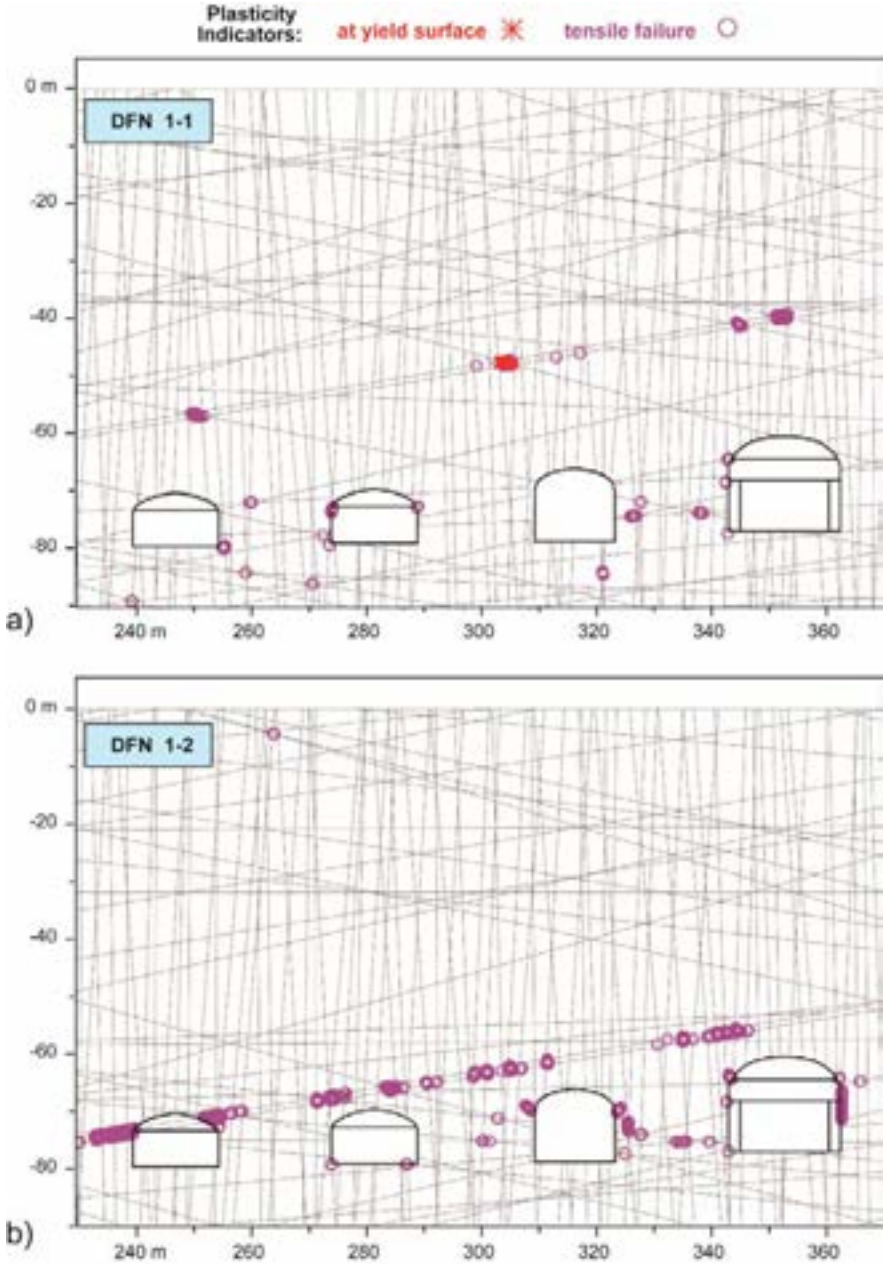


**Figure 41:** Plasticity indicators for: a) DFN 1-1 and b) DFN 1-2, comparing influence of proximity of the sub-horizontal dipping deformation zone to the rock vaults, for the SFR 1 case after excavation and backfilling.

Extended SFR 3 Repository Case

The UDEC results for the SFR 3 extension case suggest a similar response to excavation and backfilling as that for the SFR 1. The maximum displacements seen above the rock vaults are less than 2 cm when including small wedge movements (Figure 42) and less than 1 cm involving localized slip along adversely dipping persistent joints (Figure 43). As before, these figures are for the DFN realization showing the largest displacements, which in this case is DFN 3-2 (see Figure 19). The plots for all DFN realizations for the SFR 3 case are provided in Appendix 3.

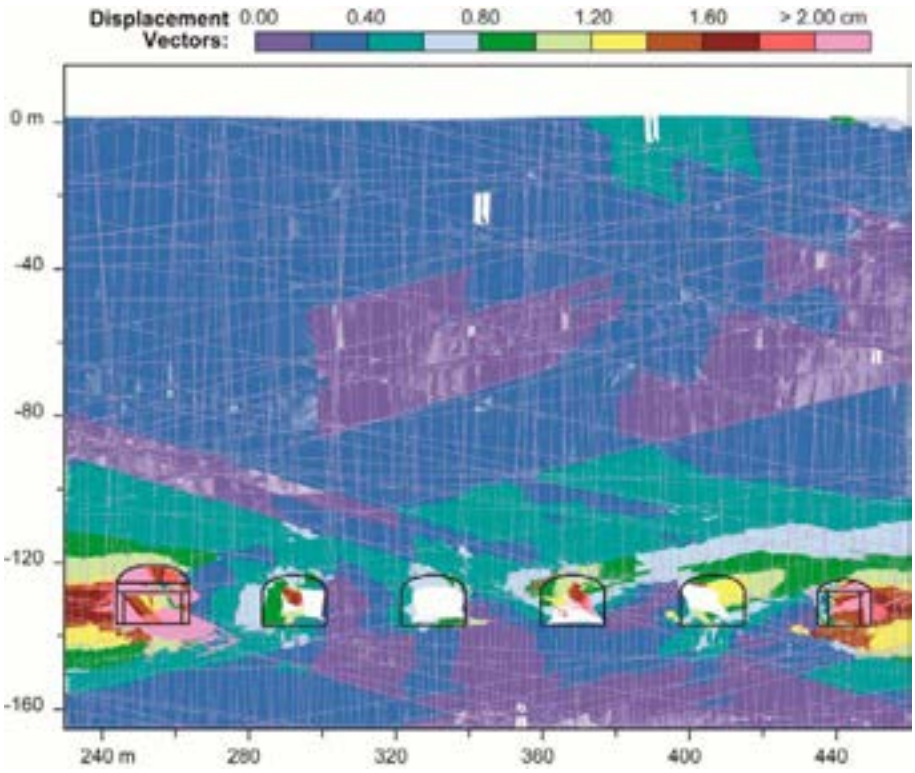


**Figure 42:** Displacement vectors for DFN 3-2 for the SFR 3 case, after excavation and backfilling.

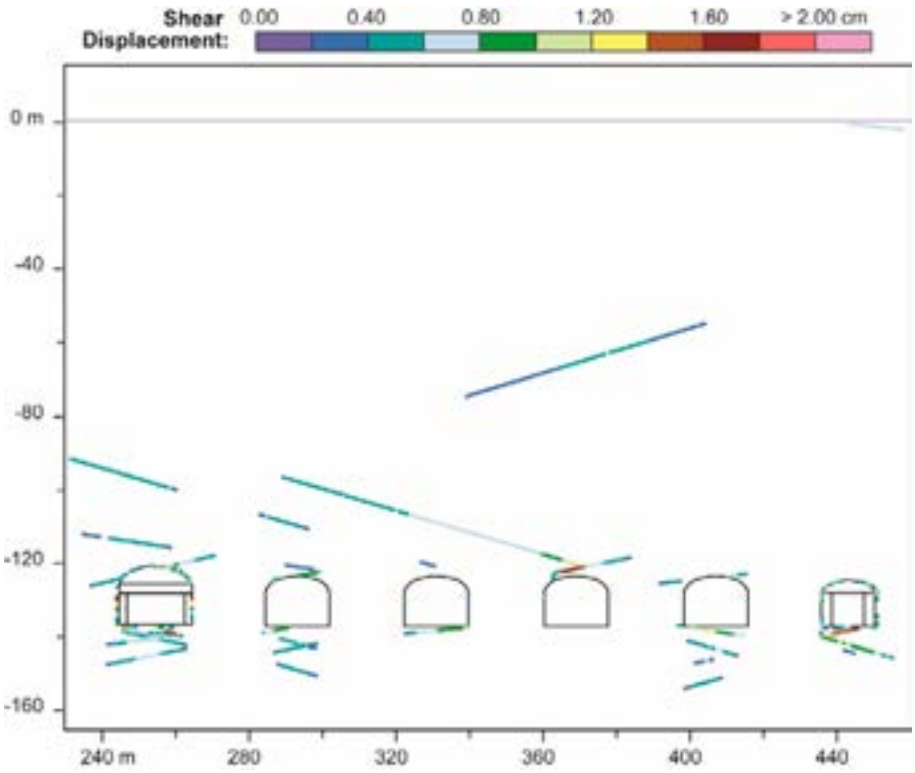


**Figure 43:** Shear displacements along fractures for DFN 3-2 for the SFR 3 case, after excavation and backfilling.

Similar to the SFR 1 case, the modelled extensometer histories in the roof of each rock vault for the SFR 3 layout shows a generalized vertical convergence response of less than a millimetre (Figure 44). Figure 45 provides the corresponding vertical displacement contours. Again, these values are comparable to the extensometer measurements made during construction of the SFR 1, which involve deformations of less than 1 mm over a 10-year period (SKB R-07-10).

With respect to plastic yielding and spalling of the intact blocks, the UDEC results for the SFR 3 extension case indicate a small increase in tensile spalling relative to the SFR 1 case (Figure 46). These are generally localized along the top arches of each rock vault and where the top headings meet the walls. This increase in spalling potential results from the slightly greater depth of the planned SFR 3 extension (i.e., 60 m deeper).

As in the case of the SFR 1, this spalling is mostly superficial and all other indicators suggest that the SFR 3 rock vaults following construction and during observations and backfilling (i.e., Year 50 in the UDEC model timeline) will be stable. This was consistently observed for each of the four DFN realizations modelled for the SFR 3 case (see Appendix 3). It should be noted that unlike the SFR 1 case where the four different DFN realizations also included varying positions for the sub-horizontal dipping deformation zone, the positions of the two SBA fracture zones crossing the SFR 3 case geometry were kept the same. The only difference between the SFR 3 models is owing to the DFN generated for each using the same statistical input.

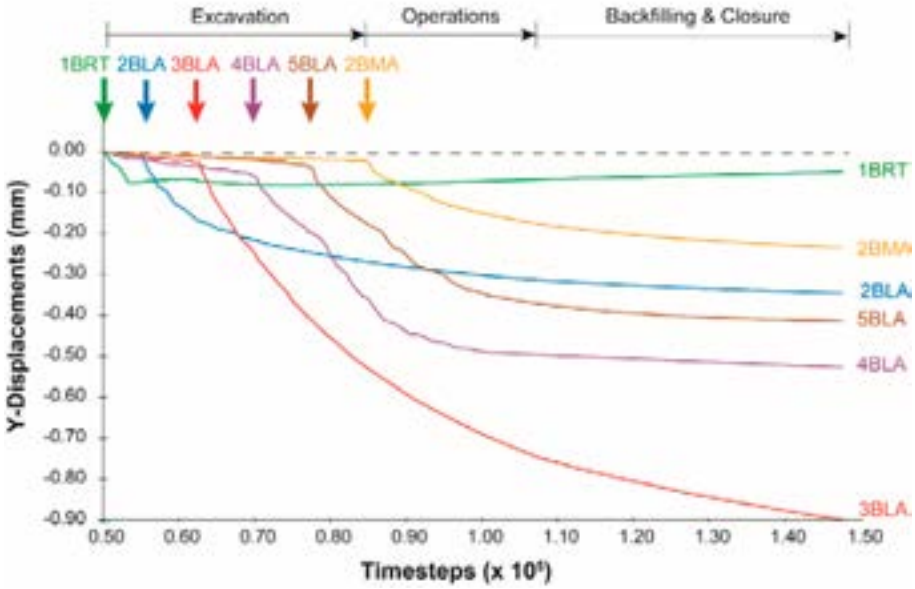


**Figure 44:** Vertical displacement histories for DFN 3-2 for the SFR 3 case for monitoring points 0.5 m above the roof of each rock vault excavation. Negative displacements are downwards.

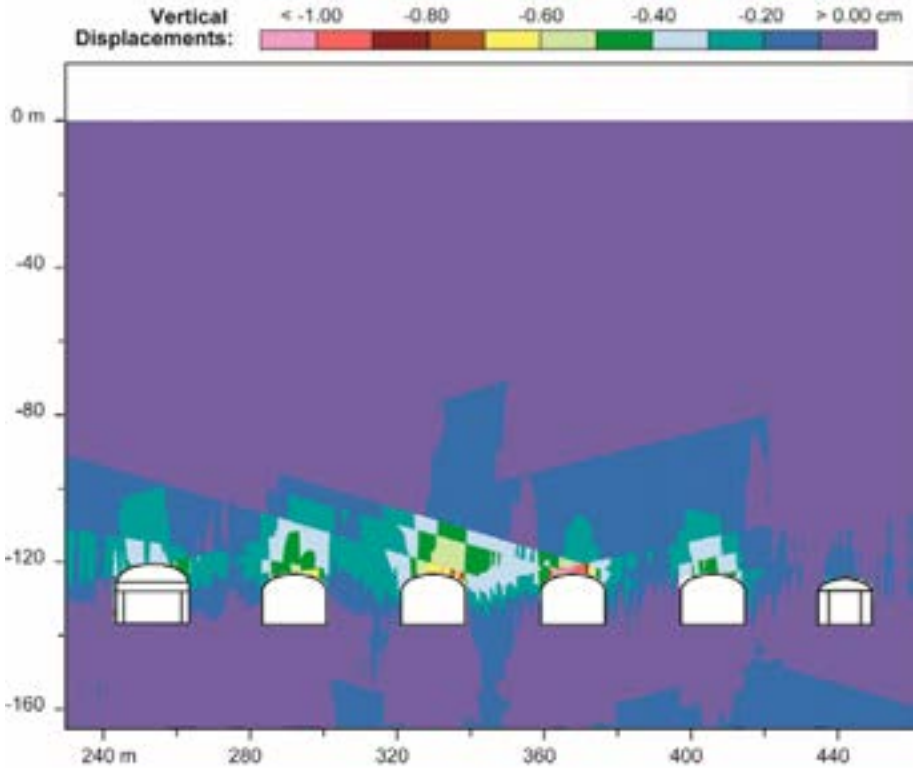


**Figure 45:** Vertical displacement contours for DFN 3-2 for the SFR 3 case, after excavation and backfilling. Negative displacements are downwards.

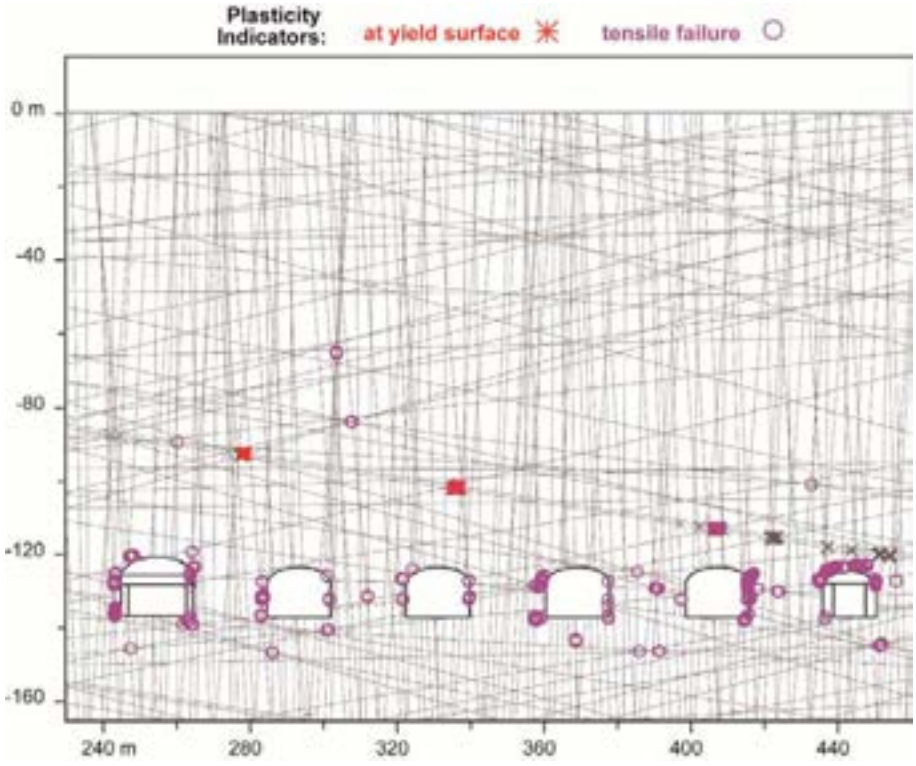


**Figure 46:** Plasticity indicators for DFN 3-2 for the SFR 3 case, after excavation and backfilling.

### 4.1.2. Year 1000 and 10,000 - Strength Degradation

In terms of overall stability, the UDEC results for modelling the long-term strength degradation between 1000 and 10,000 years do not show any indications of major failure or collapse above the SFR 1 or SFR 3 rock vaults. Instability is limited to only a small number of wedge failures that develop. With time, the amount of stress-induced damage in the intact rock blocks increases, as does the number of fractures along which shear develops. However, stability is maintained. Recall that both intact rock and fracture strength degrade with time at a rate directly dependent on driving differential stress or shear stress (relative to strength) and the confinement or normal stress. Figure 47 compares the results showing the tensile yielding for the intact rock blocks and shear along fractures for the SFR 1 case after 1000 and 10,000 years. These are for the DFN realization showing the largest displacements, which in this case is DFN 1-2 where the presence of a deformation zone several meters above the 1BMA rock vault works to concentrate the high horizontal stresses present resulting in increased tensile yield after 10,000 years of strength degradation. Note that the tensile yield indicators provide an indication for stress-induced spalling. Figure 48 provides the results for SFR 3, which in this case is DFN 3-2. Included with these figures are the results after excavation and backfilling (Year 50) for reference.

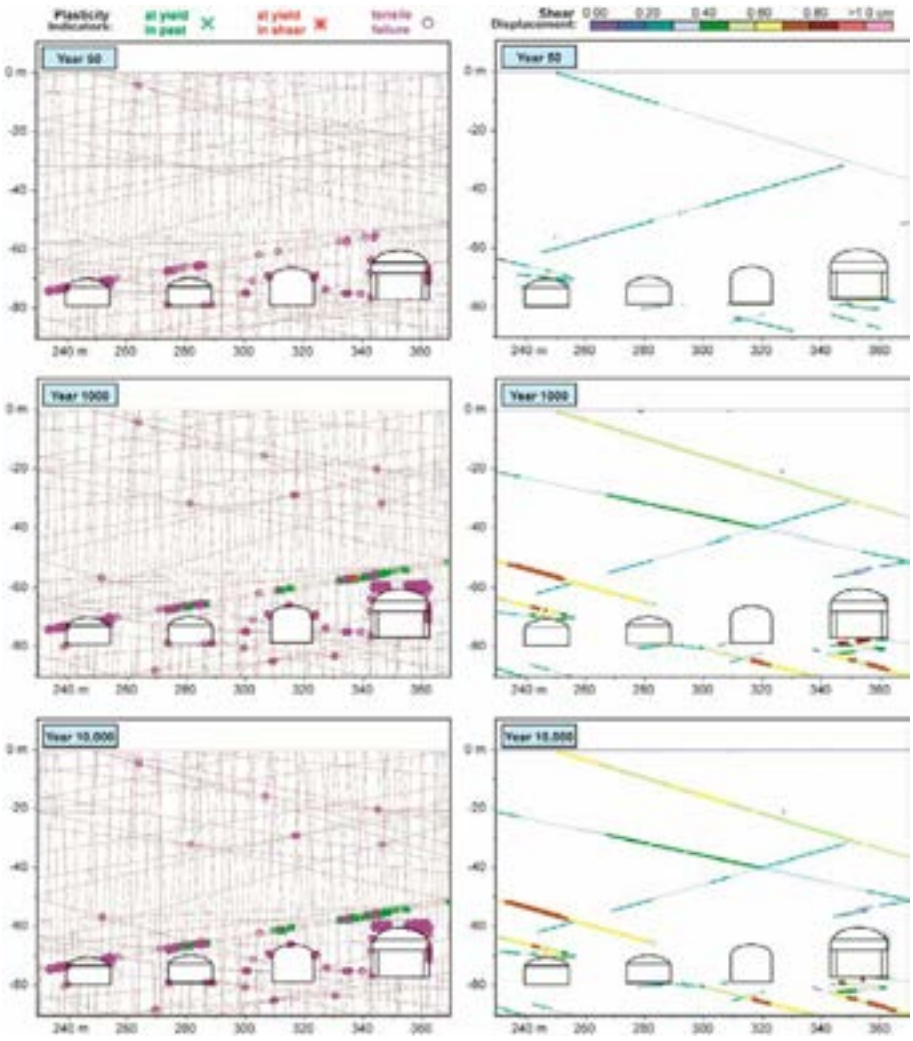


**Figure 47:** Comparison of intact rock yielding (left column) and fracture shear (right column) with increasing strength degradation over time for the SFR 1 case (DFN 1-2).

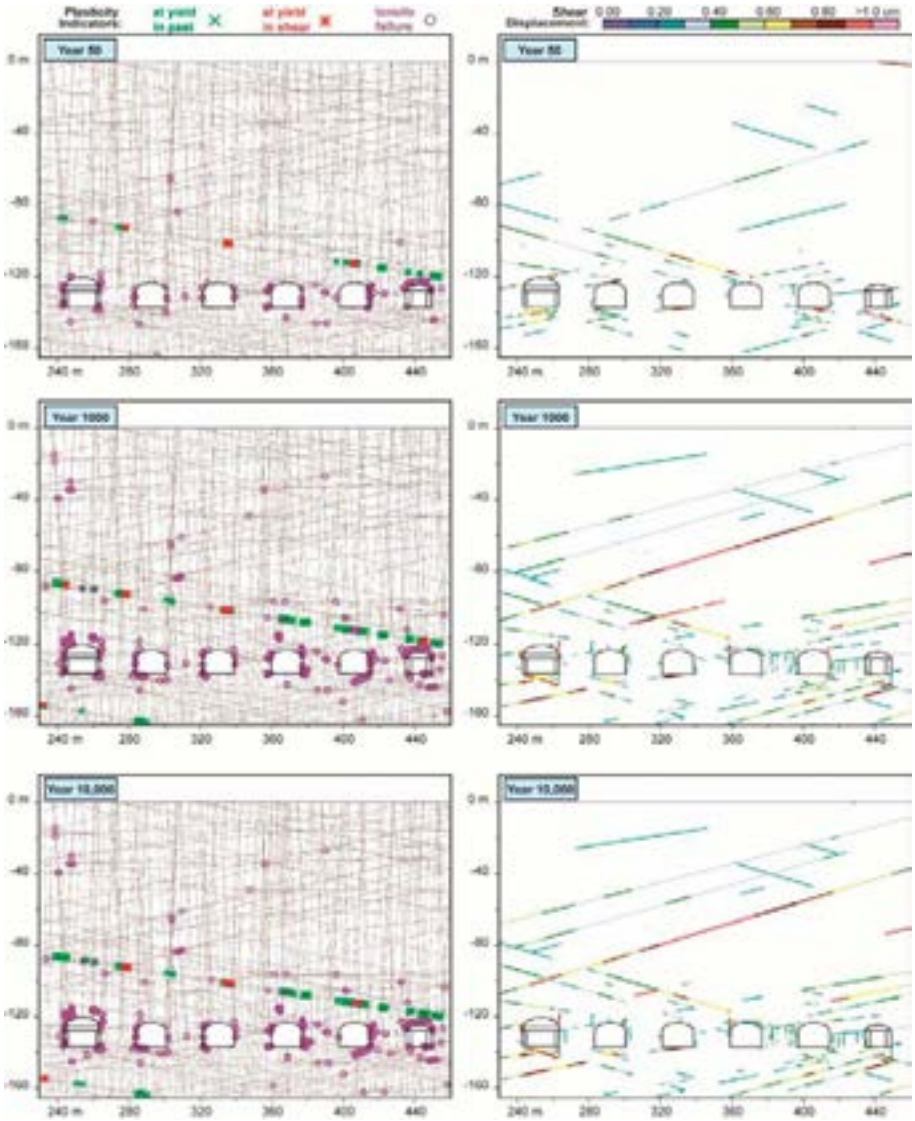

**Figure 48:** Comparison of intact rock yielding (left column) and shear displacements along fractures (right column) with increasing strength degradation over time for the SFR 3 case (DFN 3-2).

The UDEC results show that stability is primarily maintained due to the high horizontal stresses that exist above the roof of each rock vault (Figure 49). This results in high normal stresses acting across the sub-vertical fractures along which slip release is required for failure to occur. The high horizontal stresses also limit the degree of strength degradation that develops along the fractures. As previously discussed, the strength degradation logic is stress dependent and, in the case of the fracture network, requires the driving shear stress to exceed a strength threshold (based on normal stress as well as fracture cohesion and friction) before strength degradation can occur. The rate of degradation is a function of both the driving stress (versus initial strength) and the level of normal stress. This results in a heterogeneous distribution of reduced fracture strengths for each modelled time interval. The UDEC models indicate that sub-horizontal fractures are more susceptible to strength degradation than the sub-vertical fractures (Figure 50). This facilitates activation of localized wedges in the roofs above the rock vaults, but again, not to the extent of catastrophic collapse. Stress shadowing effects in the

pillars between the rock vaults initially shield them from stress-induced damage and strength degradation. However, with time and increasing strength degradation potential, the reduced normal stresses (i.e., confinement) acting on vertical fractures in the pillar allows damage to initiate, and by Year 10,000 significant strength degradation has accumulated in the pillars (Figure 50), resulting in dilation (i.e., bulking) towards the rock vaults, but again, not to the extent that catastrophic failure occurs. Figure 51 provides the results showing the strength degradation for the SFR 3 case, DFN 3-2.

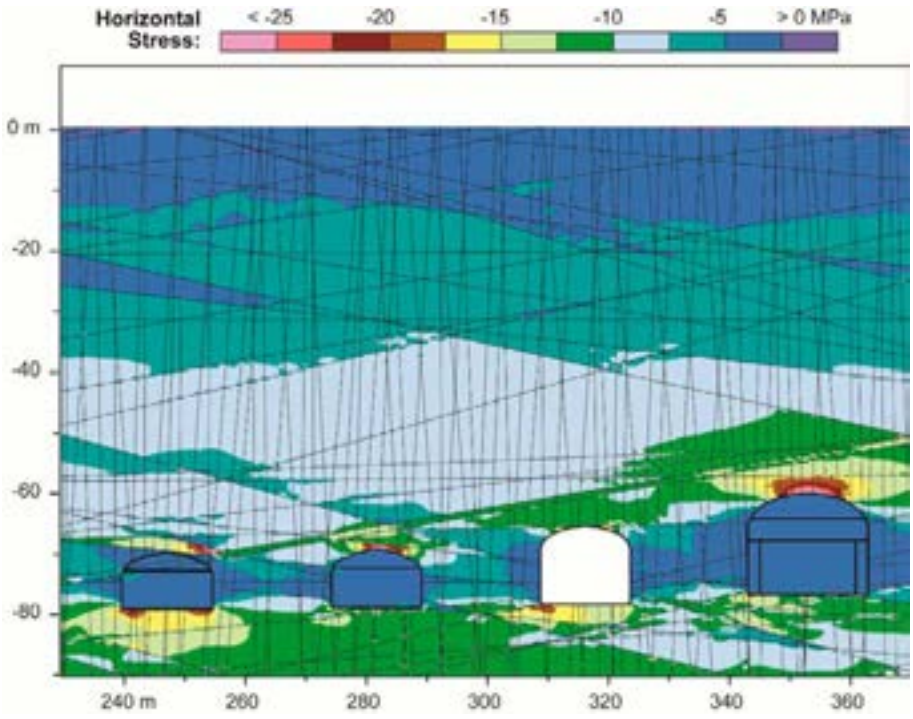


**Figure 49:** Horizontal stress contours for DFN 1-2 for the SFR 1 case at Year 10,000. Compressive stresses are negative.

Comparatively, the results for SFR 3 show a marginally higher degree of strength degradation than the SFR 1 case (compare Figure 51 to Figure 50). This is likely due to the slightly greater depth, larger number of non-backfilled BLA rock vaults, and larger number of rock vault excavations in total. The history plot of displacements above the SFR 3 rock vaults for DFN 3-2 are shown in Figure 52. These show a general trend of upward rebound (reflecting gradual movement on sub-horizontal and shallow dipping structures) with a rate that decreases over the 10,000 year period. However, above 5BLA and 3BLA, two large wedge instabilities initiate that are approximately 5 m high (Figure 53). These are localized and do not fully fail due to the high horizontal clamping stresses that help to hold the wedges in place. Overall stability is maintained.

The complete results for the UDEC 1000 and 10,000 year strength degradation models, showing the stresses, displacements, plasticity indicators, and shear slip along fractures are provided for all four DFNs for SFR 1 in Appendix 2. The results for all four DFNs for the SFR 3 case are provided in Appendix 3.

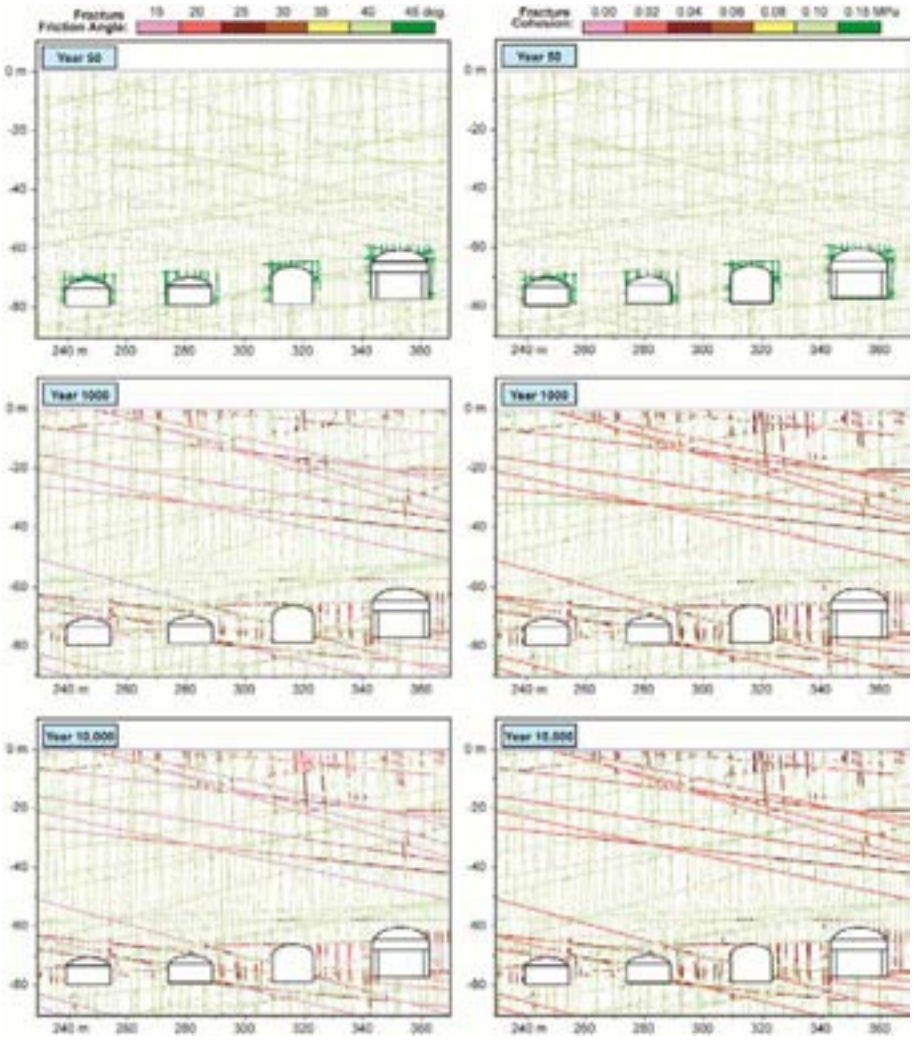


**Figure 50:** Comparison of fracture friction angle and cohesion values resulting from application of the strength degradation algorithm for the SFR 1 case (DFN 1-2). Results are shown for Year 50, 1000 and 10,000, and identify fractures where the driving and confining stress magnitudes meet the conditions required for strength degradation to occur.

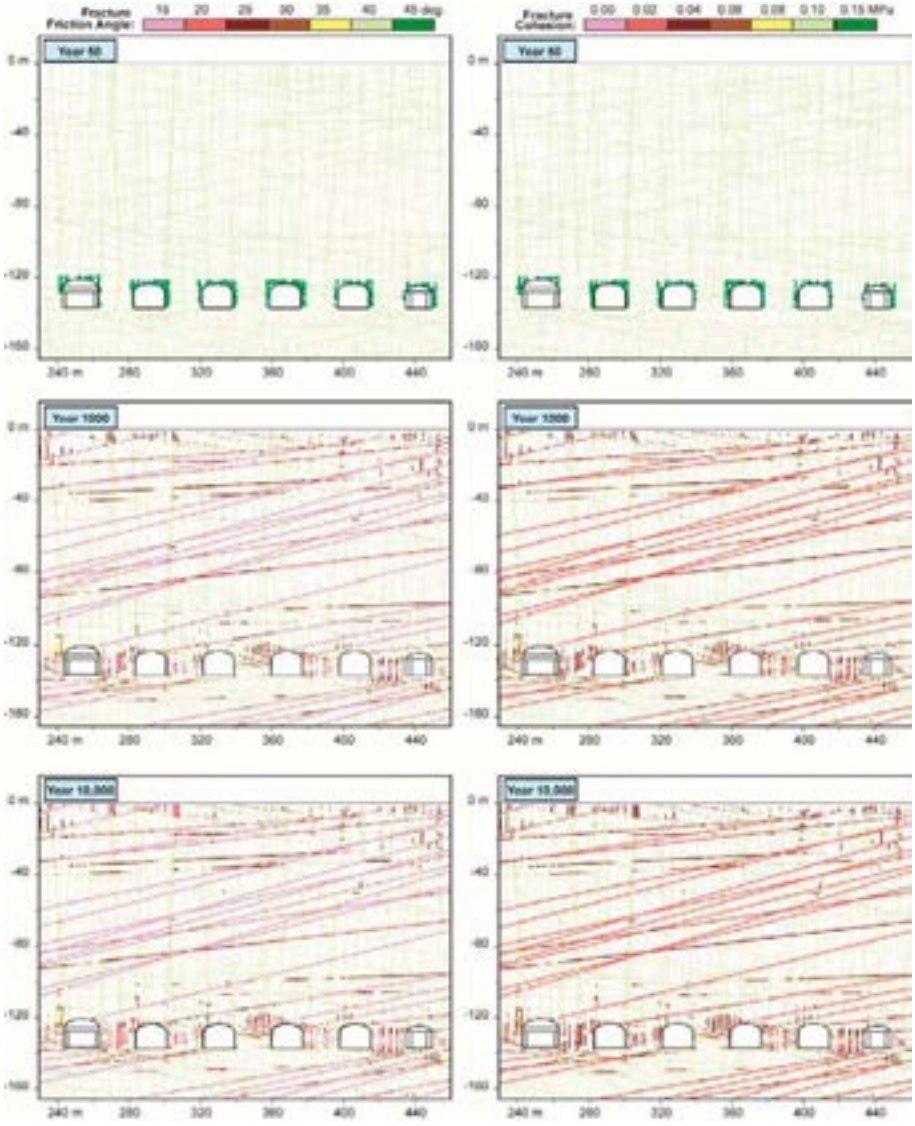


**Figure 51:** Comparison of fracture friction angle and cohesion values resulting from application of the strength degradation algorithm for the SFR 3 case (DFN 3-2). Results are shown for Year 50, 1000 and 10,000, and identify fractures where the driving and confining stress magnitudes meet the conditions required for strength degradation to occur.

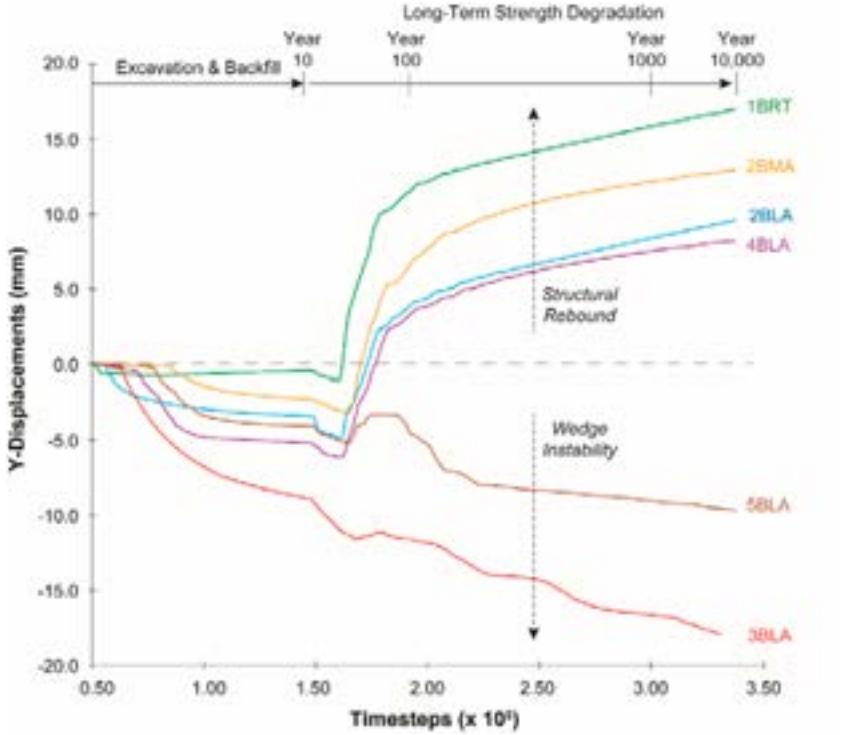


**Figure 52:** Vertical displacement histories for DFN 3-2 for the SFR 3 case after 10,000 years of strength degradation. Monitoring points are located 0.5 m above the roof of each rock vault. The structural rebound observed arises due to horizontal stress related shear on shallow dipping structures creating upward movement. Negative displacements are downwards.

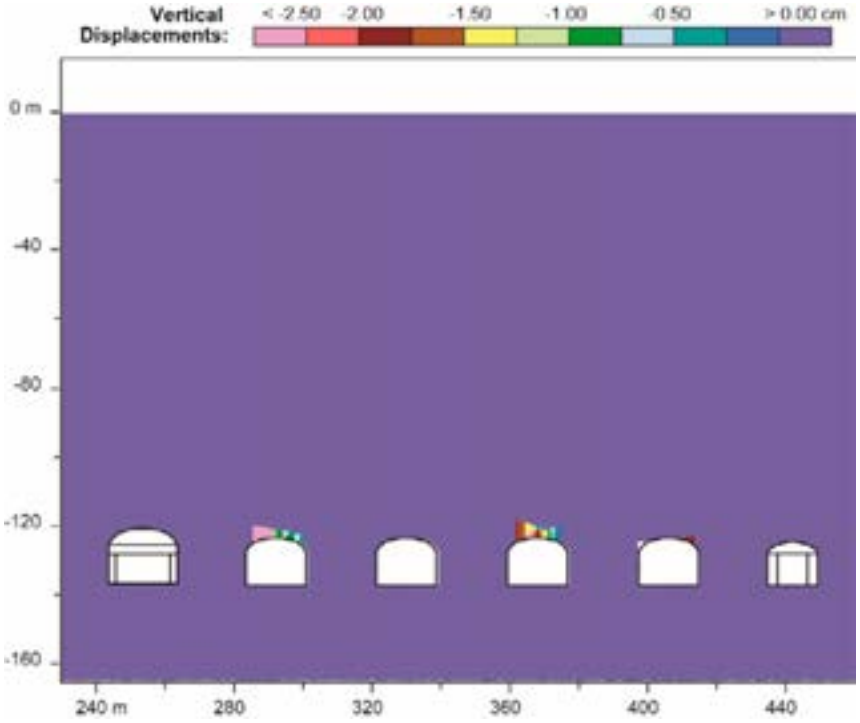


**Figure 53:** Vertical displacements showing largest wedge instabilities that develop for the SFR 3 case (DFN 3-2) after 10,000 years of strength degradation. In this case, wedges approximately 5 m high develop above 5BLA and 3BLA (see also history plots in Figure 52). Negative displacements are downwards.

### 4.1.3. Year 20,000 – Permafrost and Permafrost Melting

The simulation of permafrost at Year 20,000 and permafrost melting in Year 21,000 was seen to have only a minor effect on the models with respect to stability. It should be recalled that the permafrost modelling procedure involved adding a small amount of fracture cohesion (0.5 MPa) and a 10% increase in fracture pressure to simulate the freezing of water and expansion of ice in the fracture network in the permafrost zone. Therefore, the effects of permafrost, as modelled, involved an increase in fracture strength that helped to counteract any adverse effects the simultaneous increase of fracture pressure might have.

Existing SFR 1 Repository Case

Figure 54 shows the vertical displacement histories for the simulated multipoint extensometers above the SFR 1 rock vaults, for each of the four DFN realizations modelled. These show that stability is maintained during both permafrost and permafrost melting. Permafrost melting includes the removal of the fracture cohesion added to simulate the strength of an ice-filled fracture, and return of the fracture pore pressures to a hydrostatic state. This results in a minor vertical convergence towards the rock vaults (deflection at Year 21,000 in Figure 54). In a few cases, small wedge failures developed in response to the continued strength degradation modelled to 21,000 years combined with the temporary relaxation of normal stresses along fractures with the simulated melting of the permafrost ice.

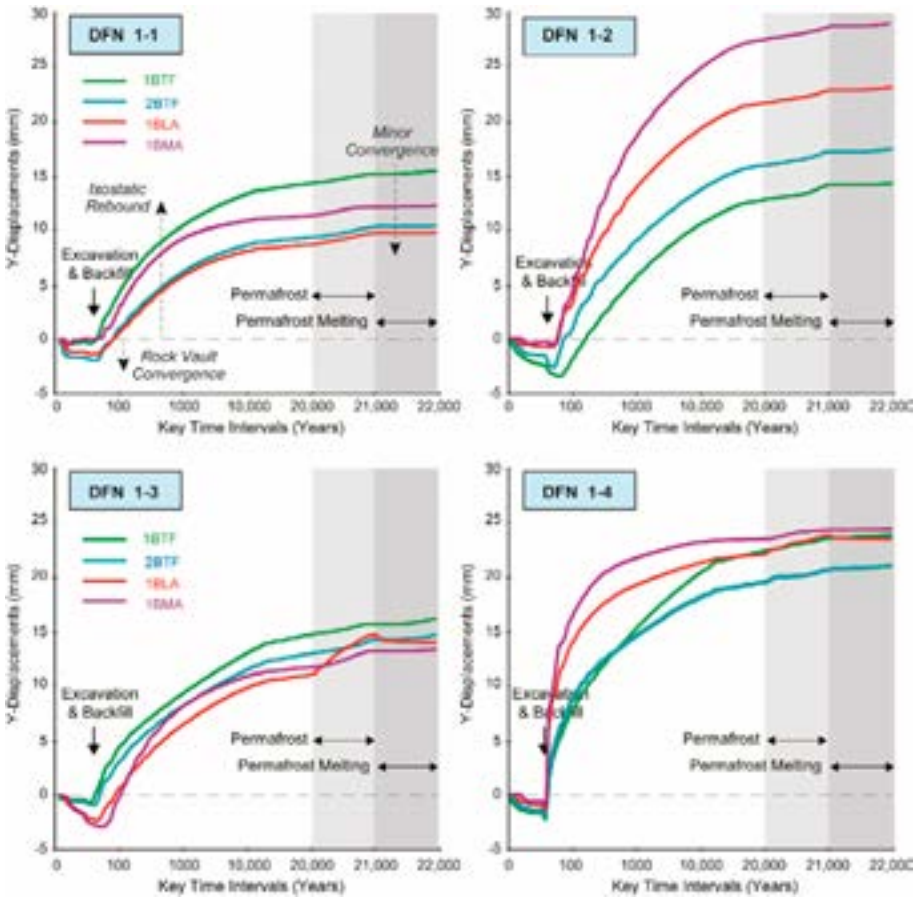


**Figure 54:** Vertical displacement histories for the four DFN realizations modelled for SFR 1 after permafrost (Year 20,000) and permafrost melting (Year 21,000), in parallel with strength degradation. Monitoring points are located 0.5 m above the roof of each rock vault. Note that down is in the negative Y-direction.

Extended SFR 3 Repository Case

The SFR 3 models also showed that stability was largely maintained during permafrost and permafrost melting. One exception was the case of DFN 3-1, where a large wedge/block failure occurs in rock vault 2BLA (Figure 55a,b). This was seen to initiate and develop in response to the simulated strength degradation between Years 10,000 and 20,000. The failure process is temporarily slowed due to the small increase in fracture cohesion added during permafrost freezing (Figure 56; see DFN 3-1). Failure then resumes and increases in extent during permafrost melting in Year 21,000 as the permafrost-enhanced fracture cohesion is removed and the normal stresses acting on the fractures relax in response to ice pressures returning to their hydrostatic levels upon melting. In total, the failure zone extends 12 m across the width of the rock vault and propagates 1-3 m into the roof. A stable arch was subsequently re-established in the roof and the failure did not propagate further. Ultimately, the failure mode and extent in this case is due to the combination of fracture orientations and intersections specific to the DFN realization as the same failure did not develop in the other three DFN realizations. Two similar sized instabilities were seen to be developing for the DFN 3-2 case above 5BLA and 3BLA (Figure 55c). However, these were still marginally stable at Year 21,000 (Figure 56; see DFN 3-2). The complete UDEC results subsequent to permafrost melting (Year 21,000) for the SFR 1 and SFR 3 cases are provided in Appendix 2 and 3, respectively.

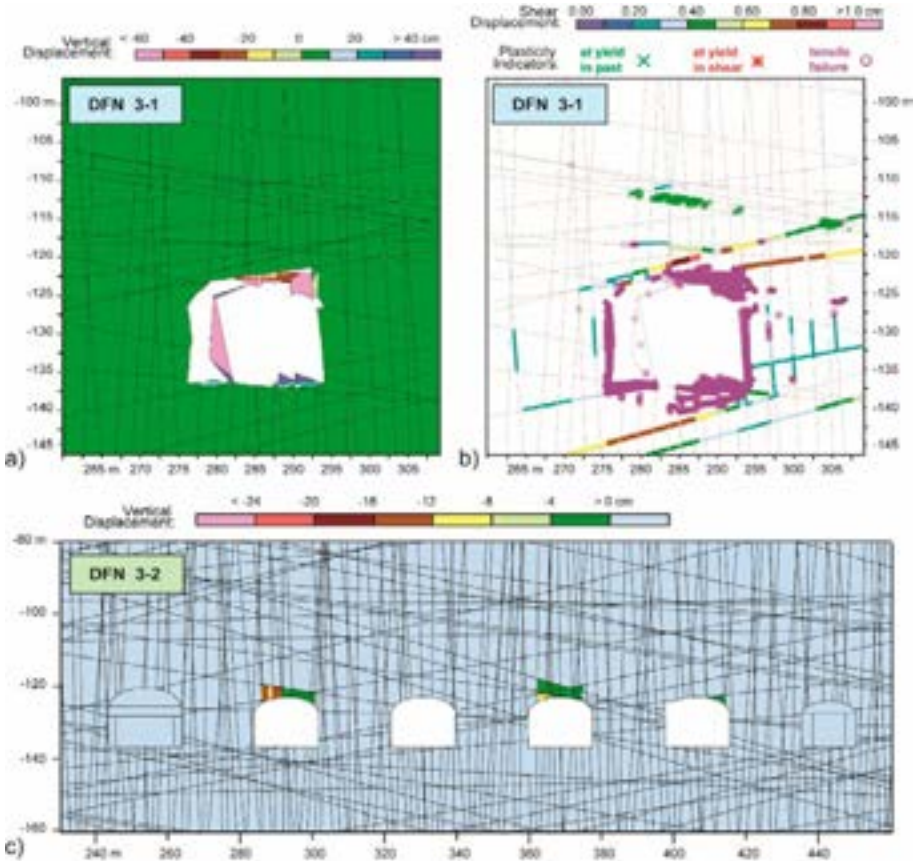


**Figure 55:** Examples of roof instabilities that develop for the SFR 3 case after strength degradation, permafrost and permafrost melting (Year 21,000): a) Vertical displacements showing roof failure above the 2BLA rock vault for DFN 3-1. b) Corresponding intact block yielding (spalling) and shear displacements along fractures. c) Roof instabilities developing above 5BLA and 3BLA for DFN 3-2. Negative displacements are downwards.

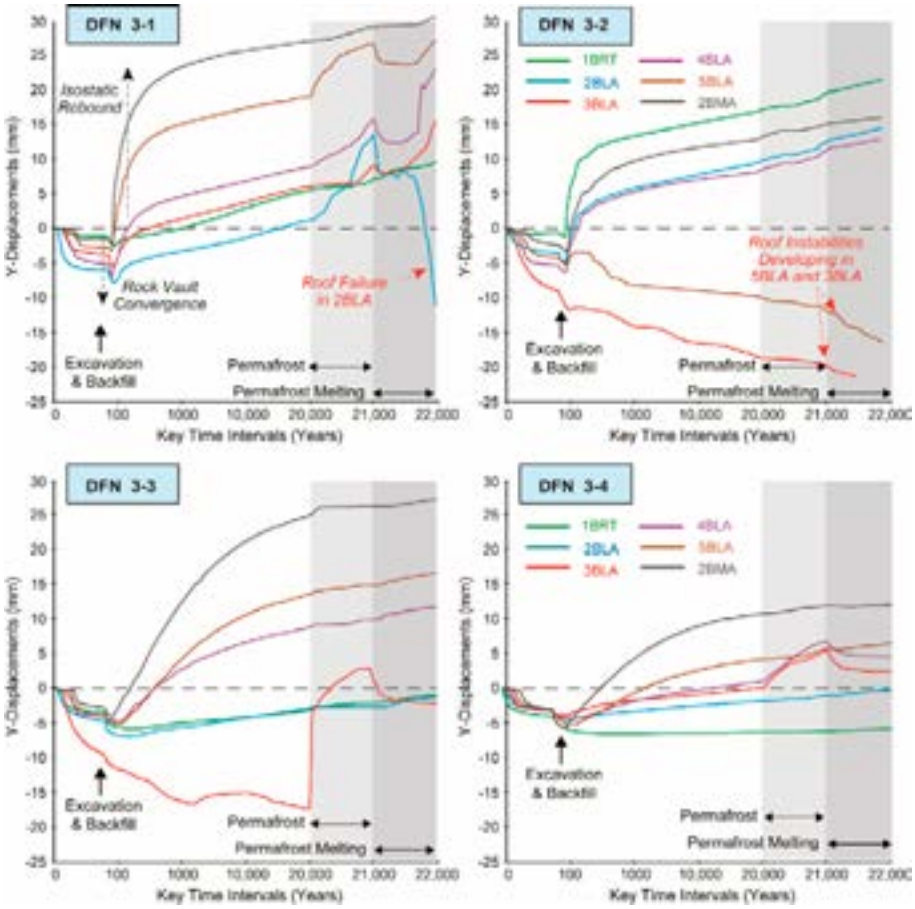


**Figure 56:** Vertical displacement histories for the four DFN realizations modelled for SFR 3 after permafrost (Year 20,000) and permafrost melting (Year 21,000), in parallel with strength degradation. Monitoring points are located 0.5 m above the roof of each rock vault. Note that down is in the negative Y-direction.

### 4.1.4. Year 50,000 to 66,000 – Glacial Loading and Unloading

The Year 50,000 glacial loading model for SFR 1 and SFR 3 involves the extension of the Year 20,000 permafrost state. Thus, the glacial loading in this case is coincident with permafrost. Under this scenario, in addition to the small cohesive strength gain and ice pressure expansion added to the permafrost zone, it was assumed that the presence of permafrost precludes elevated pore pressures and increases in hydrostatic head due to glacial ponding.

Existing SFR 1 Repository Case

In Year 50,000, the application of glacial loading to the UDEC SFR 1 models results in a significant increase in vertical stresses, with the pillars between the rock vaults experiencing a stress increase from 2-8 MPa to 20-40 MPa. This five-fold increase in vertical stress, with the horizontal confining stresses remaining relatively unchanged (slight decrease as the glacial front approaches followed by a 50% increase, at 75 m depth), results in conditions that intensify the strength degradation process in the pillars. As a result, all sub-vertical fractures located within the pillars experience significant strength degradation, and subsequently, increased shear slip (Figure 57).

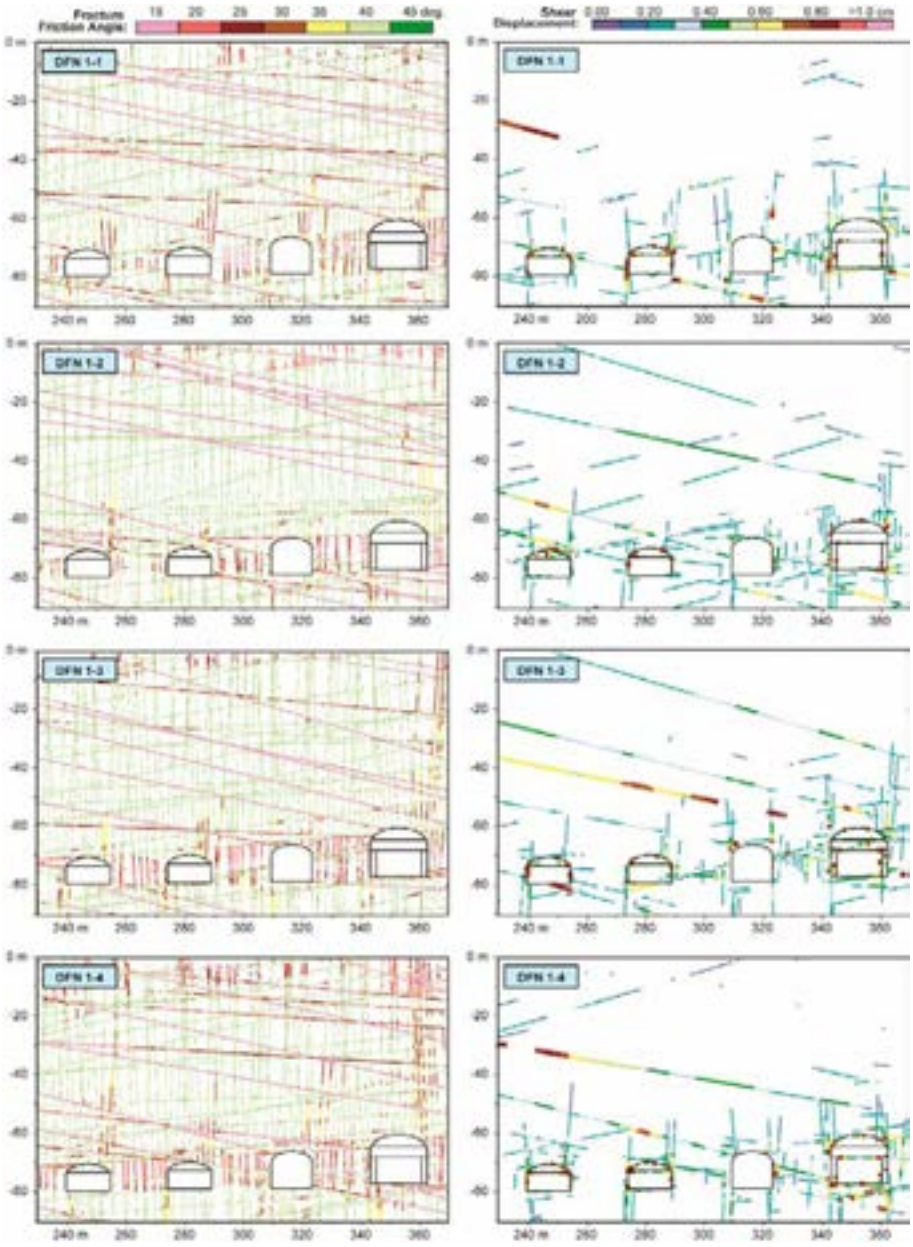


**Figure 57:** Comparison of strength degradation in the form of reduced fracture frictional strength (left column) and shear displacements along fractures (right column) resulting from glacial loading and time-dependent strength degradation over 50,000 years for the SFR 1 case.

Despite the advanced state of strength weakening in the pillars for the SFR 1 case, the orientation of these fractures relative to the excavations do not result in catastrophic failure. Instead, the history plots of vertical displacements in the roof above each rock vault (Figure 58) shows that integrity of the stabilizing arch is maintained. Again, because the permafrost is kept in place during glacial loading, the Year 50,000 model includes the accelerated time-dependent strength degradation that occurs, but also the small increase in cohesive strength provided by the permafrost. This contributes to the overall general stability for the SFR 1 case throughout glacial loading, with the exception of several small wedge failures that develop.

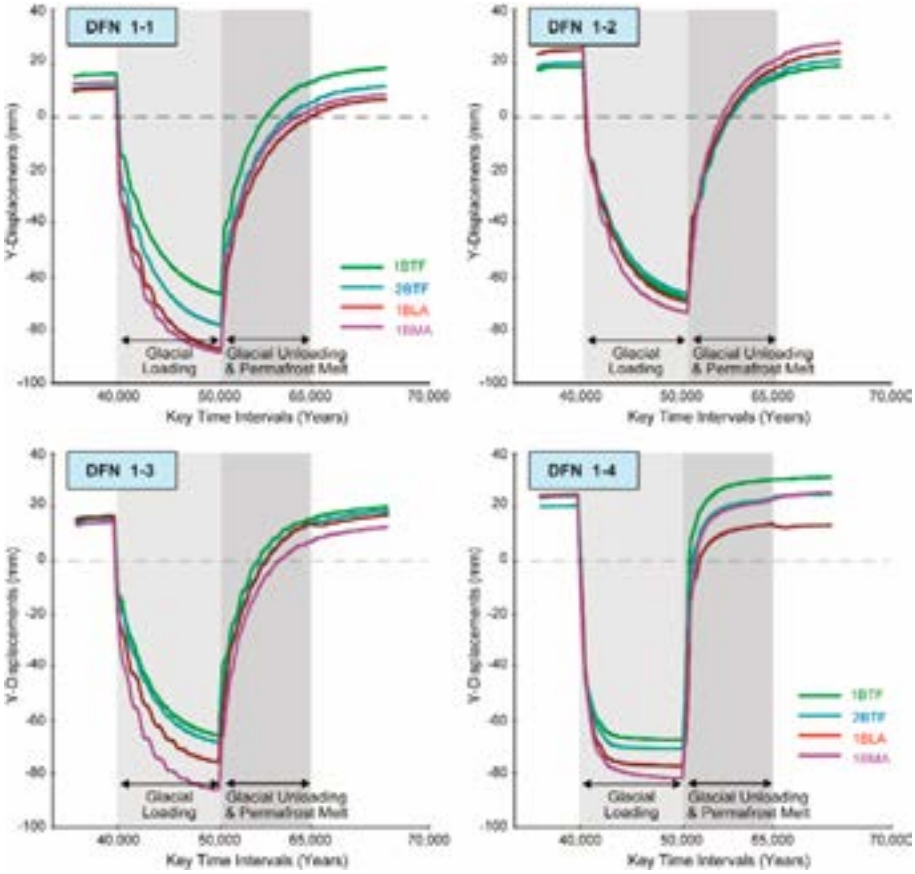


**Figure 58:** Vertical displacement histories for the SFR 1 UDEC models between Year 40,000 and 66,000, that encompasses glacial loading, glacial unloading and permafrost melting in parallel with time-dependent strength degradation. Monitoring points are located 0.5 m above the roof of each rock vault. Note that down is in the negative Y-direction.

The vertical displacement histories for SFR 1 in Figure 58 further show that stability is maintained for all four DFN realizations during subsequent glacial unloading and permafrost melting in parallel with strength degradation up to Year 66,000. These models were solved for an extended number of time-steps to confirm that the displacement trends in Figure 58 for each rock vault reach a stable equilibrium. The full results for the SFR 1 model series are included in Appendix 2.

Figure 59 shows the cumulative strength degradation in the near-field zone around the SFR 1 rock vaults as a function of the key time intervals over the full 66,000 year UDEC simulation. Shown are the percentages of fractures that experienced time-dependent shear strength decreases relative to the initial friction angle of 40 degrees at the time of excavation and backfilling. Also included is the percentage of intact block elements that yielded. Despite the significant increase in fractures that shear and reduce in strength to a friction angle of 15 degrees in response to glacial loading, unloading and permafrost melting (see Year 66,000 in Figure 59), kinematic stability is maintained because: i) the fractures most affected are sub-vertical and located in the pillars (Figure 57), which is kinematically favourable with respect to stability, and ii) the high horizontal stresses resulting from glacial unloading contribute to limiting the extent of block movements above the roofs of the rock vaults. With respect to intact rock failure, the stress conditions and degraded rock strengths are not adverse enough to allow spalling to develop and extend beyond a half meter into the rock from the boundaries of the excavations.

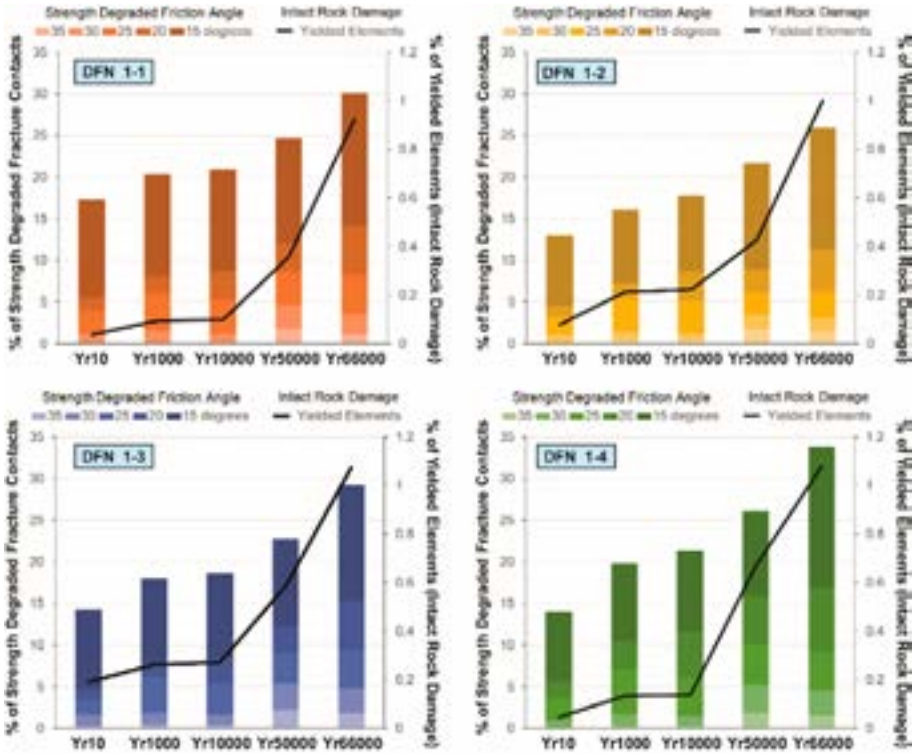


**Figure 59:** Comparison of cumulative strength degradation in the near-field zone around the SFR 1 rock vaults for several key time intervals over the full 66,000 year UDEC simulation. Shown are the percentages of fractures that experienced time-dependent shear strength decreases (relative to the initial friction angle of 40 degrees), and intact block elements that yielded. Note that the near-field zone in this case extends 10 m from the outer walls of the outside rock vaults and from 5 m below the rock vaults to the surface, encompassing approximately 60,000 fractures and 500,000 elements.

Extended SFR 3 Repository Case

A very different result was obtained for the SFR 3 case. Similar to the SFR 1 case, SFR 3 also underwent significant time-dependent strength degradation during the period of glacial loading leading to increased shear along adversely dipping fractures. As before, this was largely concentrated in the pillars between the rock vaults (Figure 60), in response to the five-fold increase in vertical stress they experience (Figure 61). Again, similar to the SFR 1 case, stability of the SFR 3 rock vaults was maintained during glacial loading despite the advanced state of strength weakening in the pillars. This can be seen in the vertical displacement histories for all for DFN realizations up to Year 50,000 (Figure 62).

However, the similarities between SFR 1 and SFR 3 begin to diverge with glacial unloading ending in Year 65,000. For the DFN 3-2 case, the same roof failure above 5BLA and 3BLA observed for the SFR 3 Year 21,000 permafrost melting case (Figure 55c) also develops and extends further. The vertical displacement histories for DFN 3-2 show that the uplift expected due to glacial unloading for these two rock vaults is countered by the downward movement of falling blocks in the roof (Figure 62). It should be noted that due to numerical convergence errors resulting from the large displacements and roof failures, the DFN 3-2 model could not be extended to the Year 65,000 permafrost melting scenario. The other three DFN realizations for SFR 3 were generally stable during glacial unloading outside of several small wedge failures, and these models were advanced to the final step of permafrost melting from Year 65,000 to Year 66,000.

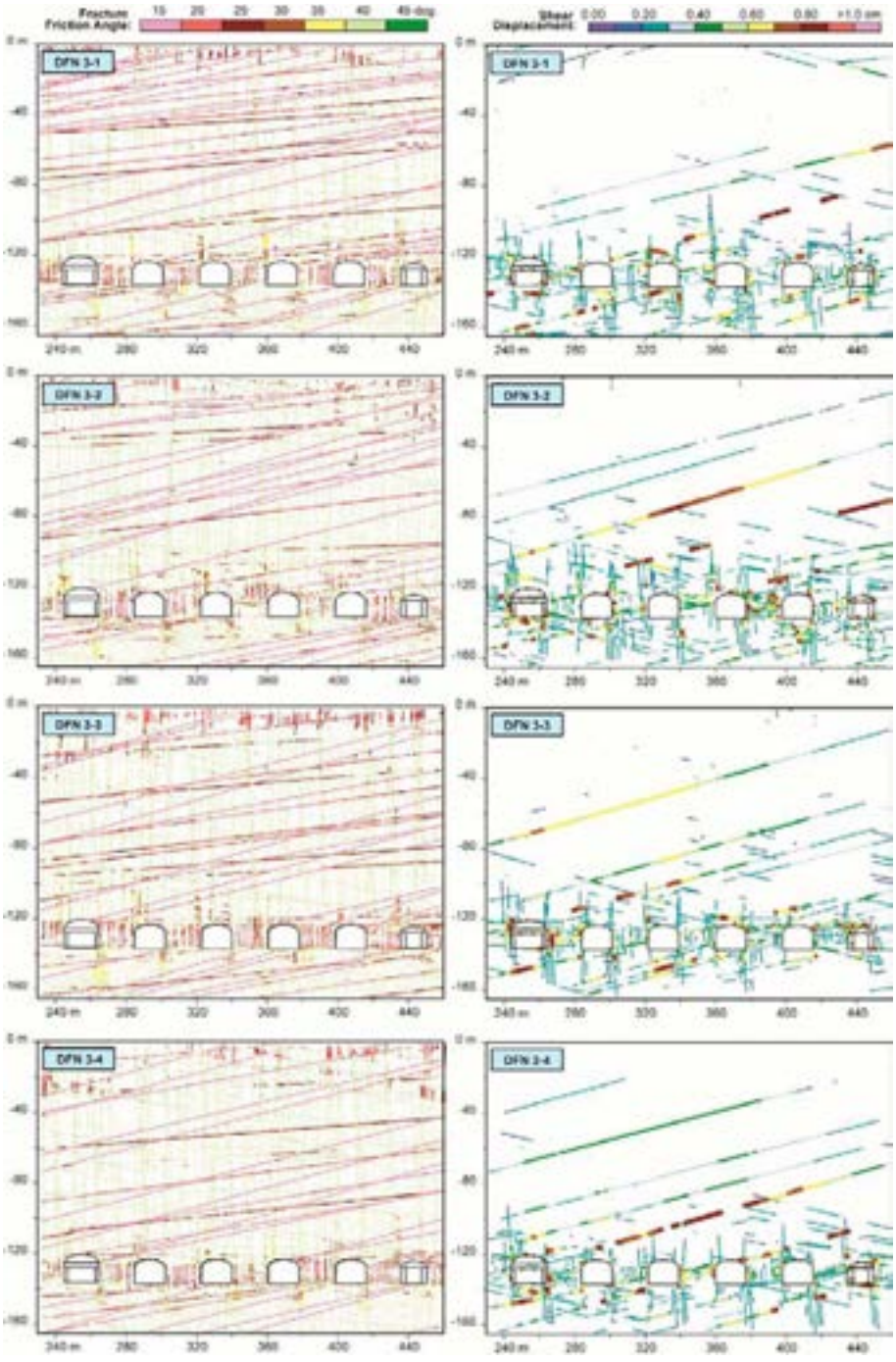


**Figure 60:** Comparison of strength degradation in the form of reduced fracture frictional strength (left column) and shear displacements along fractures (right column) resulting from glacial loading and time-dependent strength degradation over 50,000 years for the SFR 3 case.

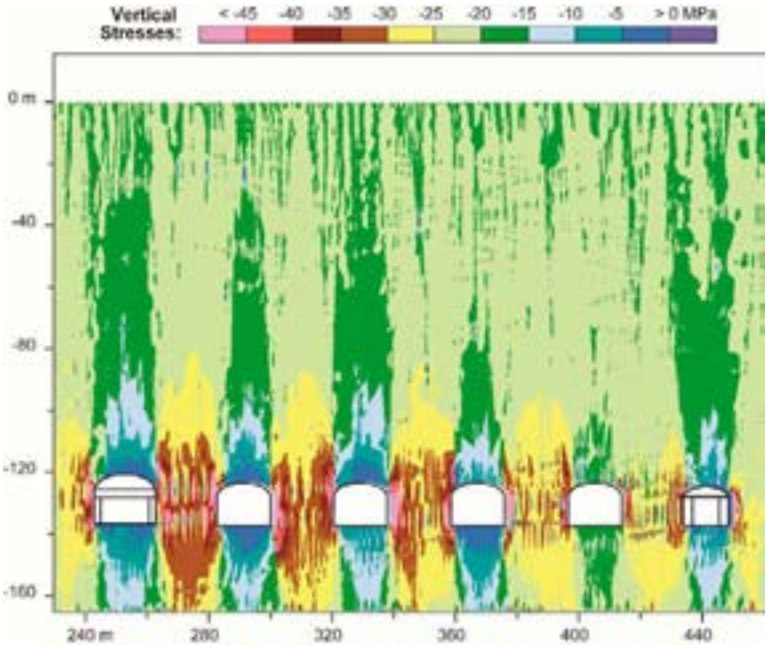


**Figure 61:** Vertical stress contours with glacial loading for DFN 3-3 for the SFR 3 case at Year 50,000. Compressive stresses are negative.

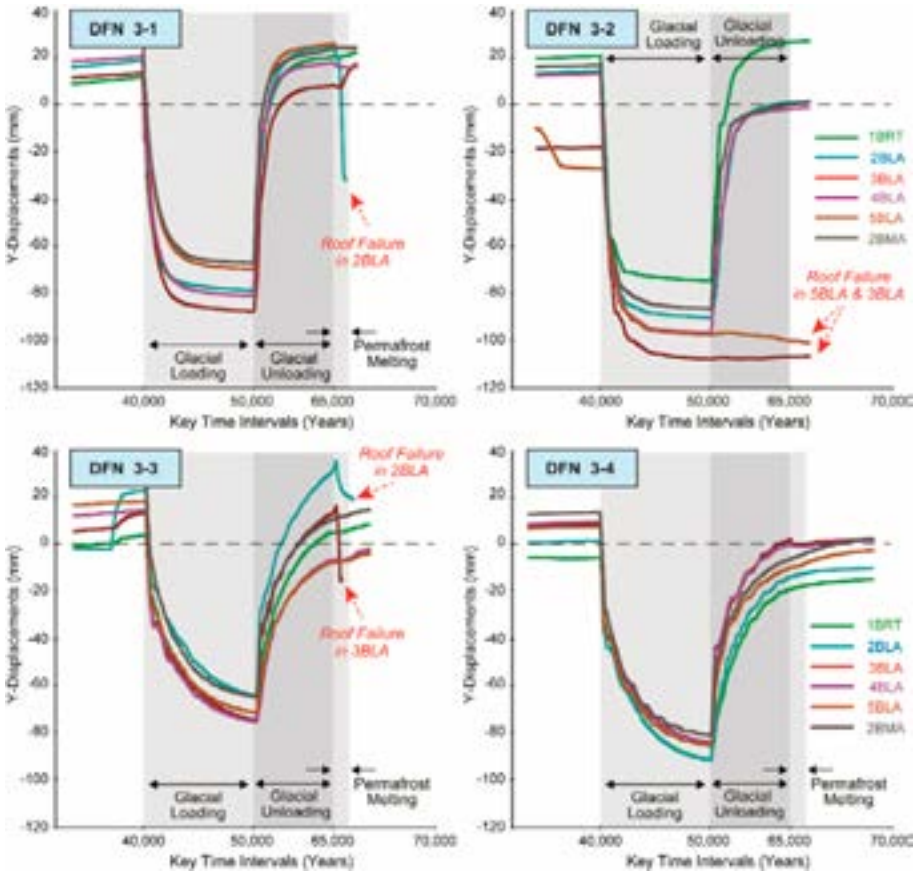


**Figure 62:** Vertical displacement histories for the SFR 3 UDEC models between Year 40,000 and 66,000, that encompasses glacial loading, glacial unloading and permafrost melting in parallel with time-dependent strength degradation. Monitoring points are located 0.5 m above the roof of each rock vault. Note that down is in the negative Y-direction.

With permafrost melting, two additional SFR 3 realizations, DFN 3-1 and DFN 3-3, experienced major instabilities and roof failures in non-backfilled rock vaults. These are seen in the history plots as sharp downward accelerations in the vertical displacements (Figure 62). Figure 63 shows that this is preceded by an increase in the number of fractures in the near-field surrounding the SFR 3 rock vaults that experience strength degradation between Year 65,000 and Year 66,000 (i.e., after permafrost melting). More importantly, this figure shows that a sharp increase in the number of intact rock elements that fail is also observed around these excavations, as indicated by the black trend lines in Figure 63.

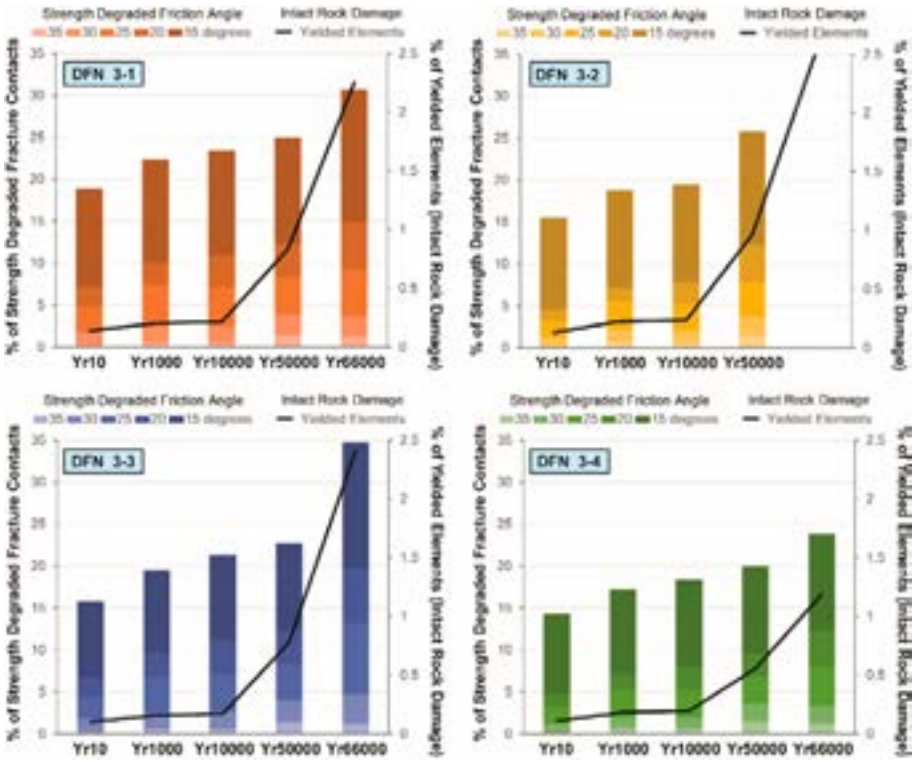


**Figure 63:** Comparison of cumulative strength degradation in the near-field zone around the SFR 3 rock vaults for several key time intervals over the full 66,000 year UDEC simulation. Shown are the percentages of fractures that experienced time-dependent shear strength decreases (relative to the initial friction angle of 40 degrees), and intact block elements that yielded. Note that the near-field zone in this case extends 10 m from the outer walls of the outside rock vaults and from 5 m below the rock vaults to the surface, encompassing approximately 145,000 fractures and 980,000 elements.

Inspection of the UDEC modelled failures for DFN 3-1 indicate that the 3BLA and 2BLA rock vaults experience major spalling leading to their limited collapse of the full span. This collapse involves ground fall at the excavation boundary and extensive damage into the rock mass. The resulting damage is most intense where the EDZ interacts with the overlying SBA fracture zone, but stabilizes in the vertical direction after 10 to 20 m from the excavation boundary (Figure 64). The sharp increase in tensile yield indicators for the intact rock (interpreted here as a proxy for spalling) is reflected in this figure. The driver for the onset of this major spalling is an increase in the horizontal to vertical stress ratio that concentrates in the roofs above the SFR 3 rock vaults during vertical rebound and stress rotation following glacial unloading (effectively, the major principal stress axis rotates from vertical during glacial loading to horizontal during glacial unloading). Figure 65 compares

the horizontal stresses during glacial unloading (ending in Year 65,000) and those after (Year 66,000). The high horizontal stresses coupled with the cumulative weakened state of the intact rock over the 66,000 year period, leaves the rock vaults highly vulnerable to severe spalling failure, which in the case of 3BLA extends several meters into the roof (Figure 64).

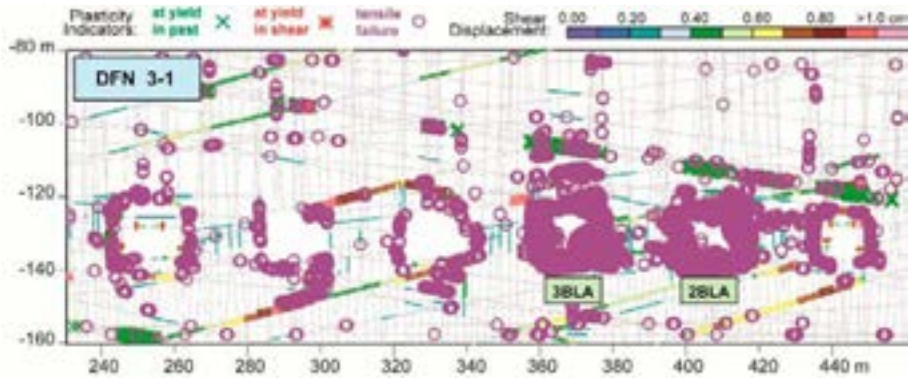


**Figure 64:** UDEC modelled slip along fractures and intact rock yielding showing the extensive EDZ and failures that develop around the 3BLA and 2BLA rock vaults for SFR 3, DFN 3-1 following glacial unloading and permafrost melting in Year 66,000.

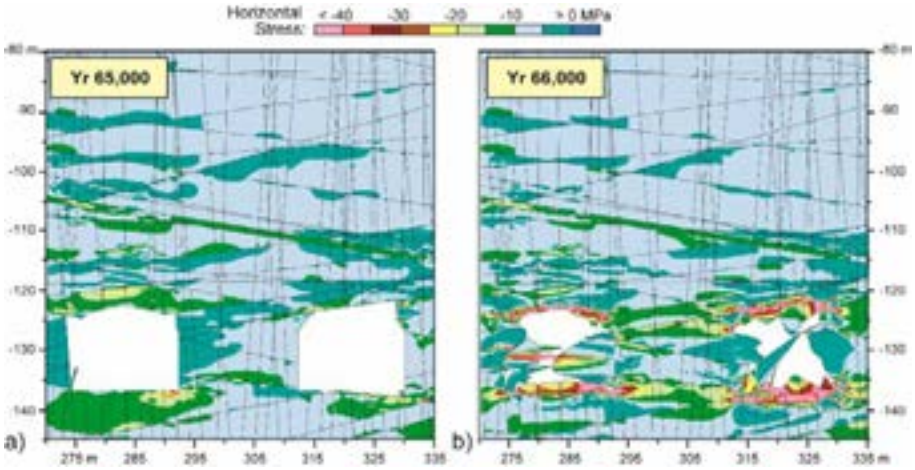


**Figure 65:** Comparison of the SFR 3 horizontal stresses in the roofs above 3BLA and 2BLA during glacial unloading (Year 65,000) and after glacial unloading (Year 66,000). Results are for DFN 3-1. Compressive stresses are negative. Note that exaggerated deformations in the walls result from kinematic block instability after failure in UDEC.

Figure 64 also shows that the pillar between 3BLA and 2BLA undergoes significant yielding. Unlike the roofs above the rock vaults, where the high horizontal stresses help to limit block movements even where fractures have experienced strength degradation over time, the walls experience relaxation in the presence of a high density of weakened vertical fractures developed in response to the earlier glacial loading. This results in a combination of slip and buckling in the walls that contribute to the overall instability and failure of 3BLA and 2BLA for the DFN 3-1 case. The same response was seen for the DFN 3-3 case, where yielding of the pillar between the 3BLA and 2BLA rock vaults (Figure 66) leads to buckling of the walls. This contributes to spalling and shear that extends into the roof. In the case of the

4BLA rock vault, interactions with the overlying SBA fracture zone allows the EDZ to extend almost 20 m above the roof (Figure 66).

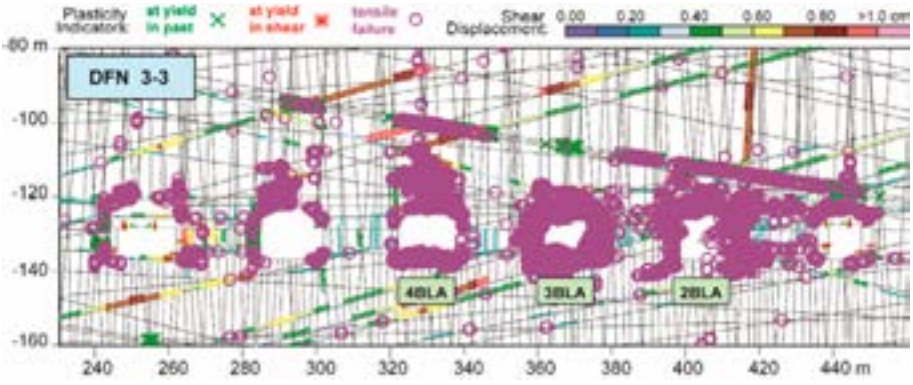


**Figure 66:** UDEC modelled slip along fractures and intact rock yielding showing the extensive EDZ and failures that develop around the 4BLA, 3BLA and 2BLA rock vaults for SFR 3, DFN 3-3 following glacial unloading and permafrost melting in Year 66,000.

In contrast to the major failures and extensive EDZ observed in three of the four DFN realizations modelled for the SFR 3 case, DFN 3-4 returned results indicating minor spalling but otherwise stable conditions. It should be recalled that for the SFR 3 case, the location of the SBA fracture zones was kept the same for all four DFN realizations and therefore the only difference between the four models was minor variations in the distribution, angles and intersections of the fractures, which were derived from the same statistical input. The full results for the SFR 3 model series are included in Appendix 3.

### 4.1.5. Backfill Loading

It should be noted that the excavation failures observed in the SFR 3 models only developed in the non-backfilled BLA rock vaults. Significant spalling failure did develop around the backfilled 1BTF, 2BTF and 1BMA rock vaults for the SFR 1 case and 1BRT and 2BMA rock vaults for the SFR 3 case, over the 66,000 year modelled interval. However, block movements and dilation of the failed intact blocks was limited by the presence of the backfilling.

Figure 67 presents the vertical and horizontal stress histories for the backfill, showing the results for the SFR 1 and SFR 3 realizations that experienced the highest loads (in this case DFN 1-1 and 3-4, respectively). These histories include both the stresses that develop in the load bearing concrete structures planned for the BTF, BMA and BRT rock vault types, and the macadam crushed rock backfill to be placed on top of the concrete structures. As expected, the UDEC results in Figure 67 show that the concrete structures carry a higher load than the rockfill, both because the rockfill sits on top of the concrete structure adding its weight to the imposed load but also because the concrete structures are much stiffer, thus attracting a higher percentage of the imposed load. Exceptions, such as in Figure 67d, involve small loose wedges in the walls of the excavation that impose an added horizontal stress on the rockfill that does not act on the lower concrete structure.

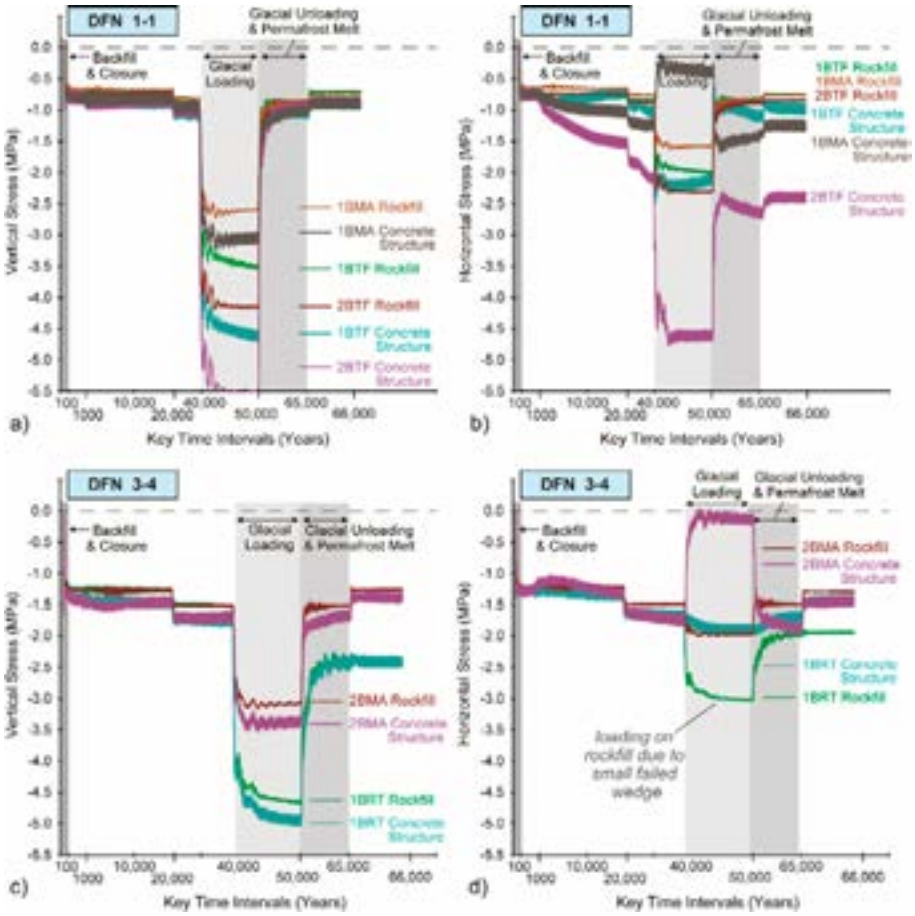


**Figure 67:** Backfill stress histories over the 66,000 year modelling period, for SFR 1 (DFN 1-1) in the: a) vertical and b) horizontal directions, and for SFR 3 (DFN 3-4) in the c) vertical and d) horizontal directions. Monitoring points are located both in the macadam (rockfill) and concrete structures as indicated. Compressive stresses are negative.

Overall, the imposed loads on the backfill for the SFR 3 case were higher than those for the SFR 1 case, except where small loose wedges imposed a higher stress. The maximum stresses coincide with glacial loading, with the concrete structure seeing loads of up to 5.5 MPa (Figure 67a). The maximum stresses during glacial loading range from 3.0 to 5.5 MPa for the SFR 1 DFN realizations, and 3.0 to 5.0 MPa for the SFR 3 DFN realizations. Otherwise, the stresses acting on the backfill separate from the glacial loading cycle, range from 0.7 to 2.4 MPa for SFR 1, and 1.2 to 2.4 MPa for SFR 3. Note that the UDEC analysis was not carried out to perform a structural analysis of the concrete load-bearing structure. Failure of the concrete structure was not considered.

### 4.1.6. Hydraulic Conductivity Changes

The UDEC results were further analysed to provide a first-order approximation of the change in hydraulic conductivity around the rock vaults for the key time intervals modelled. Changes in hydraulic conductivity in the UDEC models can be attributed to:

i) the fracture network and increases in hydraulic conductivity brought about by slip and dilation along the fractures. Relative changes in hydraulic conductivity can be quantified by comparing changes in fracture hydraulic aperture to the initial values.
ii) the intact rock and increases in hydraulic conductivity brought about by damage and spalling. In this case, plasticity indicators are used as the UDEC output to represent relative changes and estimates of EDZ depth.

SFR 1 Fracture Network

The fracture network would likely have the greatest effect on the hydraulic conductivity of the rock mass, especially if assuming a cubic law relationship whereby an increase in fracture aperture would result in an exponential increase in hydraulic conductivity along that fracture. (A 50% increase in aperture would result in a 3.4 times increase in permeability while a 100% increase in aperture would result in an 8 times increase). A fully coupled hydro-mechanical analysis was beyond the scope of this Report, and it should be emphasized that fracture flow is not only governed by the hydraulic aperture of the fracture but also the connectivity of the network. The UDEC analysis conservatively assumes full connectivity of the 2-D fracture network.

Figure 68 shows the UDEC results for SFR 1, specifically DFN 1-1, indicating fractures with hydraulic apertures greater than 0.1 mm. Note that the initial hydraulic apertures vary as a function of depth (i.e., closure stress), ranging between 0.1 mm at surface to 0.01 mm at the SFR 1 repository depth. Thus, all fractures highlighted in Figure 68 are those that have experienced increased hydraulic apertures relative to their initial values. Those that have experienced closure, where stress concentrations result in higher normal stresses, are not shown although they are accounted for in subsequent calculations of cumulative hydraulic aperture change. As would be expected, a large number of fractures experience an increase in hydraulic aperture upon excavation of the rock vaults (Figure 68), especially those that are dipping at low angles. These open in response to displacements towards the excavated rock vaults. Over time, as fracture strength degradation and slip accumulates, hydraulic aperture continues to increase but only marginally.

Figure 69 quantifies this as the percent change in the cumulative hydraulic apertures. For each key time interval, the results were analysed by summing all fracture hydraulic apertures within a given distance from each rock vault, and then calculating the percentage change relative to the sum of the initial hydraulic apertures (i.e., prior to excavation of the rock vaults). The distances analysed in Figure 69 include the “near-field” zone, which encompasses all rock vaults and extends 20 m above and below the excavation boundaries, together with 5 and 1 m windows around the excavation boundaries of each individual rock vault.

For the near-field zone encompassing 20 m around the excavations, the cumulative hydraulic aperture experiences a general increase of 15-25% upon excavation, depending on the DFN realization, and an increase of 40-50% during strength degradation to Year 20,000 and the onset of permafrost (Figure 69). During glacial loading, the apertures predictably decrease due to the added vertical load, but then increase significantly again during glacial unloading and permafrost melt. At this point (Year 66,000), the near-field window of 20 m experiences cumulative hydraulic aperture changes of up to 60%. Assuming a cubic law relationship for fracture flow, this is equivalent to a 4.1 times increase (1.6 x 1.6 x 1.6) in rock mass hydraulic conductivity.

The influence of the hydraulic aperture change on the hydraulic conductivity of the rock mass is of course greater closer to the excavation boundaries where the number of fractures experiencing slip and opening are greatest. Figure 69 shows that the percentage increase in fracture aperture increases by an additional 10% within 5 m of the excavations and 20% within 1 m of the excavation. In cases where there is some block instability and minor block movements, for example in the case of the 2BTF rock vault, Figure 69 shows that the percentage increase in the cumulative hydraulic aperture can increase by 100 to 300% in the 1 m zone around the excavation. This can be equated to a 64 times increase (4 x 4 x 4) in hydraulic conductivity of the rock mass in this zone, specific to the contribution of the fracture network for the SFR 1 case, relative to the evolution of the rock mass in response to strength degradation over time (66,000 years), glacial loading, unloading and permafrost melting.

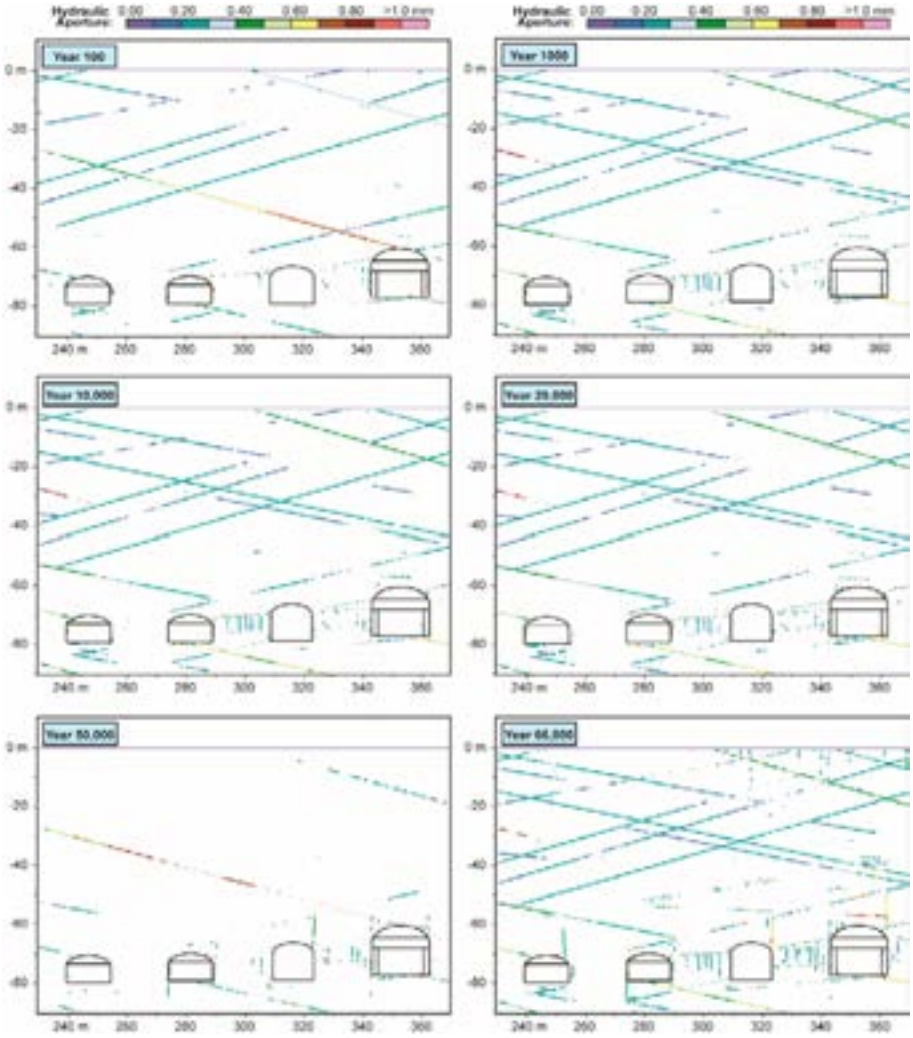


**Figure 68:** Comparison of increases in joint aperture above the initial background aperture over time resulting from application of the joint strength degradation algorithm, permafrost at Year 20,000, glacial loading at Year 50,000, and glacial unloading and permafrost melting at Year 66,000 for the SFR 1 case (DFN 1-1).

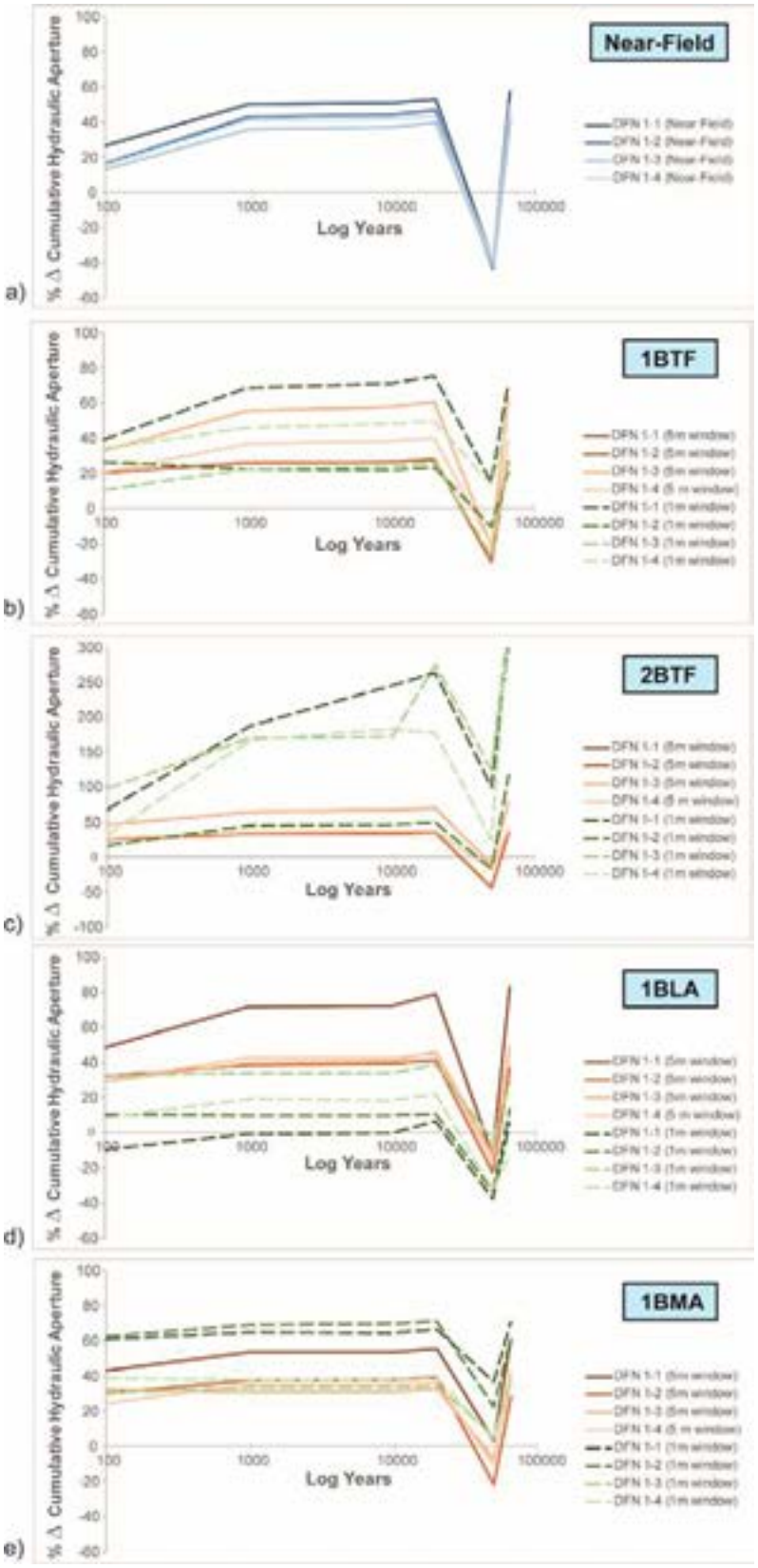


**Figure 69:** Changes in cumulative hydraulic aperture relative to the pre-excavation condition for fractures: (a) within the 20 m near-field zone around all rock vaults for the SFR 1 layout, and (b-e) those for the 5 and 1 m zones around each individual rock vault. Included in each plot are the results for all four DFN realizations.

SFR 3 Fracture Network

Figure 70 indicates that the degree of hydraulic aperture change for the SFR 3 case is greater than that for SFR 1, owing largely to a higher degree of instability modelled around the non-backfilled rock vaults (i.e., 2-5BLA). These show a similar pattern to the SFR 1 results, with an increasing number of opening fractures occurring after excavation and time-dependent strength degradation, ending with the greatest increase at Year 66,000 after glacial unloading and permafrost melting. Figure 71 shows the percent cumulative hydraulic aperture changes for each rock vault as a function of each time increment. The cumulative effect on the overall near-field zone around the rock vaults involves only a 20% increase in hydraulic aperture, which is equivalent to a 1.7 times increase in hydraulic conductivity. This increases at 66,000 years after closure to up to 40% for the 5 m window around each of the rock vaults and up to 300%, or a 64 times increase in hydraulic conductivity, for the 1 m window around 2BLA where loosening and failure of the roof develops.

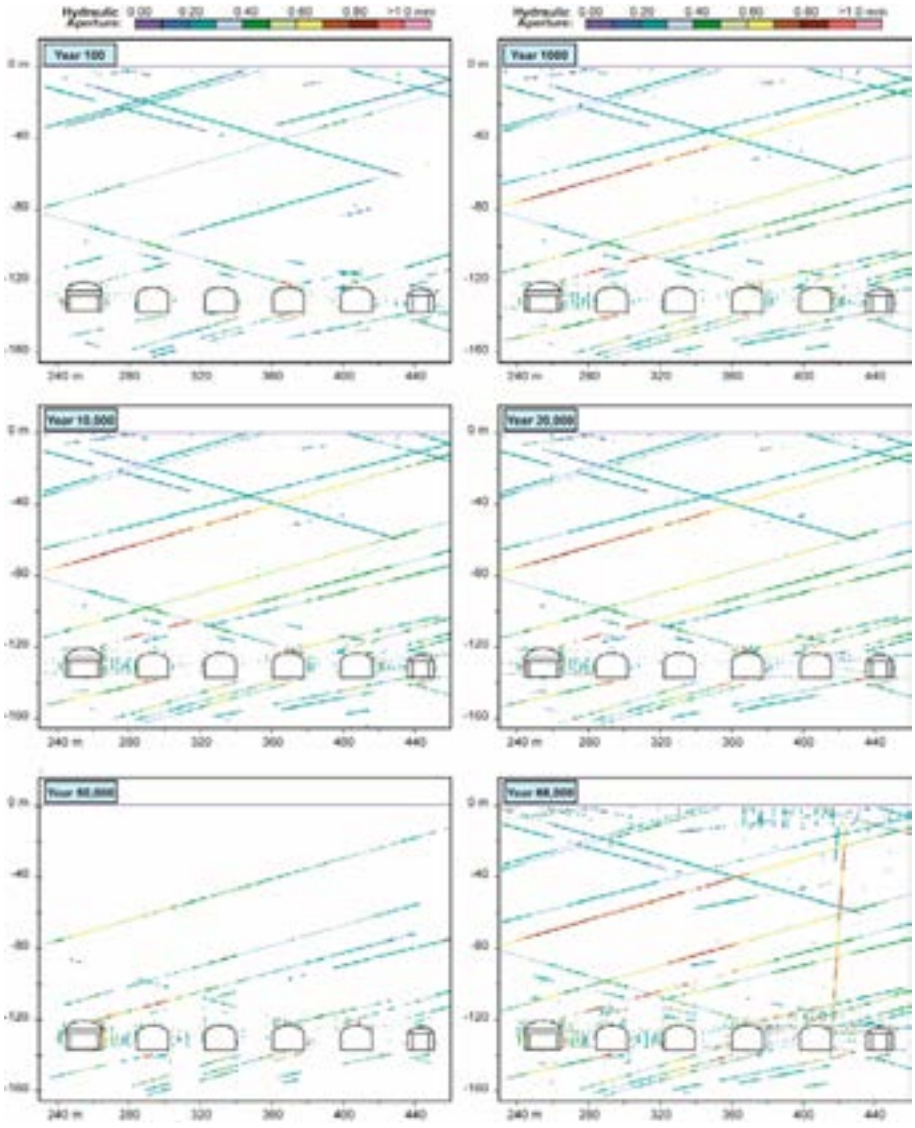


**Figure 70:** Comparison of increases in joint aperture above the initial background aperture over time resulting from application of the joint strength degradation algorithm for the SFR 3 case (DFN 3-1).

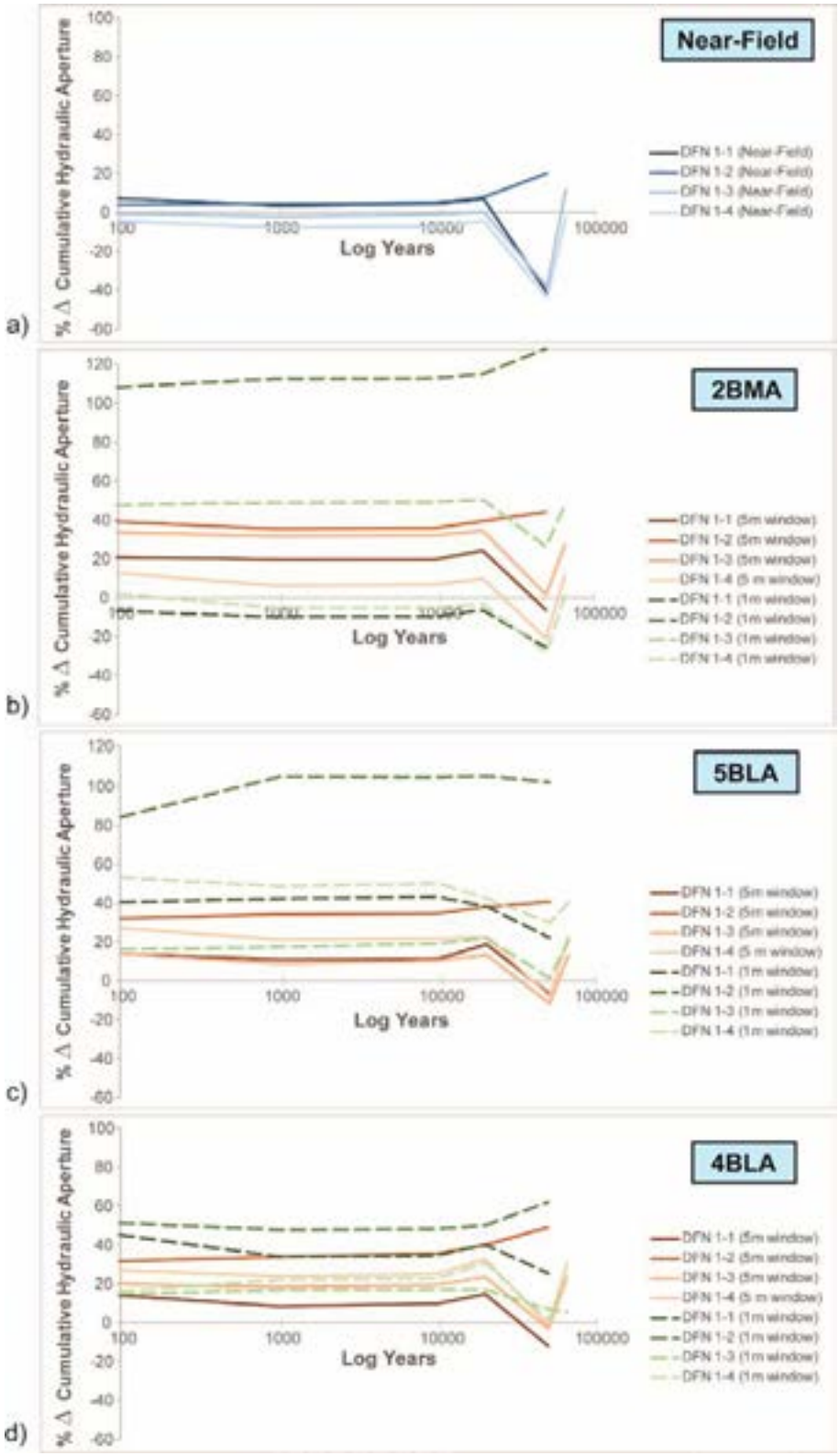


**Figure 71:** Changes in cumulative hydraulic aperture relative to the pre-excavation condition for fractures: (a) within the 20 m near-field zone around all rock vaults for the SFR 3 layout, and (b-g) those for the 5 and 1 m zones around each individual rock vault. Included in each plot are the results for all four DFN realizations. Note that this figure is continued on the next page where plots (e-g) appear.

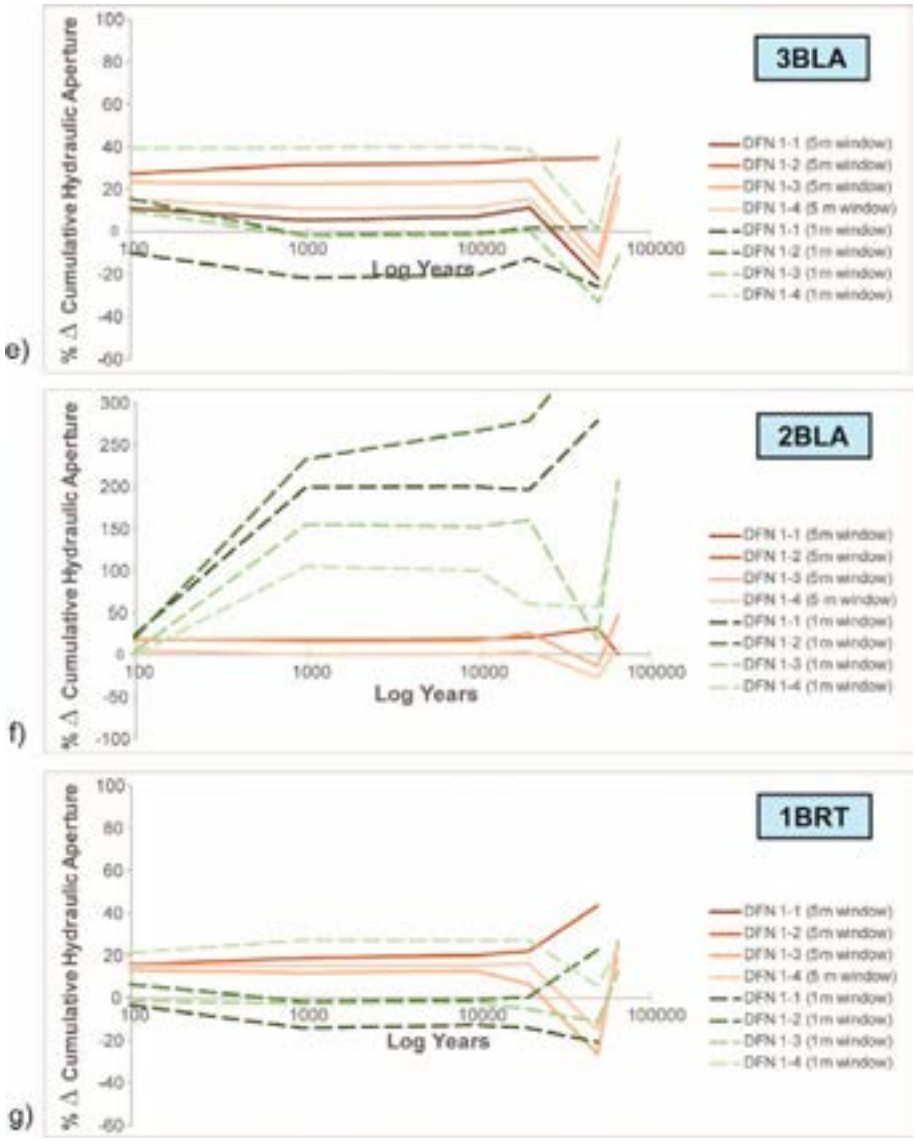


**Figure 71 (continued):** Changes in cumulative hydraulic aperture relative to the pre-excavation condition for fractures (a) within the 20 m near-field zone around all rock vaults for the SFR 3 layout, and (b-g) those for the 5 and 1 m zones around each individual rock vault. Included in each plot are the results for all four DFN realizations. Note that this figure is continued from the previous page where plots (a-d) appear.

Intact Rock and EDZ

The changes in hydraulic aperture across the fracture network would occur in parallel to stress-induced brittle fracture damage of the intact rock, which likewise would contribute to increases in the near-field rock mass hydraulic conductivity. According to connected permeability tests carried out in granitic rock at the AECL Underground Research Laboratory in Canada (Chandler et al., 1996), blast-induced damage was seen to increase the hydraulic conductivity by two to three orders of magnitude but was also discontinuous. In contrast, stress-induced damage was seen to be more continuous along the length of the excavation, and in the Highly Damaged Zone (HDZ) where damage is most extensive, the hydraulic conductivity was measured to be up to six to seven orders of magnitude greater than that of the undisturbed intact rock (Figure 72). Where the EDZ is less extensive, for example in

a lower stress environment, similar tests in granodiorite at the Kamaishi mine in Japan indicated an increase in hydraulic conductivity of two orders of magnitude (Matsui et al., 1998). Quantifying this change for the SFR 1 and 3 rock vaults is outside the scope of this Report, however the UDEC results can be used to suggest the depth of EDZ that would contribute to increases in the rock mass hydraulic conductivity.

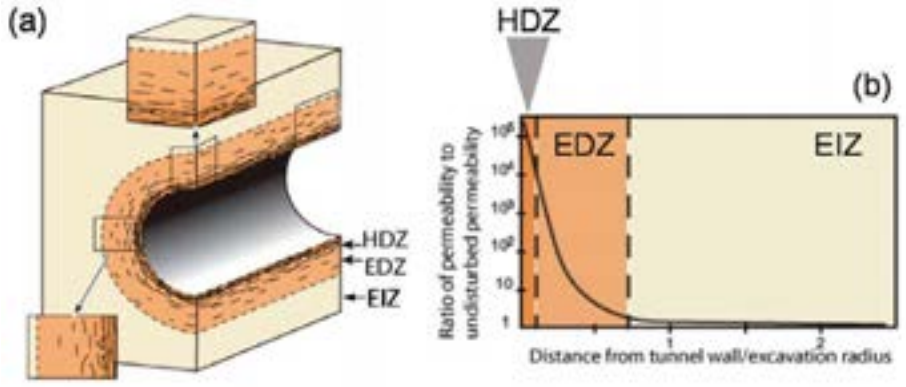


**Figure 72:** (a) Illustration of different excavation damage zones around an underground excavation resulting from stress-induced brittle fracturing. (b) Corresponding changes in rock permeability for the Highly Damaged Zone (HDZ) and Excavation Damaged Zone (EDZ).

Table 8 reports the depths of the stress-induced EDZ that develops above each of the SFR 1 rock vaults, providing the minimum and maximum values for the four DFN realizations. It should be noted that in these cases the EDZ is highly localized and is not distributed across the full width of the rock vaults (Figure 73a). This suggests that the EDZ that develops for the SFR 1 case in response to time-dependent strength degradation, permafrost, glacial loading and unloading, and permafrost melting (i.e., the 66,000 year time span modelled), would have only a relatively minor effect on the near-field rock mass hydraulic conductivity.

**Table 8:** Depth of UDEC modelled EDZ above each SFR 1 rock vault. Reported here are the minimum and maximum values derived from the four DFN realizations for each key time interval. See Figure 7 for layout of SFR 1 rock vaults.

| Year | 1BTF | 2BTF | 1BLA | 1BMA |
|---|---|---|---|---|
| Excavation | 0 - 2 m | 0 - 0.5 m | 0 - 0.1 m | 0 - 0.1 m |
| 1000 | 0 – 2 | 0 - 0.5 | 0 - 0.1 | 0 – 3 |
| 10,000 | 0 – 2 | 0 - 0.5 | 0 - 0.1 | 0.1 – 4 |
| 20,000 | 0 – 2 | 0 - 0.5 | 0.1 - 0.4 | 0.1 – 4 |
| 50,000 | 0.1 – 2 | 0 - 1 | 0.1 - 0.4 | 1 – 4 |
| 66,000 | 0.1 - 2.2 | 0.1 - 1.6 | 0.5 - 2.3 | 1.4 – 4 |

In contrast, the results for the SFR 3 case (Table 9) suggest that EDZ would be more extensive than for SFR 1. This is owing to a combination of greater depth and larger number of non-backfilled BLA rock vault types planned for the SFR 3 layout (four

compared to one for the SFR 1 layout). In several cases, the EDZ interacts with intersecting sub-vertical fractures and propagates several metres upwards towards the overlying SBA fracture zone, amplifying the extent of the EDZ (Figure 73b), most notably in response to glacial loading and unloading. This would drive the local rock permeability higher within these damage zones, up to two to three orders of magnitude (in the zone above the local failure/collapse zone), according to the literature (e.g., Chandler et al., 1996; Matsui et al., 1998).

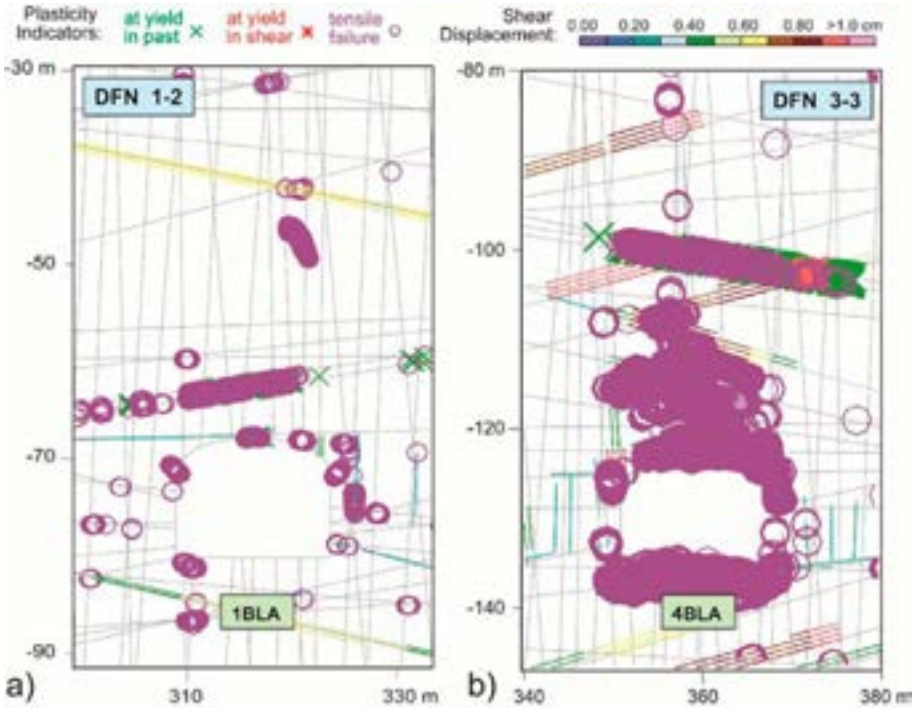


**Figure 73:** Comparison of plasticity indicators showing extent of EDZ after glacial loading, glacial unloading, permafrost melting and associated strength degradation (Year 66,000), for: a) SFR 1 and b) SFR 3. Note the localized nature of the EDZ for SFR 1, versus the more extensive nature for SFR 3.

**Table 9:** Depth of UDEC modelled EDZ above each SFR 3 rock vault. Reported here are the minimum and maximum values derived from the four DFN realizations for each key time interval. See Figure 9 for layout of SFR 3 rock vaults.

| Year | 2BMA | 5BLA | 4BLA | 3BLA | 2BLA | 1BRT |
|---|---|---|---|---|---|---|
| 10 | 0.2 - 0.4 m | 0 - 0.2 m | 0 - 0.2 m | 0 - 0.4 m | 0.2 - 1.4 m | 0 - 1.2 m |
| 1000 | 0.4 - 1.6 | 0 - 1.6 | 0 - 1.4 | 0 - 3.4 | 0.4 - 1.8 | 0.2 - 1.2 |
| 10,000 | 0.5 - 4 | 0.2 - 1.8 | 0.1 - 1.4 | 0.2 - 4 | 1 - 1.8 | 0.6 - 1.2 |
| 20,000 | 0.5 - 4 | 0.2 - 1.8 | 0.1 - 1.4 | 2.2 - 4 | 1.2 - 2.8 | 0.6 - 1.2 |
| 50,000 | 0.5 - 4 | 0.6 - 8 | 0.1 - 9.8 | 1 - 14.5 | 1.4 - 4 | 1.2 - 2.8 |
| 66,000 | 1.8 - 2.4 | 0.6 - 11 | 0.4 - 15.5 | 1 - 14.5 | 2.8 - 5.8 | 1.2 - 8.2 |

# 5. Conclusions

Results were presented from a detailed review of the evolution of the mechanical stability and associated hydraulic conductivity around the rock vaults of SKB's Final Repository for Short-Lived Radioactive Waste (SFR) at Forsmark.
The review includes a series of 2-D distinct-element analyses using the commercial code UDEC, developed and distributed by Itasca International (Itasca, 2016). UDEC was selected for its ability to account for both the complex non-linear interactions along a discrete fracture network (i.e., fracture slip and/or opening/closing), as well as the deformation and yielding of the intact rock blocks bounded by the fracture network. Both the existing SFR 1 rock vault layout and the proposed SFR 3 rock vault layout were analysed. Key features related to the geological setting and design of the SFR 1 and SFR 3 repositories were implemented in the models. These include:

- Full layouts for the SFR 1 (1BTF, 2BTF, 1BLA and 1BMA) and SFR 3 (2BMA, 5BLA, 4BLA, 3BLA, 2BLA and 1BRT) repositories were modelled. These used the dimensions, pillar spacings, excavation sequencing, and presence of backfill (where applicable), specified in SKB's long-term safety assessment (SKB TR-14-01) and associated reports.
- Discrete Fracture Networks (DFN) based on the main fracture sets mapped during construction of SFR 1 were explicitly included in the SFR 1 and SFR 3 models. A fracture set parallel to the 2-D UDEC section implicitly represents a vertical release surface in the third dimension. Four DFN realizations for each of SFR 1 and SFR 3 were modelled to account for spatial variability in the location, intersection and dip angles of critical fractures.
- Input parameters for the rock and fracture properties based on those reported in SKB R-13-53, SKB TR-14-01 and SKB R-07-31 were applied.
- Groundwater pore pressures for both the fractures and intact rock blocks were included. It was assumed that the near-field groundwater flow is parallel to the caverns, and therefore perpendicular to the 2-D section modelled. Accordingly, the total pore pressure head was assumed to be static with pore pressures equal to pressure head equal to sea level.
- Long-term rock and joint strength degradation to account for time-dependent factors such as subcritical crack growth were modelled, for reference times of 1000, 10,000, 20,000 and 50,000 years. Deterioration rates were based on extrapolated data from long-term testing of granitic rock, and implemented using functions that account for dependencies on the driving differential stress (or shear stress in the case of fractures) and the confinement (or normal stress).
- Changes in the loading conditions, concurrent with strength degradation, were modelled to include permafrost and permafrost melting, and glacial loading and unloading. These were based on the Weichselian climate case described in SKB TR-09-15.

Key findings from these models and analyses are presented below relative to several specific review questions posed by SSM:

- The appropriateness of the method used in SKB R-13-53 to model the effects of strength degradation over time, and the corresponding degraded

mechanical properties of the rock fractures used were reviewed. We found that the strength degradation procedure implemented was applied somewhat arbitrarily by reducing fracture friction angles uniformly to zones defined by set distances from the excavation boundary. Fracture shear strengths with friction angles as low as 5.7 degrees and zero cohesion were applied. This compares to the lowest values we could find in the literature of 8 degrees. As noted by the authors of SKB R-13-53, the unrealistically low friction angle was an exercise to determine the value required to produce large-scale collapse of the modelled 1BMA and 1BLA rock vaults in SFR 1. Despite this low value, it was found that the height of the loosened rock would not reach the seabed. SKB TR-14-01 concluded from this that there should be no risk of a direct connection between the rock vaults and the seabed. For the analysis presented in this Report, we have applied a more data-driven approach to time-dependent strength degradation. First, the function we developed was extrapolated from long-term strength tests performed on granite, and utilizes the driving differential stress (or shear stress in the case of the fractures) and confinement (or normal stress), to determine the degree of strength degradation to be applied. Next, as indicated, we applied the time and stress dependent strength degradation function to both the fractures and the intact rock blocks. The analysis in SKB R-13-53 assumed the intact blocks to be elastic. Despite these differences, the 2-D UDEC results obtained are similar to the 3-D results in SKB-R-13-53, and support the conclusion that rock vault collapse leading to breaching of the sea floor above is unlikely.

- The stability of the SFR 1 and SFR 3 pillars between the rock vaults and their evolution due to time-dependent strength degradation at 1000, 10,000, 20,000 and 50,000 years was modelled, with the latter time periods including simulations of permafrost and permafrost melting, and glacial loading and unloading. As noted above, this was carried out through a series of 2-D UDEC models employing a hydro-mechanical coupling to account for the influence of pore pressures on the effective stresses, and a data driven stress- and confinement-dependent relationship to model time-dependent strength degradation. Four DFN realizations were modelled for both the SFR 1 and SFR 3 cases.

  For SFR 1, the UDEC results for the full climate based scenario, through permafrost and permafrost melt, and glacial loading, unloading and permafrost melt, remain inherently stable with the exception of several minor roof failures (isolated wedges) and limited and localized spalling and structural shear. The results show that stability is primarily maintained due to the high horizontal stresses that exist, which results in high normal stresses acting across the sub-vertical fractures along which slip release is required for failure to occur.

  For SFR 3, the combination of greater depth and increased number of larger non-backfilled excavations (75% of excavations backfilled in SFR 1 versus 33% in SFR 3), resulted in a significant increase in rock mass damage above and around the excavations. For Years 1000 and 10,000, stability was generally maintained despite the increased level of rock mass damage outside of several small localized wedge failures. For the permafrost and permafrost melt scenario (Year 20,000 to 21,000), several instabilities were seen to initiate involving block movements enabled by the removal of the permafrost-enhanced strength together with the normal stresses acting on the fractures relaxing in response to ice pressures returning to their hydrostatic levels upon melting. However, only one of these in one DFN

realization (above rock vault 5BLA) evolved into a partial collapse, with a stable arch subsequently re-establishing. Ultimately, failure in this case was due to the combination of fracture orientations and intersections specific to the DFN realization as the same failure did not develop in the other three DFN realizations. For the glacial loading and unloading scenario (Year 50,000 to 66,000), significant rock mass spalling and block failures were observed, most notably for the 4BLA, 3BLA and 2BLA rock vaults. During the start of glacial loading at Year 50,000, there is a phase of stress relaxation (due to crustal flexure) followed by horizontal and vertical compression. This cycle creates significant rock mass damage and the stress conditions for accelerated time-dependent strength degradation. Subsequent glacial unloading, restoration of the pre-glacial stress state and permafrost melting (Year 66,000), then allows this damaged rock to destabilize further, creating more significant failures and limited collapse. In the worst cases, spalling and failure extends up to 20 m above the roof, although runaway collapse beyond the upper bounding SBA fracture zone does not occur.

- The effect of the supporting function of backfill in the rock vaults, where applied, was modelled. The presence of backfill was seen to have a significant benefit in promoting stability and limiting the extent of EDZ that developed. As noted above, the cases where larger failures did develop, specifically for SFR 3, these occurred above the BLA rock vault types that are not backfilled. The presence of backfill was seen to both limit block movements, thereby helping to maintain a stable arch, and reduce the stresses that develop in the pillars by carrying a greater share of the stress redistribution. It should be noted that the UDEC analysis did not include a structural analysis of the concrete load-bearing structure. Failure of the concrete structure was not considered.
- The UDEC results were analysed to provide a first-order approximation of the changes in hydraulic conductivity around the rock vaults for the key time intervals modelled, with respect to both slip and dilation along the fracture sets as well as with respect to EDZ that develops in the intact rock blocks. The change in cumulative apertures were calculated relative to the pre-excavation state for three zones: a near-field zone extending 20 m from the boundaries of the full rock vault layout, and for 5 m and 1 m windows around each individual rock vault. SFR 1 and SFR 3 after excavation through to Year 10,000, generally experienced a 10 to 40% increase in the near-field apertures, which equates to a 1.3 to 2.7 times increase in the rock mass permeability based on a cubic law fracture permeability assumption. This increased to 50 and 200% in the worst cases for the 5 m and 1 m windows, amounting to a 3.4 and 27 times increase, respectively, in the rock mass fracture permeability. The highest increases in cumulative apertures were observed upon glacial unloading and permafrost melting at the Year 66,000 scenario. The highest values were observed for the 1 m windows around the 2BTF (SFR 1) and 2BLA (SFR 3) rock vaults, where increases exceeded 300% amounting to a 64 times increase in fracture permeability. With respect to increases in the intact rock permeability owing to EDZ, the UDEC results suggest that the EDZ for the SFR 1 case through the full time-dependent strength degradation and climate based scenarios (i.e., to Year 66,000) does not evolve beyond highly localized occurrences. This suggests that the EDZ for the SFR 1 case would only have a relatively minor effect on the near-field rock mass hydraulic conductivity. For the SFR 3 case, the EDZ was seen to evolve to extend

deeper and across the full width of the rock vaults, especially above the non-backfilled BLA rock vault type. In several cases, the EDZ interacts with intersecting sub-vertical fractures and propagates several metres upwards towards the overlying SBA fracture zone, amplifying the extent of the EDZ during glacial loading and unloading. Based on relationships in the published literature, this could drive the local intact rock permeability up to 2 to 3 orders of magnitude higher within these damage zones.

# 6. References

Note that the following references are those cited separate from the review of SKB reports. The SKB reports reviewed and cited in this Report are listed in Appendix 1.


Chandler, N., Koazak, E.T. and Martin, C.D. (1996). Connected pathways in the EDZ and the potential for flow along tunnels. In *Proceedings of the International Conference on Deep Geological Disposal of Radioactive Waste - EDZ Workshop, Winnipeg*. Canadian Nuclear Society, Toronto, pp. 25-34.

Damjanac and Fairhurst (2010). Evidence for a long-term strength threshold in crystalline rock. *Rock Mechanics and Rock Engineering*, 43(5): 513-531.

Davies, M., Hamza, O., Lumsden, B. and Harris, C. (2000). Laboratory measurement of the shear strength of ice-filled rock joints. *Annals of Glaciology*, 31(1): 463-467.

Diederichs, M.S., Kaiser, P.K. and Eberhardt E. (2004). Damage initiation and propagation in hard rock tunnelling and the influence of near-face stress rotation. *International Journal of Rock Mechanics and Mining Sciences*: 41(5), 785-812.

Diederichs, M.S. (2007). The 2003 Canadian Geotechnical Colloquium: Mechanistic interpretation and practical application of damage and spalling prediction criteria for deep tunnelling. *Canadian Geotechnical Journal*, 44(9): 1082-1116.

Eberhardt, E., Diederichs, M.S. and Rahjoo, M. (2016). Pre-peak brittle fracture damage. In *Rock Mechanics and Engineering, Volume 1: Principles*. Edited by X-T. Feng. CRC Press/Balkema, Leiden, pp. 623-657.

Itasca (2016). Universal Distinct Element Code (UDEC), Version 6.00. Itasca Consulting Group Inc. Minneapolis, USA.

Jung, Y.B., Park, E.S., Chung, S.K. and Kim, H.Y. (2011). Coupled hydro-thermal modeling of ice ring formation around a pilot LNG cavern in rock. *Engineering Geology*, 118: 122-133.

Lau, J.S.O., Gorski, B., Conlon, B. and Anderson, T. (2000). Long-term loading tests on saturated granite and granodiorite. Ontario Power Generation Report 06819-REP-01300-10016 R00, Toronto, Canada.

Martin, C.D. (1997). Seventeenth Canadian Geotechnical Colloquium: The effect of cohesion loss and stress path on brittle rock strength. *Canadian Geotechnical Journal*, 34: 698-725.

Matsui, H., Sato, T., Sugihara, K. and Kikuchi, T. (1999). Overview of the excavation disturbance experiment at the Kamaishi mine. In *Proceedings, International Workshop for the Kamaishi In Situ Experiments, Kamaishi, Japan*. Japan Nuclear Cycle Development Institute, Tokai, pp. 29-44.

Nilsen, B. (1994). Analysis of potential cave-in from fault zones in hard rock subsea tunnels. *Rock Mechanics and Rock Engineering*, 27(2): 63-75.

NWMO DGR-TR-2011-17: Itasca Consulting Group (2011). Long-term geomechanical stability analysis. Nuclear Waste Management Organization, Toronto, Canada.

NWMO-TR-2015-27: Radakovic-Guzina, Z, Riahi, A. and Damjanac, B. (2015). Long-term stability analysis of APM conceptual repository design in sedimentary and crystalline rock settings. Nuclear Waste Management Organization, Toronto, Canada.

Olsson, R. and Barton, N. (2001). An improved model for hydromechanical coupling during shearing of rock joints. *International Journal of Rock Mechanics & Mining Sciences*, 38: 317-329.

Priest, S.D. (1993). Discontinuity analysis for rock engineering. Chapman & Hall.

Rocscience (2016). Rock and Soil 2-dimensional analysis program (RS2), Version 9. Rocscience Inc., Toronto, Canada.

Schmidtke, R.H. and Lajtai, E.Z. (1985). The long-term strength of Lac du Bonnet granite. *International Journal of Rock Mechanics and Mining Sciences*, 22(6): 461-465.

SSM 2016:08 (2016). SSM's external experts' reviews of SKB's safety assessment SR-PSU – hydrogeological and chemical aspects. Initial review phase. ISSN 2000-0456.

SSM 2016:12 (2016). SSM's external experts' reviews of SKB's safety assessment SR-PSU – engineered barriers, engineering geology and chemical inventory. Initial review phase. ISSN 2000-0456.

SSMFS 2008:37 (2008). The Swedish Radiation Safety Authority's regulations and general advice concerning the protection of human health and the environment in connection with the final management of spent nuclear fuel and nuclear waste. ISSN 2000-0987.

Xiao, Y., Liu, H., Chen, Y. and Jiang, J. (2014). Strength and deformation of rockfill material based on large-scale triaxial compression tests. I: Influences of density and pressure. *Journal of Geotechnical and Geoenvironmental Engineering*, 140(12): 10.1061/(ASCE)GT.1943-5606.0001176.

Zangerl, C. (2003). Analysis of surface subsidence in crystalline rocks above the Gotthard highway tunnel, Switzerland. DSc thesis, ETH Zurich, Switzerland.

**APPENDIX 1**

# Coverage of SKB reports

The following reports have been covered in this review.

**Table A1:** Coverage of SKB reports reviewed

| Reviewed report | Reviewed sections | Comments |
|---|---|---|
| R-02-32, Forsmark – site descriptive model version 0 | 5 | In situ stress magnitudes used in R-13-53 analysis. |
| R-06-38, Site descriptive modelling Forsmark stage 2.1. Feedback for completion of the site investigation including input from safety assessment and repository engineering | 2 | Mechanical properties of intact rock cited in R-07-06, which is sited in R-13-53. |
| R-07-06, Mechanical modelling of the Singö deformation zone. Site descriptive modelling Forsmark stage 2.1. | 4, 7 | Mapping of fractures during construction of SFR 1. Assessment of intact rock and fracture properties used in R-13-53 analysis. |
| R-07-10, Construction experiences from underground works at Forsmark. Compilation Report | 6, 7, 8, 9, 10 | Reporting of rock mass conditions and response to excavation during construction of SFR 1, including deformation measurements. |
| R-07-31, Rock mechanics Forsmark: Site descriptive modelling Forsmark stage 2.2 | 2, 3, 4, 5, 6, 7 | Review of intact rock, fracture and rock mass properties, and in situ stress state. |
| R-07-45, Geology Forsmark: Site descriptive modelling Forsmark stage 2.2 | 5 | Description of Singö deformation zone. |
| R-08-130, Safety analysis SFR 1, Long-term safety | 4, 6 | Initial state and evolution of SFR 1. |
| TR-09-15, Stress evolution and fault stability during the Weichselian glacial cycle | 7 | Glacial loading and stress distributions. |
| TR-11-04, Site description of the SFR area at Forsmark at completion of the site | 6 | Review of updated in situ state of stress. |

| | | |
|---|---|---|
| investigation phase. SDM-PSU Forsmark | | |
| TR-13-04, The potential for cold climate conditions and permafrost in Forsmark in the next 60,000 years | 3, 5 | Permafrost modelling results and conclusions, and exceptions. |
| TR-13-05, Climate and climate-related issues for the safety assessment SR-PSU | 3, 4 | Climate evolution and cases for permafrost and ice-sheet evolution, specifically permafrost depth and maximum ice sheet thickness. |
| R-13-53, Long term stability of rock caverns BMA and BLA of SFR, Forsmark | All | Basis for geometry, DFN and input parameters for independent stability analyses performed. |
| TR-14-01, Safety analysis for SFR Long-term safety. Main report for the safety assessment SR-PSU, Revised edition | 1, 4-11 | Mechanical evolution and use of R-13-53 for conclusions regarding collapse of rock vaults and risk of breaching the sea floor. Safety function, reference evolution, and scenarios related to geosphere barrier functions and related risk cases and dose calculations. |
| TR-14-05, Geosphere process report for the safety assessment SR-PSU | 1, 3, 4 | Hydraulic and mechanical processes with respect to boundary conditions and expected evolution. |
| TR-14-17, Site Engineering Report – SER – Projekt SFR utbyggnad | 6 | Reviewed for determination of SFR pillar widths. |

**APPENDIX 2**

# UDEC results – SFR 1

For completeness, various outputs relevant to the UDEC modelling presented in this Report are provided here to supplement those provided in the main body of the report.

## SFR 1 – Model Initialization (Stresses)

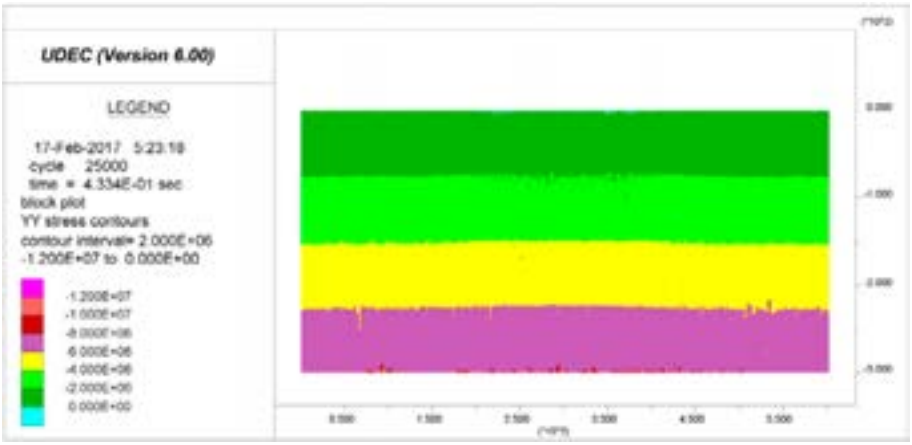


**Figure A1.** Initial vertical (YY) stress state for the SFR 1 UDEC models. Stress magnitudes are in units of Pascals, with compression negative.

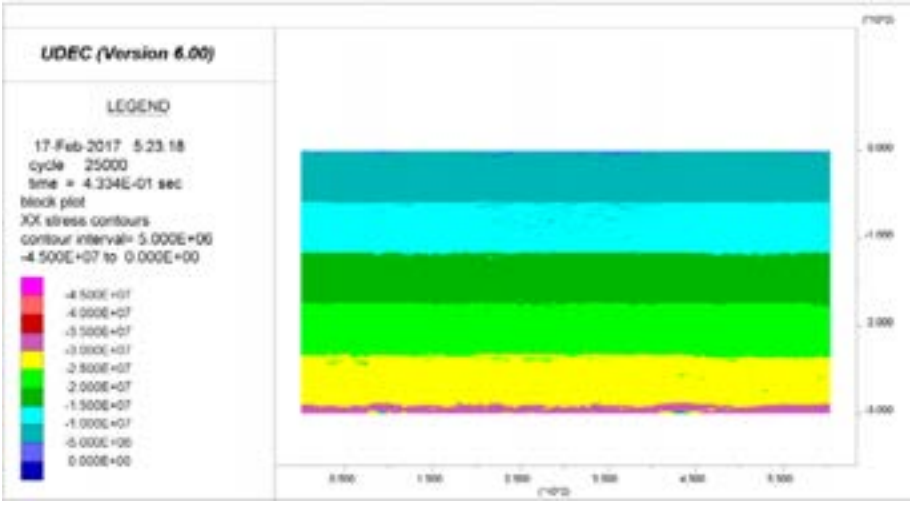


**Figure A2.** Initial horizontal (XX) stress state for the SFR 1 UDEC models. Stress magnitudes are in units of Pascals, with compression negative.

## SFR 1 – Construction and Backfilling (Vertical Stress)

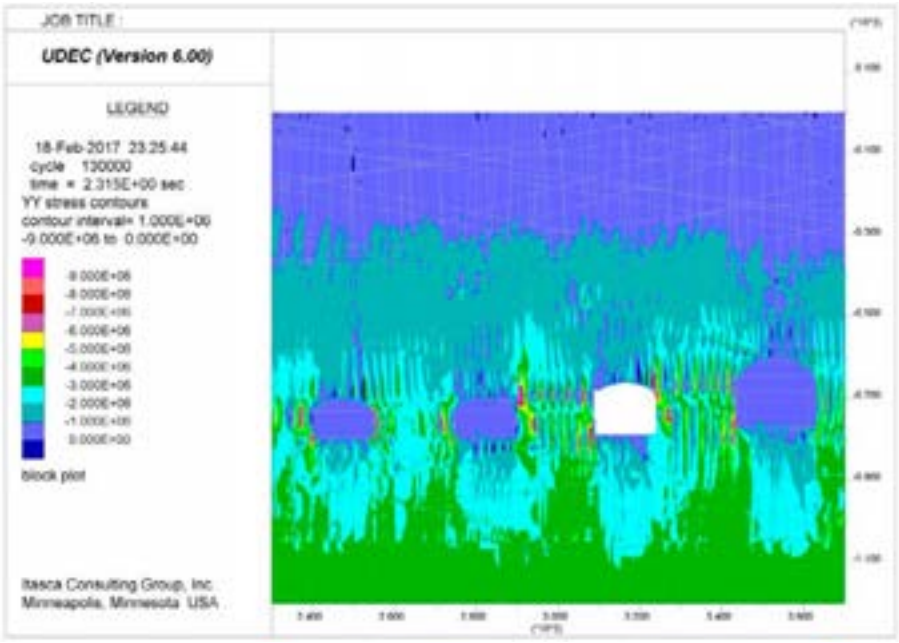


**Figure A3.** UDEC results after construction and backfilling stages, showing vertical stresses (SYY) for SFR 1, DFN 1-1. Stress magnitudes are in units of Pascals, with compression negative.

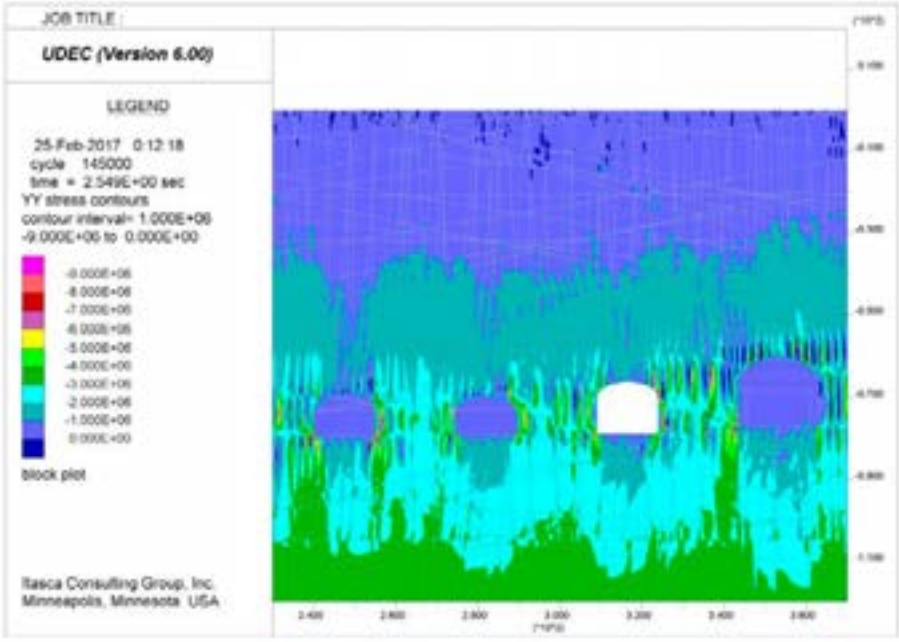


**Figure A4.** UDEC results after construction and backfilling stages, showing vertical stresses (SYY) for SFR 1, DFN 1-2. Stress magnitudes are in units of Pascals, with compression negative.

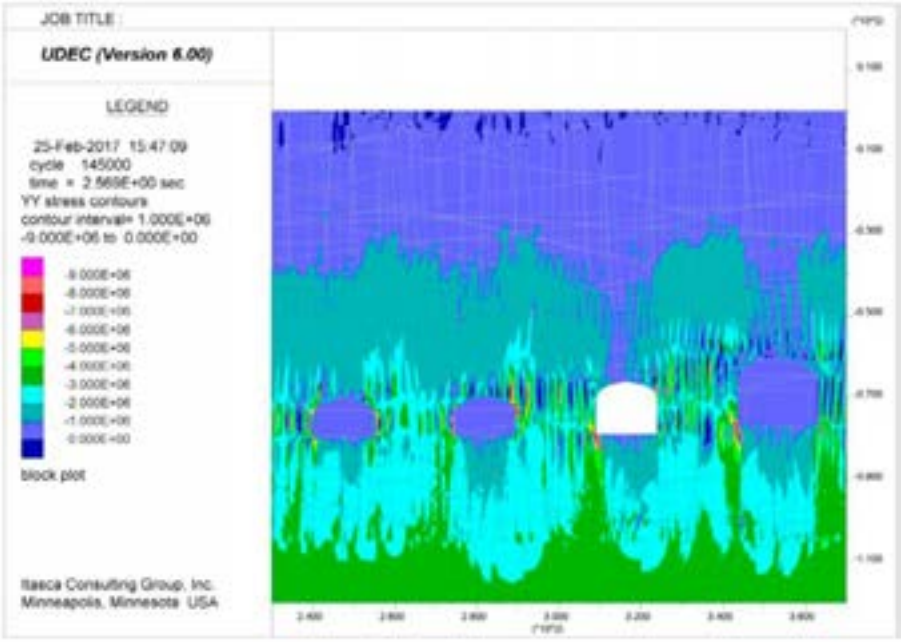


**Figure A5.** UDEC results after construction and backfilling stages, showing vertical stresses (SYY) for SFR 1, DFN 1-3. Stress magnitudes are in units of Pascals, with compression negative.

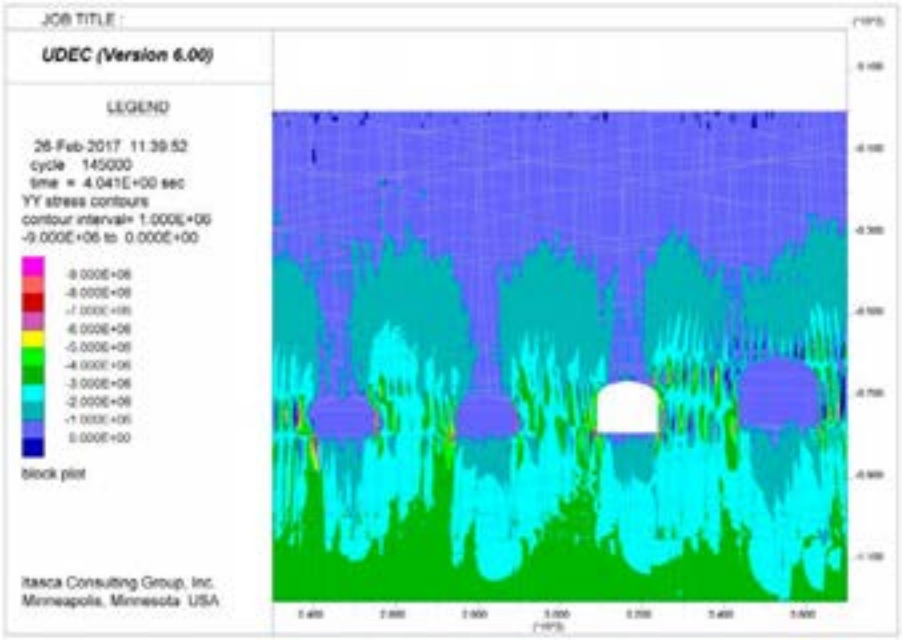


**Figure A6.** UDEC results after construction and backfilling stages, showing vertical stresses (SYY) for SFR 1, DFN 1-4. Stress magnitudes are in units of Pascals, with compression negative.

## SFR 1 – Construction and Backfilling (Horizontal Stress)

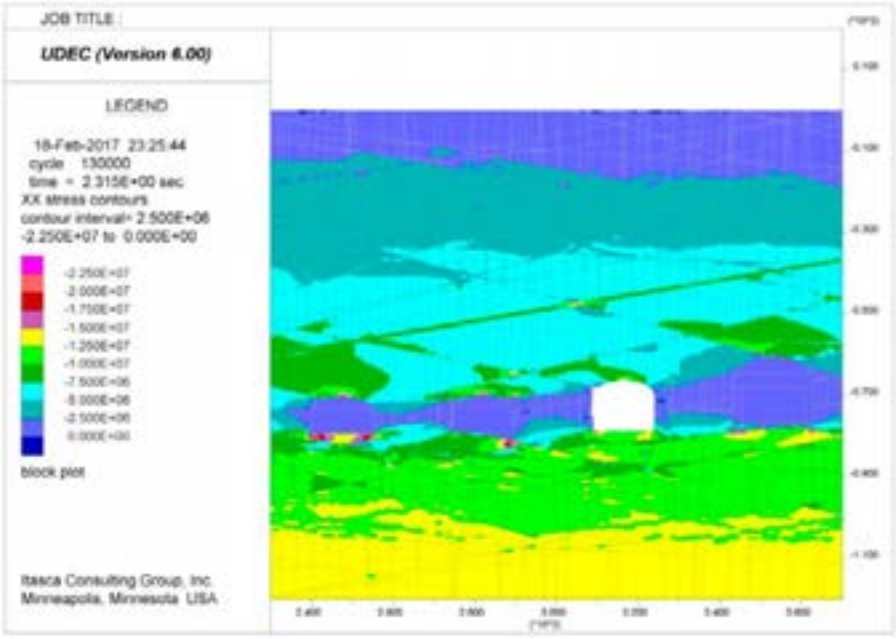


**Figure A7.** UDEC results after construction and backfilling stages, showing horizontal stresses (SXX) for SFR 1, DFN 1-1. Stress magnitudes are in units of Pascals, with compression negative.

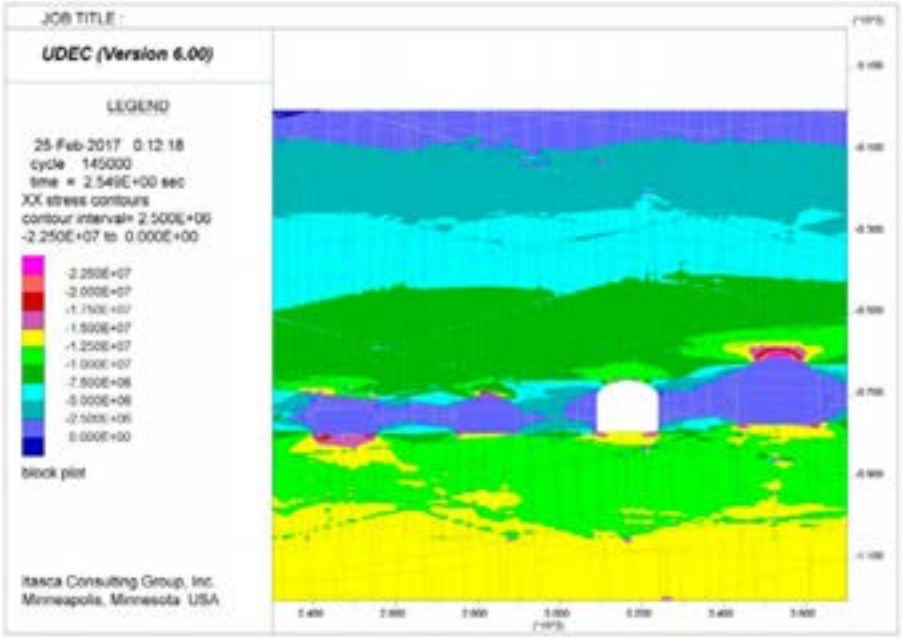


**Figure A8.** UDEC results after construction and backfilling stages, showing horizontal stresses (SXX) for SFR 1, DFN 1-2. Stress magnitudes are in units of Pascals, with compression negative.

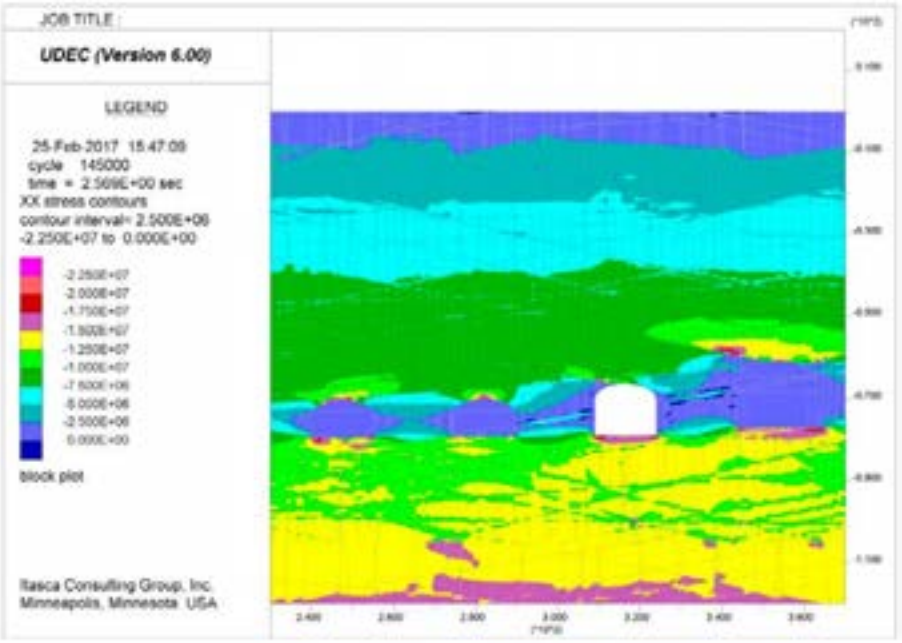


**Figure A9.** UDEC results after construction and backfilling stages, showing horizontal stresses (SXX) for SFR 1, DFN 1-3. Stress magnitudes are in units of Pascals, with compression negative.

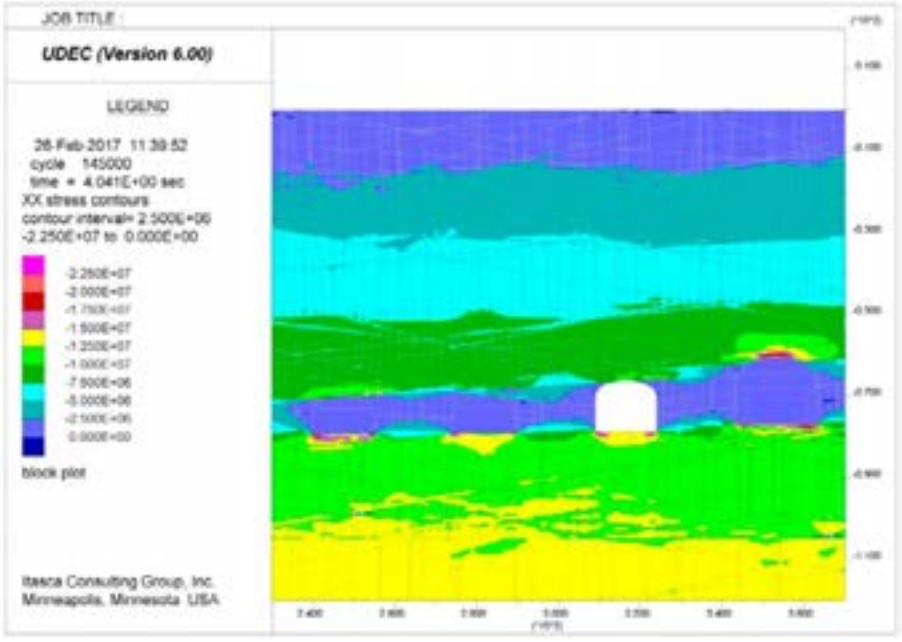


**Figure A10.** UDEC results after construction and backfilling stages, showing horizontal stresses (SXX) for SFR 1, DFN 1-4. Stress magnitudes are in units of Pascals, with compression negative.

## SFR 1 – Construction and Backfilling (Plasticity Indicators)

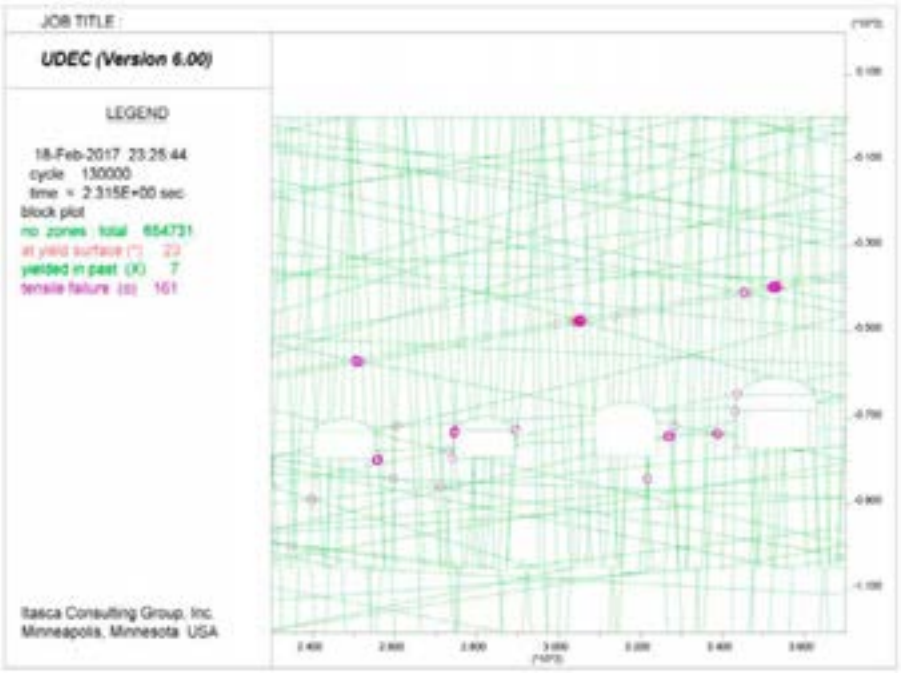


**Figure A11.** UDEC results after construction and backfilling stages, showing yielded elements for SFR 1, DFN 1-1.

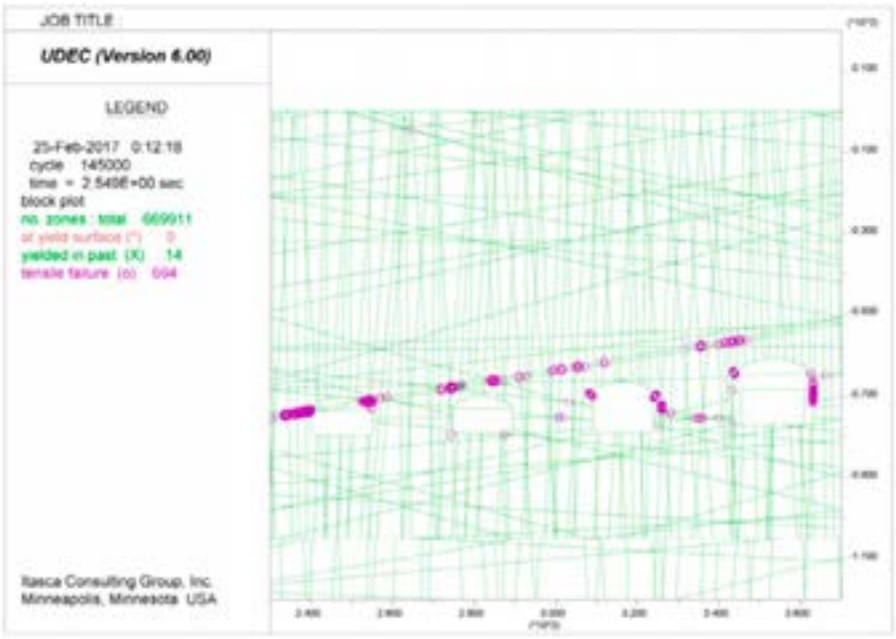


**Figure A12.** UDEC results after construction and backfilling stages, showing yielded elements for SFR 1, DFN 1-2.

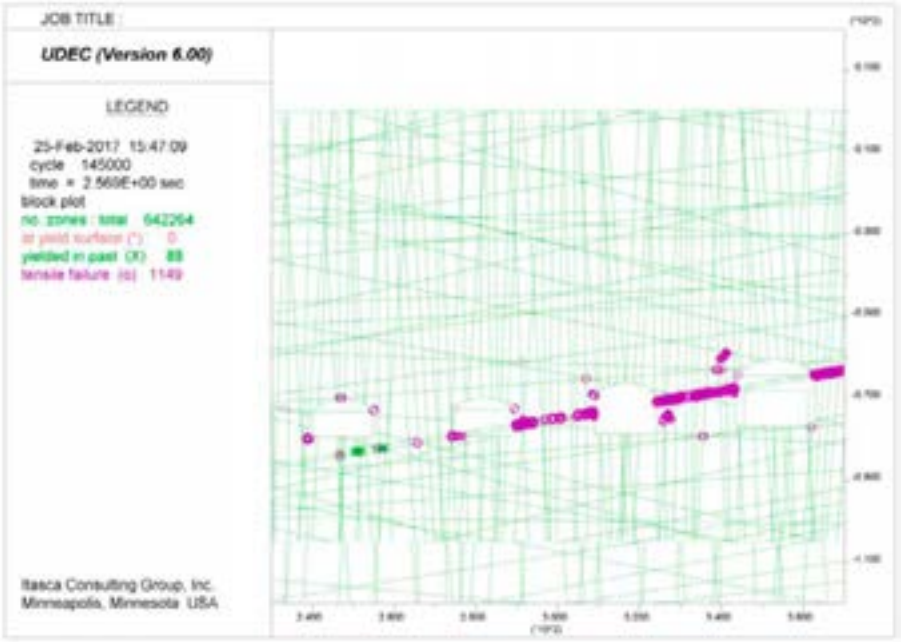


**Figure A13.** UDEC results after construction and backfilling stages, showing yielded elements for SFR 1, DFN 1-3.

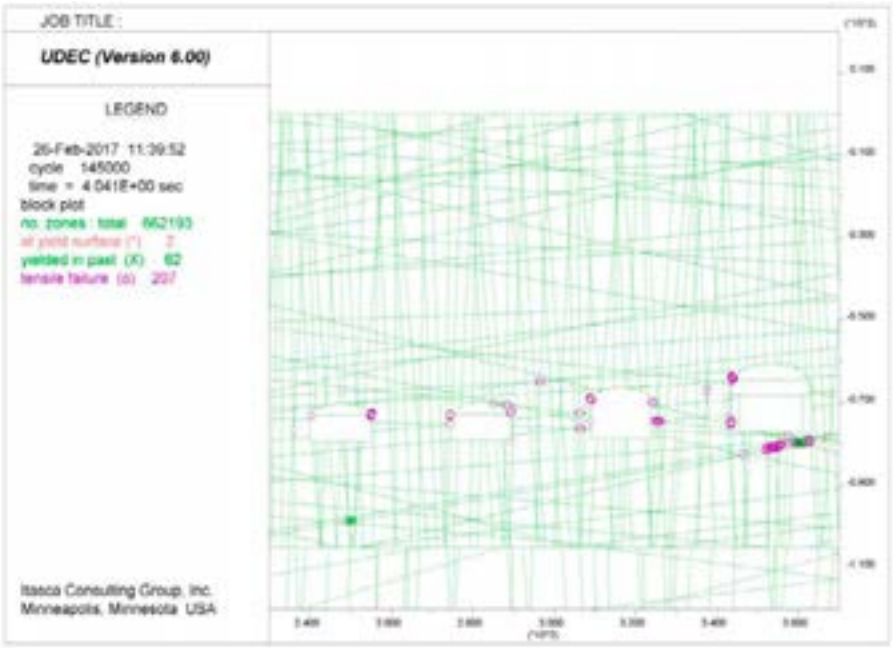


**Figure A14.** UDEC results after construction and backfilling stages, showing yielded elements for SFR 1, DFN 1-4.

## SFR 1 – Construction and Backfilling (Displacement Vectors)

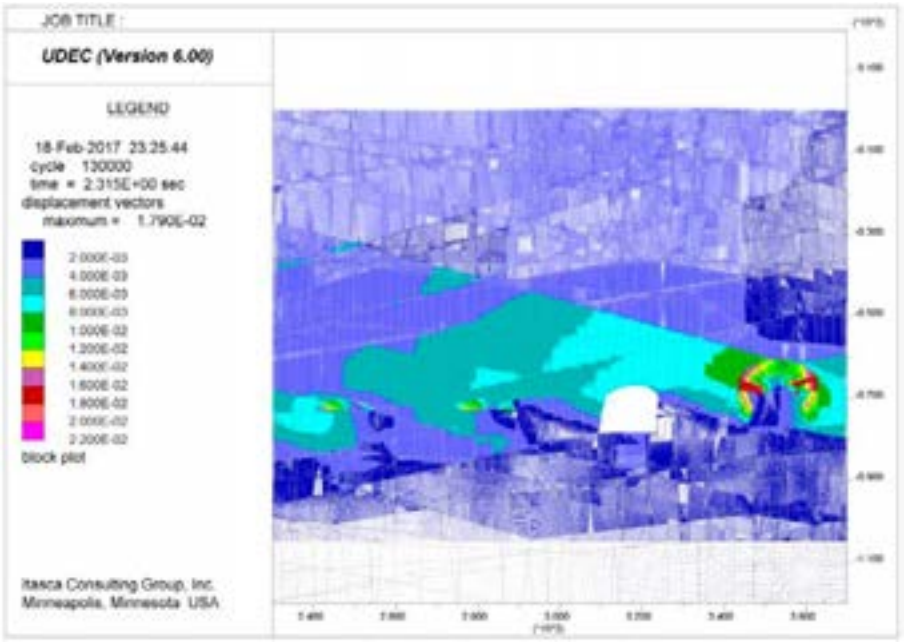


**Figure A15.** UDEC results after construction and backfilling stages, showing displacement vectors for SFR 1, DFN 1-1. Displacement magnitudes are in units of metres.

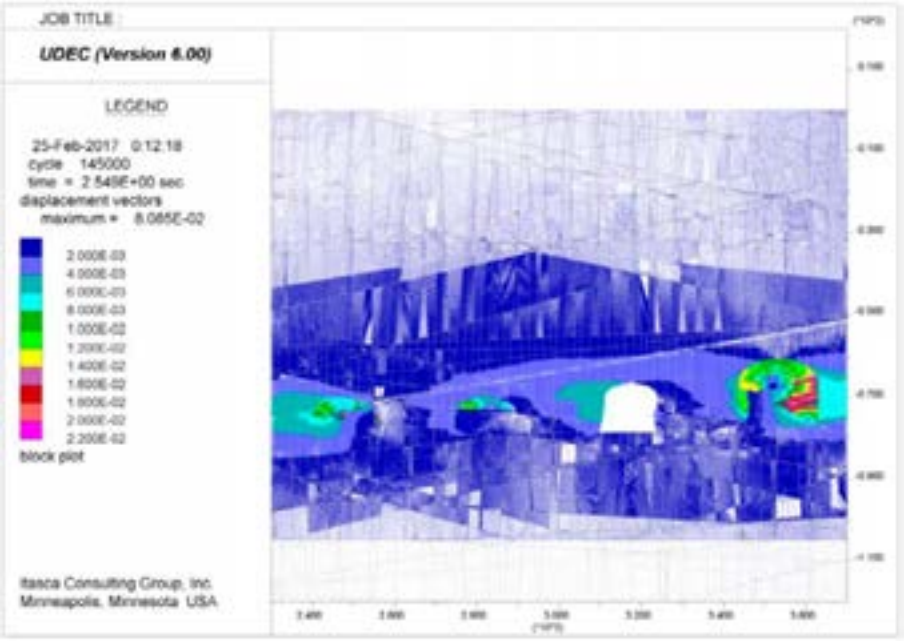


**Figure A16.** UDEC results after construction and backfilling stages, showing displacement vectors for SFR 1, DFN 1-2. Displacement magnitudes are in units of metres.

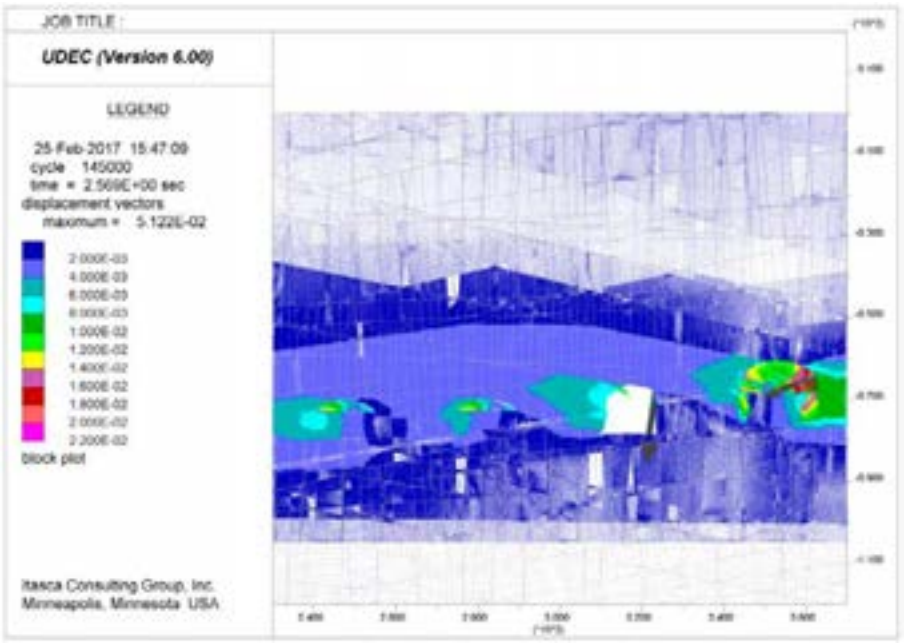


**Figure A17.** UDEC results after construction and backfilling stages, showing displacement vectors for SFR 1, DFN 1-3. Displacement magnitudes are in units of metres.

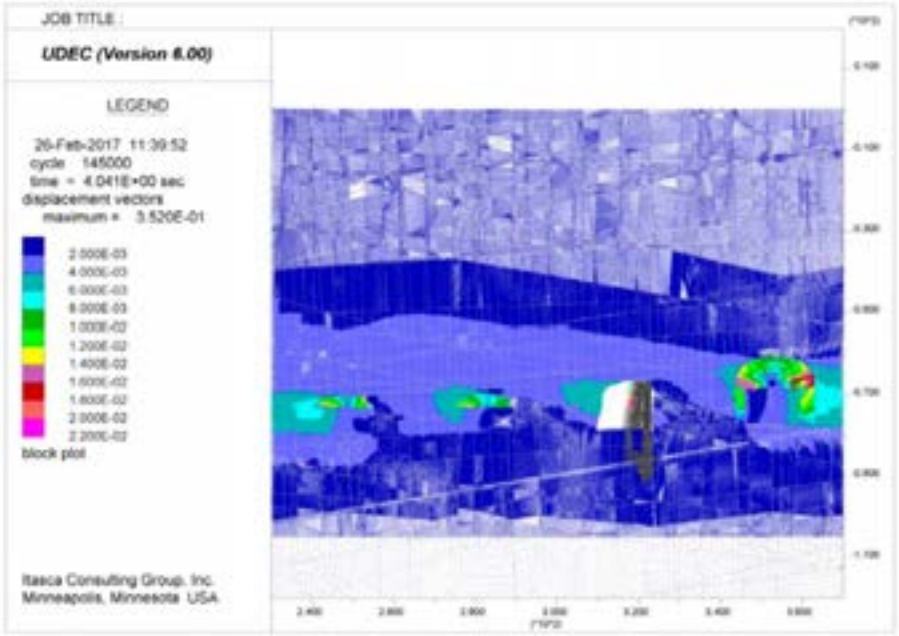


**Figure A18.** UDEC results after construction and backfilling stages, showing displacement vectors for SFR 1, DFN 1-4. Displacement magnitudes are in units of metres.

## SFR 1 – Construction and Backfilling (Fracture Shear Displacement)

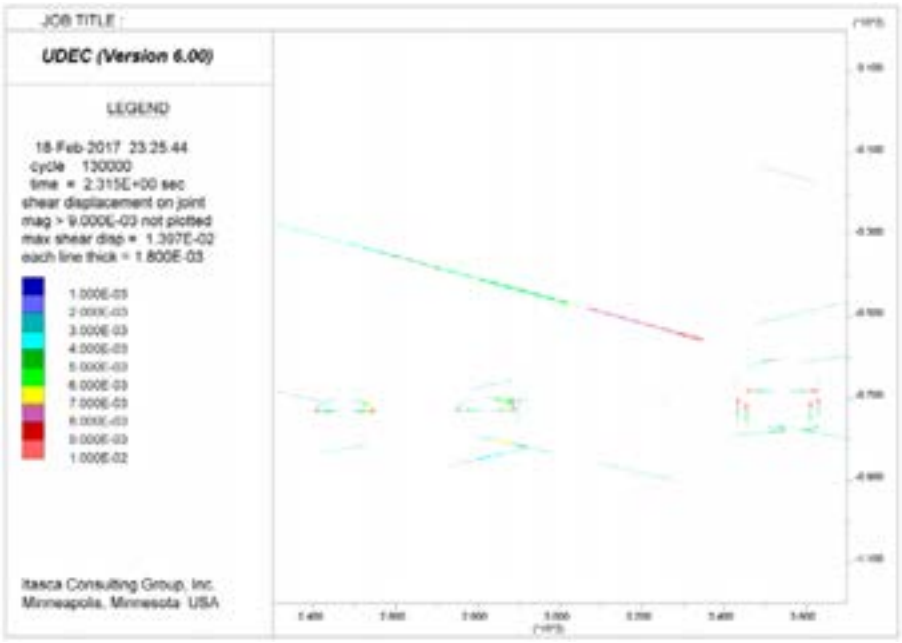


**Figure A19.** UDEC results after construction and backfilling stages, showing shear displacements along fractures for SFR 1, DFN 1-1. Displacements are in units of metres.

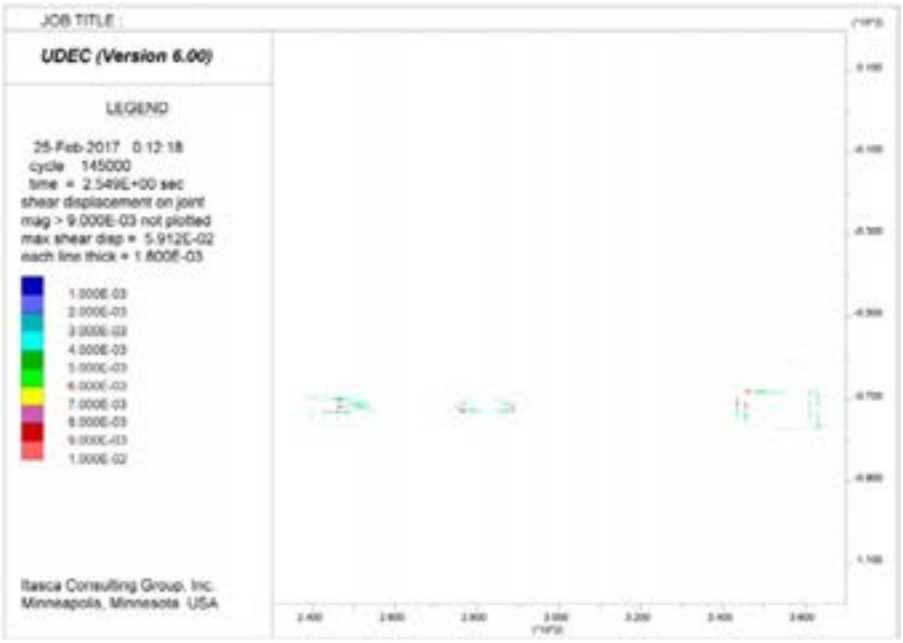


**Figure A20.** UDEC results after construction and backfilling stages, showing shear displacements along fractures for SFR 1, DFN 1-2. Displacements are in units of metres.

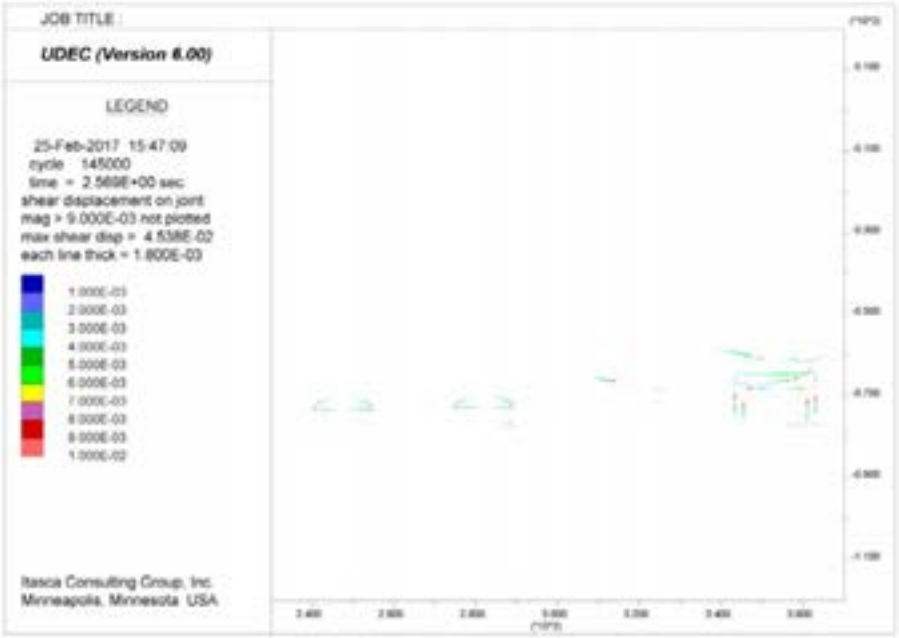


**Figure A21.** UDEC results after construction and backfilling stages, showing shear displacements along fractures for SFR 1, DFN 1-3. Displacements are in units of metres.

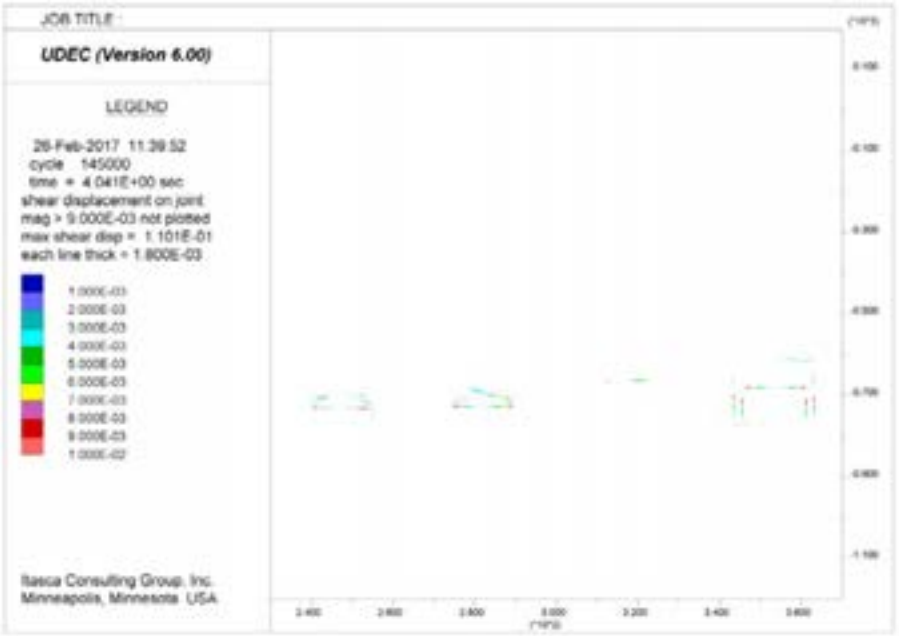


**Figure A22.** UDEC results after construction and backfilling stages, showing shear displacements along fractures for SFR 1, DFN 1-4. Displacements are in units of metres.

## SFR 1 – Construction and Backfilling (Vertical Displacements)

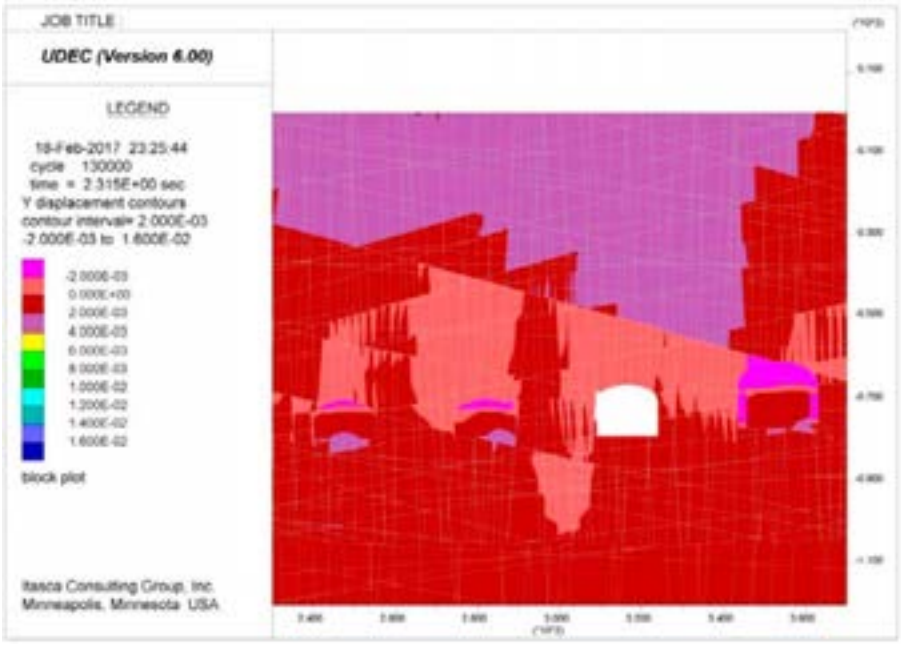


**Figure A23.** UDEC results after construction and backfilling stages, showing vertical displacements for SFR 1, DFN 1-1. Displacements are in units of metres, with positive up.

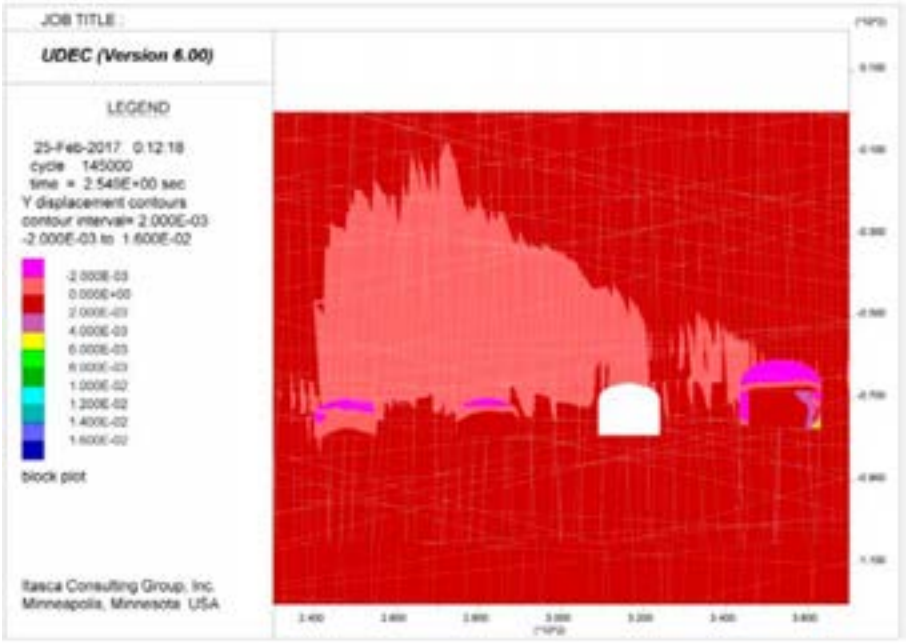


**Figure A24.** UDEC results after construction and backfilling stages, showing vertical displacements for SFR 1, DFN 1-2. Displacements are in units of metres, with positive up.

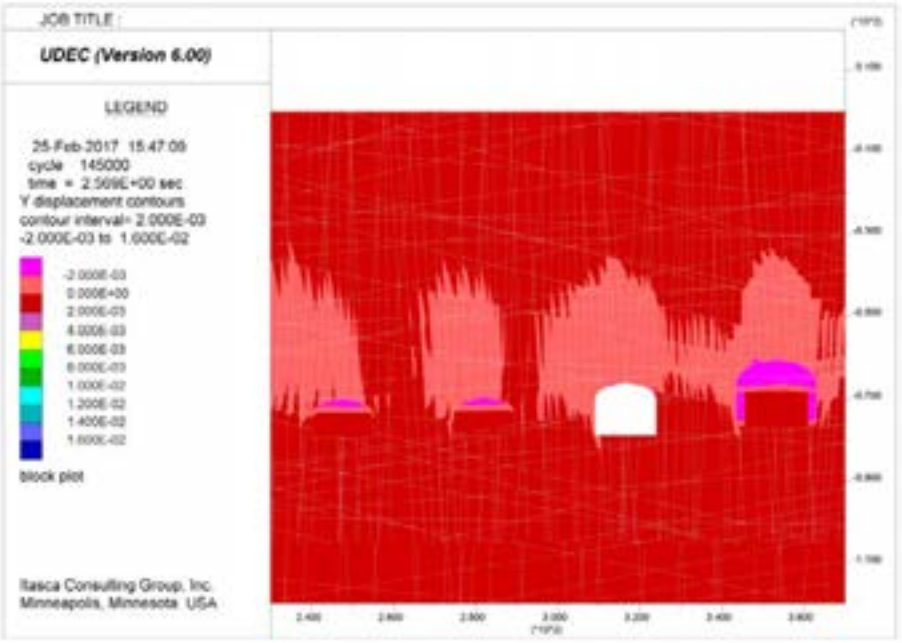


**Figure A25.** UDEC results after construction and backfilling stages, showing vertical displacements for SFR 1, DFN 1-3. Displacements are in units of metres, with positive up.

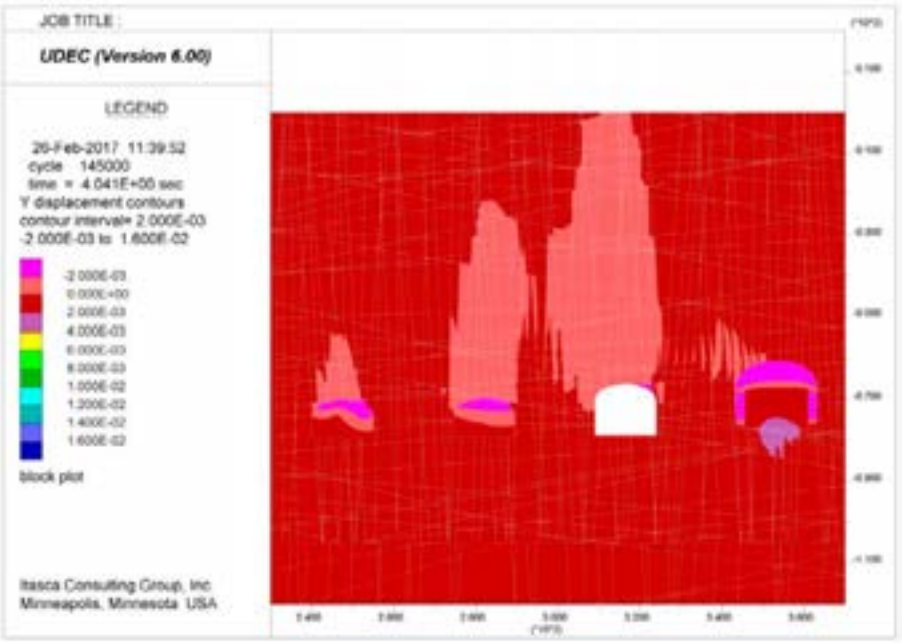


**Figure A26.** UDEC results after construction and backfilling stages, showing vertical displacements for SFR 1, DFN 1-4. Displacements are in units of metres, with positive up.

## SFR 1 – Construction and Backfilling (Horizontal Displacements)

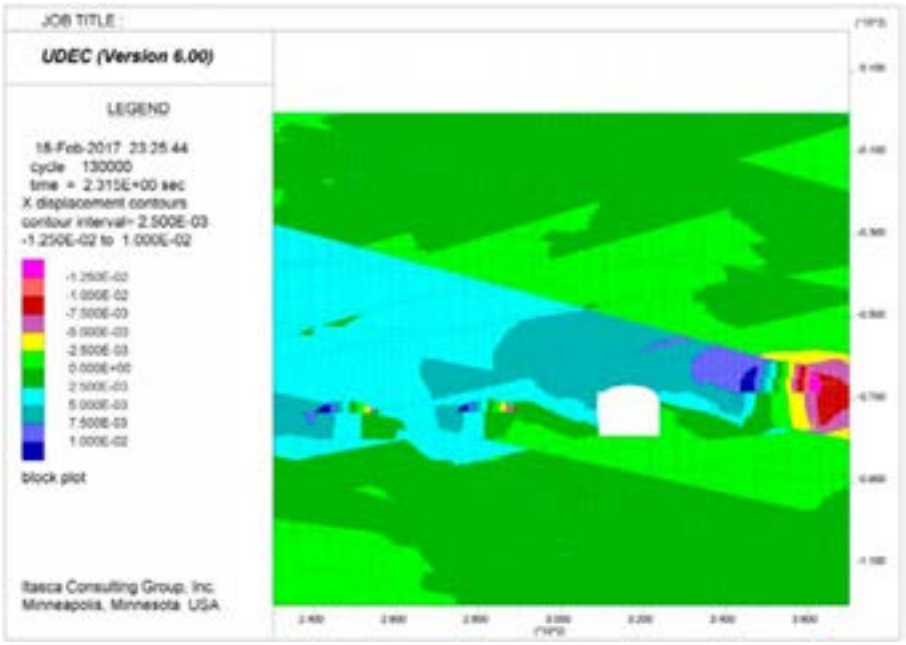


**Figure A27.** UDEC results after construction and backfilling stages, showing horizontal displacements for SFR 1, DFN 1-1. Displacements are in units of metres, with positive to the right.

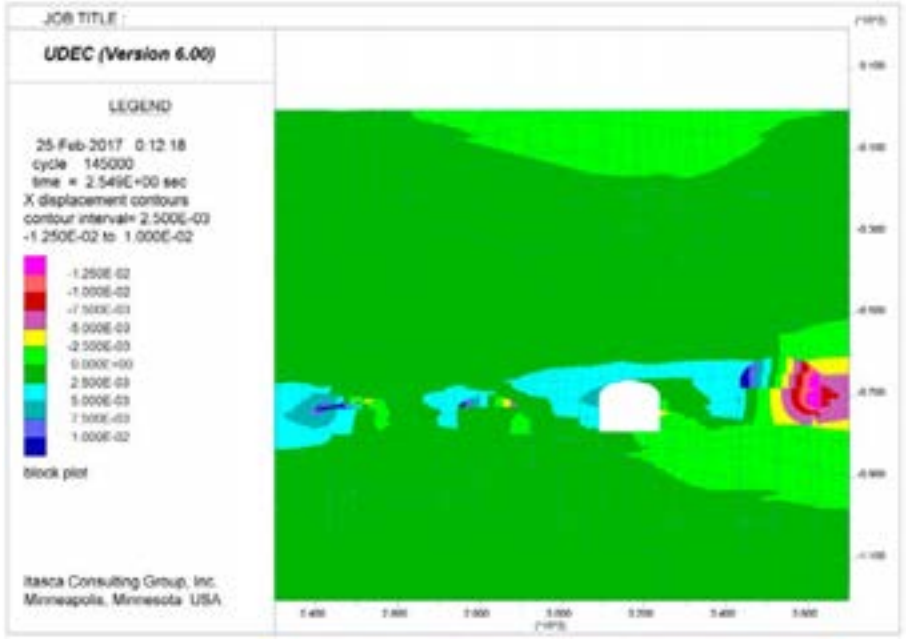


**Figure A28.** UDEC results after construction and backfilling stages, showing horizontal displacements for SFR 1, DFN 1-2. Displacements are in units of metres, with positive to the right.

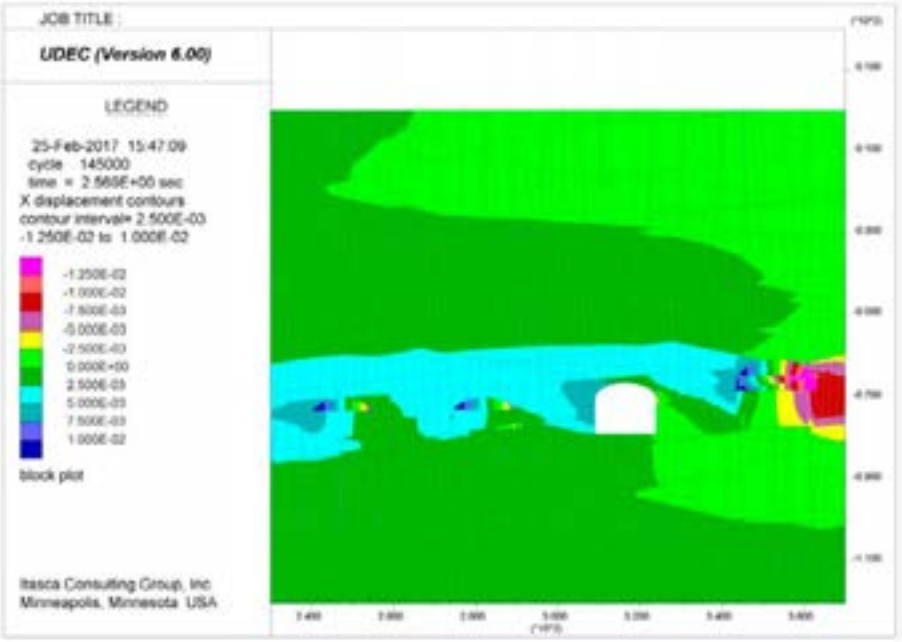


**Figure A29.** UDEC results after construction and backfilling stages, showing horizontal displacements for SFR 1, DFN 1-3. Displacements are in units of metres, with positive to the right.

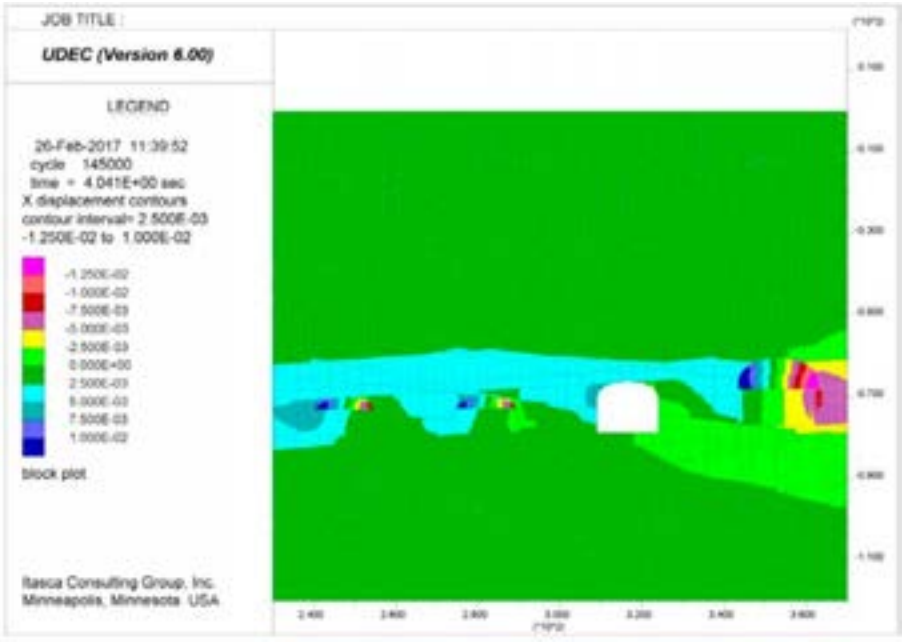


**Figure A30.** UDEC results after construction and backfilling stages, showing horizontal displacements for SFR 1, DFN 1-4. Displacements are in units of metres, with positive to the right.

## SFR 1 – Year 1000 Strength Degradation (Vertical Stress)

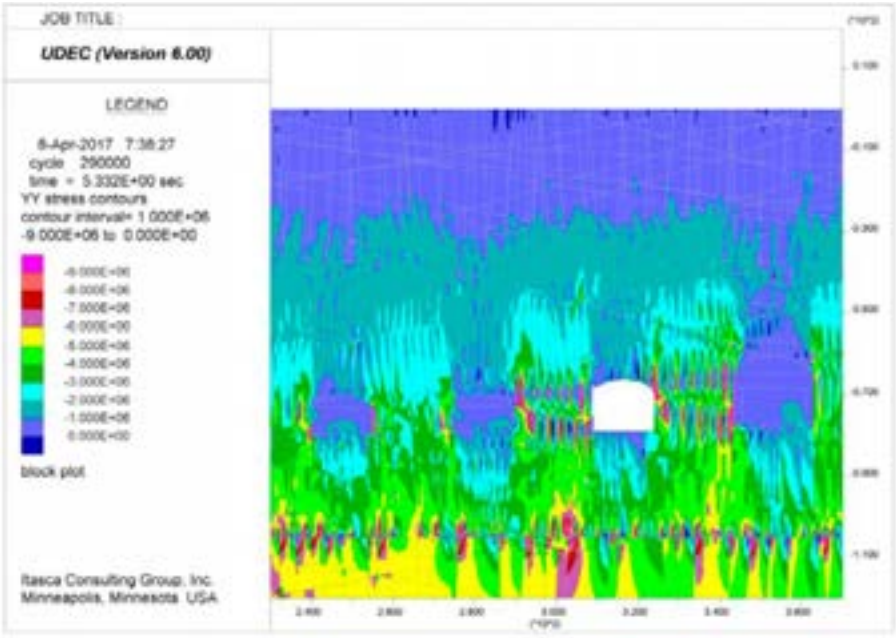


**Figure A31.** UDEC results after strength degradation up to Year 1000, showing vertical stresses (SYY) for SFR 1, DFN 1-1. Stress magnitudes are in units of Pascals, with compression negative.

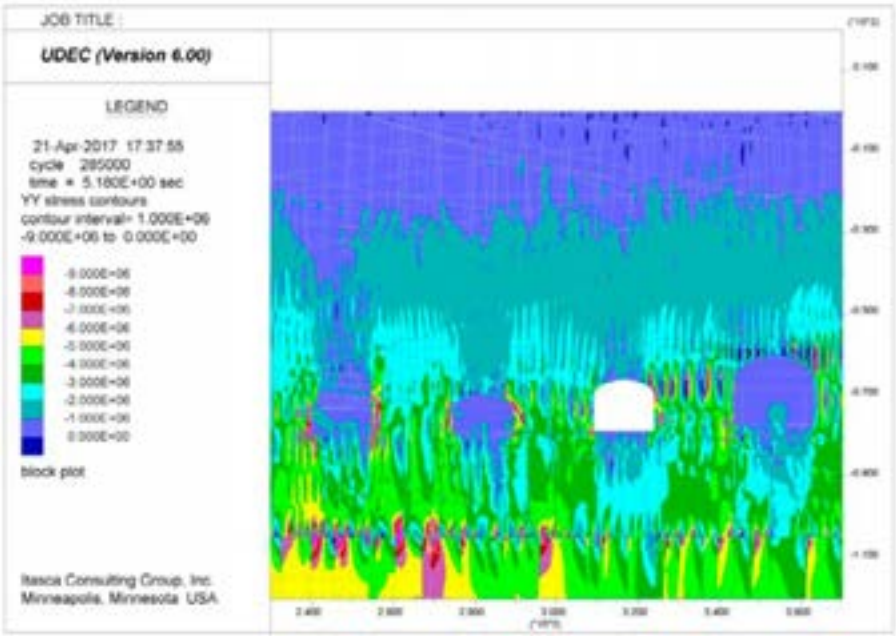


**Figure A32.** UDEC results after strength degradation up to Year 1000, showing vertical stresses (SYY) for SFR 1, DFN 1-2. Stress magnitudes are in units of Pascals, with compression negative.

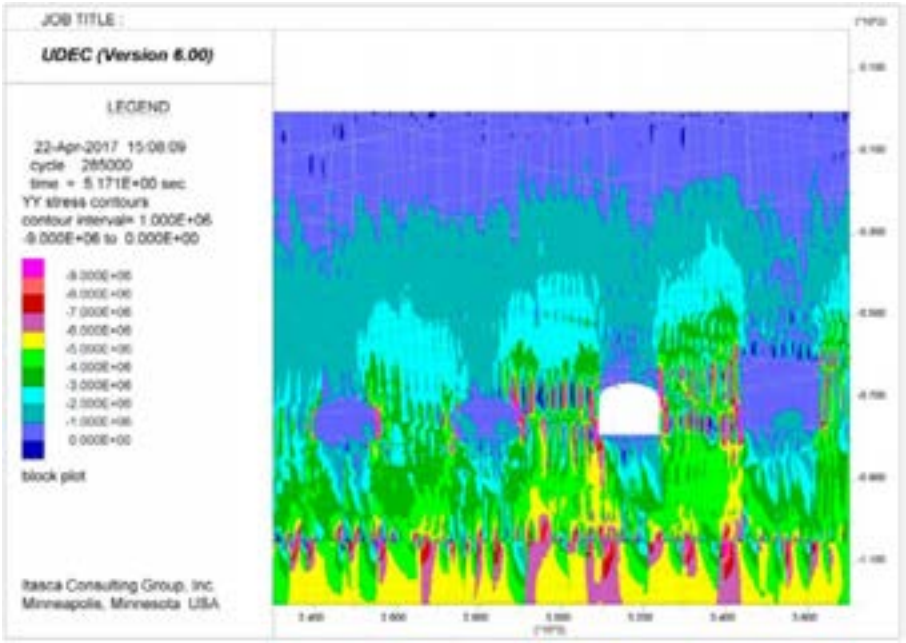


**Figure A33.** UDEC results after strength degradation up to Year 1000, showing vertical stresses (SYY) for SFR 1, DFN 1-3. Stress magnitudes are in units of Pascals, with compression negative.

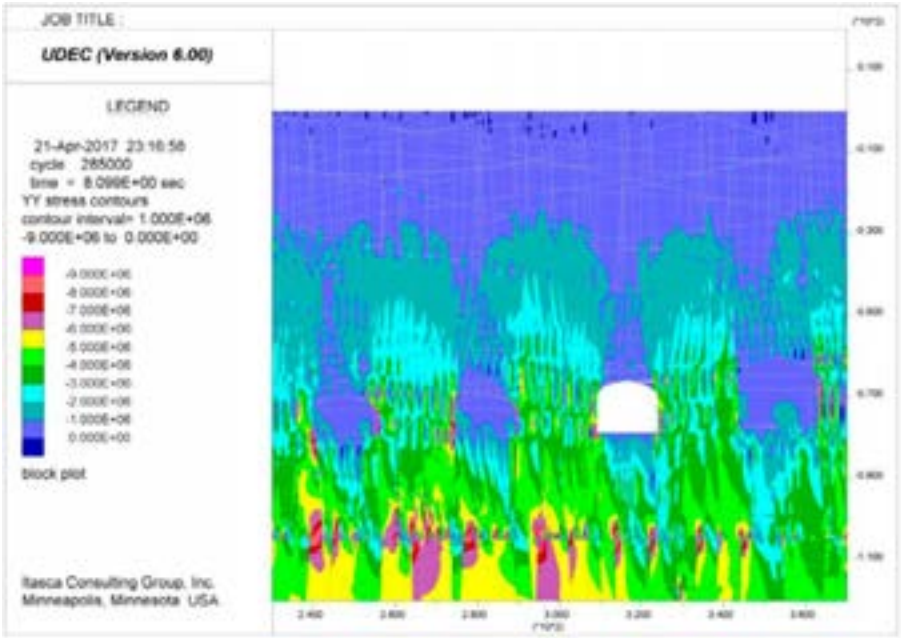


**Figure A34.** UDEC results after strength degradation up to Year 1000, showing vertical stresses (SYY) for SFR 1, DFN 1-4. Stress magnitudes are in units of Pascals, with compression negative.

## SFR 1 – Year 1000 Strength Degradation (Horizontal Stress)

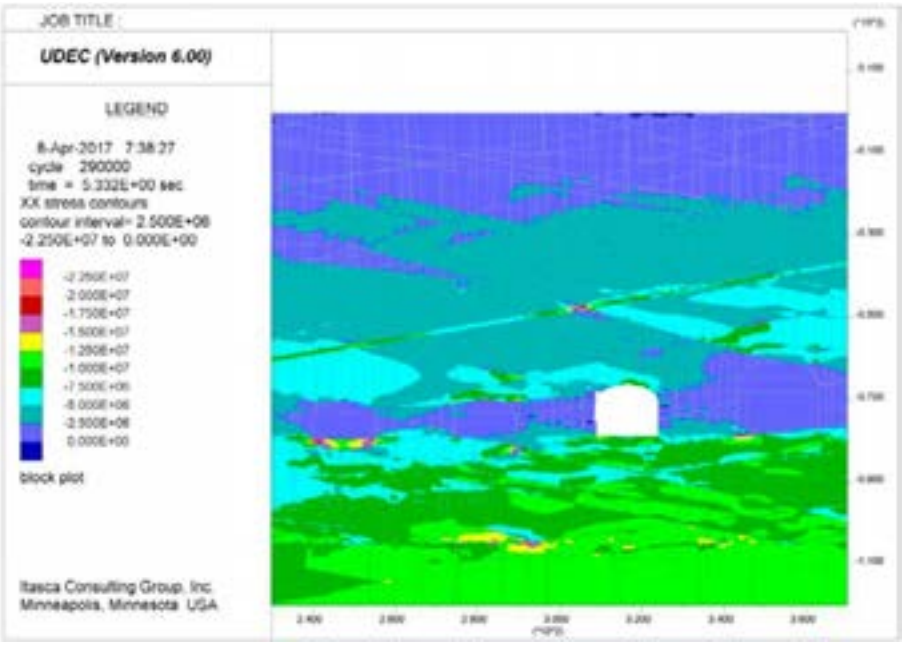


**Figure A35.** UDEC results after strength degradation up to Year 1000, showing horizontal stresses (SXX) for SFR 1, DFN 1-1. Stress magnitudes are in units of Pascals, with compression negative.

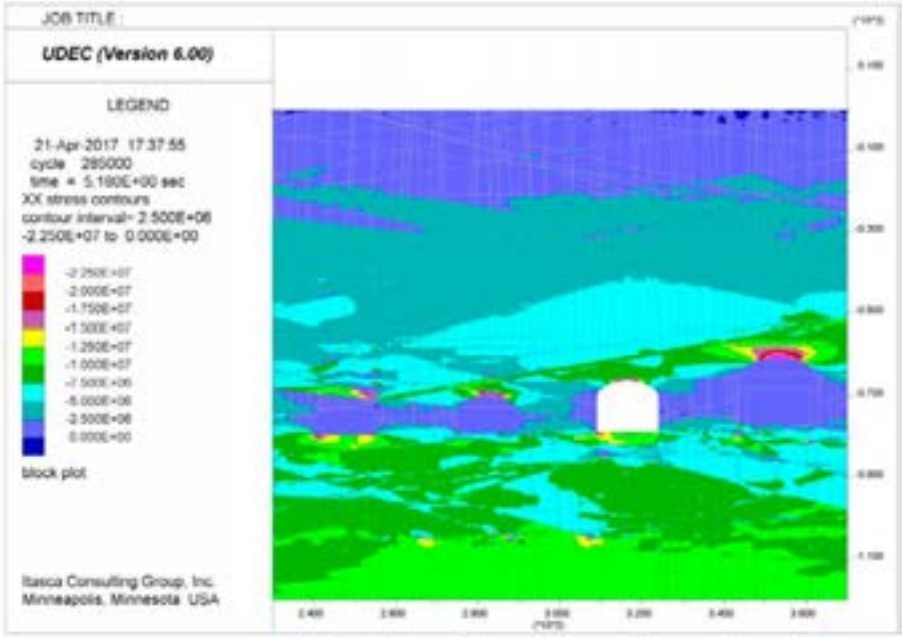


**Figure A36.** UDEC results after strength degradation up to Year 1000, showing horizontal stresses (SXX) for SFR 1, DFN 1-2. Stress magnitudes are in units of Pascals, with compression negative.

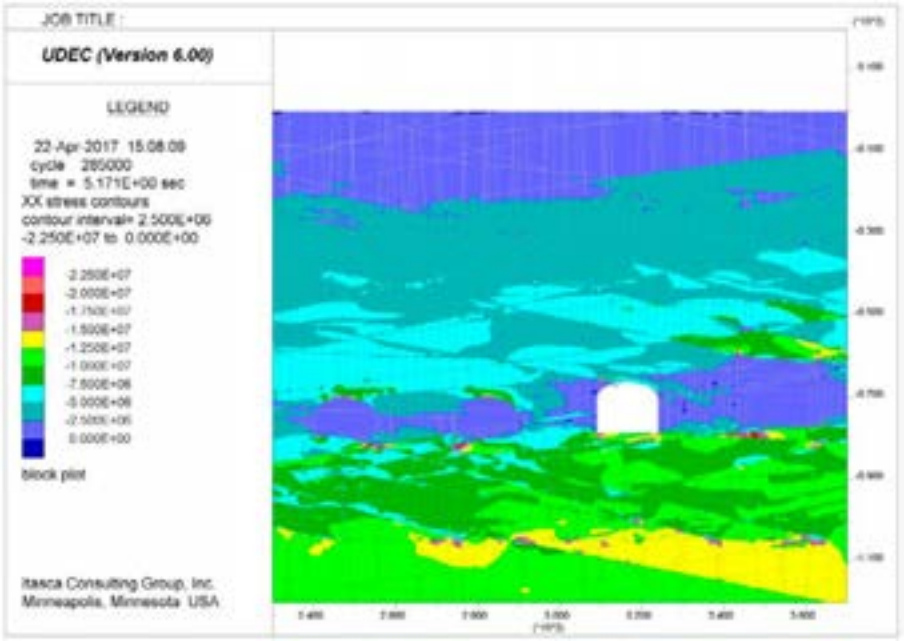


**Figure A37.** UDEC results after strength degradation up to Year 1000, showing horizontal stresses (SXX) for SFR 1, DFN 1-3. Stress magnitudes are in units of Pascals, with compression negative.

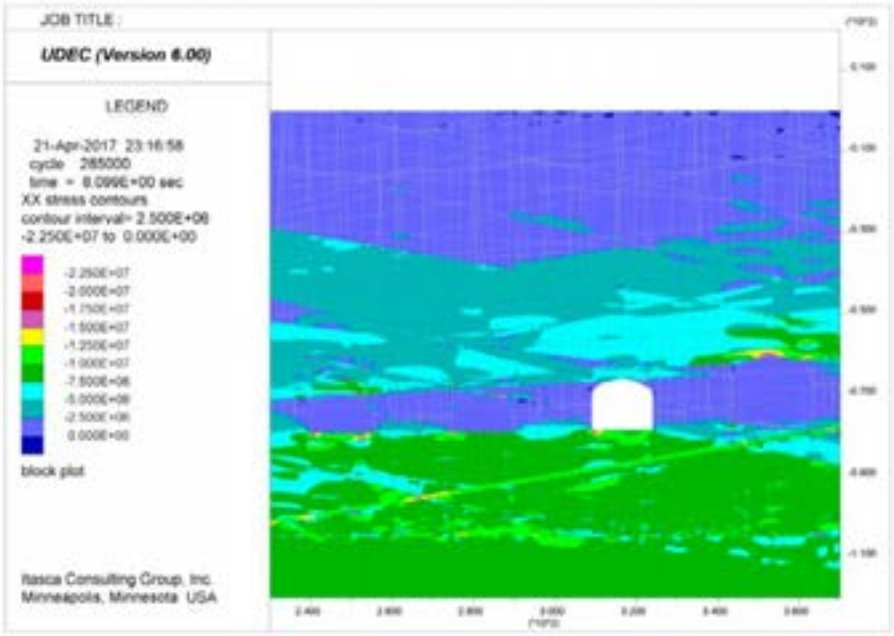


**Figure A38.** UDEC results after strength degradation up to Year 1000, showing horizontal stresses (SXX) for SFR 1, DFN 1-4. Stress magnitudes are in units of Pascals, with compression negative.

## SFR 1 – Year 1000 Strength Degradation (Plasticity Indicators)

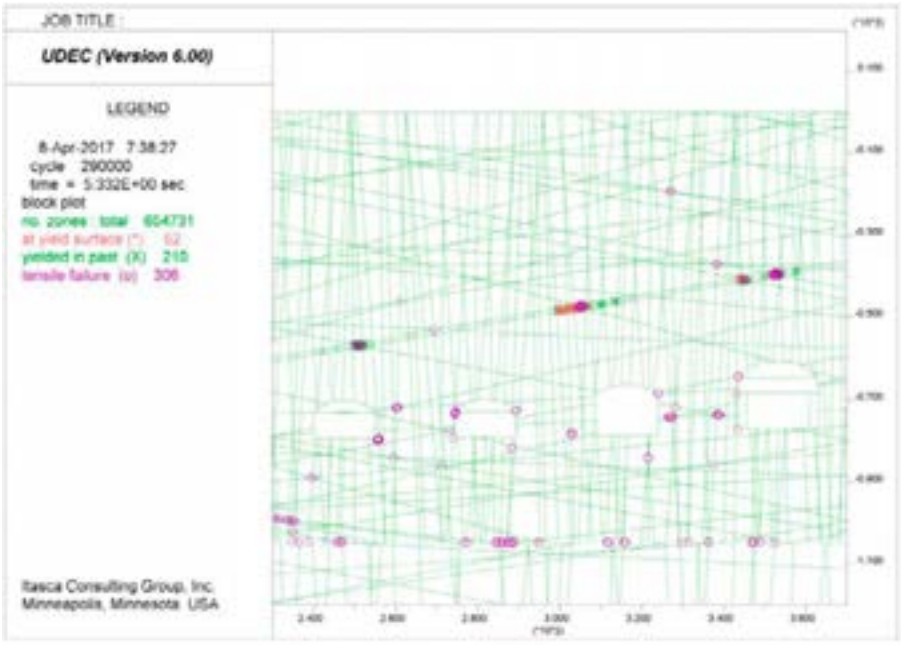


**Figure A39.** UDEC results after strength degradation up to Year 1000, showing yielded elements for SFR 1, DFN 1-1.

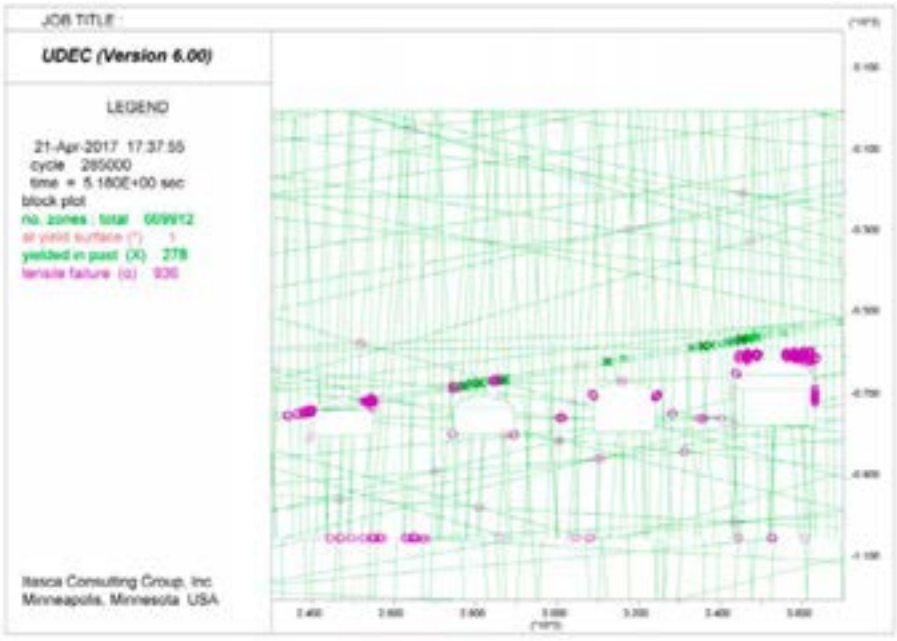


**Figure A40.** UDEC results after strength degradation up to Year 1000, showing yielded elements for SFR 1, DFN 1-2.

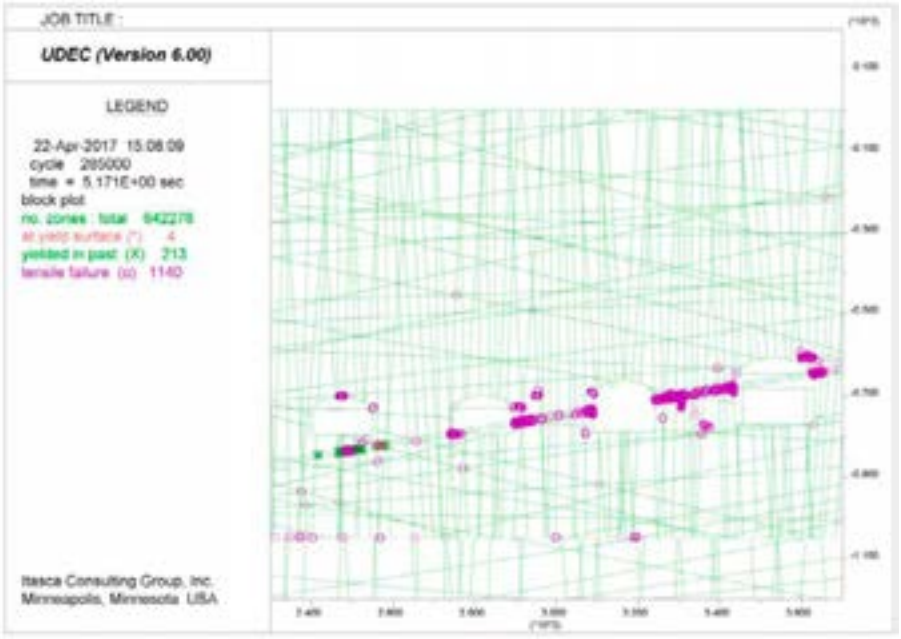


**Figure A41.** UDEC results after strength degradation up to Year 1000, showing yielded elements for SFR 1, DFN 1-3.

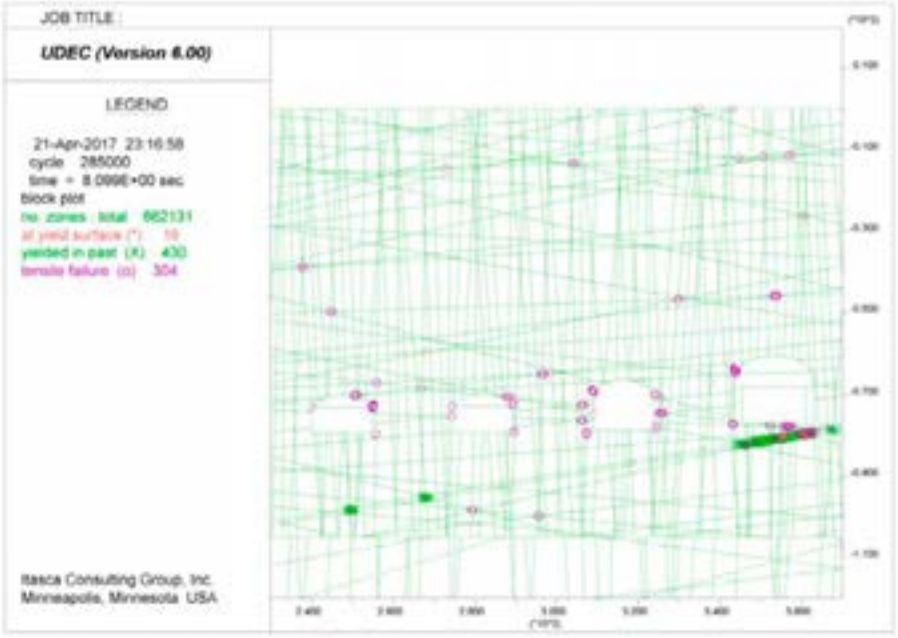


**Figure A42.** UDEC results after strength degradation up to Year 1000, showing yielded elements for SFR 1, DFN 1-4.

## SFR 1 – Year 1000 Strength Degradation (Displacement Vectors)

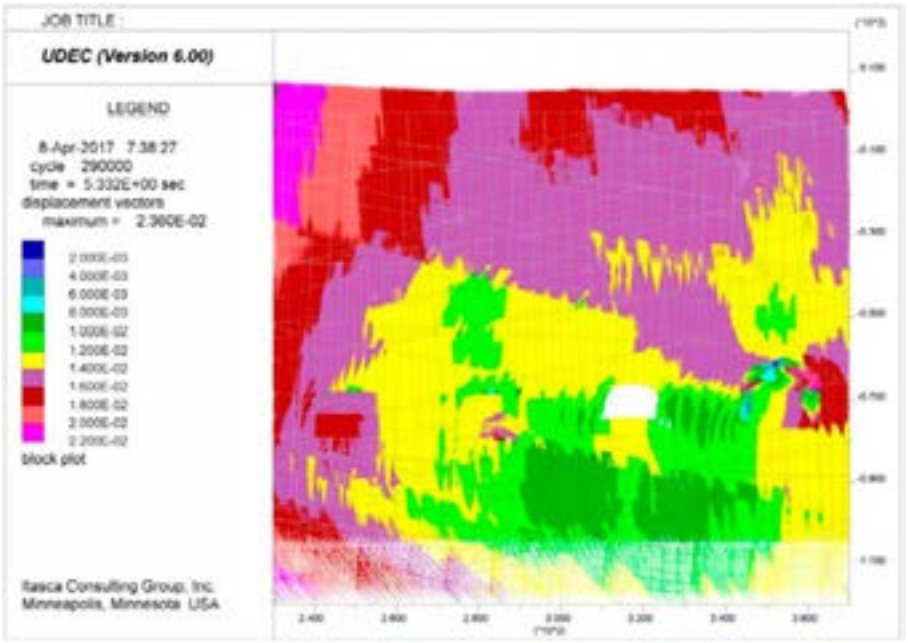


**Figure A43.** UDEC results after strength degradation up to Year 1000, showing displacement vectors for SFR 1, DFN 1-1. Displacement magnitudes are in units of metres.

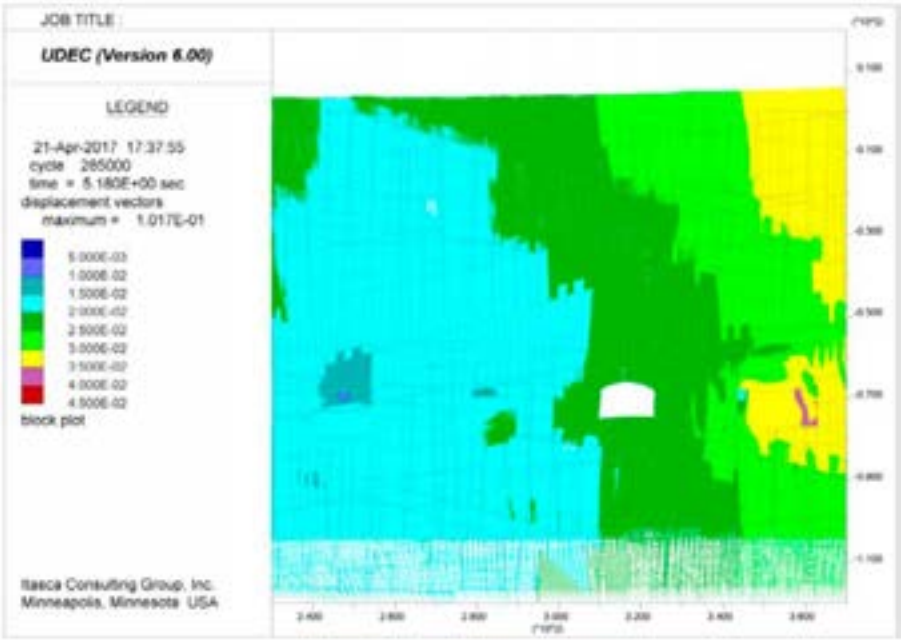


**Figure A44.** UDEC results after strength degradation up to Year 1000, showing displacement vectors for SFR 1, DFN 1-2. Displacement magnitudes are in units of metres.

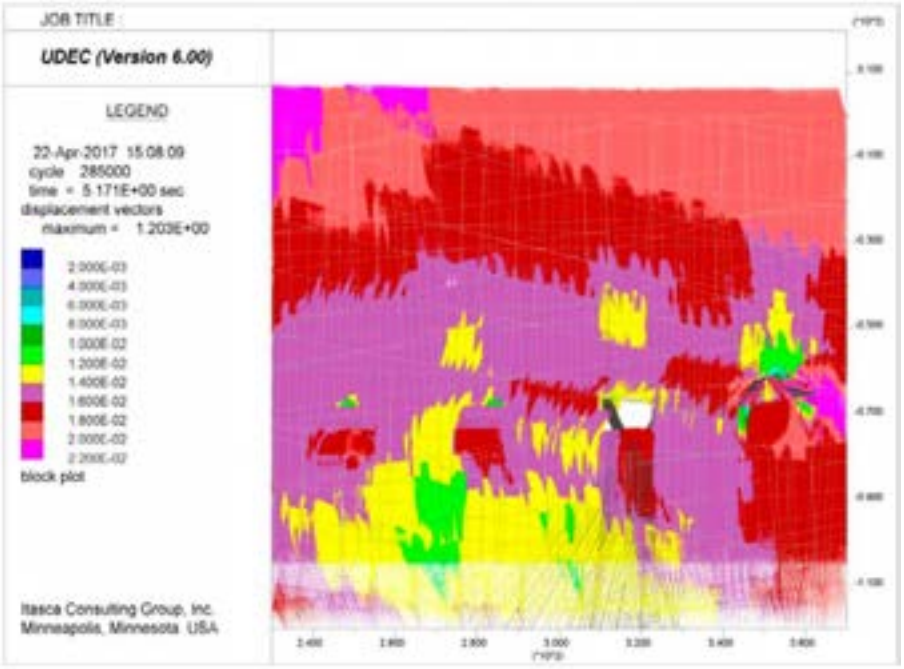


**Figure A45.** UDEC results after strength degradation up to Year 1000, showing displacement vectors for SFR 1, DFN 1-3. Displacement magnitudes are in units of metres.

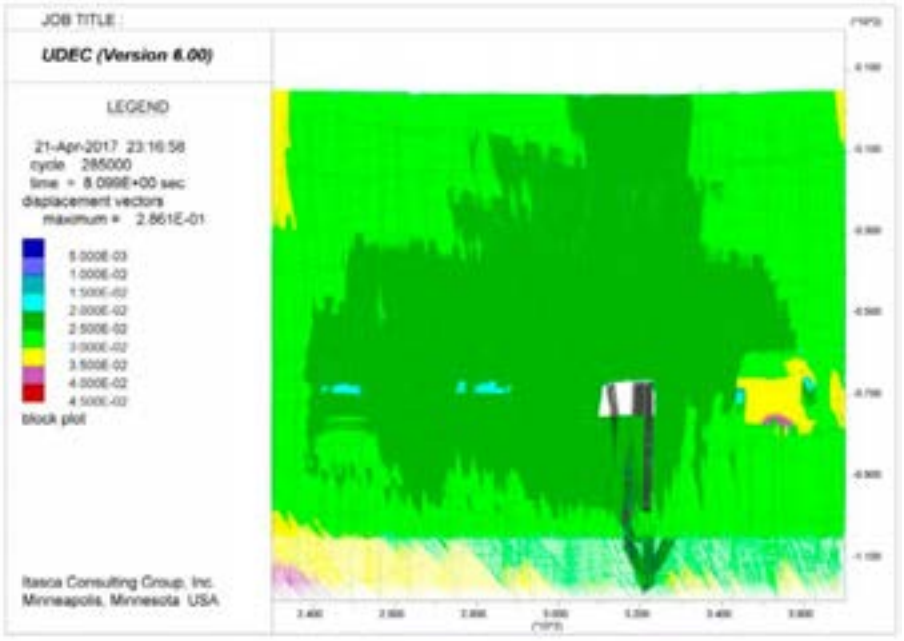


**Figure A46.** UDEC results after strength degradation up to Year 1000, showing displacement vectors for SFR 1, DFN 1-4. Displacement magnitudes are in units of metres.

## SFR 1 – Year 1000 Strength Degradation (Fracture Shear Displacement)

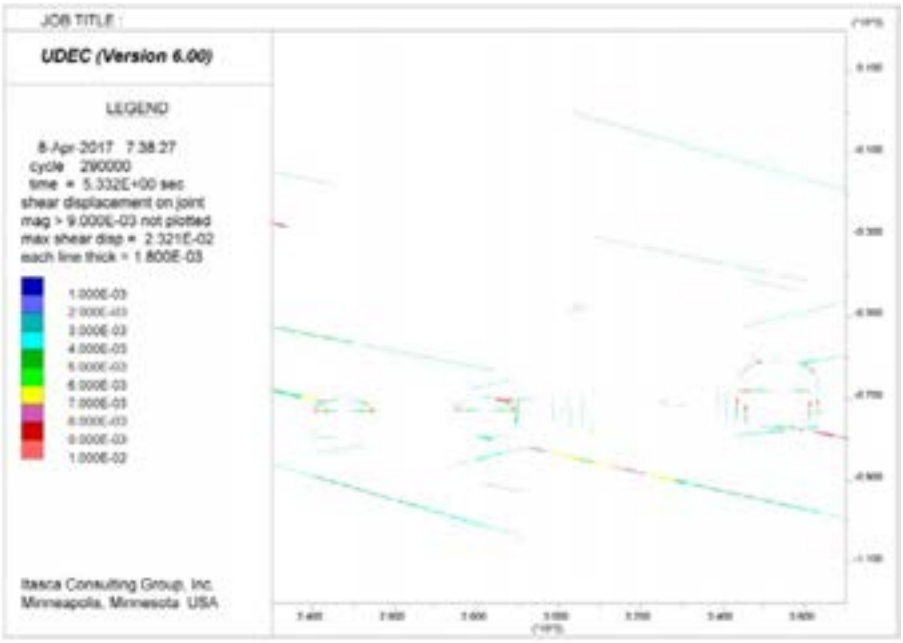


**Figure A47.** UDEC results after strength degradation up to Year 1000, showing shear displacements along fractures for SFR 1, DFN 1-1. Displacements are in units of metres.

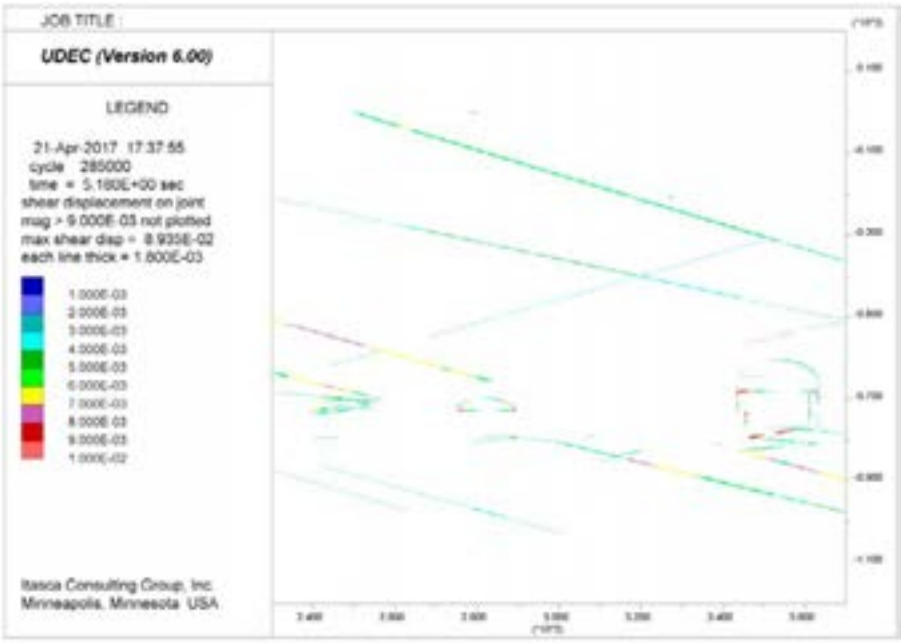


**Figure A48.** UDEC results after strength degradation up to Year 1000, showing shear displacements along fractures for SFR 1, DFN 1-2. Displacements are in units of metres.

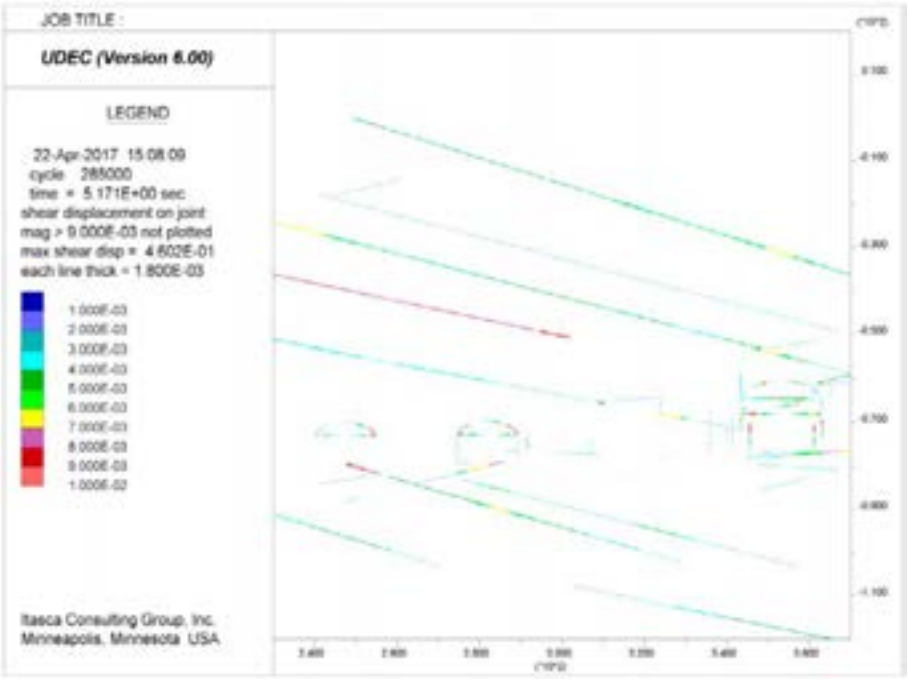


**Figure A49.** UDEC results after strength degradation up to Year 1000, showing shear displacements along fractures for SFR 1, DFN 1-3. Displacements are in units of metres.

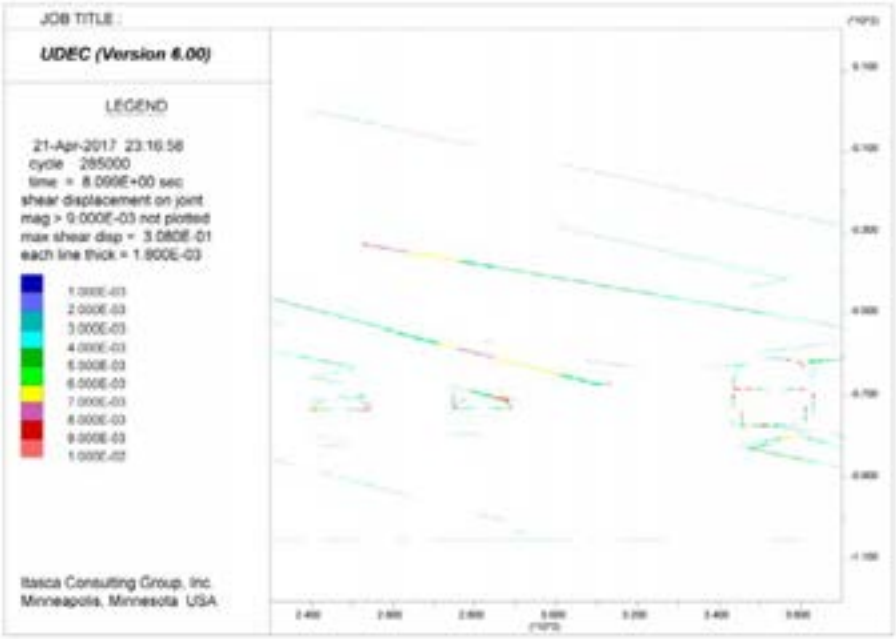


**Figure A50.** UDEC results after strength degradation up to Year 1000, showing shear displacements along fractures for SFR 1, DFN 1-4. Displacements are in units of metres.

## SFR 1 – Year 1000 Strength Degradation (Vertical Displacements)

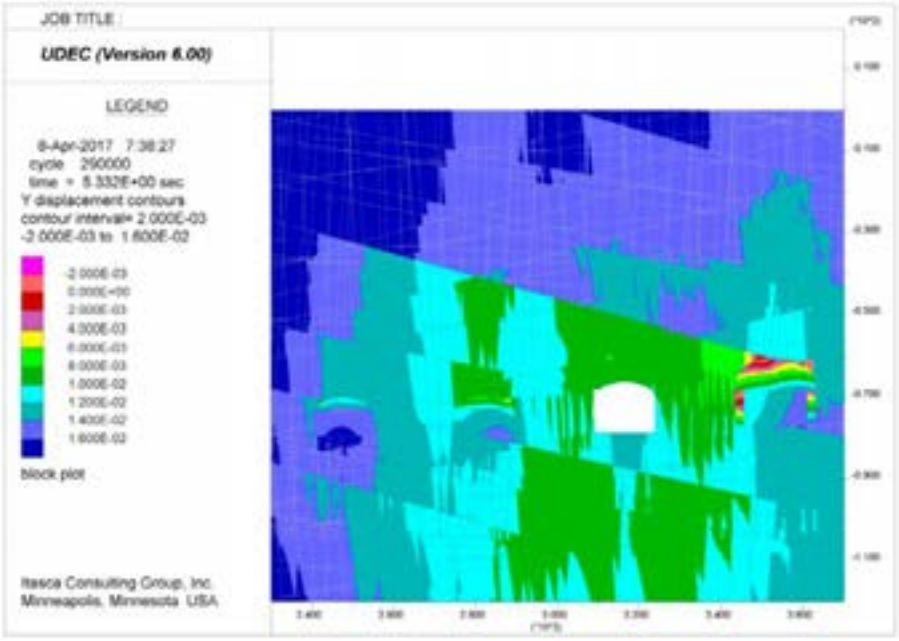


**Figure A51.** UDEC results after strength degradation up to Year 1000, showing vertical displacements for SFR 1, DFN 1-1. Displacements are in units of metres, with positive up.

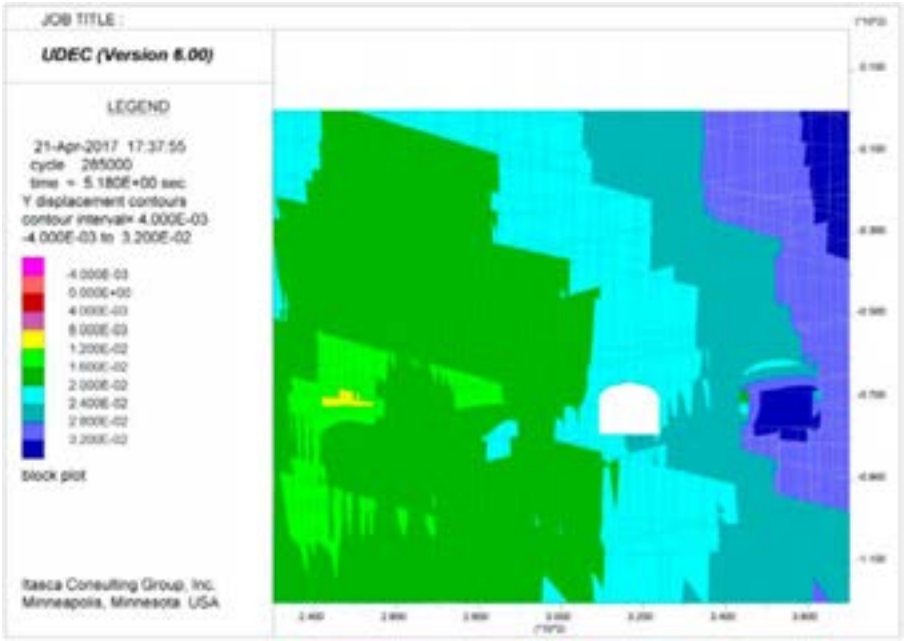


**Figure A52.** UDEC results after strength degradation up to Year 1000, showing vertical displacements for SFR 1, DFN 1-2. Displacements are in units of metres, with positive up.

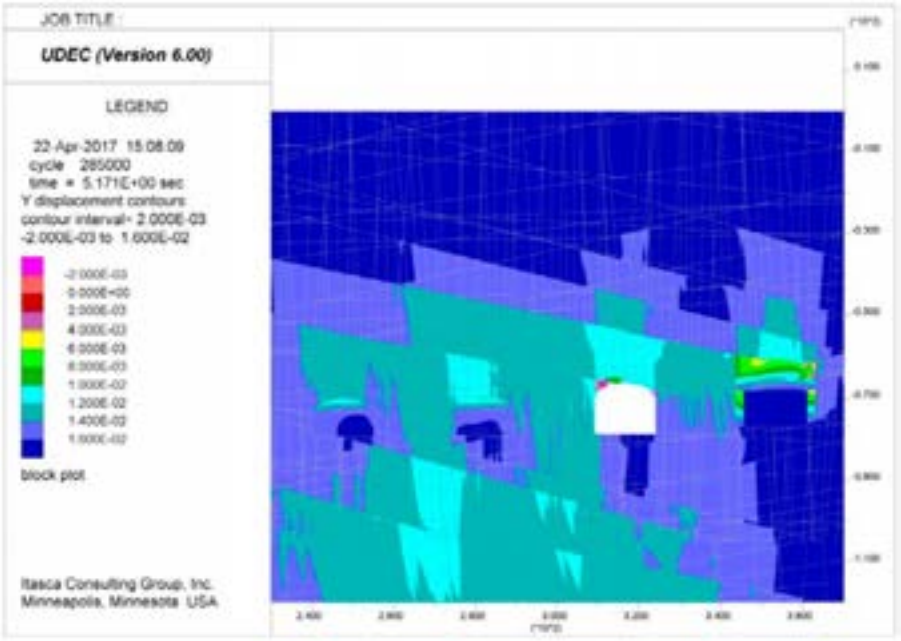


**Figure A53.** UDEC results after strength degradation up to Year 1000, showing vertical displacements for SFR 1, DFN 1-3. Displacements are in units of metres, with positive up.

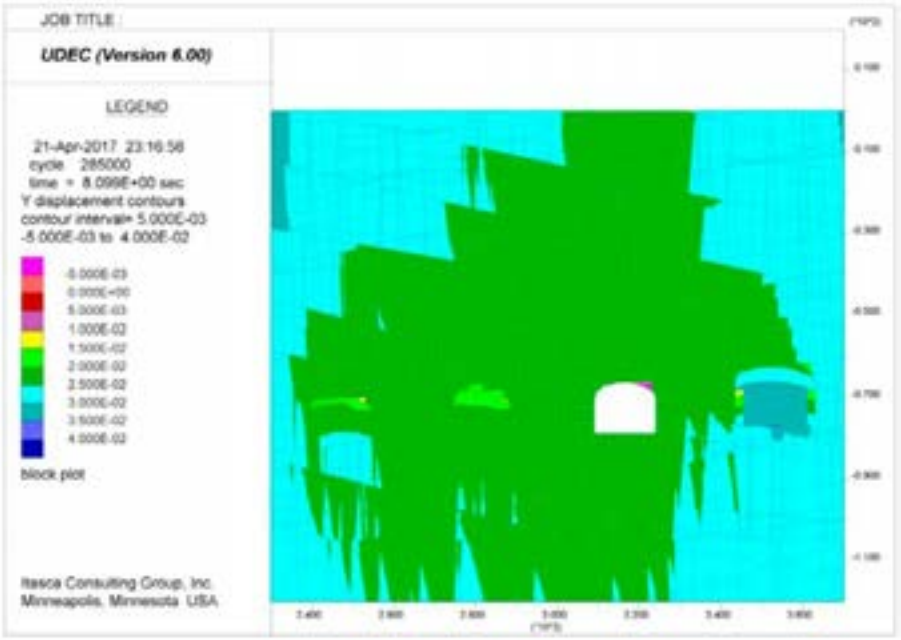


**Figure A54.** UDEC results after strength degradation up to Year 1000, showing vertical displacements for SFR 1, DFN 1-4. Displacements are in units of metres, with positive up.

## SFR 1 – Year 1000 Strength Degradation (Horizontal Displacements)

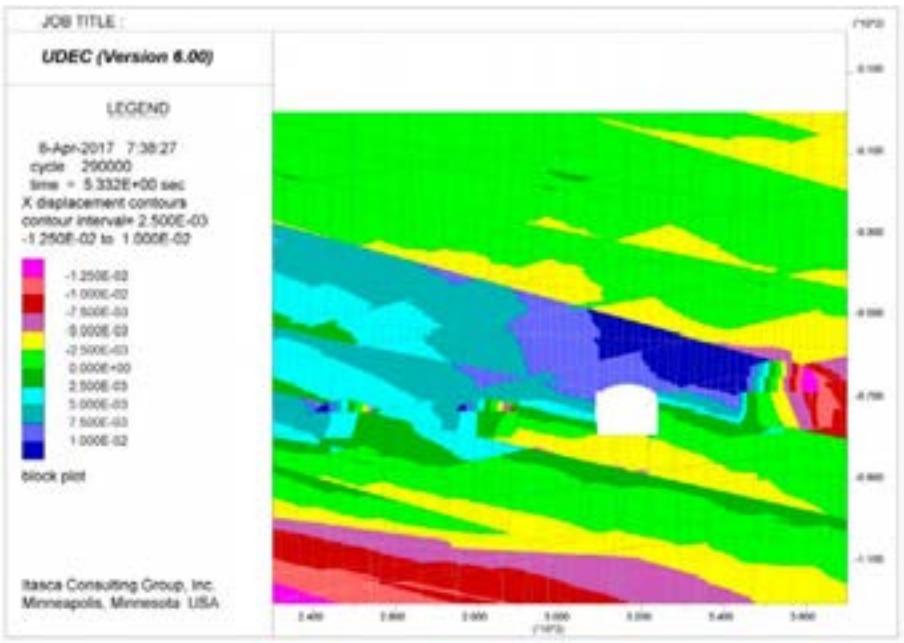


**Figure A55.** UDEC results after strength degradation up to Year 1000, showing horizontal displacements for SFR 1, DFN 1-1. Displacements are in units of metres, with positive to the right.

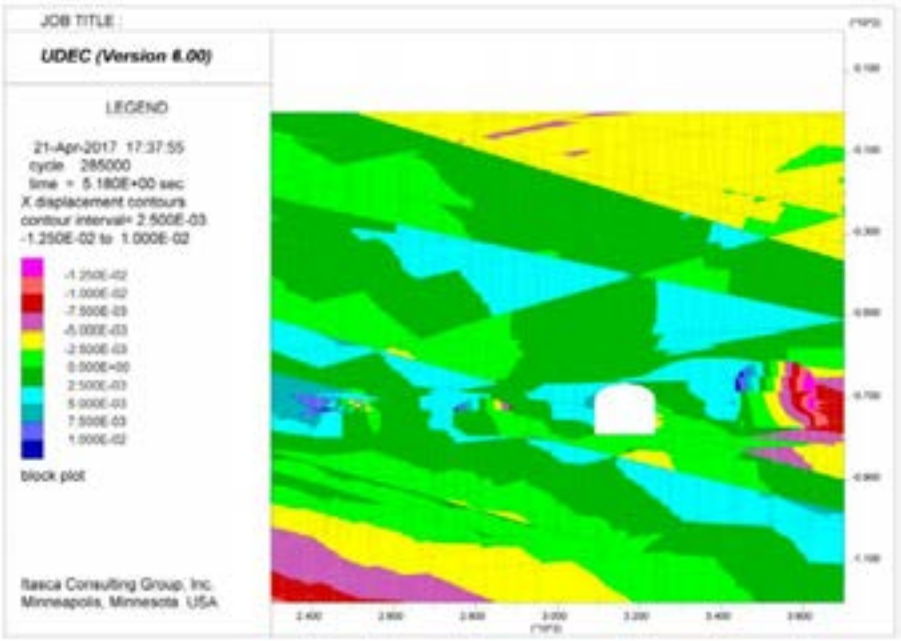


**Figure A56.** UDEC results after strength degradation up to Year 1000, showing horizontal displacements for SFR 1, DFN 1-2. Displacements are in units of metres, with positive to the right.

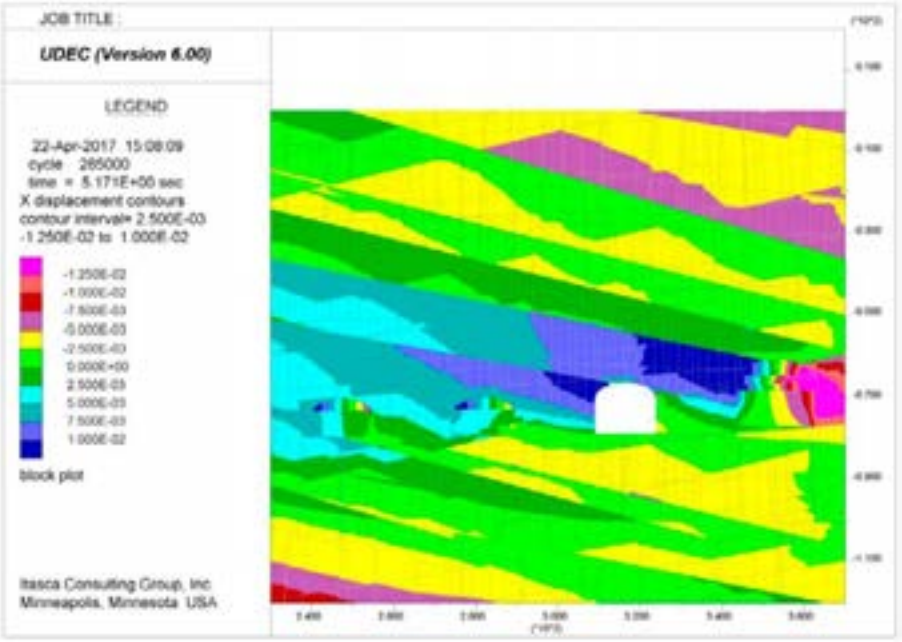


**Figure A57.** UDEC results after strength degradation up to Year 1000, showing horizontal displacements for SFR 1, DFN 1-3. Displacements are in units of metres, with positive to the right.

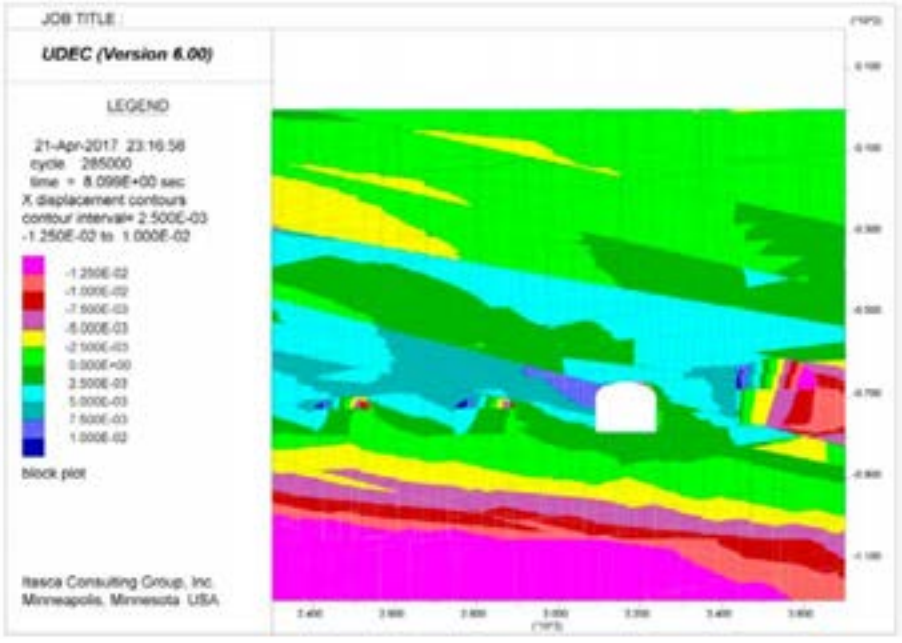


**Figure A58.** UDEC results after strength degradation up to Year 1000, showing horizontal displacements for SFR 1, DFN 1-4. Displacements are in units of metres, with positive to the right.

## SFR 1 – Year 10,000 Strength Degradation (Vertical Stress)

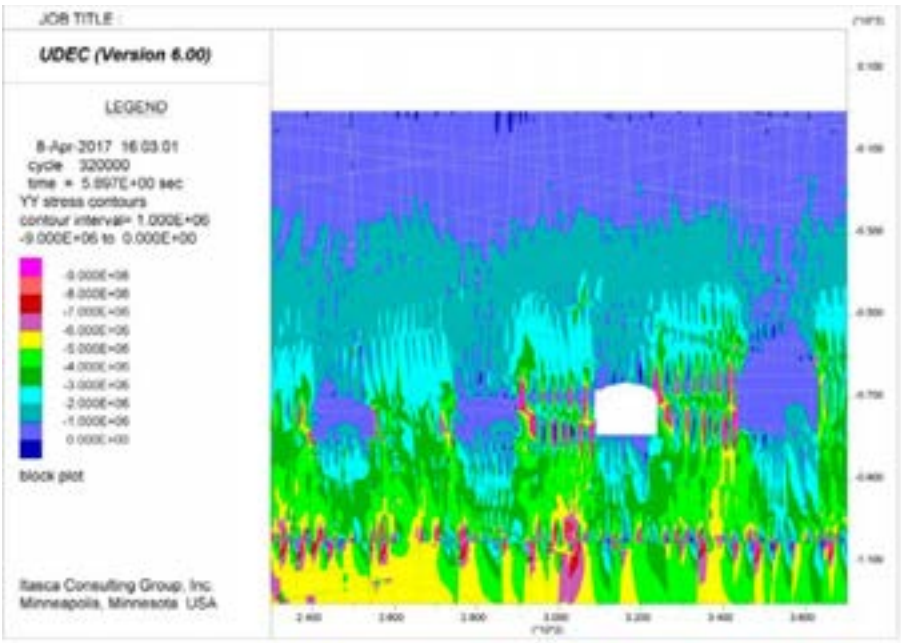


**Figure A59.** UDEC results after strength degradation up to Year 10,000, showing vertical stresses (SYY) for SFR 1, DFN 1-1. Stress magnitudes are in units of Pascals, with compression negative.

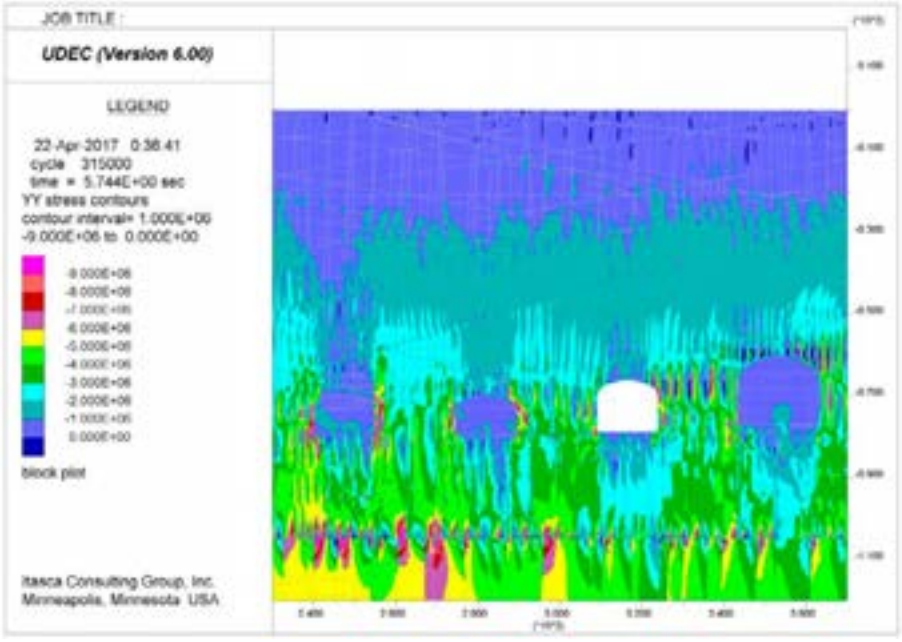


**Figure A60.** UDEC results after strength degradation up to Year 10,000, showing vertical stresses (SYY) for SFR 1, DFN 1-2. Stress magnitudes are in units of Pascals, with compression negative.

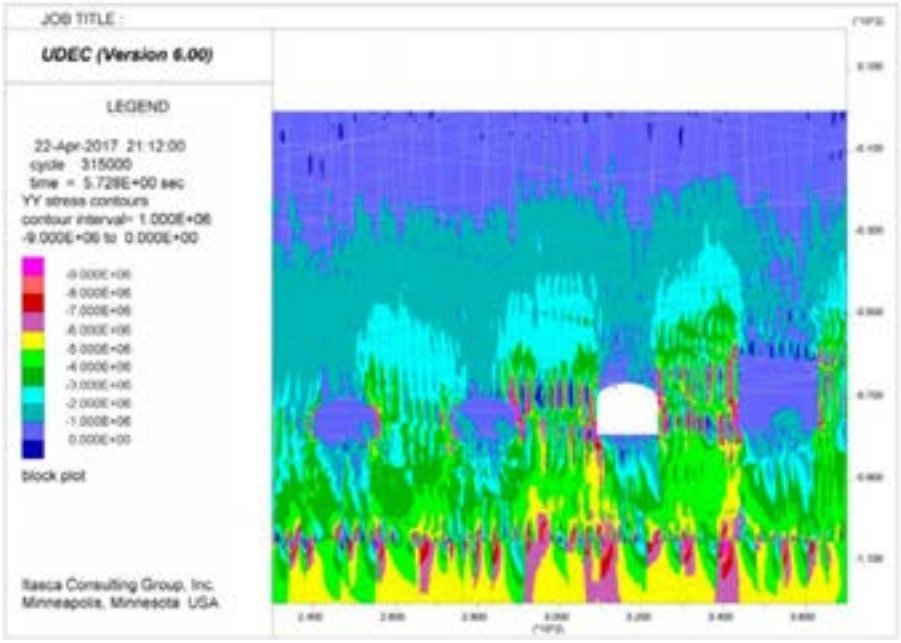


**Figure A61.** UDEC results after strength degradation up to Year 10,000, showing vertical stresses (SYY) for SFR 1, DFN 1-3. Stress magnitudes are in units of Pascals, with compression negative.

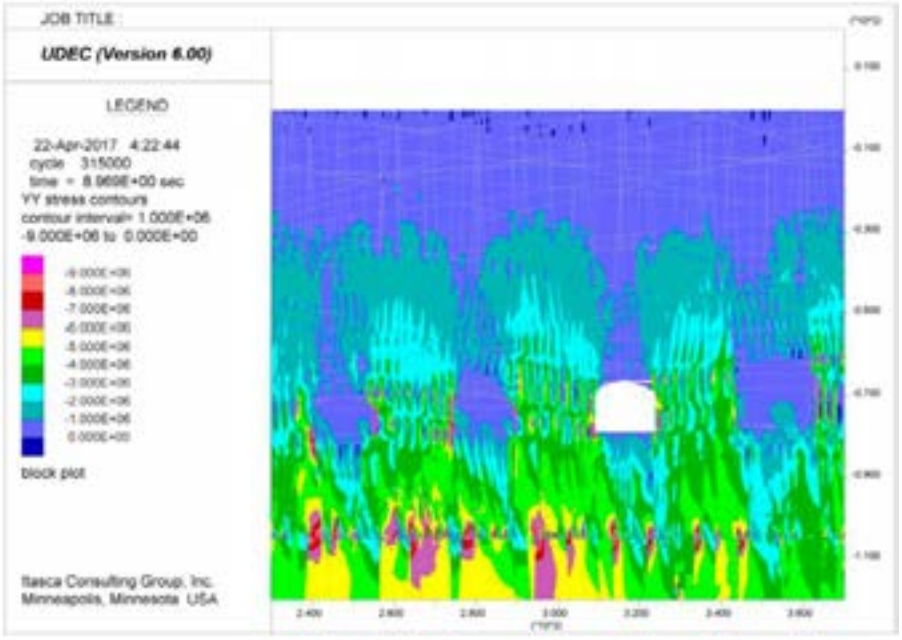


**Figure A62.** UDEC results after strength degradation up to Year 10.000, showing vertical stresses (SYY) for SFR 1, DFN 1-4. Stress magnitudes are in units of Pascals, with compression negative.

## SFR 1 – Year 10,000 Strength Degradation (Horizontal Stress)

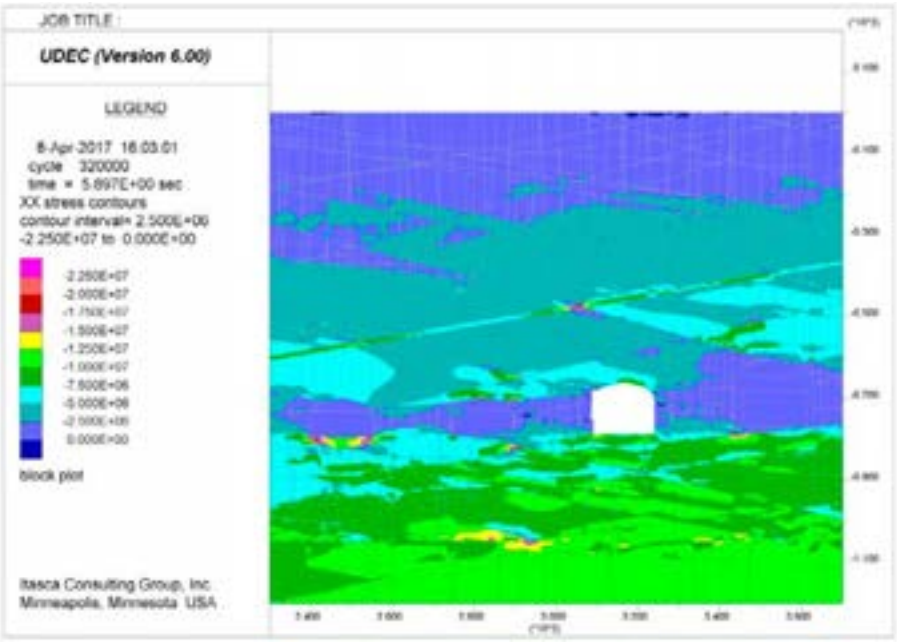


**Figure A63.** UDEC results after strength degradation up to Year 10,000, showing horizontal stresses (SXX) for SFR 1, DFN 1-1. Stress magnitudes are in units of Pascals, with compression negative.

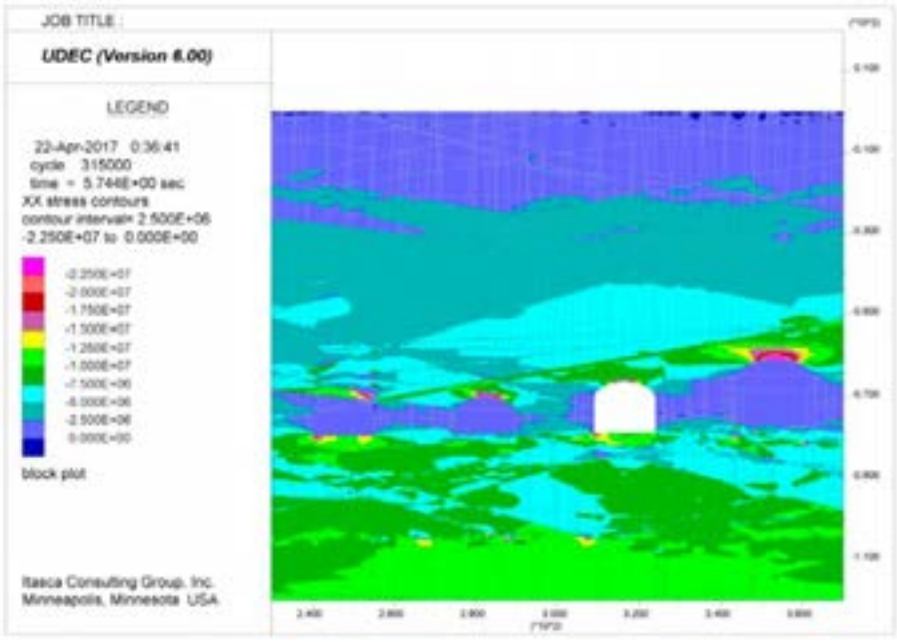


**Figure A64.** UDEC results after strength degradation up to Year 10,000, showing horizontal stresses (SXX) for SFR 1, DFN 1-2. Stress magnitudes are in units of Pascals, with compression negative.

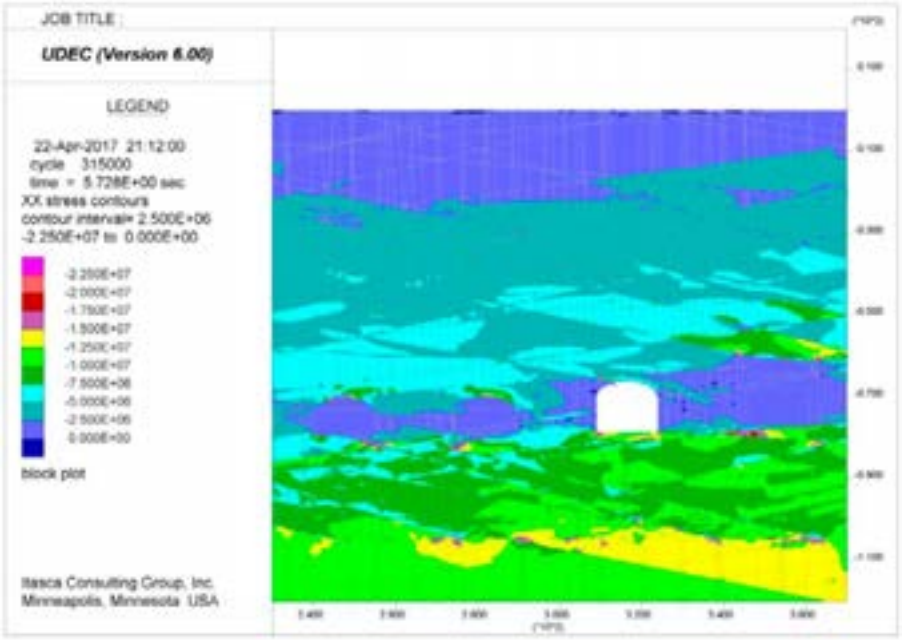


**Figure A65.** UDEC results after strength degradation up to Year 10,000, showing horizontal stresses (SXX) for SFR 1, DFN 1-3. Stress magnitudes are in units of Pascals, with compression negative.

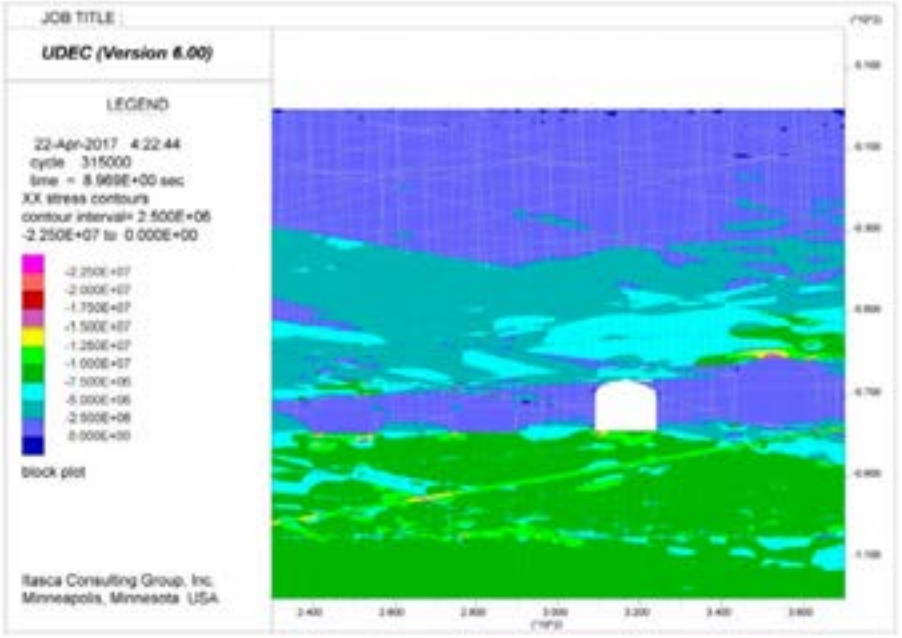


**Figure A66.** UDEC results after strength degradation up to Year 10,000, showing horizontal stresses (SXX) for SFR 1, DFN 1-4. Stress magnitudes are in units of Pascals, with compression negative.

## SFR 1 – Year 10,000 Strength Degradation (Plasticity Indicators)

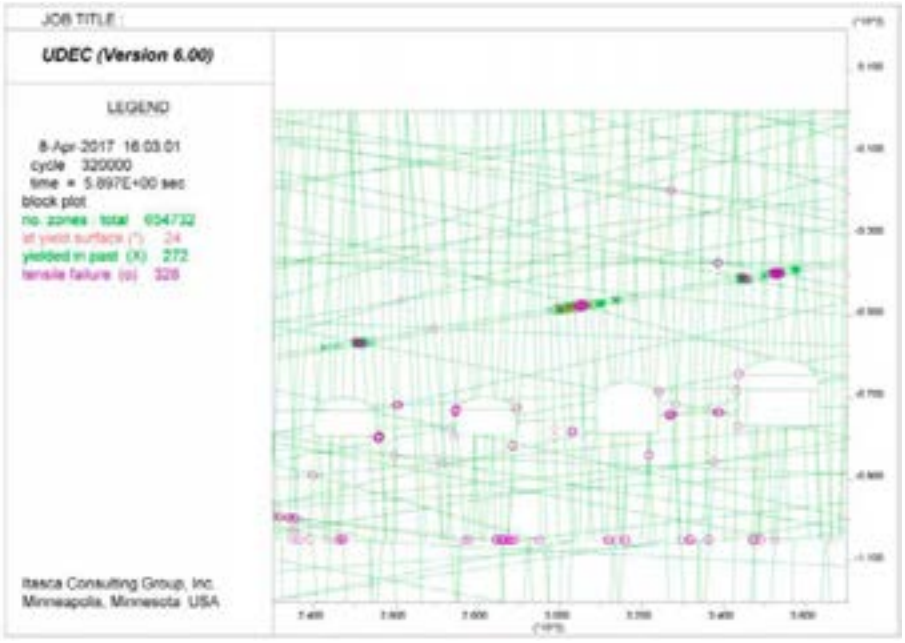


**Figure A67.** UDEC results after strength degradation up to Year 10,000, showing yielded elements for SFR 1, DFN 1-1.

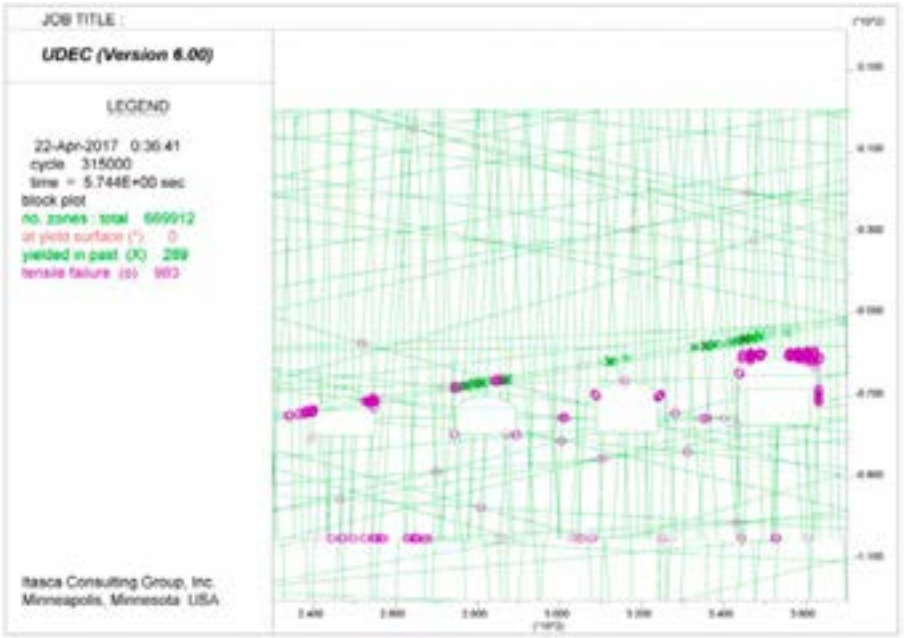


**Figure A68.** UDEC results after strength degradation up to Year 10,000, showing yielded elements for SFR 1, DFN 1-2.

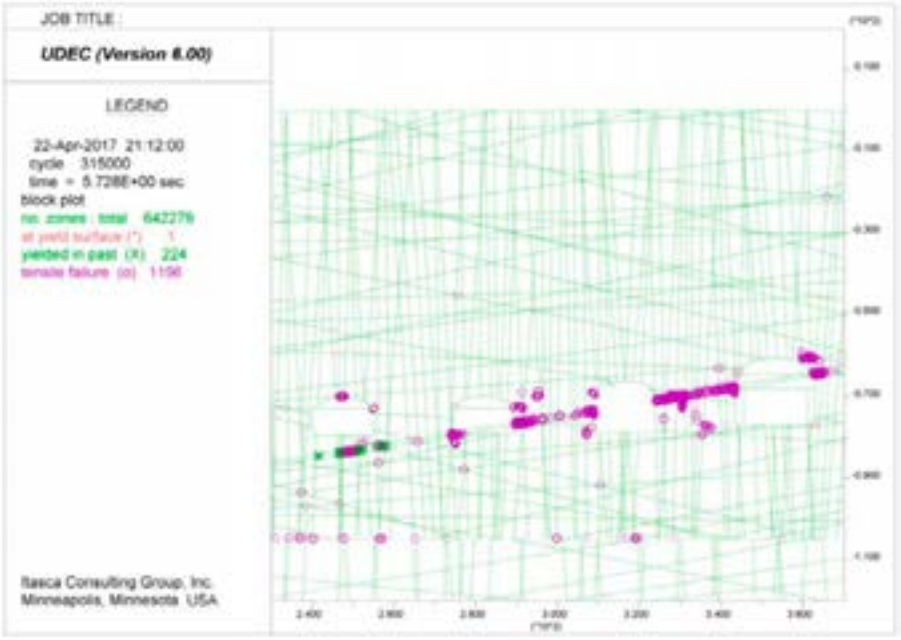


**Figure A69.** UDEC results after strength degradation up to Year 10,000, showing yielded elements for SFR 1, DFN 1-3.

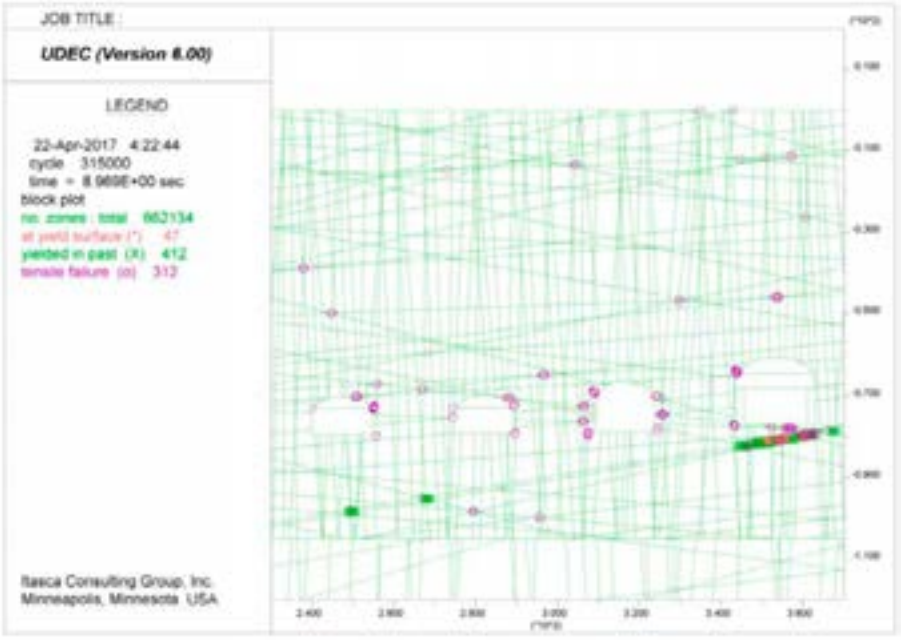


**Figure A70.** UDEC results after strength degradation up to Year 10,000, showing yielded elements for SFR 1, DFN 1-4.

## SFR 1 – Year 10,000 Strength Degradation (Displacement Vectors)

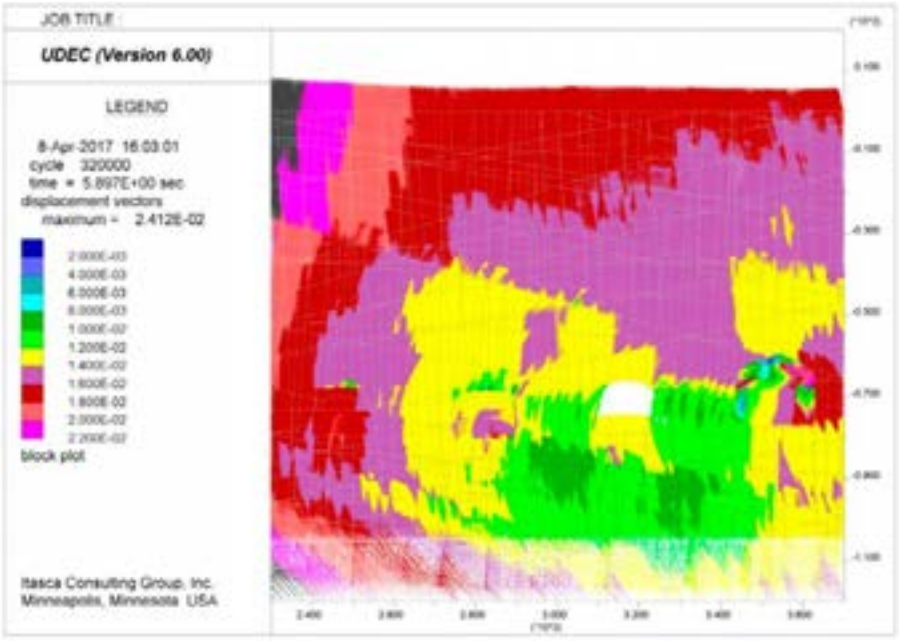


**Figure A71.** UDEC results after strength degradation up to Year 10,000, showing displacement vectors for SFR 1, DFN 1-1. Displacement magnitudes are in units of metres.

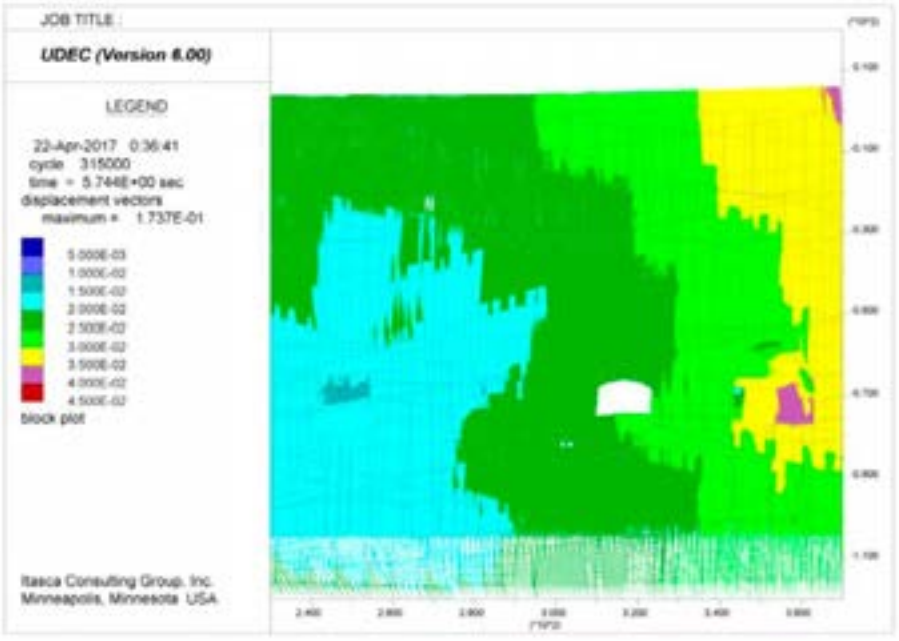


**Figure A72.** UDEC results after strength degradation up to Year 10,000, showing displacement vectors for SFR 1, DFN 1-2. Displacement magnitudes are in units of metres.

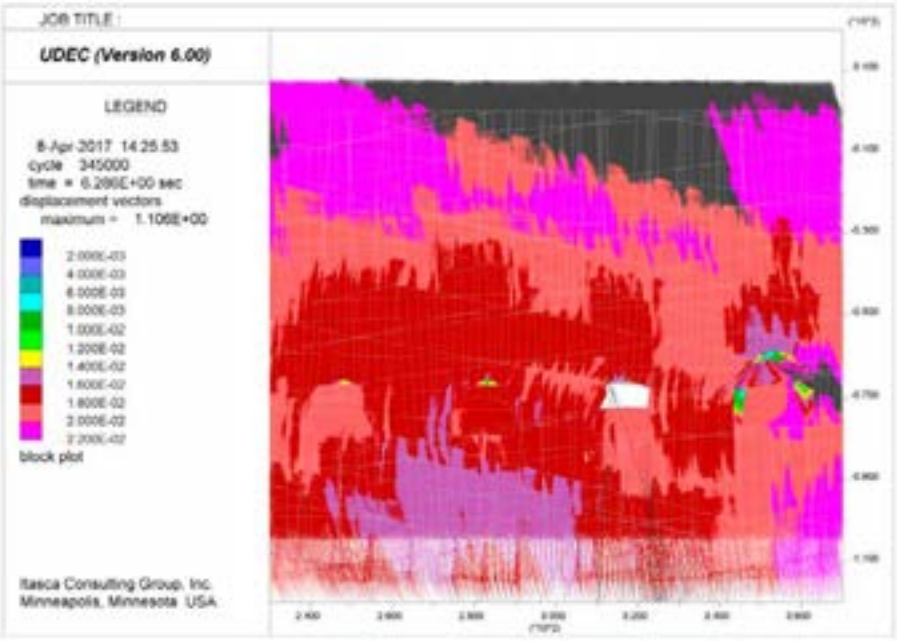


**Figure A73.** UDEC results after strength degradation up to Year 10,000, showing displacement vectors for SFR 1, DFN 1-3. Displacement magnitudes are in units of metres.

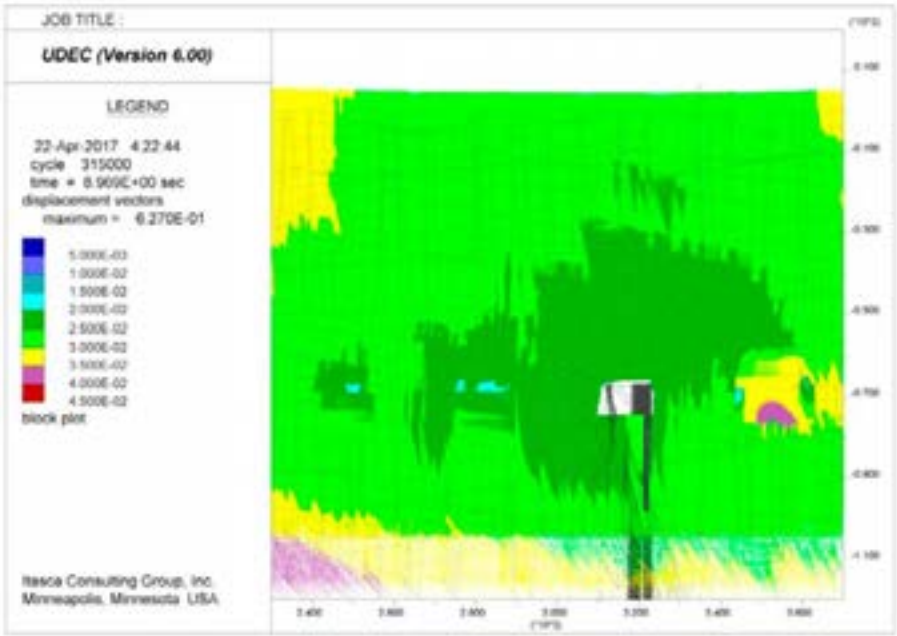


**Figure A74.** UDEC results after strength degradation up to Year 10,000, showing displacement vectors for SFR 1, DFN 1-4. Displacement magnitudes are in units of metres.

## SFR 1 – Year 10,000 Strength Degradation (Fracture Shear Displ.)

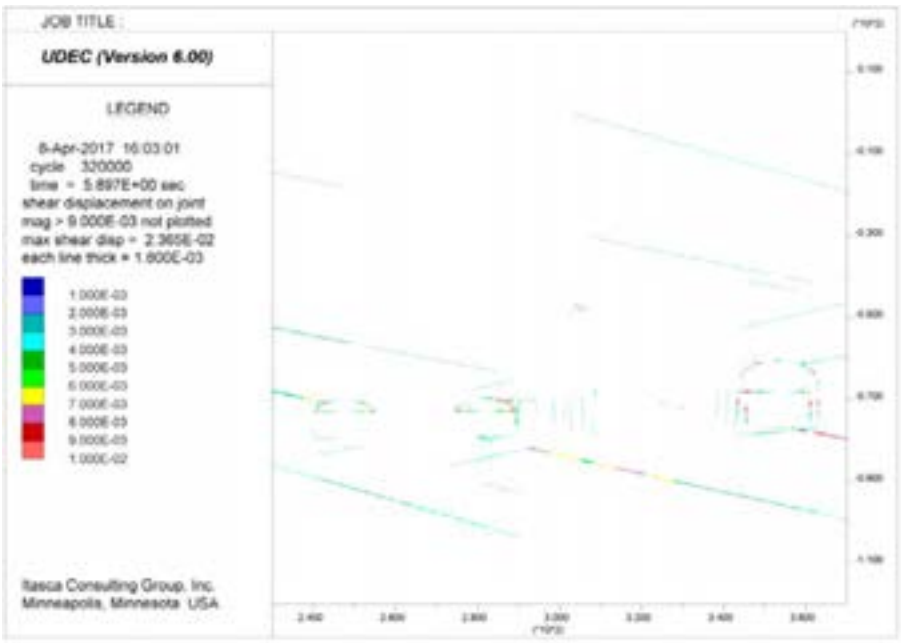


**Figure A75.** UDEC results after strength degradation up to Year 10,000, showing shear displacements along fractures for SFR 1, DFN 1-1. Displacements are in units of metres.

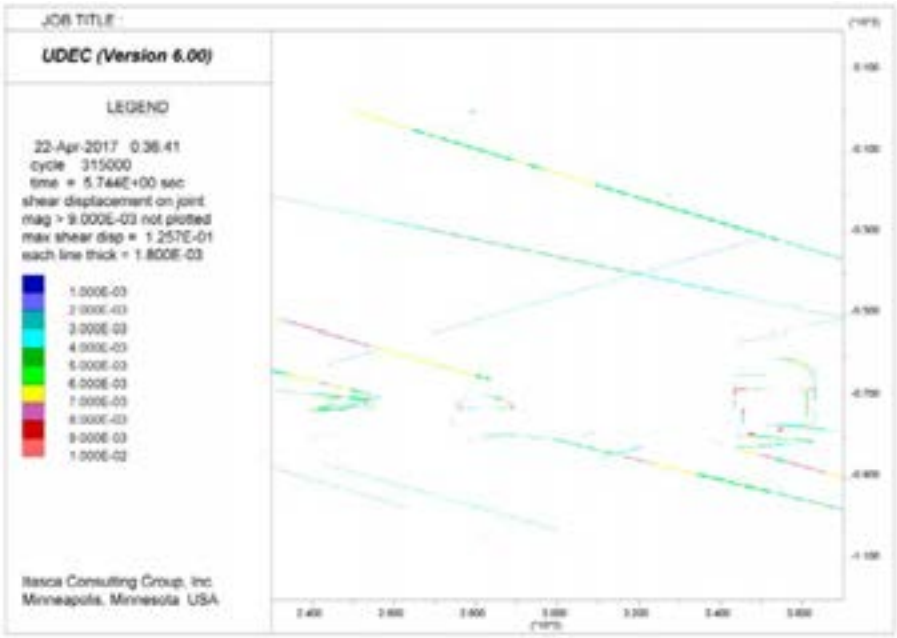


**Figure A76.** UDEC results after strength degradation up to Year 10,000, showing shear displacements along fractures for SFR 1, DFN 1-2. Displacements are in units of metres.

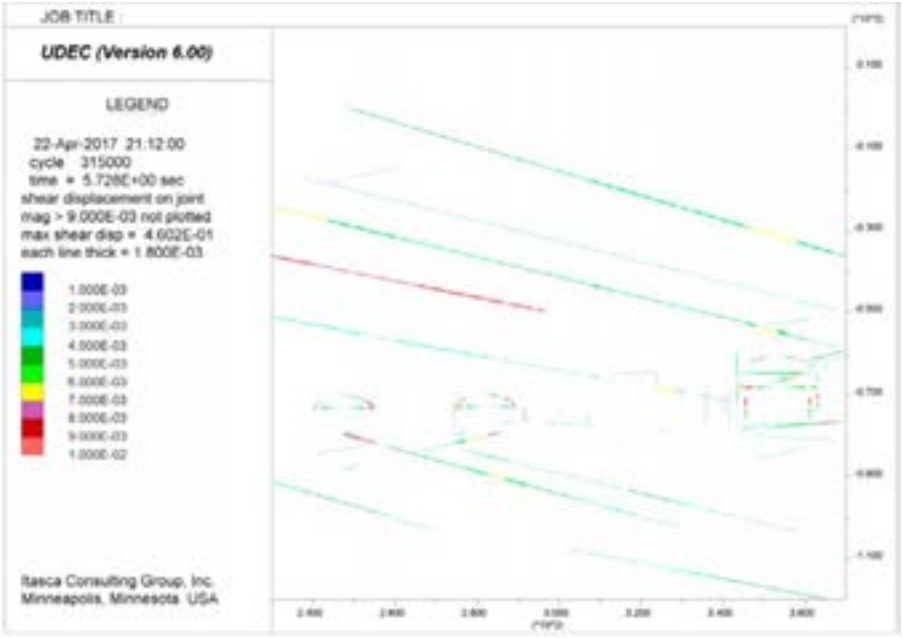


**Figure A77.** UDEC results after strength degradation up to Year 10,000, showing shear displacements along fractures for SFR 1, DFN 1-3. Displacements are in units of metres.

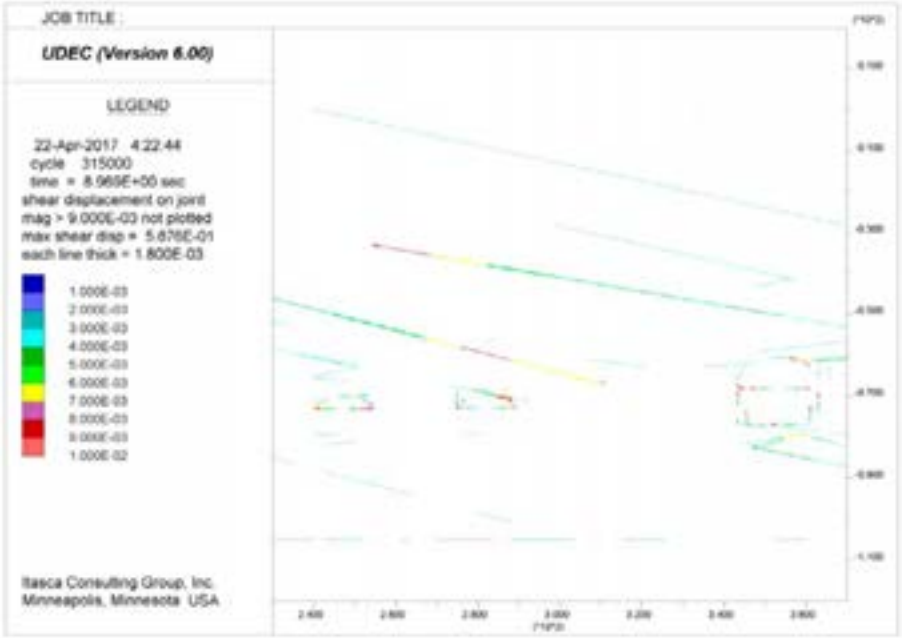


**Figure A78.** UDEC results after strength degradation up to Year 10,000, showing shear displacements along fractures for SFR 1, DFN 1-4. Displacements are in units of metres.

## SFR 1 – Year 10,000 Strength Degradation (Vertical Displacements)

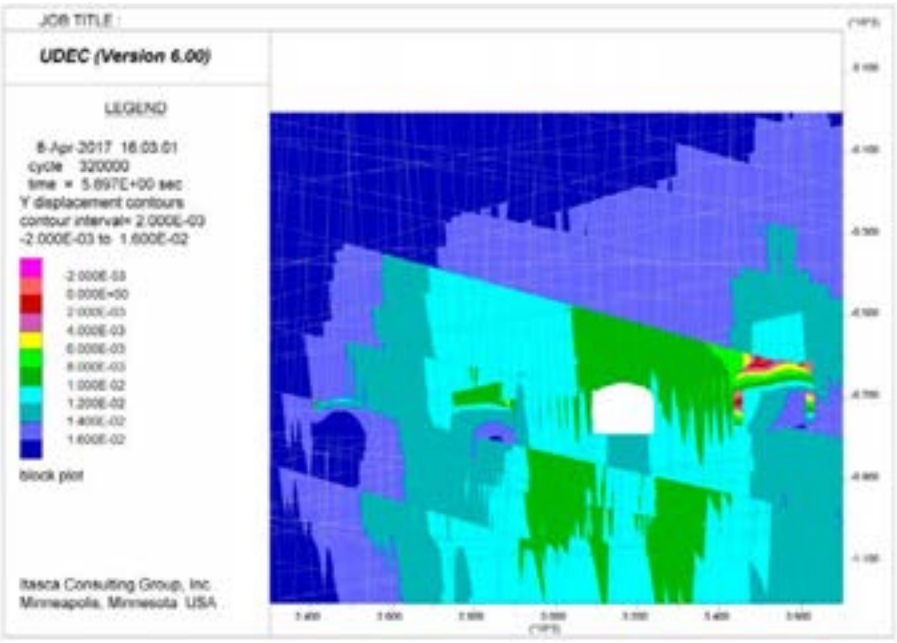


**Figure A79.** UDEC results after strength degradation up to Year 10,000, showing vertical displacements for SFR 1, DFN 1-1. Displacements are in units of metres, with positive up.

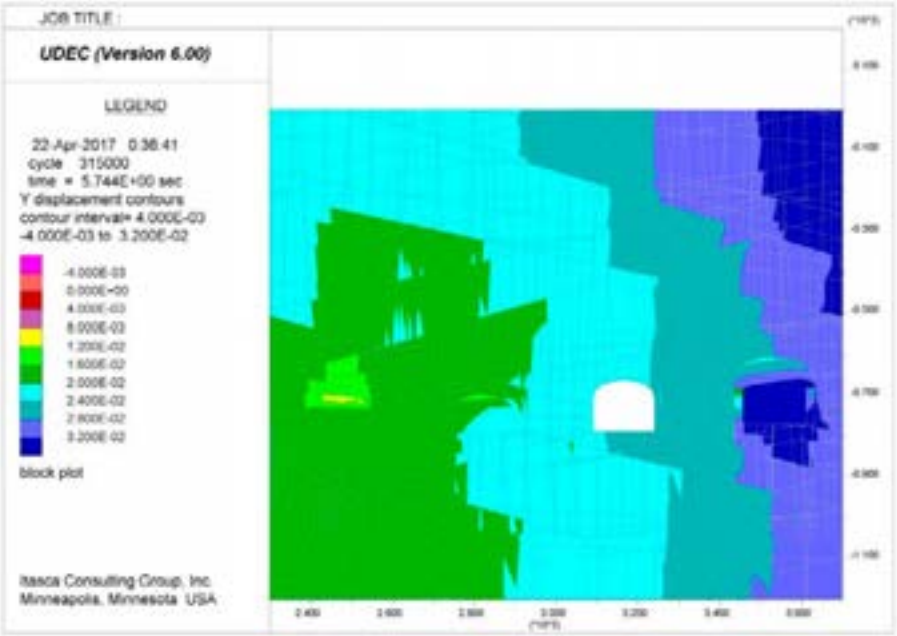


**Figure A80.** UDEC results after strength degradation up to Year 10,000, showing vertical displacements for SFR 1, DFN 1-2. Displacements are in units of metres, with positive up.

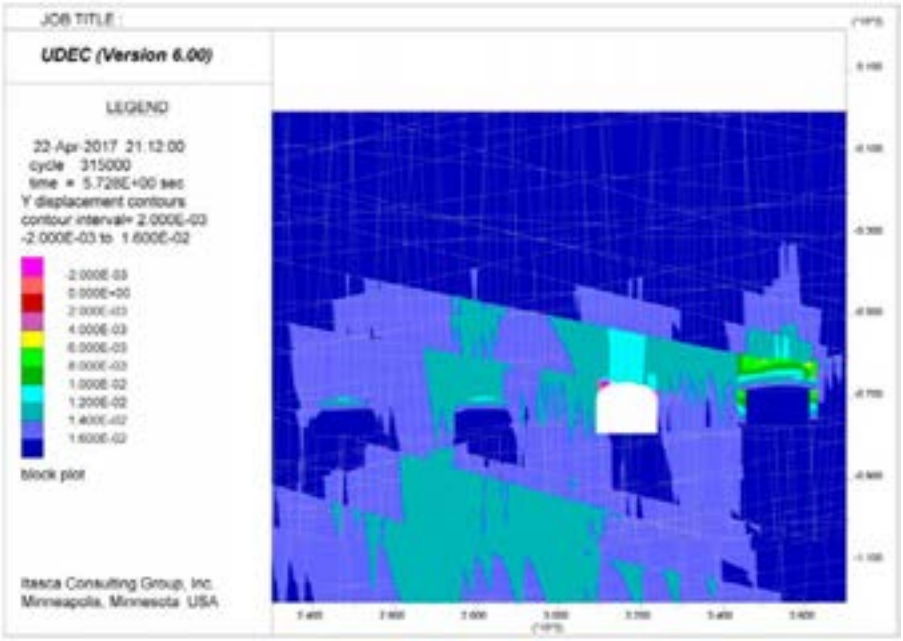


**Figure A81.** UDEC results after strength degradation up to Year 10,000, showing vertical displacements for SFR 1, DFN 1-3. Displacements are in units of metres, with positive up.

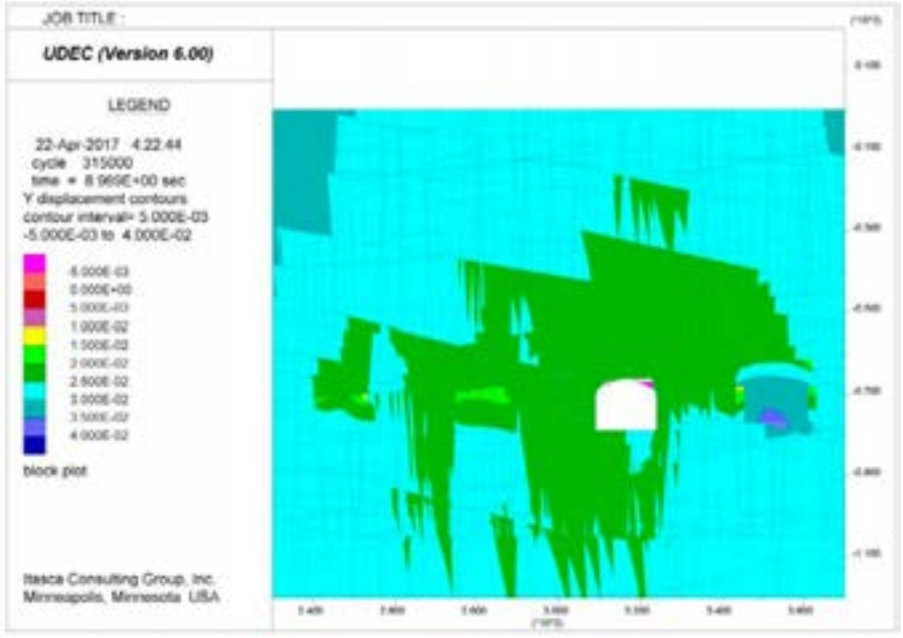


**Figure A82.** UDEC results after strength degradation up to Year 10,000, showing vertical displacements for SFR 1, DFN 1-4. Displacements are in units of metres, with positive up.

## SFR 1 – Year 10,000 Strength Degradation (Horizontal Displacements)

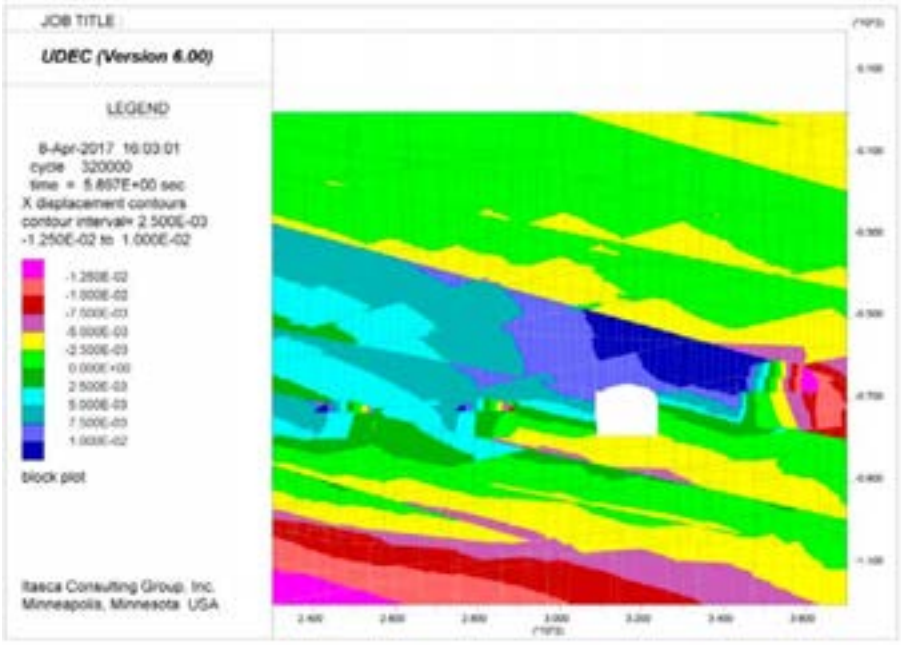


**Figure A83.** UDEC results after strength degradation up to Year 10,000, showing horizontal displacements for SFR 1, DFN 1-1. Displacements are in units of metres, with positive to the right.

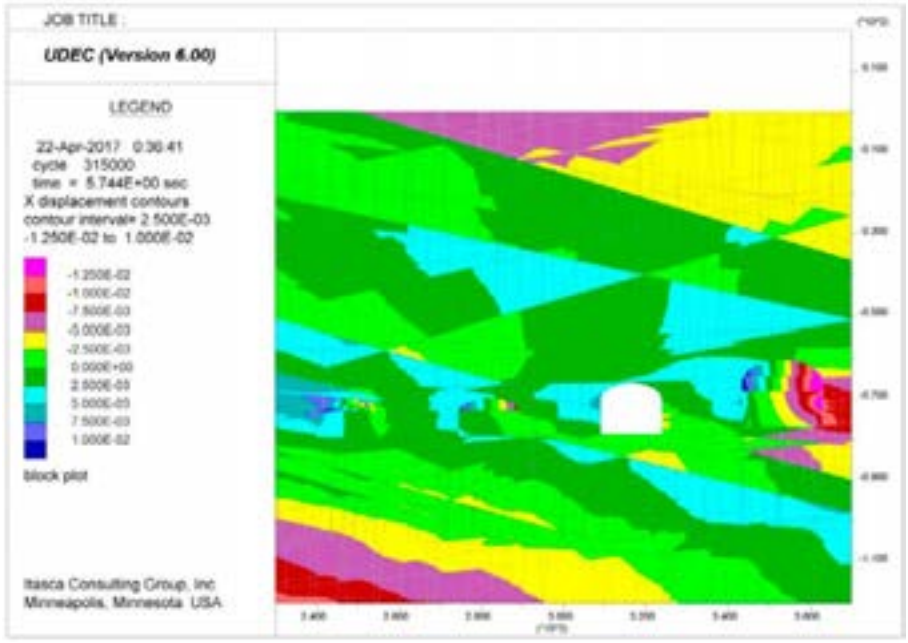


**Figure A84.** UDEC results after strength degradation up to Year 10,000, showing horizontal displacements for SFR 1, DFN 1-2. Displacements are in units of metres, with positive to the right.

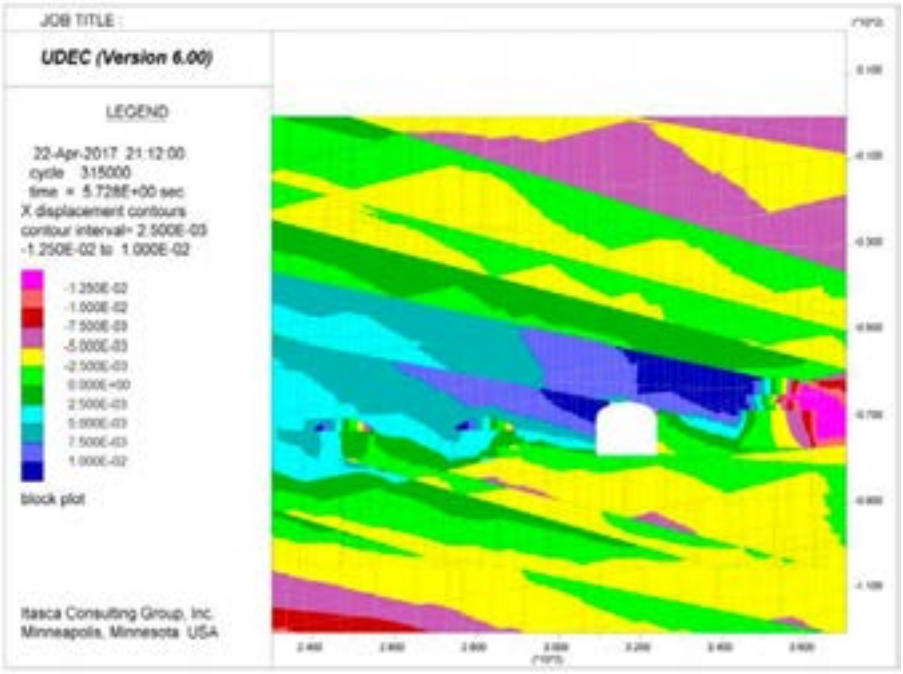


**Figure A85.** UDEC results after strength degradation up to Year 10,000, showing horizontal displacements for SFR 1, DFN 1-3. Displacements are in units of metres, with positive to the right.

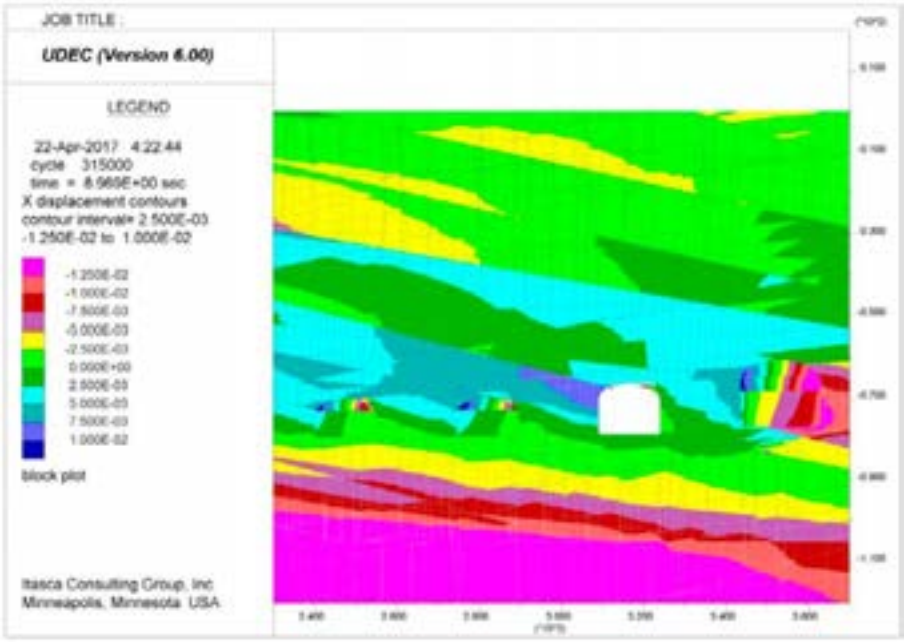


**Figure A86.** UDEC results after strength degradation up to Year 10,000, showing horizontal displacements for SFR 1, DFN 1-4. Displacements are in units of metres, with positive to the right.

## SFR 1 – Year 21,000 Permafrost Melting (Vertical Stress)

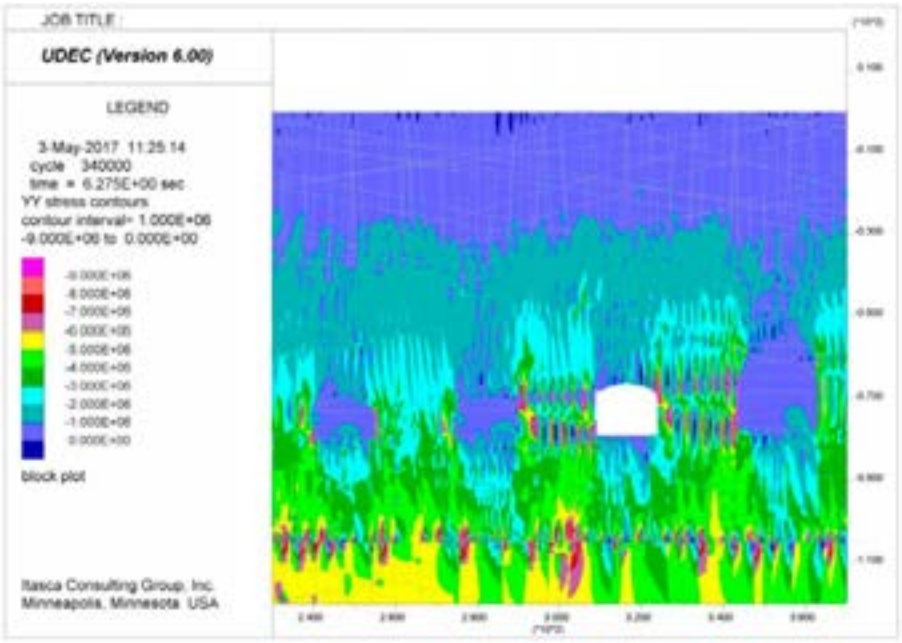


**Figure A87.** UDEC results after strength degradation and permafrost melting at Year 21,000, showing vertical stresses (SYY) for SFR 1, DFN 1-1. Stress magnitudes are in units of Pascals, with compression negative.

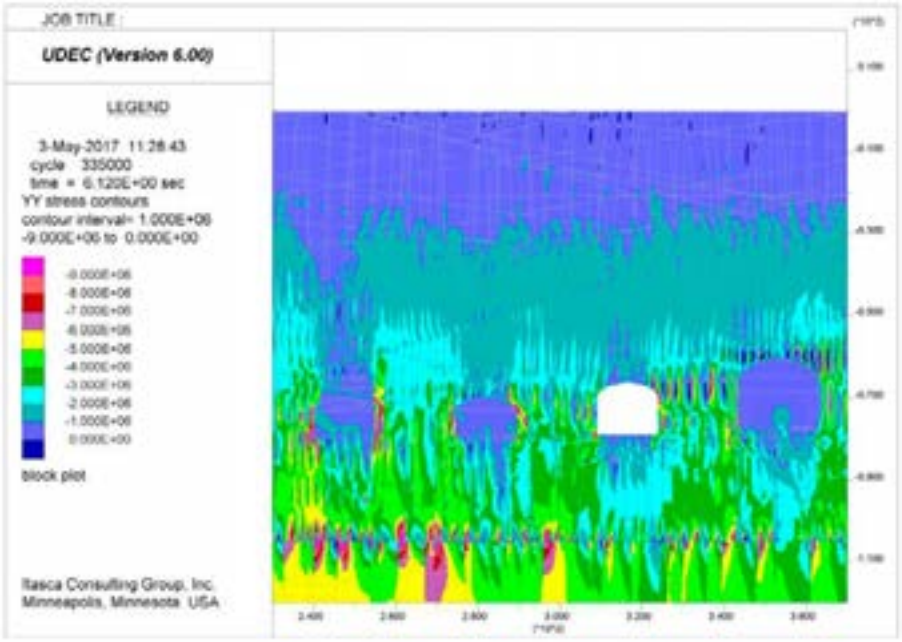


**Figure A88.** UDEC results after strength degradation and permafrost melting at Year 21,000, showing vertical stresses (SYY) for SFR 1, DFN 1-2. Stress magnitudes are in units of Pascals, with compression negative.

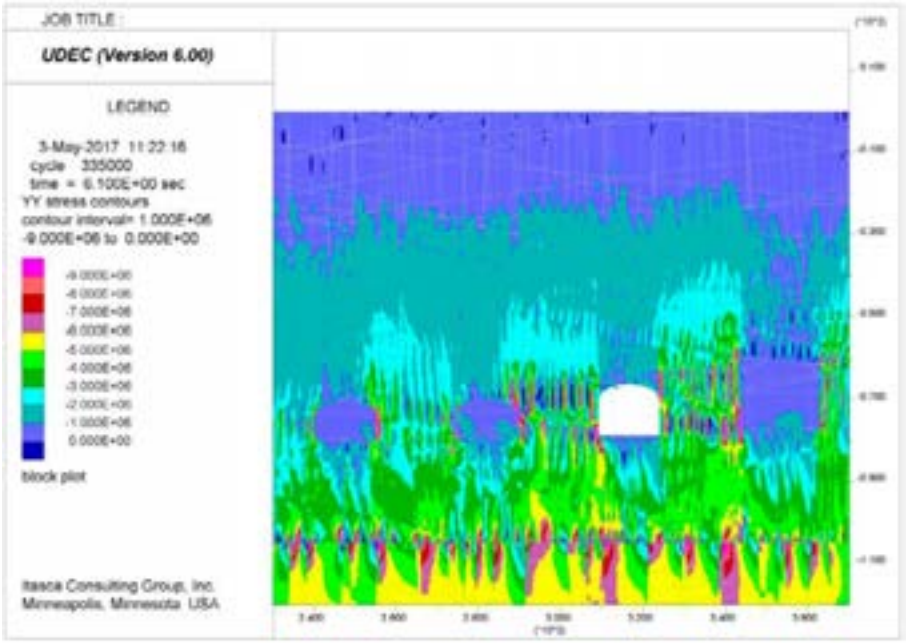


**Figure A89.** UDEC results after strength degradation and permafrost melting at Year 21,000, showing vertical stresses (SYY) for SFR 1, DFN 1-3. Stress magnitudes are in units of Pascals, with compression negative.

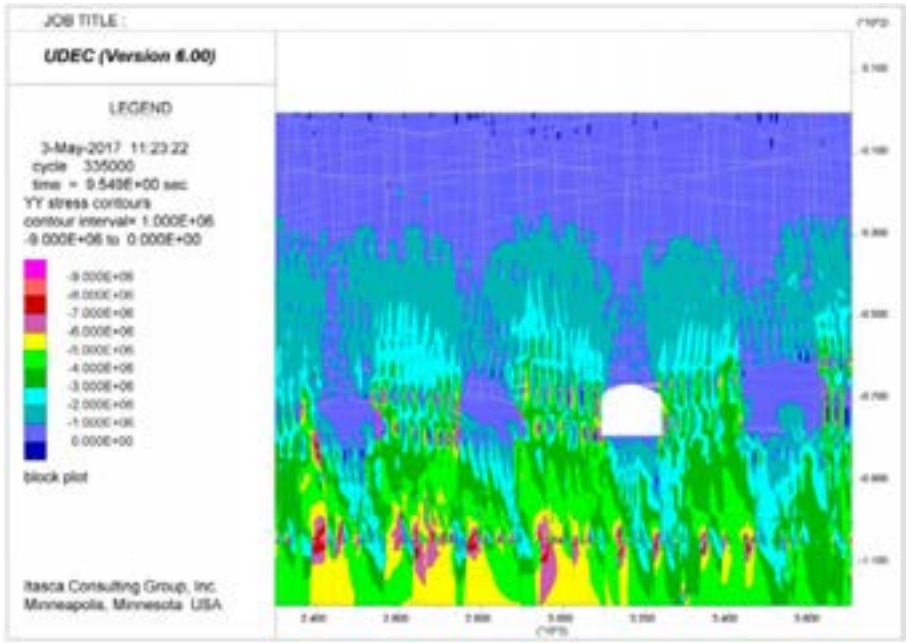


**Figure A90.** UDEC results after strength degradation and permafrost melting at Year 21,000, showing vertical stresses (SYY) for SFR 1, DFN 1-4. Stress magnitudes are in units of Pascals, with compression negative.

## SFR 1 – Year 21,000 Permafrost Melting (Horizontal Stress)

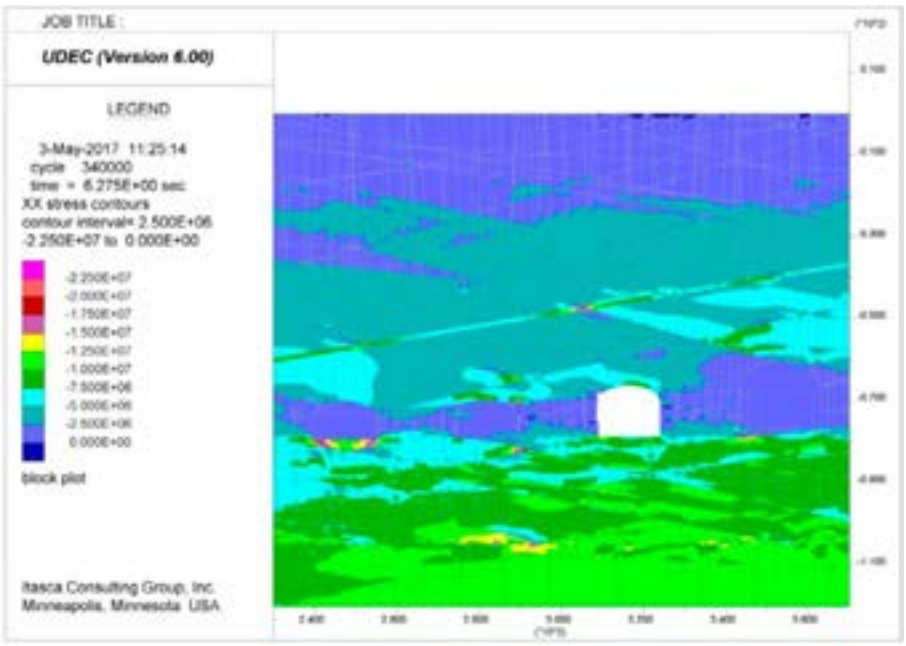


**Figure A91.** UDEC results after strength degradation and permafrost melting at Year 21,000, showing horizontal stresses (SXX) for SFR 1, DFN 1-1. Stress magnitudes are in units of Pascals, with compression negative.

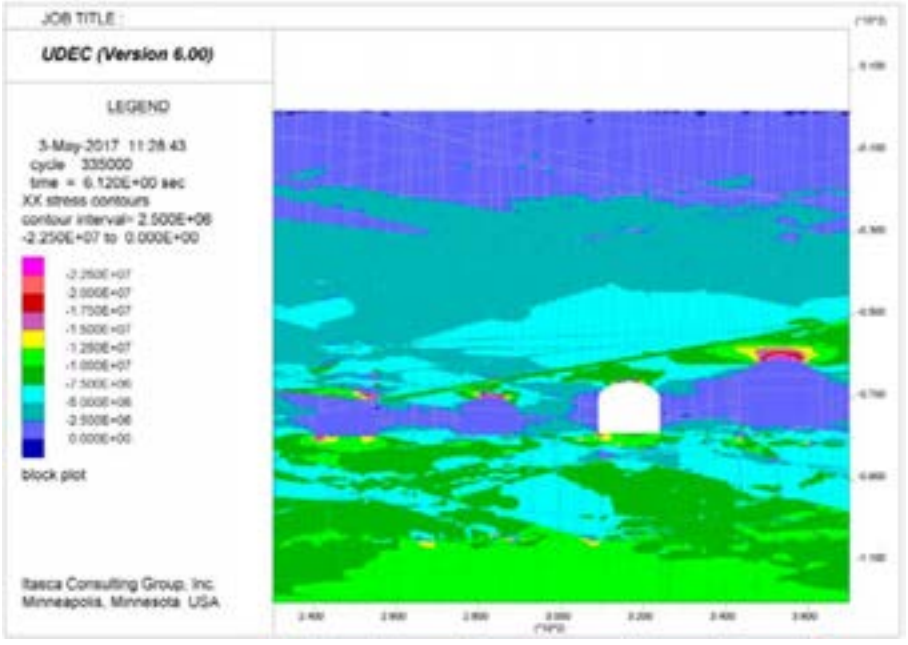


**Figure A92.** UDEC results after strength degradation and permafrost melting at Year 21,000, showing horizontal stresses (SXX) for SFR 1, DFN 1-2. Stress magnitudes are in units of Pascals, with compression negative.

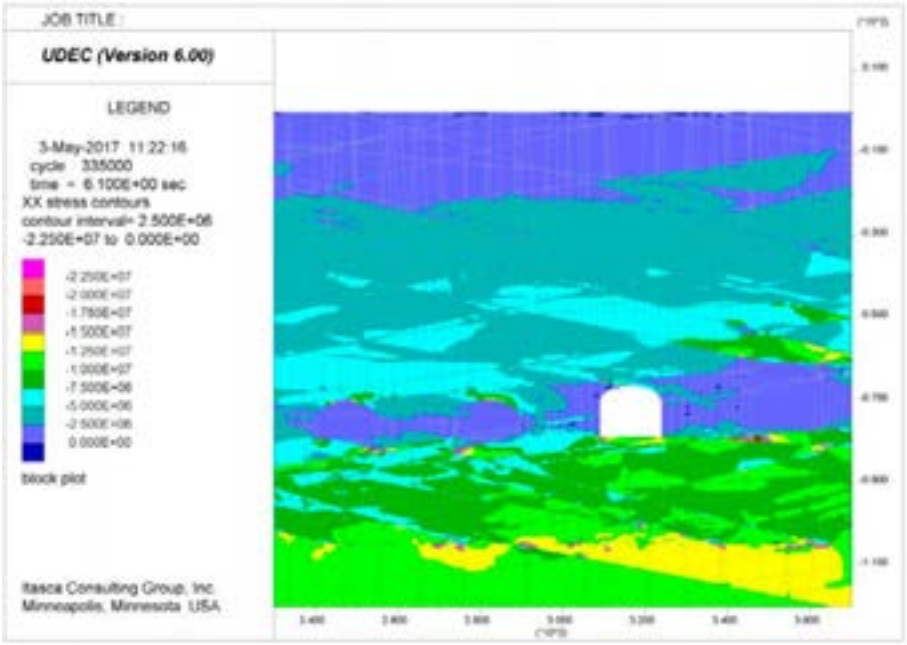


**Figure A93.** UDEC results after strength degradation and permafrost melting at Year 21,000, showing horizontal stresses (SXX) for SFR 1, DFN 1-3. Stress magnitudes are in units of Pascals, with compression negative.

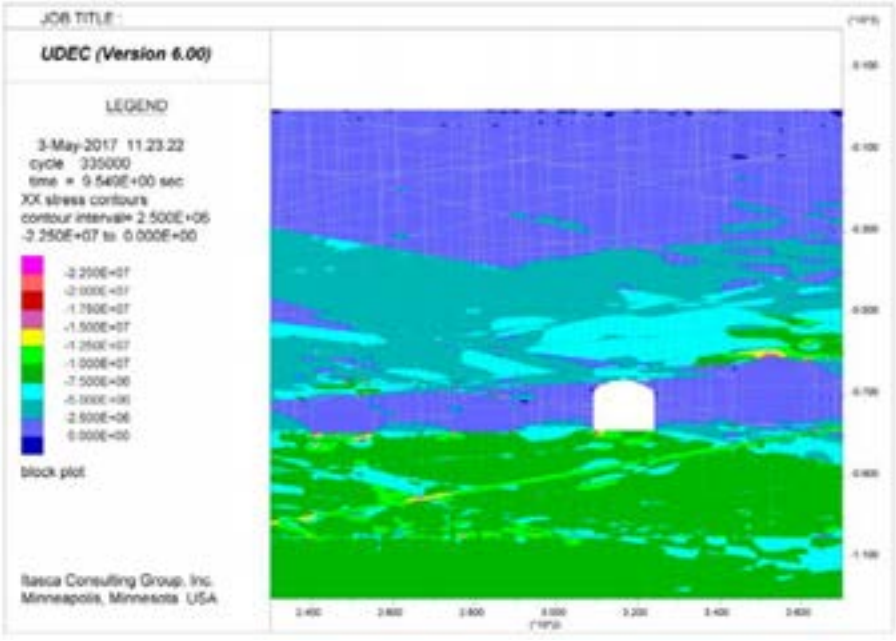


**Figure A94.** UDEC results after strength degradation and permafrost melting at Year 21,000, showing horizontal stresses (SXX) for SFR 1, DFN 1-4. Stress magnitudes are in units of Pascals, with compression negative.

## SFR 1 – Year 21,000 Permafrost Melting (Plasticity Indicators)

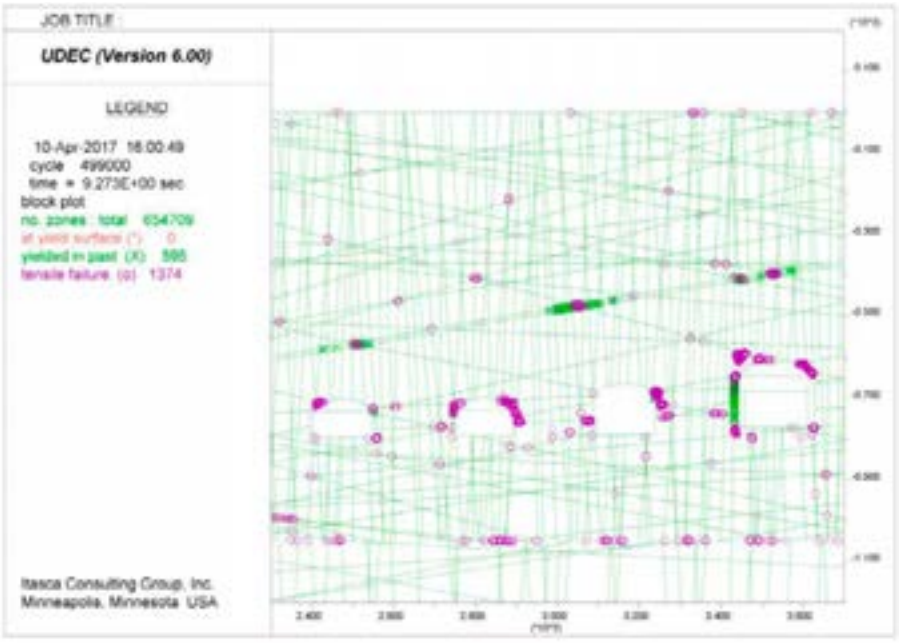


**Figure A95.** UDEC results after strength degradation and permafrost melting at Year 21,000, showing yielded elements for SFR 1, DFN 1-1.


**Figure A96.** UDEC results after strength degradation and permafrost melting at Year 21,000, showing yielded elements for SFR 1, DFN 1-2.

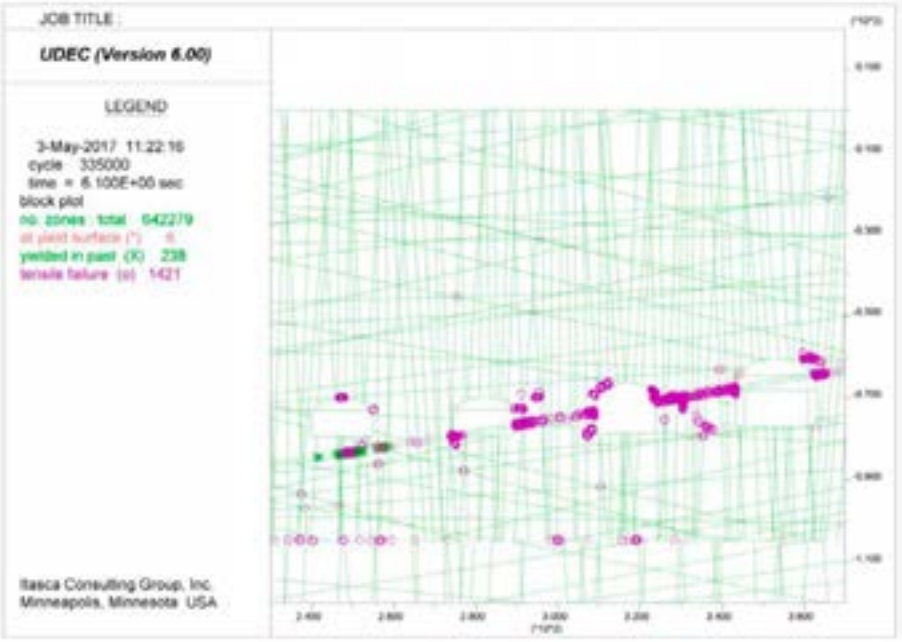


**Figure A97.** UDEC results after strength degradation and permafrost melting at Year 21,000, showing yielded elements for SFR 1, DFN 1-3.

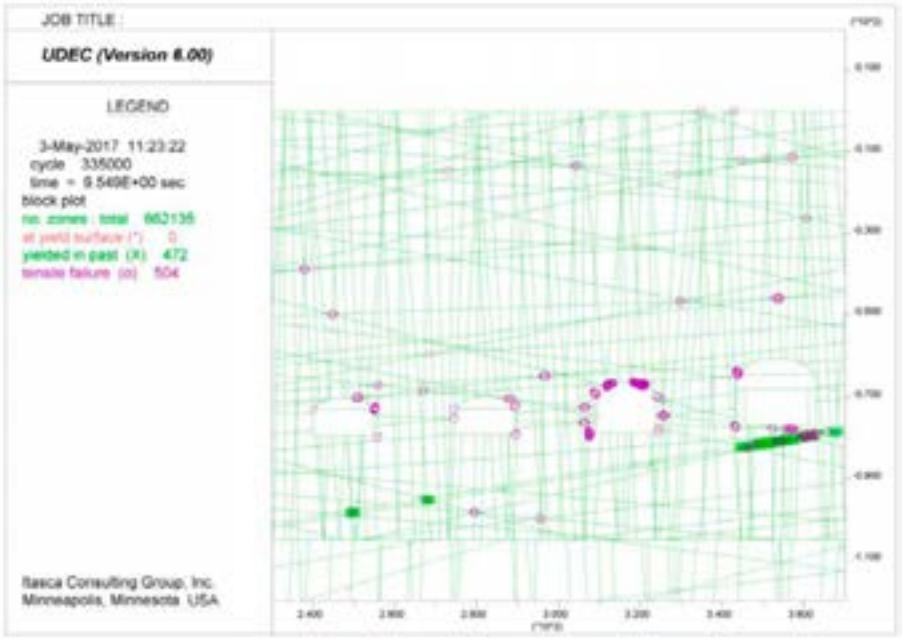


**Figure A98.** UDEC results after strength degradation and permafrost melting at Year 21,000, showing yielded elements for SFR 1, DFN 1-4.

## SFR 1 – Year 21,000 Permafrost Melting (Displacement Vectors)

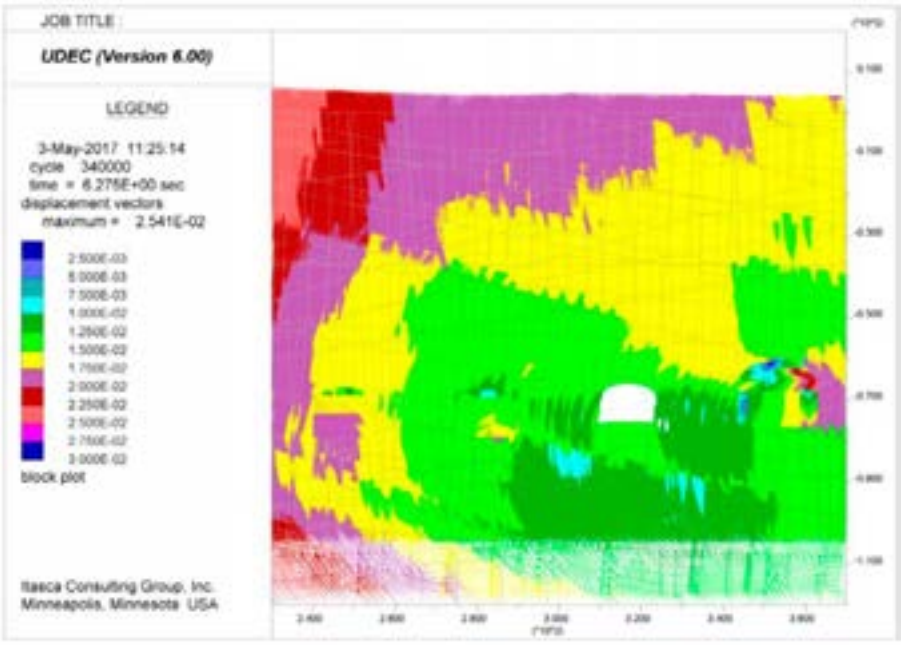


**Figure A99.** UDEC results after strength degradation and permafrost melting at Year 21,000, showing displacement vectors for SFR 1, DFN 1-1. Displacement magnitudes are in units of metres.

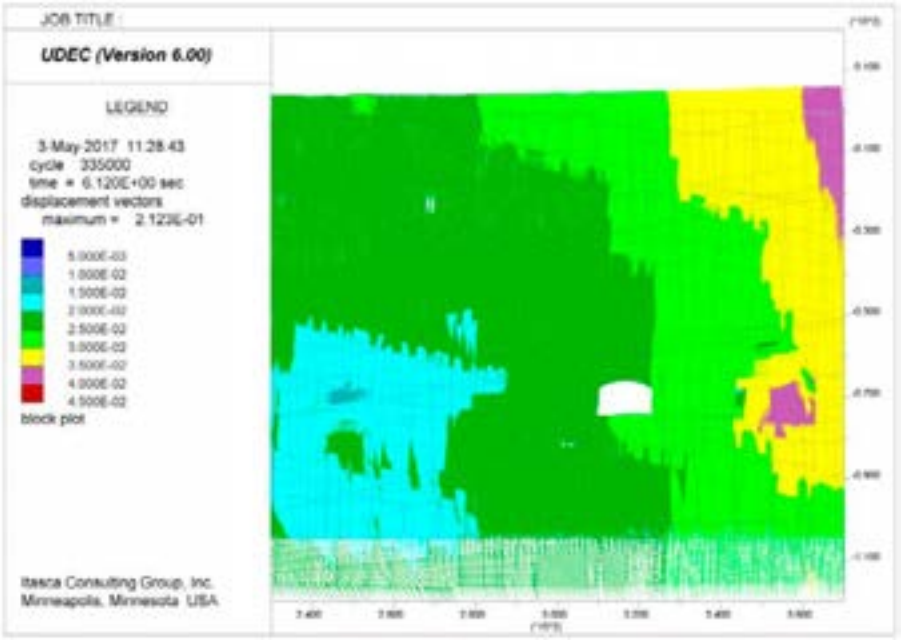


**Figure A100.** UDEC results after strength degradation and permafrost melting at Year 21,000, showing displacement vectors for SFR 1, DFN 1-2. Displacement magnitudes are in units of metres.

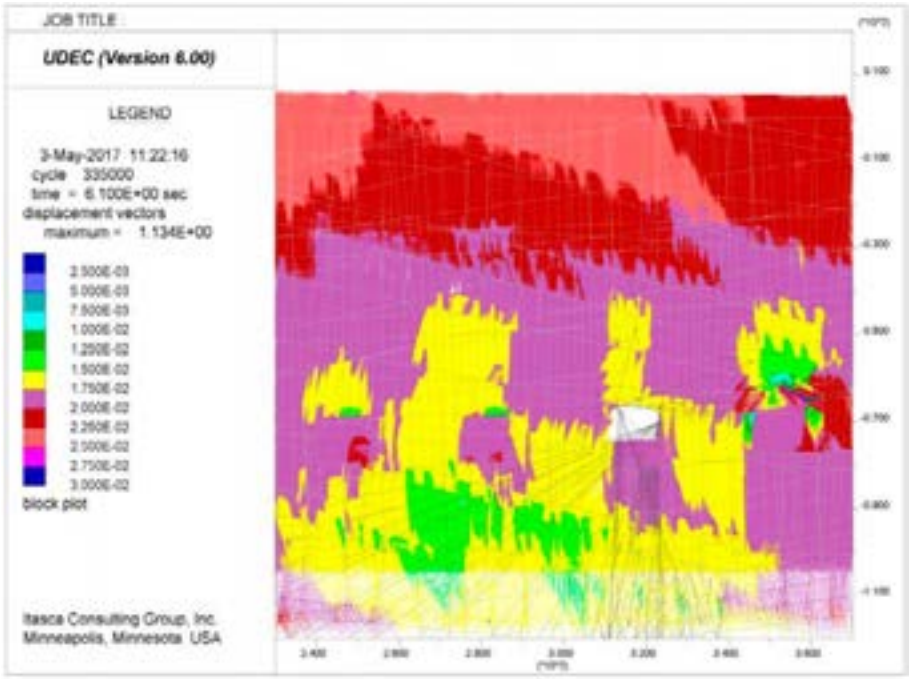


**Figure A101.** UDEC results after strength degradation and permafrost melting at Year 21,000, showing displacement vectors for SFR 1, DFN 1-3. Displacement magnitudes are in units of metres.

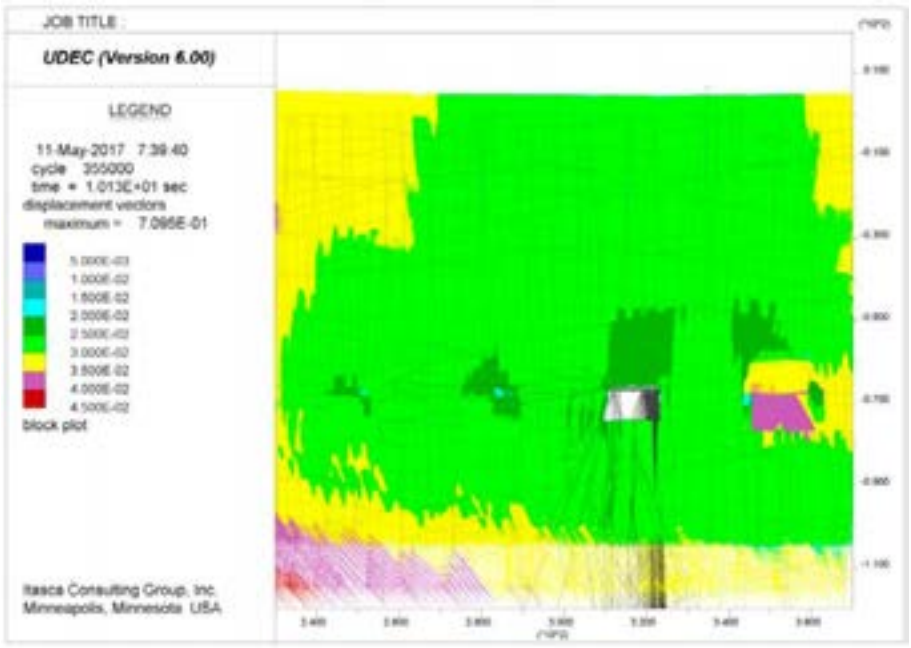


**Figure A102.** UDEC results after strength degradation and permafrost melting at Year 21,000, showing displacement vectors for SFR 1, DFN 1-4. Displacement magnitudes are in units of metres.

## SFR 1 – Year 21,000 Permafrost Melting (Fracture Shear Displacement)

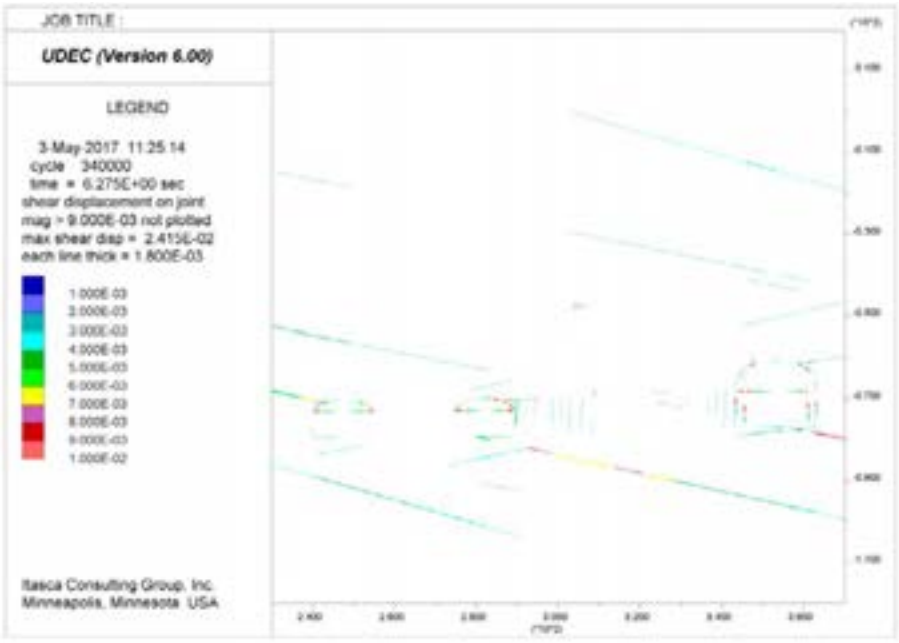


**Figure A103.** UDEC results after strength degradation and permafrost melting at Year 21,000, showing shear displacements along fractures for SFR 1, DFN 1-1. Displacements are in units of metres.

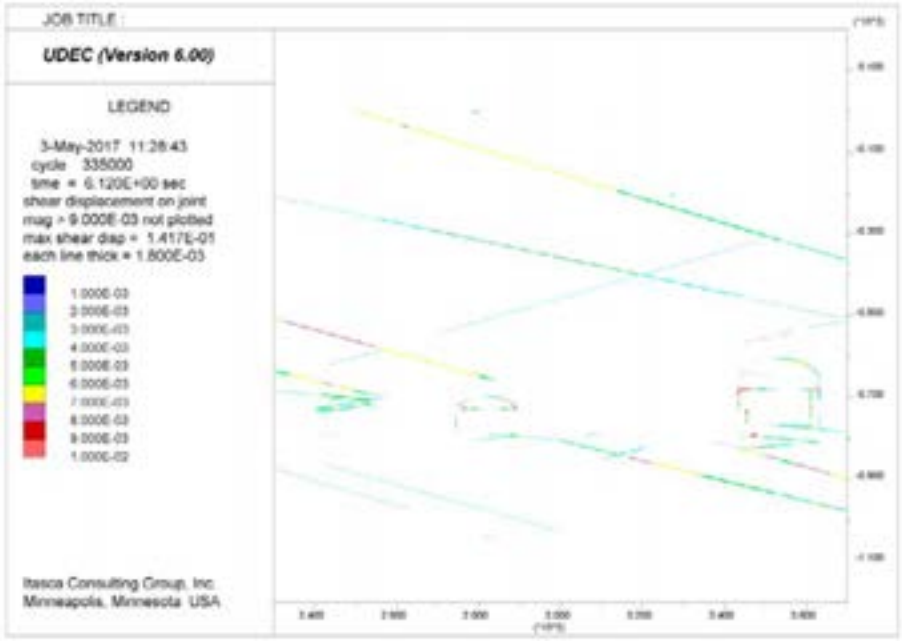


**Figure A104.** UDEC results after strength degradation and permafrost melting at Year 21,000, showing shear displacements along fractures for SFR 1, DFN 1-2. Displacements are in units of metres.

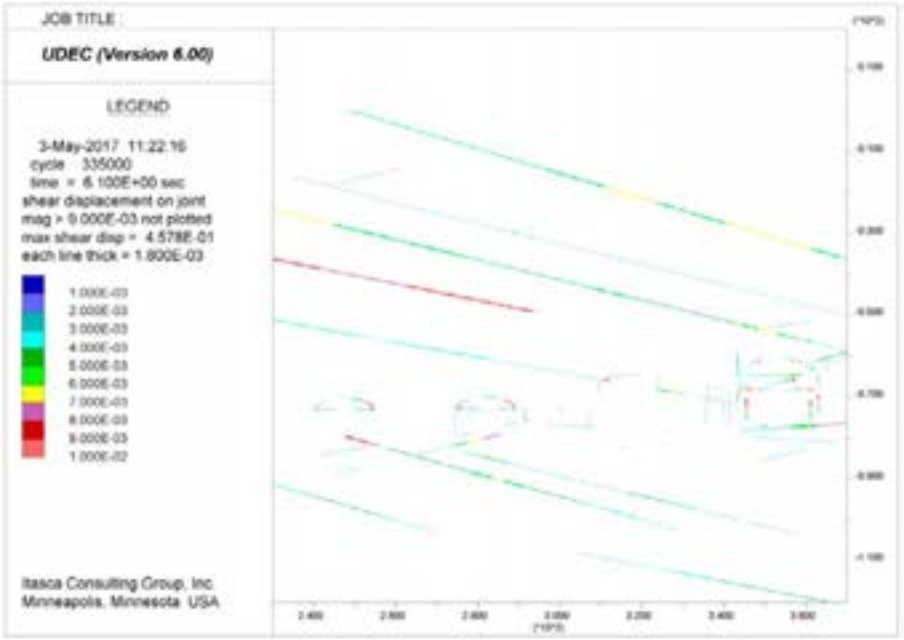


**Figure A105.** UDEC results after strength degradation and permafrost melting at Year 21,000, showing shear displacements along fractures for SFR 1, DFN 1-3. Displacements are in units of metres.

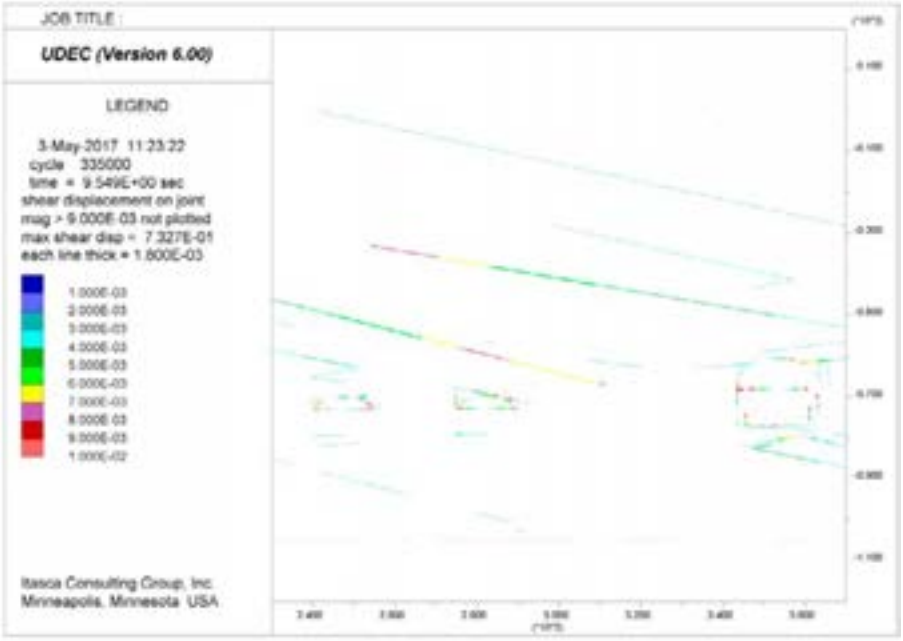


**Figure A106.** UDEC results after strength degradation and permafrost melting at Year 21,000, showing shear displacements along fractures for SFR 1, DFN 1-4. Displacements are in units of metres.

## SFR 1 – Year 21,000 Permafrost Melting (Vertical Displacements)

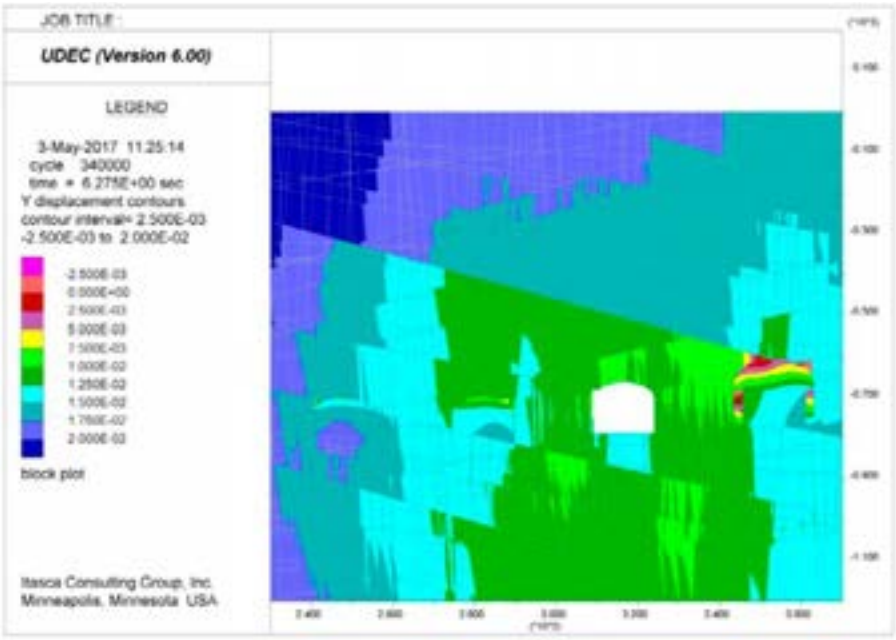


**Figure A107.** UDEC results after strength degradation and permafrost melting at Year 21,000, showing vertical displacements for SFR 1, DFN 1-1. Displacements are in units of metres, with positive up.

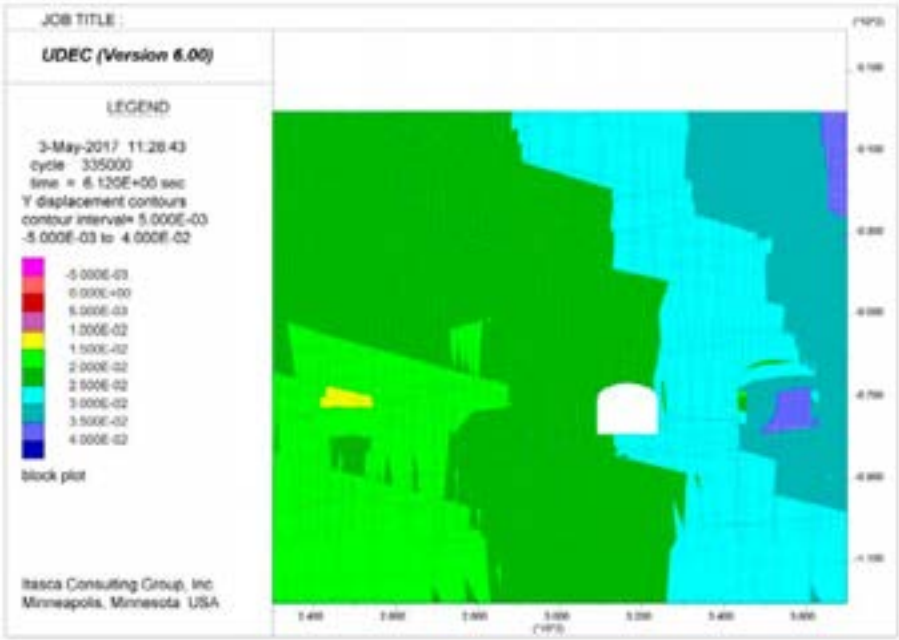


**Figure A108.** UDEC results after strength degradation and permafrost melting at Year 21,000, showing vertical displacements for SFR 1, DFN 1-2. Displacements are in units of metres, with positive up.

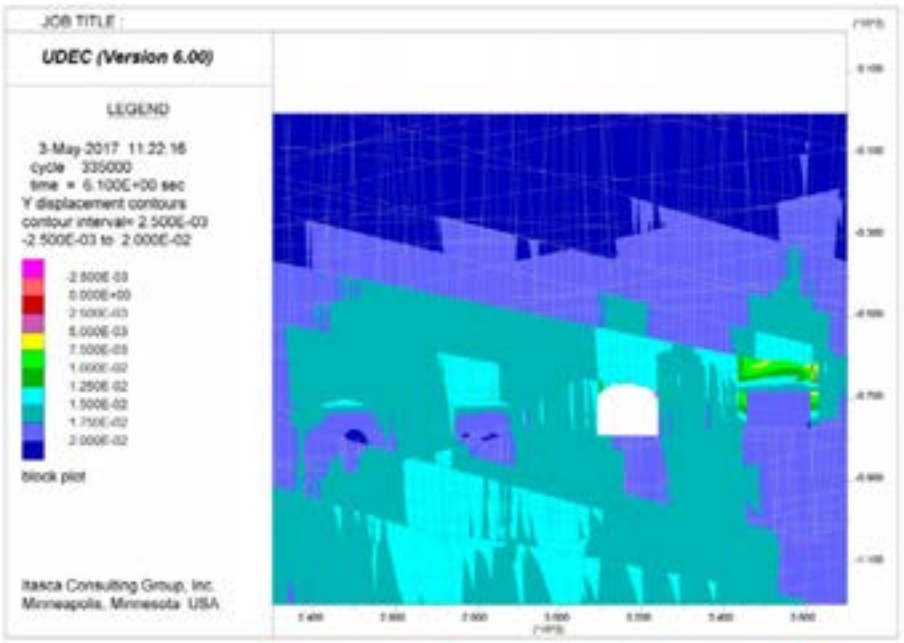


**Figure A109.** UDEC results after strength degradation and permafrost melting at Year 21,000, showing vertical displacements for SFR 1, DFN 1-3. Displacements are in units of metres, with positive up.

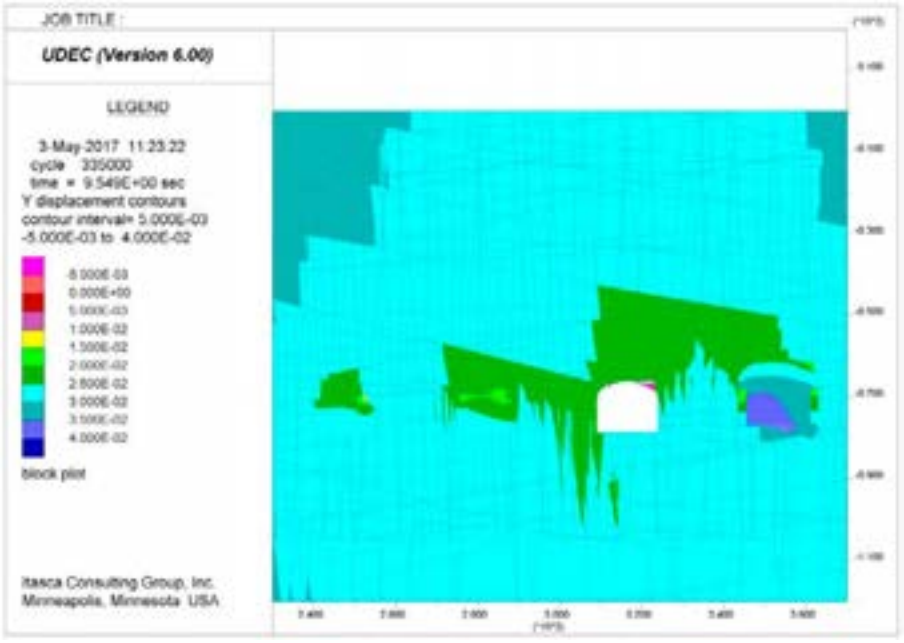


**Figure A110.** UDEC results after strength degradation and permafrost melting at Year 21,000, showing vertical displacements for SFR 1, DFN 1-4. Displacements are in units of metres, with positive up.

## SFR 1 – Year 21,000 Permafrost Melting (Horizontal Displacements)

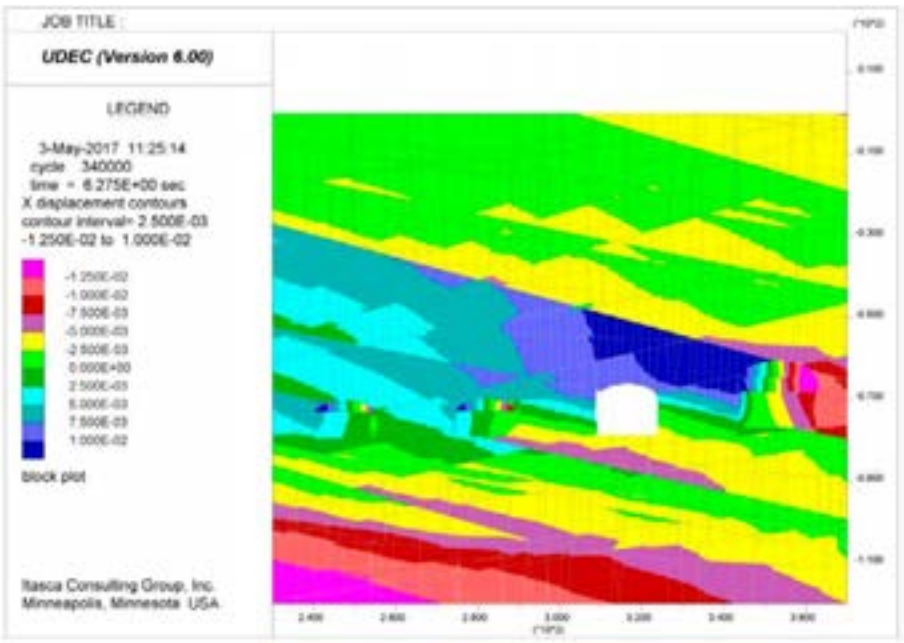


**Figure A111.** UDEC results after strength degradation and permafrost melting at Year 21,000, showing horizontal displacements for SFR 1, DFN 1-1. Displacements are in units of metres, with positive to the right.

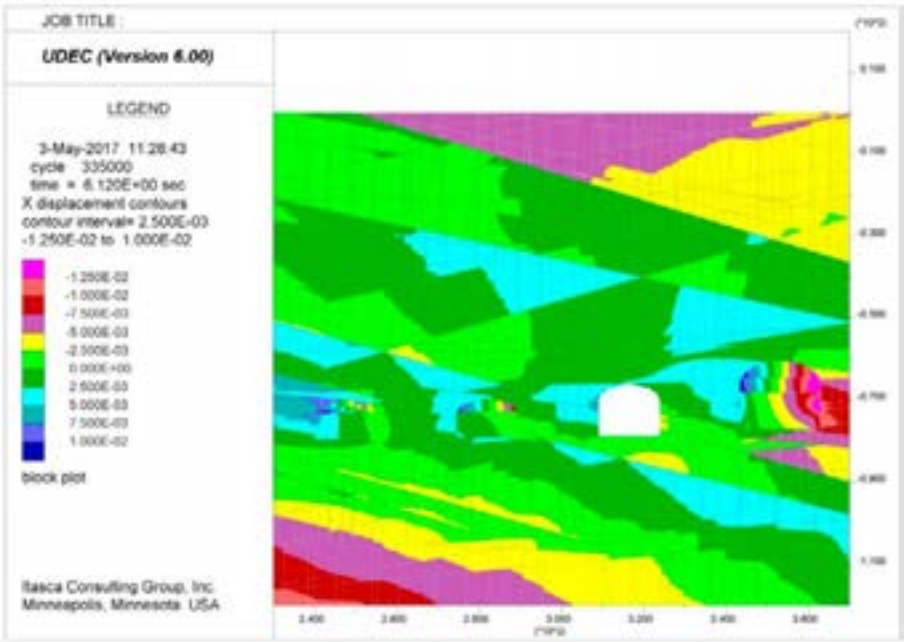


**Figure A112.** UDEC results after strength degradation and permafrost melting at Year 21,000, showing horizontal displacements for SFR 1, DFN 1-2. Displacements are in units of metres, with positive to the right.

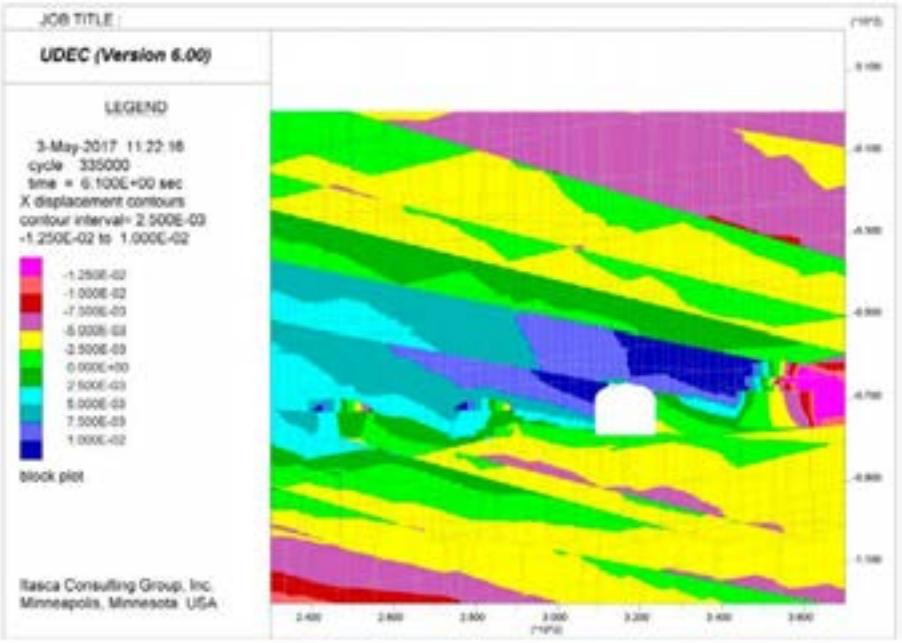


**Figure A113.** UDEC results after strength degradation and permafrost melting at Year 21,000, showing horizontal displacements for SFR 1, DFN 1-3. Displacements are in units of metres, with positive to the right.

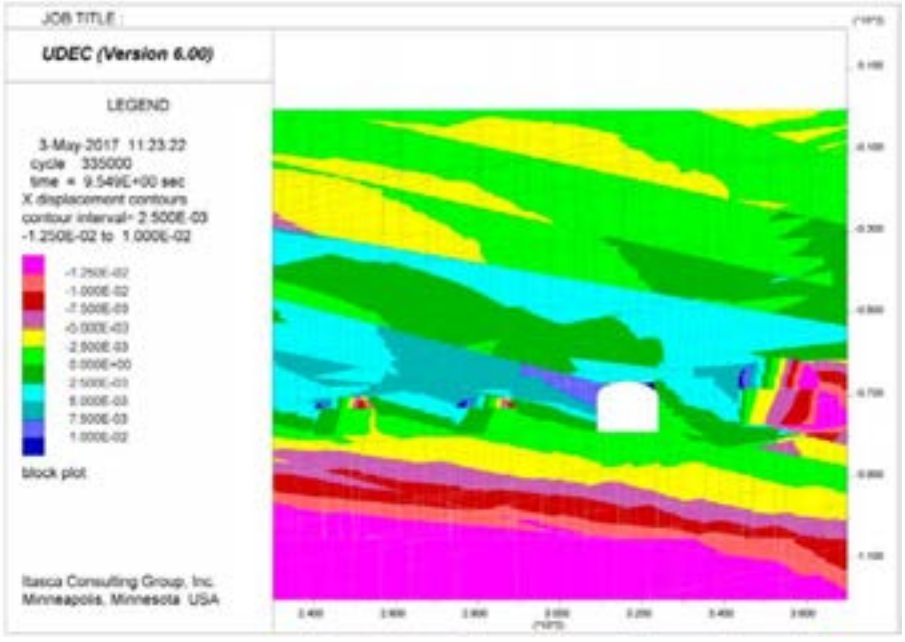


**Figure A114.** UDEC results after strength degradation and permafrost melting at Year 21,000, showing horizontal displacements for SFR 1, DFN 1-4. Displacements are in units of metres, with positive to the right.

## SFR 1 – Year 50,000 Glacial Loading (Vertical Stress)

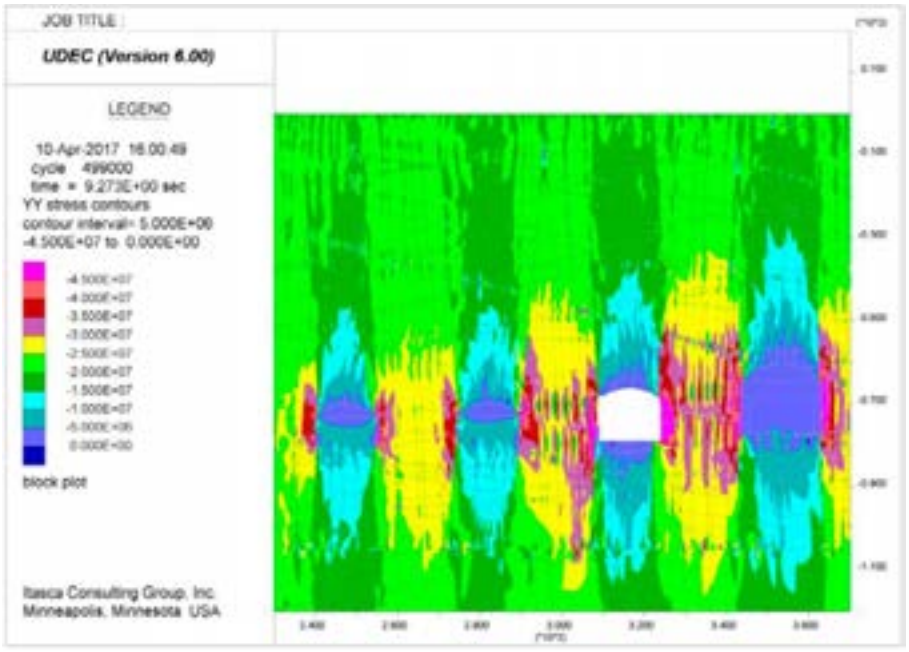


**Figure A115.** UDEC results after strength degradation and glacial loading at Year 50,000, showing vertical stresses (SYY) for SFR 1, DFN 1-1. Stress magnitudes are in units of Pascals, with compression negative.

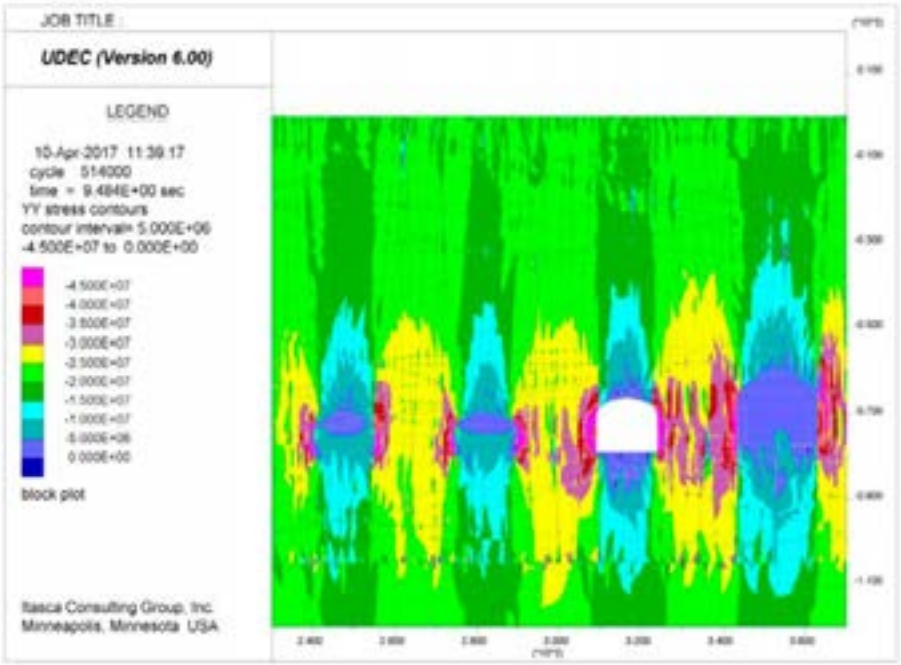


**Figure A116.** UDEC results after strength degradation and glacial loading at Year 50,000, showing vertical stresses (SYY) for SFR 1, DFN 1-2. Stress magnitudes are in units of Pascals, with compression negative.

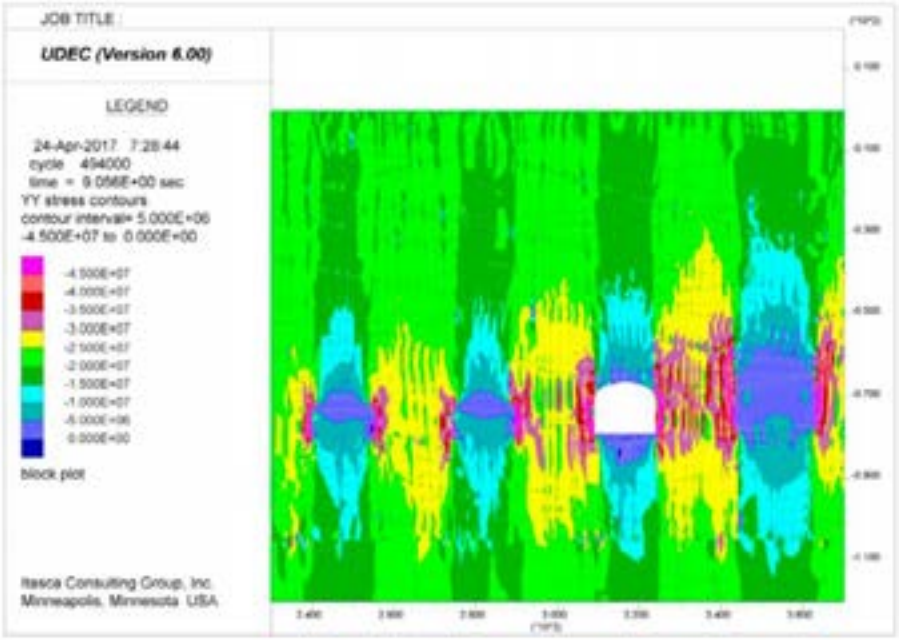


**Figure A117.** UDEC results after strength degradation and glacial loading at Year 50,000, showing vertical stresses (SYY) for SFR 1, DFN 1-3. Stress magnitudes are in units of Pascals, with compression negative.

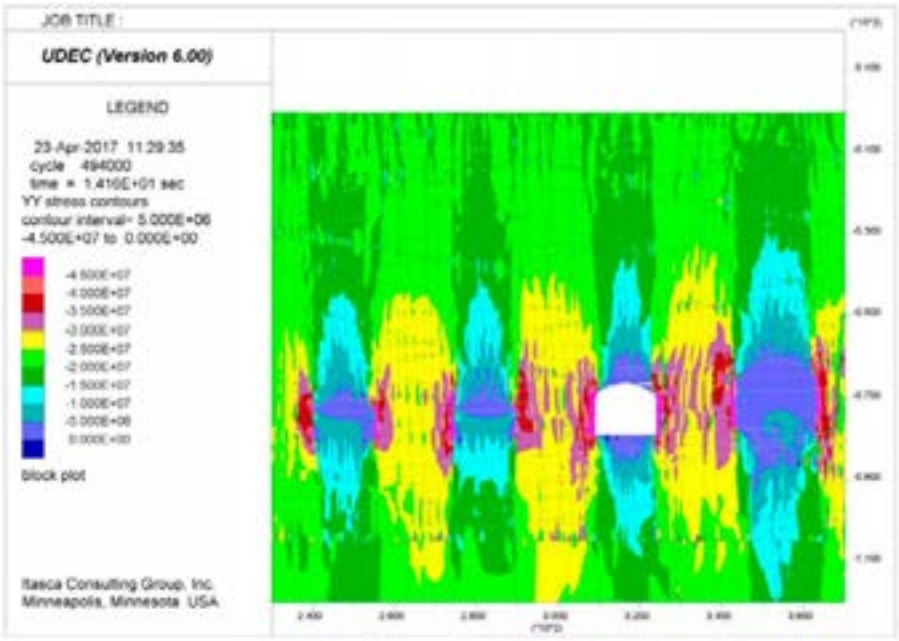


**Figure A118.** UDEC results after strength degradation and glacial loading at Year 50,000, showing vertical stresses (SYY) for SFR 1, DFN 1-4. Stress magnitudes are in units of Pascals, with compression negative.

## SFR 1 – Year 50,000 Glacial Loading (Horizontal Stress)

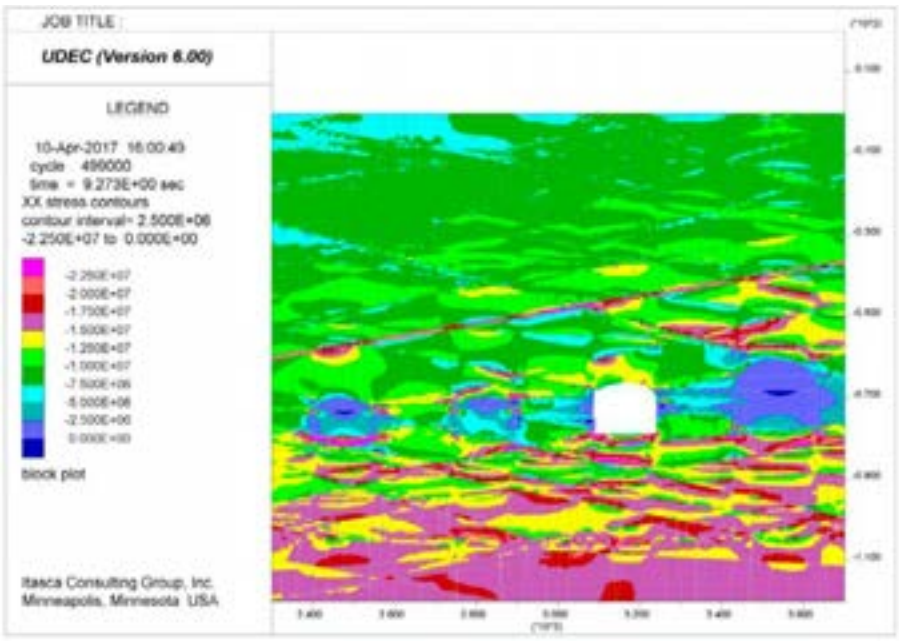


**Figure A119.** UDEC results after strength degradation and glacial loading at Year 50,000, showing horizontal stresses (SXX) for SFR 1, DFN 1-1. Stress magnitudes are in units of Pascals, with compression negative.

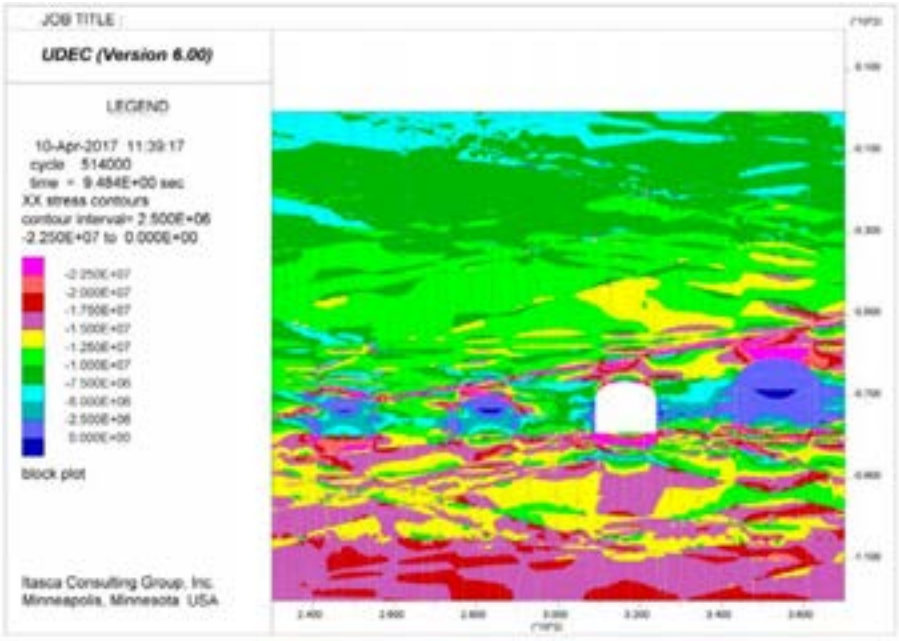


**Figure A120.** UDEC results after strength degradation and glacial loading at Year 50,000, showing horizontal stresses (SXX) for SFR 1, DFN 1-2. Stress magnitudes are in units of Pascals, with compression negative.

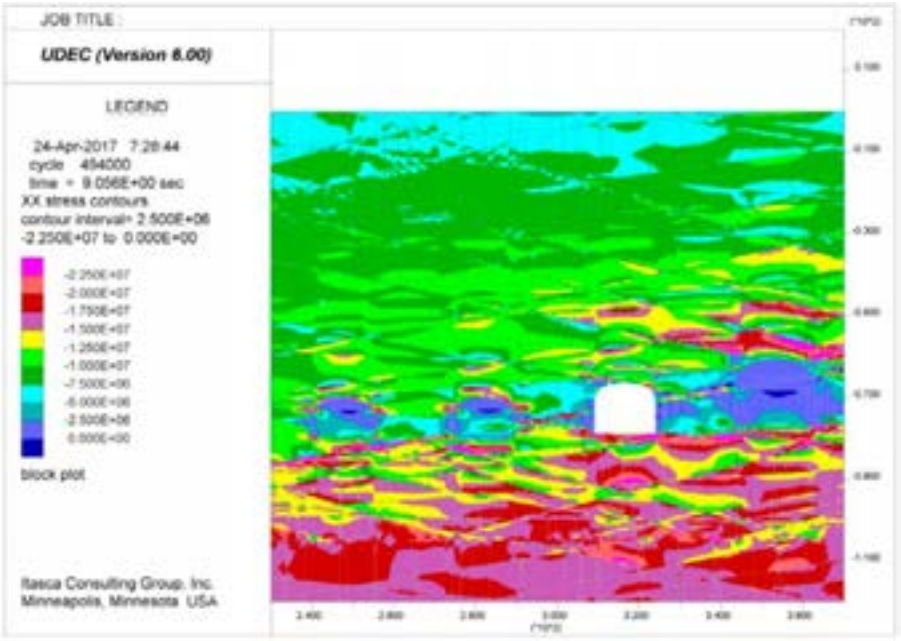


**Figure A121.** UDEC results after strength degradation and glacial loading at Year 50,000, showing horizontal stresses (SXX) for SFR 1, DFN 1-3. Stress magnitudes are in units of Pascals, with compression negative.

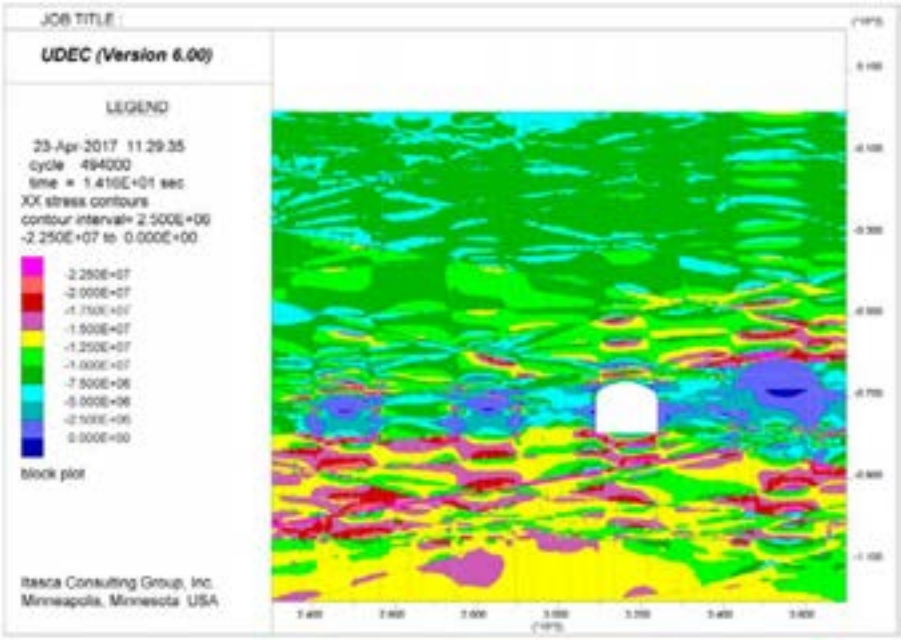


**Figure A122.** UDEC results after strength degradation and glacial loading at Year 50,000, showing horizontal stresses (SXX) for SFR 1, DFN 1-4. Stress magnitudes are in units of Pascals, with compression negative.

## SFR 1 – Year 50,000 Glacial Loading (Plasticity Indicators)

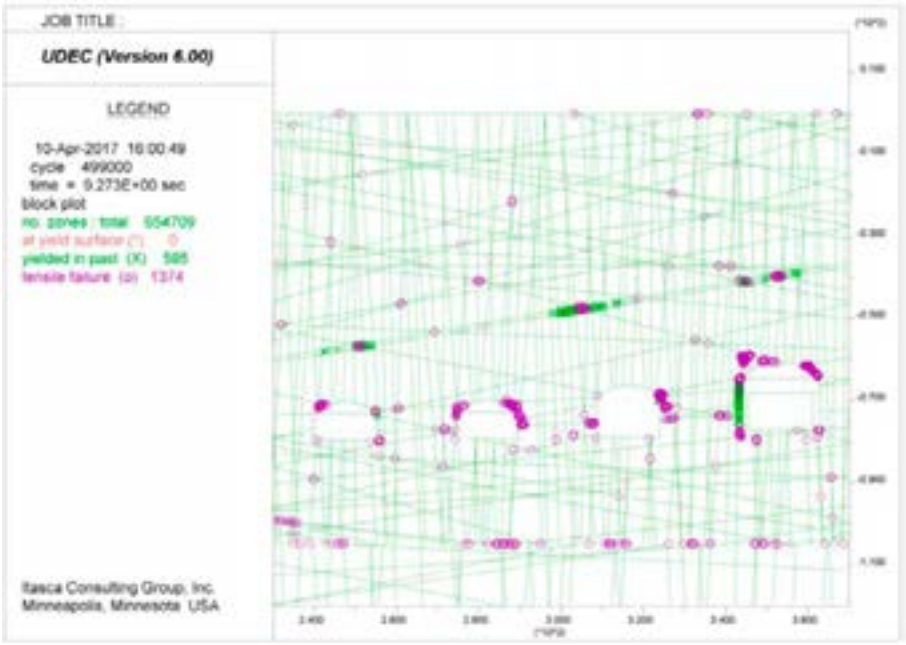


**Figure A123.** UDEC results after strength degradation and glacial loading at Year 50,000, showing yielded elements for SFR 1, DFN 1-1.

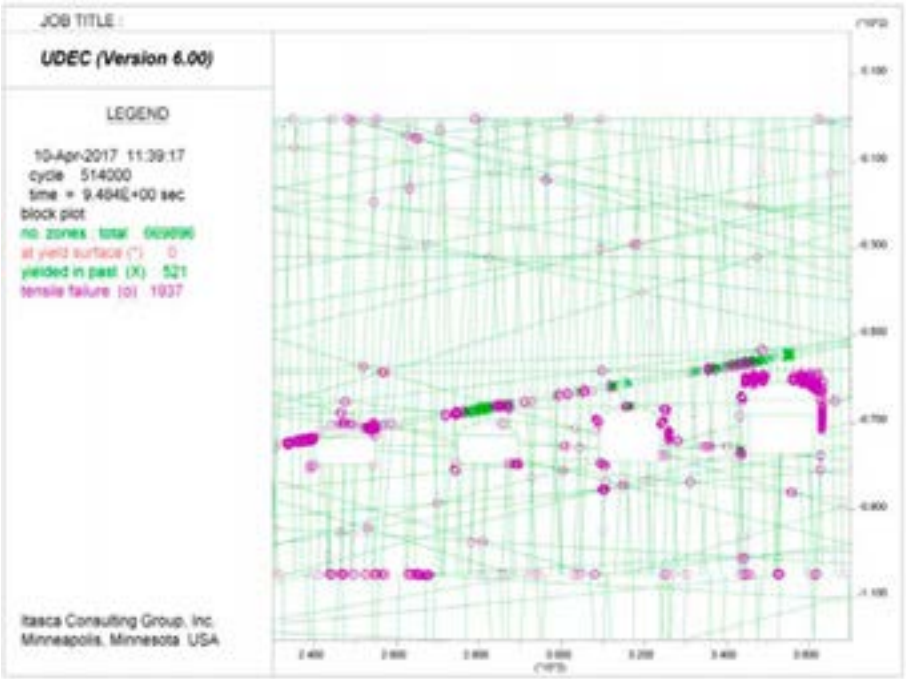


**Figure A124.** UDEC results after strength degradation and glacial loading at Year 50,000, showing yielded elements for SFR 1, DFN 1-2.

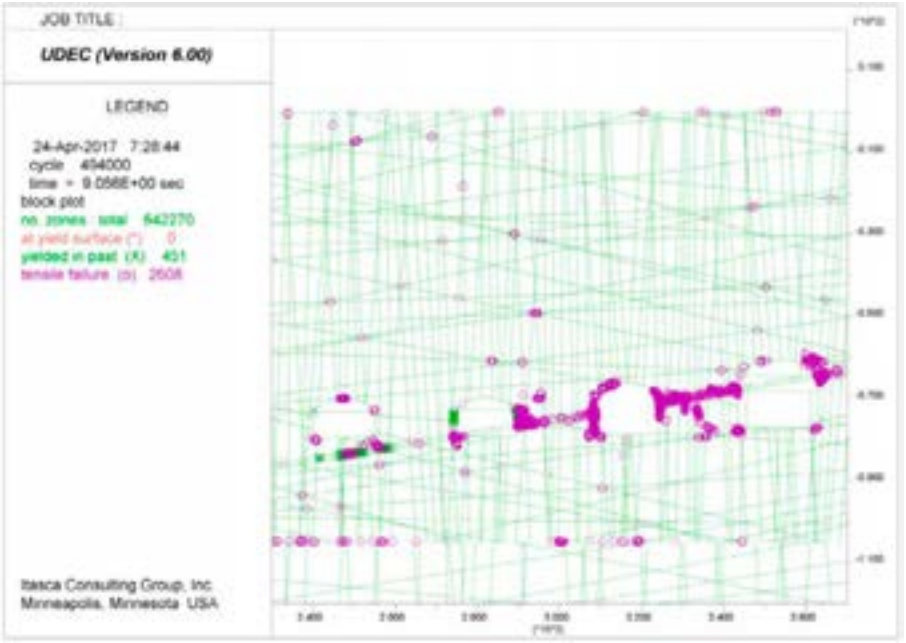


**Figure A125.** UDEC results after strength degradation and glacial loading at Year 50,000, showing yielded elements for SFR 1, DFN 1-3.

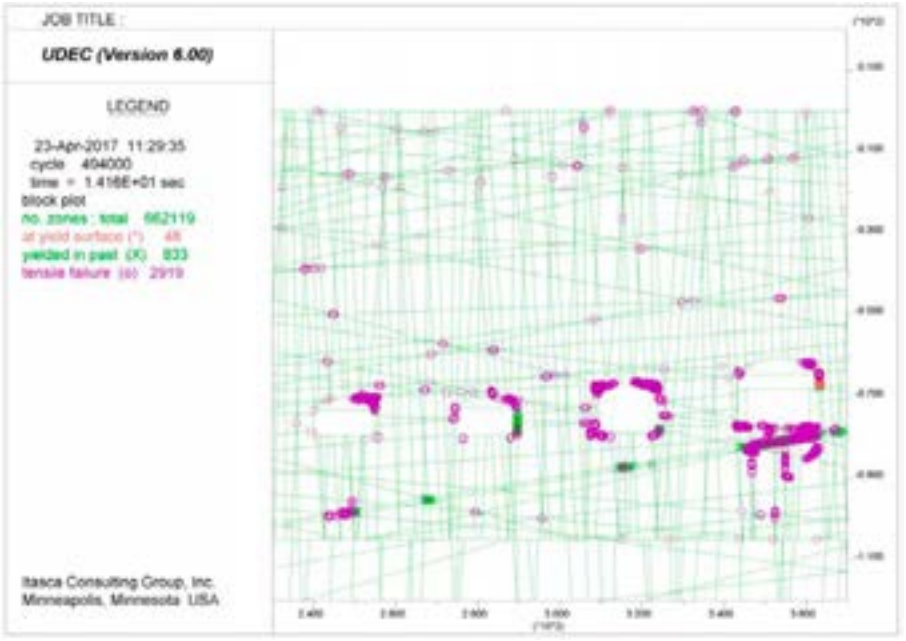


**Figure A126.** UDEC results after strength degradation and glacial loading at Year 50,000, showing yielded elements for SFR 1, DFN 1-4.

## SFR 1 – Year 50,000 Glacial Loading (Displacement Vectors)

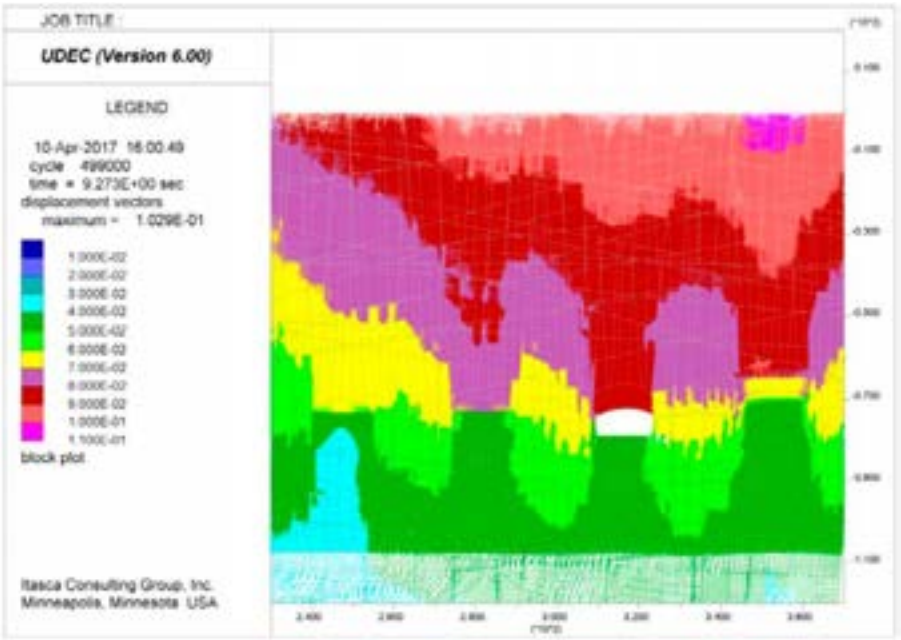


**Figure A127.** UDEC results after strength degradation and glacial loading at Year 50,000, showing displacement vectors for SFR 1, DFN 1-1. Displacement magnitudes are in units of metres.

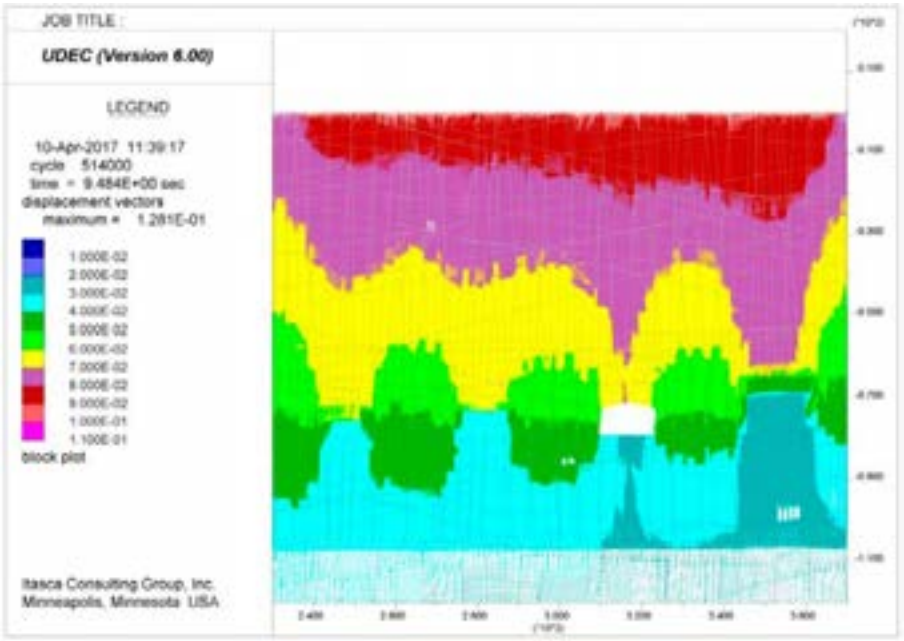


**Figure A128.** UDEC results after strength degradation and glacial loading at Year 50,000, showing displacement vectors for SFR 1, DFN 1-2. Displacement magnitudes are in units of metres.

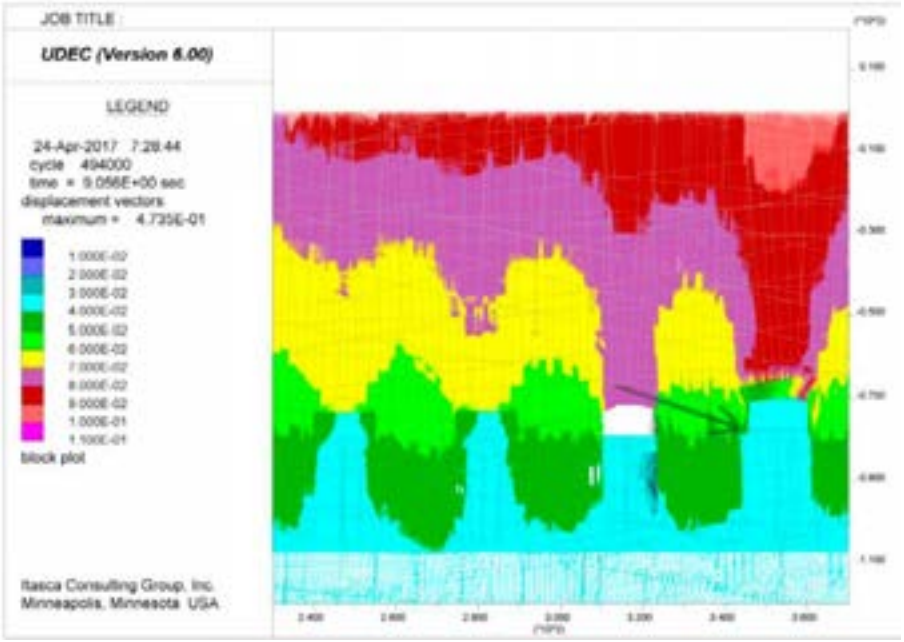


**Figure A129.** UDEC results after strength degradation and glacial loading at Year 50,000, showing displacement vectors for SFR 1, DFN 1-3. Displacement magnitudes are in units of metres.

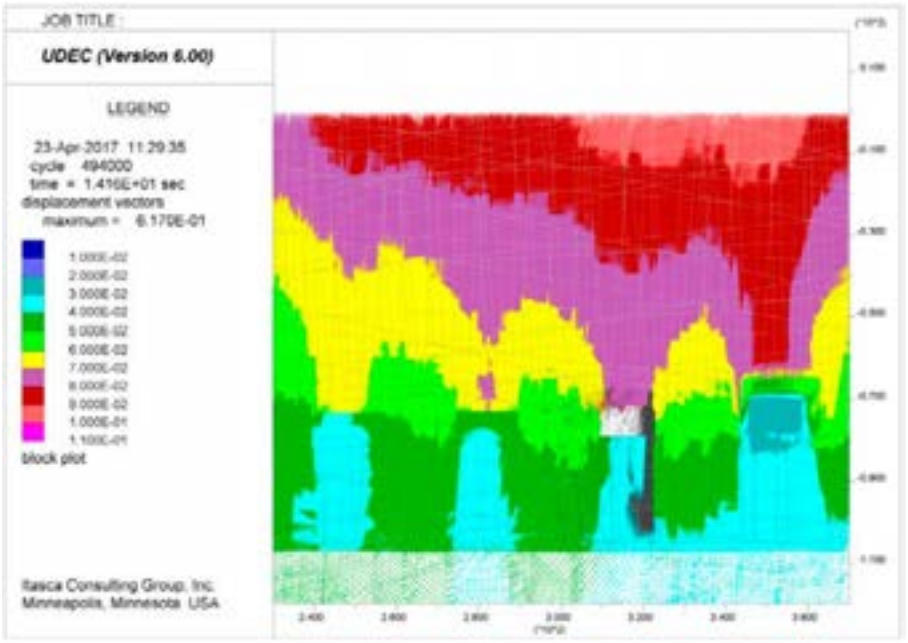


**Figure A130.** UDEC results after strength degradation and glacial loading at Year 50,000, showing displacement vectors for SFR 1, DFN 1-4. Displacement magnitudes are in units of metres.

## SFR 1 – Year 50,000 Glacial Loading (Fracture Shear Displacement)

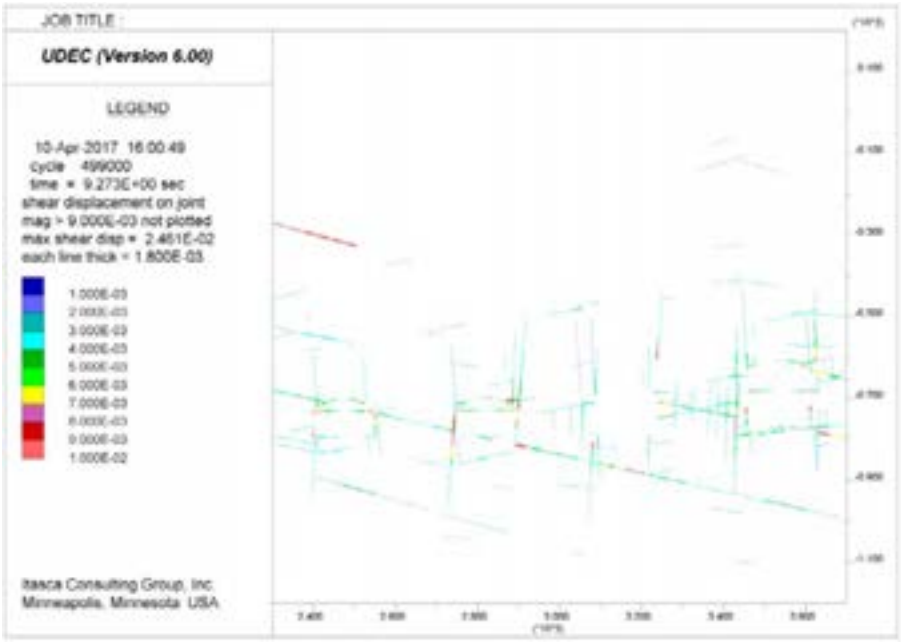


**Figure A131.** UDEC results after strength degradation and glacial loading at Year 50,000, showing shear displacements along fractures for SFR 1, DFN 1-1. Displacements are in units of metres.

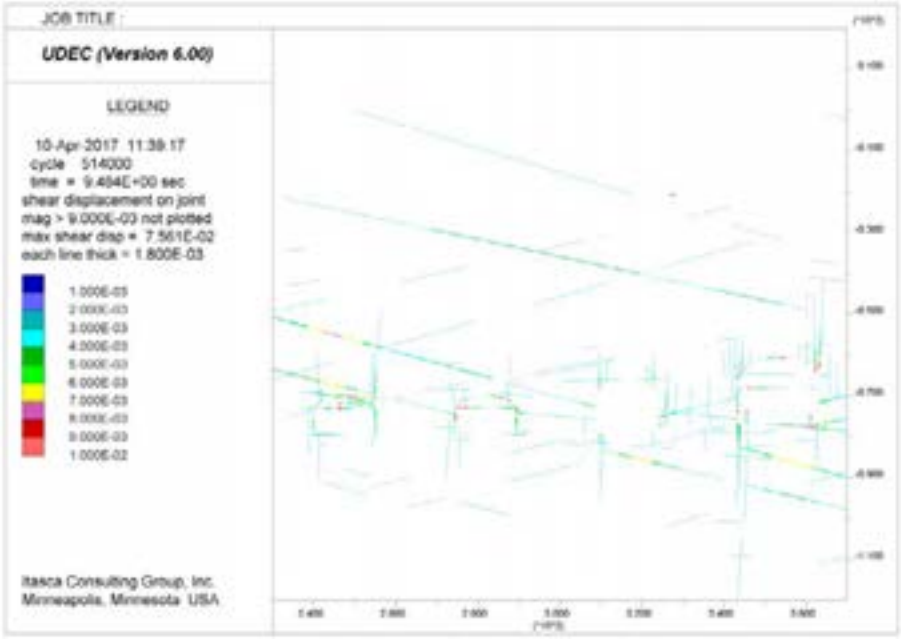


**Figure A132.** UDEC results after strength degradation and glacial loading at Year 50,000, showing shear displacements along fractures for SFR 1, DFN 1-2. Displacements are in units of metres.

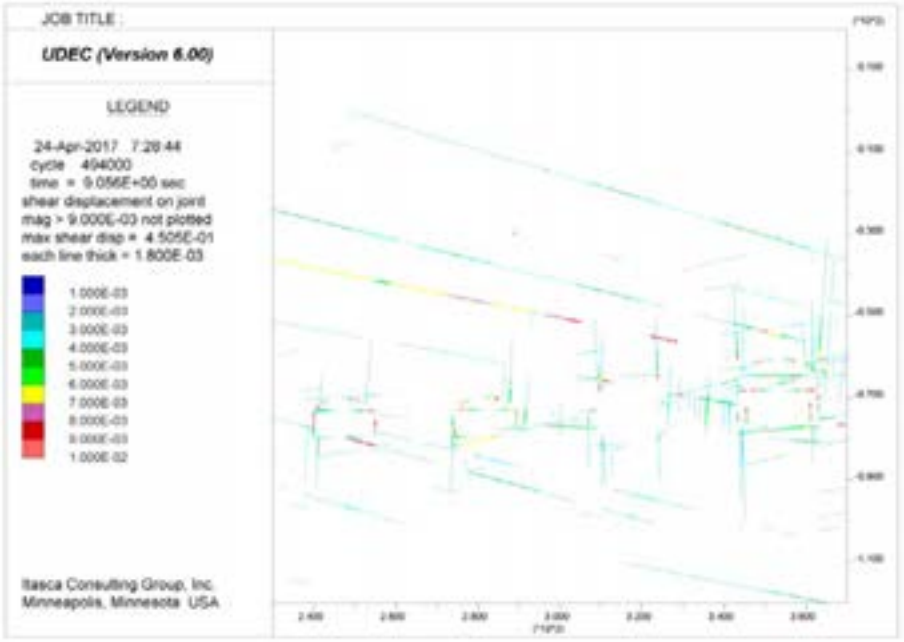


**Figure A133.** UDEC results after strength degradation and glacial loading at Year 50,000, showing shear displacements along fractures for SFR 1, DFN 1-3. Displacements are in units of metres.

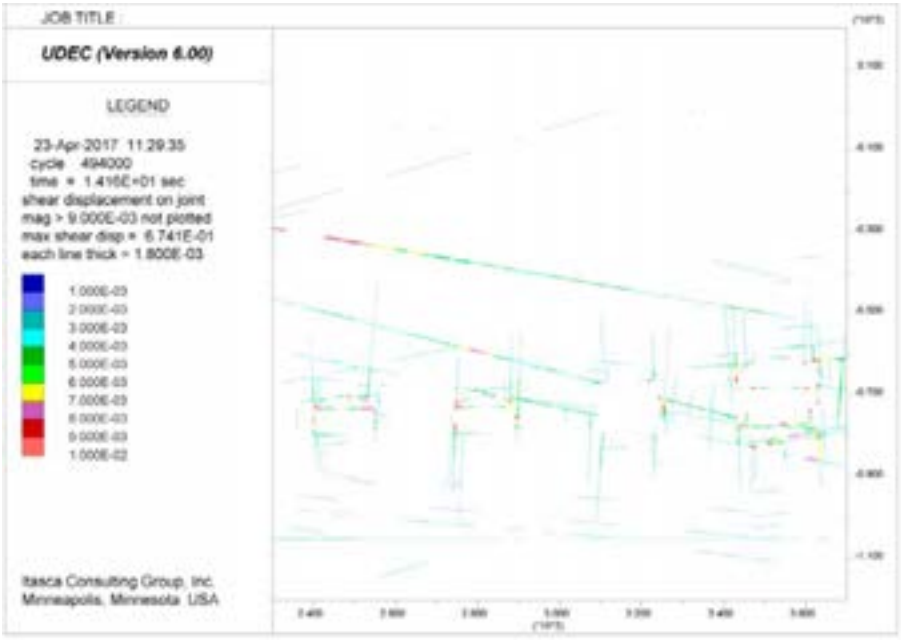


**Figure A134.** UDEC results after strength degradation and glacial loading at Year 50,000, showing shear displacements along fractures for SFR 1, DFN 1-4. Displacements are in units of metres.

## SFR 1 – Year 50,000 Glacial Loading (Vertical Displacements)

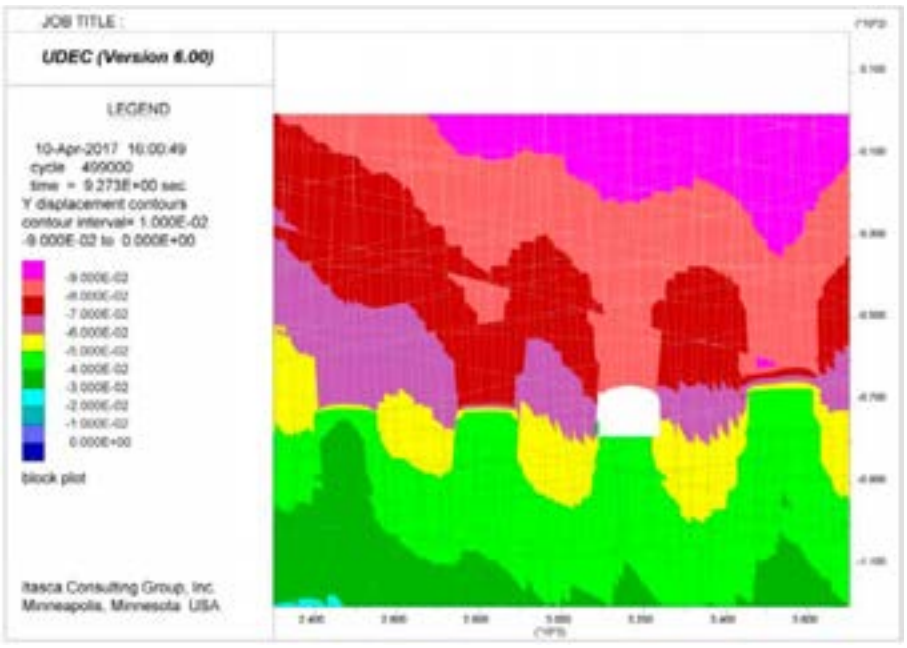


**Figure A135.** UDEC results after strength degradation and glacial loading at Year 50,000, showing vertical displacements for SFR 1, DFN 1-1. Displacements are in units of metres, with positive up.

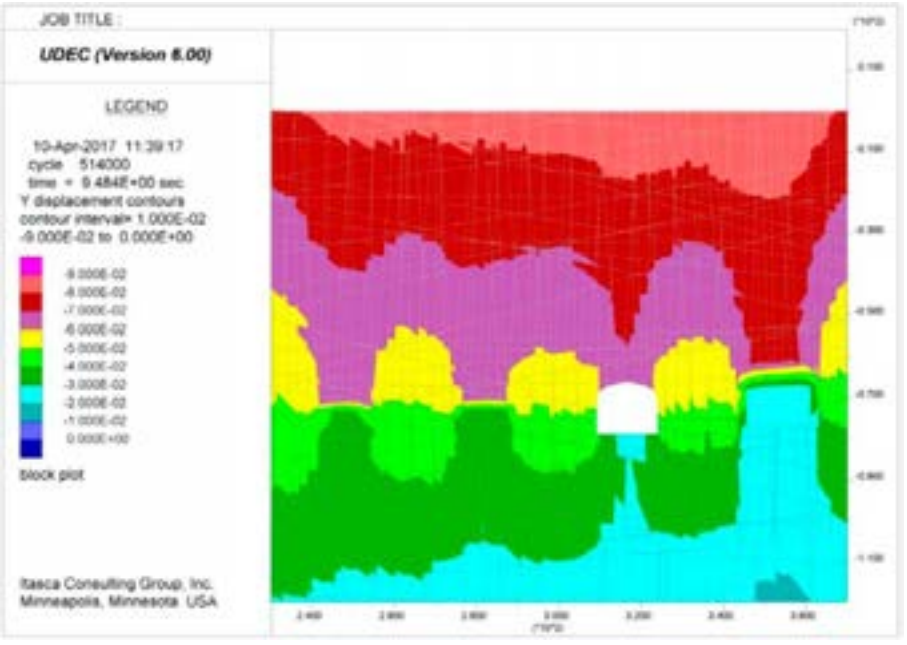


**Figure A136.** UDEC results after strength degradation and glacial loading at Year 50,000, showing vertical displacements for SFR 1, DFN 1-2. Displacements are in units of metres, with positive up.

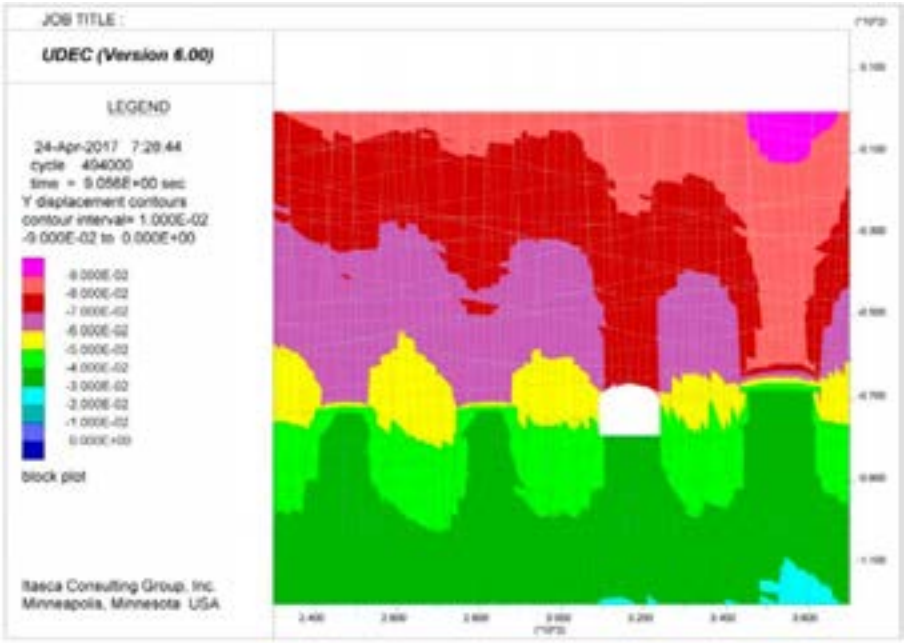


**Figure A137.** UDEC results after strength degradation and glacial loading at Year 50,000, showing vertical displacements for SFR 1, DFN 1-3. Displacements are in units of metres, with positive up.

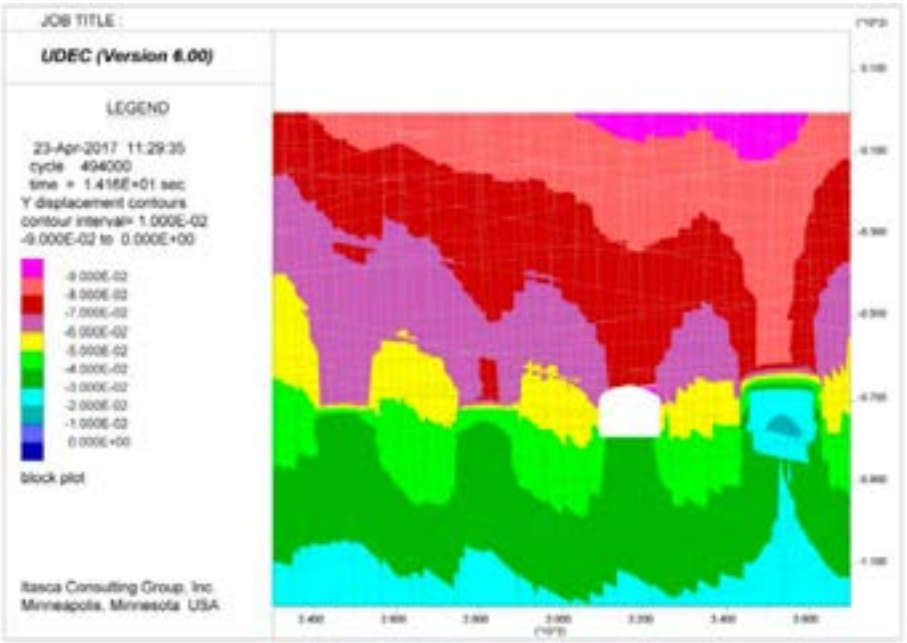


**Figure A138.** UDEC results after strength degradation and glacial loading at Year 50,000, showing vertical displacements for SFR 1, DFN 1-4. Displacements are in units of metres, with positive up.

## SFR 1 – Year 50,000 Glacial Loading (Horizontal Displacements)

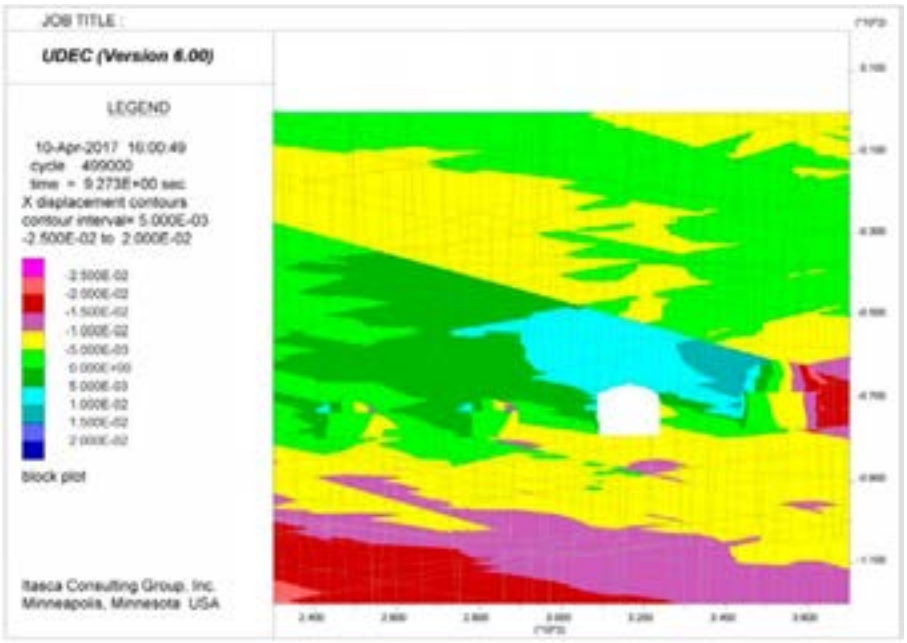


**Figure A139.** UDEC results after strength degradation and glacial loading at Year 50,000, showing horizontal displacements for SFR 1, DFN 1-1. Displacements are in units of metres, with positive to the right.

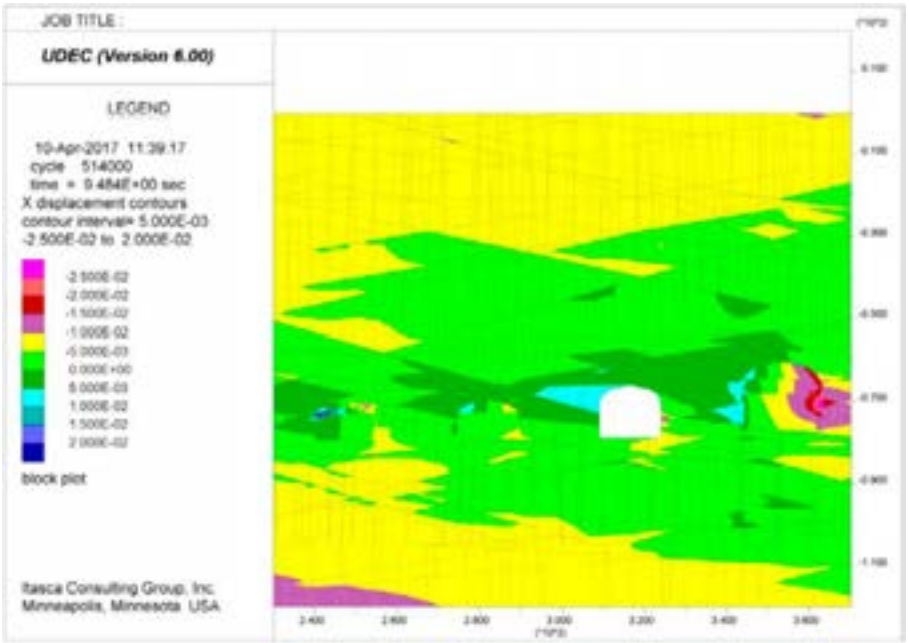

**Figure A140.** UDEC results after strength degradation and glacial loading at Year 50,000, showing horizontal displacements for SFR 1, DFN 1-2. Displacements are in units of metres, with positive to the right.

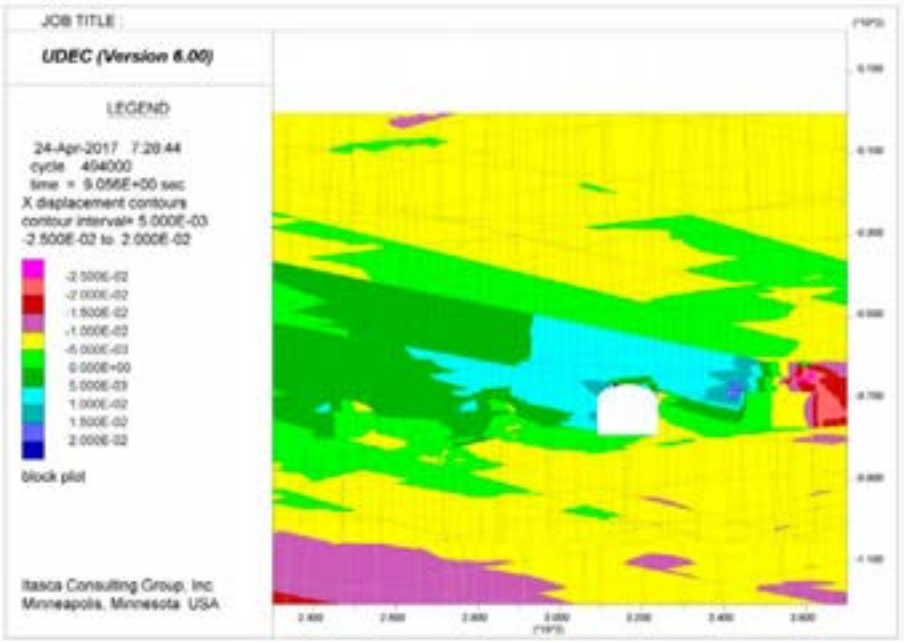


**Figure A141.** UDEC results after strength degradation and glacial loading at Year 50,000, showing horizontal displacements for SFR 1, DFN 1-3. Displacements are in units of metres, with positive to the right.

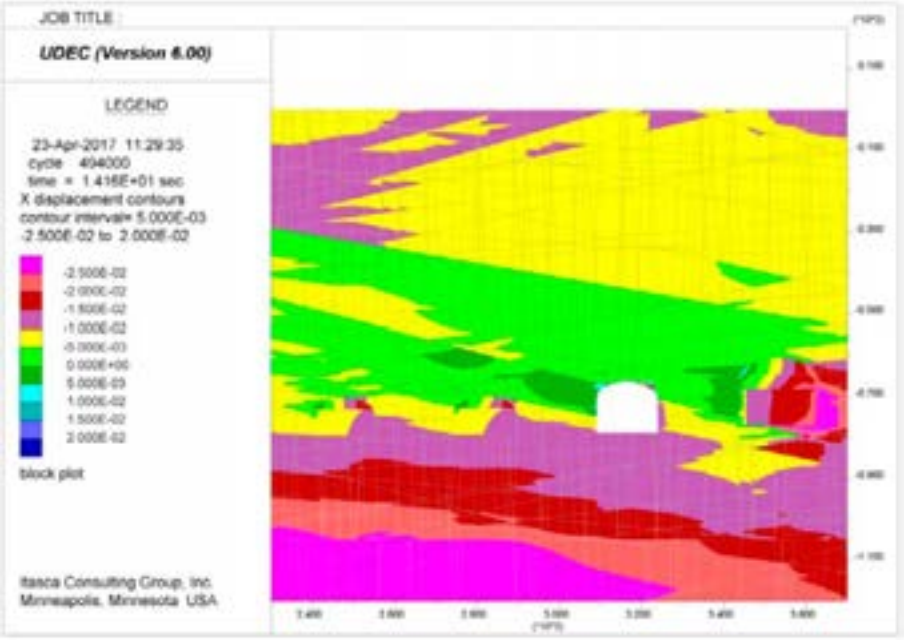


**Figure A142.** UDEC results after strength degradation and glacial loading at Year 50,000, showing horizontal displacements for SFR 1, DFN 1-4. Displacements are in units of metres, with positive to the right.

## SFR 1 – Year 66,000 Glacial Unloading (Vertical Stress)

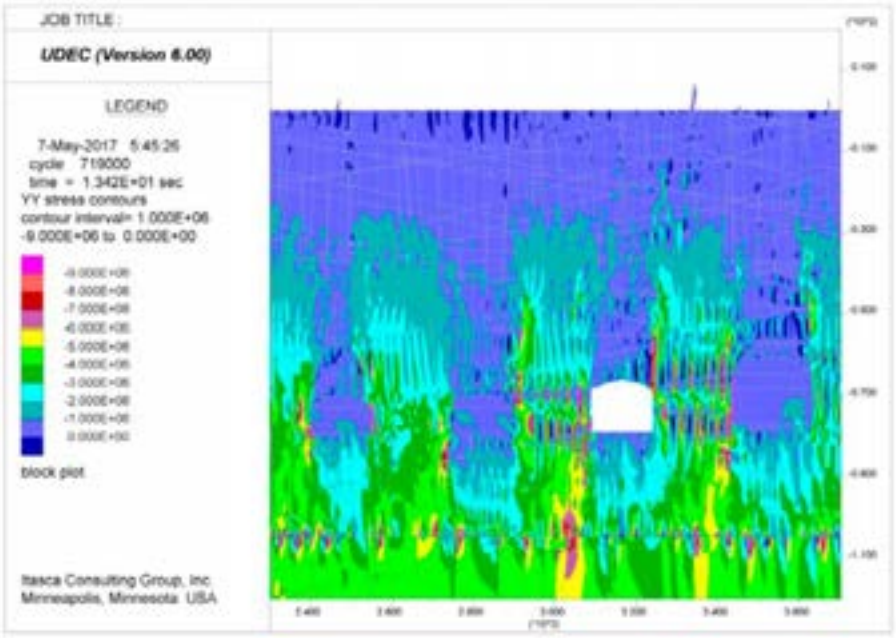


**Figure A143.** UDEC results after strength degradation, glacial unloading and permafrost melting at Year 66,000, showing vertical stresses (SYY) for SFR 1, DFN 1-1. Stress magnitudes are in units of Pascals, with compression negative.

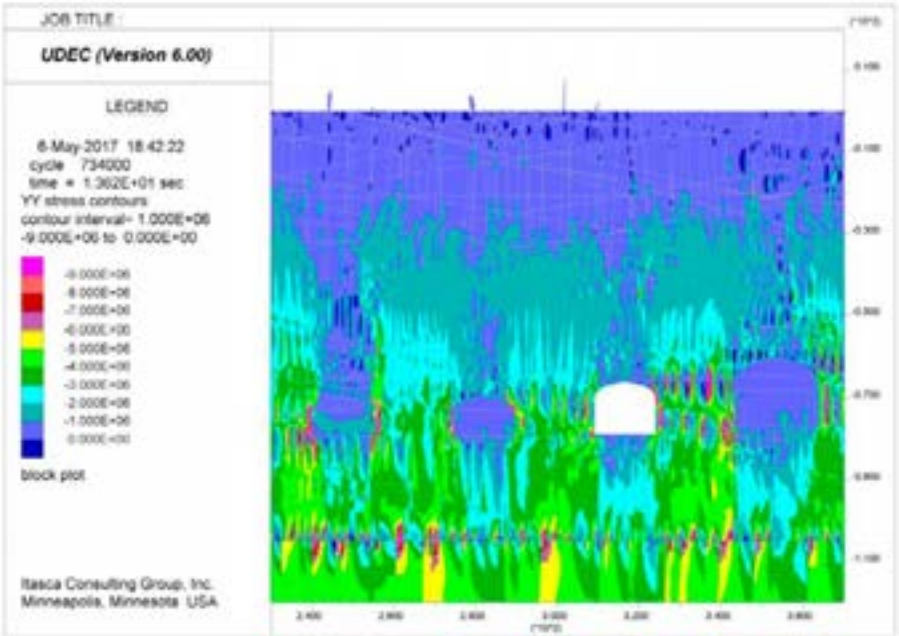

**Figure A144.** UDEC results after strength degradation, glacial unloading and permafrost melting at Year 66,000, showing vertical stresses (SYY) for SFR 1, DFN 1-2. Stress magnitudes are in units of Pascals, with compression negative.

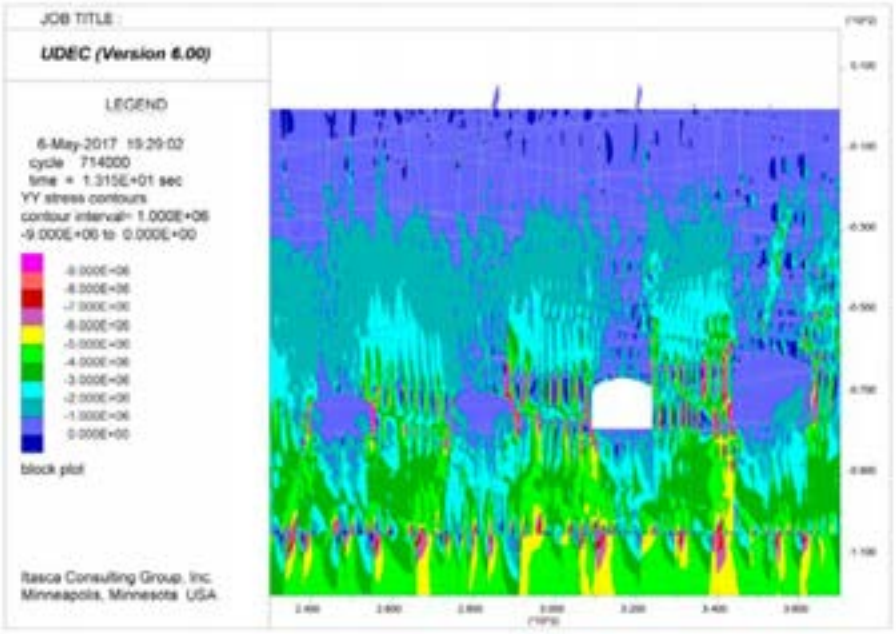


**Figure A145.** UDEC results after strength degradation, glacial unloading and permafrost melting at Year 66,000, showing vertical stresses (SYY) for SFR 1, DFN 1-3. Stress magnitudes are in units of Pascals, with compression negative.

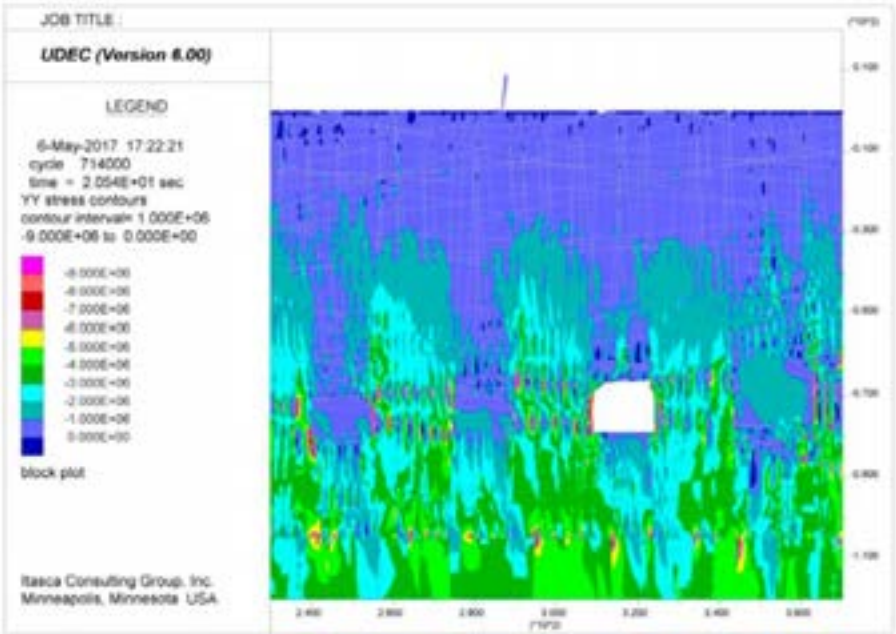


**Figure A146.** UDEC results after strength degradation, glacial unloading and permafrost melting at Year 66,000, showing vertical stresses (SYY) for SFR 1, DFN 1-4. Stress magnitudes are in units of Pascals, with compression negative.

## SFR 1 – Year 66,000 Glacial Unloading (Horizontal Stress)

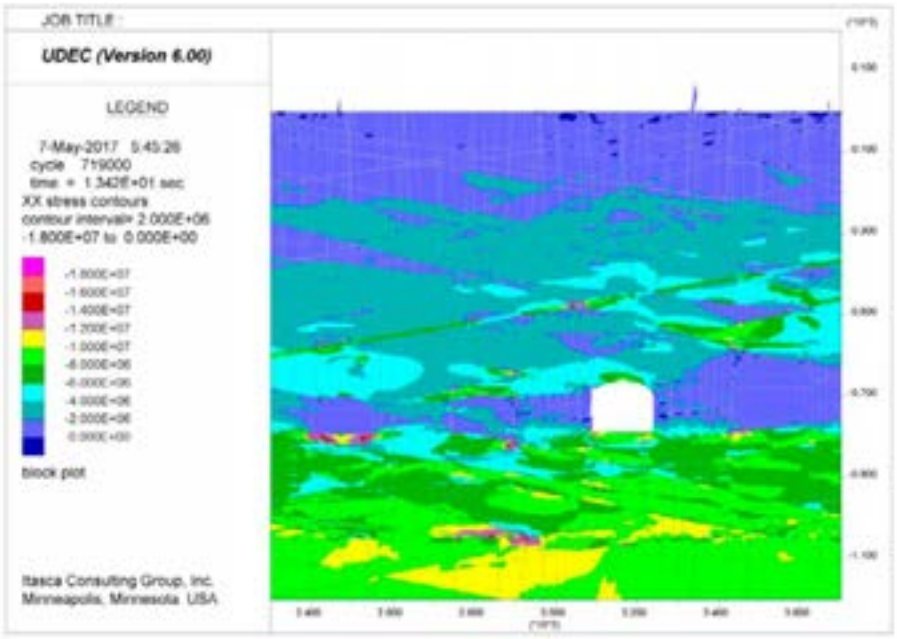


**Figure A147.** UDEC results after strength degradation, glacial unloading and permafrost melting at Year 66,000, showing horizontal stresses (SXX) for SFR 1, DFN 1-1. Stress magnitudes are in units of Pascals, with compression negative.

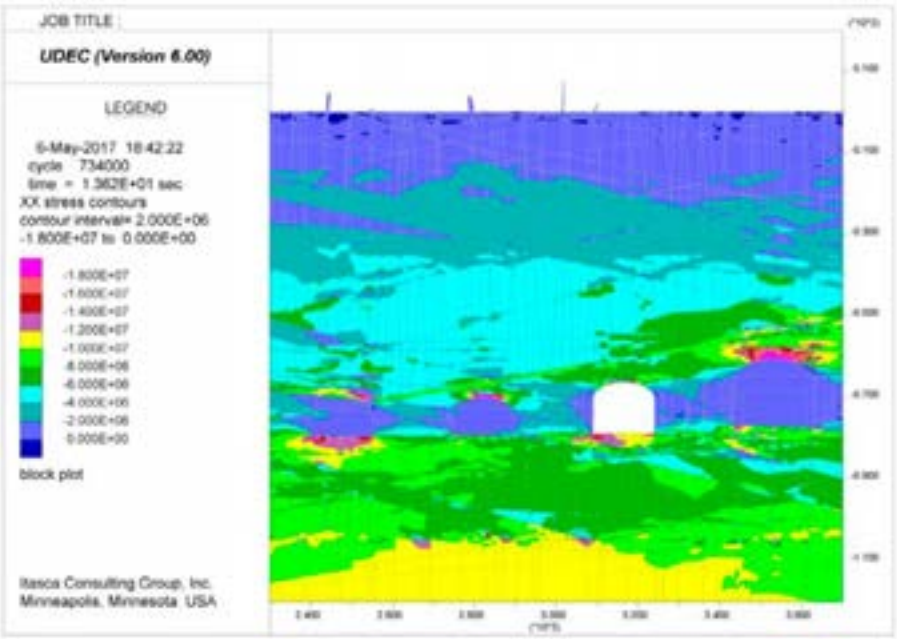

**Figure A148.** UDEC results after strength degradation, glacial unloading and permafrost melting at Year 66,000, showing horizontal stresses (SXX) for SFR 1, DFN 1-2. Stress magnitudes are in units of Pascals, with compression negative.

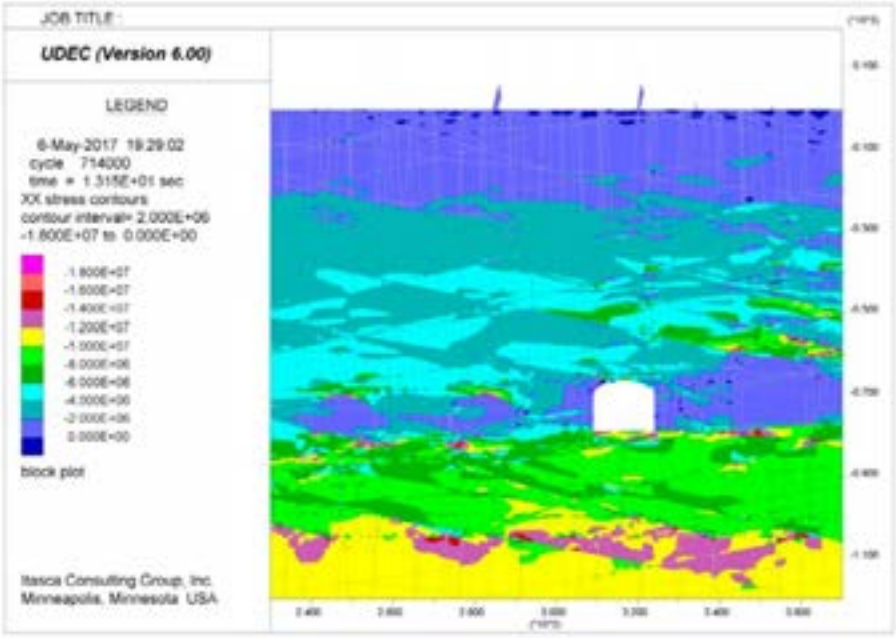


**Figure A149.** UDEC results after strength degradation, glacial unloading and permafrost melting at Year 66,000, showing horizontal stresses (SXX) for SFR 1, DFN 1-3. Stress magnitudes are in units of Pascals, with compression negative.

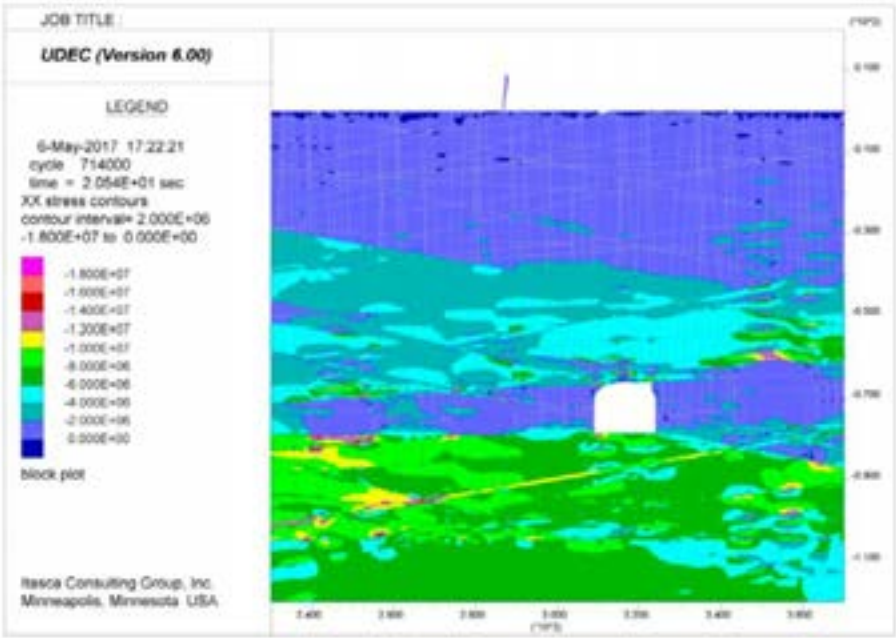


**Figure A150.** UDEC results after strength degradation, glacial unloading and permafrost melting at Year 66,000, showing horizontal stresses (SXX) for SFR 1, DFN 1-4. Stress magnitudes are in units of Pascals, with compression negative.

## SFR 1 – Year 66,000 Glacial Unloading (Plasticity Indicators)

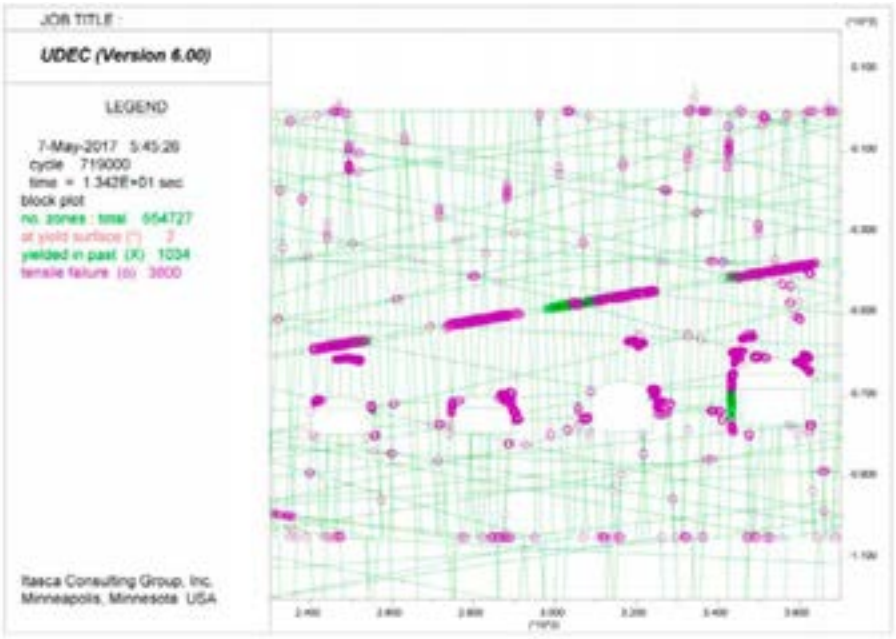


**Figure A151.** UDEC results after strength degradation, glacial unloading and permafrost melting at Year 66,000, showing yielded elements for SFR 1, DFN 1-1.

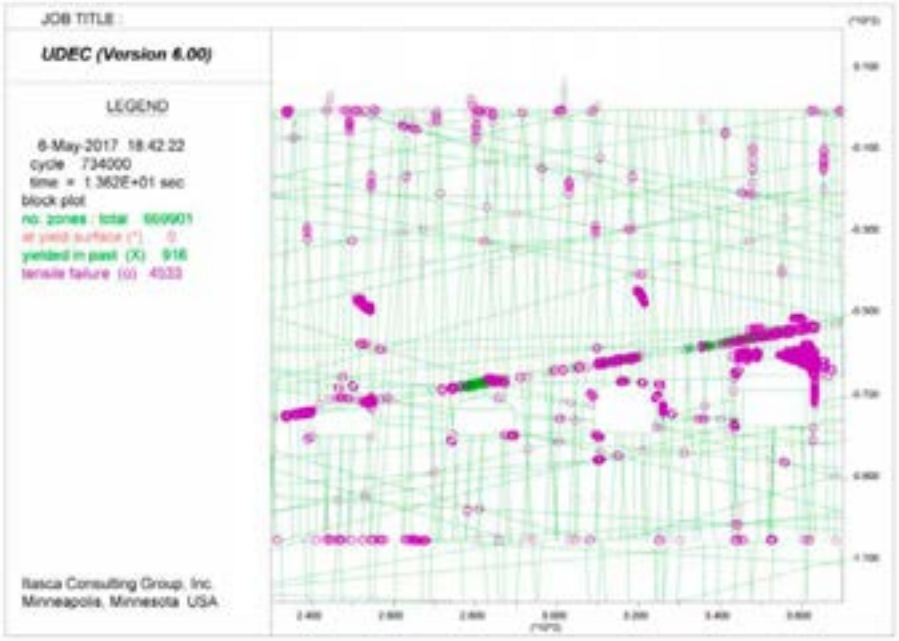

**Figure A152.** UDEC results after strength degradation, glacial unloading and permafrost melting at Year 66,000, showing yielded elements for SFR 1, DFN 1-2.

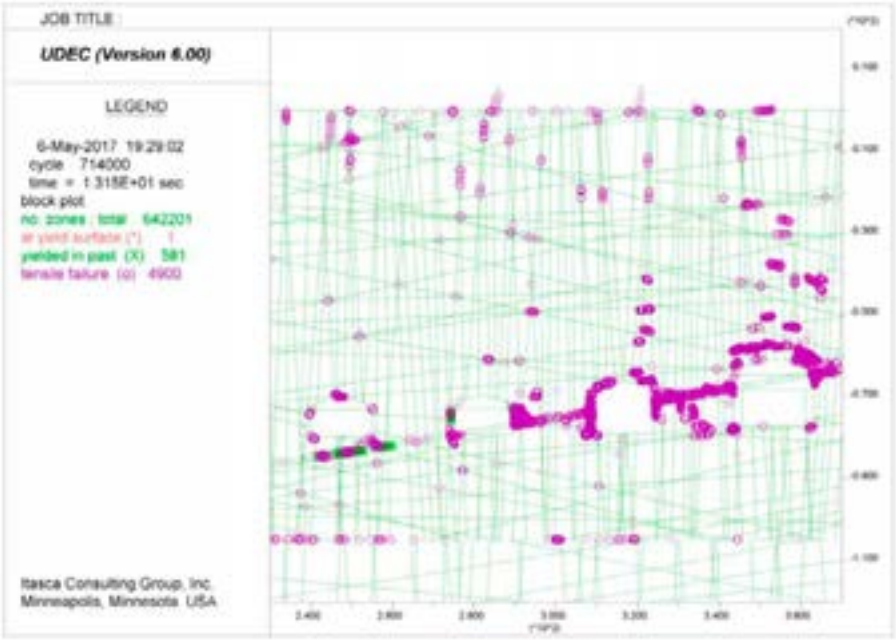


**Figure A153.** UDEC results after strength degradation, glacial unloading and permafrost melting at Year 66,000, showing yielded elements for SFR 1, DFN 1-3.

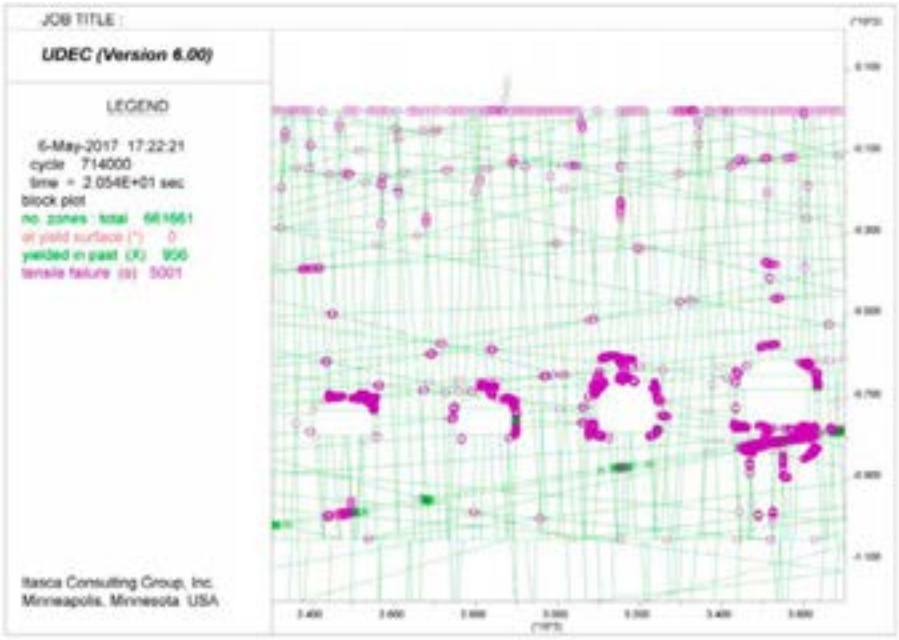


**Figure A154.** UDEC results after strength degradation, glacial unloading and permafrost melting at Year 66,000, showing yielded elements for SFR 1, DFN 1-4.

## SFR 1 – Year 66,000 Glacial Unloading (Displacement Vectors)

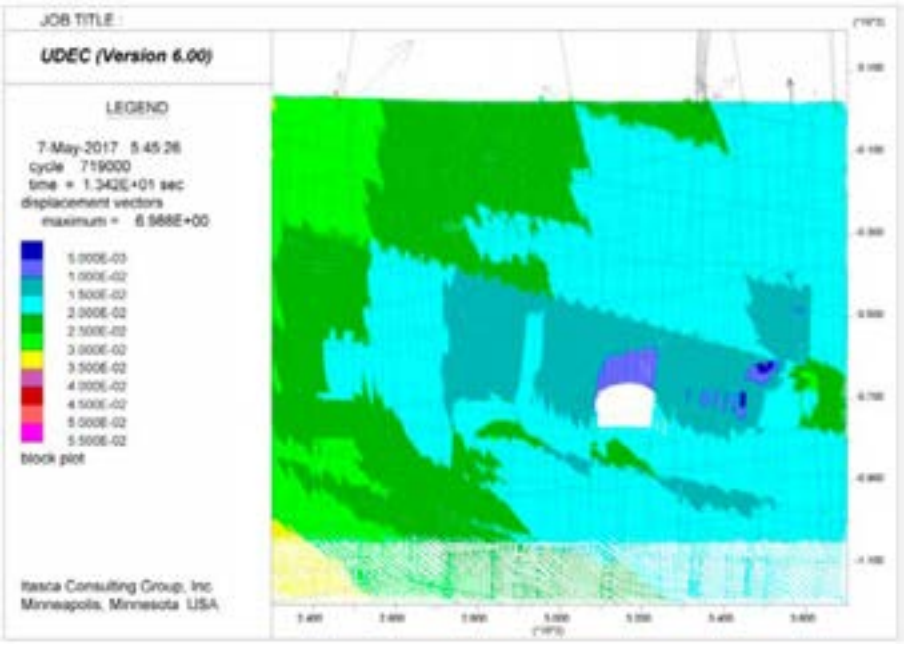


**Figure A155.** UDEC results after strength degradation, glacial unloading and permafrost melting at Year 66,000, showing displacement vectors for SFR 1, DFN 1-1. Displacement magnitudes are in units of metres.

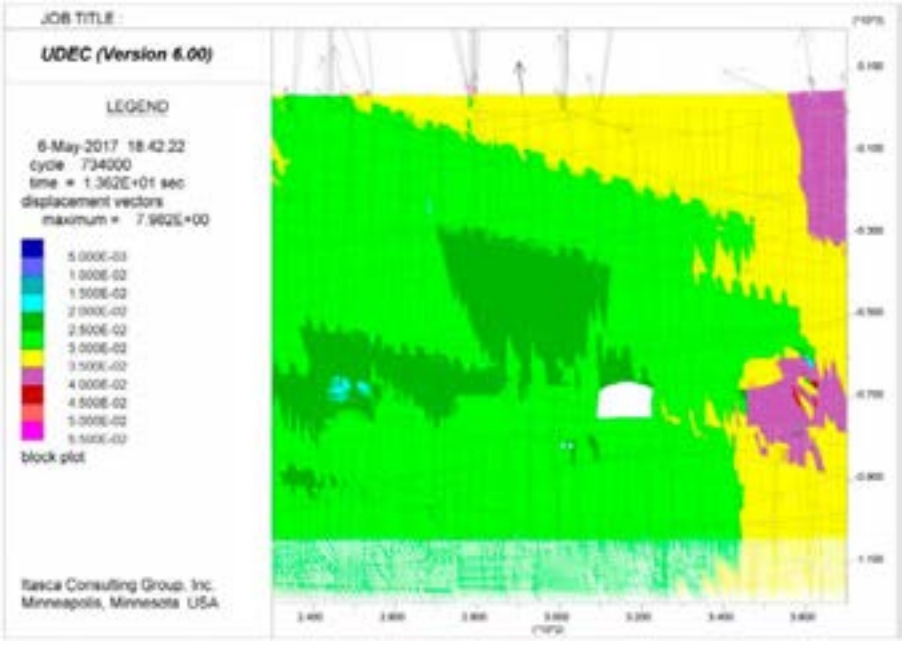

**Figure A156.** UDEC results after strength degradation, glacial unloading and permafrost melting at Year 66,000, showing displacement vectors for SFR 1, DFN 1-2. Displacement magnitudes are in units of metres.

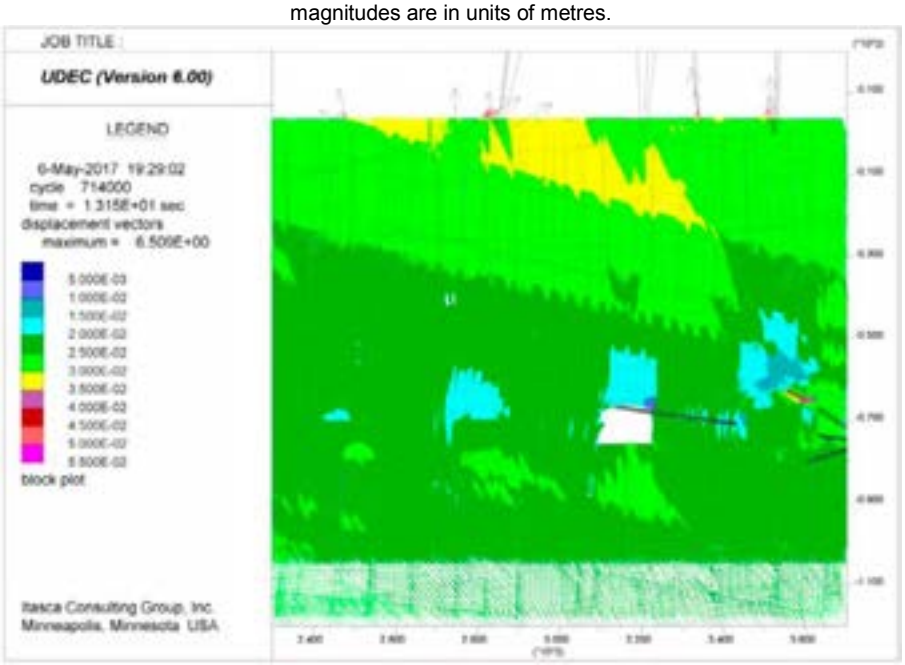


**Figure A157.** UDEC results after strength degradation, glacial unloading and permafrost melting at Year 66,000, showing displacement vectors for SFR 1, DFN 1-3. Displacement magnitudes are in units of metres.

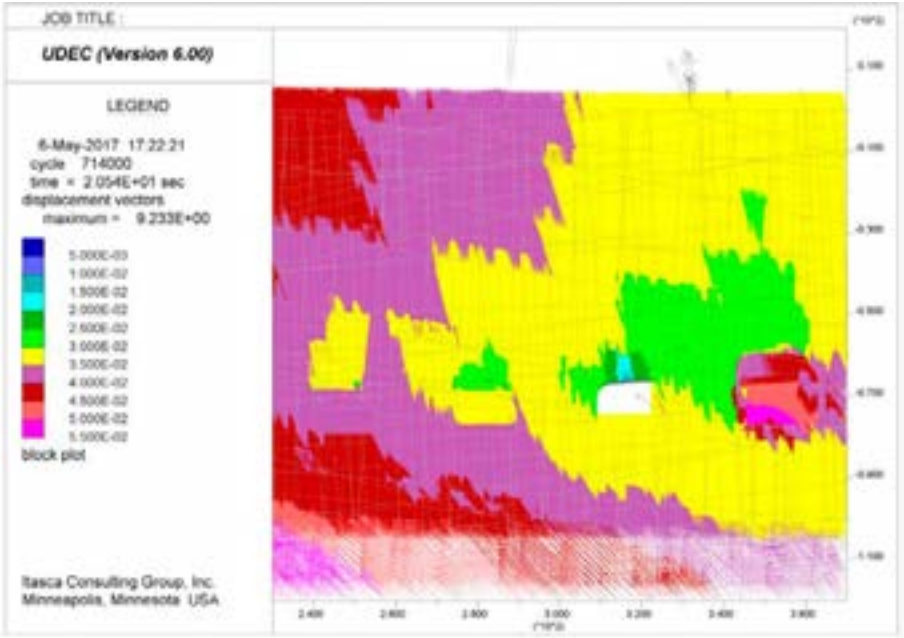

**Figure A158.** UDEC results after strength degradation, glacial unloading and permafrost melting at Year 66,000, showing displacement vectors for SFR 1, DFN 1-4. Displacement magnitudes are in units of metres.

## SFR 1 – Year 66,000 Glacial Unloading (Fracture Shear Displacement)

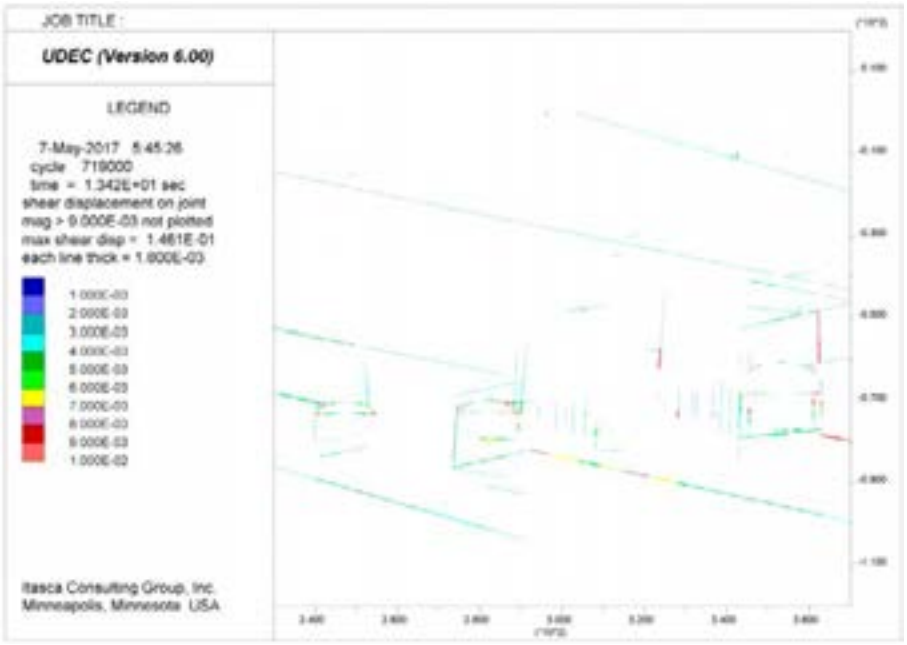


**Figure A159.** UDEC results after strength degradation, glacial unloading and permafrost melting at Year 66,000, showing shear displacements along fractures for SFR 1, DFN 1-1. Displacements are in units of metres.

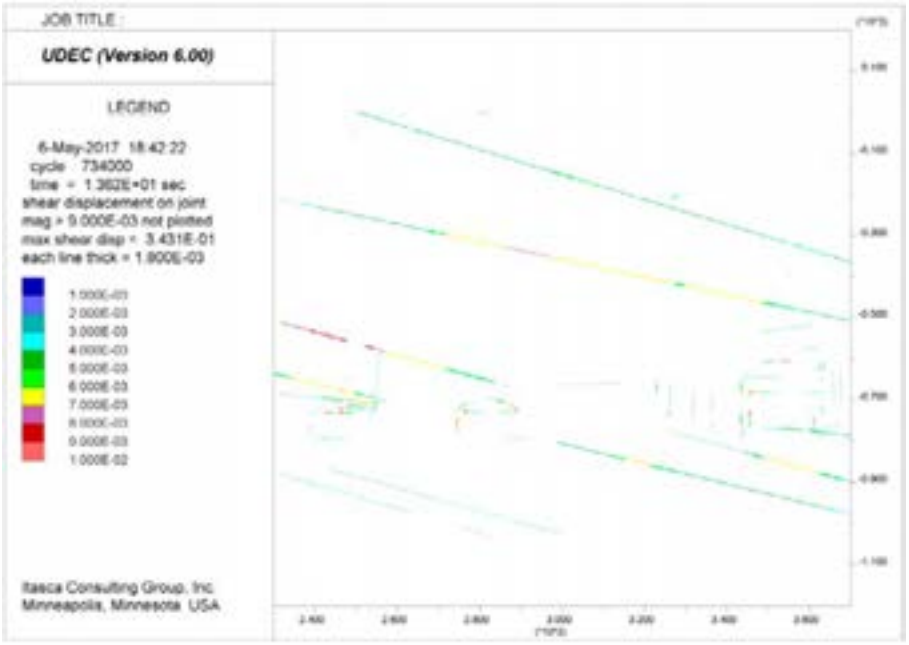


**Figure A160.** UDEC results after strength degradation, glacial unloading and permafrost melting at Year 66,000, showing shear displacements along fractures for SFR 1, DFN 1-2. Displacements are in units of metres.

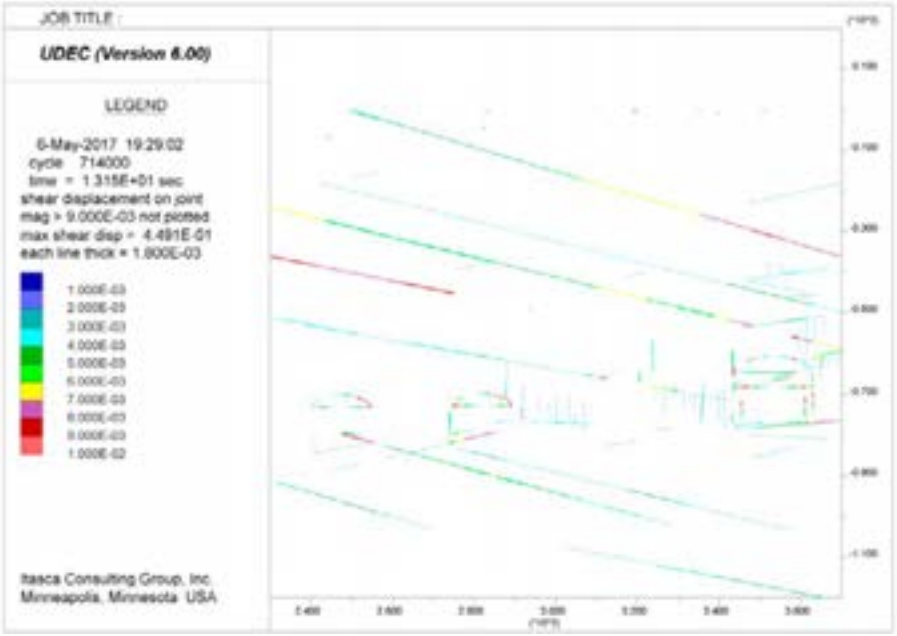


**Figure A161.** UDEC results after strength degradation, glacial unloading and permafrost melting at Year 66,000, showing shear displacements along fractures for SFR 1, DFN 1-3. Displacements are in units of metres.

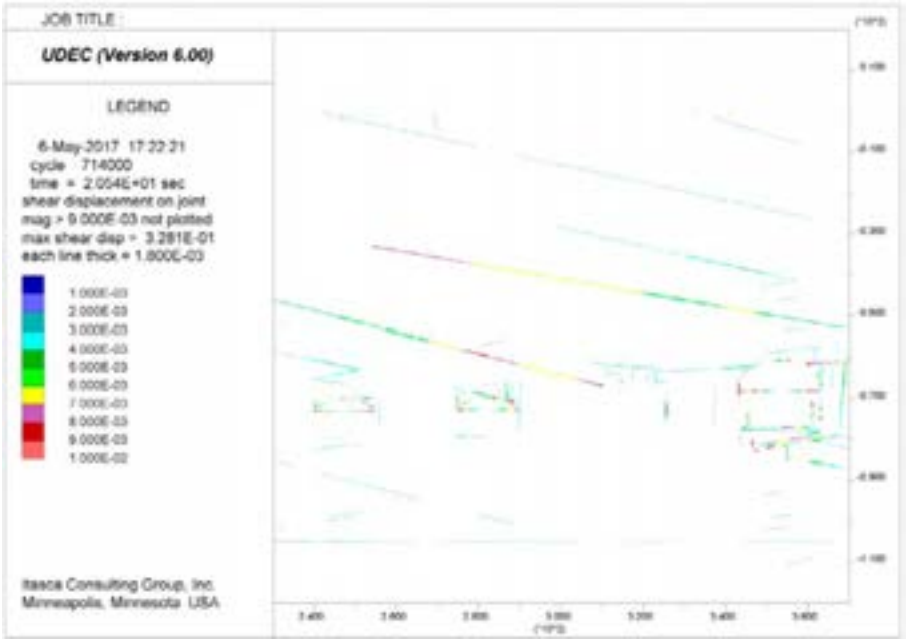


**Figure A162.** UDEC results after strength degradation, glacial unloading and permafrost melting at Year 66,000, showing shear displacements along fractures for SFR 1, DFN 1-4. Displacements are in units of metres.

## SFR 1 – Year 66,000 Glacial Unloading (Vertical Displacements)

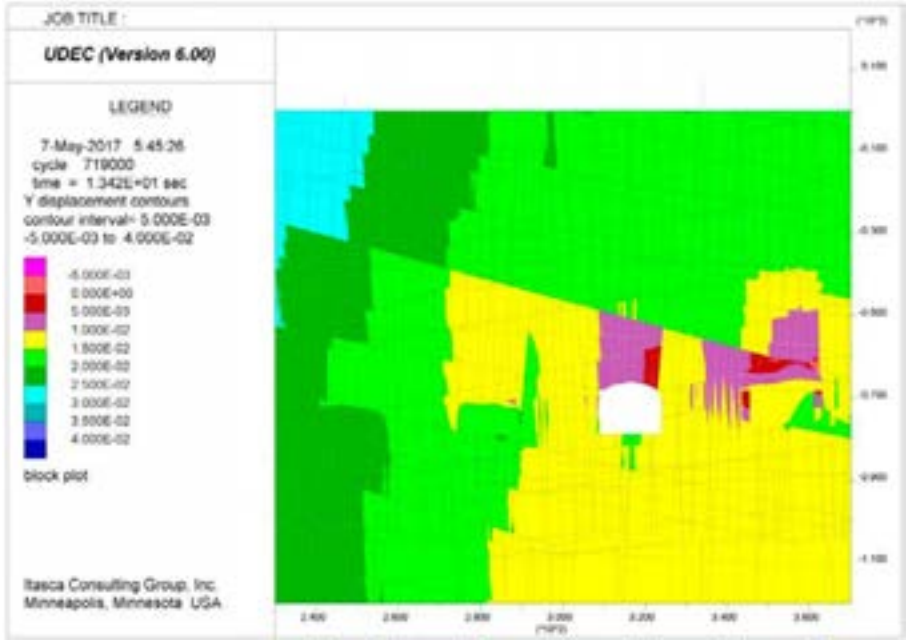

**Figure A163.** UDEC results after strength degradation, glacial unloading and permafrost melting at Year 66,000, showing vertical displacements for SFR 1, DFN 1-1. Displacements are in units of metres, with positive up.

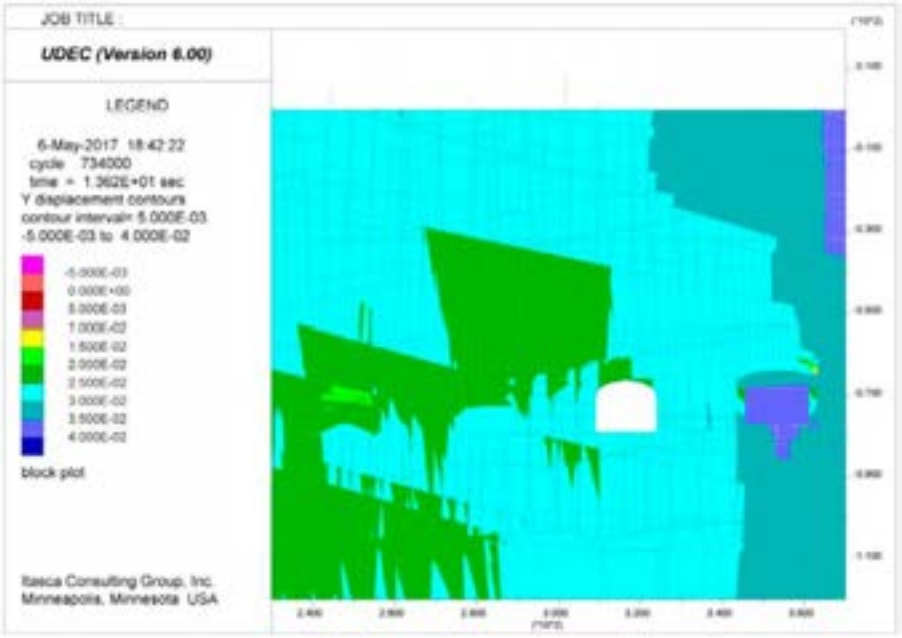


**Figure A164.** UDEC results after strength degradation, glacial unloading and permafrost melting at Year 66,000, showing vertical displacements for SFR 1, DFN 1-2. Displacements are in units of metres, with positive up.

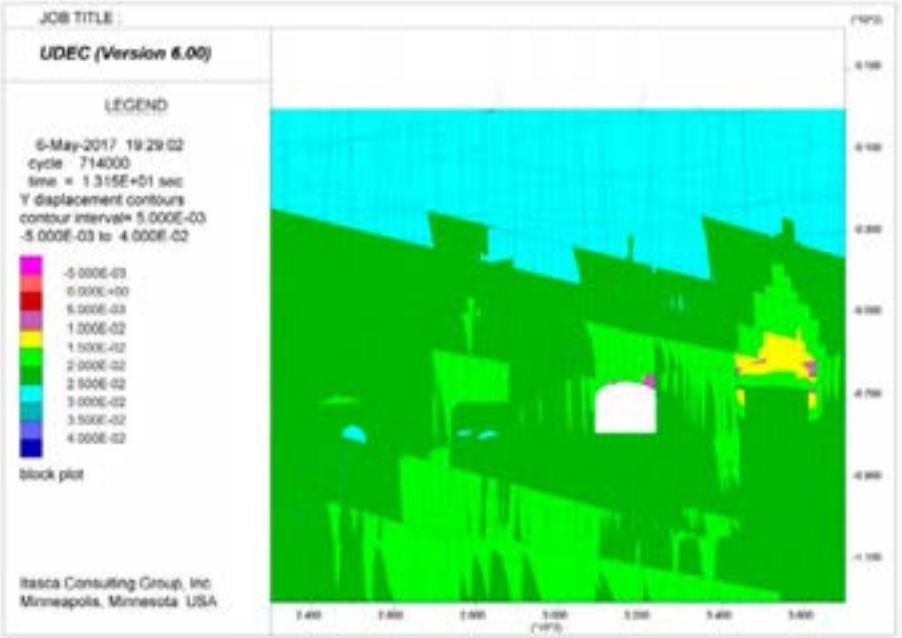


**Figure A165.** UDEC results after strength degradation, glacial unloading and permafrost melting at Year 66,000, showing vertical displacements for SFR 1, DFN 1-3. Displacements are in units of metres, with positive up.

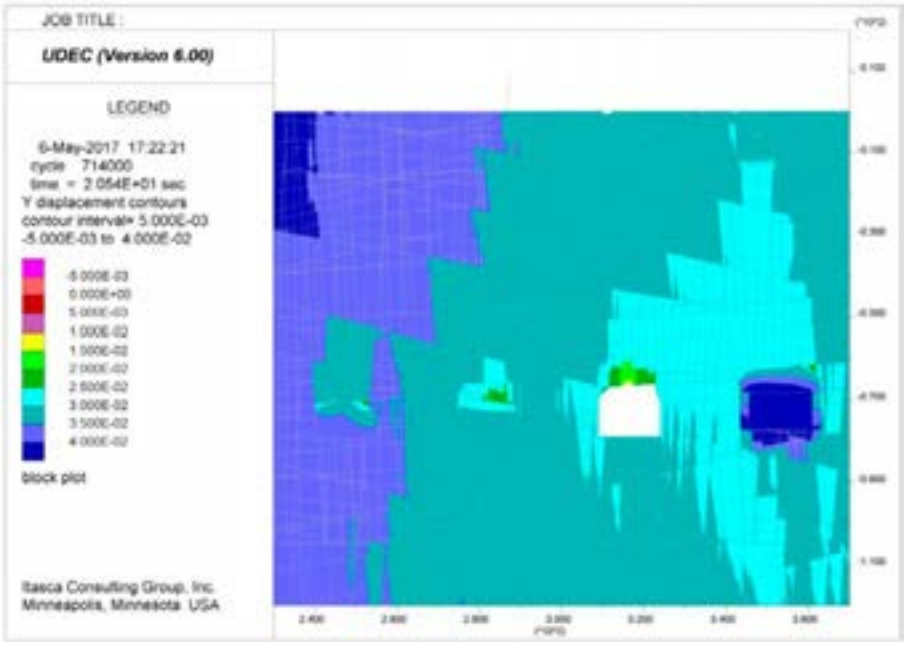


**Figure A166.** UDEC results after strength degradation, glacial unloading and permafrost melting at Year 66,000, showing vertical displacements for SFR 1, DFN 1-4. Displacements are in units of metres, with positive up.

## SFR 1 – Year 66,000 Glacial Unloading (Horizontal Displacements)

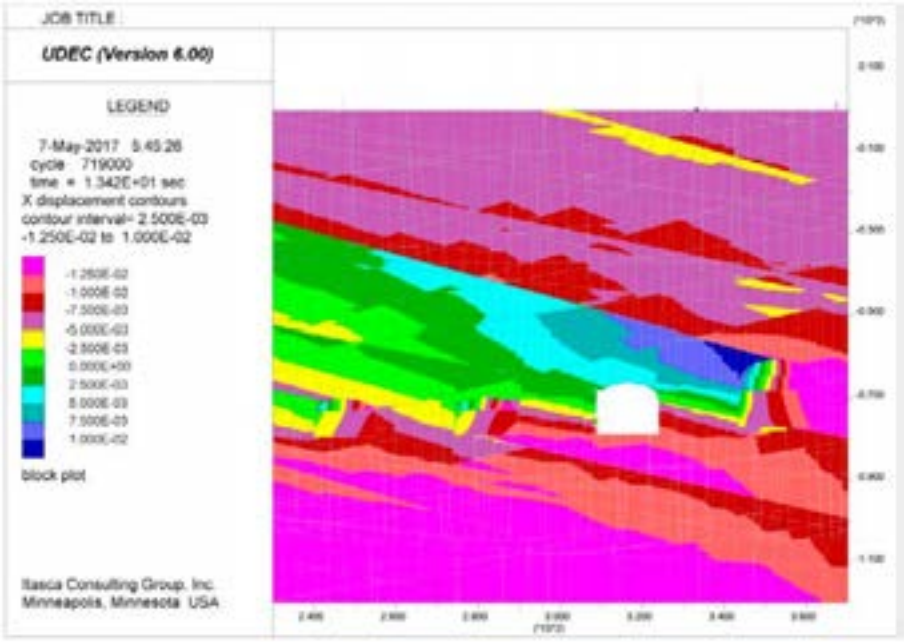

**Figure A167.** UDEC results after strength degradation, glacial unloading and permafrost melting at Year 66,000, showing horizontal displacements for SFR 1, DFN 1-1. Displacements are in units of metres, with positive to the right.

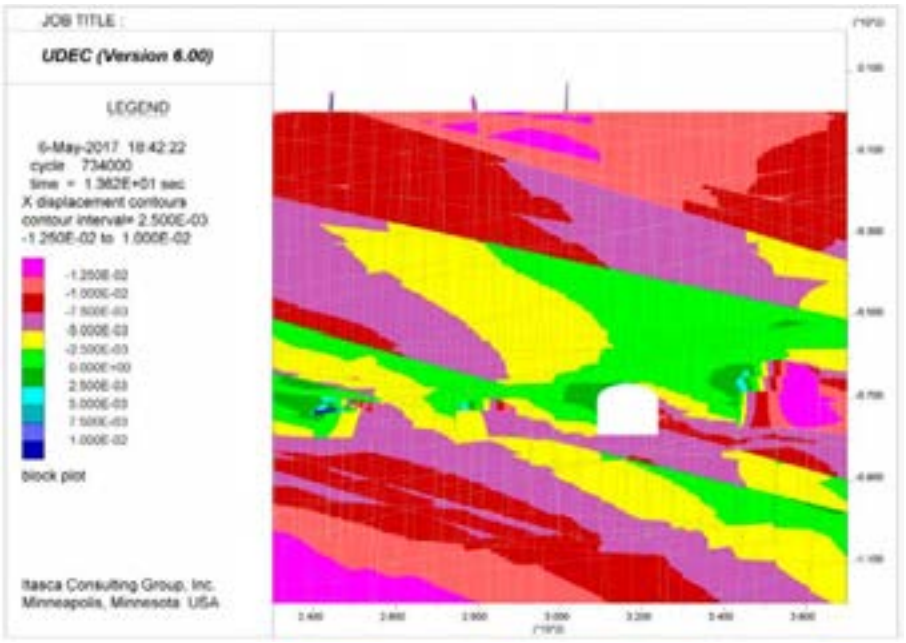


**Figure A168.** UDEC results after strength degradation, glacial unloading and permafrost melting at Year 66,000, showing horizontal displacements for SFR 1, DFN 1-2. Displacements are in units of metres, with positive to the right.

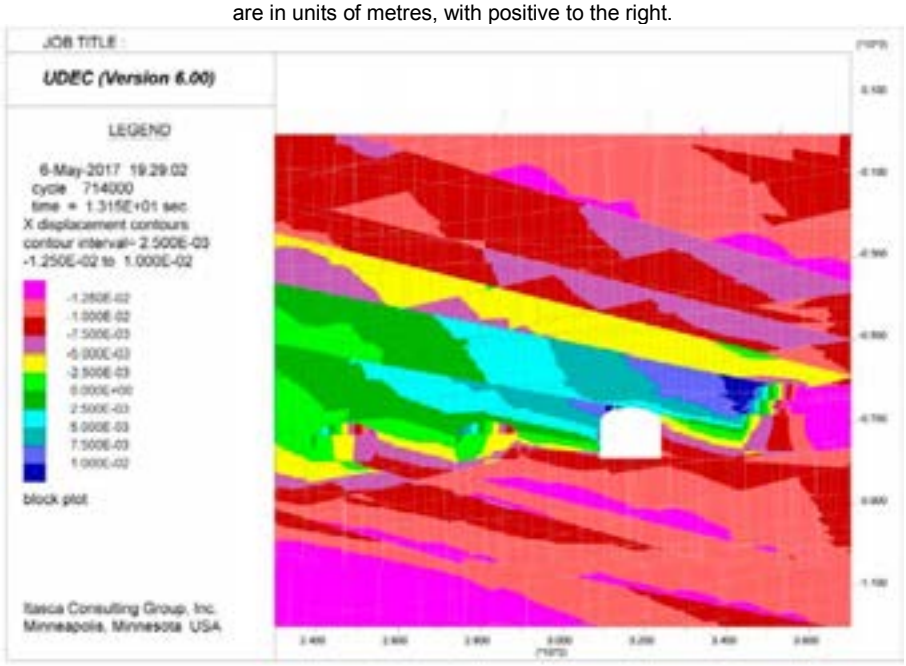


**Figure A169.** UDEC results after strength degradation, glacial unloading and permafrost melting at Year 66,000, showing horizontal displacements for SFR 1, DFN 1-3. Displacements are in units of metres, with positive to the right.

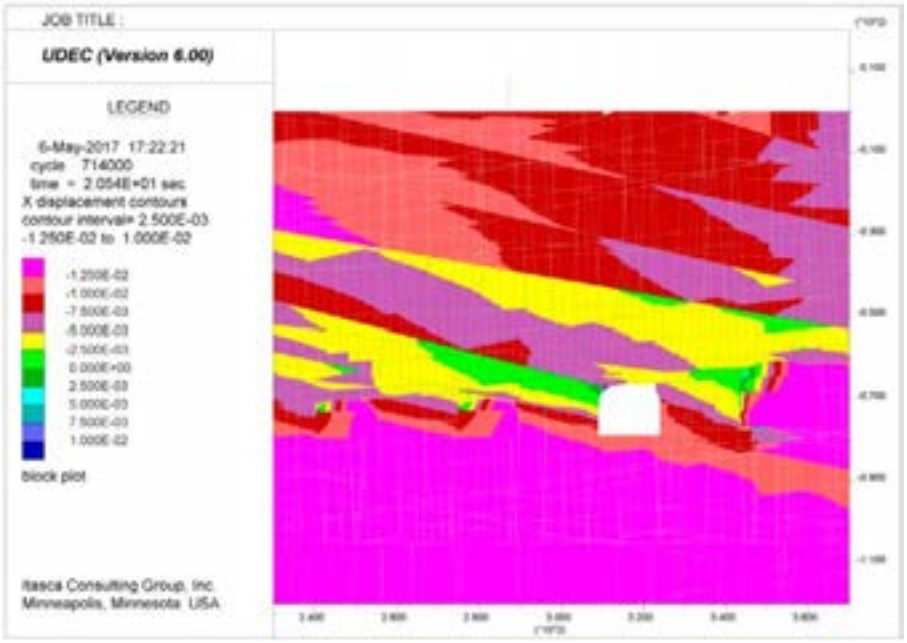


**Figure A170.** UDEC results after strength degradation, glacial unloading and permafrost melting at Year 66,000, showing horizontal displacements for SFR 1, DFN 1-4. Displacements are in units of metres, with positive to the right.

APPENDIX 3

# UDEC results – SFR 3

For completeness, various outputs relevant to the UDEC modelling presented in this Report are provided here to supplement those provided in the main body of the report.

## SFR 3 – Model Initialization (Stresses)

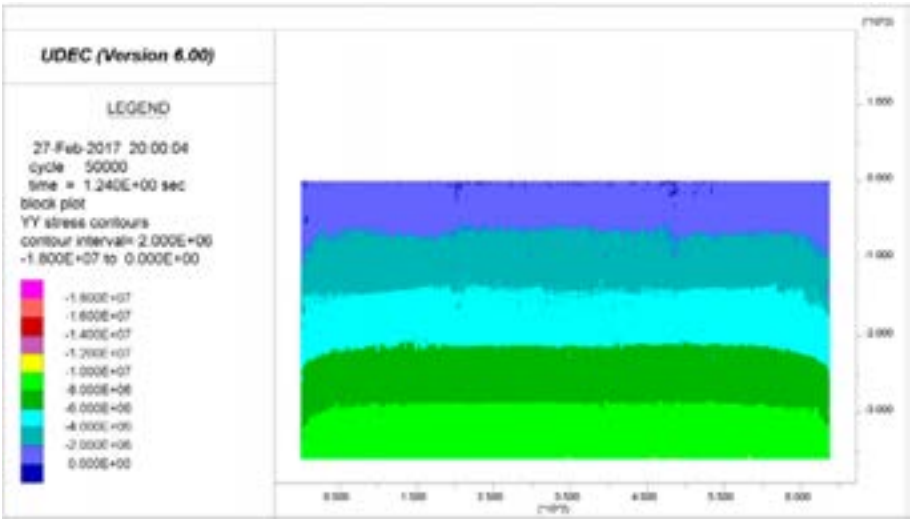


**Figure A171.** Initial vertical (YY) stress state for the SFR 3 UDEC models. Stress magnitudes are in units of Pascals, with compression negative.

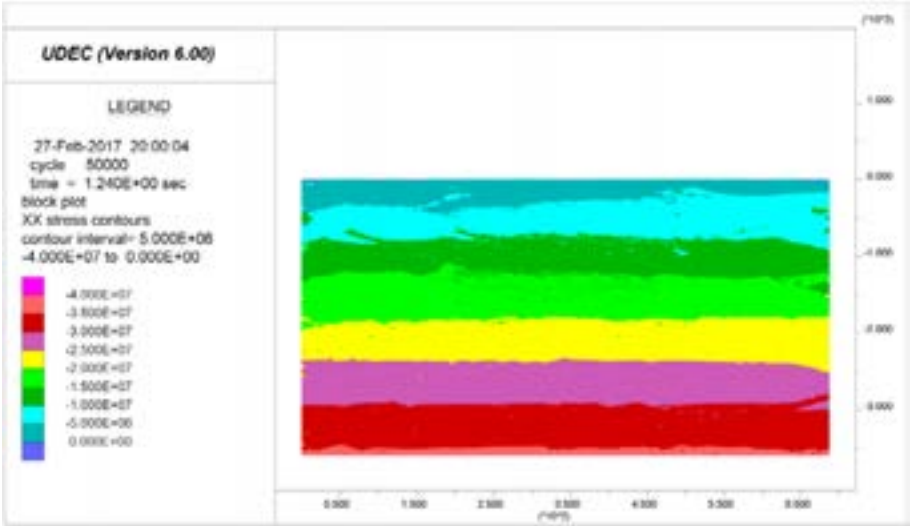


**Figure A172.** Initial horizontal (XX) stress state for the SFR 3 UDEC models. Stress magnitudes are in units of Pascals, with compression negative.

## SFR 3 – Construction and Backfilling (Vertical Stress)

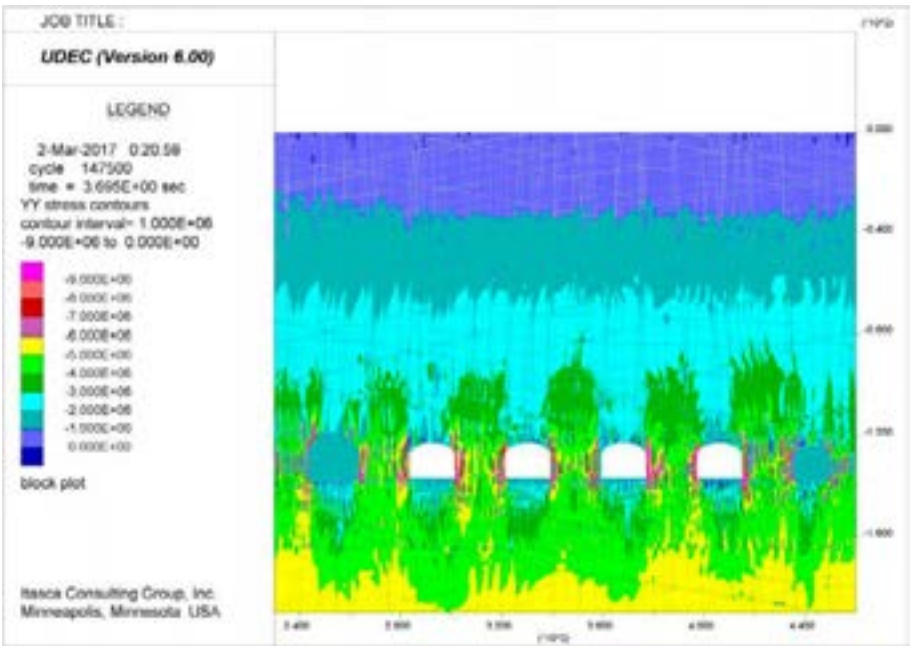


**Figure A173.** UDEC results after construction and backfilling stages, showing vertical stresses (SYY) for SFR 3, DFN 3-1. Stress magnitudes are in units of Pascals, with compression negative.

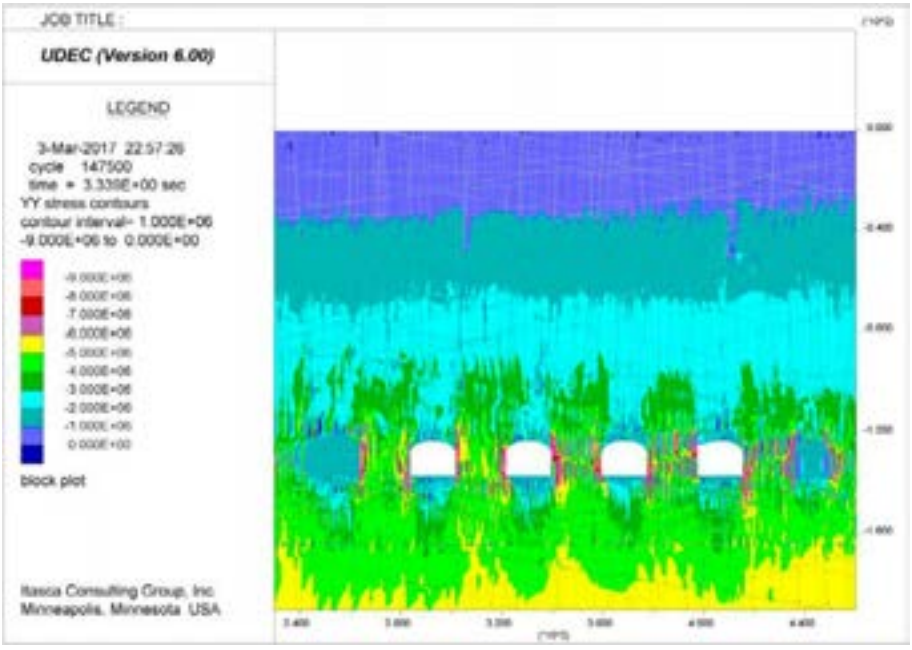


**Figure A174.** UDEC results after construction and backfilling stages, showing vertical stresses (SYY) for SFR 3, DFN 3-2. Stress magnitudes are in units of Pascals, with compression negative.

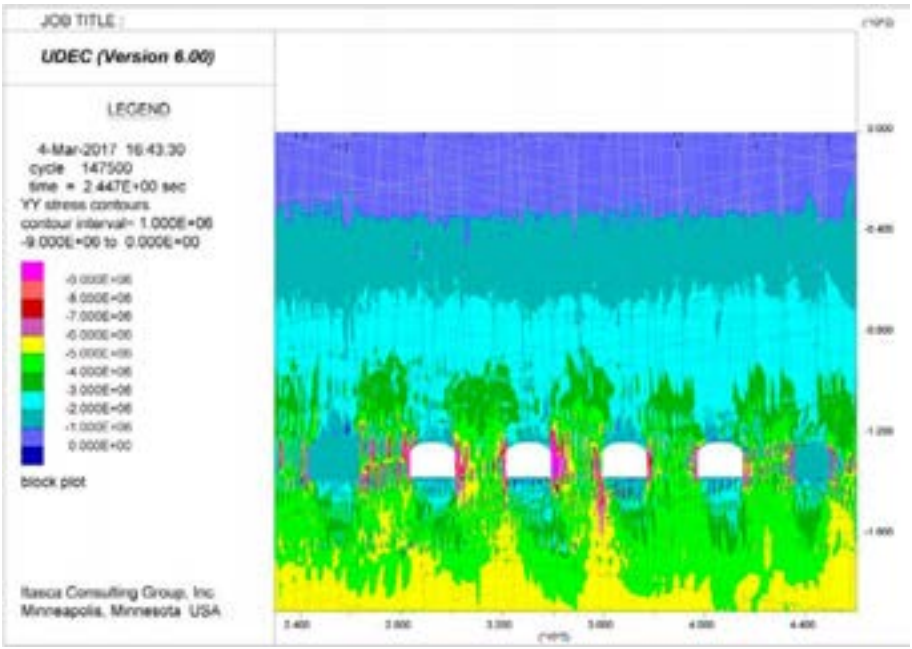


**Figure A175.** UDEC results after construction and backfilling stages, showing vertical stresses (SYY) for SFR 3, DFN 3-3. Stress magnitudes are in units of Pascals, with compression negative.

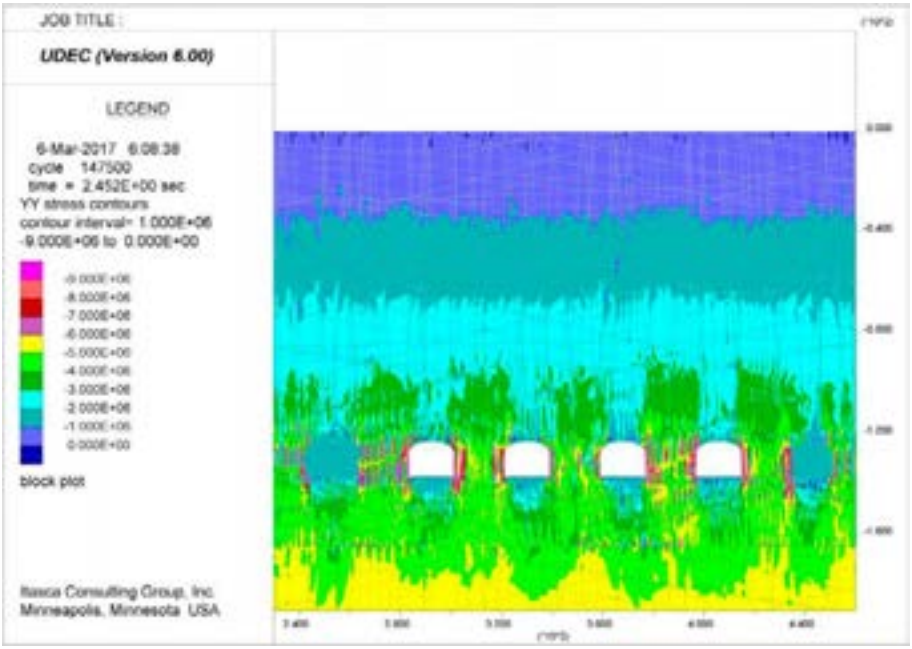


**Figure A176.** UDEC results after construction and backfilling stages, showing vertical stresses (SYY) for SFR 3, DFN 3-4. Stress magnitudes are in units of Pascals, with compression negative.

## SFR 3 – Construction and Backfilling (Horizontal Stress)

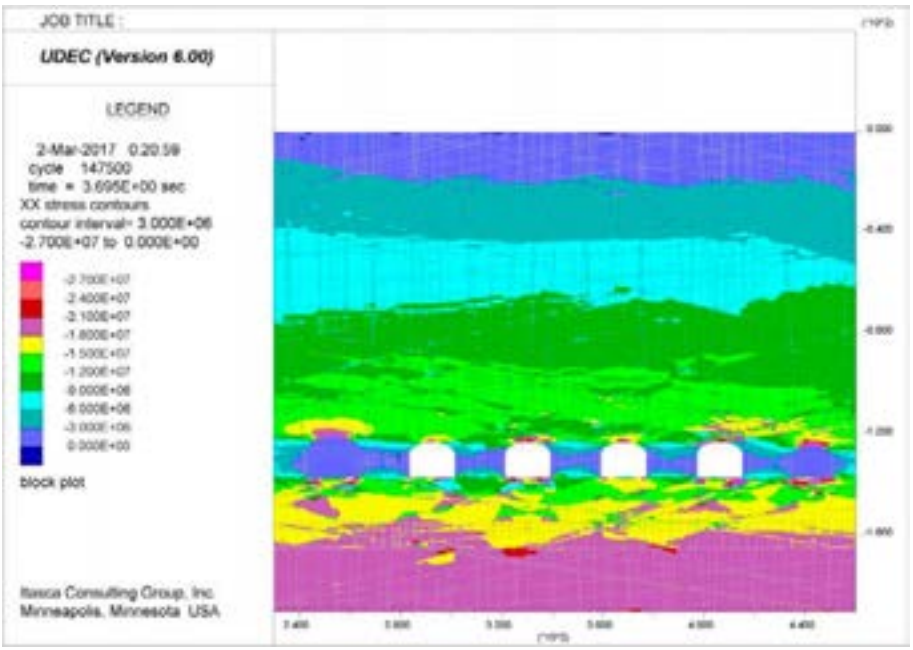


**Figure A177.** UDEC results after construction and backfilling stages, showing horizontal stresses (SXX) for SFR 3, DFN 3-1. Stress magnitudes are in units of Pascals, with compression negative.

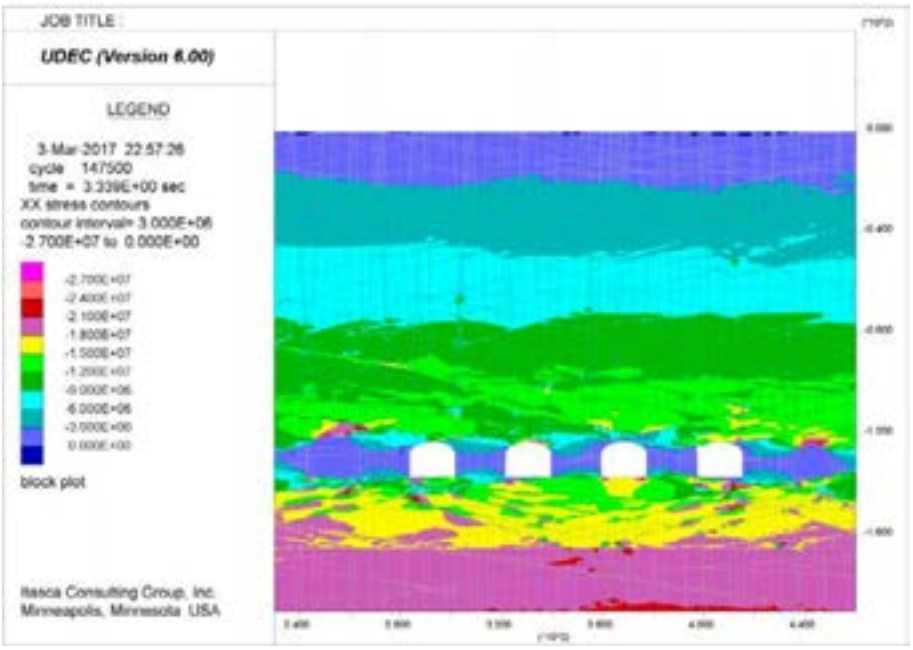


**Figure A178.** UDEC results after construction and backfilling stages, showing horizontal stresses (SXX) for SFR 3, DFN 3-2. Stress magnitudes are in units of Pascals, with compression negative.

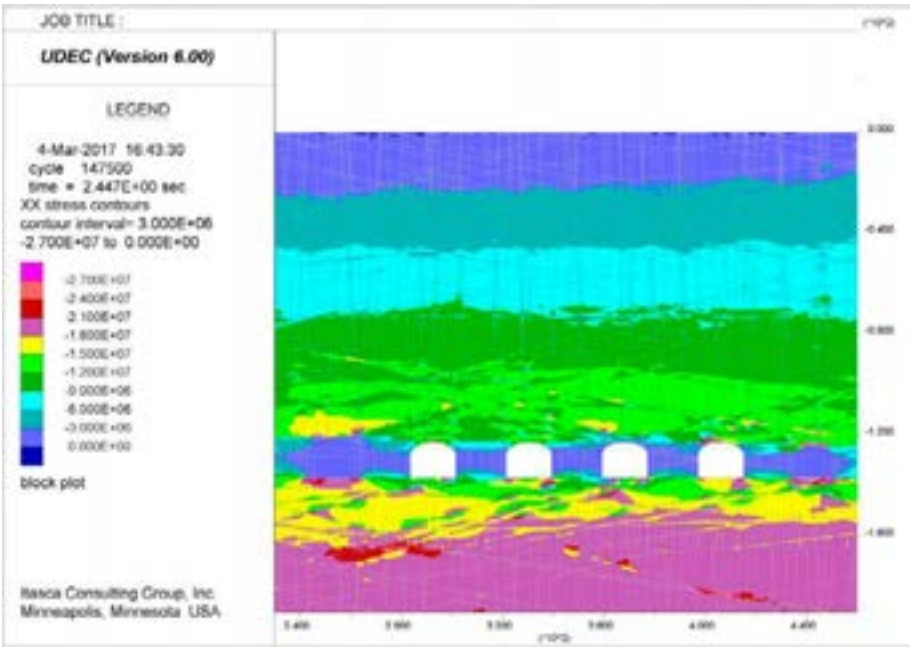


**Figure A179.** UDEC results after construction and backfilling stages, showing horizontal stresses (SXX) for SFR 3, DFN 3-3. Stress magnitudes are in units of Pascals, with compression negative.

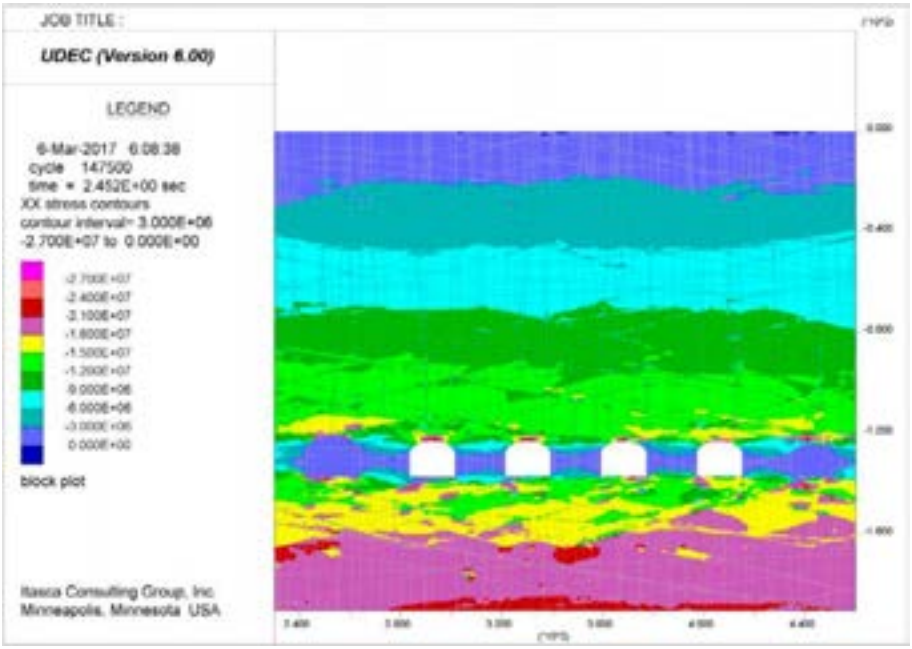


**Figure A180.** UDEC results after construction and backfilling stages, showing horizontal stresses (SXX) for SFR 3, DFN 3-4. Stress magnitudes are in units of Pascals, with compression negative.

## SFR 3 – Construction and Backfilling (Plasticity Indicators)

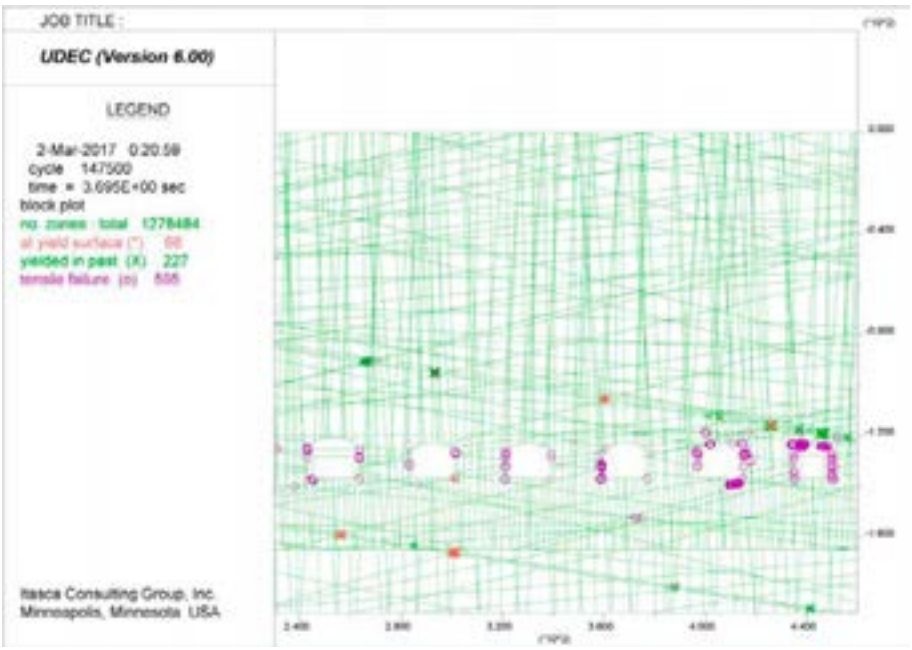


**Figure A181.** UDEC results after construction and backfilling stages, showing yielded elements for SFR 3, DFN 3-1.

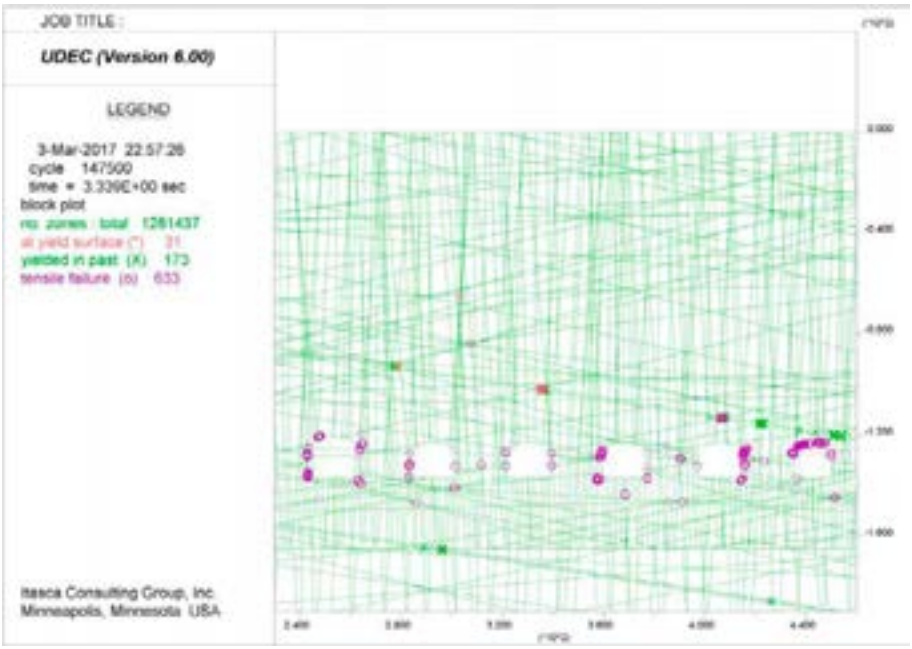


**Figure A182.** UDEC results after construction and backfilling stages, showing yielded elements for SFR 3, DFN 3-2.

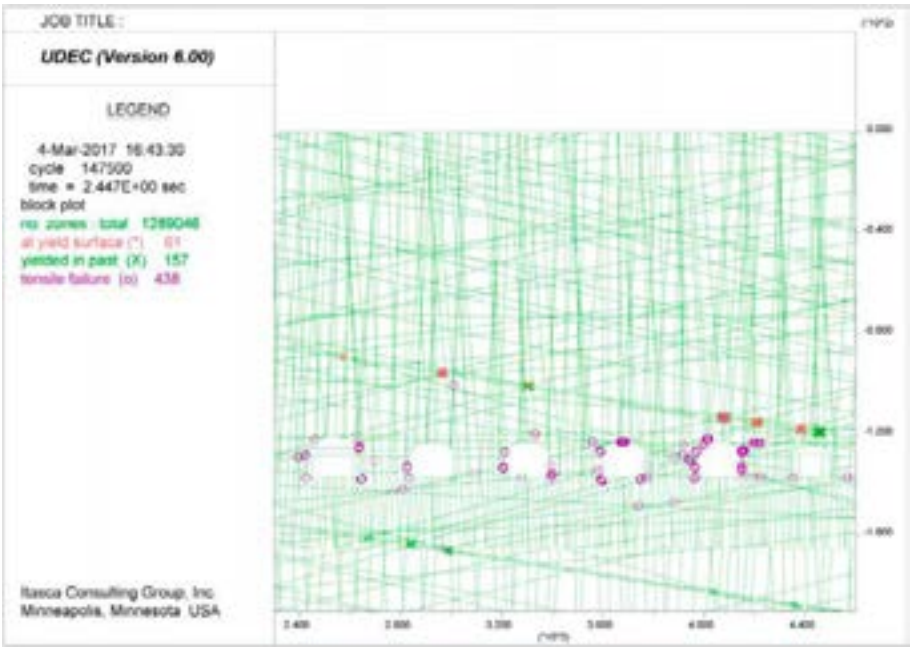


**Figure A183.** UDEC results after construction and backfilling stages, showing yielded elements for SFR 3, DFN 3-3.

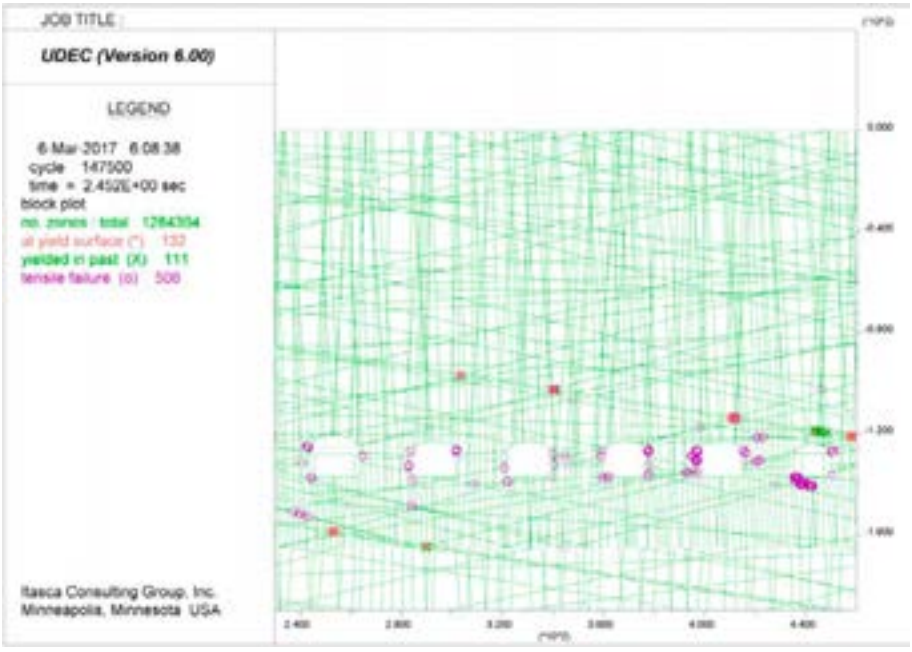


**Figure A184.** UDEC results after construction and backfilling stages, showing yielded elements for SFR 3, DFN 3-4.

## SFR 3 – Construction and Backfilling (Displacement Vectors)

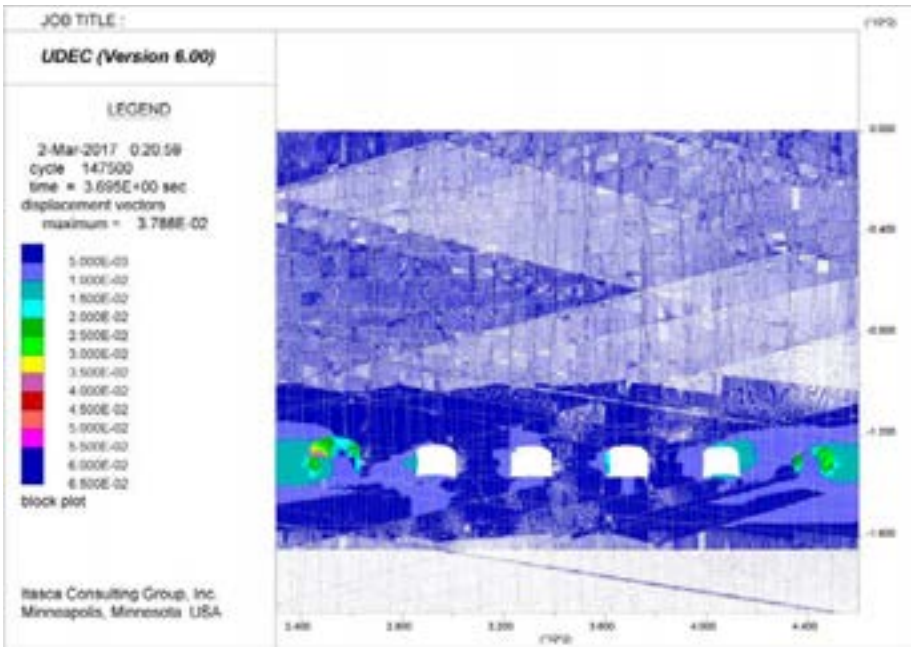


**Figure A185.** UDEC results after construction and backfilling stages, showing displacement vectors for SFR 3, DFN 3-1. Displacement magnitudes are in units of metres.

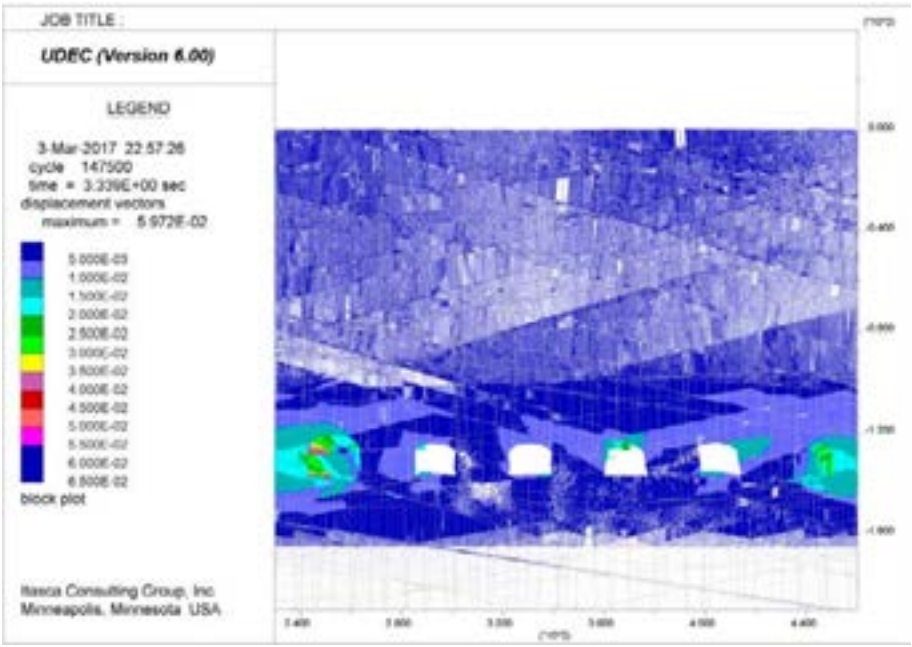


**Figure A186.** UDEC results after construction and backfilling stages, showing displacement vectors for SFR 3, DFN 3-2. Displacement magnitudes are in units of metres.

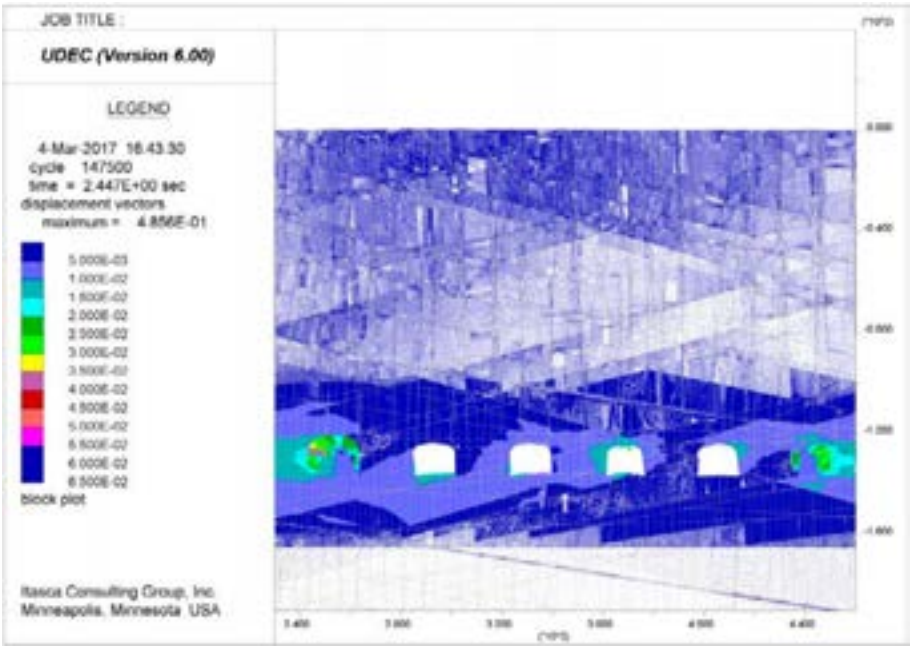


**Figure A187.** UDEC results after construction and backfilling stages, showing displacement vectors for SFR 3, DFN 3-3. Displacement magnitudes are in units of metres.

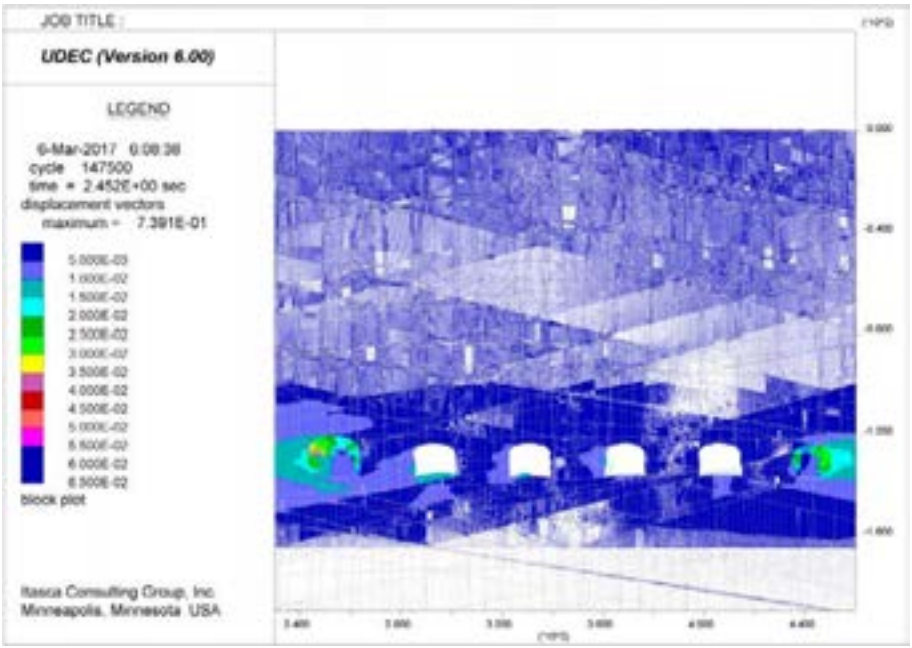


**Figure A188.** UDEC results after construction and backfilling stages, showing displacement vectors for SFR 3, DFN 3-4. Displacement magnitudes are in units of metres.

## SFR 3 – Construction and Backfilling (Fracture Shear Displacement)

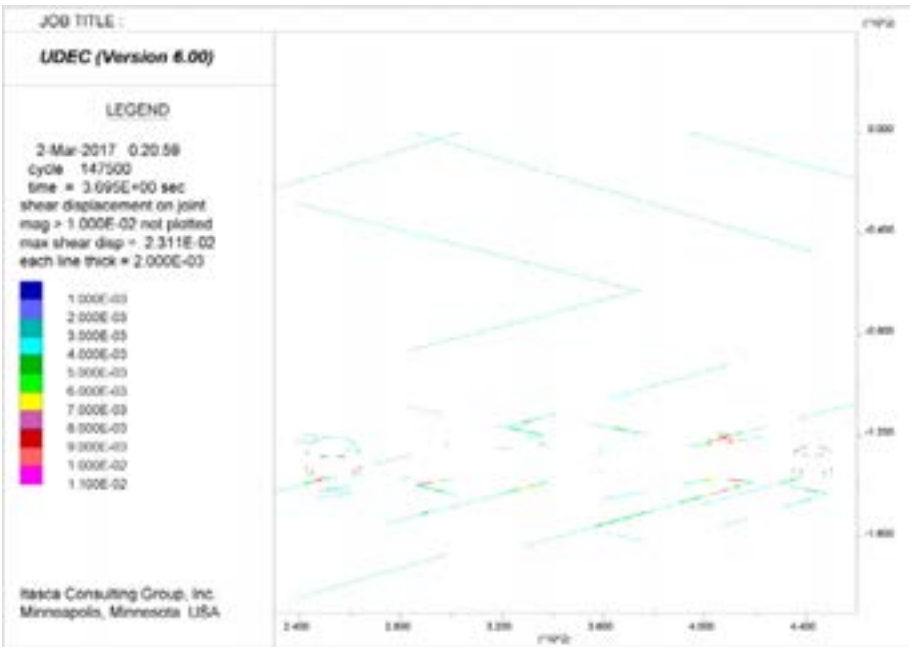


**Figure A189.** UDEC results after construction and backfilling stages, showing shear displacements along fractures for SFR 3, DFN 3-1. Displacements are in units of metres.

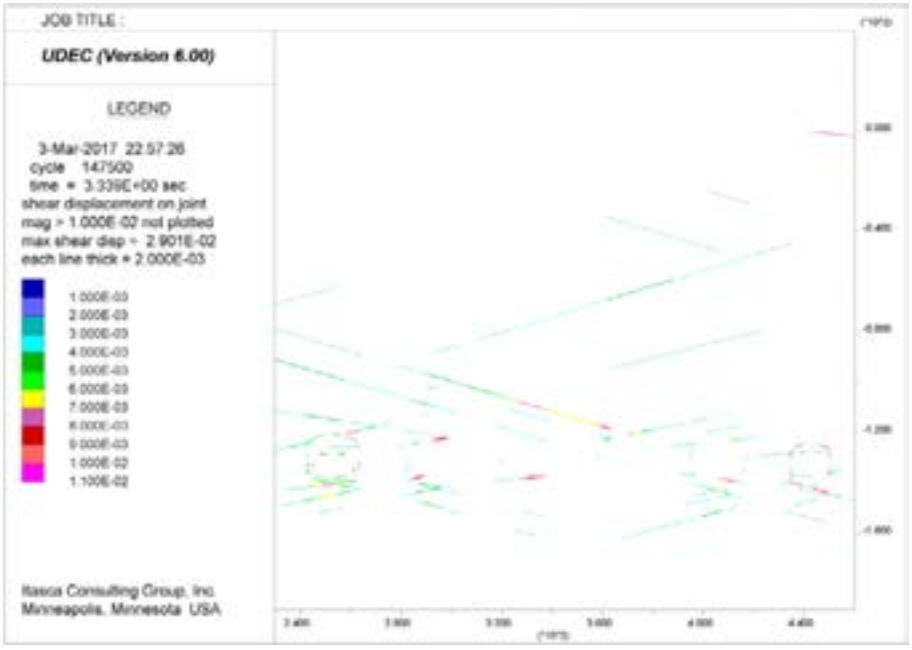


**Figure A190.** UDEC results after construction and backfilling stages, showing shear displacements along fractures for SFR 3, DFN 3-2. Displacements are in units of metres.

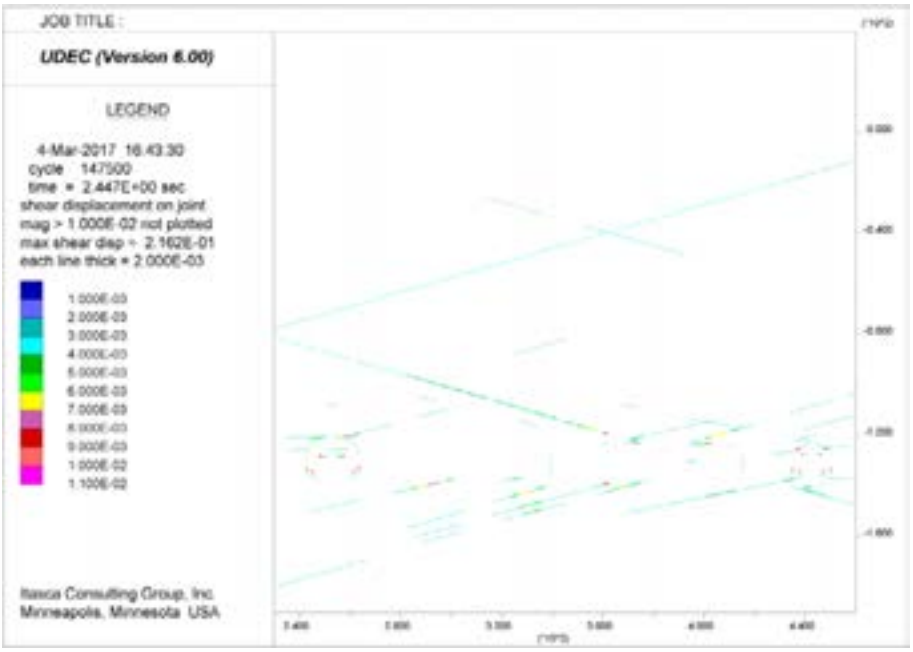


**Figure A191.** UDEC results after construction and backfilling stages, showing shear displacements along fractures for SFR 3, DFN 3-3. Displacements are in units of metres.

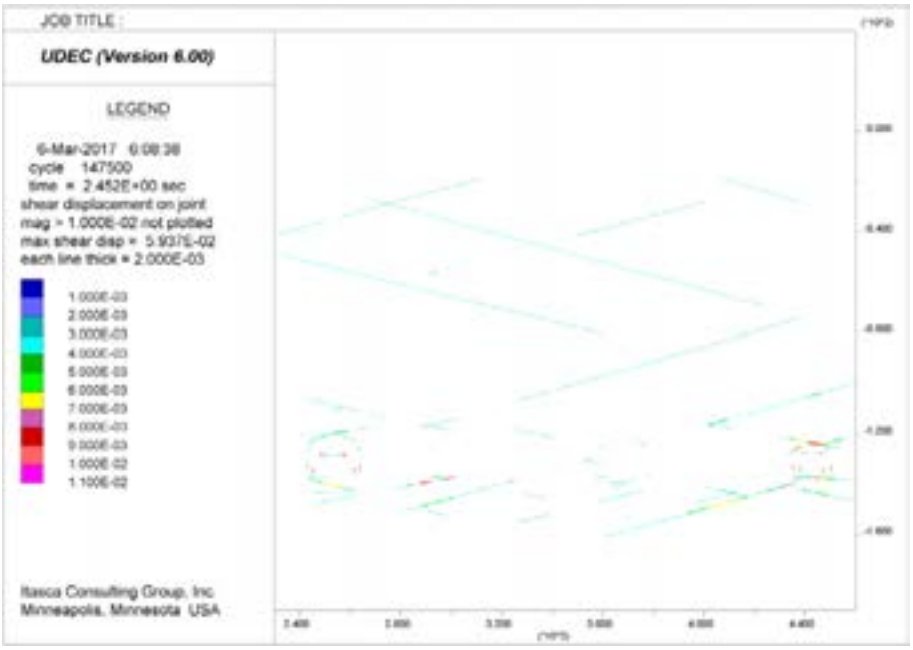


**Figure A192.** UDEC results after construction and backfilling stages, showing shear displacements along fractures for SFR 3, DFN 3-4. Displacements are in units of metres.

## SFR 3 – Construction and Backfilling (Vertical Displacements)

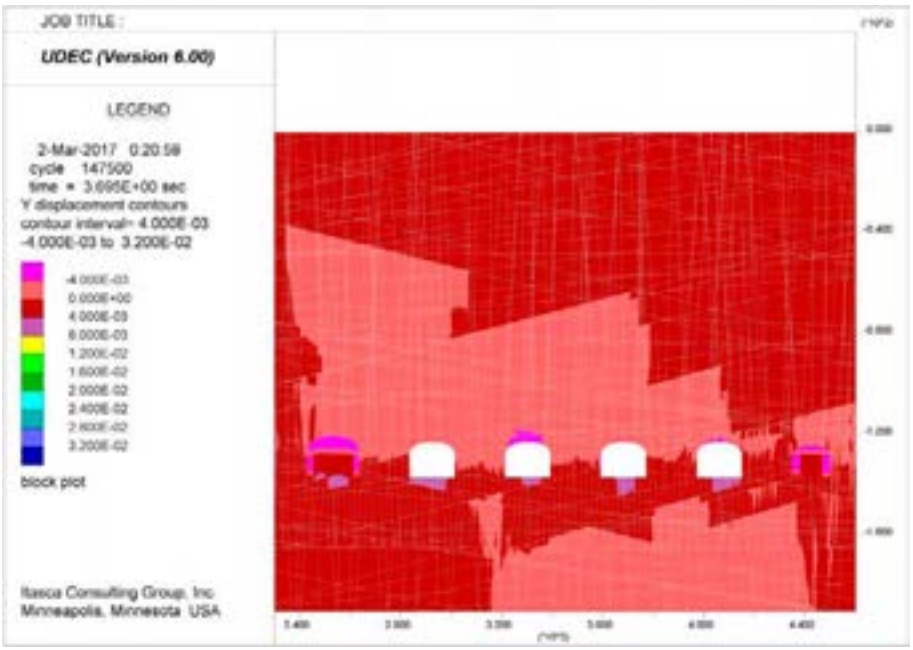


**Figure A193.** UDEC results after construction and backfilling stages, showing vertical displacements for SFR 3, DFN 3-1. Displacements are in units of metres, with positive up.

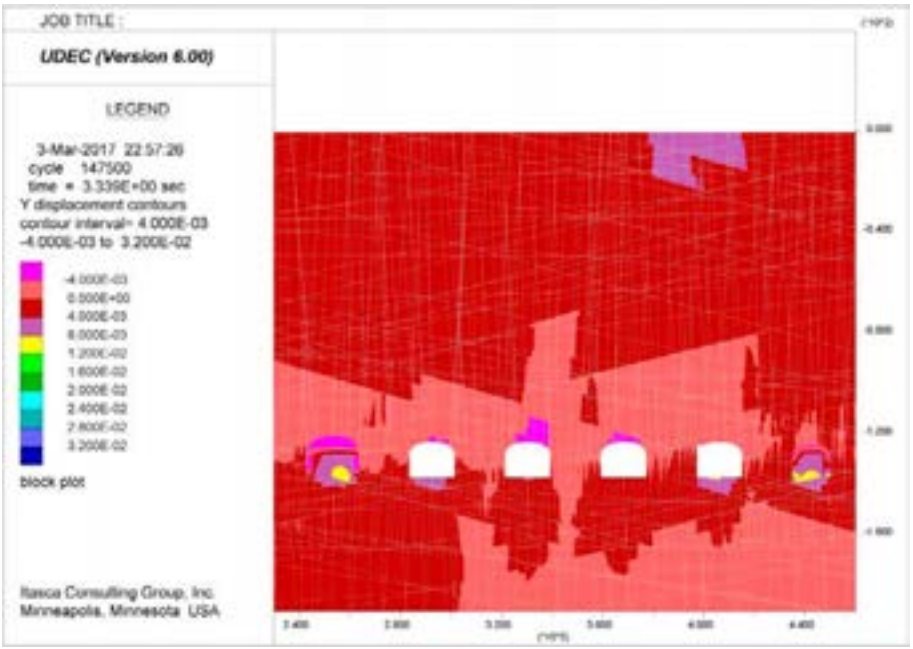


**Figure A194.** UDEC results after construction and backfilling stages, showing vertical displacements for SFR 3, DFN 3-2. Displacements are in units of metres, with positive up.

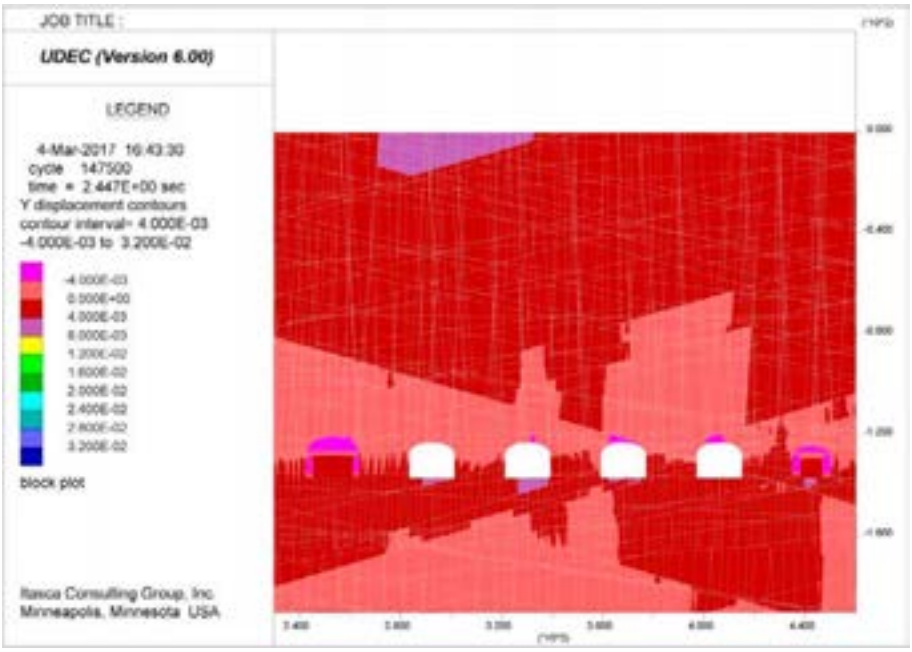


**Figure A195.** UDEC results after construction and backfilling stages, showing vertical displacements for SFR 3, DFN 3-3. Displacements are in units of metres, with positive up.

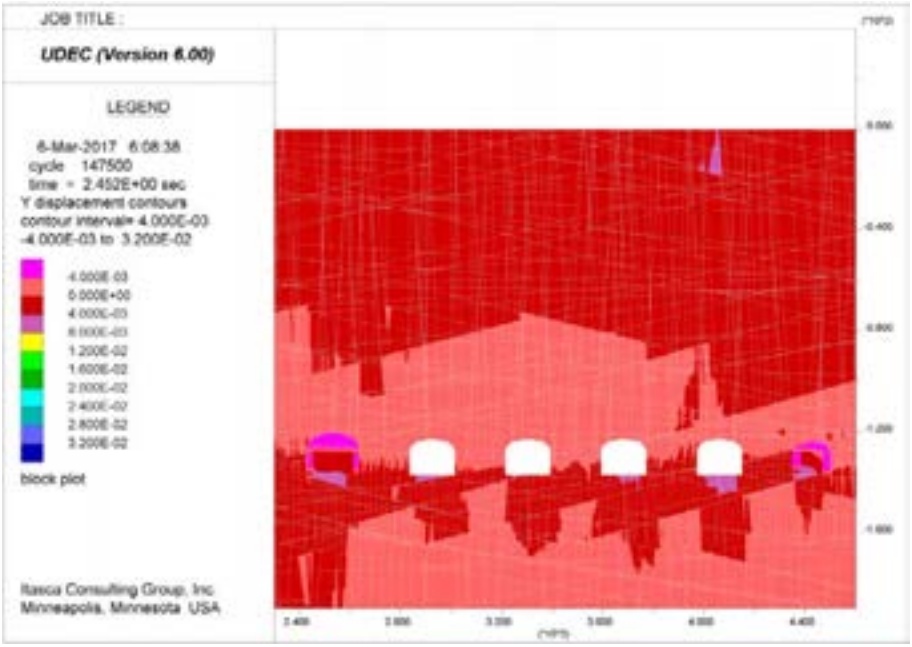


**Figure A196.** UDEC results after construction and backfilling stages, showing vertical displacements for SFR 3, DFN 3-4. Displacements are in units of metres, with positive up.

## SFR 3 – Construction and Backfilling (Horizontal Displacements)

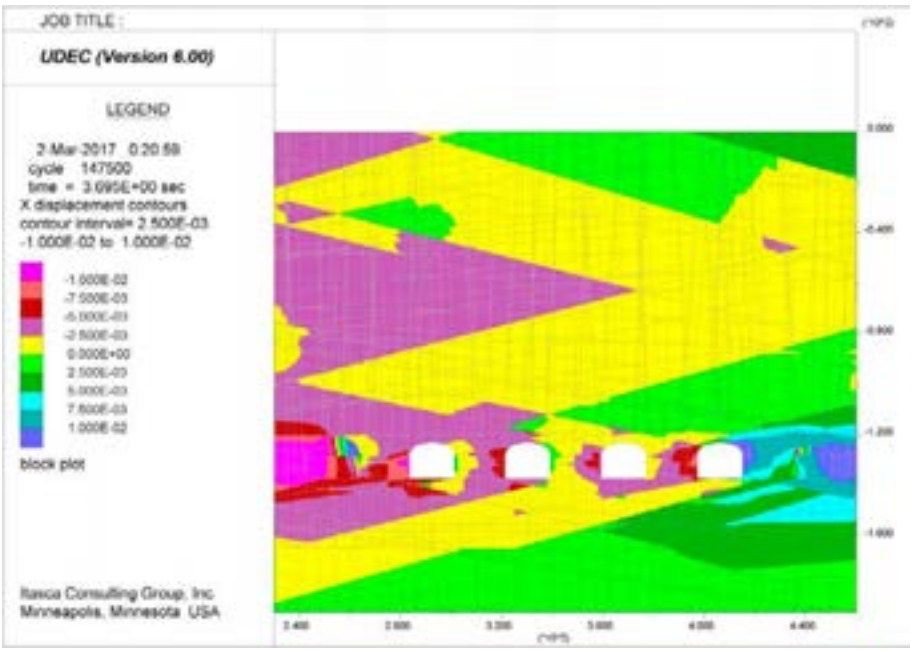


**Figure A197.** UDEC results after construction and backfilling stages, showing horizontal displacements for SFR 3, DFN 3-1. Displacements are in units of metres, with positive to the right.

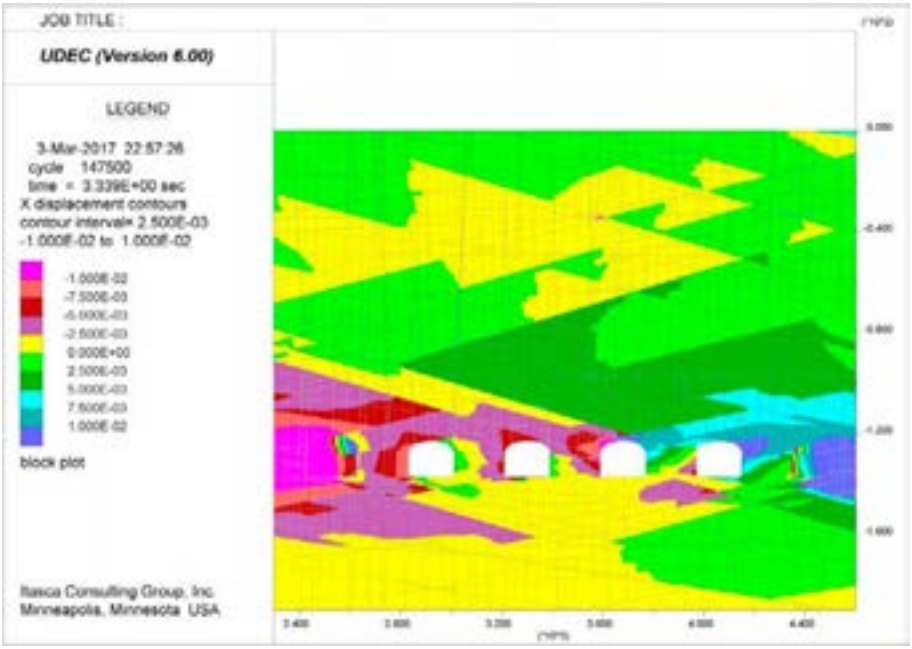


**Figure A198.** UDEC results after construction and backfilling stages, showing horizontal displacements for SFR 3, DFN 3-2. Displacements are in units of metres, with positive to the right.

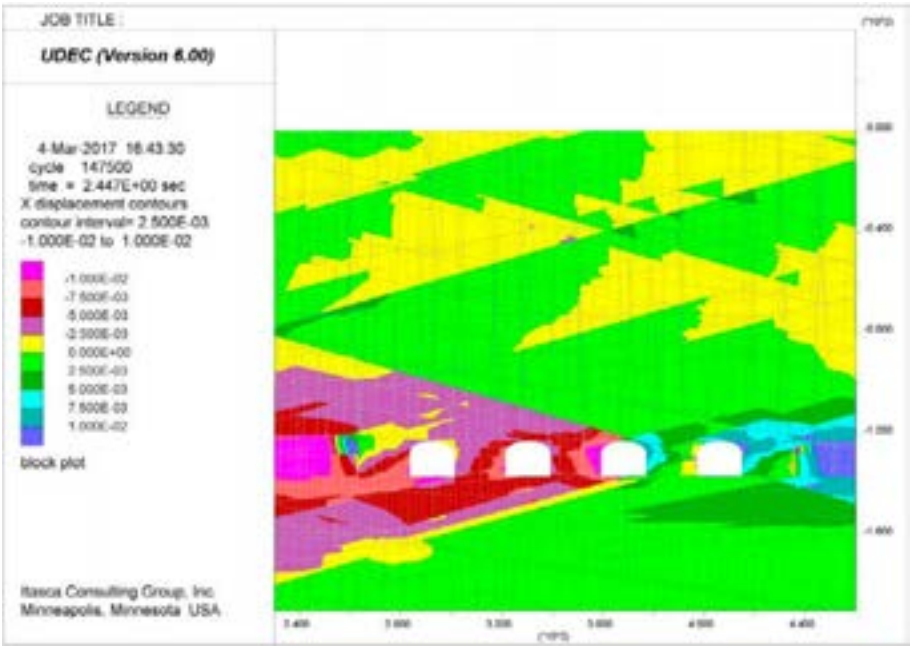


**Figure A199.** UDEC results after construction and backfilling stages, showing horizontal displacements for SFR 3, DFN 3-3. Displacements are in units of metres, with positive to the right.

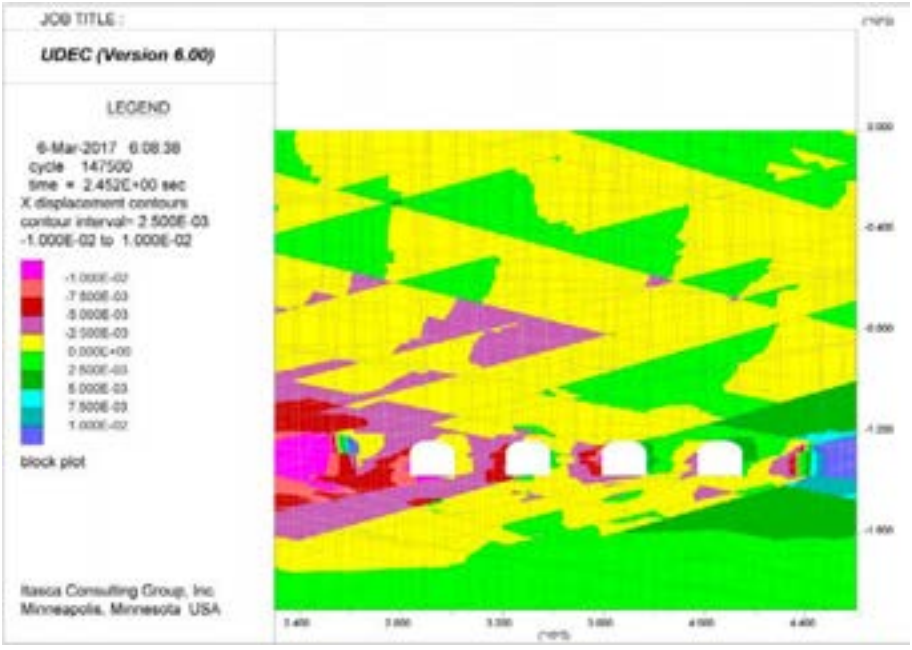


**Figure A200.** UDEC results after construction and backfilling stages, showing horizontal displacements for SFR 3, DFN 3-4. Displacements are in units of metres, with positive to the right.

## SFR 3 – Year 1000 Strength Degradation (Vertical Stress)

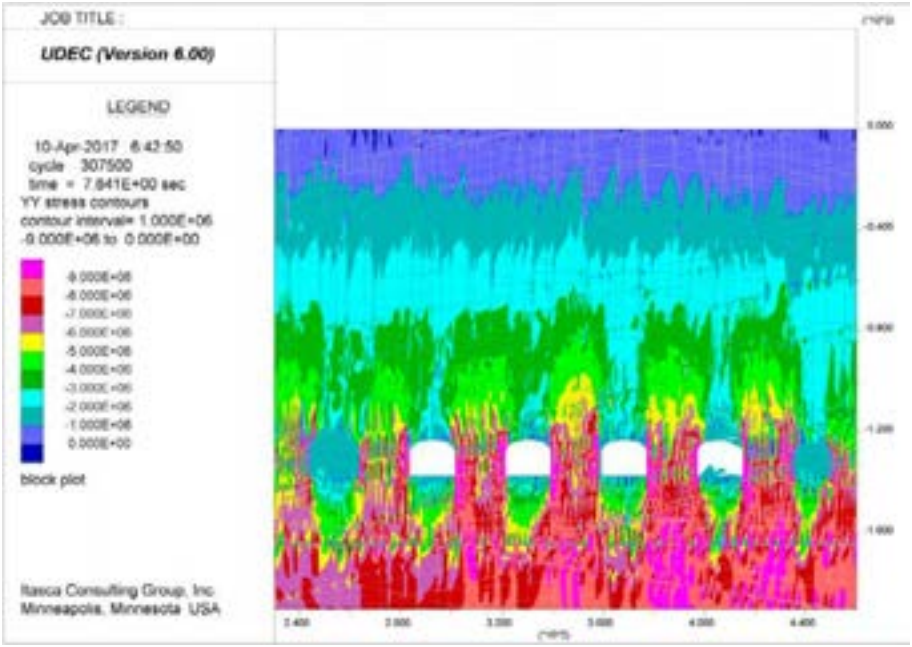


**Figure A201.** UDEC results after strength degradation up to Year 1000, showing vertical stresses (SYY) for SFR 3, DFN 3-1. Stress magnitudes are in units of Pascals, with compression negative.

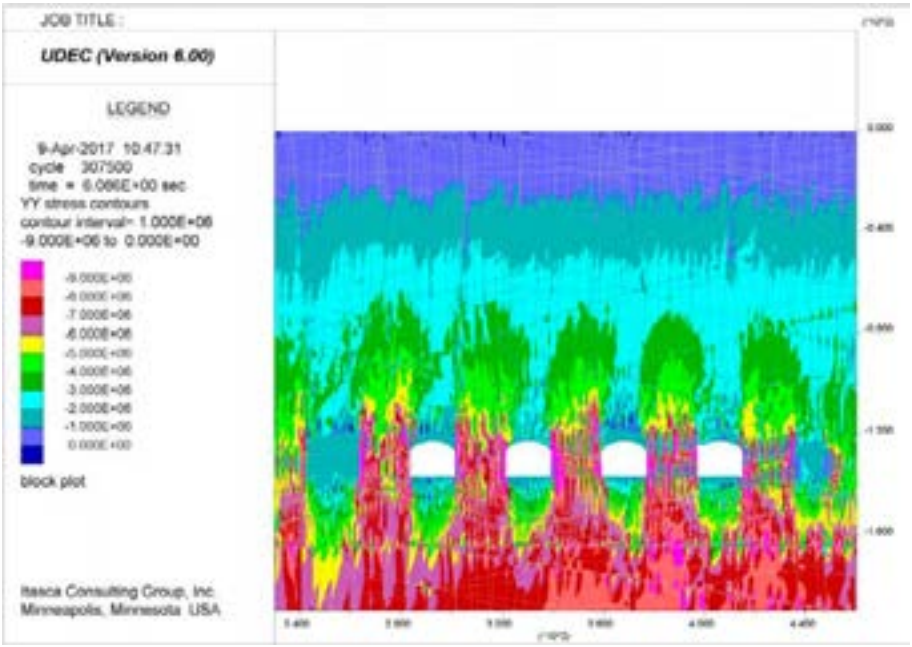


**Figure A202.** UDEC results after strength degradation up to Year 1000, showing vertical stresses (SYY) for SFR 3, DFN 3-2. Stress magnitudes are in units of Pascals, with compression negative.

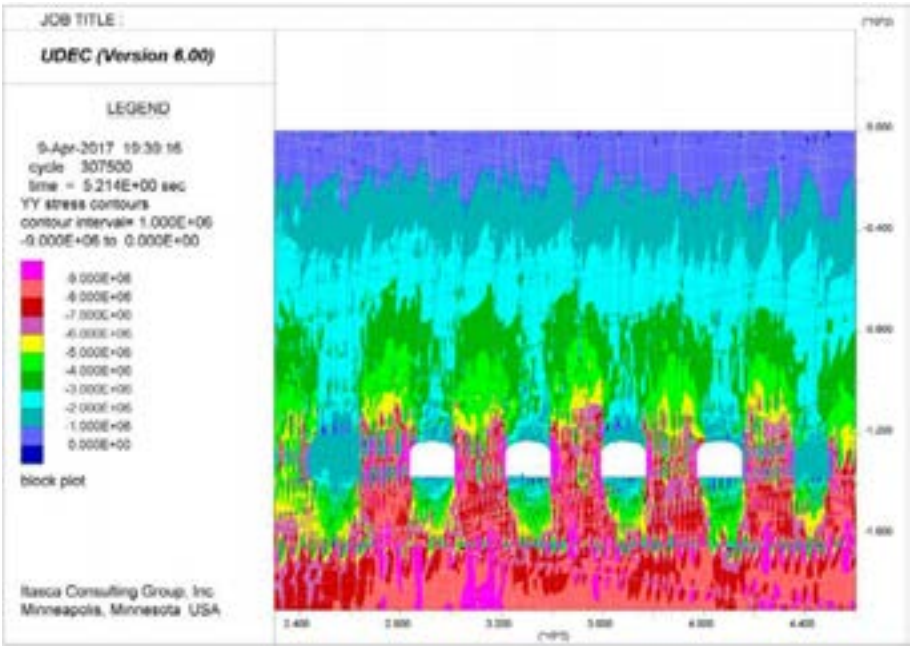


**Figure A203.** UDEC results after strength degradation up to Year 1000, showing vertical stresses (SYY) for SFR 3, DFN 3-3. Stress magnitudes are in units of Pascals, with compression negative.

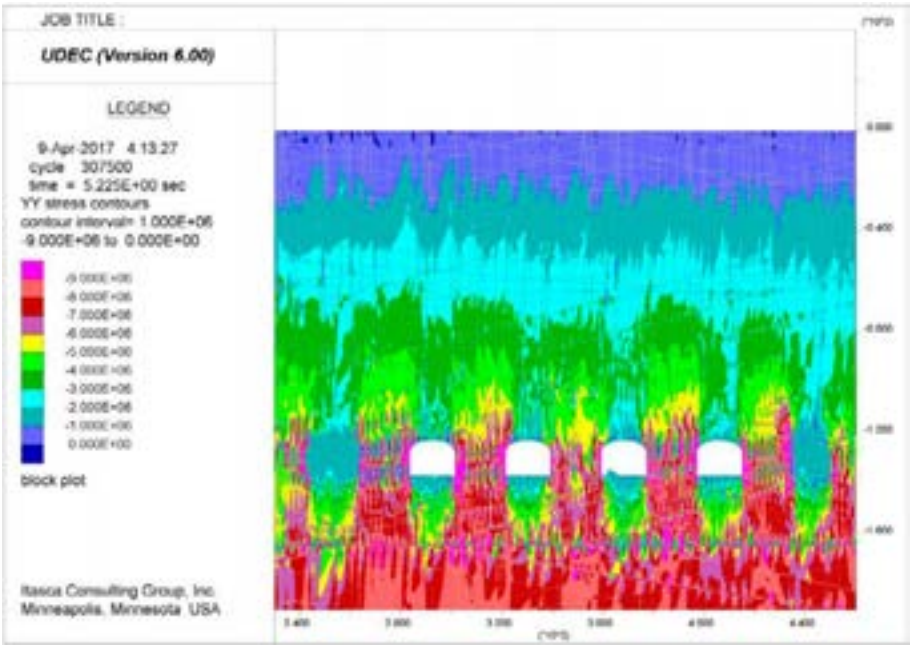


**Figure A204.** UDEC results after strength degradation up to Year 1000, showing vertical stresses (SYY) for SFR 3, DFN 3-4. Stress magnitudes are in units of Pascals, with compression negative.

## SFR 3 – Year 1000 Strength Degradation (Horizontal Stress)

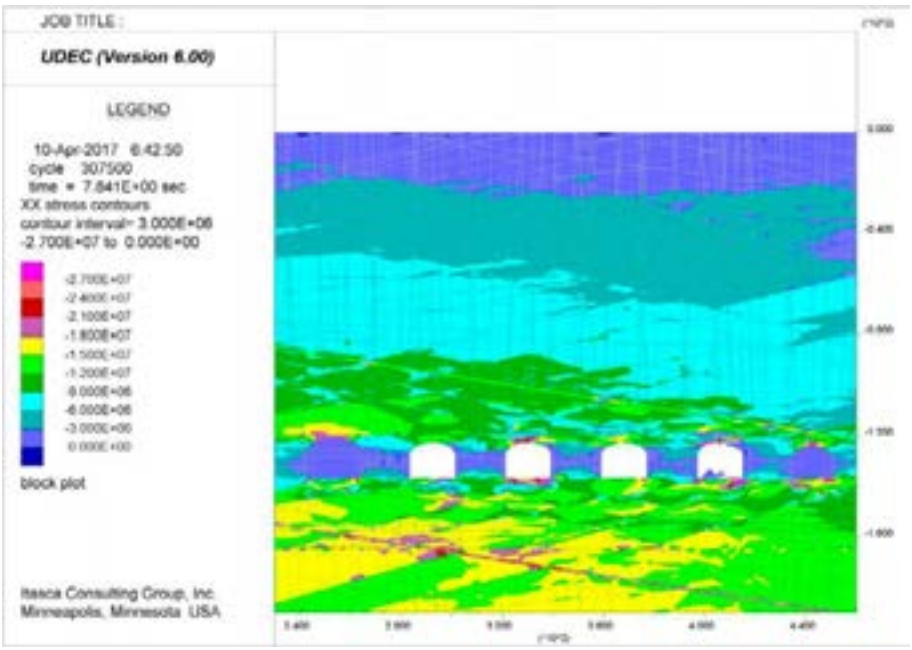


**Figure A205.** UDEC results after strength degradation up to Year 1000, showing horizontal stresses (SXX) for SFR 3, DFN 3-1. Stress magnitudes are in units of Pascals, with compression negative.

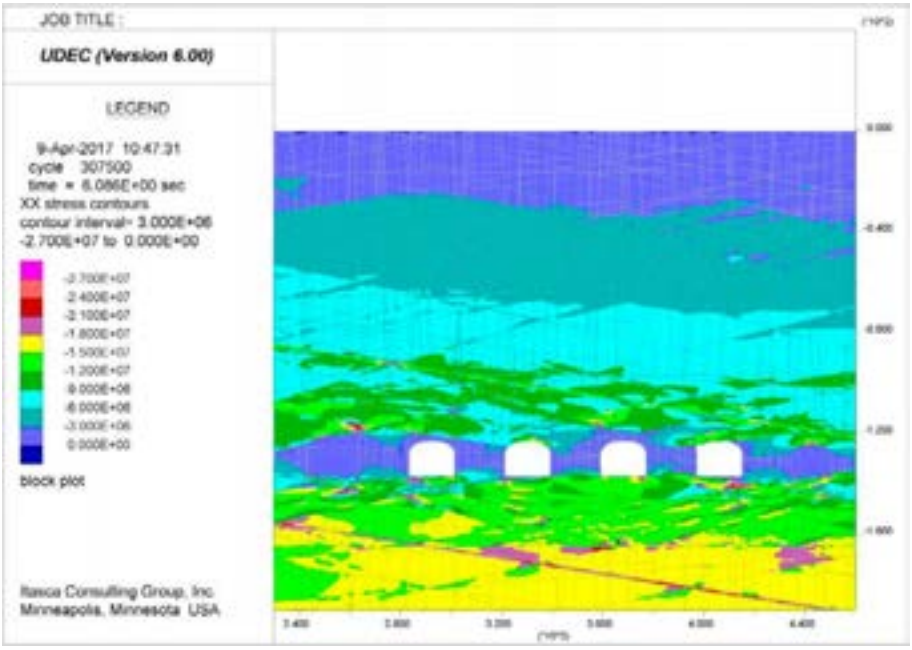


**Figure A206.** UDEC results after strength degradation up to Year 1000, showing horizontal stresses (SXX) for SFR 3, DFN 3-2. Stress magnitudes are in units of Pascals, with compression negative.

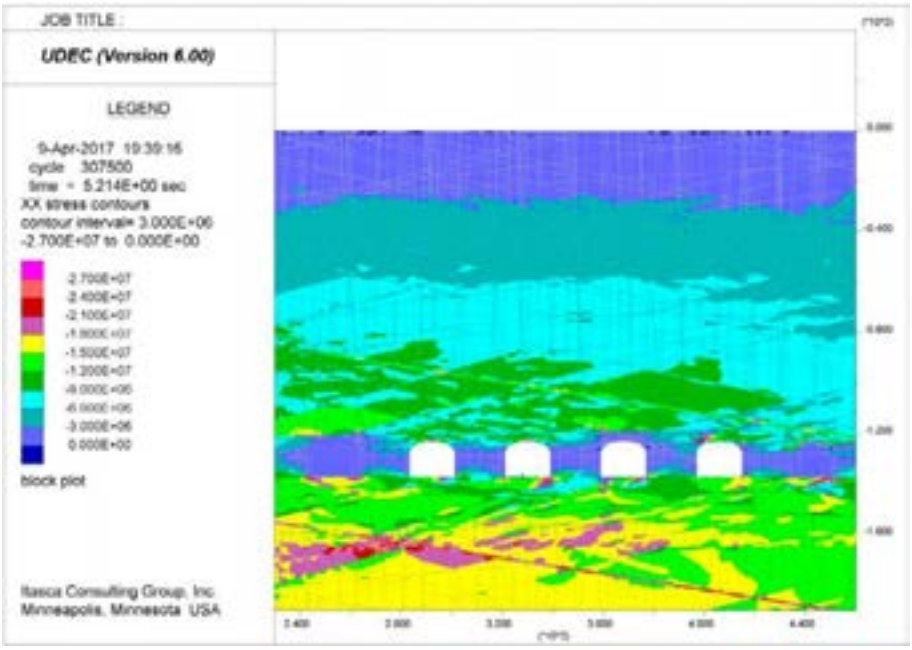


**Figure A207.** UDEC results after strength degradation up to Year 1000, showing horizontal stresses (SXX) for SFR 3, DFN 3-3. Stress magnitudes are in units of Pascals, with compression negative.

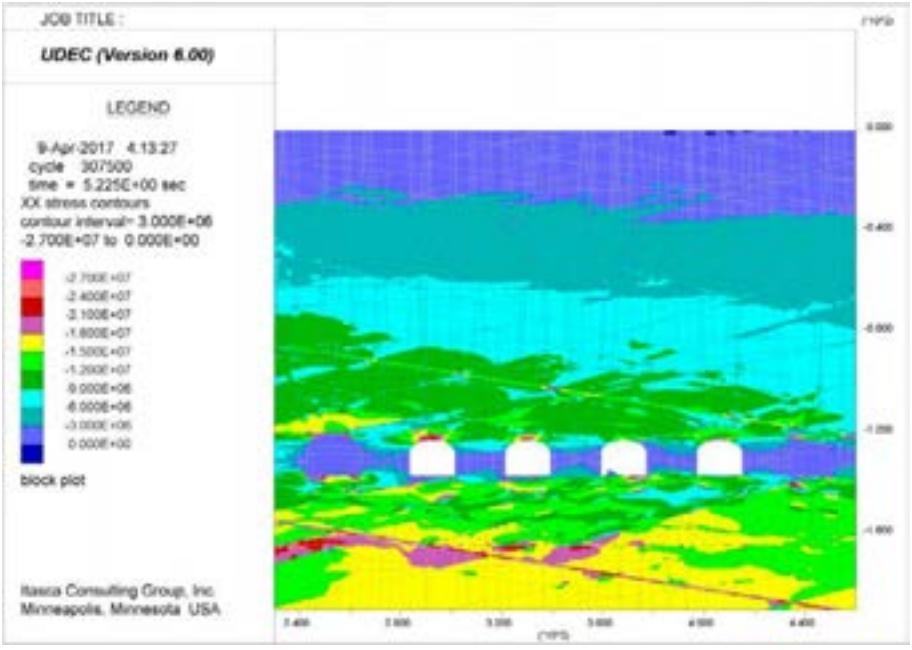


**Figure A208.** UDEC results after strength degradation up to Year 1000, showing horizontal stresses (SXX) for SFR 3, DFN 3-4. Stress magnitudes are in units of Pascals, with compression negative.

## SFR 3 – Year 1000 Strength Degradation (Plasticity Indicators)

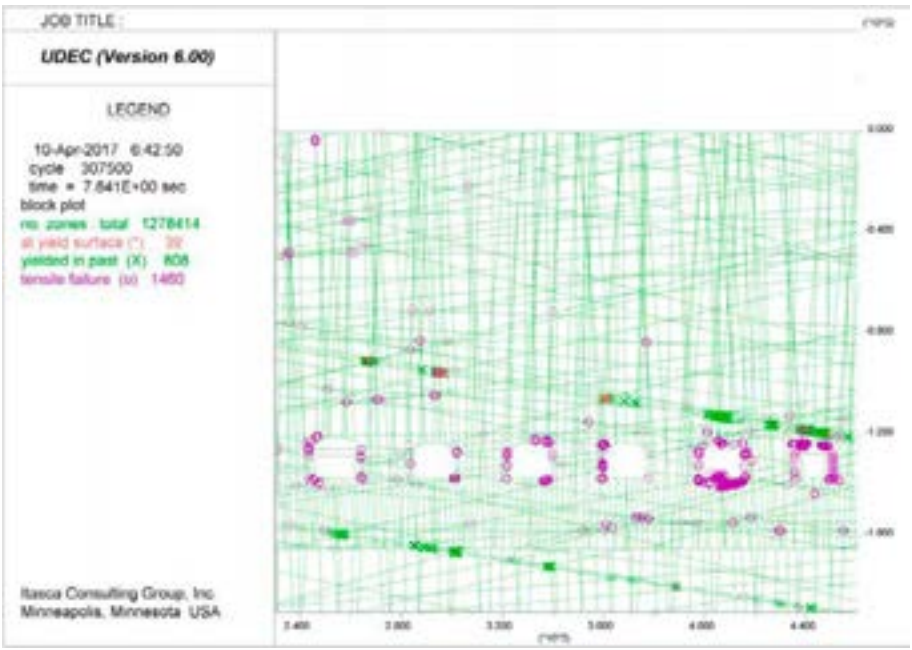


**Figure A209.** UDEC results after strength degradation up to Year 1000, showing yielded elements for SFR 3, DFN 3-1.

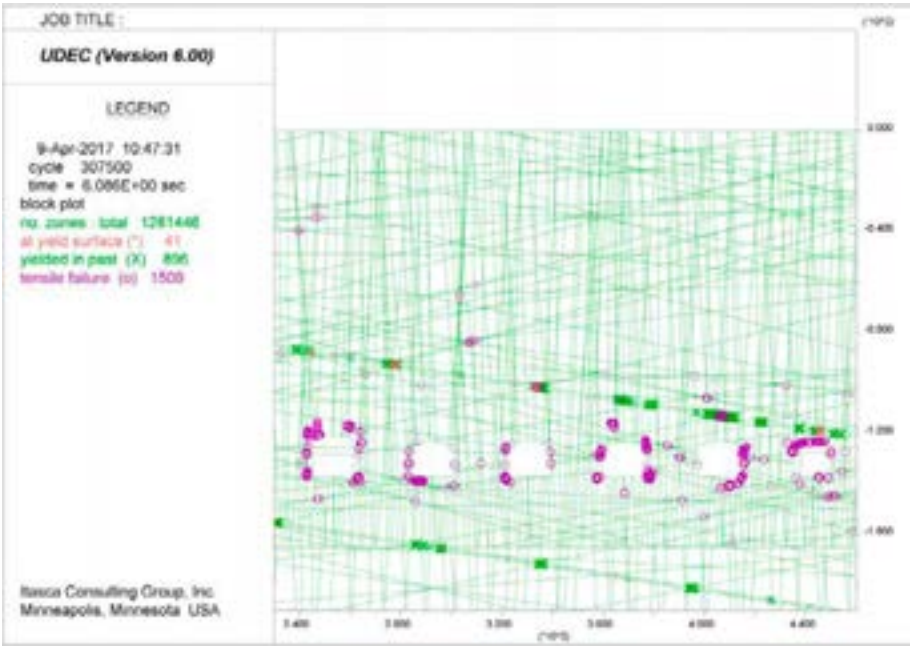


**Figure A210.** UDEC results after strength degradation up to Year 1000, showing yielded elements for SFR 3, DFN 3-2.

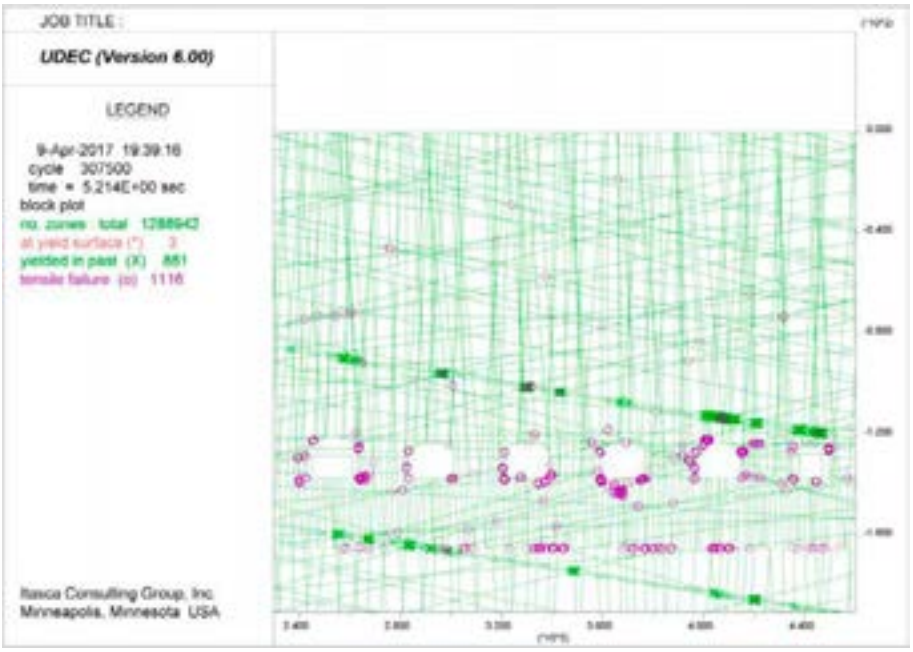


**Figure A211.** UDEC results after strength degradation up to Year 1000, showing yielded elements for SFR 3, DFN 3-3.

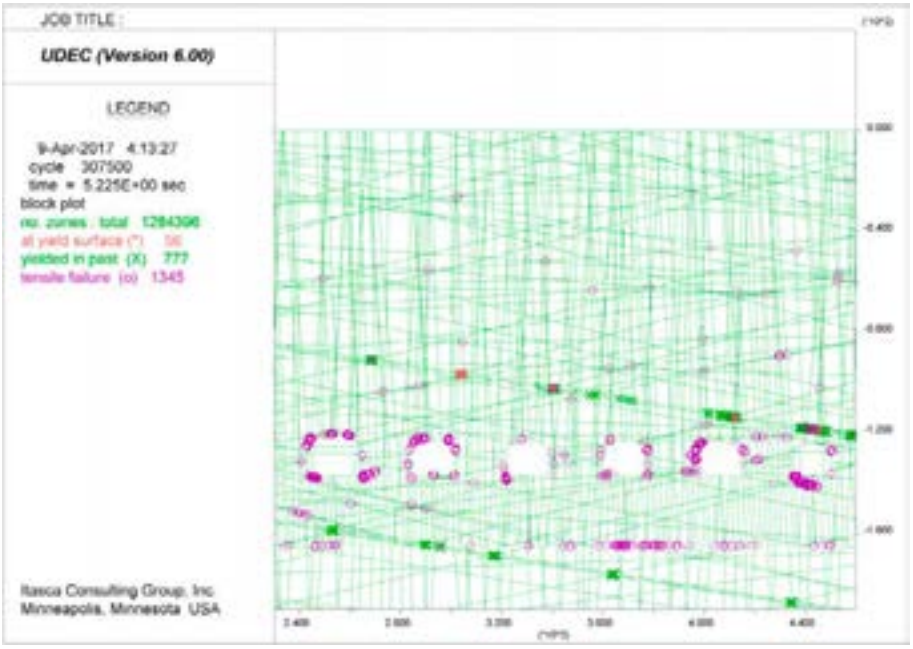


**Figure A212.** UDEC results after strength degradation up to Year 1000, showing yielded elements for SFR 3, DFN 3-4.

## SFR 3 – Year 1000 Strength Degradation (Displacement Vectors)

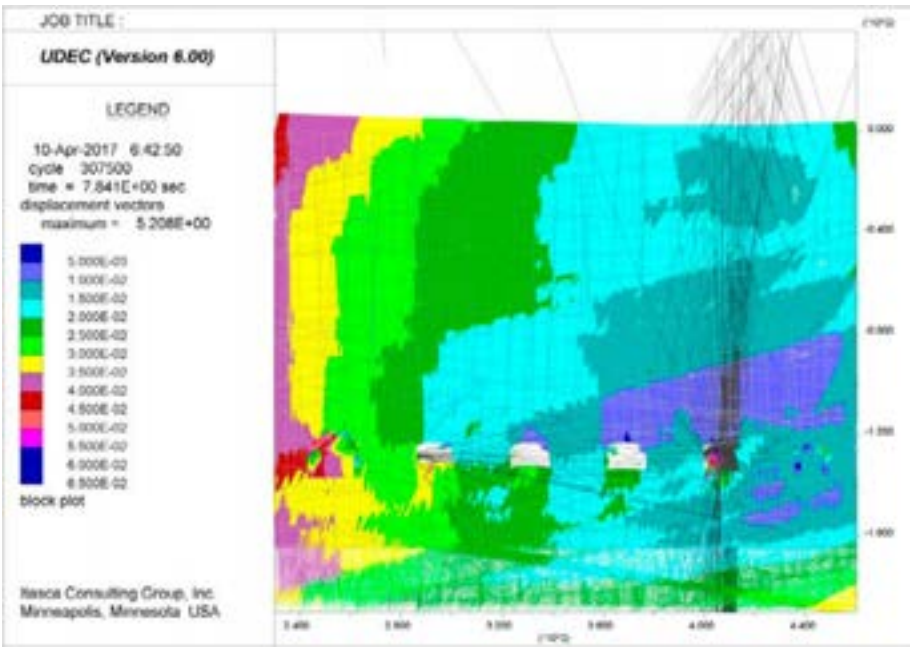


**Figure A213.** UDEC results after strength degradation up to Year 1000, showing displacement vectors for SFR 3, DFN 3-1. Displacement magnitudes are in units of metres.

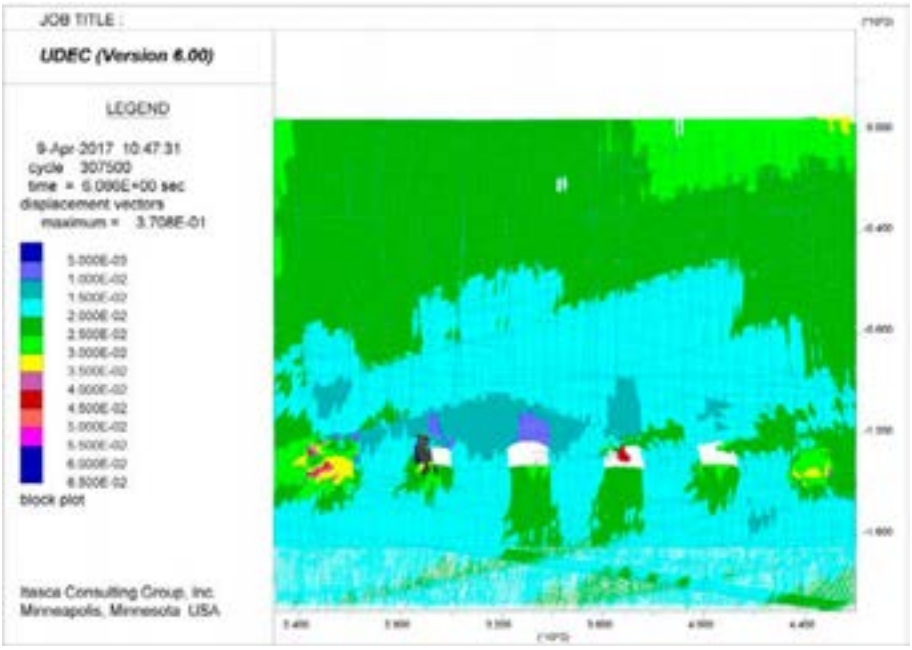


**Figure A214.** UDEC results after strength degradation up to Year 1000, showing displacement vectors for SFR 3, DFN 3-2. Displacement magnitudes are in units of metres.

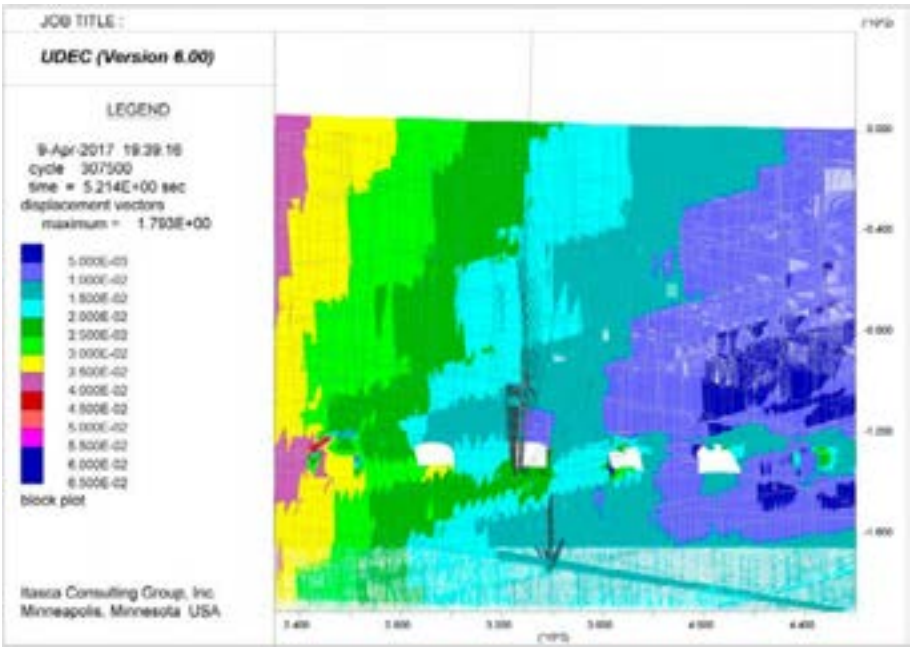


**Figure A215.** UDEC results after strength degradation up to Year 1000, showing displacement vectors for SFR 3, DFN 3-3. Displacement magnitudes are in units of metres.

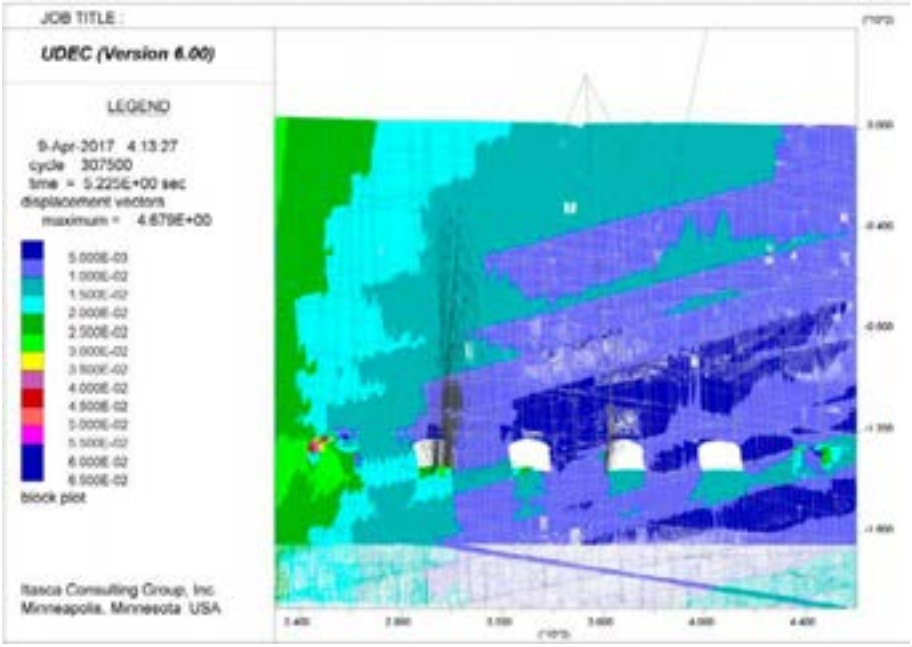


**Figure A216.** UDEC results after strength degradation up to Year 1000, showing displacement vectors for SFR 3, DFN 3-4. Displacement magnitudes are in units of metres.

## SFR 3 – Year 1000 Strength Degradation (Fracture Shear Displacement)

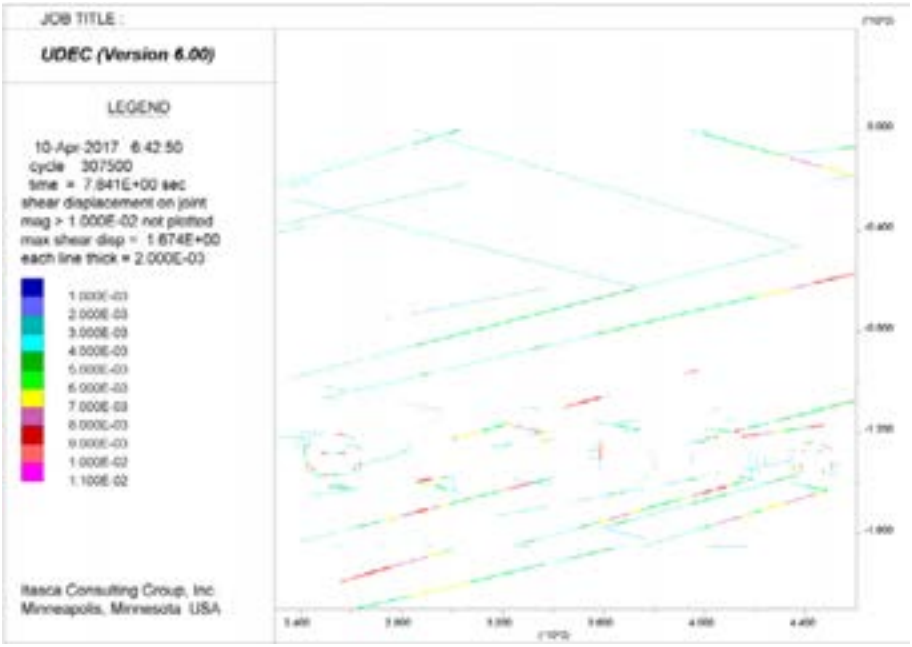


**Figure A217.** UDEC results after strength degradation up to Year 1000, showing shear displacements along fractures for SFR 3, DFN 3-1. Displacements are in units of metres.

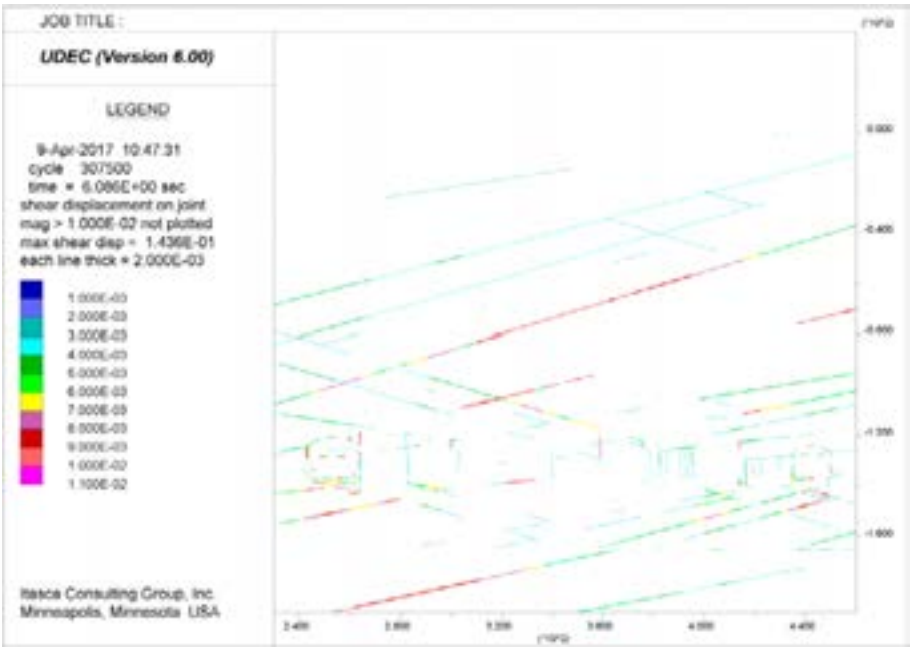


**Figure A218.** UDEC results after strength degradation up to Year 1000, showing shear displacements along fractures for SFR 3, DFN 3-2. Displacements are in units of metres.

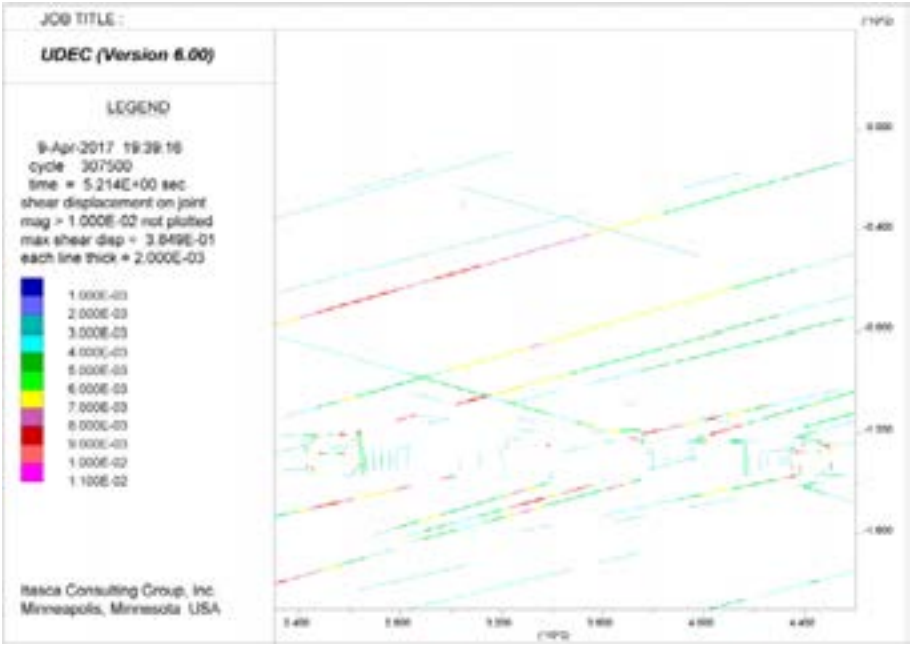


**Figure A219.** UDEC results after strength degradation up to Year 1000, showing shear displacements along fractures for SFR 3, DFN 3-3. Displacements are in units of metres.

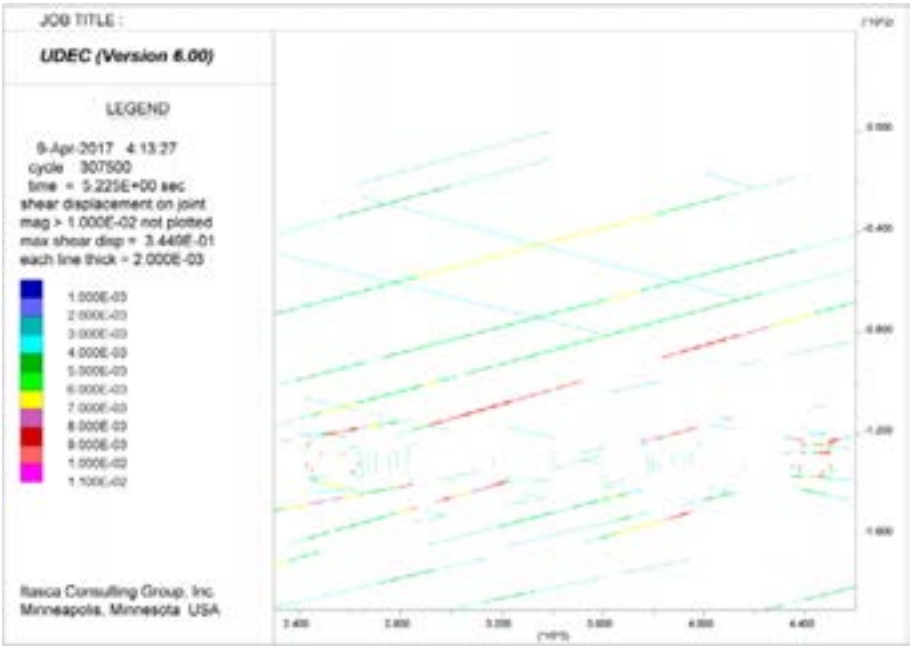


**Figure A220.** UDEC results after strength degradation up to Year 1000, showing shear displacements along fractures for SFR 3, DFN 3-4. Displacements are in units of metres.

## SFR 3 – Year 1000 Strength Degradation (Vertical Displacements)

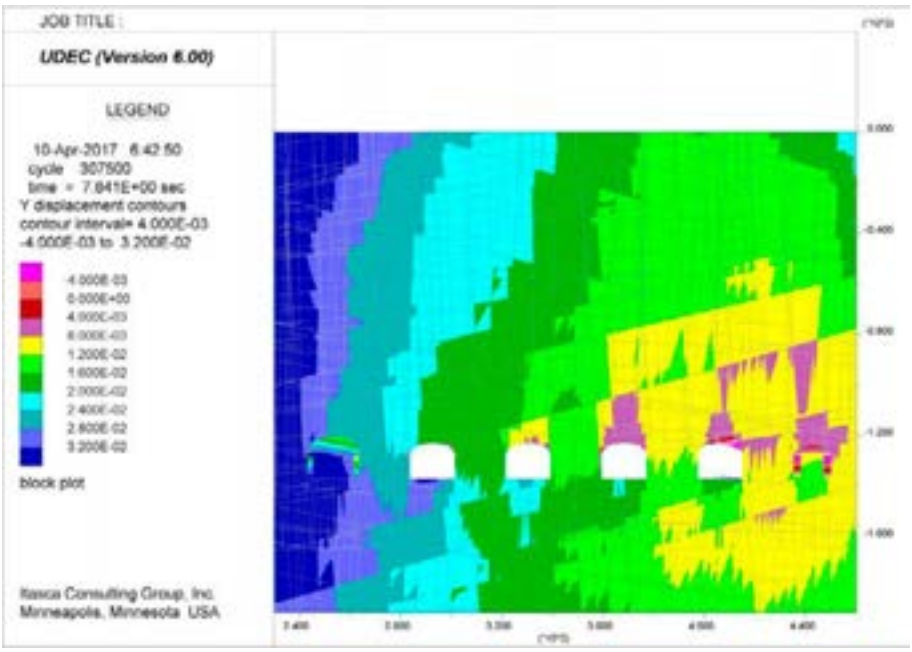


**Figure A221.** UDEC results after strength degradation up to Year 1000, showing vertical displacements for SFR 3, DFN 3-1. Displacements are in units of metres, with positive up.

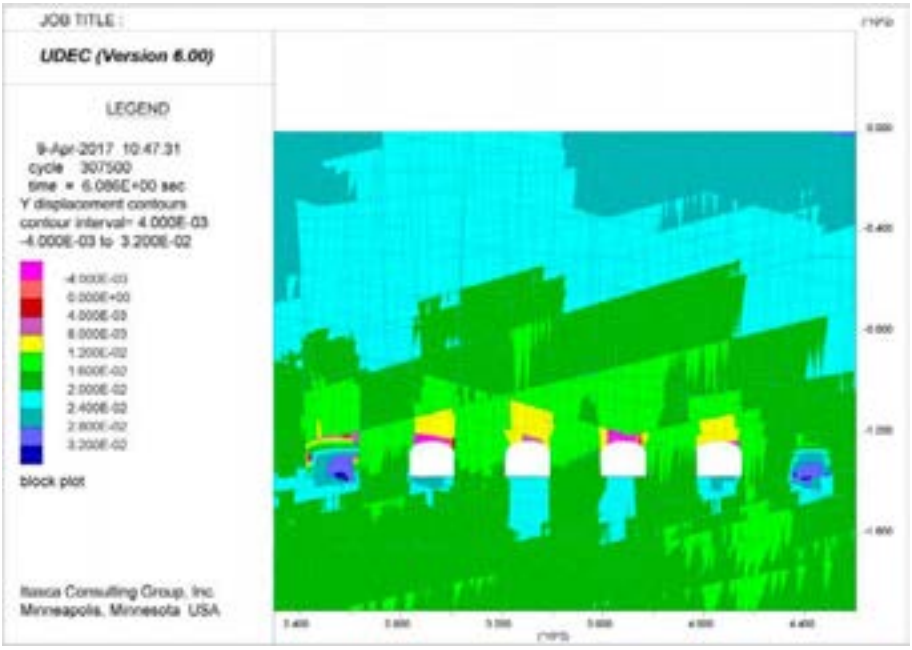


**Figure A222.** UDEC results after strength degradation up to Year 1000, showing vertical displacements for SFR 3, DFN 3-2. Displacements are in units of metres, with positive up.

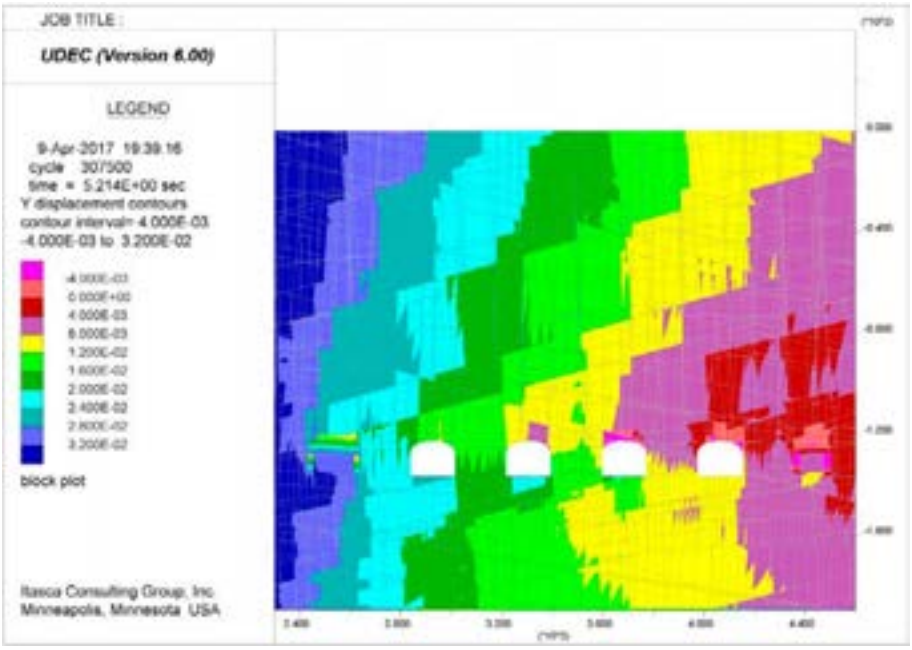


**Figure A223.** UDEC results after strength degradation up to Year 1000, showing vertical displacements for SFR 3, DFN 3-3. Displacements are in units of metres, with positive up.

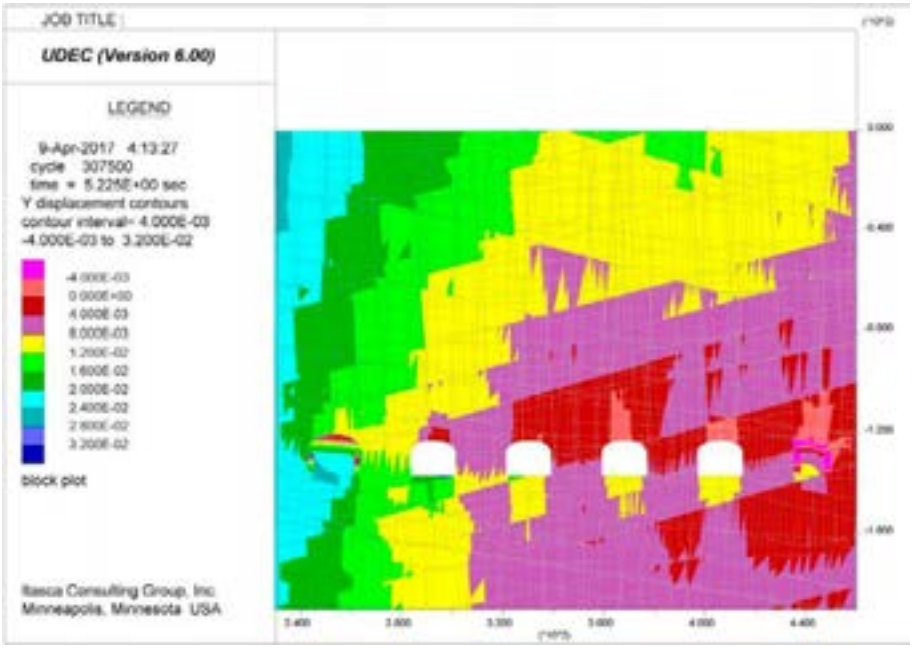


**Figure A224.** UDEC results after strength degradation up to Year 1000, showing vertical displacements for SFR 3, DFN 3-4. Displacements are in units of metres, with positive up.

## SFR 3 – Year 1000 Strength Degradation (Horizontal Displacements)

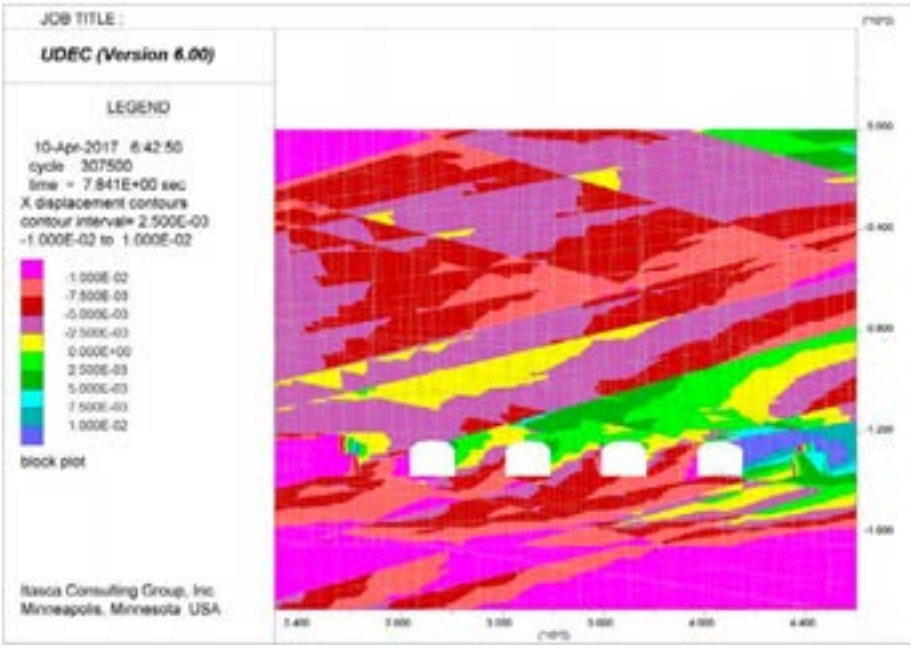


**Figure A225.** UDEC results after strength degradation up to Year 1000, showing horizontal displacements for SFR 3, DFN 3-1. Displacements are in units of metres, with positive to the right.

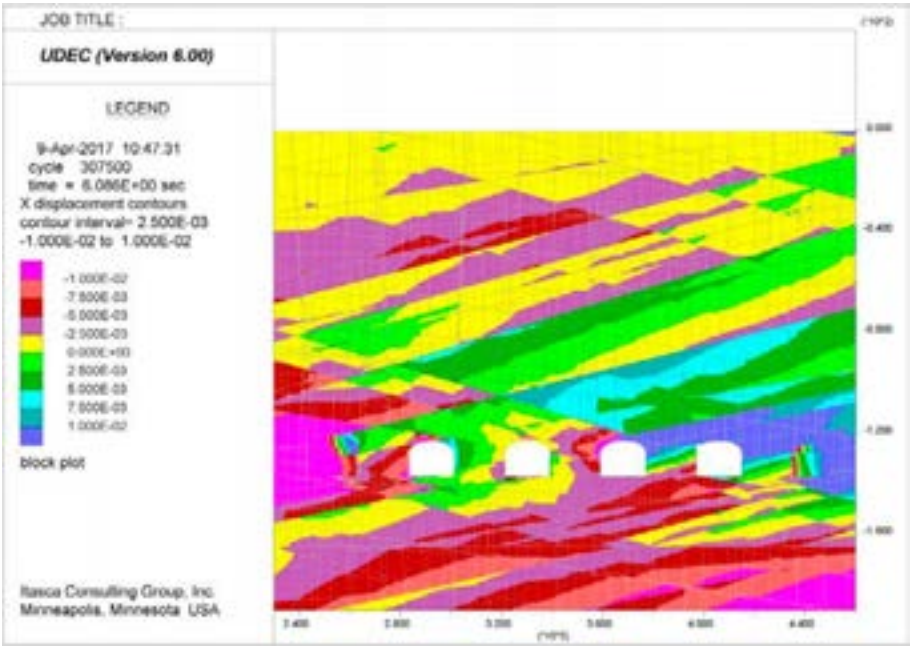


**Figure A226.** UDEC results after strength degradation up to Year 1000, showing horizontal displacements for SFR 3, DFN 3-2. Displacements are in units of metres, with positive to the right.

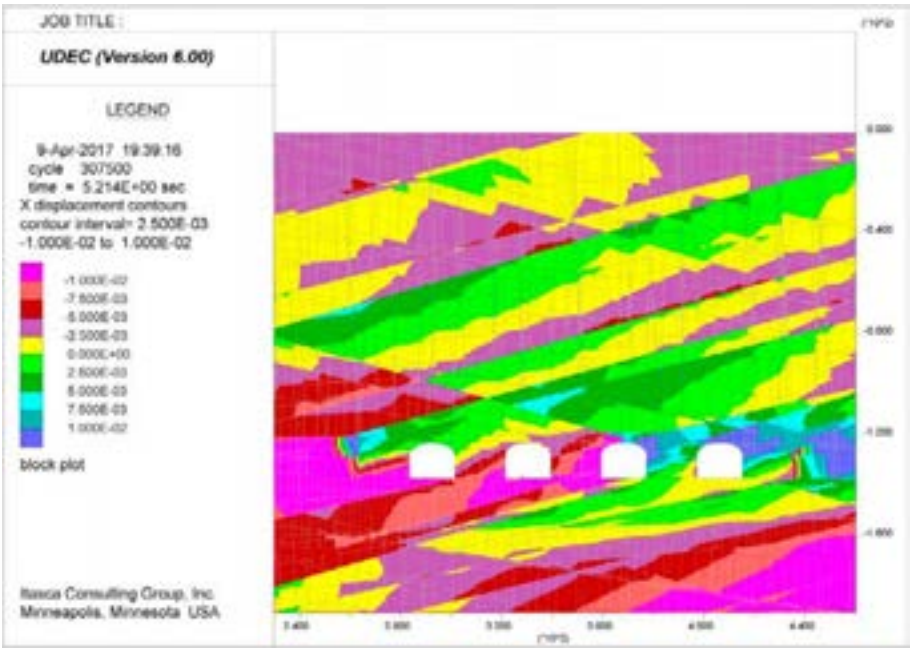


**Figure A227.** UDEC results after strength degradation up to Year 1000, showing horizontal displacements for SFR 3, DFN 3-3. Displacements are in units of metres, with positive to the right.

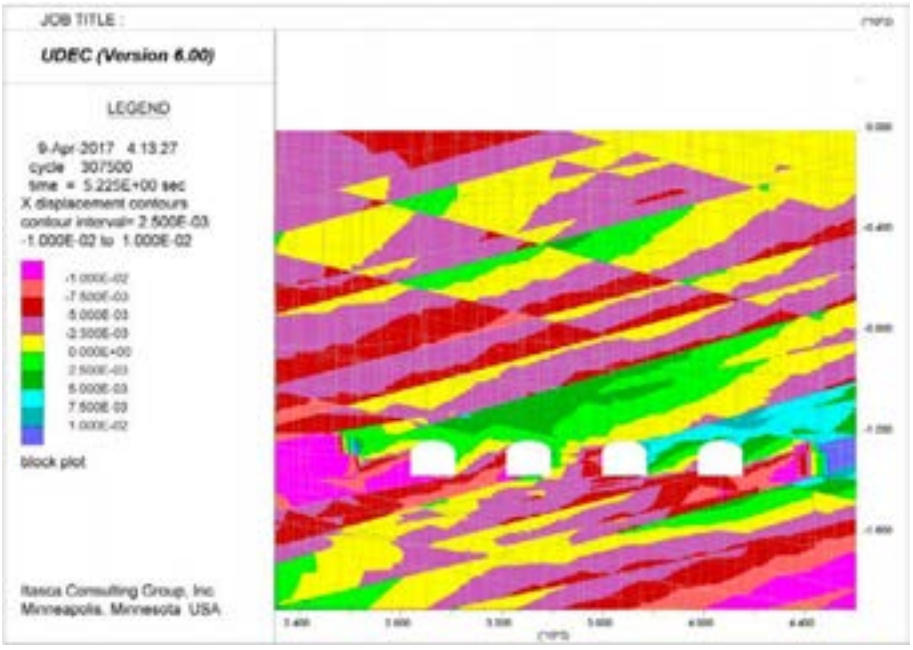


**Figure A228.** UDEC results after strength degradation up to Year 1000, showing horizontal displacements for SFR 3, DFN 3-4. Displacements are in units of metres, with positive to the right.

## SFR 3 – Year 10,000 Strength Degradation (Vertical Stress)

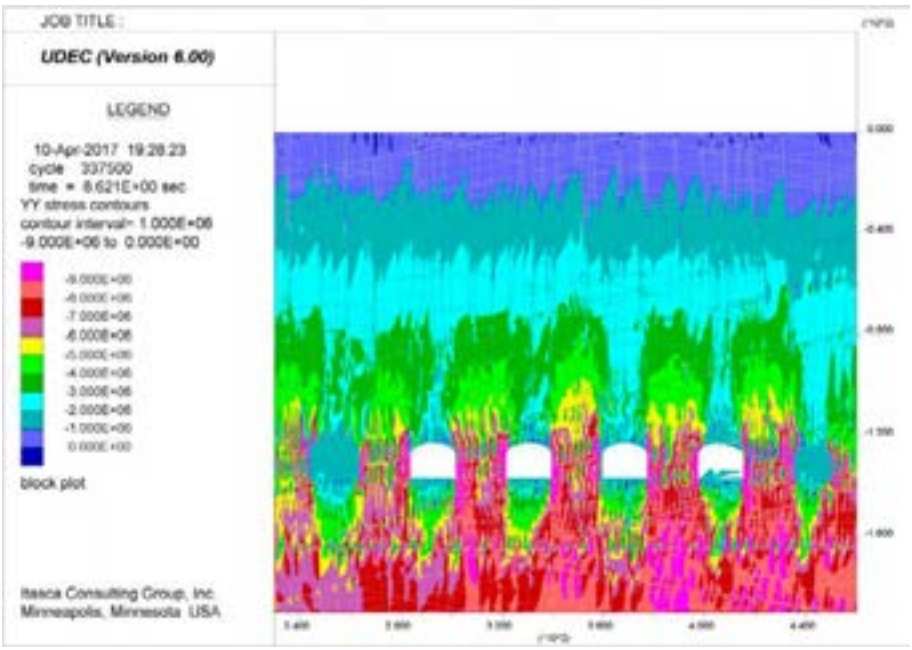


**Figure A229.** UDEC results after strength degradation up to Year 10,000, showing vertical stresses (SYY) for SFR 3, DFN 3-1. Stress magnitudes are in units of Pascals, with compression negative.

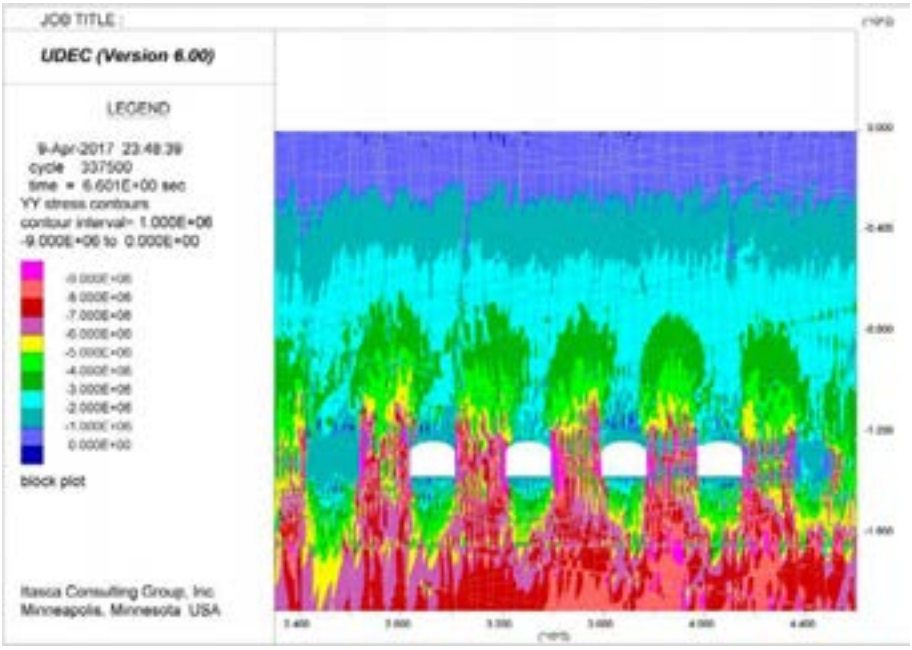


**Figure A230.** UDEC results after strength degradation up to Year 10,000, showing vertical stresses (SYY) for SFR 3, DFN 3-2. Stress magnitudes are in units of Pascals, with compression negative.

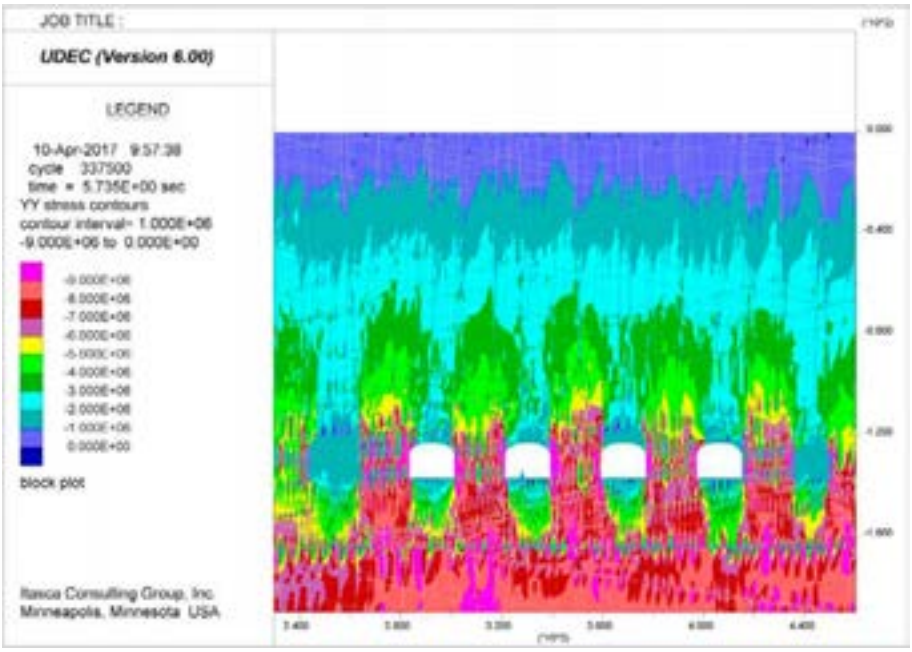


**Figure A231.** UDEC results after strength degradation up to Year 10,000, showing vertical stresses (SYY) for SFR 3, DFN 3-3. Stress magnitudes are in units of Pascals, with compression negative.

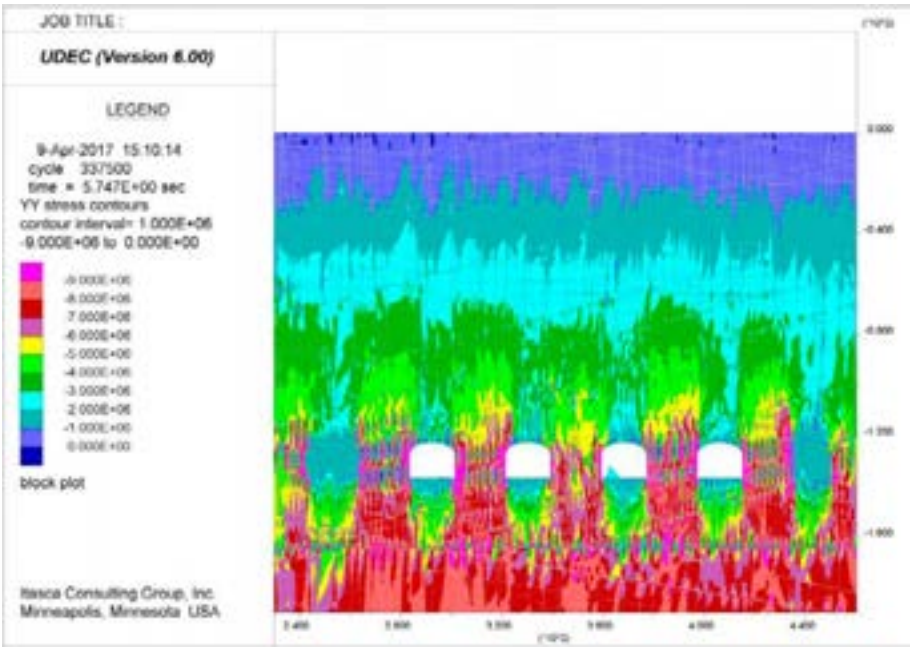


**Figure A232.** UDEC results after strength degradation up to Year 10.000, showing vertical stresses (SYY) for SFR 3, DFN 3-4. Stress magnitudes are in units of Pascals, with compression negative.

## SFR 3 – Year 10,000 Strength Degradation (Horizontal Stress)

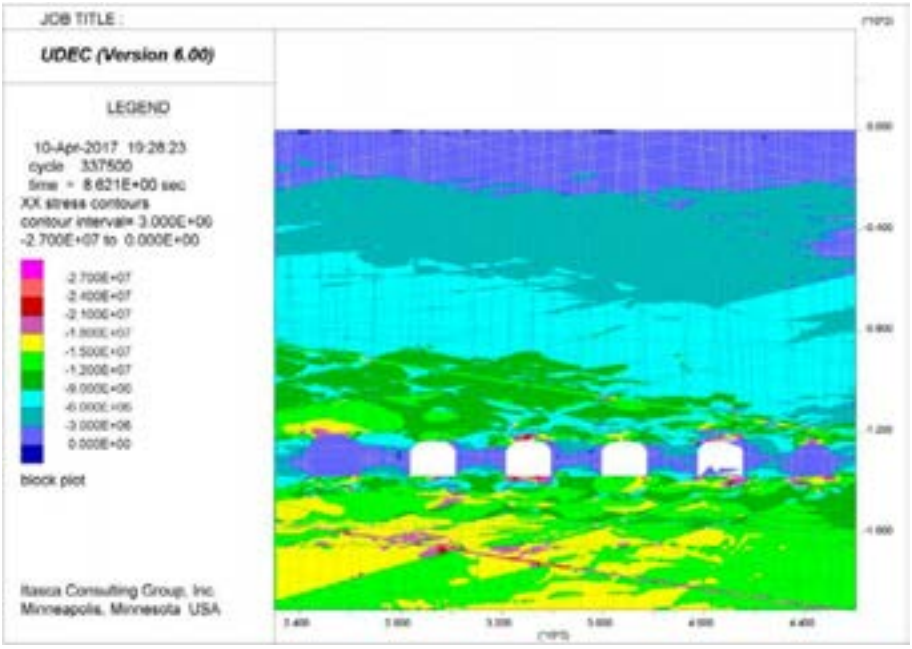


**Figure A233.** UDEC results after strength degradation up to Year 10,000, showing horizontal stresses (SXX) for SFR 3, DFN 3-1. Stress magnitudes are in units of Pascals, with compression negative.

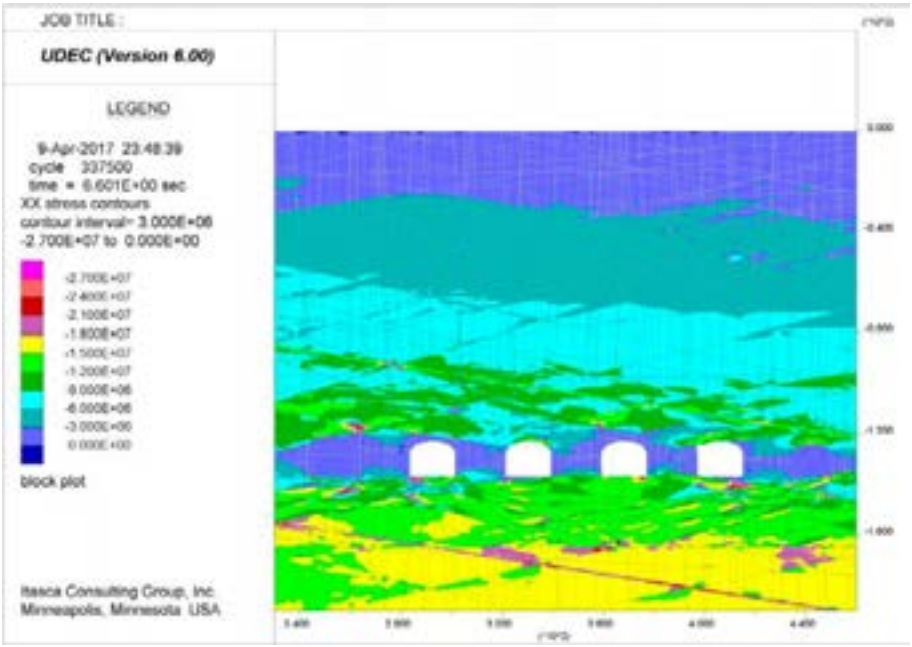


**Figure A234.** UDEC results after strength degradation up to Year 10,000, showing horizontal stresses (SXX) for SFR 3, DFN 3-2. Stress magnitudes are in units of Pascals, with compression negative.

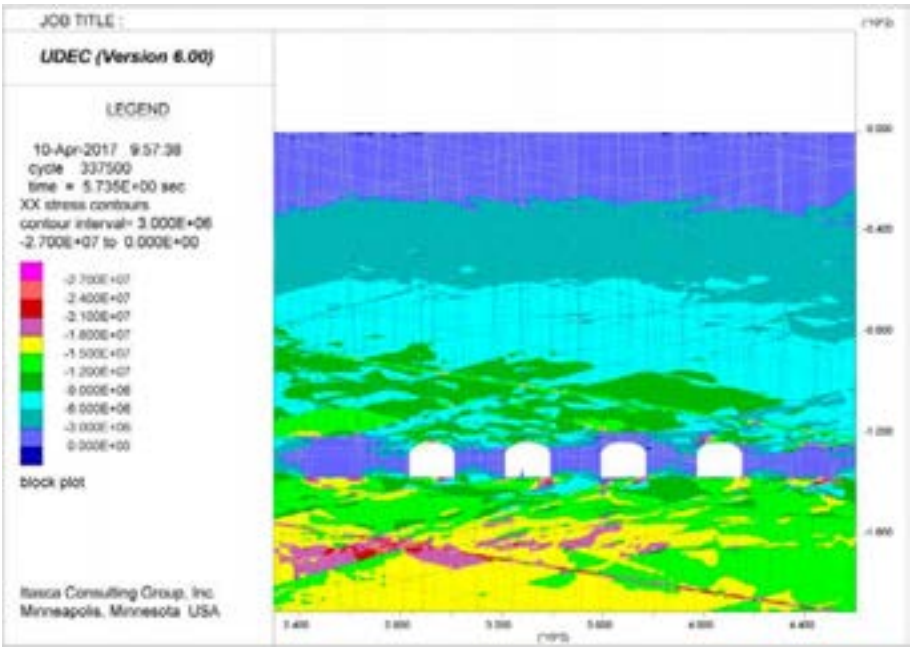


**Figure A235.** UDEC results after strength degradation up to Year 10,000, showing horizontal stresses (SXX) for SFR 3, DFN 3-3. Stress magnitudes are in units of Pascals, with compression negative.

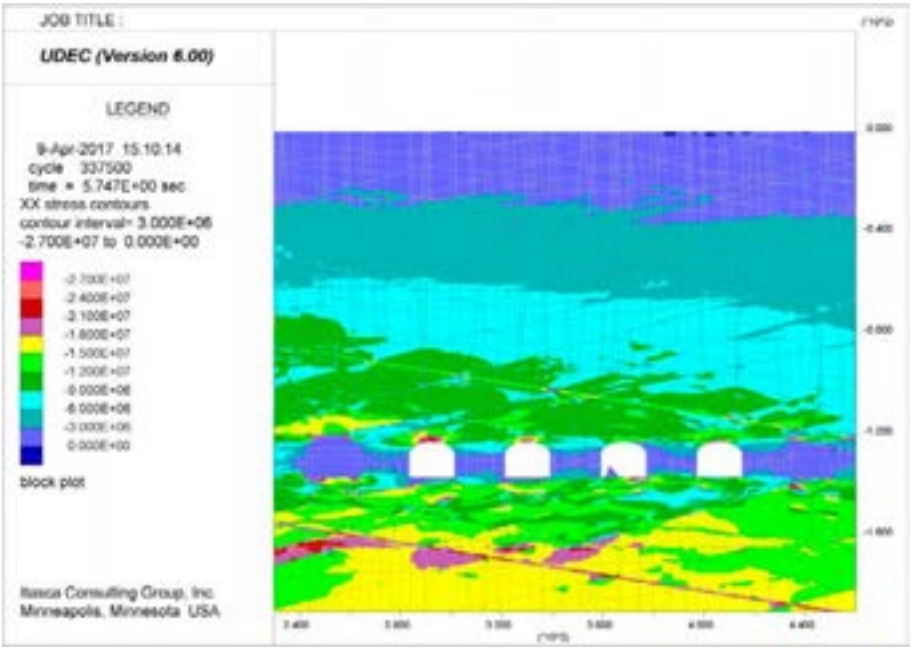


**Figure A236.** UDEC results after strength degradation up to Year 10,000, showing horizontal stresses (SXX) for SFR 3, DFN 3-4. Stress magnitudes are in units of Pascals, with compression negative.

## SFR 3 – Year 10,000 Strength Degradation (Plasticity Indicators)

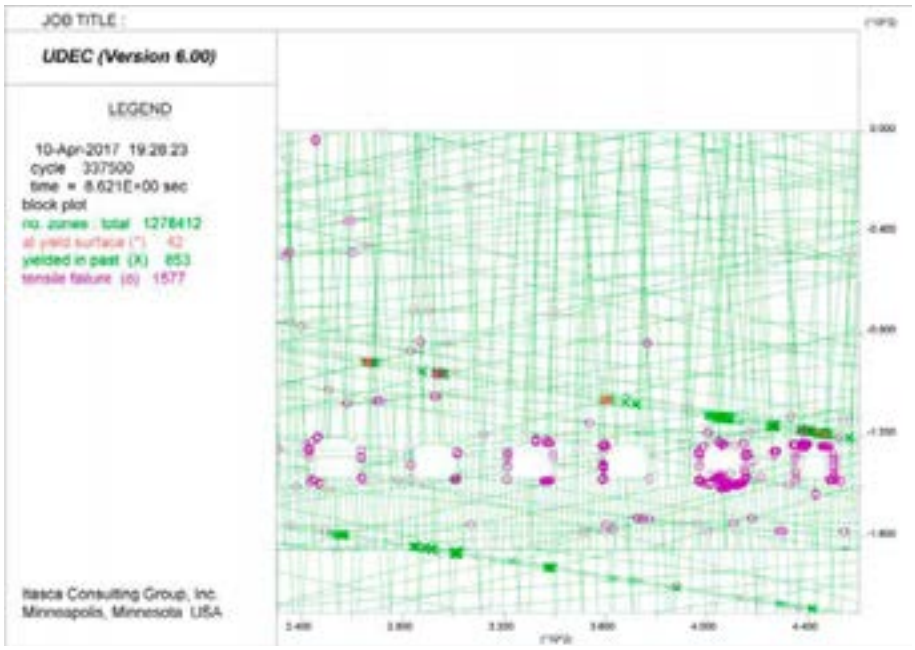


**Figure A237.** UDEC results after strength degradation up to Year 10,000, showing yielded elements for SFR 3, DFN 3-1.

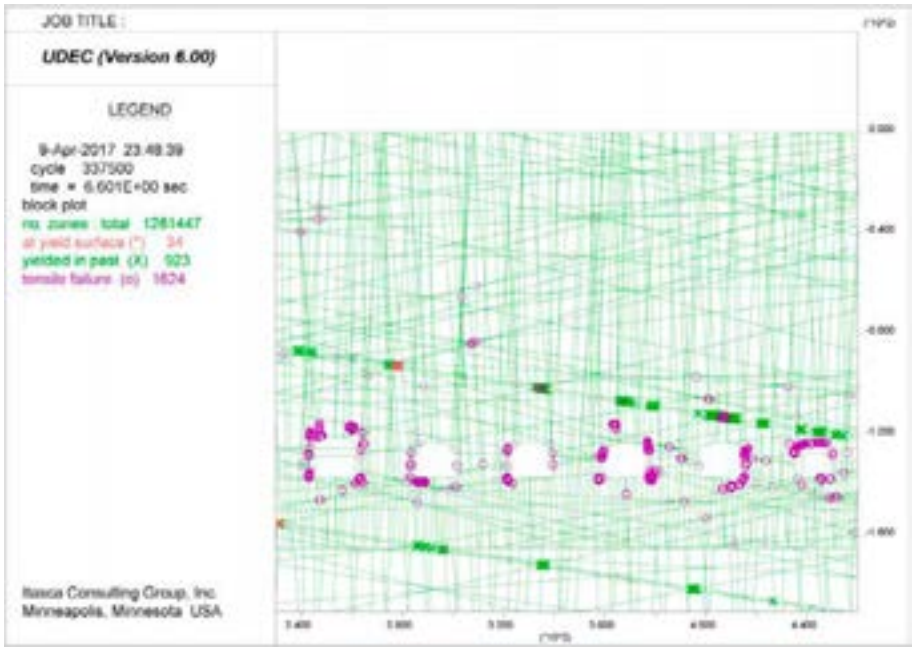


**Figure A238.** UDEC results after strength degradation up to Year 10,000, showing yielded elements for SFR 3, DFN 3-2.

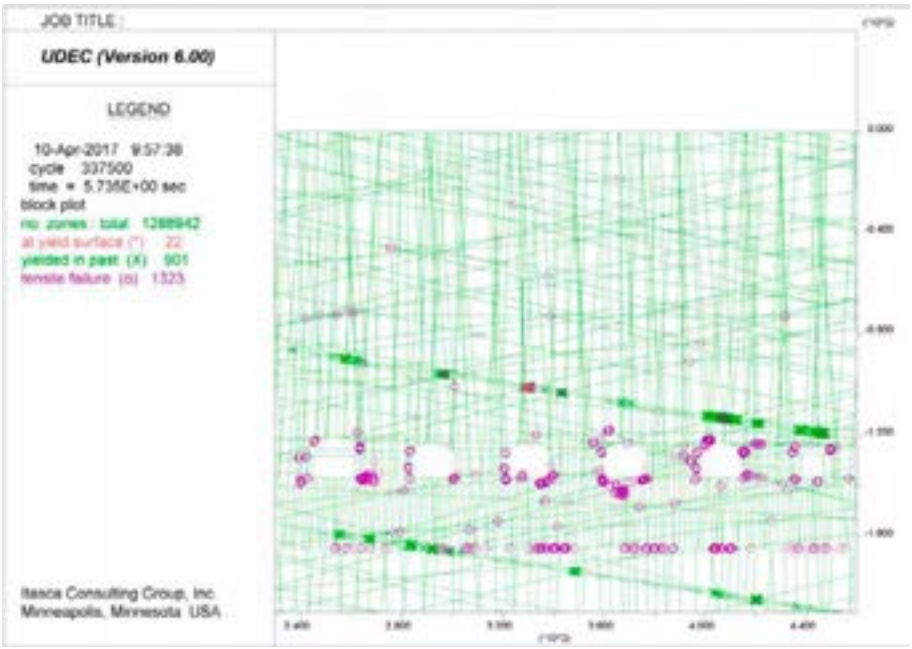


**Figure A239.** UDEC results after strength degradation up to Year 10,000, showing yielded elements for SFR 3, DFN 3-3.

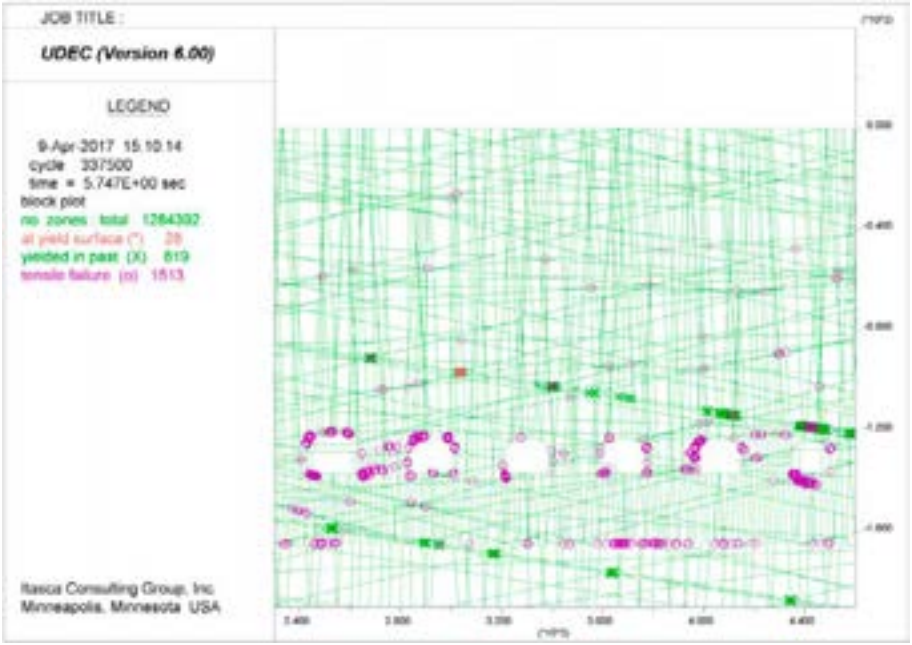


**Figure A240.** UDEC results after strength degradation up to Year 10,000, showing yielded elements for SFR 3, DFN 3-4.

## SFR 3 – Year 10,000 Strength Degradation (Displacement Vectors)

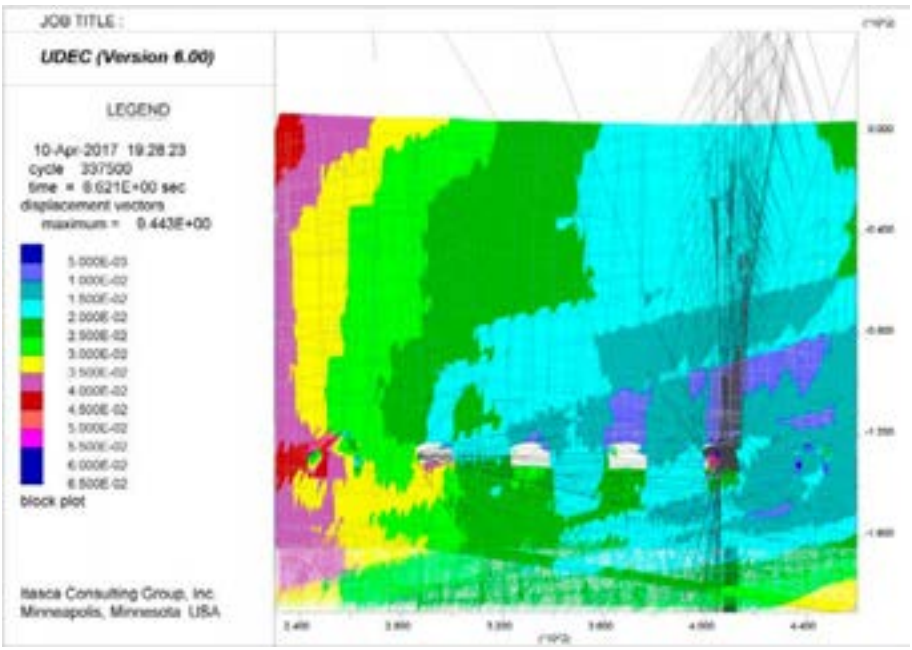


**Figure A241.** UDEC results after strength degradation up to Year 10,000, showing displacement vectors for SFR 3, DFN 3-1. Displacement magnitudes are in units of metres.

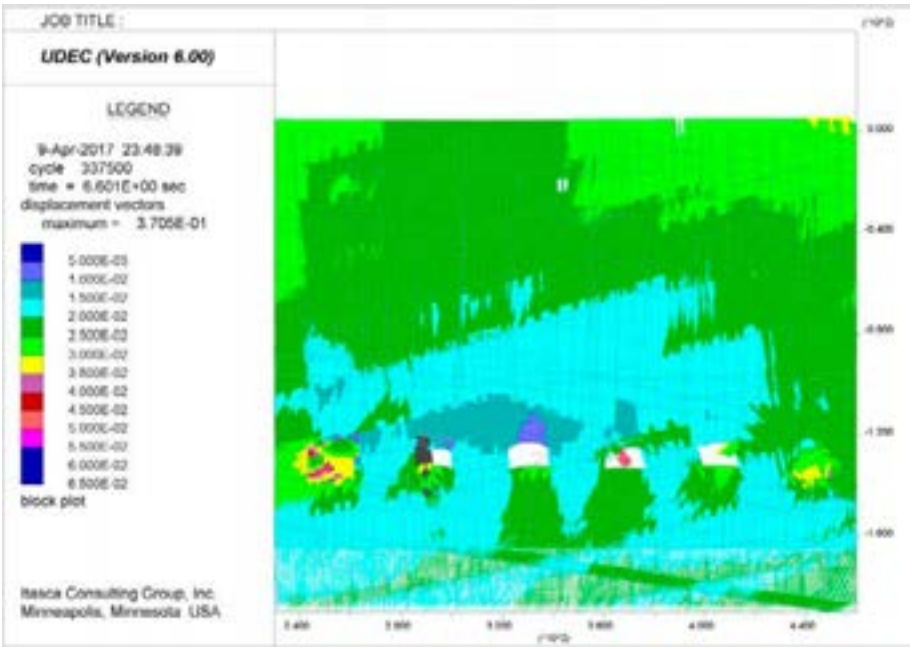


**Figure A242.** UDEC results after strength degradation up to Year 10,000, showing displacement vectors for SFR 3, DFN 3-2. Displacement magnitudes are in units of metres.

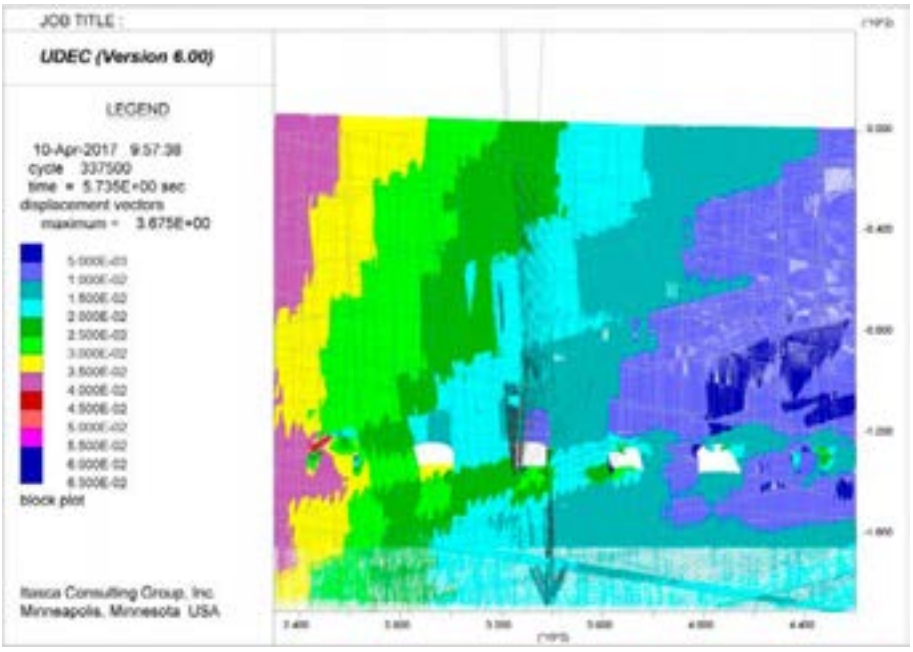


**Figure A243.** UDEC results after strength degradation up to Year 10,000, showing displacement vectors for SFR 3, DFN 3-3. Displacement magnitudes are in units of metres.

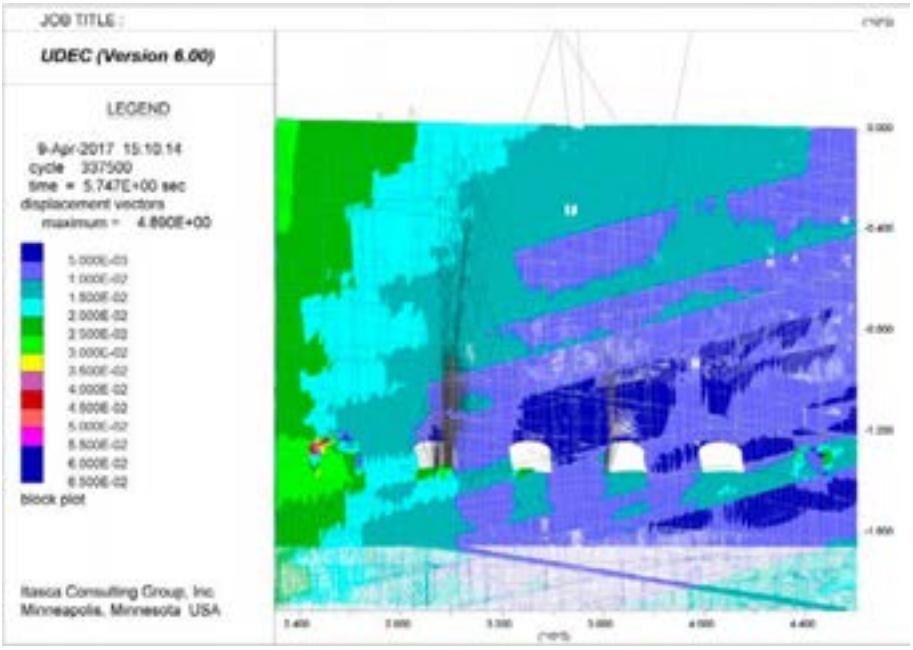


**Figure A244.** UDEC results after strength degradation up to Year 10,000, showing displacement vectors for SFR 3, DFN 3-4. Displacement magnitudes are in units of metres.

## SFR 3 – Year 10,000 Strength Degradation (Fracture Shear Displ.)

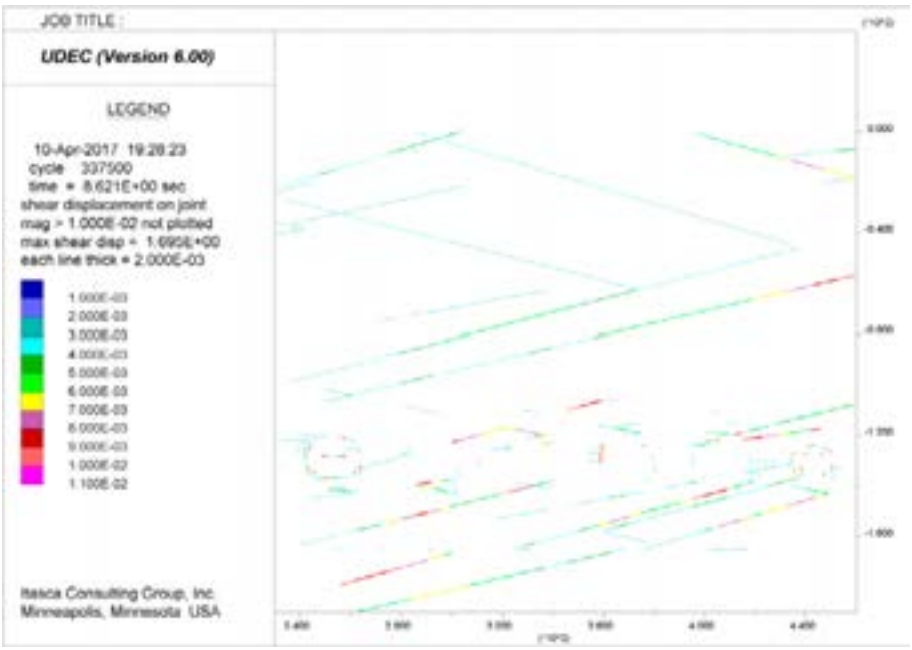


**Figure A245.** UDEC results after strength degradation up to Year 10,000, showing shear displacements along fractures for SFR 3, DFN 3-1. Displacements are in units of metres.

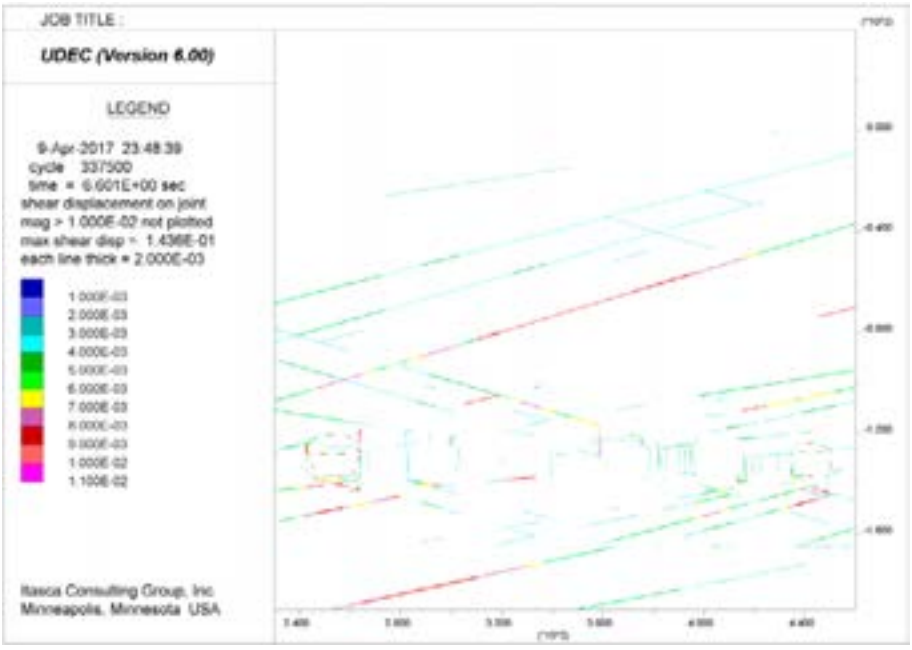


**Figure A246.** UDEC results after strength degradation up to Year 10,000, showing shear displacements along fractures for SFR 3, DFN 3-2. Displacements are in units of metres.

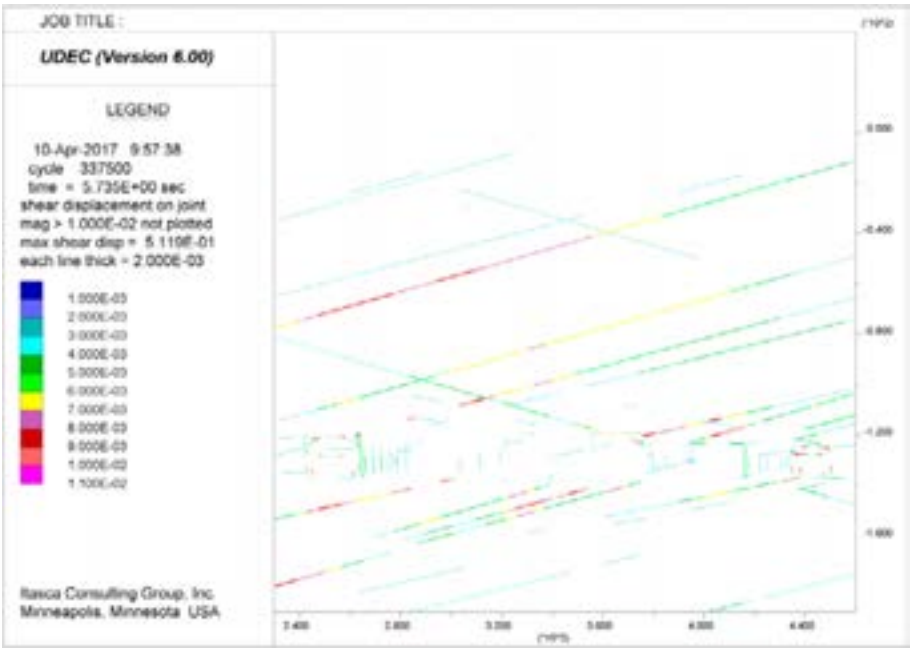


**Figure A247.** UDEC results after strength degradation up to Year 10,000, showing shear displacements along fractures for SFR 3, DFN 3-3. Displacements are in units of metres.

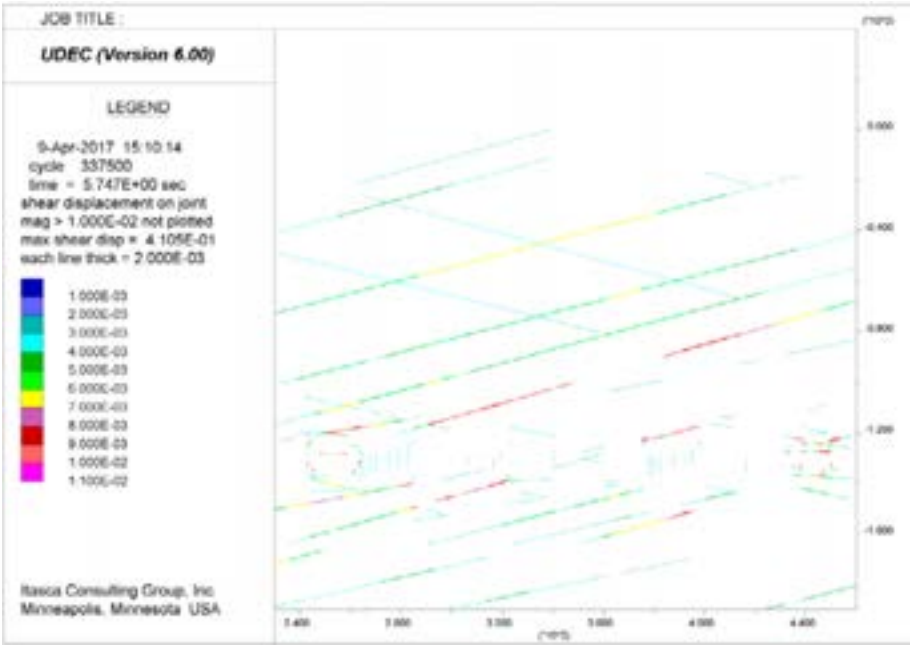


**Figure A248.** UDEC results after strength degradation up to Year 10,000, showing shear displacements along fractures for SFR 3, DFN 3-4. Displacements are in units of metres.

## SFR 3 – Year 10,000 Strength Degradation (Vertical Displacements)

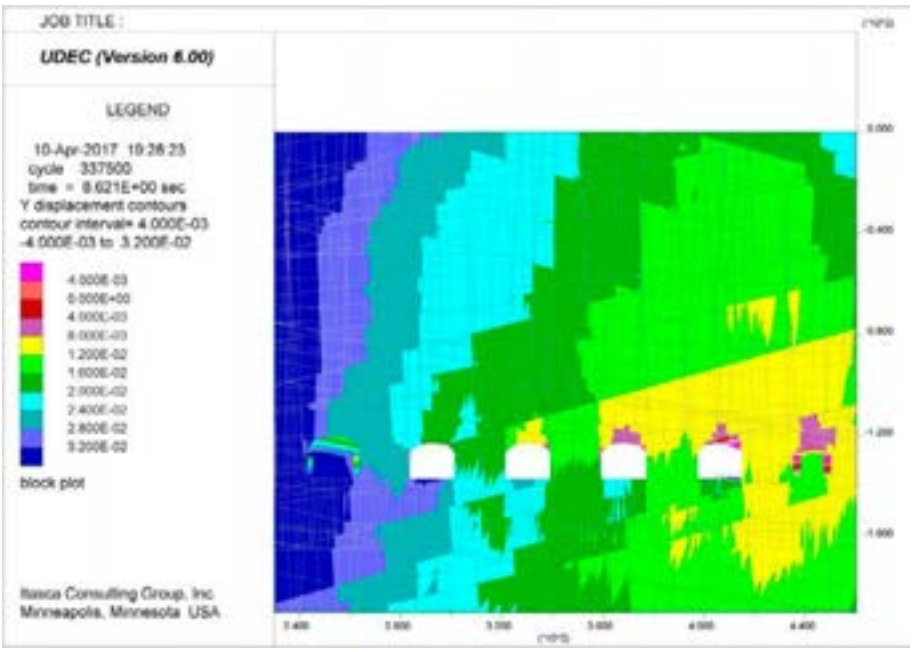


**Figure A249.** UDEC results after strength degradation up to Year 10,000, showing vertical displacements for SFR 3, DFN 3-1. Displacements are in units of metres, with positive up.

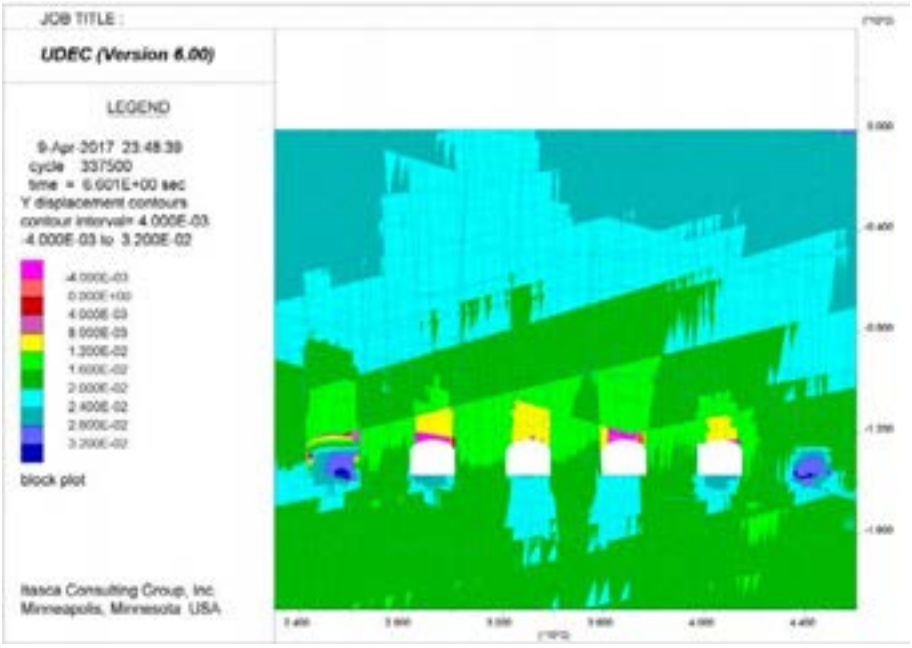


**Figure A250.** UDEC results after strength degradation up to Year 10,000, showing vertical displacements for SFR 3, DFN 3-2. Displacements are in units of metres, with positive up.

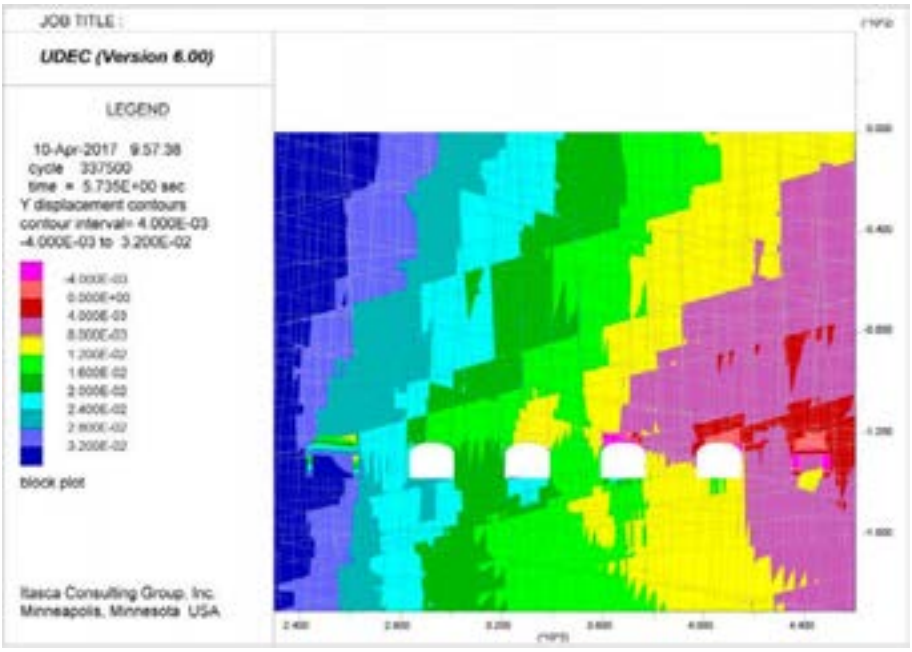


**Figure A251.** UDEC results after strength degradation up to Year 10,000, showing vertical displacements for SFR 3, DFN 3-3. Displacements are in units of metres, with positive up.

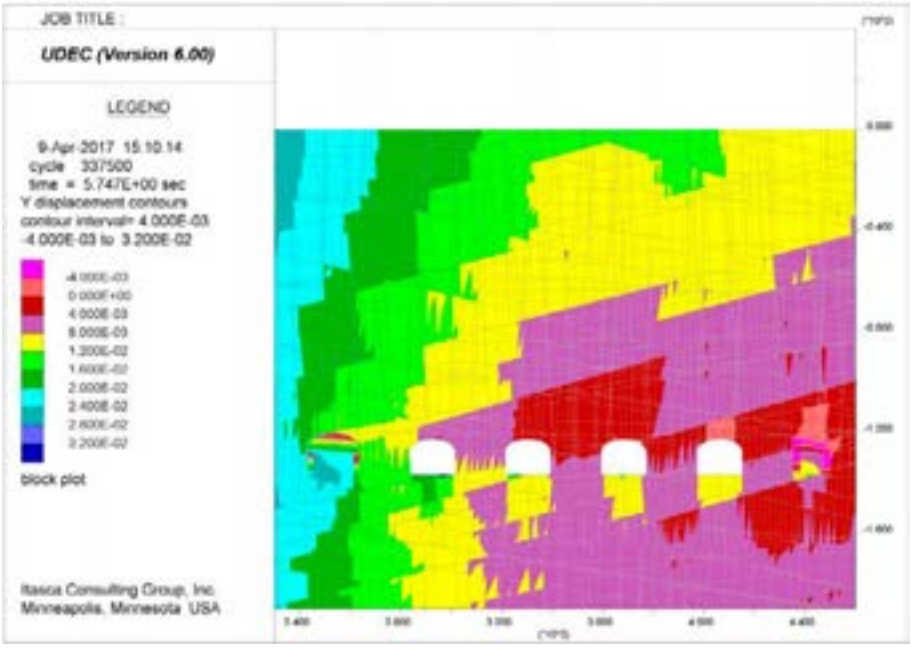


**Figure A252.** UDEC results after strength degradation up to Year 10,000, showing vertical displacements for SFR 3, DFN 3-4. Displacements are in units of metres, with positive up.

## SFR 3 – Year 10,000 Strength Degradation (Horizontal Displacements)

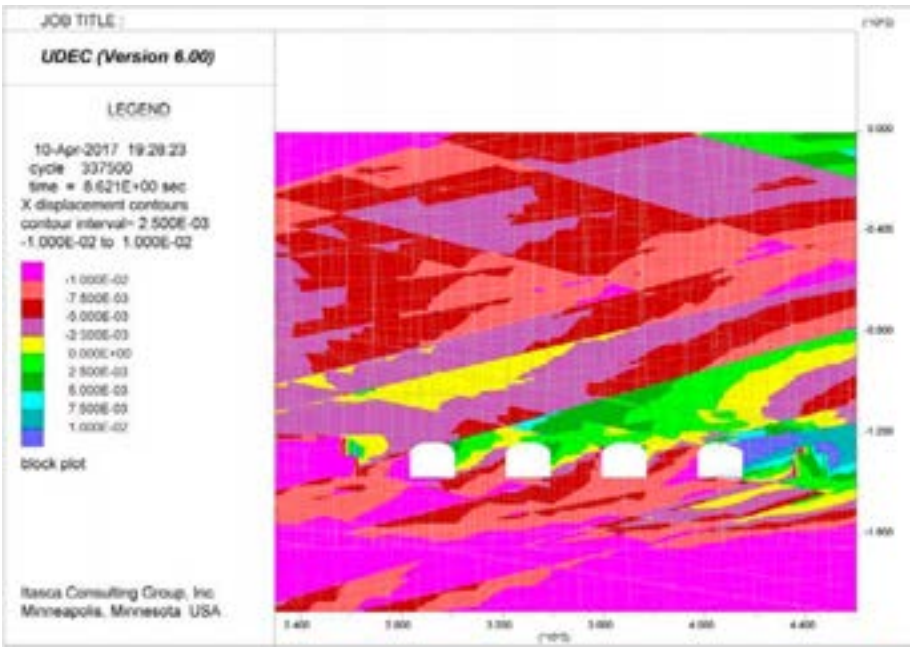


**Figure A253.** UDEC results after strength degradation up to Year 10,000, showing horizontal displacements for SFR 3, DFN 3-1. Displacements are in units of metres, with positive to the right.

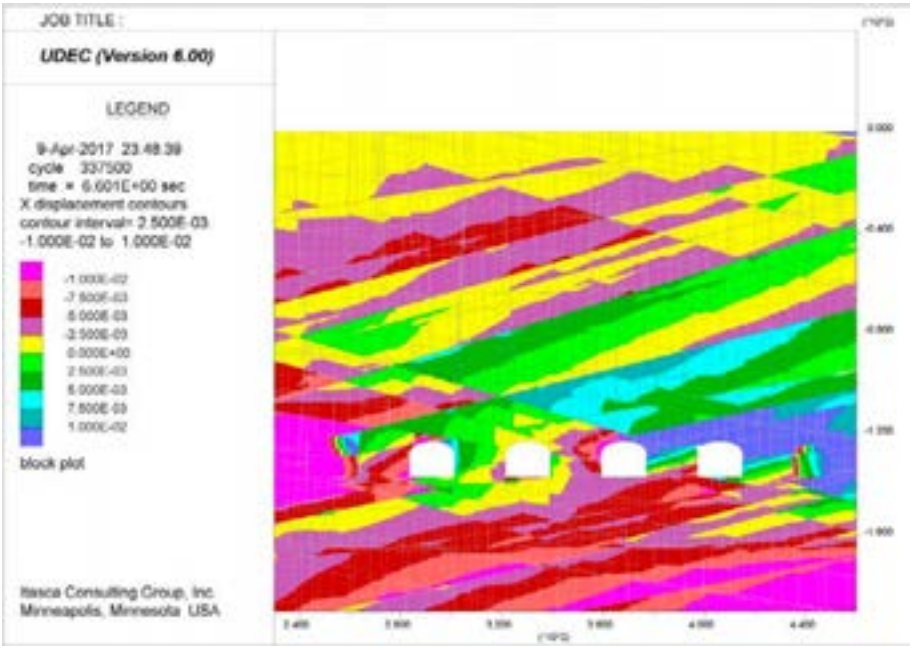


**Figure A254.** UDEC results after strength degradation up to Year 10,000, showing horizontal displacements for SFR 3, DFN 3-2. Displacements are in units of metres, with positive to the right.

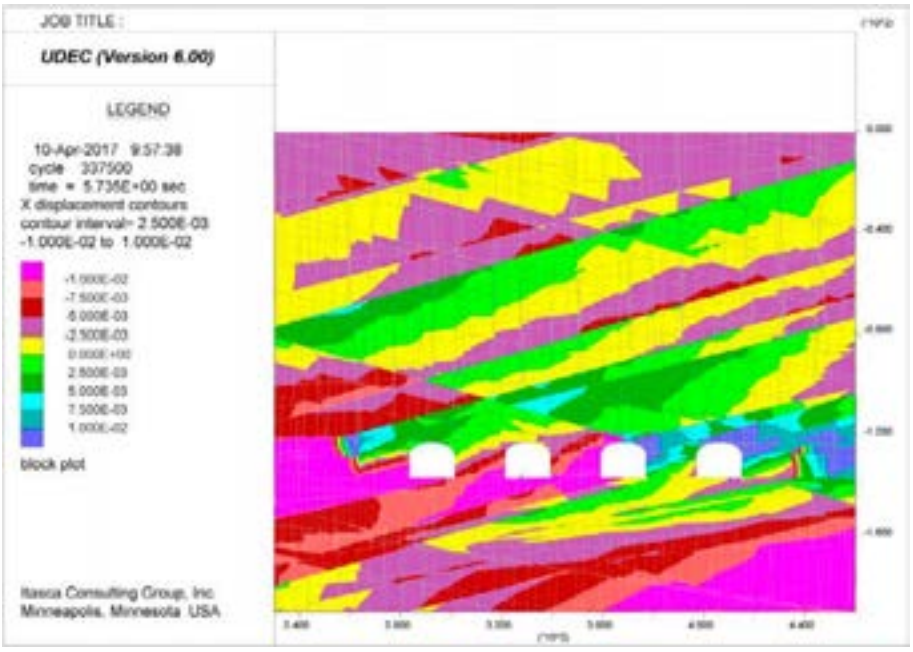


**Figure A255.** UDEC results after strength degradation up to Year 10,000, showing horizontal displacements for SFR 3, DFN 3-3. Displacements are in units of metres, with positive to the right.

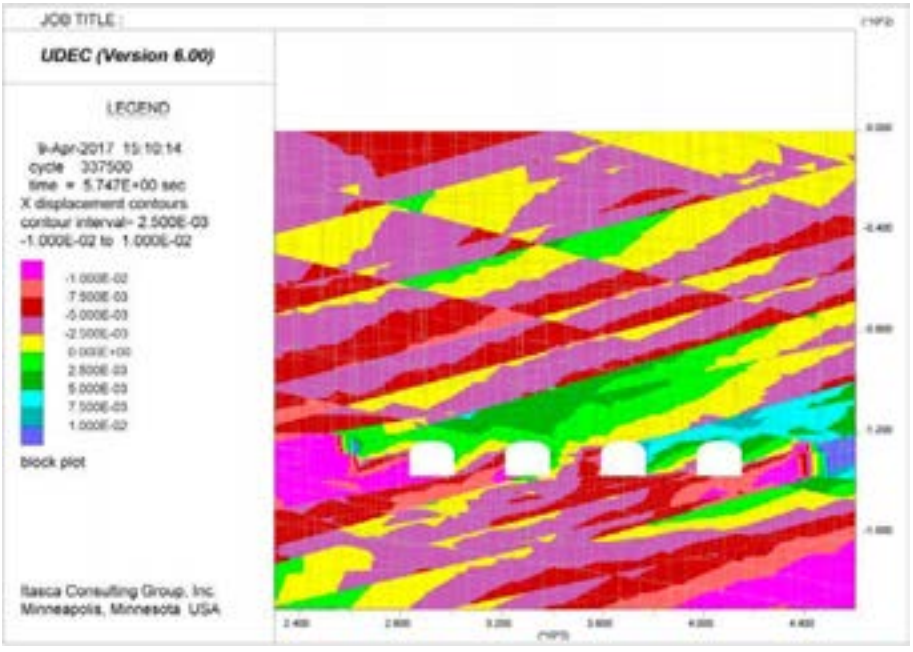


**Figure A256.** UDEC results after strength degradation up to Year 10,000, showing horizontal displacements for SFR 3, DFN 3-4. Displacements are in units of metres, with positive to the right.

## SFR 3 – Year 21,000 Permafrost Melting (Vertical Stress)

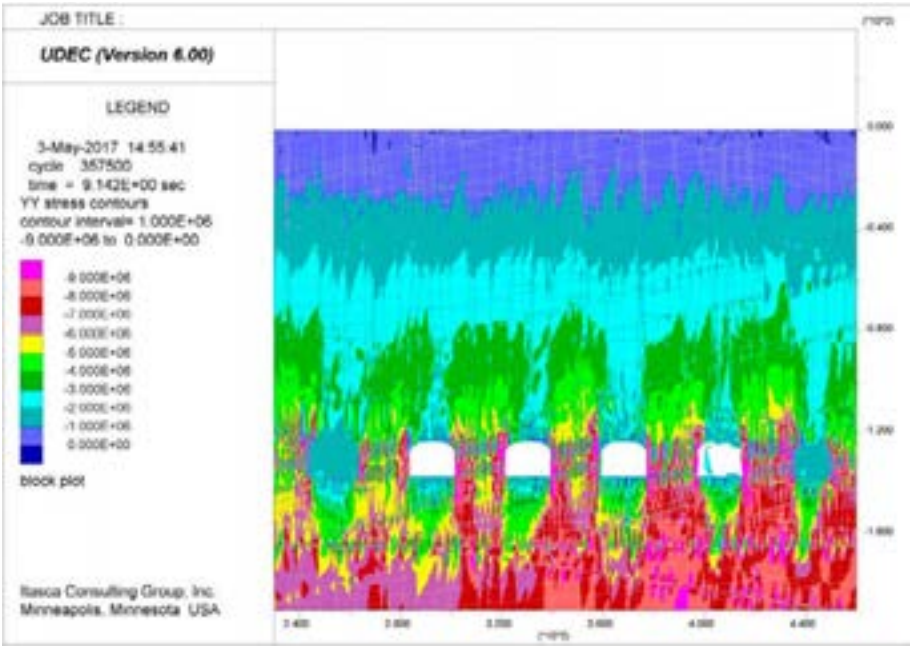


**Figure A257.** UDEC results after strength degradation and permafrost melting at Year 21,000, showing vertical stresses (SYY) for SFR 3, DFN 3-1. Stress magnitudes are in units of Pascals, with compression negative.

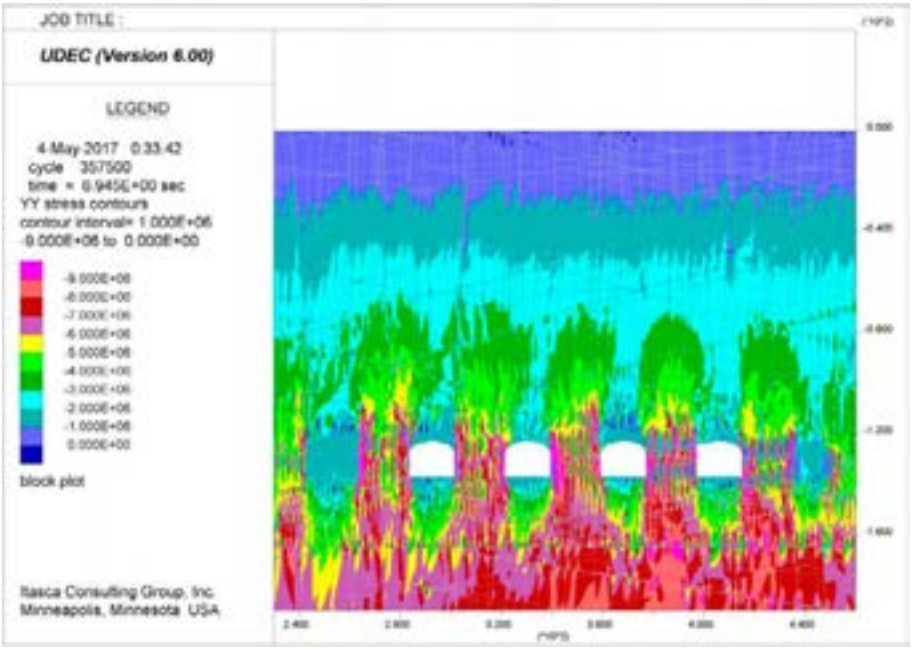


**Figure A258.** UDEC results after strength degradation and permafrost melting at Year 21,000, showing vertical stresses (SYY) for SFR 3, DFN 3-2. Stress magnitudes are in units of Pascals, with compression negative.

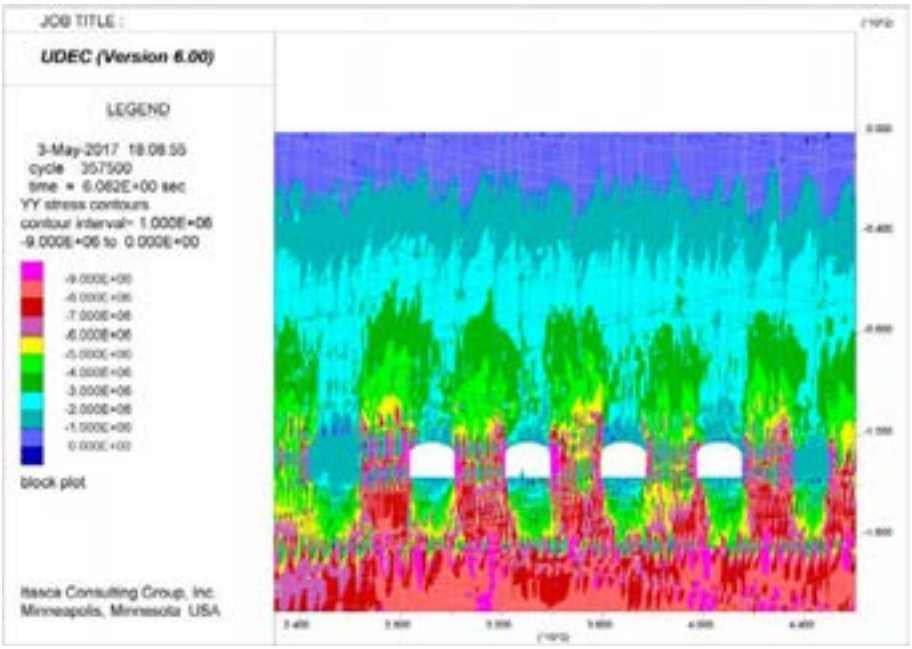


**Figure A259.** UDEC results after strength degradation and permafrost melting at Year 21,000, showing vertical stresses (SYY) for SFR 3, DFN 3-3. Stress magnitudes are in units of Pascals, with compression negative.

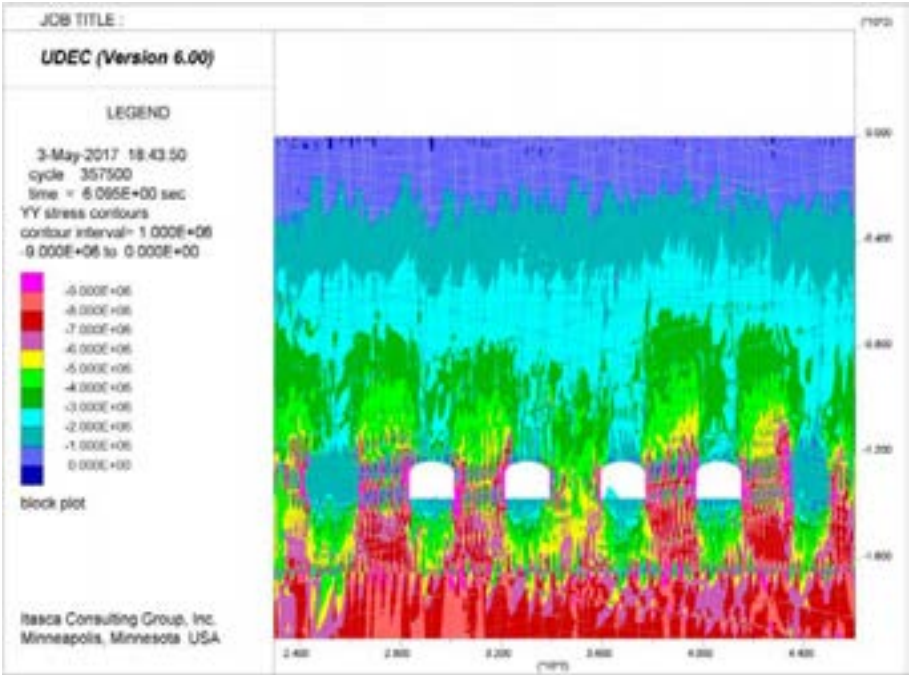


**Figure A260.** UDEC results after strength degradation and permafrost melting at Year 21,000, showing vertical stresses (SYY) for SFR 3, DFN 3-4. Stress magnitudes are in units of Pascals, with compression negative.

## SFR 3 – Year 21,000 Permafrost Melting (Horizontal Stress)

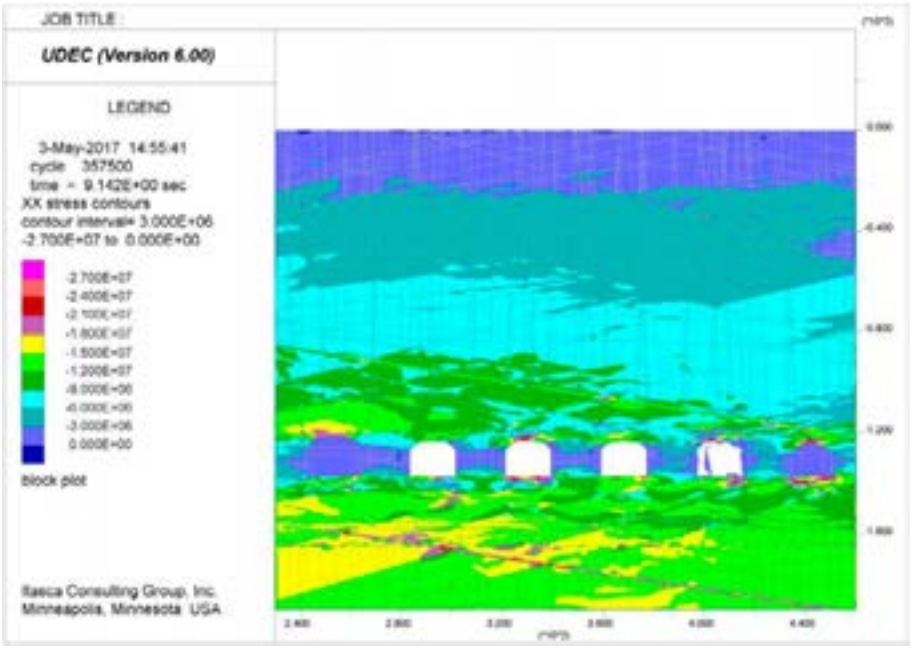


**Figure A261.** UDEC results after strength degradation and permafrost melting at Year 21,000, showing horizontal stresses (SXX) for SFR 3, DFN 3-1. Stress magnitudes are in units of Pascals, with compression negative.

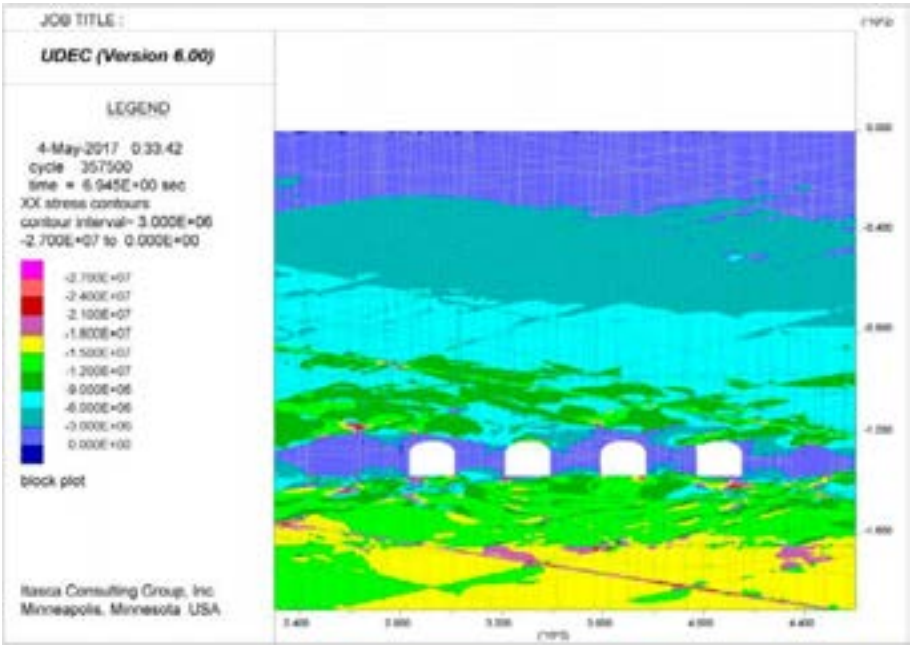


**Figure A262.** UDEC results after strength degradation and permafrost melting at Year 21,000, showing horizontal stresses (SXX) for SFR 3, DFN 3-2. Stress magnitudes are in units of Pascals, with compression negative.

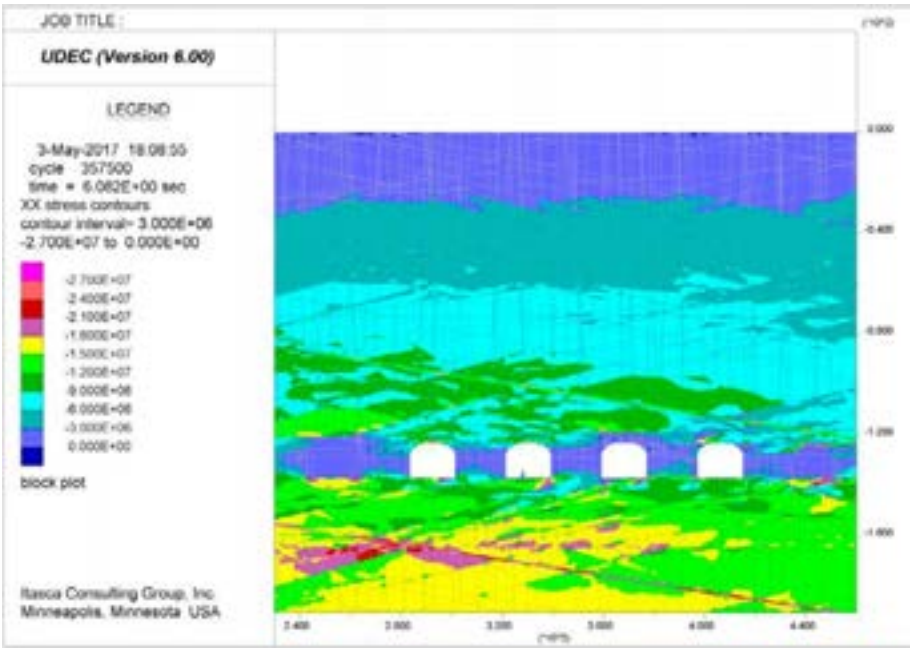


**Figure A263.** UDEC results after strength degradation and permafrost melting at Year 21,000, showing horizontal stresses (SXX) for SFR 3, DFN 3-3. Stress magnitudes are in units of Pascals, with compression negative.

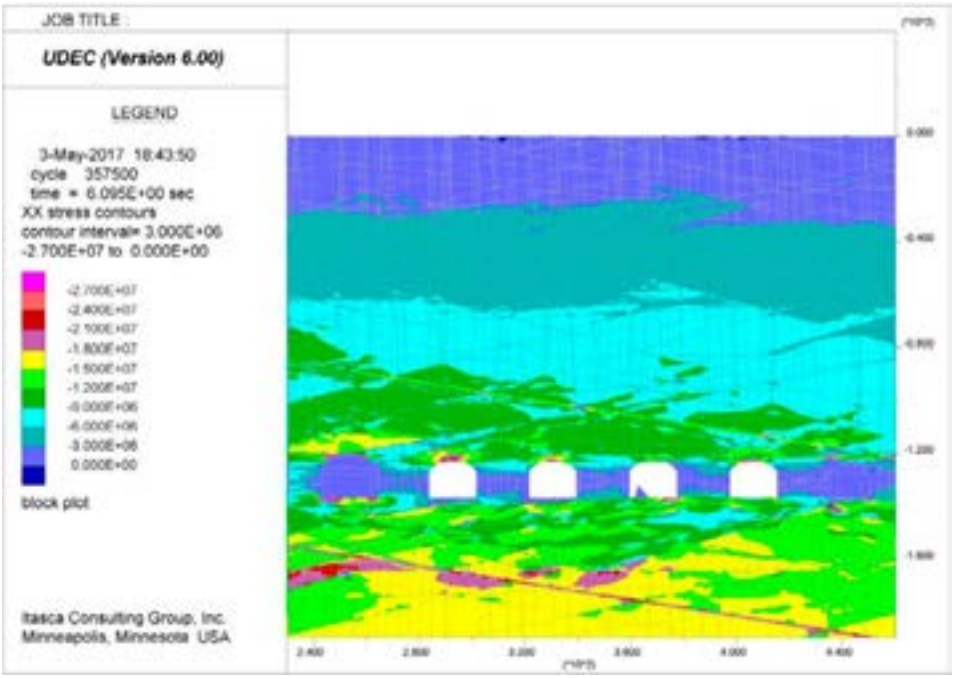


**Figure A264.** UDEC results after strength degradation and permafrost melting at Year 21,000, showing horizontal stresses (SXX) for SFR 3, DFN 3-4. Stress magnitudes are in units of Pascals, with compression negative.

## SFR 3 – Year 21,000 Permafrost Melting (Plasticity Indicators)

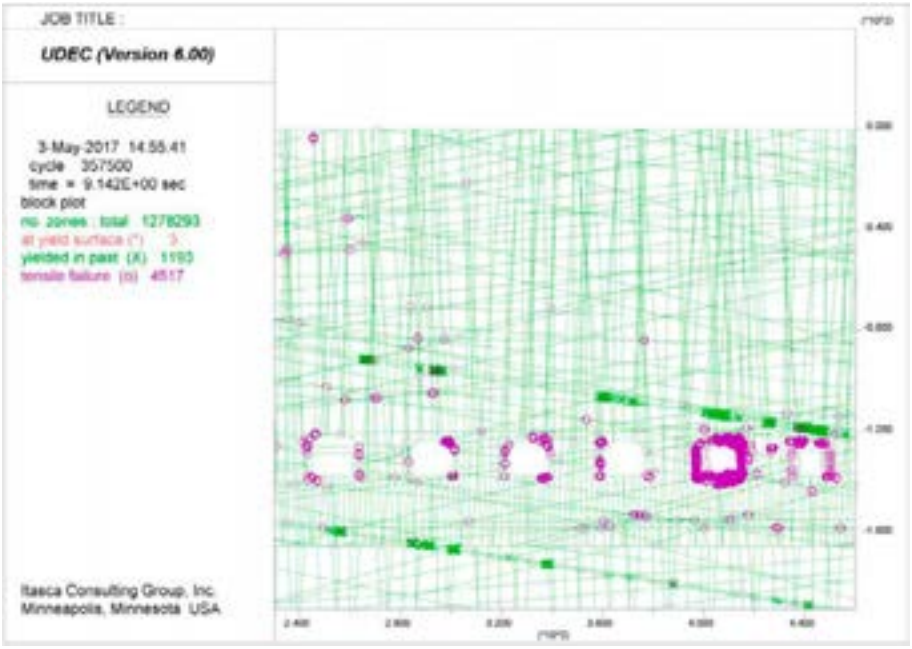


**Figure A265.** UDEC results after strength degradation and permafrost melting at Year 21,000, showing yielded elements for SFR 3, DFN 3-1.

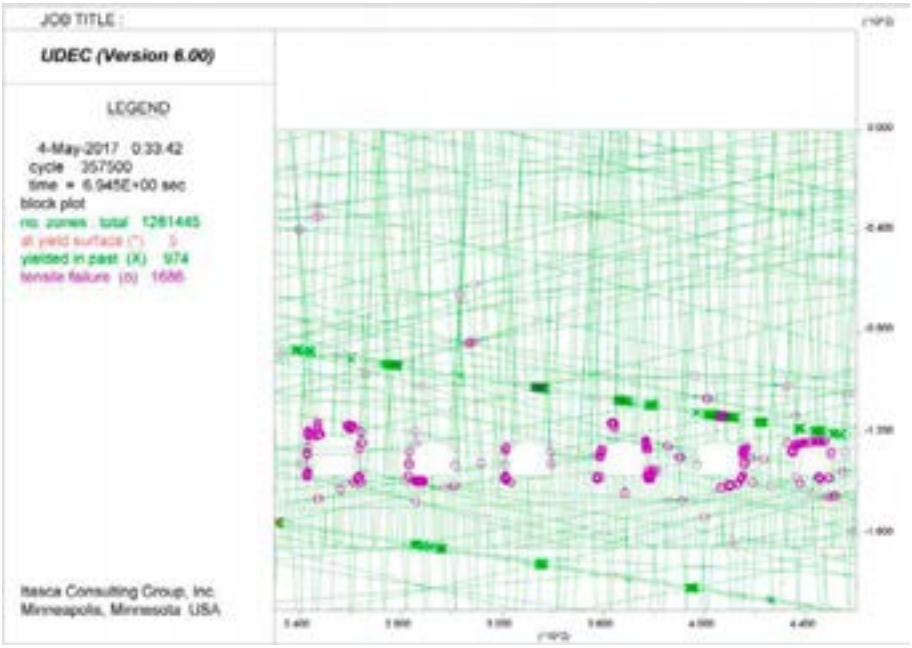


**Figure A266.** UDEC results after strength degradation and permafrost melting at Year 21,000, showing yielded elements for SFR 3, DFN 3-2.

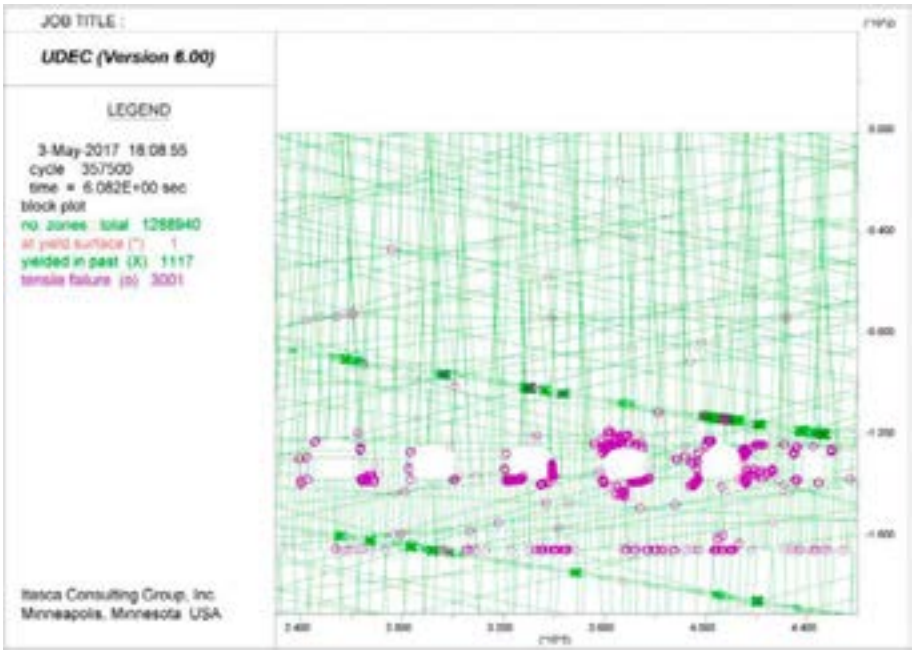


**Figure A267.** UDEC results after strength degradation and permafrost melting at Year 21,000, showing yielded elements for SFR 3, DFN 3-3.

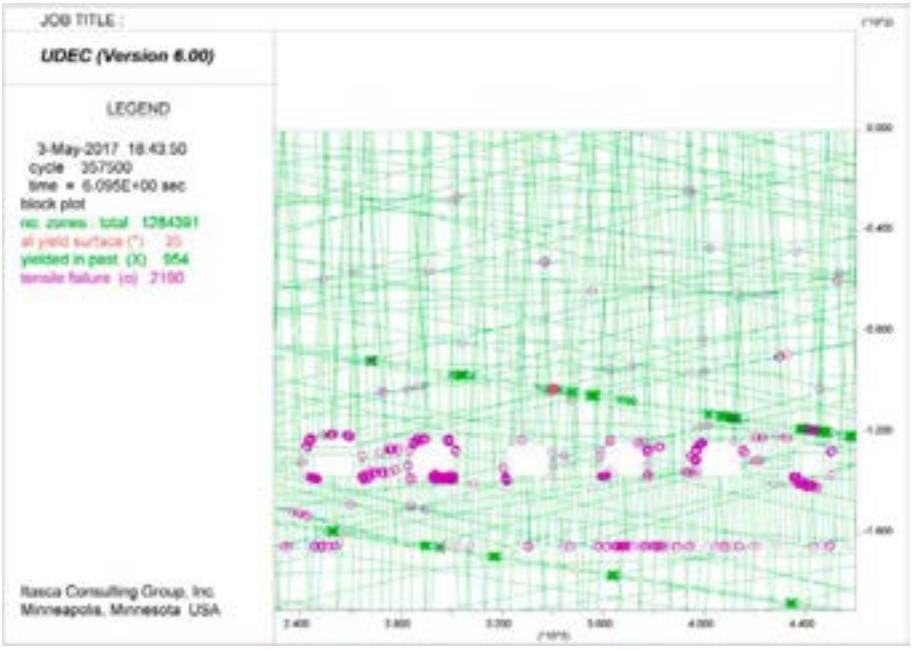


**Figure A268.** UDEC results after strength degradation and permafrost melting at Year 21,000, showing yielded elements for SFR 3, DFN 3-4.

## SFR 3 – Year 21,000 Permafrost Melting (Displacement Vectors)

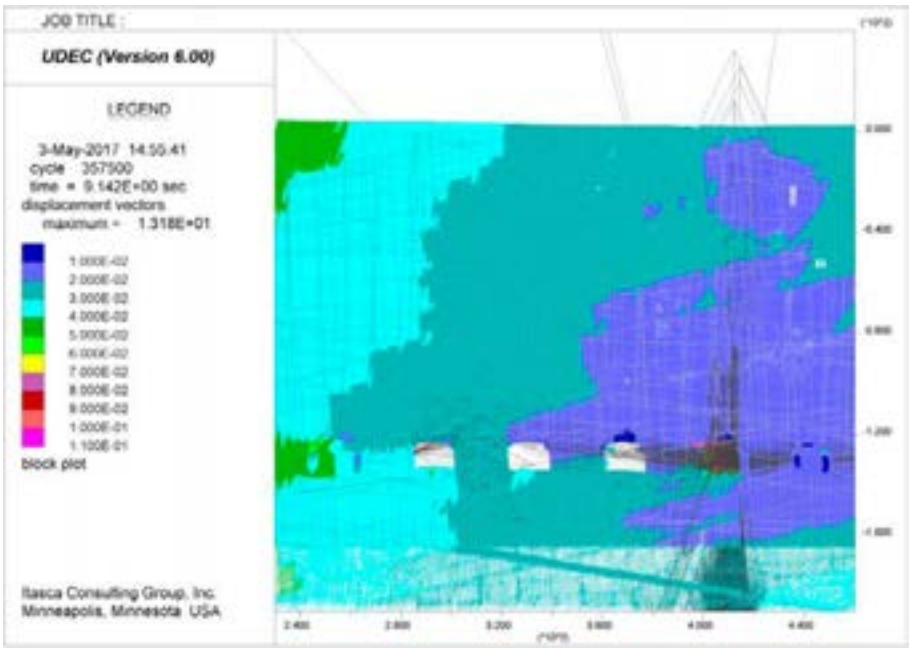


**Figure A269.** UDEC results after strength degradation and permafrost melting at Year 21,000, showing displacement vectors for SFR 3, DFN 3-1. Displacement magnitudes are in units of metres.

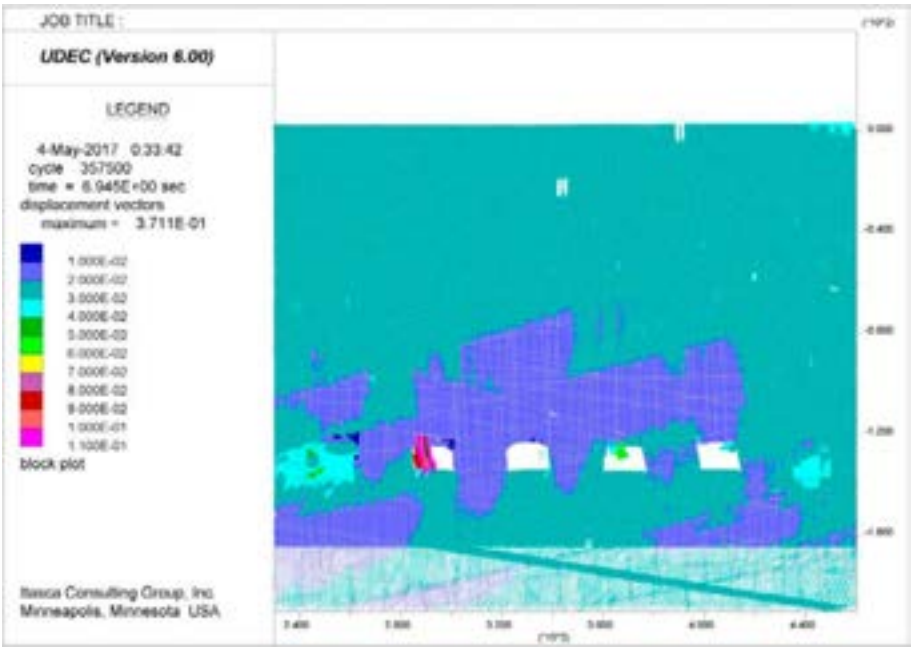


**Figure A270.** UDEC results after strength degradation and permafrost melting at Year 21,000, showing displacement vectors for SFR 3, DFN 3-2. Displacement magnitudes are in units of metres.

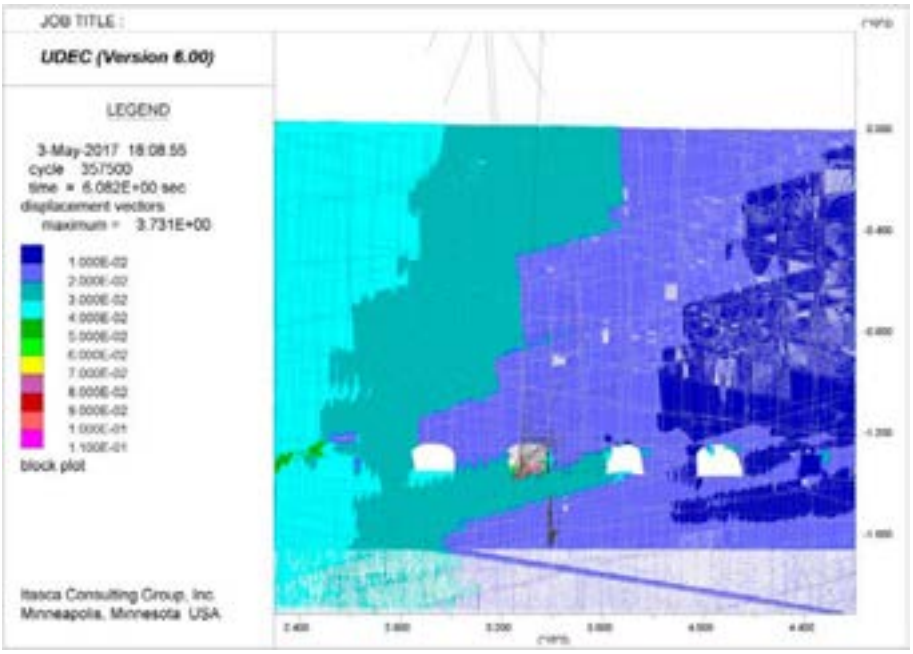


**Figure A271.** UDEC results after strength degradation and permafrost melting at Year 21,000, showing displacement vectors for SFR 3, DFN 3-3. Displacement magnitudes are in units of metres.

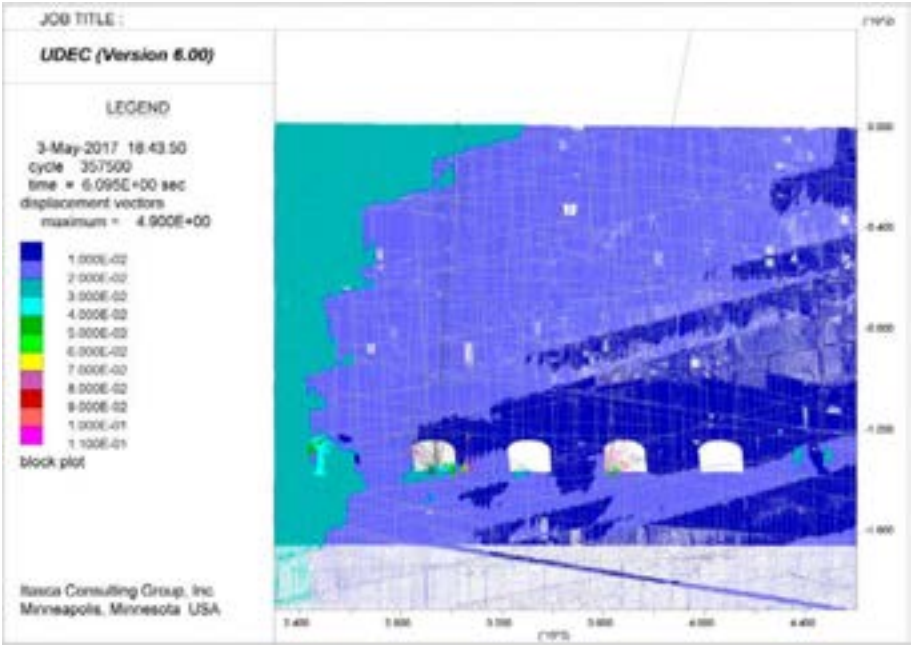


**Figure A272.** UDEC results after strength degradation and permafrost melting at Year 21,000, showing displacement vectors for SFR 3, DFN 3-4. Displacement magnitudes are in units of metres.

## SFR 3 – Year 21,000 Permafrost Melting (Fracture Shear Displacement)

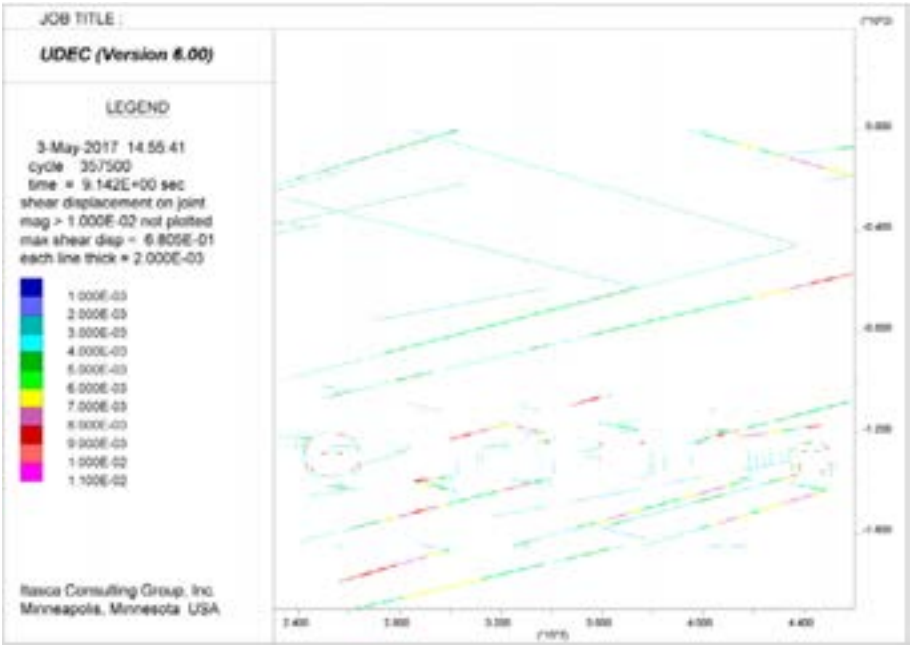


**Figure A273.** UDEC results after strength degradation and permafrost melting at Year 21,000, showing shear displacements along fractures for SFR 3, DFN 3-1. Displacements are in units of metres.

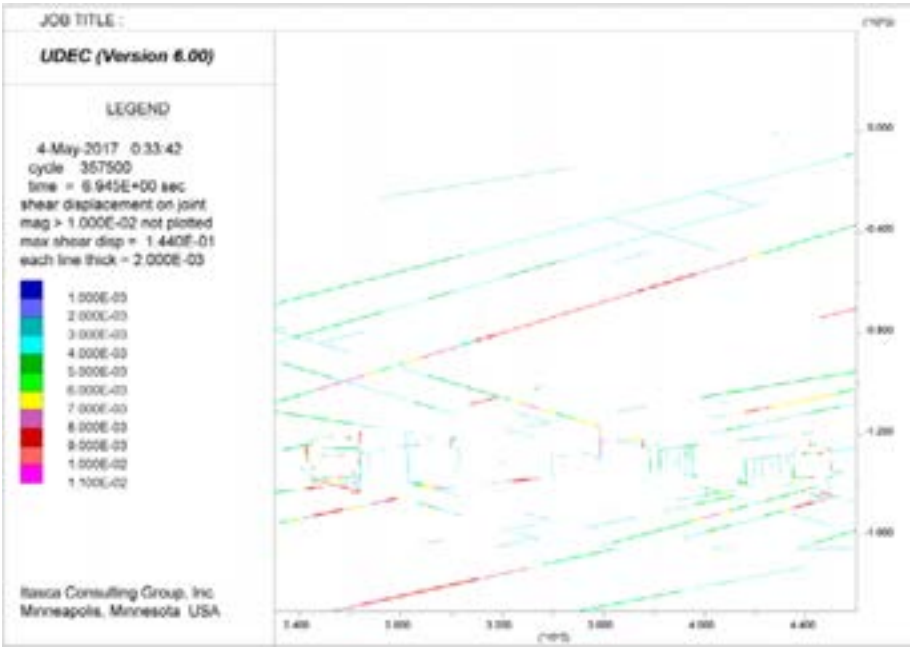


**Figure A274.** UDEC results after strength degradation and permafrost melting at Year 21,000, showing shear displacements along fractures for SFR 3, DFN 3-2. Displacements are in units of metres.

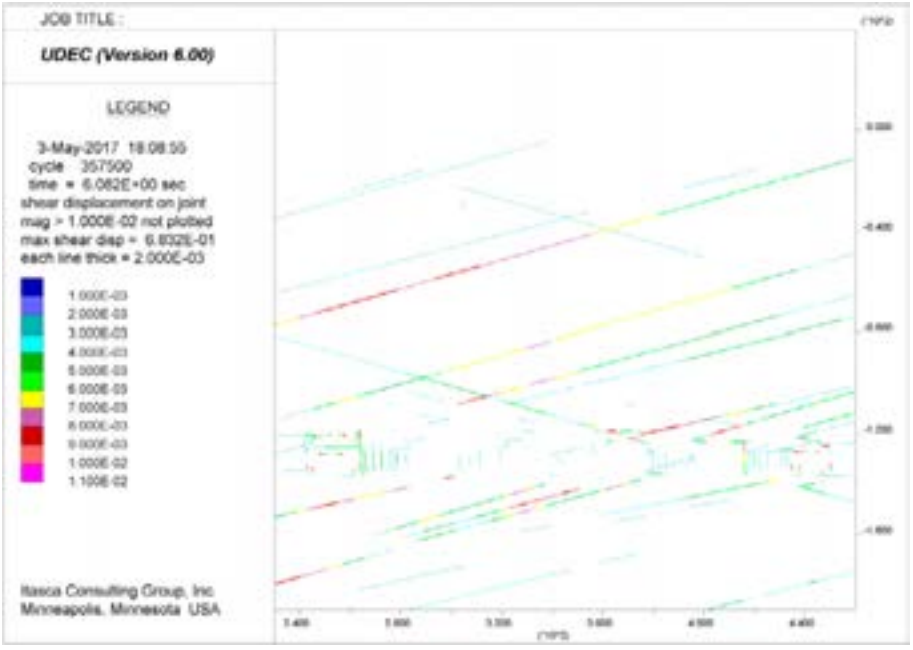


**Figure A275.** UDEC results after strength degradation and permafrost melting at Year 21,000, showing shear displacements along fractures for SFR 3, DFN 3-3. Displacements are in units of metres.

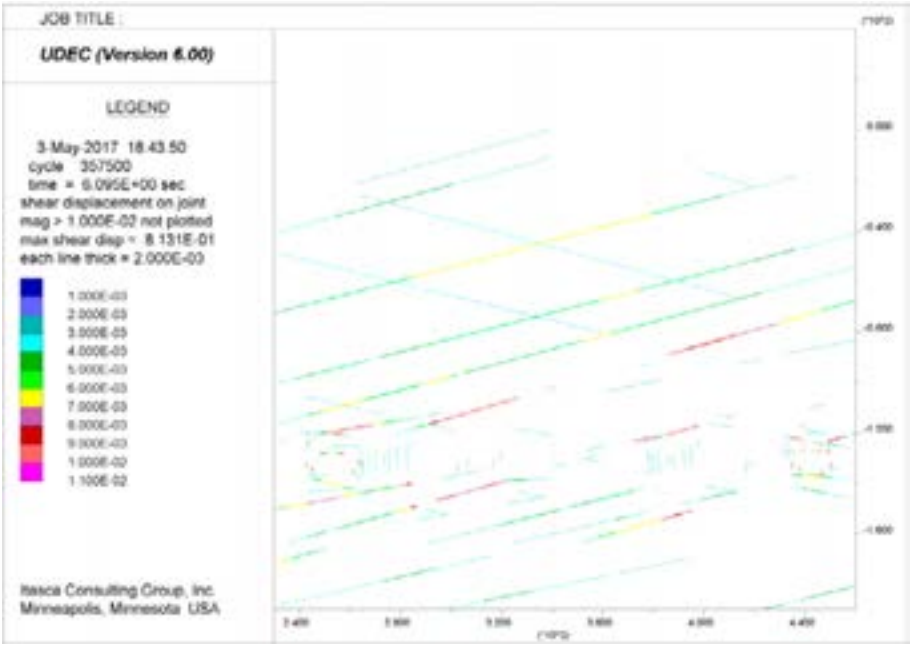


**Figure A276.** UDEC results after strength degradation and permafrost melting at Year 21,000, showing shear displacements along fractures for SFR 3, DFN 3-4. Displacements are in units of metres.

## SFR 3 – Year 21,000 Permafrost Melting (Vertical Displacements)

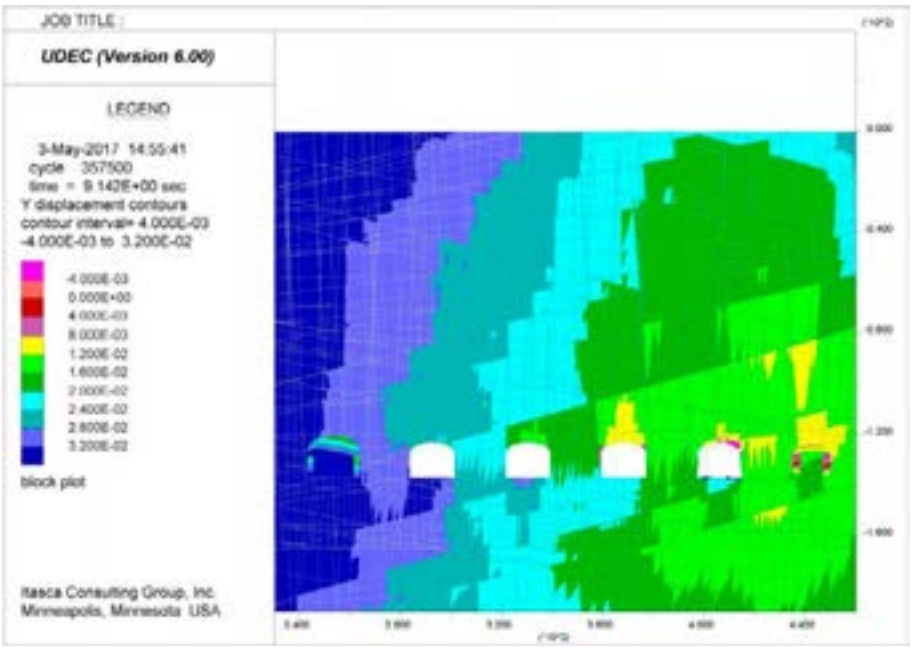


**Figure A277.** UDEC results after strength degradation and permafrost melting at Year 21,000, showing vertical displacements for SFR 3, DFN 3-1. Displacements are in units of metres, with positive up.

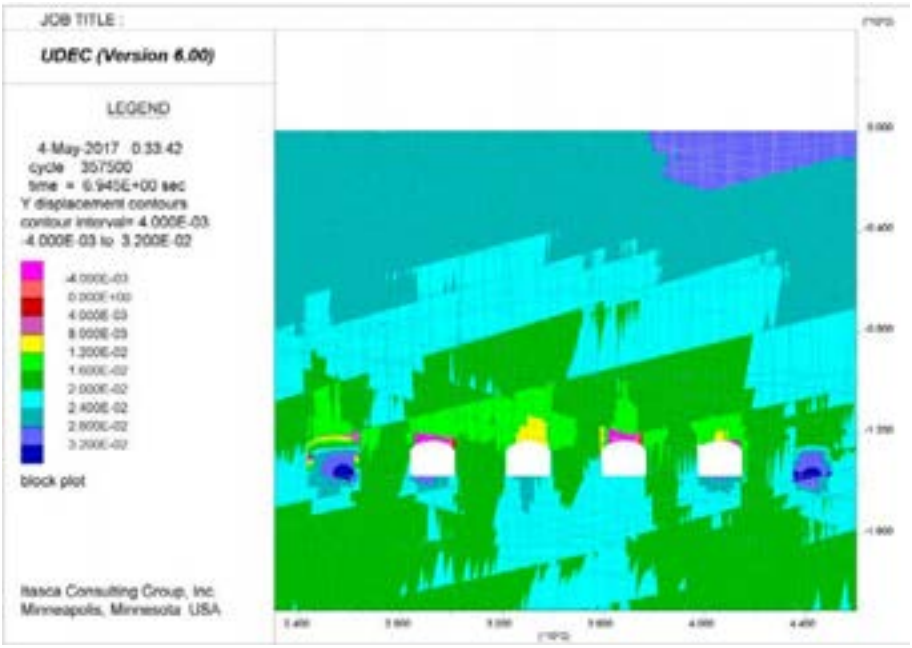


**Figure A278.** UDEC results after strength degradation and permafrost melting at Year 21,000, showing vertical displacements for SFR 3, DFN 3-2. Displacements are in units of metres, with positive up.

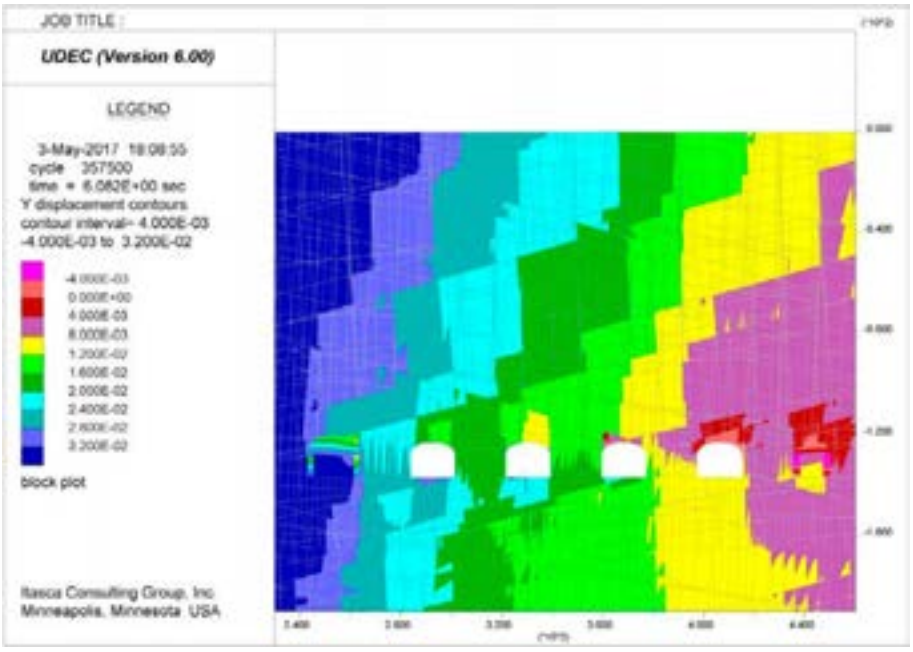


**Figure A279.** UDEC results after strength degradation and permafrost melting at Year 21,000, showing vertical displacements for SFR 3, DFN 3-3. Displacements are in units of metres, with positive up.

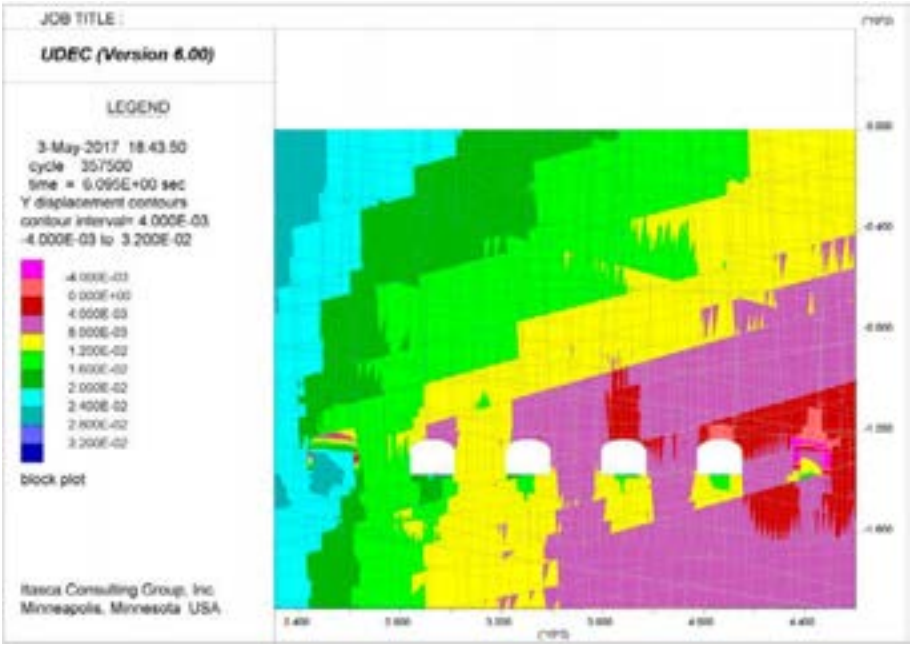


**Figure A280.** UDEC results after strength degradation and permafrost melting at Year 21,000, showing vertical displacements for SFR 3, DFN 3-4. Displacements are in units of metres, with positive up.

## SFR 3 – Year 21,000 Permafrost Melting (Horizontal Displacements)

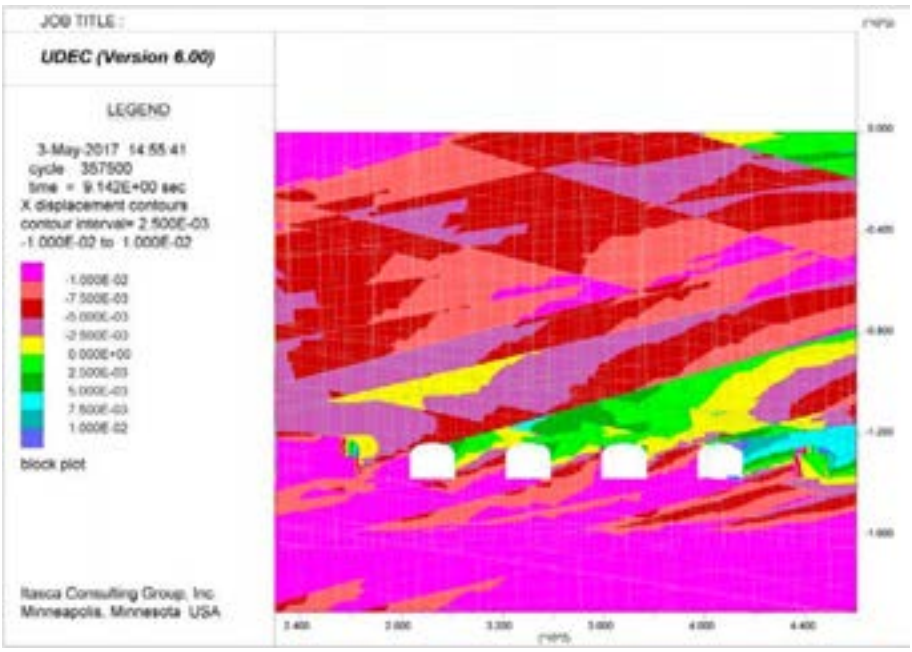


**Figure A281.** UDEC results after strength degradation and permafrost melting at Year 21,000, showing horizontal displacements for SFR 3, DFN 3-1. Displacements are in units of metres, with positive to the right.

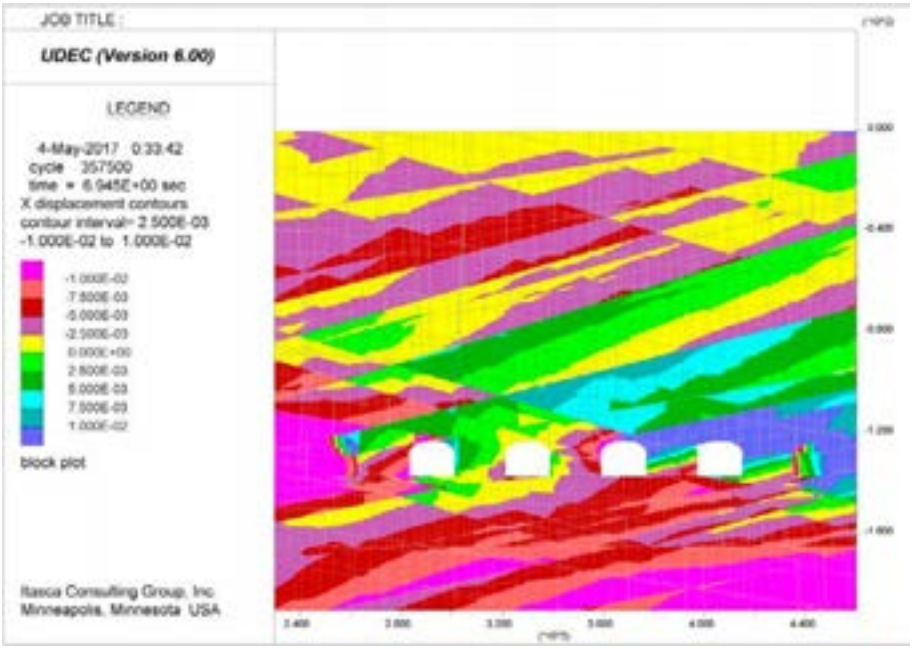


**Figure A282.** UDEC results after strength degradation and permafrost melting at Year 21,000, showing horizontal displacements for SFR 3, DFN 3-2. Displacements are in units of metres, with positive to the right.

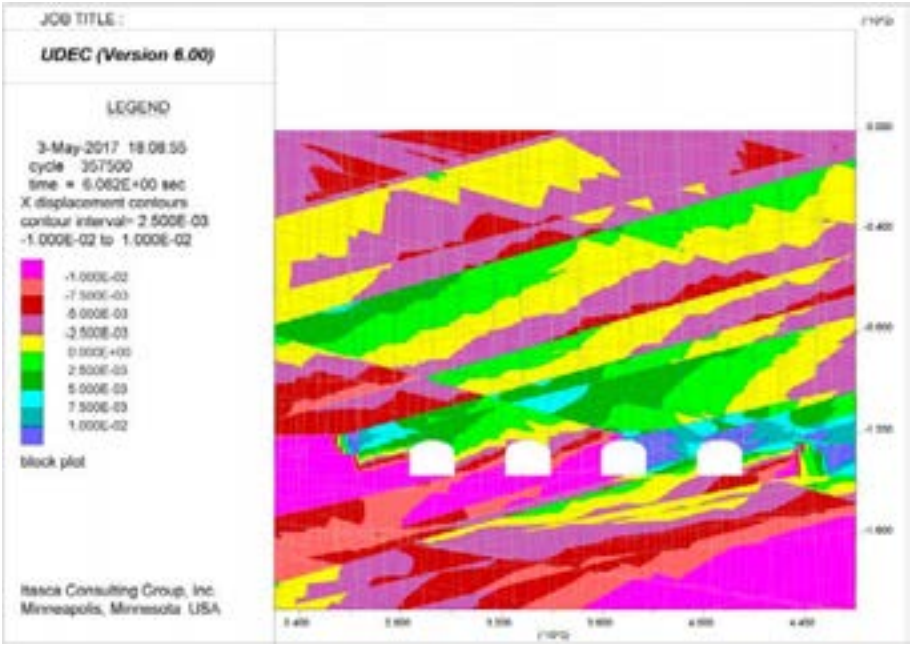


**Figure A283.** UDEC results after strength degradation and permafrost melting at Year 21,000, showing horizontal displacements for SFR 3, DFN 3-3. Displacements are in units of metres, with positive to the right.

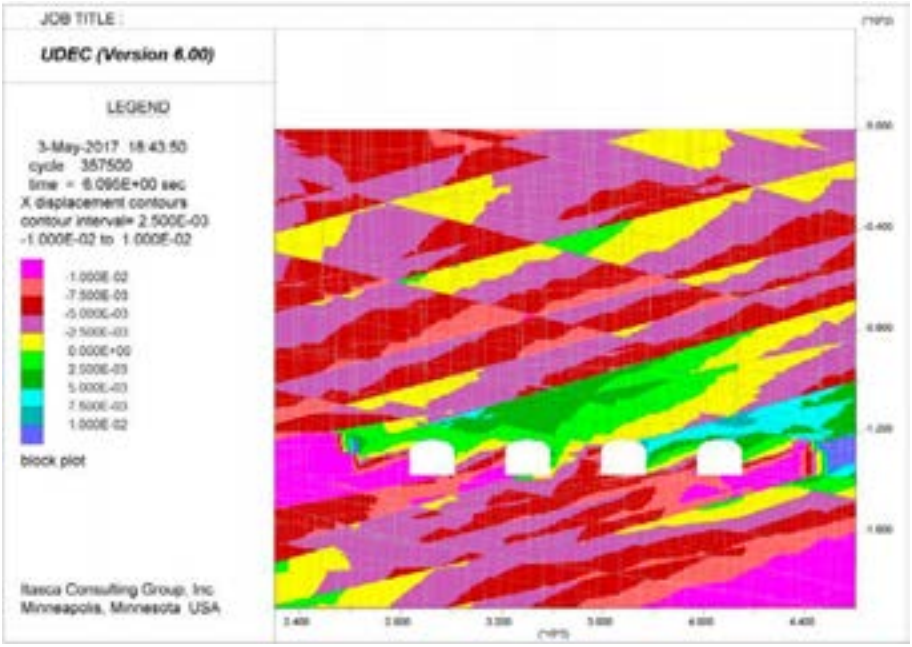


**Figure A284.** UDEC results after strength degradation and permafrost melting at Year 21,000, showing horizontal displacements for SFR 3, DFN 3-4. Displacements are in units of metres, with positive to the right.

## SFR 3 – Year 50,000 Glacial Loading (Vertical Stress)

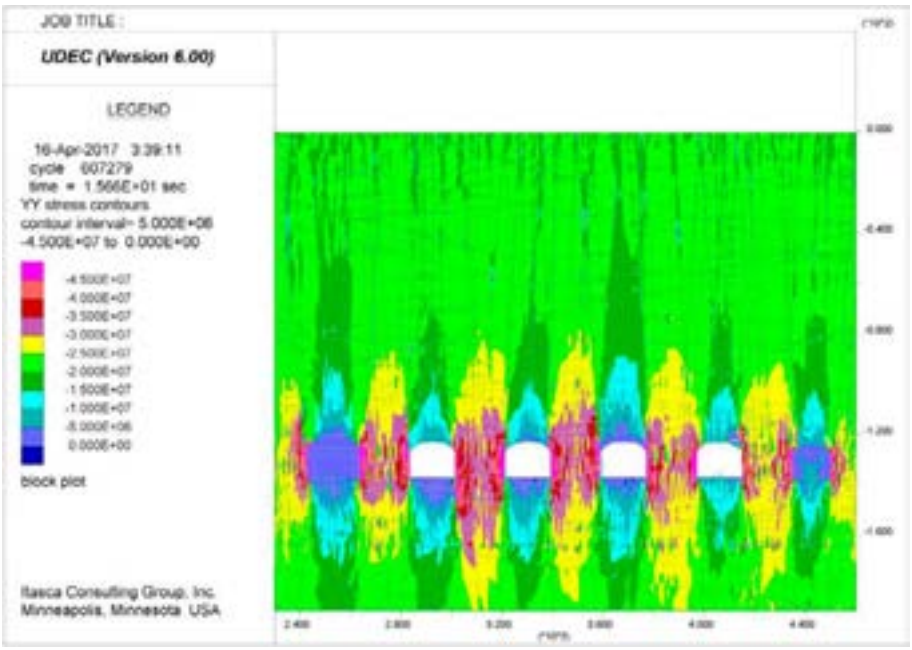


**Figure A285.** UDEC results after strength degradation and glacial loading at Year 50,000, showing vertical stresses (SYY) for SFR 3, DFN 3-1. Stress magnitudes are in units of Pascals, with compression negative.

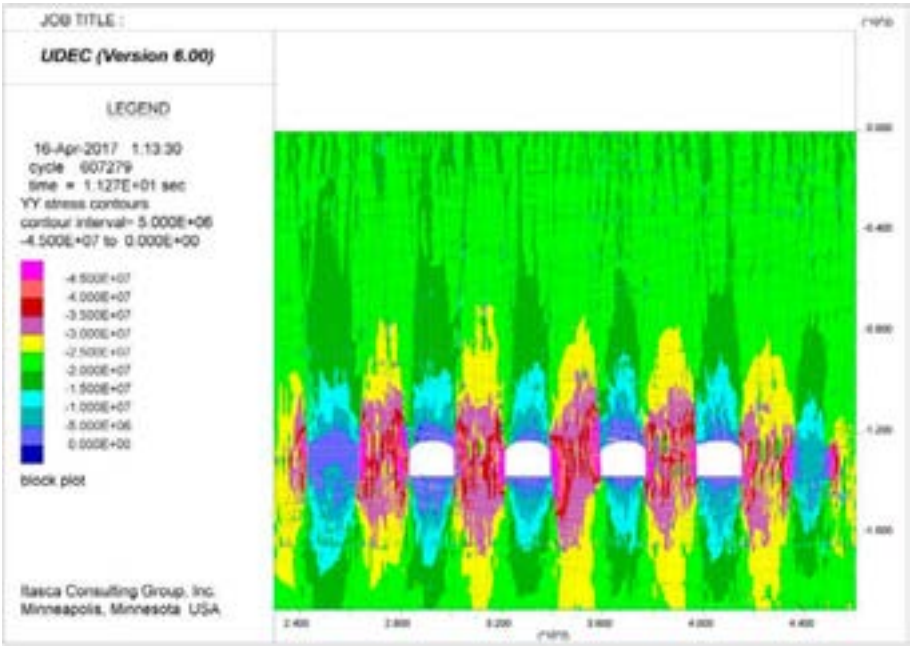


**Figure A286.** UDEC results after strength degradation and glacial loading at Year 50,000, showing vertical stresses (SYY) for SFR 3, DFN 3-2. Stress magnitudes are in units of Pascals, with compression negative.

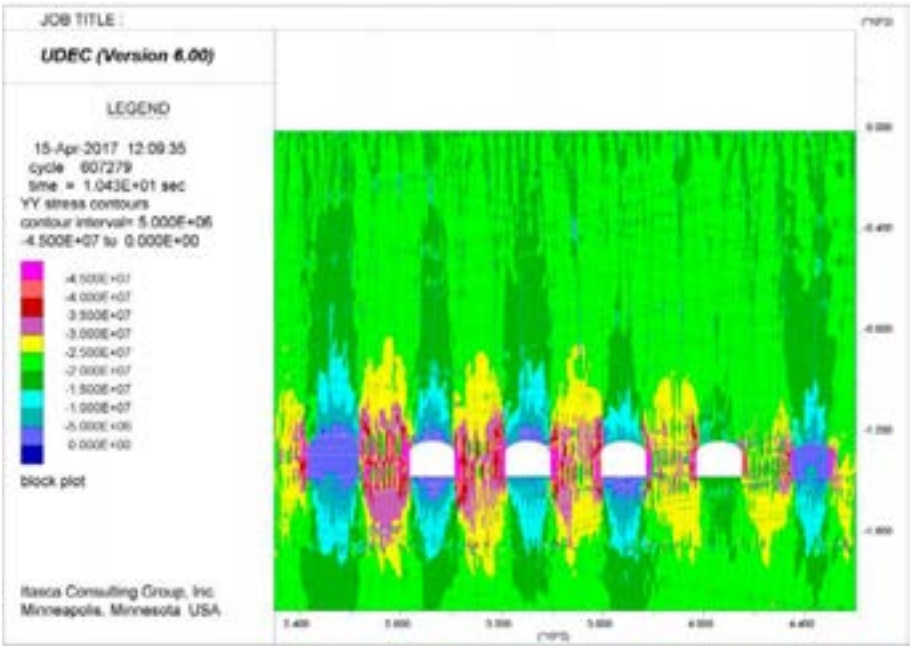


**Figure A287.** UDEC results after strength degradation and glacial loading at Year 50,000, showing vertical stresses (SYY) for SFR 3, DFN 3-3. Stress magnitudes are in units of Pascals, with compression negative.

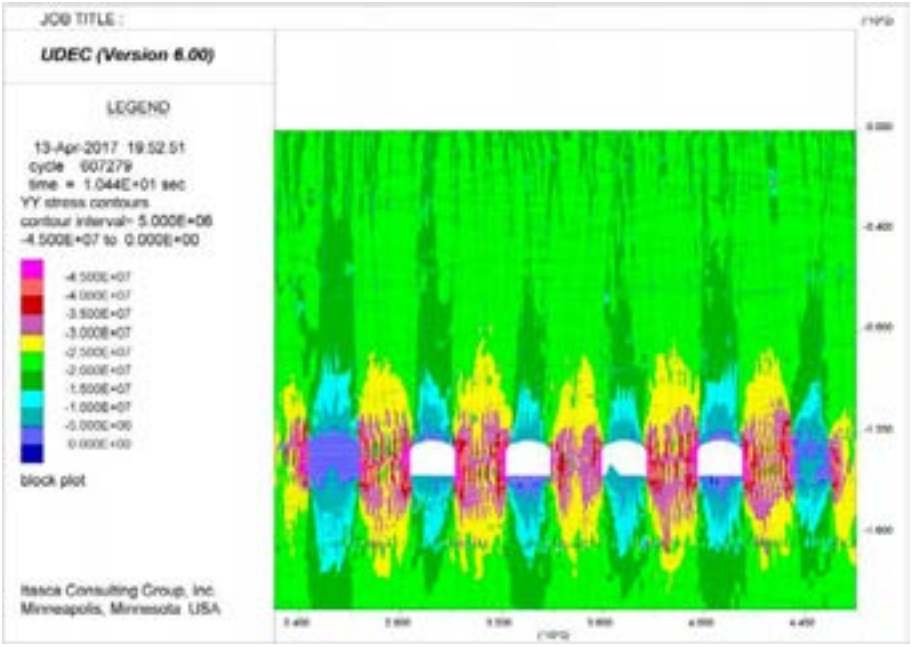


**Figure A288.** UDEC results after strength degradation and glacial loading at Year 50,000, showing vertical stresses (SYY) for SFR 3, DFN 3-4. Stress magnitudes are in units of Pascals, with compression negative.

## SFR 3 – Year 50,000 Glacial Loading (Horizontal Stress)

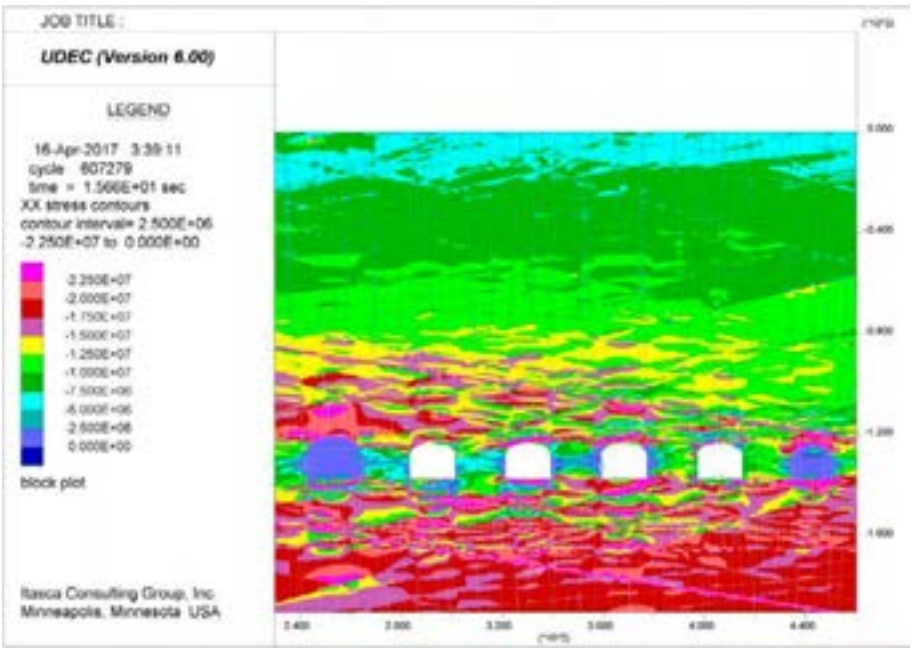


**Figure A289.** UDEC results after strength degradation and glacial loading at Year 50,000, showing horizontal stresses (SXX) for SFR 3, DFN 3-1. Stress magnitudes are in units of Pascals, with compression negative.

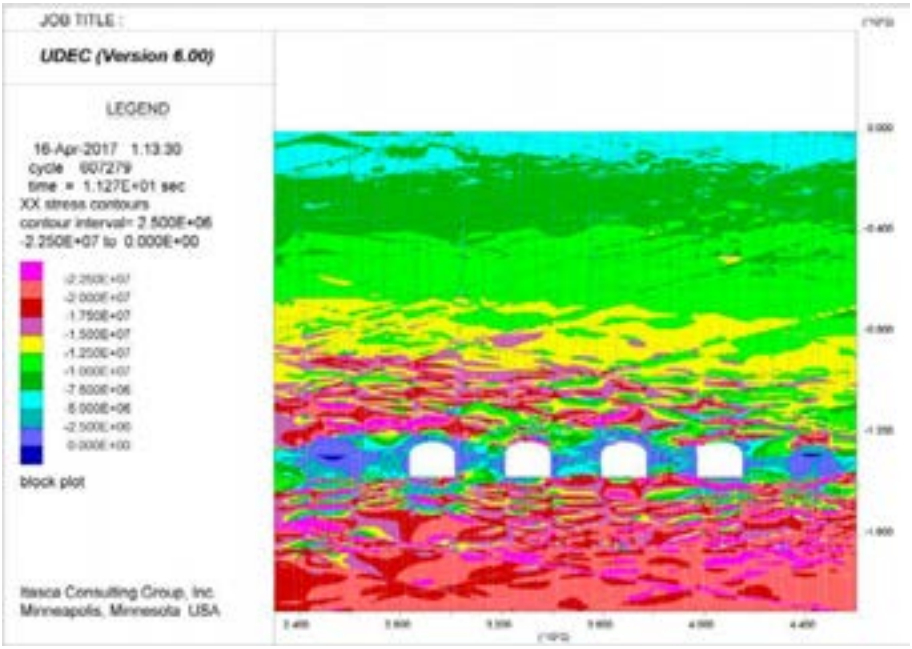


**Figure A290.** UDEC results after strength degradation and glacial loading at Year 50,000, showing horizontal stresses (SXX) for SFR 3, DFN 3-2. Stress magnitudes are in units of Pascals, with compression negative.

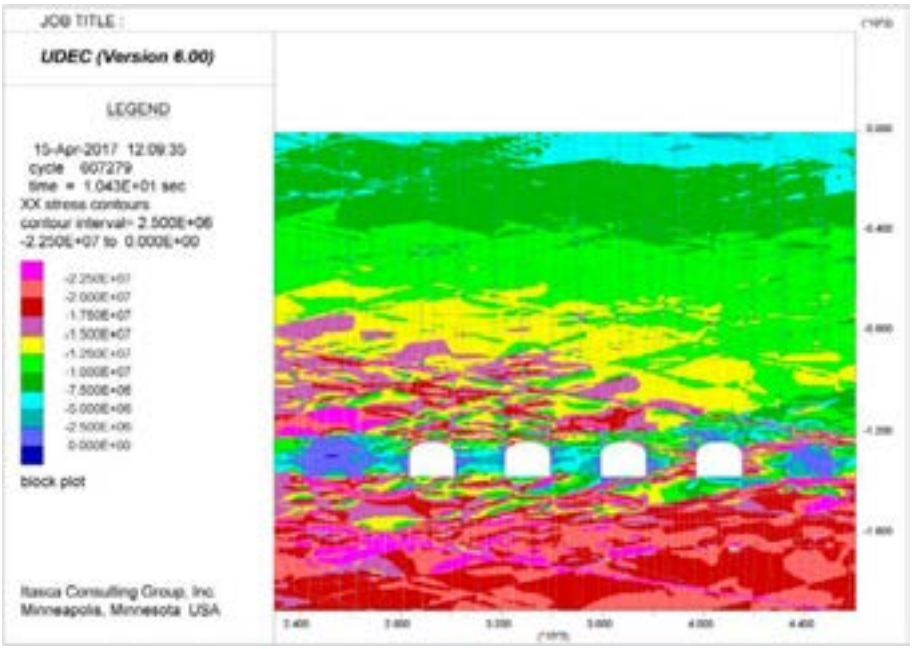


**Figure A291.** UDEC results after strength degradation and glacial loading at Year 50,000, showing horizontal stresses (SXX) for SFR 3, DFN 3-3. Stress magnitudes are in units of Pascals, with compression negative.

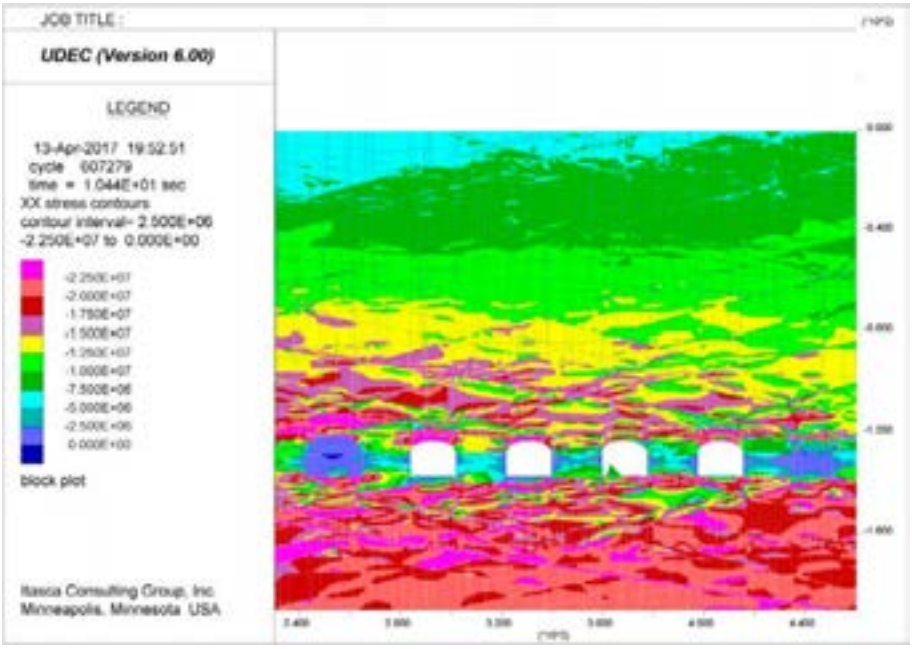


**Figure A292.** UDEC results after strength degradation and glacial loading at Year 50,000, showing horizontal stresses (SXX) for SFR 3, DFN 3-4. Stress magnitudes are in units of Pascals, with compression negative.

## SFR 3 – Year 50,000 Glacial Loading (Plasticity Indicators)

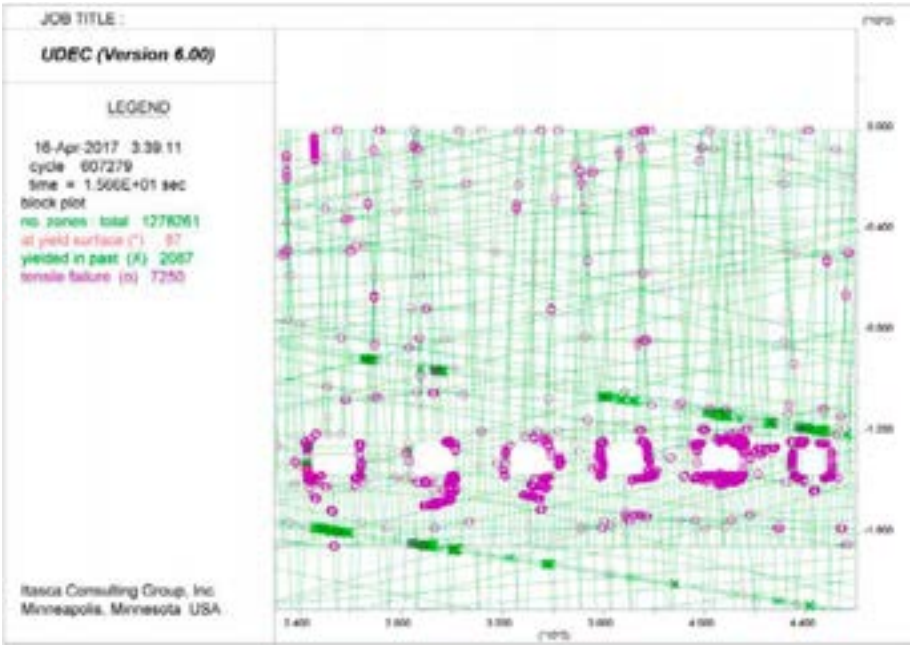


**Figure A293.** UDEC results after strength degradation and glacial loading at Year 50,000, showing yielded elements for SFR 3, DFN 3-1.

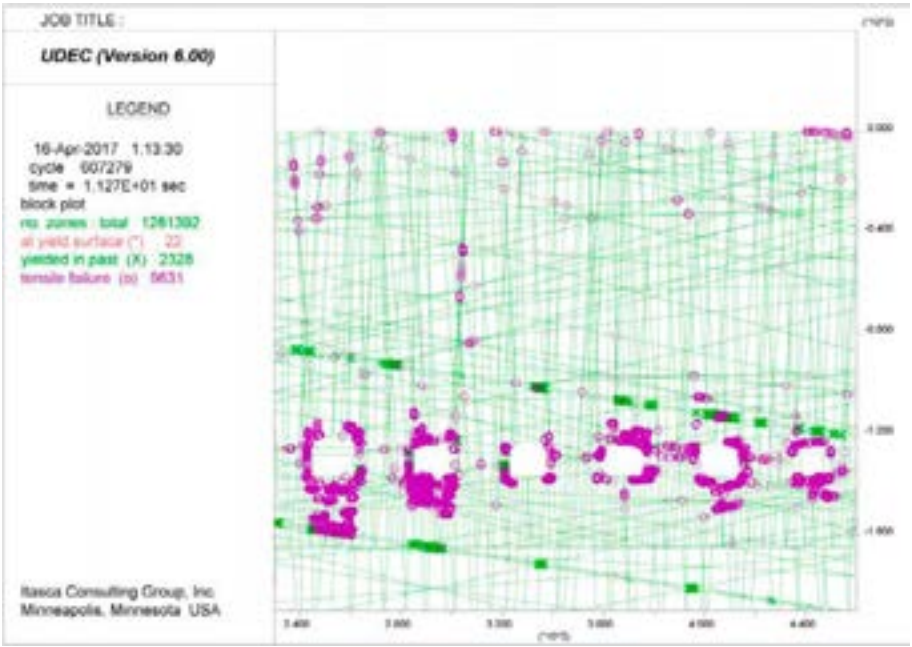


**Figure A294.** UDEC results after strength degradation and glacial loading at Year 50,000, showing yielded elements for SFR 3, DFN 3-2.

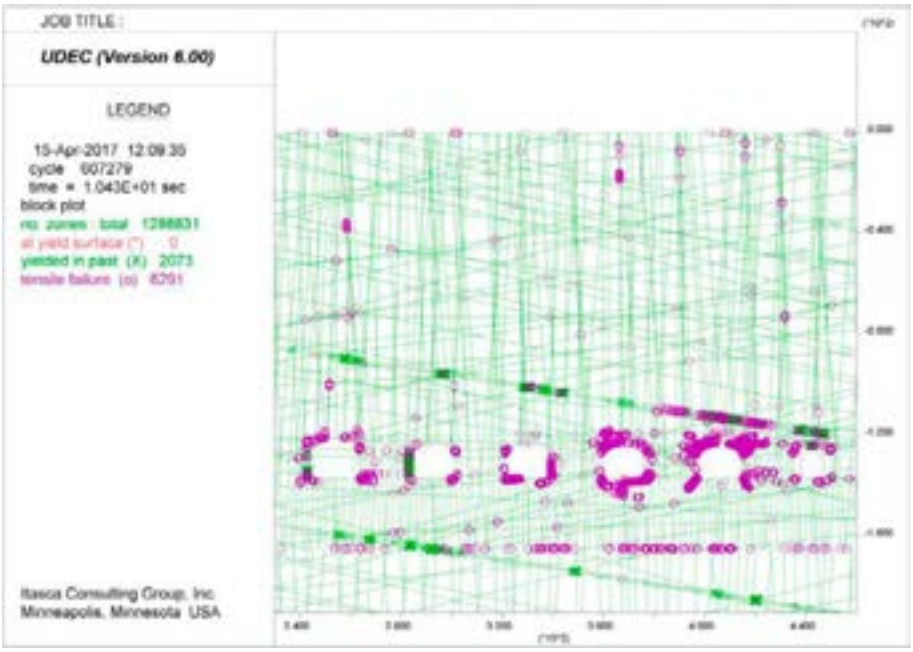


**Figure A295.** UDEC results after strength degradation and glacial loading at Year 50,000, showing yielded elements for SFR 3, DFN 3-3.

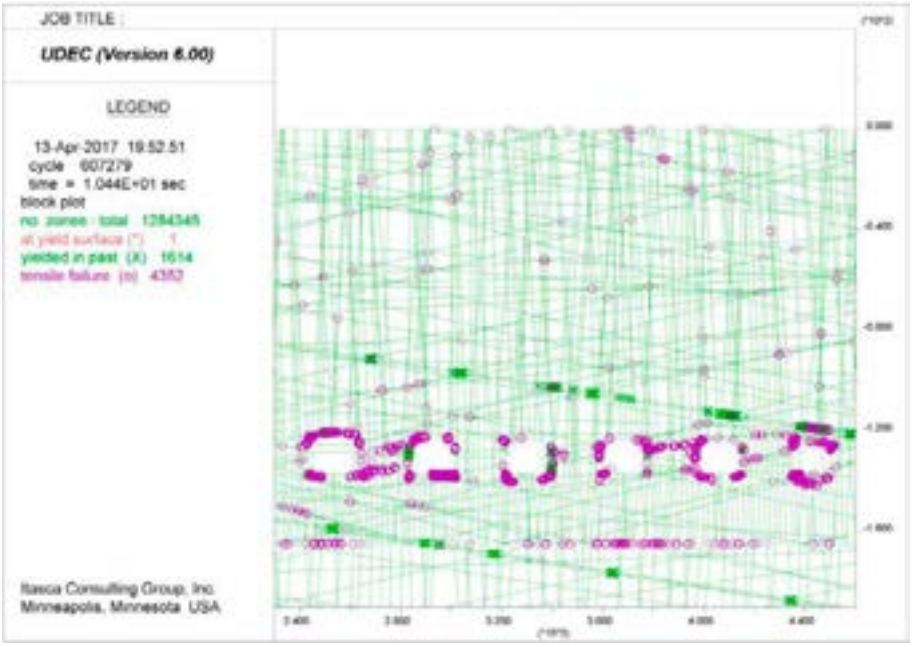


**Figure A296.** UDEC results after strength degradation and glacial loading at Year 50,000, showing yielded elements for SFR 3, DFN 3-4.

## SFR 3 – Year 50,000 Glacial Loading (Displacement Vectors)

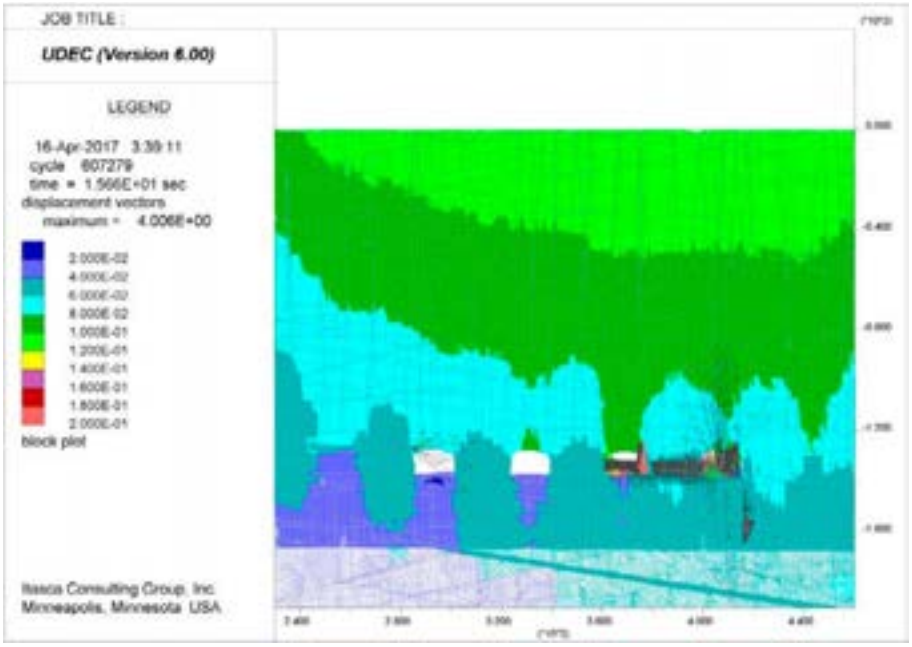


**Figure A297.** UDEC results after strength degradation and glacial loading at Year 50,000, showing displacement vectors for SFR 3, DFN 3-1. Displacement magnitudes are in units of metres.

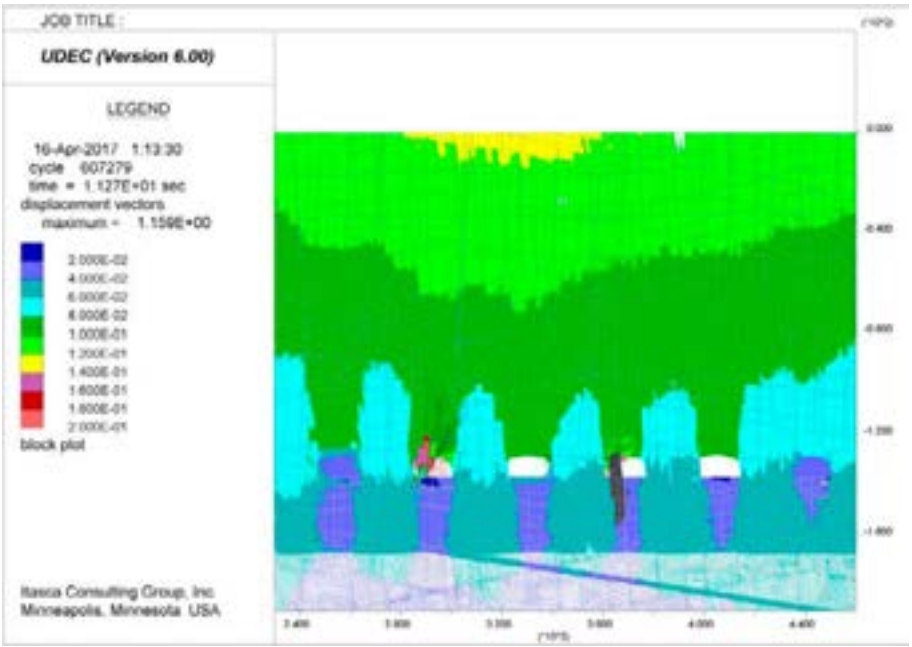


**Figure A298.** UDEC results after strength degradation and glacial loading at Year 50,000, showing displacement vectors for SFR 3, DFN 3-2. Displacement magnitudes are in units of metres.

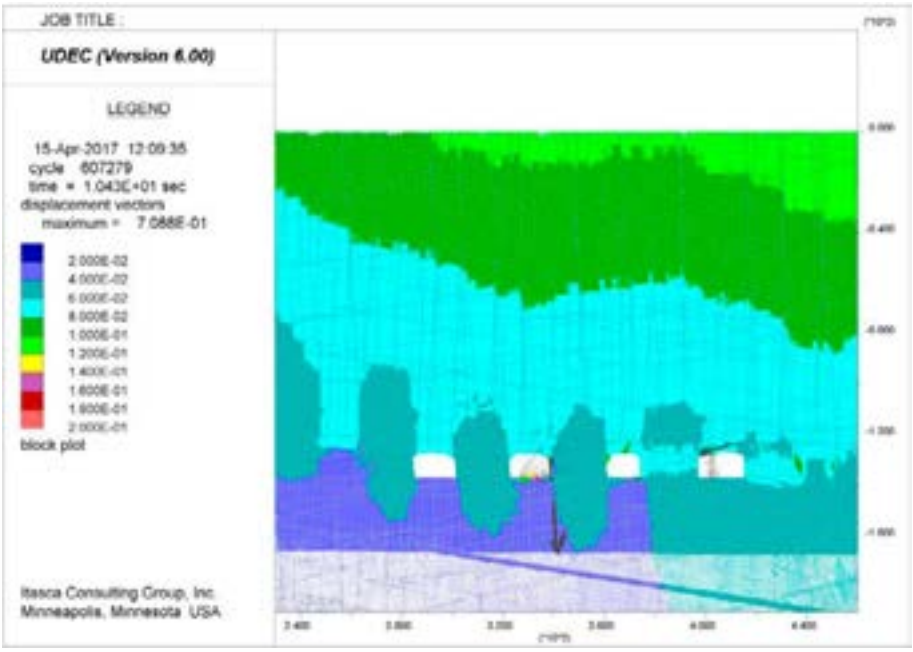


**Figure A299.** UDEC results after strength degradation and glacial loading at Year 50,000, showing displacement vectors for SFR 3, DFN 3-3. Displacement magnitudes are in units of metres.

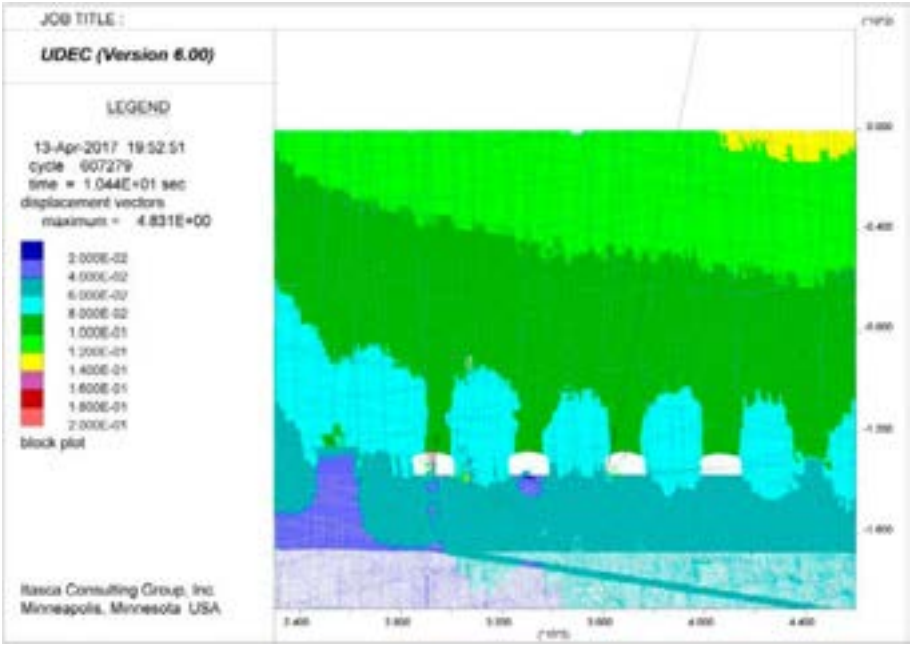


**Figure A300.** UDEC results after strength degradation and glacial loading at Year 50,000, showing displacement vectors for SFR 3, DFN 3-4. Displacement magnitudes are in units of metres.

## SFR 3 – Year 50,000 Glacial Loading (Fracture Shear Displacement)

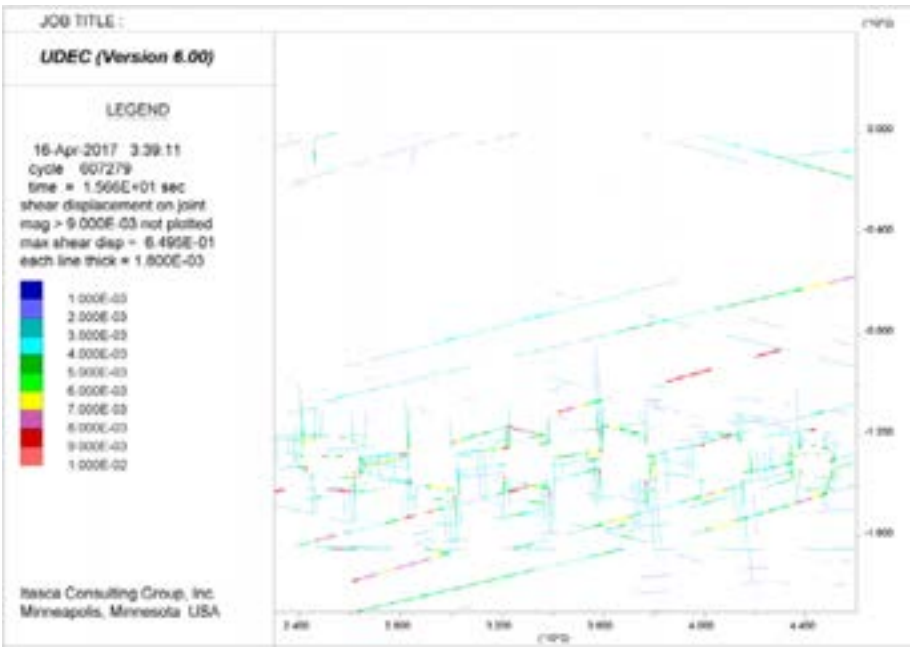


**Figure A301.** UDEC results after strength degradation and glacial loading at Year 50,000, showing shear displacements along fractures for SFR 3, DFN 3-1. Displacements are in units of metres.

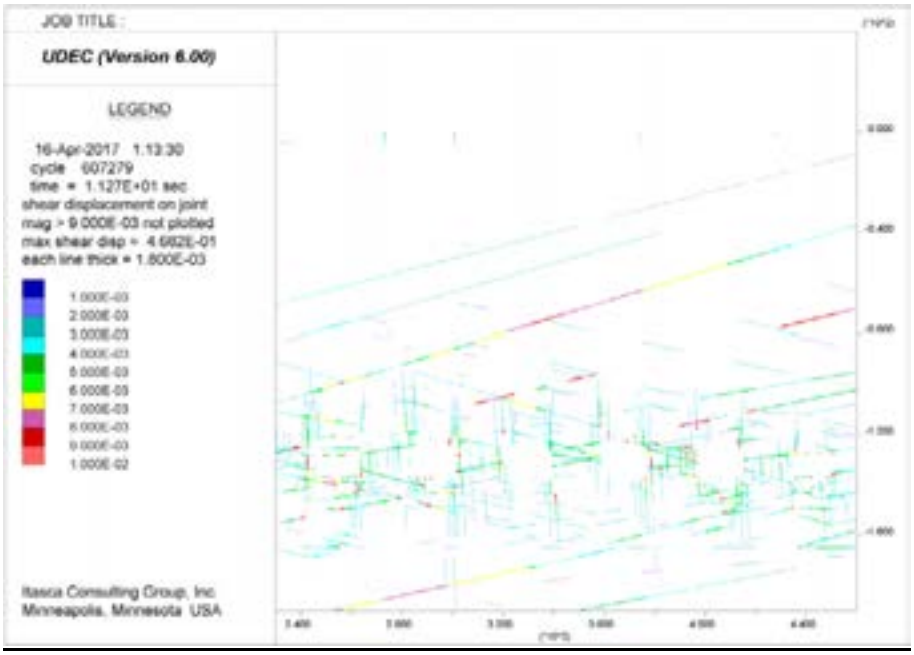


**Figure A302.** UDEC results after strength degradation and glacial loading at Year 50,000, showing shear displacements along fractures for SFR 3, DFN 3-2. Displacements are in units of metres.

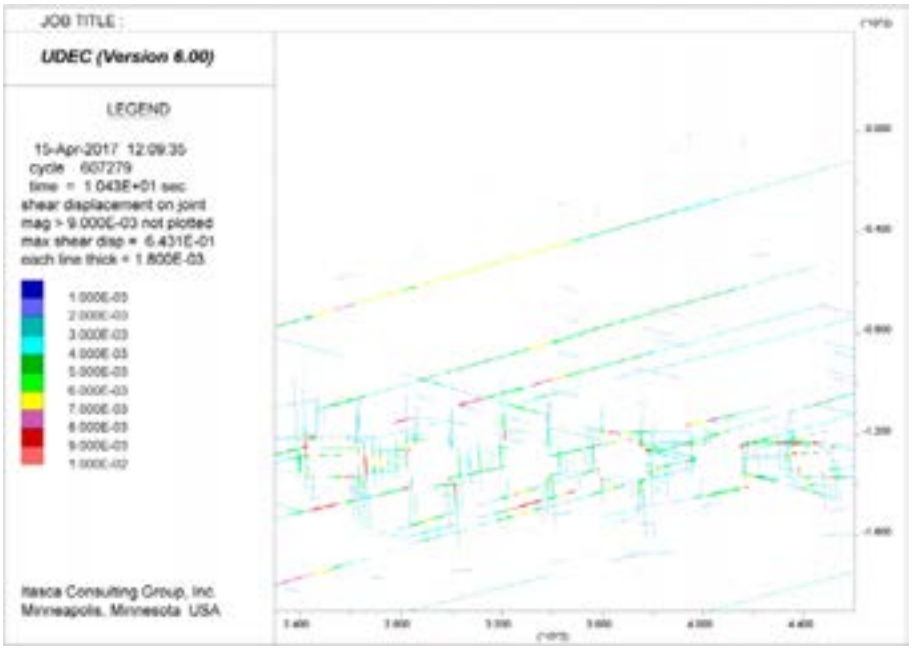


**Figure A303.** UDEC results after strength degradation and glacial loading at Year 50,000, showing shear displacements along fractures for SFR 3, DFN 3-3. Displacements are in units of metres.

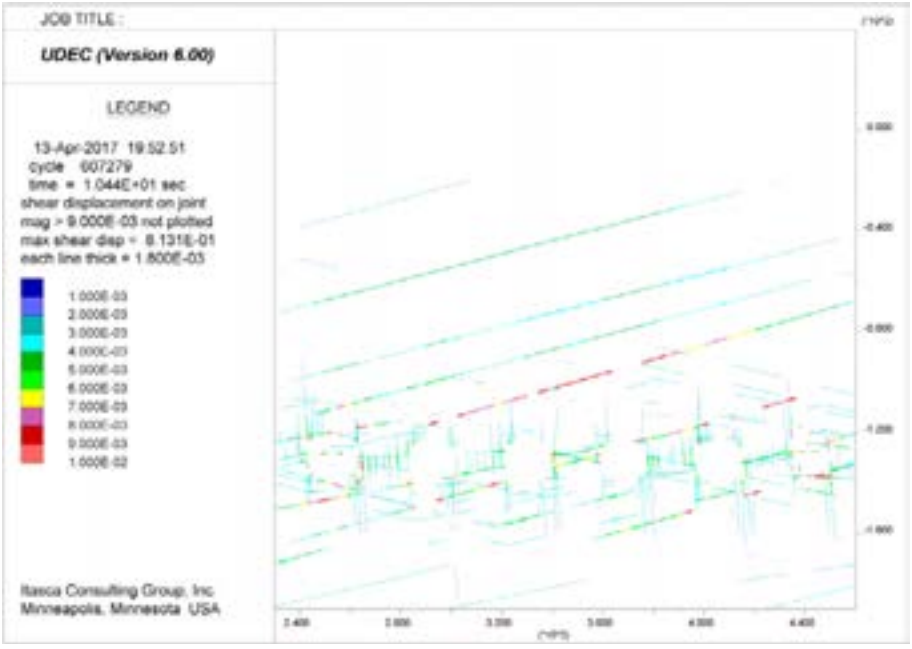


**Figure A304.** UDEC results after strength degradation and glacial loading at Year 50,000, showing shear displacements along fractures for SFR 3, DFN 3-4. Displacements are in units of metres.

## SFR 3 – Year 50,000 Glacial Loading (Vertical Displacements)

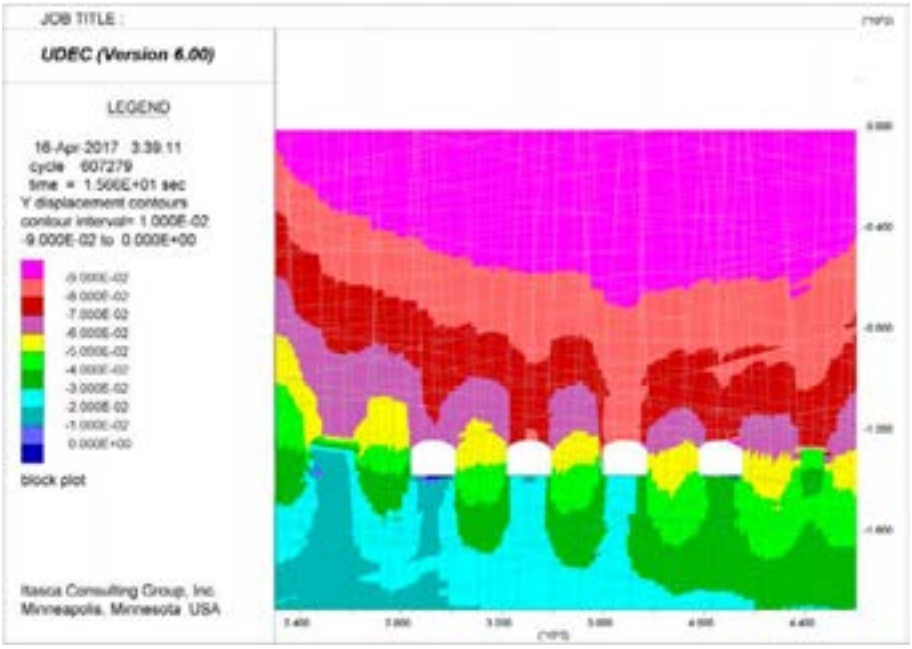


**Figure A305.** UDEC results after strength degradation and glacial loading at Year 50,000, showing vertical displacements for SFR 3, DFN 3-1. Displacements are in units of metres, with positive up.

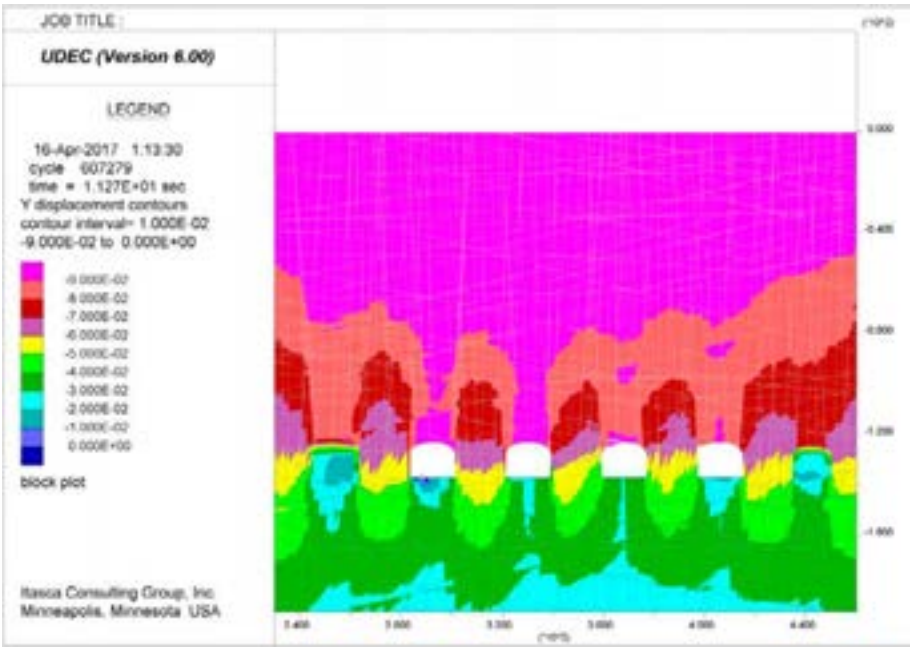


**Figure A306.** UDEC results after strength degradation and glacial loading at Year 50,000, showing vertical displacements for SFR 3, DFN 3-2. Displacements are in units of metres, with positive up.

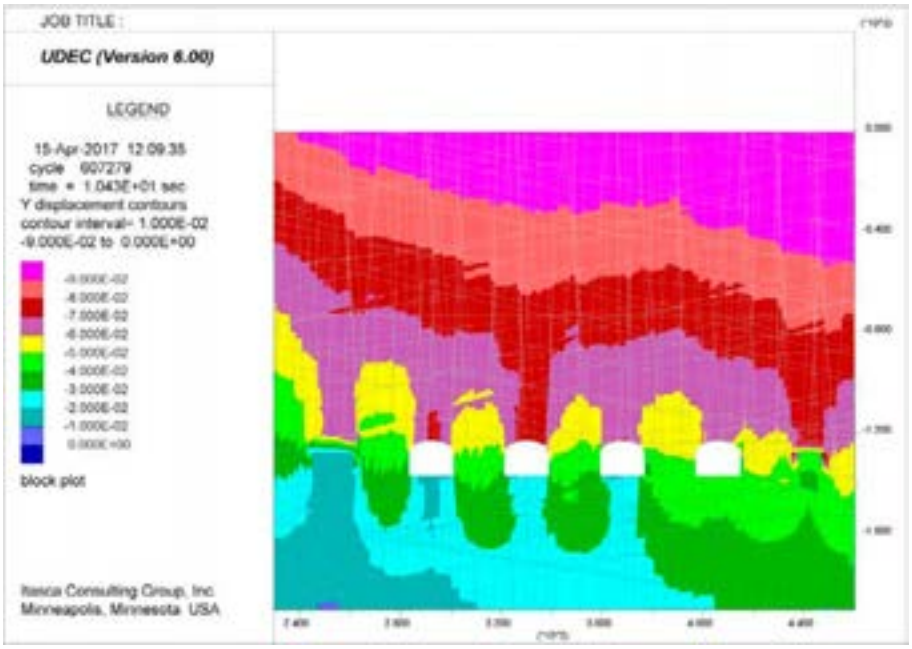


**Figure A307.** UDEC results after strength degradation and glacial loading at Year 50,000, showing vertical displacements for SFR 3, DFN 3-3. Displacements are in units of metres, with positive up.

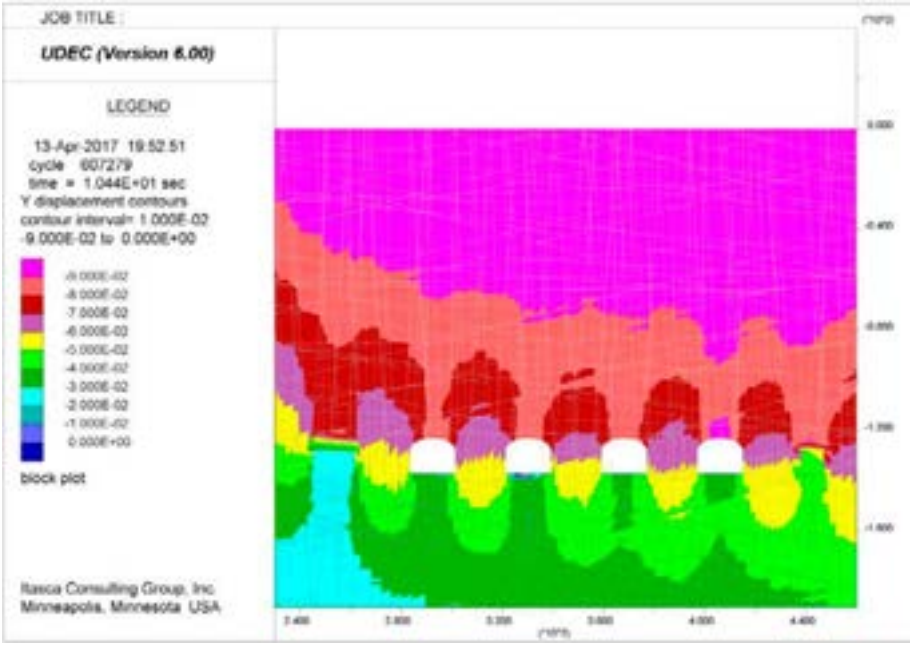


**Figure A308.** UDEC results after strength degradation and glacial loading at Year 50,000, showing vertical displacements for SFR 3, DFN 3-4. Displacements are in units of metres, with positive up.

## SFR 3 – Year 50,000 Glacial Loading (Horizontal Displacements)

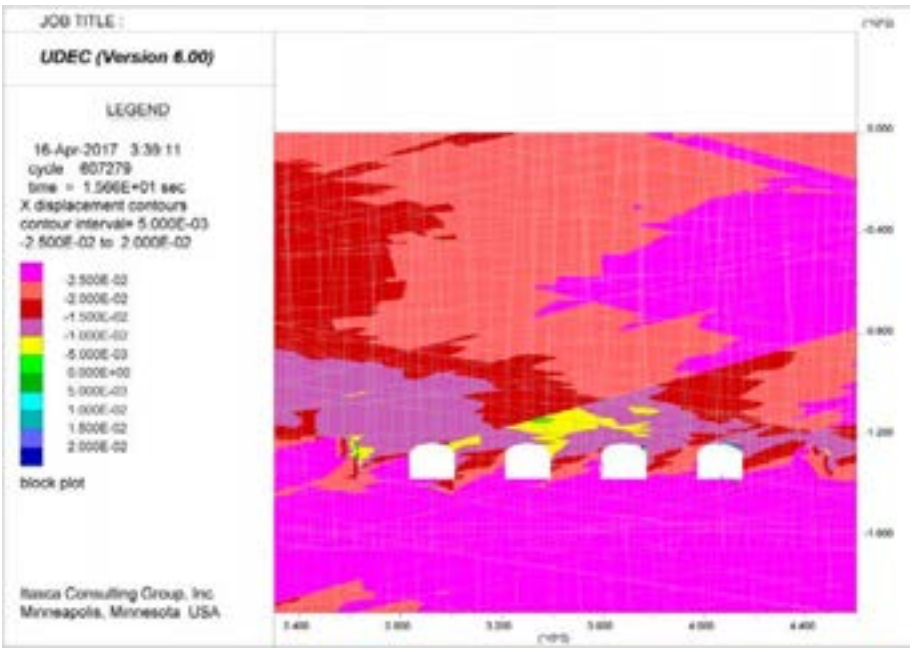


**Figure A309.** UDEC results after strength degradation and glacial loading at Year 50,000, showing horizontal displacements for SFR 3, DFN 3-1. Displacements are in units of metres, with positive to the right.

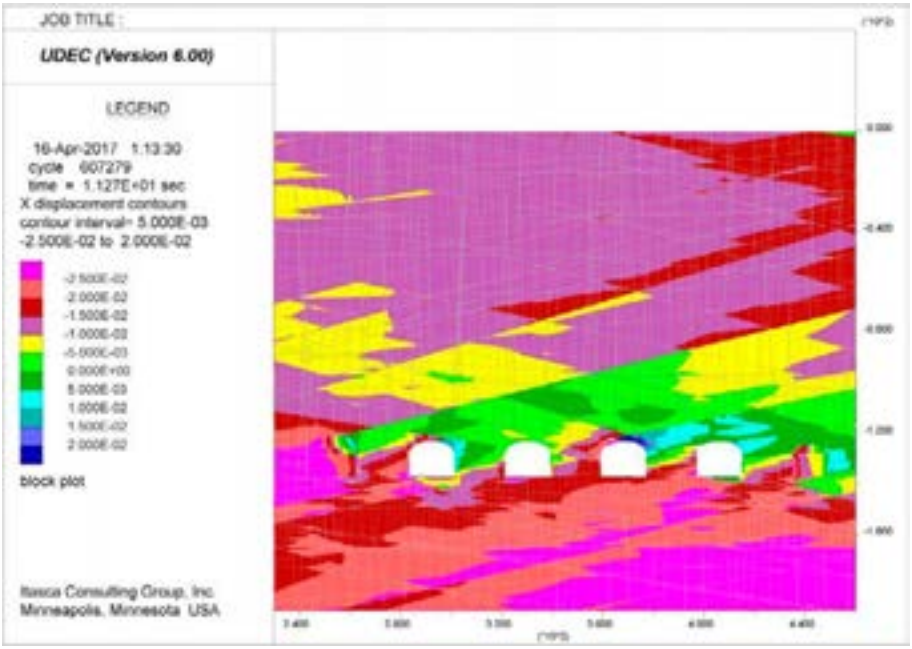


**Figure A310.** UDEC results after strength degradation and glacial loading at Year 50,000, showing horizontal displacements for SFR 3, DFN 3-2. Displacements are in units of metres, with positive to the right.

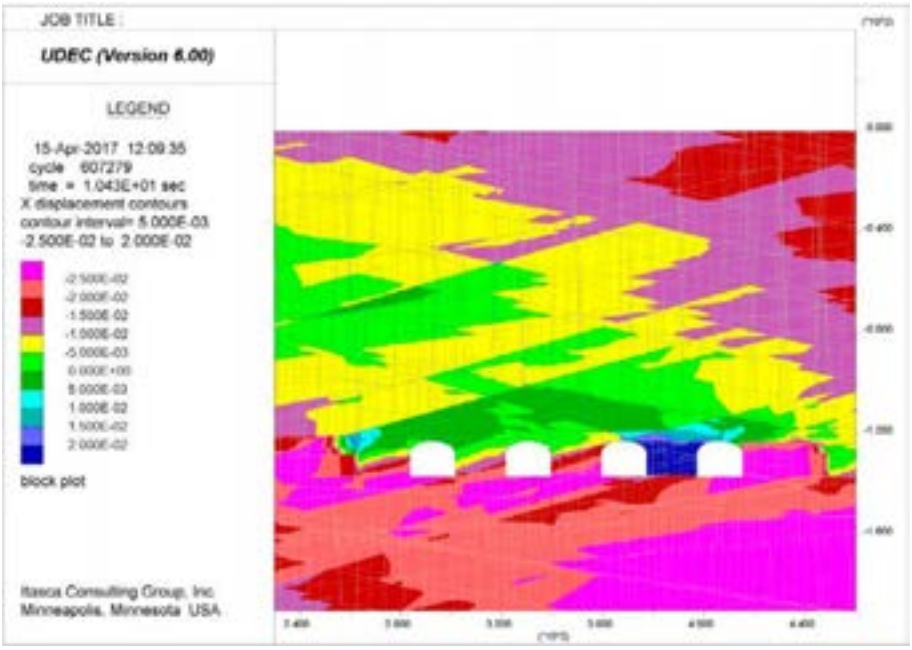


**Figure A311.** UDEC results after strength degradation and glacial loading at Year 50,000, showing horizontal displacements for SFR 3, DFN 3-3. Displacements are in units of metres, with positive to the right.

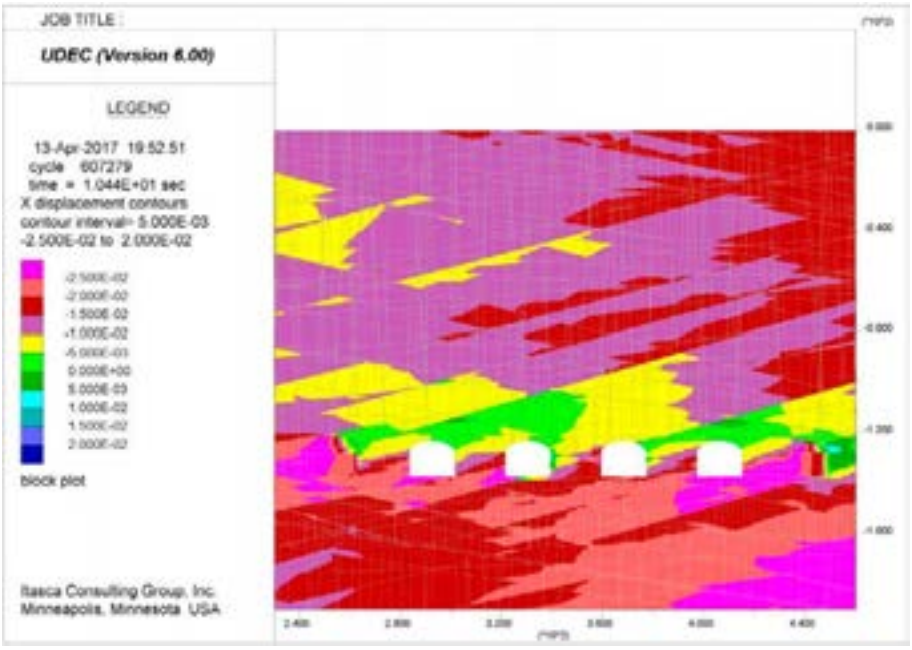


**Figure A312.** UDEC results after strength degradation and glacial loading at Year 50,000, showing horizontal displacements for SFR 3, DFN 3-4. Displacements are in units of metres, with positive to the right.

## SFR 3 – Year 66,000 Glacial Unloading (Vertical Stress)

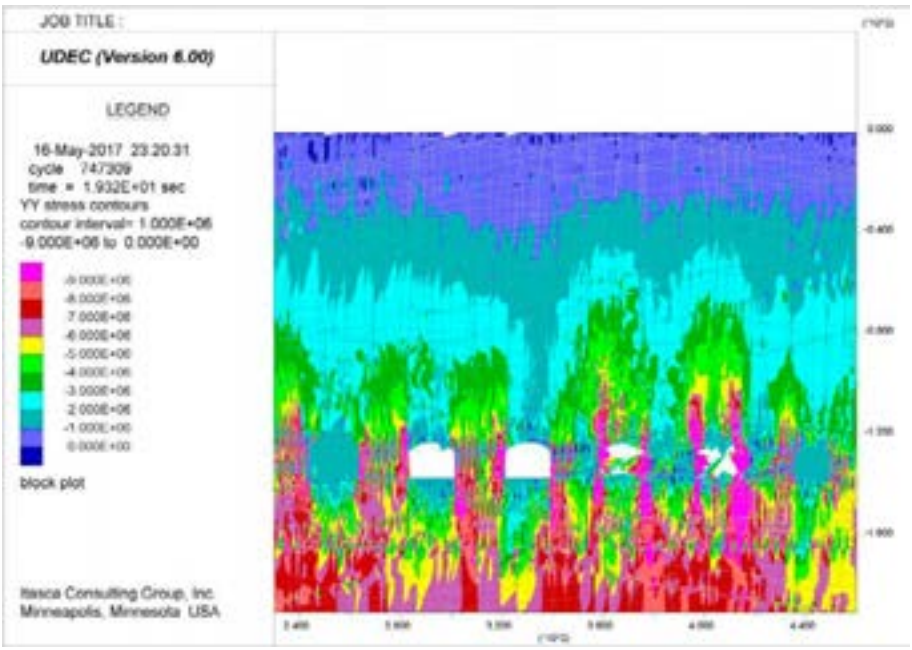


**Figure A313.** UDEC results after strength degradation, glacial unloading and permafrost melting at Year 66,000, showing vertical stresses (SYY) for SFR 3, DFN 3-1. Stress magnitudes are in units of Pascals, with compression negative.

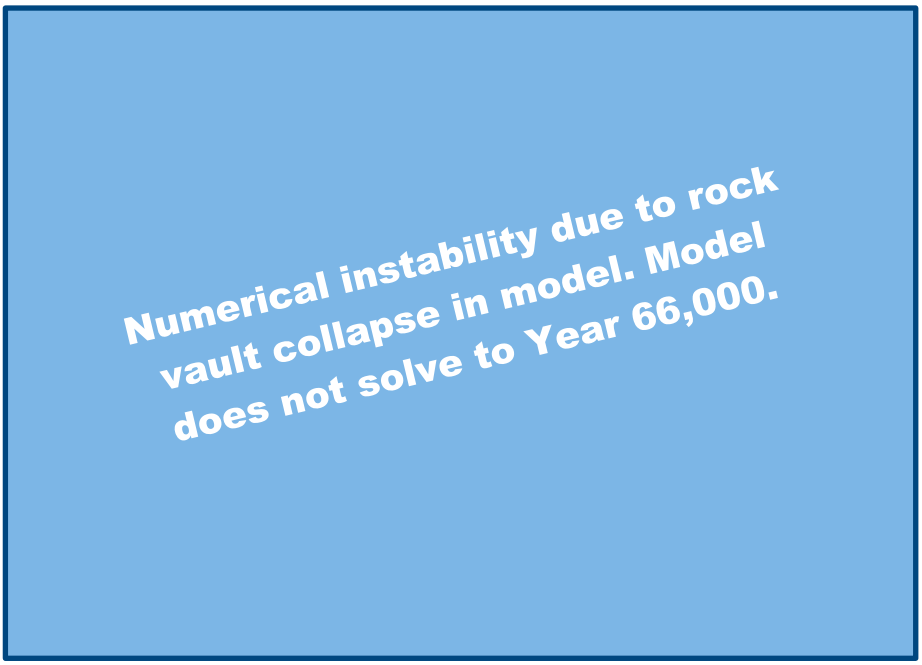


**Figure A314.** UDEC results after strength degradation, glacial unloading and permafrost melting at Year 66,000, showing vertical stresses (SYY) for SFR 3, DFN 3-2. Stress magnitudes are in units of Pascals, with compression negative.

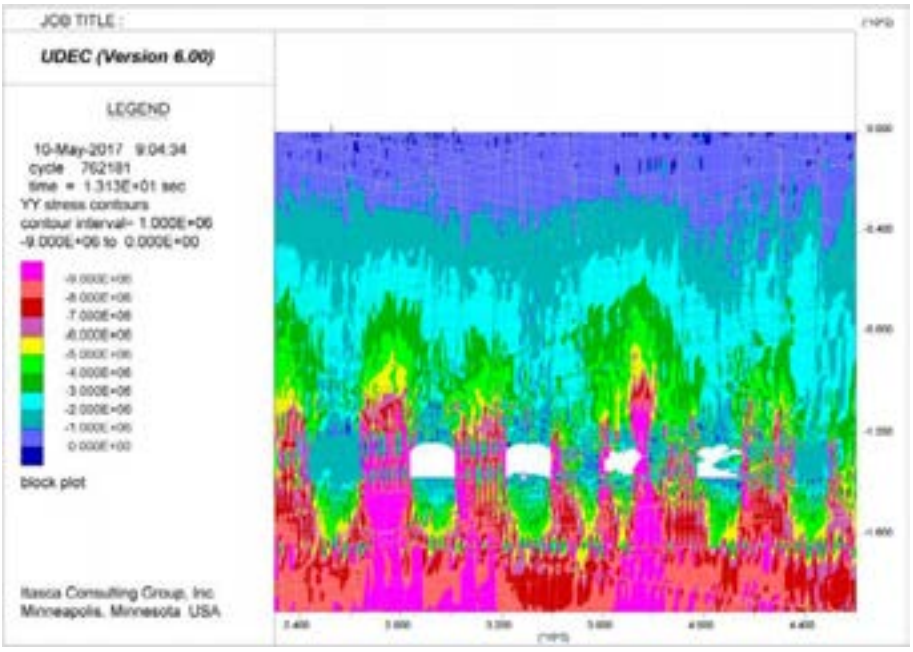


**Figure A315.** UDEC results after strength degradation, glacial unloading and permafrost melting at Year 66,000, showing vertical stresses (SYY) for SFR 3, DFN 3-3. Stress magnitudes are in units of Pascals, with compression negative.

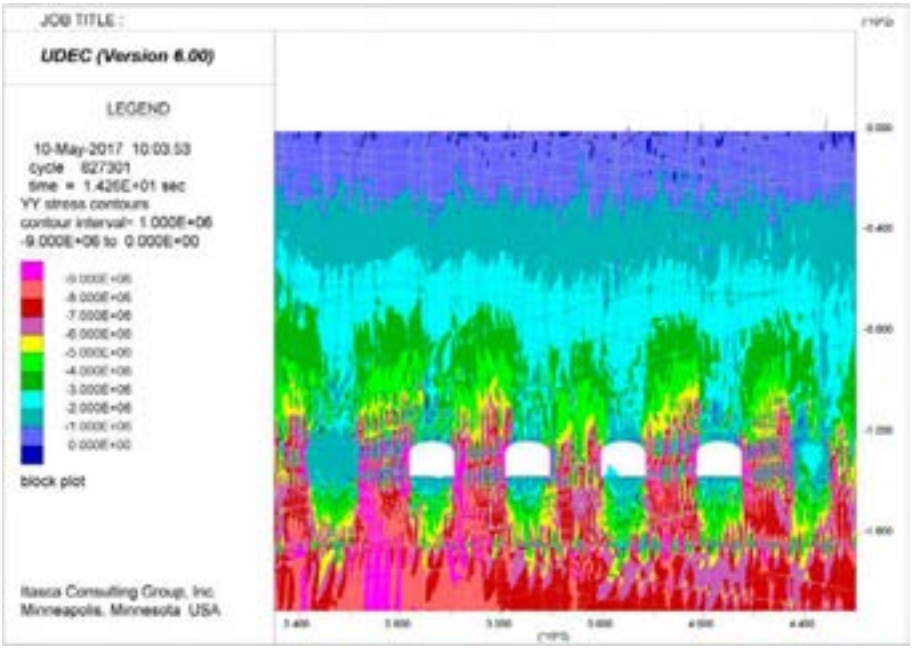


**Figure A316.** UDEC results after strength degradation, glacial unloading and permafrost melting at Year 66,000, showing vertical stresses (SYY) for SFR 3, DFN 3-4. Stress magnitudes are in units of Pascals, with compression negative.

## SFR 3 – Year 66,000 Glacial Unloading (Horizontal Stress)

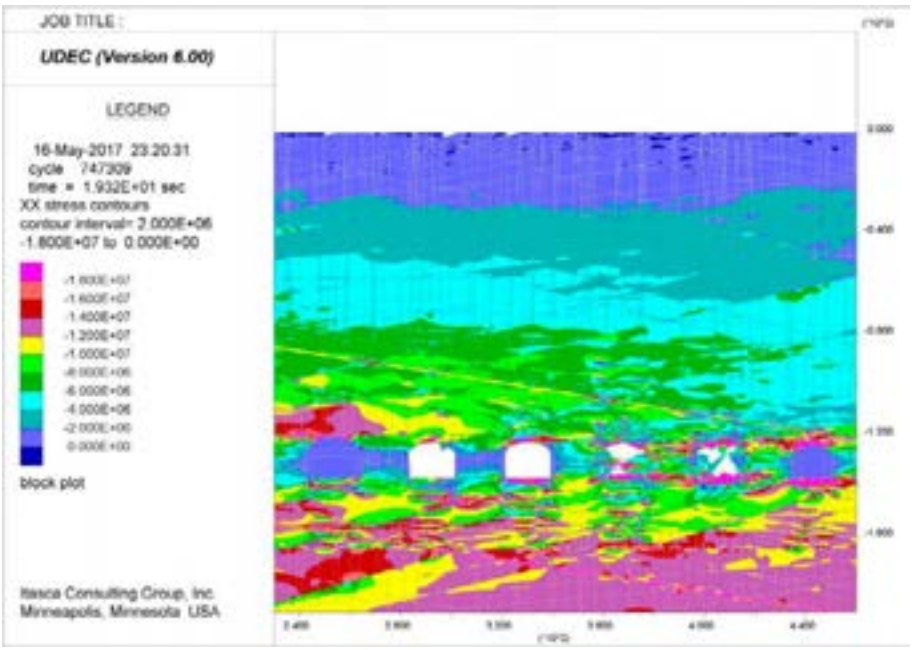


**Figure A317.** UDEC results after strength degradation, glacial unloading and permafrost melting at Year 66,000, showing horizontal stresses (SXX) for SFR 3, DFN 3-1. Stress magnitudes are in units of Pascals, with compression negative.

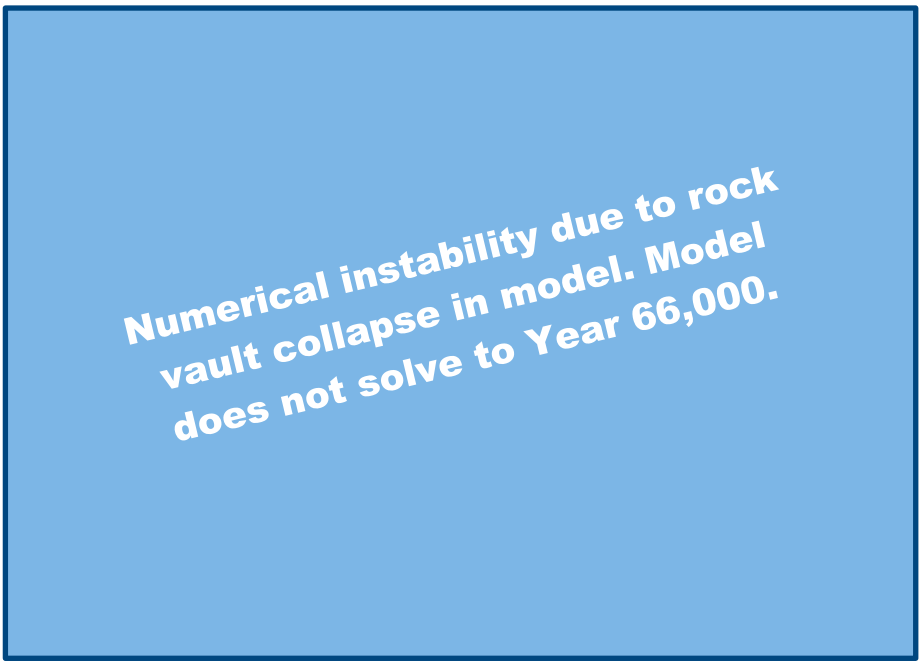


**Figure A318.** UDEC results after strength degradation, glacial unloading and permafrost melting at Year 66,000, showing horizontal stresses (SXX) for SFR 3, DFN 3-2. Stress magnitudes are in units of Pascals, with compression negative.

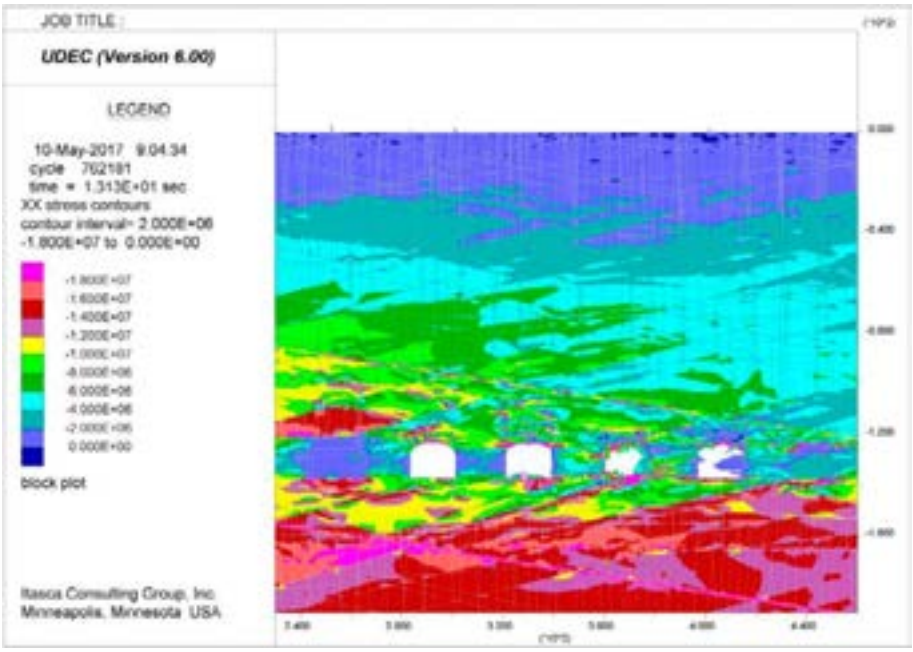


**Figure A319.** UDEC results after strength degradation, glacial unloading and permafrost melting at Year 66,000, showing horizontal stresses (SXX) for SFR 3, DFN 3-3. Stress magnitudes are in units of Pascals, with compression negative.

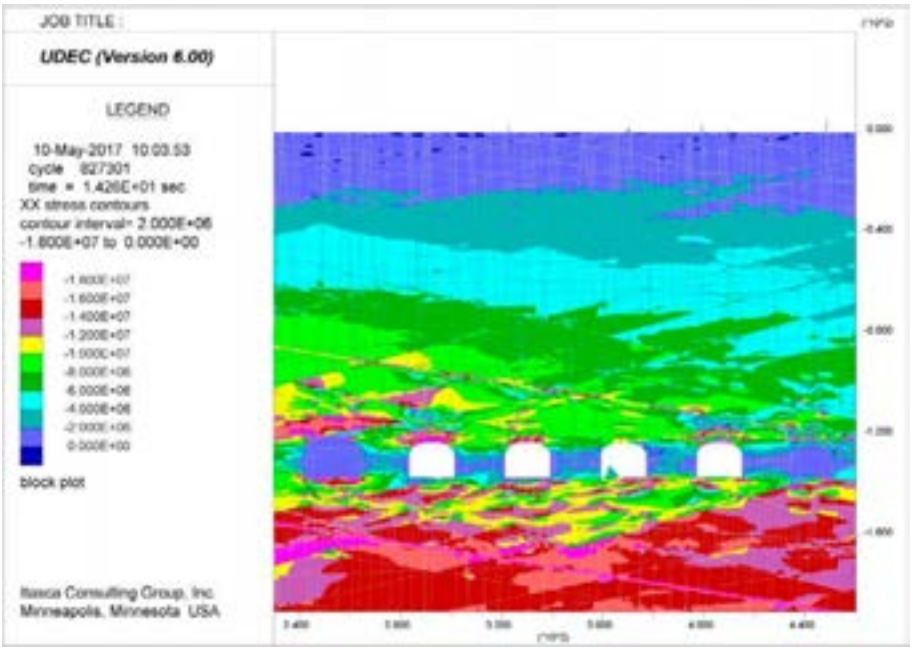


**Figure A320.** UDEC results after strength degradation, glacial unloading and permafrost melting at Year 66,000, showing horizontal stresses (SXX) for SFR 3, DFN 3-4. Stress magnitudes are in units of Pascals, with compression negative.

## SFR 3 – Year 66,000 Glacial Unloading (Plasticity Indicators)

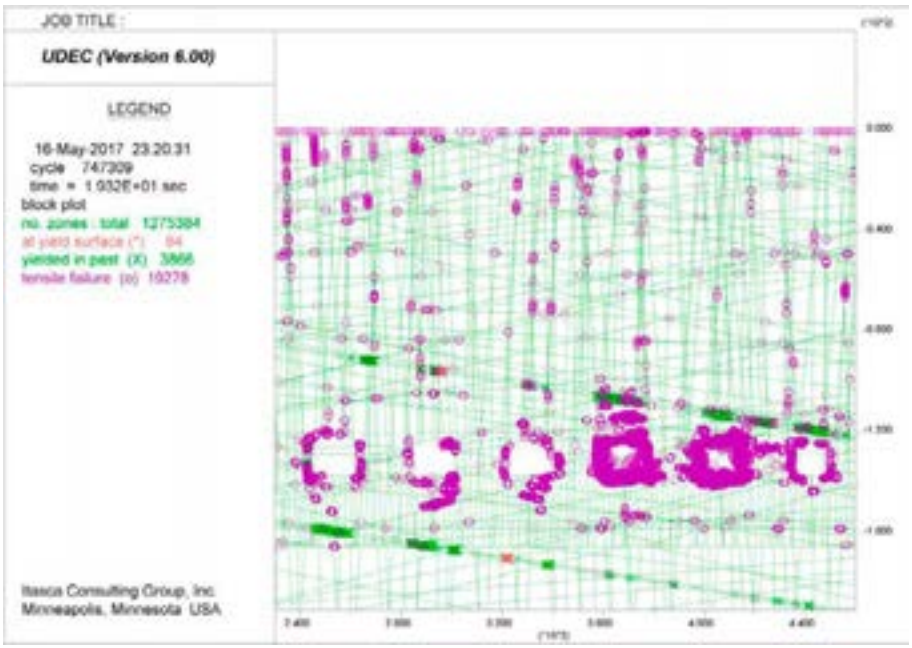


**Figure A321.** UDEC results after strength degradation, glacial unloading and permafrost melting at Year 66,000, showing yielded elements for SFR 3, DFN 3-1.

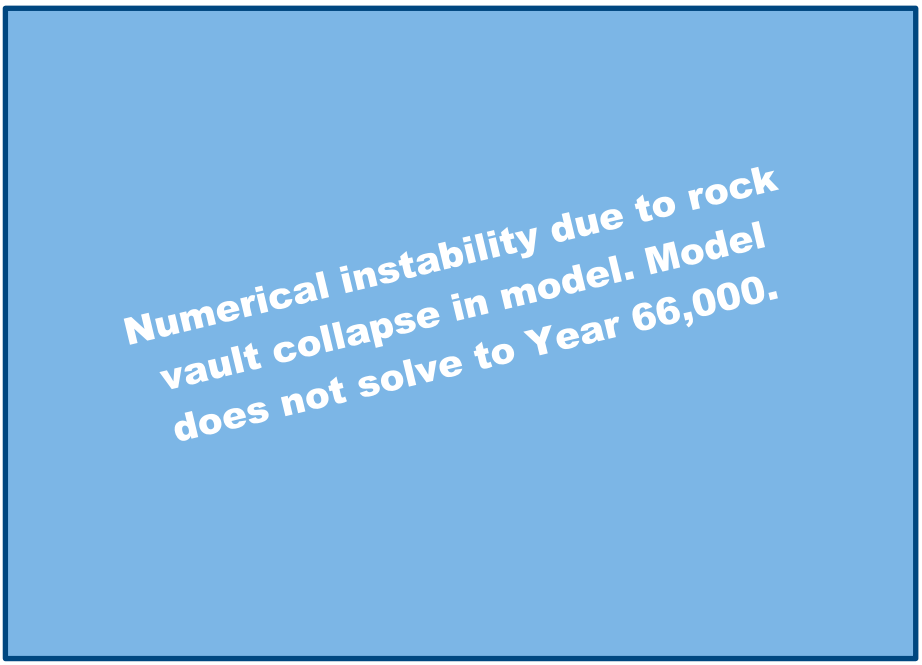


**Figure A322.** UDEC results after strength degradation, glacial unloading and permafrost melting at Year 66,000, showing yielded elements for SFR 3, DFN 3-2.

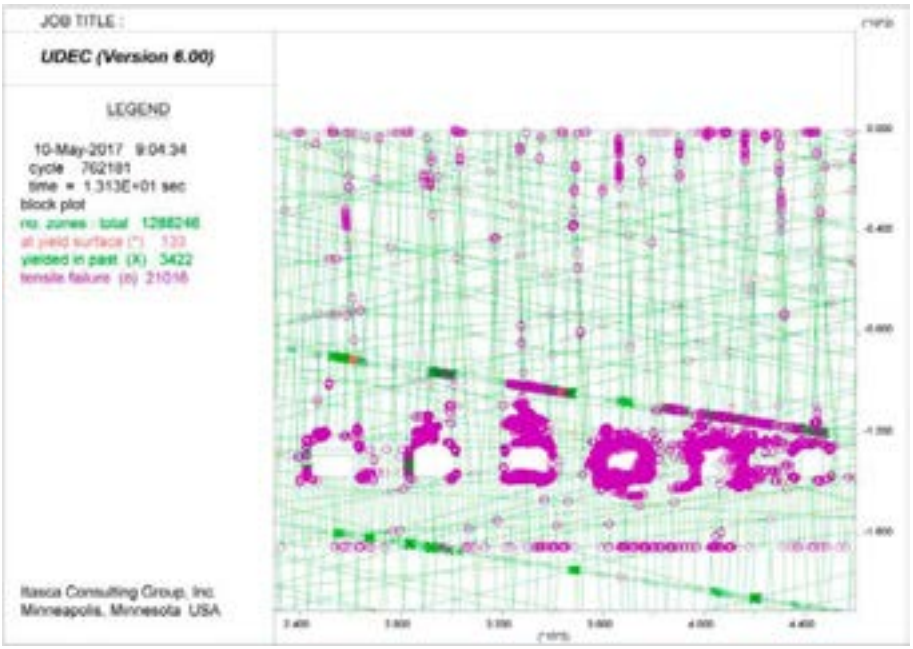


**Figure A323.** UDEC results after strength degradation, glacial unloading and permafrost melting at Year 66,000, showing yielded elements for SFR 3, DFN 3-3.

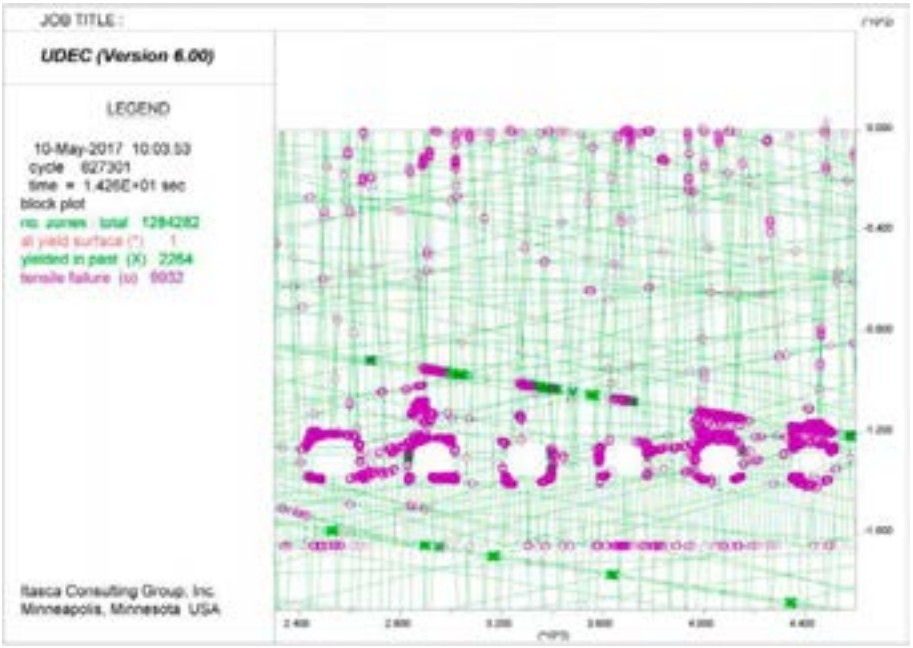


**Figure A324.** UDEC results after strength degradation, glacial unloading and permafrost melting at Year 66,000, showing yielded elements for SFR 3, DFN 3-4.

## SFR 3 – Year 66,000 Glacial Unloading (Displacement Vectors)

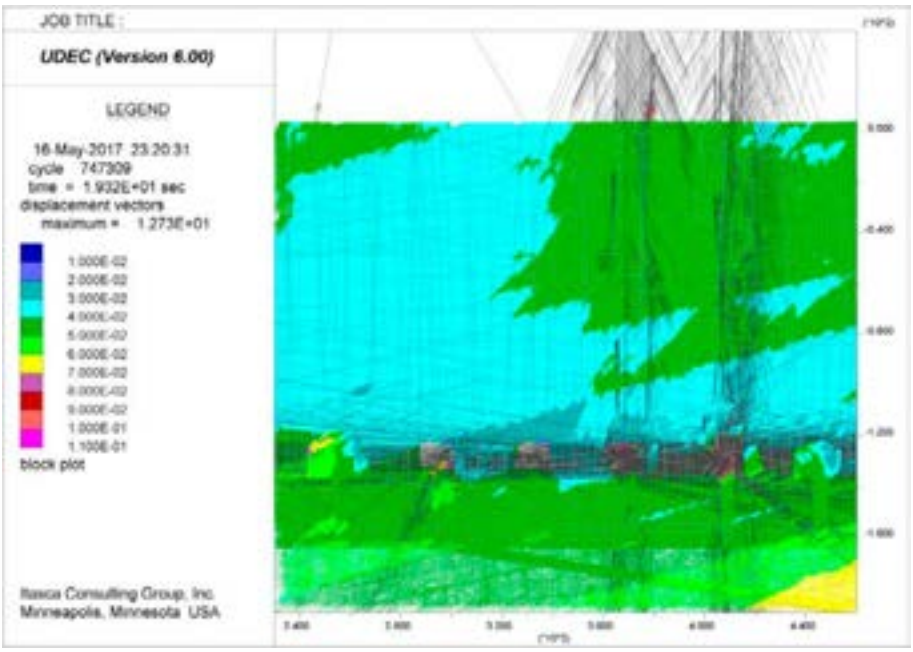


**Figure A325.** UDEC results after strength degradation, glacial unloading and permafrost melting at Year 66,000, showing displacement vectors for SFR 3, DFN 3-1. Displacement magnitudes are in units of metres.

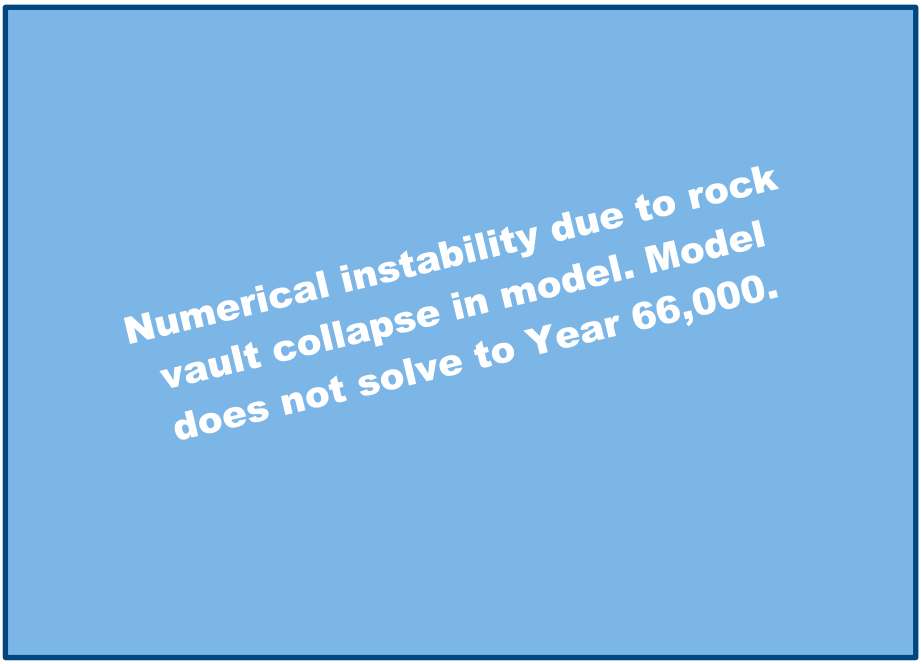


**Figure A326.** UDEC results after strength degradation, glacial unloading and permafrost melting at Year 66,000, showing displacement vectors for SFR 3, DFN 3-2. Displacement magnitudes are in units of metres.

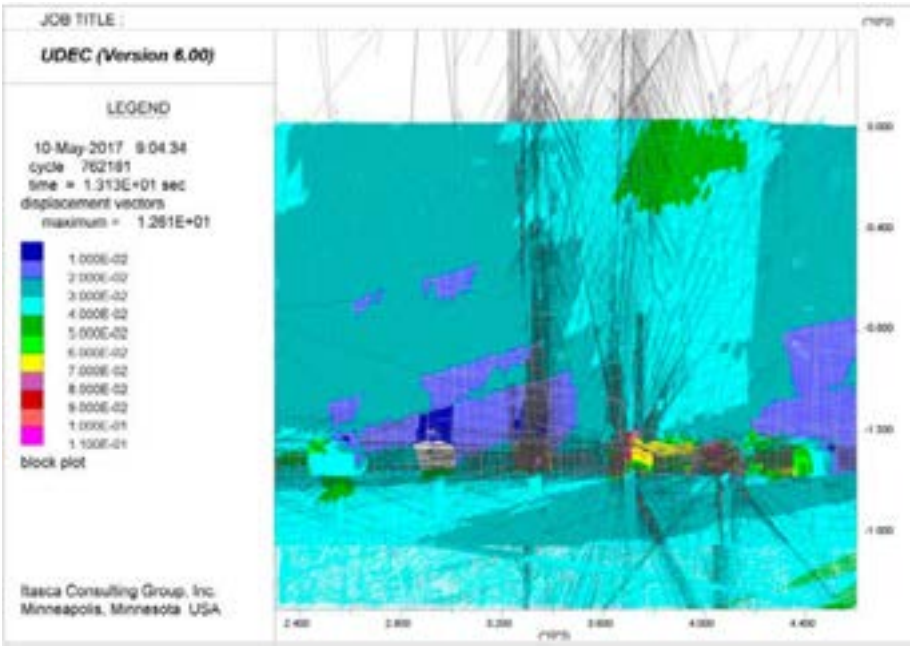


**Figure A327.** UDEC results after strength degradation, glacial unloading and permafrost melting at Year 66,000, showing displacement vectors for SFR 3, DFN 3-3. Displacement magnitudes are in units of metres.

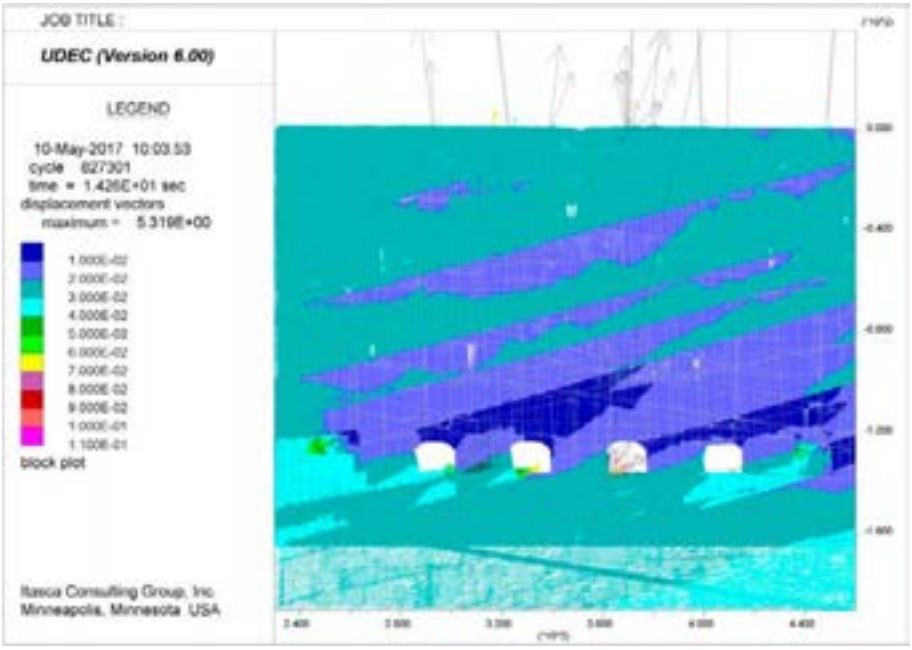


**Figure A328.** UDEC results after strength degradation, glacial unloading and permafrost melting at Year 66,000, showing displacement vectors for SFR 3, DFN 3-4. Displacement magnitudes are in units of metres.

## SFR 3 – Year 66,000 Glacial Unloading (Fracture Shear Displacement)

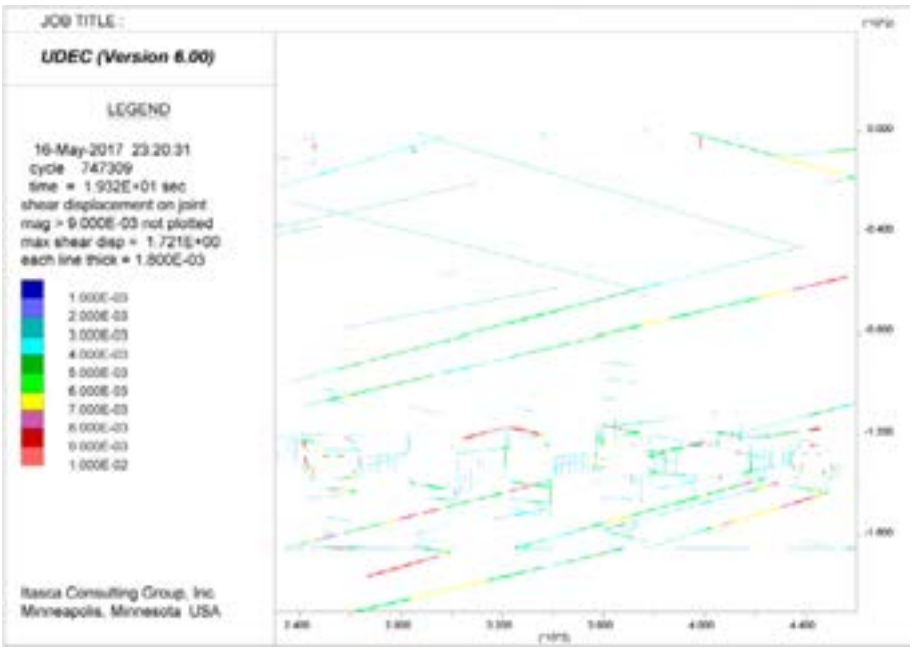


**Figure A329.** UDEC results after strength degradation, glacial unloading and permafrost melting at Year 66,000, showing shear displacements along fractures for SFR 3, DFN 3-1. Displacements are in units of metres.

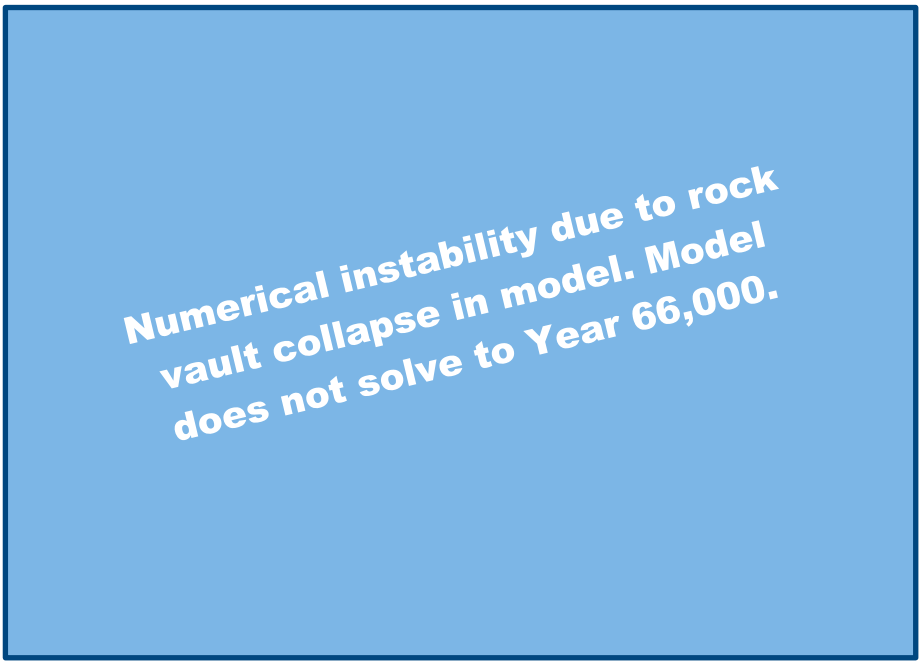


**Figure A330.** UDEC results after strength degradation, glacial unloading and permafrost melting at Year 66,000, showing shear displacements along fractures for SFR 3, DFN 3-2. Displacements are in units of metres.

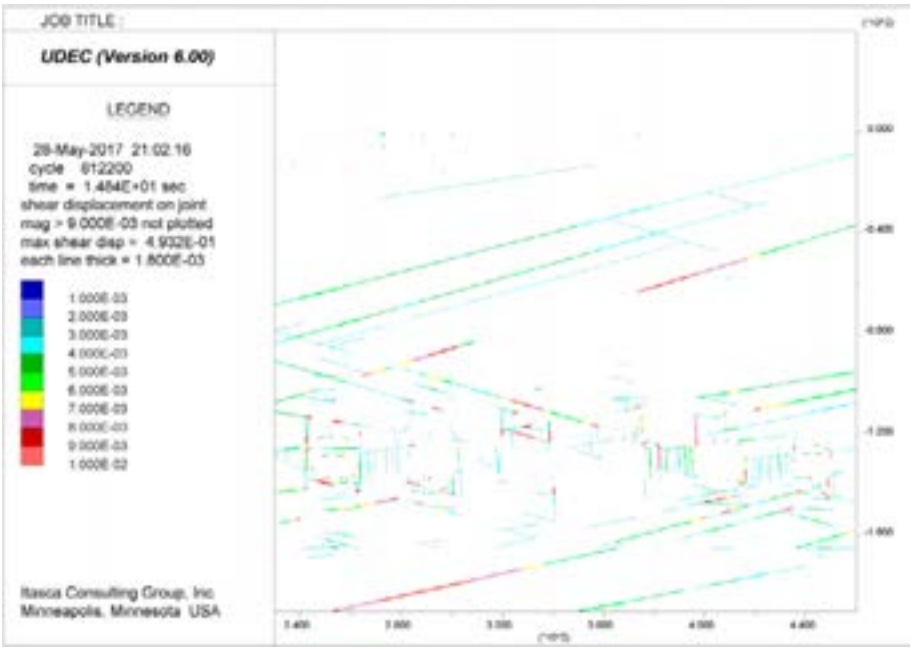


**Figure A331.** UDEC results after strength degradation, glacial unloading and permafrost melting at Year 66,000, showing shear displacements along fractures for SFR 3, DFN 3-3. Displacements are in units of metres.

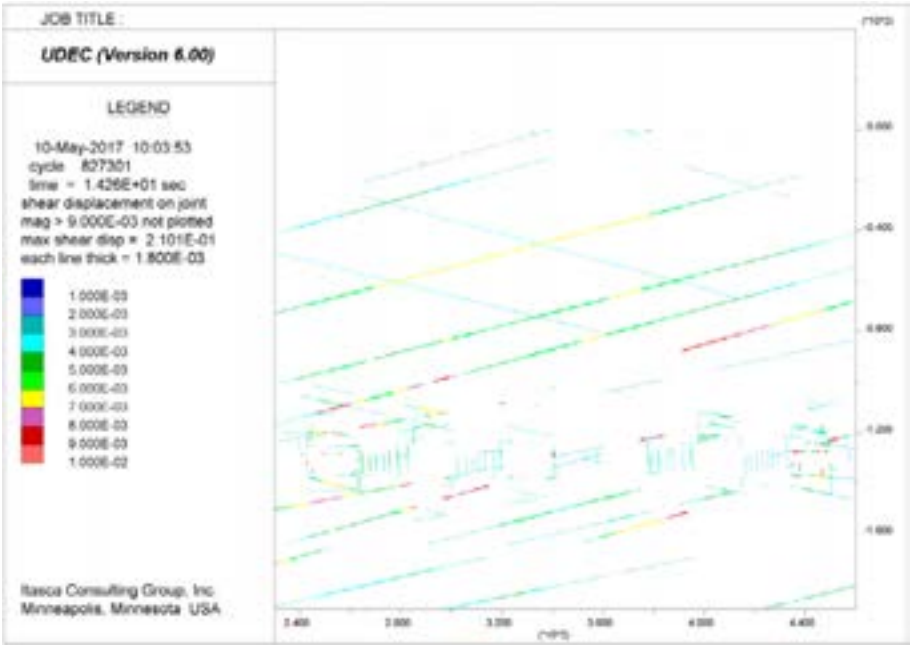


**Figure A332.** UDEC results after strength degradation, glacial unloading and permafrost melting at Year 66,000, showing shear displacements along fractures for SFR 3, DFN 3-4. Displacements are in units of metres.

## SFR 3 – Year 66,000 Glacial Unloading (Vertical Displacements)

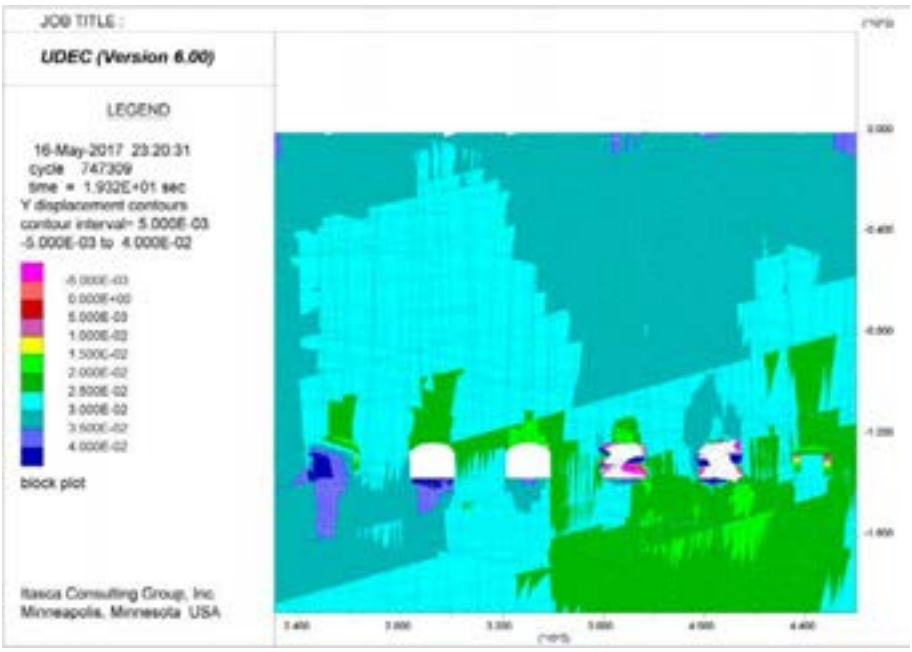


**Figure A333.** UDEC results after strength degradation, glacial unloading and permafrost melting at Year 66,000, showing vertical displacements for SFR 3, DFN 3-1. Displacements are in units of metres, with positive up.

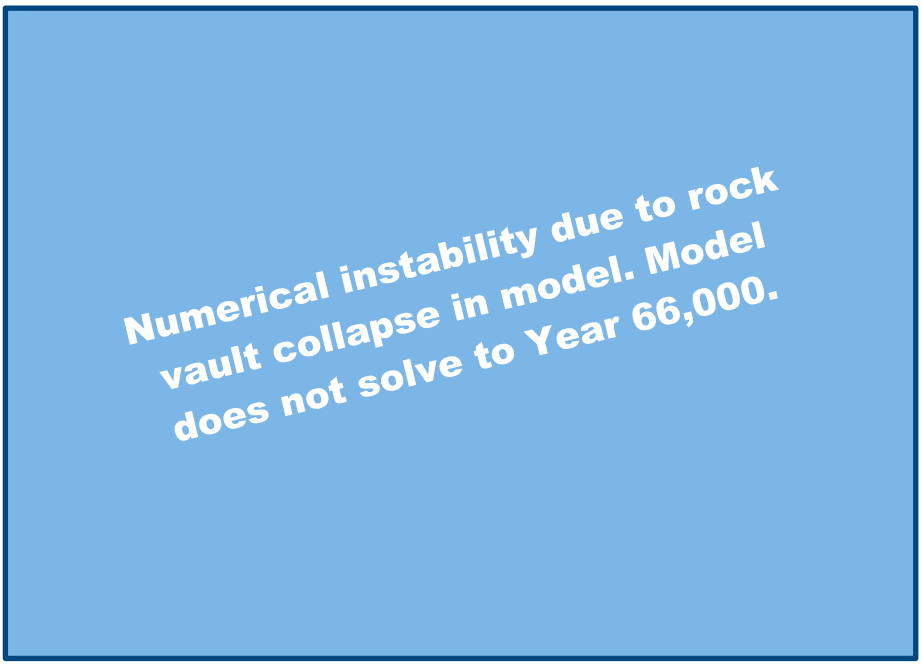


**Figure A334.** UDEC results after strength degradation, glacial unloading and permafrost melting at Year 66,000, showing vertical displacements for SFR 3, DFN 3-2. Displacements are in units of metres, with positive up.

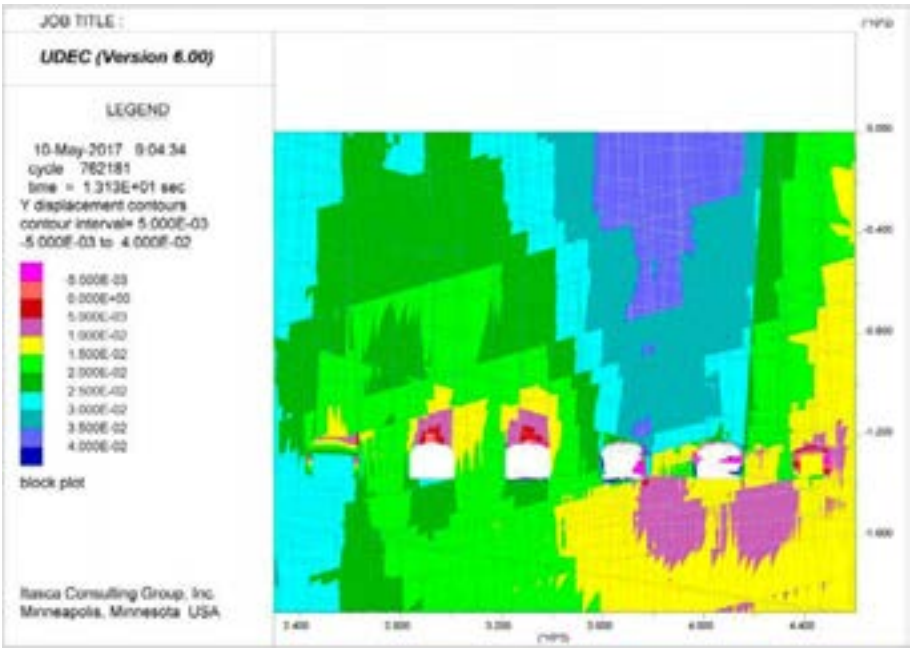


**Figure A335.** UDEC results after strength degradation, glacial unloading and permafrost melting at Year 66,000, showing vertical displacements for SFR 3, DFN 3-3. Displacements are in units of metres, with positive up.

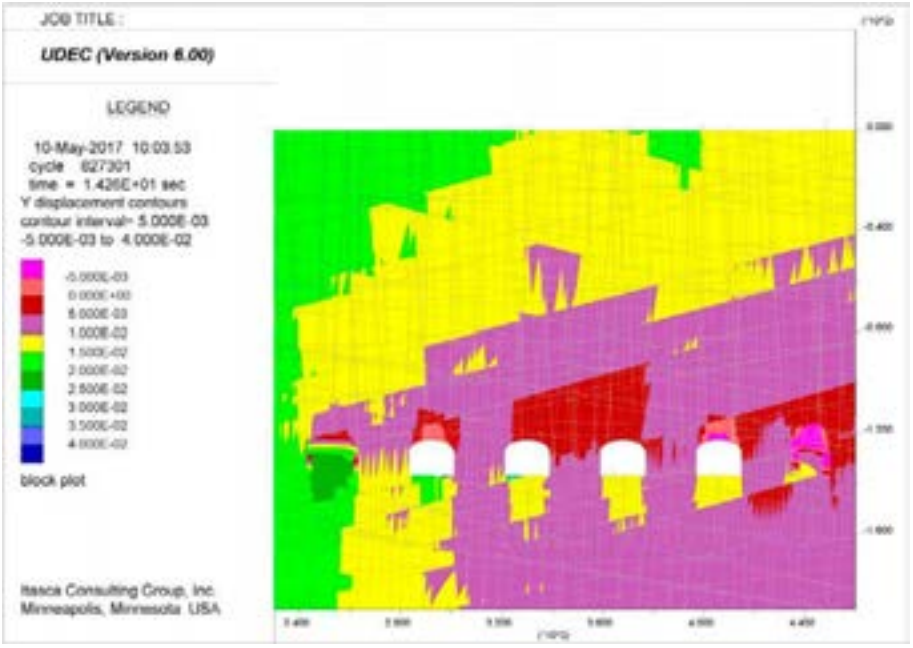


**Figure A336.** UDEC results after strength degradation, glacial unloading and permafrost melting at Year 66,000, showing vertical displacements for SFR 3, DFN 3-4. Displacements are in units of metres, with positive up.

## SFR 3 – Year 66,000 Glacial Unloading (Horizontal Displacements)

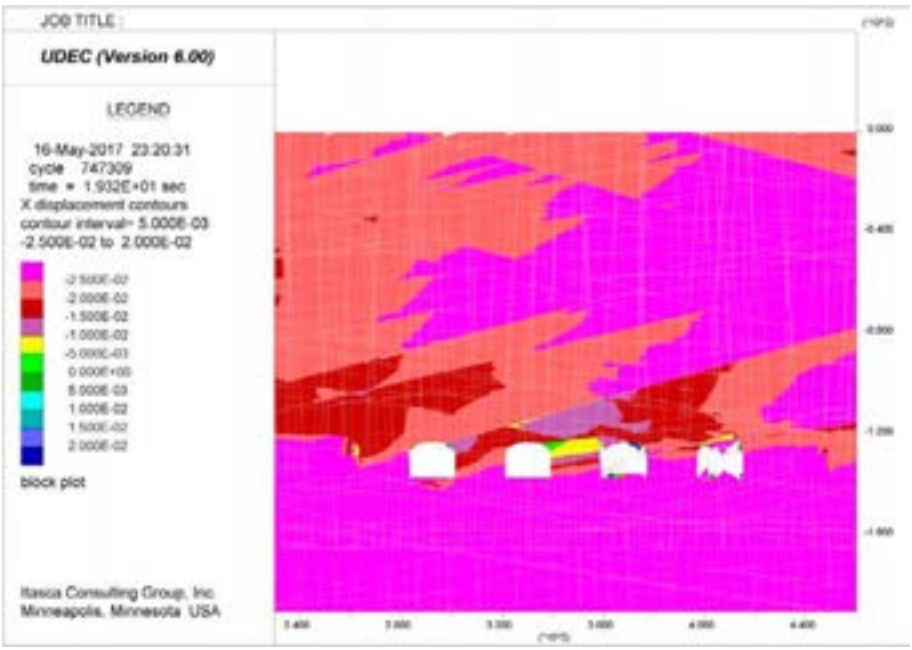


**Figure A337.** UDEC results after strength degradation, glacial unloading and permafrost melting at Year 66,000, showing horizontal displacements for SFR 3, DFN 3-1. Displacements are in units of metres, with positive to the right.

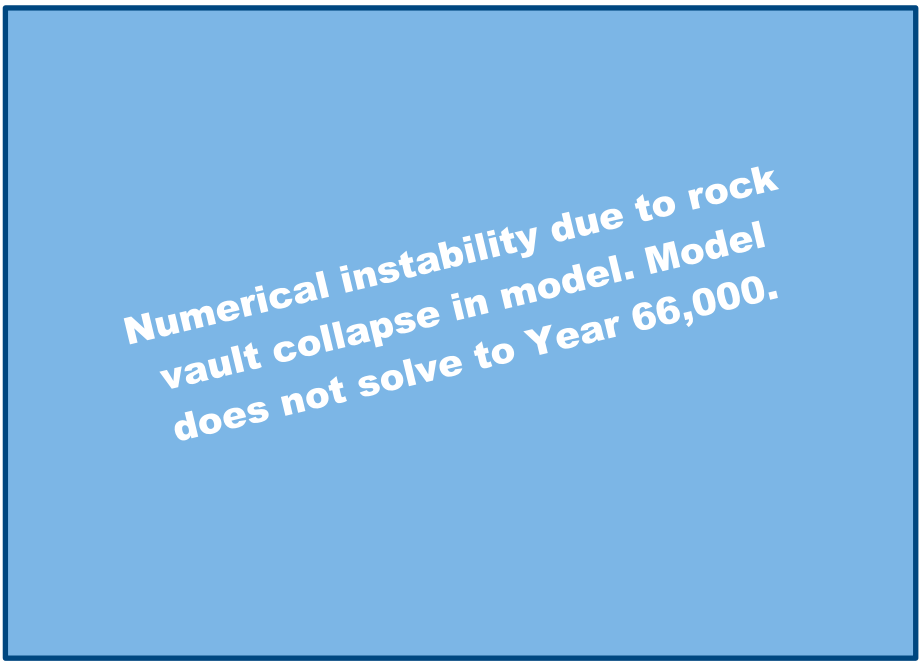


**Figure A338.** UDEC results after strength degradation, glacial unloading and permafrost melting at Year 66,000, showing horizontal displacements for SFR 3, DFN 3-2. Displacements are in units of metres, with positive to the right.

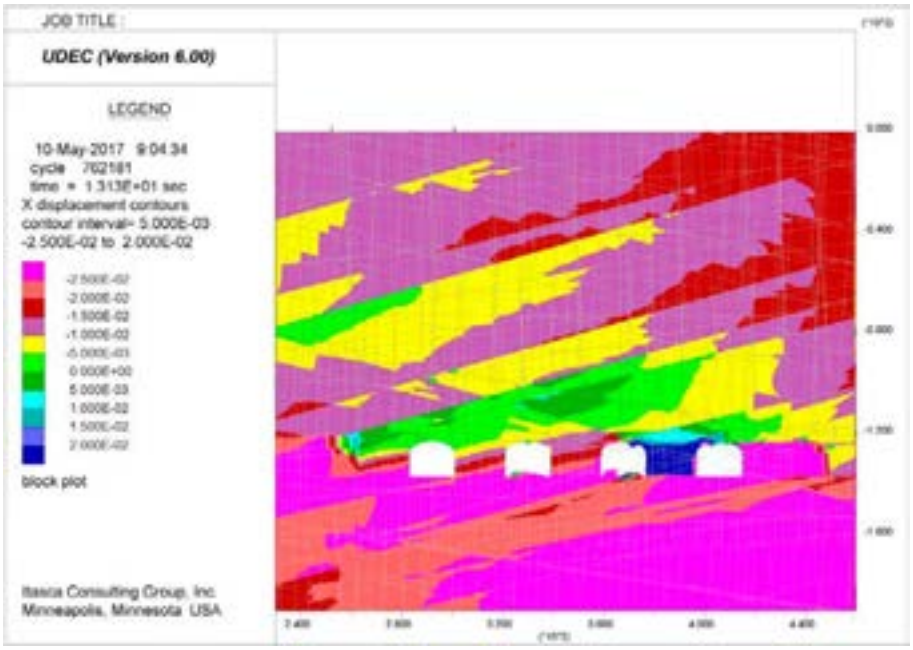


**Figure A339.** UDEC results after strength degradation, glacial unloading and permafrost melting at Year 66,000, showing horizontal displacements for SFR 3, DFN 3-3. Displacements are in units of metres, with positive to the right.

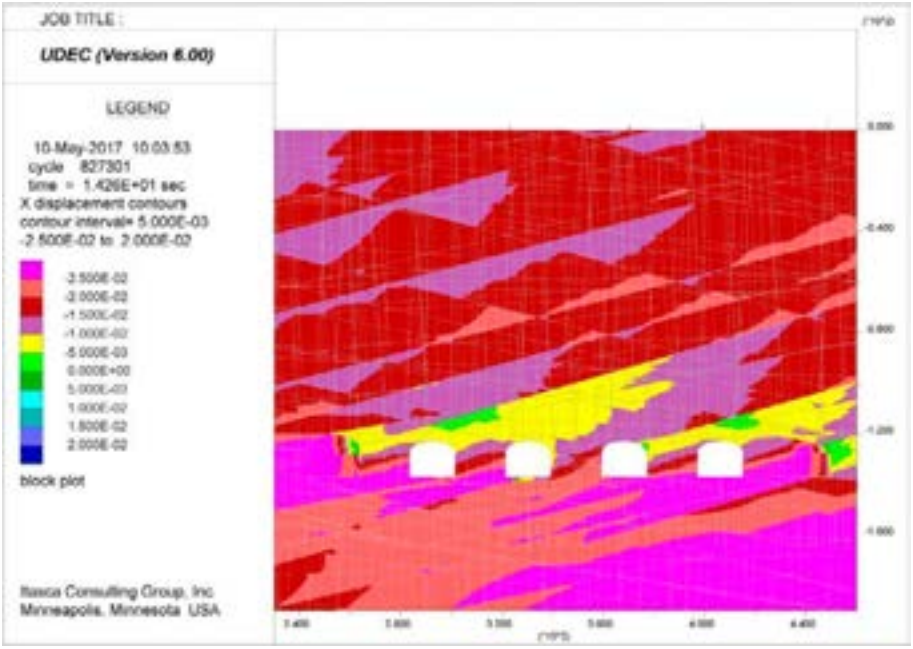


**Figure A340.** UDEC results after strength degradation, glacial unloading and permafrost melting at Year 66,000, showing horizontal displacements for SFR 3, DFN 3-4. Displacements are in units of metres, with positive to the right.

**APPENDIX 4**

# UDEC command inputs

For transparency purposes, the command inputs used to develop the UDEC models are included below. These include one of the DFN realizations for the SFR 1 series of models, and one for the extended SFR 3 series of models.

## SFR 1 Geometry and Mesh

```
new
config fluid
round 0.05

; Far-Field Rock Mass
block 0,0 603.1,0 603.1,-300 0,-300
change mat 1 cons 1

; Deformation Zone (dip in 2D plane = 9.5 deg.), 20 m above BMA (mid-room section)
crack 0,-99.1 592.3,0
crack 0,-98.1 586.4,0
change mat 3 cons 1 range atbl 1,-98.5

; Near-Field Rock Mass
crack 200,0 200,-105 join
crack 403.1,0 403.1,-105 join
crack 200,-105 403.1,-105 join
change mat 2 cons 1 range atbl 205,-25 205,-95

; 1-BTF Vault Geometry
  crack 247.5,-79.5 246.5,-105
  crack 240,-79.5 255,-79.5
  crack 240,-79.5 240,-73.5
  crack 255,-79.5 255,-73.5
  crack 240.0,-73.5 240.5,-72.4  ; begin arch
  crack 240.5,-72.4 241.0,-72.0
  crack 241.0,-72.0 241.5,-71.7
  crack 241.5,-71.7 242.0,-71.4
  crack 242.0,-71.4 242.5,-71.2
  crack 242.5,-71.2 243.0,-71.0
  crack 243.0,-71.0 243.5,-70.8
  crack 243.5,-70.8 244.0,-70.6
  crack 244.0,-70.6 244.5,-70.5
  crack 244.5,-70.5 245.0,-70.4
  crack 245.0,-70.4 245.5,-70.3
  crack 245.5,-70.3 246.0,-70.2
  crack 246.0,-70.2 246.5,-70.1
  crack 246.5,-70.1 247.0,-70.0
  crack 247.0,-70.0 247.5,-70.0
  crack 247.5,-70.0 248.0,-70.0
  crack 248.0,-70.0 248.5,-70.1
  crack 248.5,-70.1 249.0,-70.2
  crack 249.0,-70.2 249.5,-70.3
  crack 249.5,-70.3 250.0,-70.4
  crack 250.0,-70.4 250.5,-70.5
  crack 250.5,-70.5 251.0,-70.6
  crack 251.0,-70.6 251.5,-70.8
  crack 251.5,-70.8 252.0,-71.0
  crack 252.0,-71.0 252.5,-71.2
  crack 252.5,-71.2 253.0,-71.4
  crack 253.0,-71.4 253.5,-71.7
  crack 253.5,-71.7 254.0,-72.0
  crack 254.0,-72.0 254.5,-72.4
  crack 254.5,-72.4 255.0,-73.5 ; end arch

; 2-BTF Vault Geometry
  crack 282,-79.2 281,-105
  crack 274.5,-79.2 289.5,-79.2
  crack 274.5,-79.2 274.5,-73.2
  crack 289.5,-79.2 289.5,-73.2
  crack 274.5,-73.2 275.0,-72.1  ; begin arch
  crack 275.0,-72.1 275.5,-71.7
  crack 281.0,-69.8 281.5,-69.7
  crack 281.5,-69.7 282.0,-69.7
  crack 282.0,-69.7 282.5,-69.7
  crack 282.5,-69.7 283.0,-69.8
  crack 283.0,-69.8 283.5,-69.9
  crack 283.5,-69.9 284.0,-70.0
```

```
crack 275.5,-71.7 276.0,-71.4
crack 276.0,-71.4 276.5,-71.1
crack 276.5,-71.1 277.0,-70.9
crack 277.0,-70.9 277.5,-70.7
crack 277.5,-70.7 278.0,-70.5
crack 278.0,-70.5 278.5,-70.3
crack 278.5,-70.3 279.0,-70.2
crack 279.0,-70.2 279.5,-70.1
crack 279.5,-70.1 280.0,-70.0
crack 280.0,-70.0 280.5,-69.9
crack 280.5,-69.9 281.0,-69.8
crack 284.0,-70.0 284.5,-70.1
crack 284.5,-70.1 285.0,-70.2
crack 285.0,-70.2 285.5,-70.3
crack 285.5,-70.3 286.0,-70.5
crack 286.0,-70.5 286.5,-70.7
crack 286.5,-70.7 287.0,-70.9
crack 287.0,-70.9 287.5,-71.1
crack 287.5,-71.1 288.0,-71.4
crack 288.0,-71.4 288.5,-71.7
crack 288.5,-71.7 289.0,-72.1
crack 289.0,-72.1 289.5,-73.2 ; end arch

; 1-BLA Vault Geometry
crack 316.5,-78.8 315.5,-105
crack 309,-78.8 324,-78.8
crack 309,-78.8 309,-70.3
crack 324,-78.8 324,-70.3
crack 309.0,-70.3 309.25,-69.3 ; begin arch
crack 309.25,-69.3 309.5,-68.7
crack 309.5,-68.7 310.0,-68.2
crack 310.0,-68.2 310.5,-67.8
crack 310.5,-67.8 311.0,-67.4
crack 311.0,-67.4 311.5,-67.2
crack 311.5,-67.2 312.0,-67.0
crack 312.0,-67.0 312.5,-66.8
crack 312.5,-66.8 313.0,-66.7
crack 313.0,-66.7 313.5,-66.6
crack 313.5,-66.6 314.0,-66.5
crack 314.0,-66.5 314.5,-66.4
crack 314.5,-66.4 315.0,-66.3
crack 315.0,-66.3 315.5,-66.2
crack 315.5,-66.2 316.0,-66.1
crack 316.0,-66.1 316.5,-66.1
crack 316.5,-66.1 317.0,-66.1
crack 317.0,-66.1 317.5,-66.2
crack 317.5,-66.2 318.0,-66.3
crack 318.0,-66.3 318.5,-66.4
crack 318.5,-66.4 319.0,-66.5
crack 319.0,-66.5 319.5,-66.6
crack 319.5,-66.6 320.0,-66.7
crack 320.0,-66.7 320.5,-66.8
crack 320.5,-66.8 321.0,-67.0
crack 321.0,-67.0 321.5,-67.2
crack 321.5,-67.2 322.0,-67.4
crack 322.0,-67.4 322.5,-67.8
crack 322.5,-67.8 323.0,-68.2
crack 323.0,-68.2 323.5,-68.7
crack 323.5,-68.7 323.75,-69.3
crack 323.75,-69.3 324.0,-70.3 ; end arch

; 1-BMA Vault Geometry
crack 353.3,-77 352.3,-105
crack 343.5,-77 363.1,-77
crack 343.5,-77 343.5,-65.5
crack 363.1,-77 363.1,-65.5
crack 343.5,-65.5 344.0,-64.5 ; begin arch
crack 344.0,-64.5 344.5,-63.7
crack 344.5,-63.7 345.0,-63.2
crack 345.0,-63.2 345.5,-62.8
crack 345.5,-62.8 346.0,-62.4
crack 346.0,-62.4 346.5,-62.0
crack 346.5,-62.0 347.0,-61.7
crack 347.0,-61.7 347.5,-61.5
crack 347.5,-61.5 348.0,-61.3
crack 348.0,-61.3 348.5,-61.1
crack 348.5,-61.1 349.0,-61.0
crack 349.0,-61.0 349.5,-60.9
crack 349.5,-60.9 350.0,-60.8
crack 350.0,-60.8 350.5,-60.7
crack 350.5,-60.7 351.0,-60.6
crack 351.0,-60.6 351.5,-60.6
crack 351.5,-60.6 352.0,-60.5
crack 352.0,-60.5 352.6,-60.5
crack 352.6,-60.5 353.1,-60.5
crack 353.1,-60.5 353.6,-60.5
crack 353.6,-60.5 354.1,-60.5
crack 354.1,-60.5 354.6,-60.5
crack 354.6,-60.5 355.1,-60.6
crack 355.1,-60.6 355.6,-60.6
crack 355.6,-60.6 356.1,-60.7
crack 356.1,-60.7 356.6,-60.8
crack 356.6,-60.8 357.1,-60.9
crack 357.1,-60.9 357.6,-61.0
crack 357.6,-61.0 358.1,-61.1
crack 358.1,-61.1 358.6,-61.3
crack 358.6,-61.3 359.1,-61.5
crack 359.1,-61.5 359.6,-61.7
crack 359.6,-61.7 360.1,-62.0
crack 360.1,-62.0 360.6,-62.4
crack 360.6,-62.4 361.1,-62.8
crack 361.1,-62.8 361.6,-63.2
crack 361.6,-63.2 362.1,-63.7
crack 362.1,-63.7 362.6,-64.5
crack 362.6,-64.5 363.1,-65.5 ; end arch

; Define Vaults Excavation Sequence/Backfill Boundaries (approx. 4 m benches)
crack 240,-73.1 255,-73.1       ; 1-BTF bench (bottom vault/upper backfill)
crack 274.5,-72.8 289.5,-72.8   ; 2-BTF bench (bottom vault/upper backfill)
crack 309,-74.3 324,-74.3       ; 1-BLA lower bench
crack 309,-70.3 324,-70.3       ; 1-BLA upper bench (top of concrete containers)
crack 343.5,-68.1 363.1,-68.1   ; 1-BMA lower bench (top of concrete enclosure)
crack 345.5,-77 345.5,-68.1     ; 1-BMA left wall of concrete enclosure
```

```
crack 361.1,-77 361.1,-68.1      ; 1-BMA right wall of concrete enclosure
crack 343.5,-64.5 363.1,-64.5   ; 1-BMA upper bench

change mat 4 cons 1 range atbl 247 -78      ; 1-BTF room (grouted concrete tanks)
change mat 5 cons 1 range atbl 247 -72      ; 1-BTF rockfill (macadam backfill)
change mat 6 cons 1 range atbl 282 -78      ; 2-BTF room (grouted concrete tanks)
change mat 7 cons 1 range atbl 282 -71      ; 2-BTF rockfill (macadam backfill)
change mat 8 cons 1 range atbl 316,-76      ; 1-BLA room lower bench (no backfill)
change mat 8 cons 1 range atbl 316,-72      ; 1-BLA room upper bench (no backfill)
change mat 8 cons 1 range atbl 316,-68      ; 1-BLA top heading (no backfill)
change mat 9 cons 1 range atbl 351,-76      ; 1-BMA room (reinforced concrete storage)
change mat 10 cons 1 range atbl 344,-76     ; 1-BMA rockfill (left wall)
change mat 10 cons 1 range atbl 362.6,-76  ; 1-BMA rockfill (right wall)
change mat 10 cons 1 range atbl 351,-66     ; 1-BMA rockfill (lower top heading)
change mat 10 cons 1 range atbl 351,-62     ; 1-BMA rockfill (upper top heading)

; Jointing in Far-Field (2x Spacing)
; #1 dip = 0 +/- 17 deg, 6 m spacing
; #2 dip = 90 +/- 5 deg, 4 m spacing
jset id=1 ang 0,17 spa 6,1 tra 1000,0 range mat 1
jset id=2 ang 90,5 spa 4,1 tra 1000,0 range mat 1
jdelete

; Jointing in Near-Field (1x Spacing)
; #3 dip = 0 +/- 17 deg, 3 m spacing
; #4 dip = 90 +/- 5 deg, 2 m spacing
hide range mat 1 4 5 6 7 8 9 10
jset id=3 ang 0,17 spa 3,0.5 tra 1000,0 range mat 2
jset id=4 ang 90,5 spa 2,0.5 tra 1000,0 range mat 2 3
jdelete
show
del bl range area 0.05

save 01a-geometry.sav

; Mesh Generation
gen edge 0.5 ra mat 3
table 1   150,0 453.1,0 453.1,-155 150,-155 150,0
gen edge 4 range outside table 1
gen edge 2 range mat 1
table 2   220,-40 383.1,-40 383.1,-100 220,-100 220,-40
gen quad 0.5 range outside table 2
gen edge 0.5 range outside table 2
gen quad 0.25
gen edge 0.25

save 02a-mesh.sav
```

## SFR 3 Geometry and Mesh

```
new
config fluid
round 0.05

; Far-Field Rock Mass
block 0,0 687,0 687,-360 0,-360
change mat 1 cons 1

; SBA2 Deformation Zone (dip in 2D plane = 9 deg.)
; 4 m above 1BRT
```

```
crack 0,-50 687,-158
crack 0,-49 687,-157
change mat 3 cons 1 range atbl 1,-49.5

; SBA6 Deformation Zone (dip in 2D plane = 9 deg.)
; 70 m below SBA2
crack 0,-120 687,-228
crack 0,-119 687,-227
change mat 3 cons 1 range atbl 1,-119.4

; Near-Field Zone
crack 200,0 200,-165 join
crack 487,0 487,-165 join
crack 200,-165 487,-165 join
change mat 2 cons 1 range atbl 475,-156 475,-115 475,-40

;  2-BMA Vault Geometry
  crack 244.8,-137 244,-157.5
  crack 234.6,-137 255,-137
  crack 234.6,-137 234.6,-125.5
  crack 255,-137 255,-125.5
  crack 234.6,-125.5 235.1,-124.5 ; begin arch
  crack 235.1,-124.5 235.6,-123.7
  crack 235.6,-123.7 236.1,-123.2
  crack 236.1,-123.2 236.6,-122.8
  crack 236.6,-122.8 237.1,-122.4
  crack 237.1,-122.4 237.6,-122.0
  crack 237.6,-122.0 238.1,-121.8
  crack 238.1,-121.8 238.6,-121.6
  crack 238.6,-121.6 239.1,-121.4
  crack 239.1,-121.4 239.6,-121.2
  crack 239.6,-121.2 240.1,-121.1
  crack 240.1,-121.1 240.6,-121.0
  crack 240.6,-121.0 241.1,-120.9
  crack 241.1,-120.9 241.6,-120.8
  crack 241.6,-120.8 242.1,-120.7
  crack 242.1,-120.7 242.6,-120.6
  crack 242.6,-120.6 243.1,-120.6
  crack 243.1,-120.6 243.6,-120.6
  crack 243.6,-120.6 244.1,-120.6
  crack 244.1,-120.6 245.5,-120.6
  crack 245.5,-120.6 246,-120.6
  crack 246,-120.6 246.5,-120.6
  crack 246.5,-120.6 247,-120.6
  crack 247,-120.6 247.5,-120.7
  crack 247.5,-120.7 248,-120.8
  crack 248,-120.8 248.5,-120.9
  crack 248.5,-120.9 249,-121.0
  crack 249,-121.0 249.5,-121.1
  crack 249.5,-121.1 250,-121.2
  crack 250,-121.2 250.5,-121.4
  crack 250.5,-121.4 251,-121.6
  crack 251,-121.6 251.5,-121.8
  crack 251.5,-121.8 252,-122
  crack 252,-122 252.5,-122.4
  crack 252.5,-122.4 253,-122.8
  crack 253,-122.8 253.5,-123.2
  crack 253.5,-123.2 254,-123.7
  crack 254,-123.7 254.5,-124.5
  crack 254.5,-124.5 255,-125.5 ; end arch

; 5-BLA Vault Geometry
  crack 284,-137 283,-165
  crack 275,-137 292.9,-137
  crack 275,-137 275,-127.1
  crack 292.9,-137 292.9,-127.1
  crack 275,-127.1 275.5,-126.1 ; begin arch
  crack 275.5,-126.1 276,-125.5
  crack 276,-125.5 276.5,-125
  crack 276.5,-125 277,-124.6
  crack 277,-124.6 277.5,-124.2
  crack 277.5,-124.2 278,-124
  crack 278,-124 278.5,-123.8
  crack 278.5,-123.8 279,-123.6
  crack 279,-123.6 279.5,-123.5
  crack 279.5,-123.5 280,-123.4
  crack 280,-123.4 280.5,-123.3
  crack 280.5,-123.3 281,-123.2
  crack 281,-123.2 281.5,-123.1
  crack 281.5,-123.1 282,-123
  crack 282,-123 283,-122.9
  crack 283,-122.9 284.4,-122.9
  crack 284.4,-122.9 285.4,-122.9
  crack 285.4,-122.9 285.9,-123
  crack 285.9,-123 286.4,-123.1
  crack 286.4,-123.1 286.9,-123.2
  crack 286.9,-123.2 287.4,-123.3
  crack 287.4,-123.3 287.9,-123.4
  crack 287.9,-123.4 288.4,-123.5
  crack 288.4,-123.5 288.9,-123.6
  crack 288.9,-123.6 289.4,-123.8
  crack 289.4,-123.8 289.9,-124
  crack 289.9,-124 290.4,-124.2
  crack 290.4,-124.2 290.9,-124.6
  crack 290.9,-124.6 291.4,-125
  crack 291.4,-125 291.9,-125.5
  crack 291.9,-125.5 292.4,-126.1
  crack 292.4,-126.1 292.9,-127.1 ; end arch

; 4-BLA Vault Geometry
  crack 321.9,-137 320.9,-165
  crack 312.9,-137 330.8,-137
  crack 319.9,-123 320.9,-122.9
  crack 320.9,-122.9 322.3,-122.9
```

```
crack 312.9,-137 312.9,-127.1
crack 330.8,-137 330.8,-127.1
crack 312.9,-127.1 313.4,-126.1; begin arch
crack 313.4,-126.1 313.9,-125.5
crack 313.9,-125.5 314.4,-125
crack 314.4,-125 314.9,-124.6
crack 314.9,-124.6 315.4,-124.2
crack 315.4,-124.2 315.9,-124
crack 315.9,-124 316.4,-123.8
crack 316.4,-123.8 316.9,-123.6
crack 316.9,-123.6 317.4,-123.5
crack 317.4,-123.5 317.9,-123.4
crack 317.9,-123.4 318.4,-123.3
crack 318.4,-123.3 318.9,-123.2
crack 318.9,-123.2 319.4,-123.1
crack 319.4,-123.1 319.9,-123
crack 322.3,-122.9 323.3,-122.9
crack 323.3,-122.9 323.8,-123
crack 323.8,-123 324.3,-123.1
crack 324.3,-123.1 324.8,-123.2
crack 324.8,-123.2 325.3,-123.3
crack 325.3,-123.3 325.8,-123.4
crack 325.8,-123.4 326.3,-123.5
crack 326.3,-123.5 326.8,-123.6
crack 326.8,-123.6 327.3,-123.8
crack 327.3,-123.8 327.8,-124
crack 327.8,-124 328.3,-124.2
crack 328.3,-124.2 328.8,-124.6
crack 328.8,-124.6 329.3,-125
crack 329.3,-125 329.8,-125.5
crack 329.8,-125.5 330.3,-126.1
crack 330.3,-126.1 330.8,-127.1 ; end arch

; 3-BLA Vault Geometry
crack 360,-137 359,-165
crack 350.8,-137 368.7,-137
crack 350.8,-137 350.8,-127.1
crack 368.7,-137 368.7,-127.1
crack 350.8,-127.1 351.3,-126.1; begin arch
crack 351.3,-126.1 351.8,-125.5
crack 351.8,-125.5 352.3,-125
crack 352.3,-125 352.8,-124.6
crack 352.8,-124.6 353.3,-124.2
crack 353.3,-124.2 353.8,-124
crack 353.8,-124 354.3,-123.8
crack 354.3,-123.8 354.8,-123.6
crack 354.8,-123.6 355.3,-123.5
crack 355.3,-123.5 355.8,-123.4
crack 355.8,-123.4 356.3,-123.3
crack 356.3,-123.3 356.8,-123.2
crack 356.8,-123.2 357.3,-123.1
crack 357.3,-123.1 357.8,-123
crack 357.8,-123 358.8,-122.9
crack 358.8,-122.9 360.2,-122.9
crack 360.2,-122.9 361.2,-122.9
crack 361.2,-122.9 361.7,-123
crack 361.7,-123 362.2,-123.1
crack 362.2,-123.1 362.7,-123.2
crack 362.7,-123.2 363.2,-123.3
crack 363.2,-123.3 363.7,-123.4
crack 363.7,-123.4 364.2,-123.5
crack 364.2,-123.5 364.7,-123.6
crack 364.7,-123.6 365.2,-123.8
crack 365.2,-123.8 365.7,-124
crack 365.7,-124 366.2,-124.2
crack 366.2,-124.2 366.7,-124.6
crack 366.7,-124.6 367.2,-125
crack 367.2,-125 367.7,-125.5
crack 367.7,-125.5 368.2,-126.1
crack 368.2,-126.1 368.7,-127.1 ; end arch

; 2-BLA Vault Geometry
crack 397.7,-137 396.7,-165
crack 388.7,-137 406.6,-137
crack 388.7,-137 388.7,-127.1
crack 406.6,-137 406.6,-127.1
crack 388.7,-127.1 389.2,-126.1; begin arch
crack 389.2,-126.1 389.7,-125.5
crack 389.7,-125.5 390.2,-125
crack 390.2,-125 390.7,-124.6
crack 390.7,-124.6 391.2,-124.2
crack 391.2,-124.2 391.7,-124
crack 391.7,-124 392.2,-123.8
crack 392.2,-123.8 392.7,-123.6
crack 392.7,-123.6 393.2,-123.5
crack 393.2,-123.5 393.7,-123.4
crack 393.7,-123.4 394.2,-123.3
crack 394.2,-123.3 394.7,-123.2
crack 394.7,-123.2 395.2,-123.1
crack 395.2,-123.1 395.7,-123
crack 395.7,-123 396.7,-122.9
crack 396.7,-122.9 398.1,-122.9
crack 398.1,-122.9 399.1,-122.9
crack 399.1,-122.9 399.6,-123
crack 399.6,-123 400.1,-123.1
crack 400.1,-123.1 400.6,-123.2
crack 400.6,-123.2 401.1,-123.3
crack 401.1,-123.3 401.6,-123.4
crack 401.6,-123.4 402.1,-123.5
crack 402.1,-123.5 402.6,-123.6
crack 402.6,-123.6 403.1,-123.8
crack 403.1,-123.8 403.6,-124
crack 403.6,-124 404.1,-124.2
crack 404.1,-124.2 404.6,-124.6
crack 404.6,-124.6 405.1,-125
crack 405.1,-125 405.6,-125.5
crack 405.6,-125.5 406.1,-126.1
crack 406.1,-126.1 406.6,-127.1 ; end arch

; 1-BRT Vault Geometry
crack 434.1,-137 433.1,-165
crack 426.6,-137 441.6,-137
crack 426.6,-137 426.6,-127.5
crack 441.6,-137 441.6,-127.5
crack 426.6,-127.5 427.1,-126.4  ; begin arch
crack 433.1,-124.1 433.6,-124.0
crack 433.6,-124.0 434.1,-124.0
crack 434.1,-124.0 434.6,-124.0
crack 434.6,-124.0 435.1,-124.1
crack 435.1,-124.1 435.6,-124.2
```

```
crack 427.1,-126.4 427.6,-126.0
crack 427.6,-126.0 428.1,-125.7
crack 428.1,-125.7 428.6,-125.4
crack 428.6,-125.4 429.1,-125.2
crack 429.1,-125.2 429.6,-125.0
crack 429.6,-125.0 430.1,-124.8
crack 430.1,-124.8 430.6,-124.6
crack 430.6,-124.6 431.1,-124.5
crack 431.1,-124.5 431.6,-124.4
crack 431.6,-124.4 432.1,-124.3
crack 432.1,-124.3 432.6,-124.2
crack 432.6,-124.2 433.1,-124.1
crack 435.6,-124.2 436.1,-124.3
crack 436.1,-124.3 436.6,-124.4
crack 436.6,-124.4 437.1,-124.5
crack 437.1,-124.5 437.6,-124.6
crack 437.6,-124.6 438.1,-124.8
crack 438.1,-124.8 438.6,-125.0
crack 438.6,-125.0 439.1,-125.2
crack 439.1,-125.2 439.6,-125.4
crack 439.6,-125.4 440.1,-125.7
crack 440.1,-125.7 440.6,-126.0
crack 440.6,-126.0 441.1,-126.4
crack 441.1,-126.4 441.6,-127.5 ; end arch

; Define Vaults/Material Boundaries (approx. 4 m benches)
crack 234.6,-128.2 255,-128.2      ; 2-BMA lower bench (top of concrete enclosure)
crack 236.7,-137 236.7,-128.2      ;      left wall of concrete enclosure
crack 252.9,-137 252.9,-128.2      ;      right wall of concrete enclosure
crack 234.6,-125.5 255,-125.5      ;      upper bench

crack 275,-132 292.9,-132          ; 5-BLA lower bench
crack 275,-127.1 292.9,-127.1      ;      upper bench (top of containers)

crack 312.9,-132 330.8,-132        ; 4-BLA lower bench
crack 312.9,-127.1 330.8,-127.1    ;      upper bench (top of containers)

crack 350.8,-132 368.7,-132        ; 3-BLA lower bench
crack 350.8,-127.1 368.7,-127.1    ;      upper bench (top of containers)

crack 388.7,-132 406.6,-132        ; 2-BLA lower bench
crack 388.7,-127.1 406.6,-127.1    ;      upper bench (top of containers)

crack 426.6,-127.5 441.6,-127.5    ; 1-BRT bench (bottom vault/concrete)
crack 429.6,-137 429.6,-127.5      ; 1-BRT bench (bottom vault/backfill)
crack 438.6,-137 438.6,-127.5      ; 1-BRT bench (bottom vault/backfill)
jdelete

change mat 4 cons 1 range atbl 433.6 -132     ; 1-BRT room (grouted concrete tanks)
change mat 5 cons 1 range atbl 439.6 -132     ; 1-BRT rockfill (macadam backfill)
change mat 5 cons 1 range atbl 427.6 -132     ; 1-BRT rockfill (macadam backfill)
change mat 5 cons 1 range atbl 433.6 -125     ; 1-BRT rockfill (macadam backfill)

change mat 6 cons 1 range atbl 284,-134       ; 5-BLA room lower bench (no backfill)
change mat 6 cons 1 range atbl 284,-130       ; 5-BLA room upper bench (no backfill)
change mat 6 cons 1 range atbl 284,-125       ; 5-BLA top heading (no backfill)

change mat 7 cons 1 range atbl 320,-134       ; 4-BLA room lower bench (no backfill)
change mat 7 cons 1 range atbl 320,-130       ; 4-BLA room upper bench (no backfill)
change mat 7 cons 1 range atbl 320,-125       ; 4-BLA top heading (no backfill)

change mat 8 cons 1 range atbl 360,-134       ; 3-BLA room lower bench (no backfill)
change mat 8 cons 1 range atbl 360,-130       ; 3-BLA room upper bench (no backfill)
change mat 8 cons 1 range atbl 360,-125       ; 3-BLA top heading (no backfill)

change mat 9 cons 1 range atbl 400,-134       ; 2-BLA room lower bench (no backfill)
change mat 9 cons 1 range atbl 400,-130       ; 2-BLA room upper bench (no backfill)
change mat 9 cons 1 range atbl 400,-125       ; 2-BLA top heading (no backfill)

change mat 10 cons 1 range atbl 250.4,-133    ; 2-BMA room (reinforced concrete storage)
change mat 11 cons 1 range atbl 236,-133      ; 2-BMA rockfill (left wall)
change mat 11 cons 1 range atbl 254,-133      ; 2-BMA rockfill (right wall)
change mat 11 cons 1 range atbl 250.4,-127    ; 2-BMA rockfill (lower top heading)
change mat 11 cons 1 range atbl 250.4,-123    ; 2-BMA rockfill (upper top heading)
```

```
; Jointing in Far-Field (2x Spacing)
; #1 dip = 0 +/- 17 deg, 6 m spacing
; #2 dip = 90 +/- 5 deg, 4 m spacing
jset id=1 ang 0,17 spa 6,1 tra 1000,0 range mat 1
jset id=2 ang 90,5 spa 4,1 tra 1000,0 range mat 1
jdelete

; Jointing in Near-Field
; #3 dip = 0 +/- 17 deg, 3 m spacing
; #4 dip = 90 +/- 5 deg, 2 m spacing
hide range mat 1 4 5 6 7 8 9 10
jset id=3 ang 0,17 spa 3,0.5 tra 1000,0 range mat 2
jset id=4 ang 90,5 spa 2,0.5 tra 1000,0 range mat 2 3
jdelete
show
del bl range area 0.05

save 01-3a-geometry.sav

; Mesh Generation
gen edge 0.5 ra mat 3
table 1   150,0 537,0 537,-200 150,-200 150,0
gen edge 4 range outside table 1
gen edge 2 range mat 1
table 2   220,-100 467,-100 467,-160 220,-160 220,-100
gen quad 0.5 range outside table 2
gen edge 0.5 range outside table 2
gen quad 0.25
gen edge 0.25

save 02-3a-mesh.sav
```

## Stress and Pore Pressure Initialization

Provided here for SFR 1 geometry. Minor differences for SFR 3 relating to geometry differences.

```
; Rock Mass & Joint Properties (elastic for stress initialization)

; Far- & Near-Field (RFR02: E=60 GPa, v=0.23)
zone model elastic dens 2700 bu 37e9 sh 24.4e9 biot 0.9

; Deformation Zones (E=16 GPa, v = 0.43)
zone model elastic dens 2600 bu 38e9 sh 5.6e9 range mat 3

; Joint Properties (stress initialization)
joint model area jkn 80e9 jks 2e9 jfric 40 jcoh 10e6 jt 10e6 jdil 5 &
            jperm 80 azero 1e-4 ares 1e-5

fluid density 1000
set flow off
grav 0 -9.81

; In Situ Stress State (R-13-53; p. 16)
insitu str -5e6 0 0 szz 0 xgrad 0 0 0 ygrad 7e4 0 2.7e4 zgrad 0 7e4 ywtable 0 zone_pp

; Boundary Conditions
bound xvel 0 range -1 1 -301 1
bound xvel 0 range 602 604 -301 1
bound yvel 0 range -1 604 -301 -299
```

```
step 25000

save 03a-IniStress.sav

;-----------------------------------------------------------------------

; Switch Rock Mass Properties to Mohr-Coulomb

reset disp jdisp vel rot

; Near-Field (RFR02: E=60 GPa, v=0.23)
zone model mohr dens 2700 bu 37e9 sh 24.4e9 fric 40 c 23.3e6 &
            ten 6.8e6 dil 15 biot 0.9 range mat 2

; Deformation Zones (E=16 GPa, v = 0.43)
zone model mohr dens 2600 bu 38e9 sh 5.6e9 fric 51 c 2e6 ten 0.1e6 dil 15  range mat 3

; Joint Properties
joint model area jkn 80e9 jks 2e9 jfric 40 jcoh 0.1e6 jt 0 jdil 5 &
            jperm 80 azero 1e-4 ares 1e-5

step 25000

save 04a-IniStateMC.sav
```

## SFR 1 Rock Vault Excavation and Subsequent Backfilling

```
reset disp jdisp vel rot

; Joint Properties
joint model area jkn 80e9 jks 2e9 jfric 40 jcoh 0.1e6 jt 0 jdil 5 &
            jperm 80 azero 1e-4 ares 1e-5

set jcond area jkn 80e9 jks 2e9 jfric 40 jcoh 0.1e6 jt 0 jdil 5 &
            jperm 80 azero 1e-4 ares 1e-5

;-------------------------------------------------------------------------------
; history points - tunnel convergence

; 1-BTF
his xd 239,-75       ; his 1 left wall (1m)
his xd 256,-75       ; his 2 right wall (1m)
his yd 241.3,-70.7   ; his 3 left roof (1m)
his yd 252,-70       ; his 4 right roof (1m)
his yd 247.5,-69.5   ; his 5 mid roof (EDZ 0.5m)
his yd 247.5,-69     ; his 6 mid roof (EDZ 1m)
his yd 247.5,-68     ; his 7 mid roof (EDZ 2m)
his yd 247.5,-65     ; his 8 mid roof (EDZ 5m)
his yd 247.5,-60     ; his 9 mid roof (10m)

; 2-BTF
his xd 273.5,-75     ; his 10 left wall (1m)
his xd 290.5,-75     ; his 11 right wall (1m)
his yd 276,-70       ; his 12 left roof (1m)
his yd 289,-71       ; his 13 right roof (1m)
his yd 282,-69       ; his 14 mid roof (EDZ 0.5m)
```

```
his yd 282,-68.5     ; his 15 mid roof (EDZ 1m)
his yd 282,-67.5     ; his 16 mid roof (EDZ 2m)
his yd 282,-64.5     ; his 17 mid roof (EDZ 5m)
his yd 282,-59.5     ; his 18 mid roof (10m)

; 1-BLA
his xd 308,-72       ; his 19 left wall (1m)
his xd 325,-72       ; his 20 right wall (1m)
his yd 311,-66.4     ; his 21 left roof (1m)
his yd 322,-66.4     ; his 22 right roof (1m)
his yd 316,-65.5     ; his 23 mid roof (EDZ 0.5m)
his yd 316,-65       ; his 24 mid roof (EDZ 1m)
his yd 316,-64       ; his 25 mid roof (EDZ 2m)
his yd 316,-61       ; his 26 mid roof (EDZ 5m)
his yd 316,-56       ; his 27 mid roof (10m)

; 1-BMA
his xd 342.5,-69     ; his 28 left wall (1m)
his xd 364,-69       ; his 29 right wall (1m)
his yd 347,-60.5     ; his 30 left roof (1m)
his yd 359,-60.5     ; his 31 right roof (1m)
his yd 353.5,-60     ; his 32 mid roof (EDZ 0.5m)
his yd 353.5,-59.5   ; his 33 mid roof (EDZ 1m)
his yd 353.5,-58.5   ; his 34 mid roof (EDZ 2m)
his yd 353.5,-55.5   ; his 35 mid roof (EDZ 5m)
his yd 353.5,-50.5   ; his 36 mid roof (10m)
his yd 353.5,-45.5   ; his 37 mid roof (15m)
his yd 353.5,-40.5   ; his 38 mid roof (20m)
his yd 353.5,-35.5   ; his 39 mid roof (25m)
;--------------------------------------------------------------------------------

; ---- Excavate 1-BTF First ------------------
joint model area jkn 80e9 jks 2e9 jfric 45 jcoh 0.15e6 jt 0.1e6 jdil 5 &
              jperm 80 azero 1e-4 ares 1e-5 range reg 238,-73 238,-68 257,-68 257,-73
zone model null dens 2700 bu 37e9 sh 24.4e9 range mat 5
step 2500
joint model area jkn 80e9 jks 2e9 jfric 45 jcoh 0.15e6 jt 0.1e6 jdil 5 &
             jperm 80 azero 1e-4 ares 1e-5 range reg 238,-79 238,-68 257,-68 257,-79
zone model null dens 2700 bu 37e9 sh 24.4e9 range mat 4
step 2500
save 05a-Excavate-1BTF.sav

; ---- Excavate 2-BTF Second ------------------
joint model area jkn 80e9 jks 2e9 jfric 45 jcoh 0.15e6 jt 0.1e6 jdil 5 jperm 80 &
            azero 1e-4 ares 1e-5 range reg 272.5,-73 272.5,-67.5 291.5,-67.5 291.5,-73
zone model null dens 2700 bu 37e9 sh 24.4e9 range mat 7
step 2500
joint model area jkn 80e9 jks 2e9 jfric 45 jcoh 0.15e6 jt 0.1e6 jdil 5 jperm 80 &
           azero 1e-4 ares 1e-5 range reg 272.5,-79 272.5,-67.5 291.5,-67.5 291.5,-79
zone model null dens 2700 bu 37e9 sh 24.4e9 range mat 6
; scaling (loose block, later to be replaced with backfill)
zone model null dens 2700 bu 37e9 sh 24.4e9 range bl 4138363 4140491
step 2500
save 06a-Excavate-2BTF.sav
```

```
; ---- Excavate 1-BLA Third ------------------
joint model area jkn 80e9 jks 2e9 jfric 45 jcoh 0.15e6 jt 0.1e6 jdil 5 jperm 80 &
                azero 1e-4 ares 1e-5 range reg 307,-70 307,-64 326,-64 326,-70
zone model null dens 2700 bu 37e9 sh 24.4e9 &
        range mat 8 above 309,-70.3 324,-70.3
step 2500
joint model area jkn 80e9 jks 2e9 jfric 45 jcoh 0.15e6 jt 0.1e6 jdil 5 jperm 80 &
                azero 1e-4 ares 1e-5 range reg 307,-74 307,-64 326,-64 326,-74
zone model null dens 2700 bu 37e9 sh 24.4e9 &
        range mat 8 above 309,-74.3 324,-74.3
; scaling (loose blocks deleted, non-backfilled excavation)
del bl 3187771 3203045 3188347 4036484
step 2500
joint model area jkn 80e9 jks 2e9 jfric 45 jcoh 0.15e6 jt 0.1e6 jdil 5 jperm 80 &
                azero 1e-4 ares 1e-5 range reg 307,-78 307,-64 326,-64 326,-78
zone model null dens 2700 bu 37e9 sh 24.4e9 range mat 8
step 2500
save 07a-Excavate-1BLA.sav

; ---- Excavate 1-BMA Fourth ------------------
joint model area jkn 80e9 jks 2e9 jfric 45 jcoh 0.15e6 jt 0.1e6 jdil 5 jperm 80 &
        azero 1e-4 ares 1e-5 range reg 341.5,-64.5 341.5,-58.5 365.1,-58.5 365.1,-64.5
zone model null dens 2700 bu 37e9 sh 24.4e9 &
        range mat 10 above 343.5,-64.5 363.1,-64.5
step 2500
joint model area jkn 80e9 jks 2e9 jfric 45 jcoh 0.15e6 jt 0.1e6 jdil 5 jperm 80 &
        azero 1e-4 ares 1e-5 range reg 341.5,-68 341.5,-58.5 365.1,-58.5 365.1,-68
zone model null dens 2700 bu 37e9 sh 24.4e9 &
        range mat 10 above 343.5,-68.1 363.1,-68.1
step 2500
joint model area jkn 80e9 jks 2e9 jfric 45 jcoh 0.15e6 jt 0.1e6 jdil 5 jperm 80 &
        azero 1e-4 ares 1e-5 range reg 341.5,-77 341.5,-58.5 365.1,-58.5 365.1,-77
zone model null dens 2700 bu 37e9 sh 24.4e9 range mat 9 10
step 17500
save 08a-Excavate-1BMA.sav

;-----------------------------------------------------------------
; Backfilling after repository closure
; Concrete (model as elastic w/ properties from Table 2-7 in R-13-53)
; E = 17 GPa, v = 0.15
zone model elastic dens 2400 bu 8.1e9 sh 7.4e9 range mat 4 6 9

; Macadam backfilling (model as elastic w/ properties)
; E = 300 MPa, v = 0.3
zone model elastic dens 1900 bu 250e6 sh 115e6 range mat 5 7 10
zone model elastic dens 1900 bu 250e6 sh 115e6 range bl 4138363 4140491

; history points - backfill pressures
his sxx 247,-72  ; his 40 (1-BTF rockfill)
his syy 247,-72  ; his 41 (1-BTF rockfill)
his sxx 247,-75  ; his 42 (1-BTF concrete)
his syy 247,-75  ; his 43 (1-BTF concrete)

his sxx 282,-72  ; his 44 (2-BTF rockfill)
```

```
his syy 282,-72  ; his 45 (2-BTF rockfill)
his sxx 282,-75  ; his 46 (2-BTF concrete)
his syy 282,-75  ; his 47 (2-BTF concrete)

his sxx 353,-64  ; his 48 (1-BMA rockfill)
his syy 353,-64  ; his 49 (1-BMA rockfill)
his sxx 353,-70  ; his 50 (1-BMA concrete)
his syy 353,-70  ; his 51 (1-BMA concrete)

step 40000
save 09a-Backfill.sav
```

**SFR 3 Rock Vault Excavation and Subsequent Backfilling**

```
reset disp jdisp vel rot

; Joint Properties
joint model area jkn 80e9 jks 2e9 jfric 40 jcoh 0.1e6 jt 0 jdil 5 &
        jperm 80 azero 1e-4 ares 1e-5

set jcond area jkn 80e9 jks 2e9 jfric 40 jcoh 0.1e6 jt 0 jdil 5 &
        jperm 80 azero 1e-4 ares 1e-5

;-------------------------------------------------------------------------------
; history points - tunnel convergence

; 1-BRT
his xd 425.6,-132     ; his 1 left wall (1m)
his xd 442.6,-132     ; his 2 right wall (1m)
his yd 428.6,-123     ; his 3 left roof (1m)
his yd 439.6,-123     ; his 4 right roof (1m)
his yd 434.1,-123.5  ; his 5 mid roof (EDZ 0.5m)
his yd 434.1,-123    ; his 6 mid roof (EDZ 1m)
his yd 434.1,-122    ; his 7 mid roof (EDZ 2m)
his yd 434.1,-119    ; his 8 mid roof (EDZ 5m)
his yd 434.1,-114    ; his 9 mid roof (10m)

; 5-BLA
his xd 274,-132     ; his 10 left wall (1m)
his xd 294,-132     ; his 11 right wall (1m)
his yd 277,-121.9    ; his 12 left roof (1m)
his yd 291,-121.9    ; his 13 right roof (1m)
his yd 284,-122.4    ; his 14 mid roof (EDZ 0.5m)
his yd 284,-121.9     ; his 15 mid roof (EDZ 1m)
his yd 284,-120.9     ; his 16 mid roof (EDZ 2m)
his yd 284,-117.9     ; his 17 mid roof (EDZ 5m)
his yd 284,-112.9     ; his 18 mid roof (10m)

; 4-BLA
his xd 312,-132     ; his 19 left wall (1m)
his xd 332,-132     ; his 20 right wall (1m)
his yd 316,-121.9    ; his 21 left roof (1m)
```

```
his yd 328,-121.9    ; his 22 right roof (1m)
his yd 322,-122.4    ; his 23 mid roof (EDZ 0.5m)
his yd 322,-121.9      ; his 24 mid roof (EDZ 1m)
his yd 322,-120.9      ; his 25 mid roof (EDZ 2m)
his yd 322,-117.9      ; his 26 mid roof (EDZ 5m)
his yd 322,-112.9      ; his 27 mid roof (10m)

; 3-BLA
his xd 350,-132      ; his 28 left wall (1m)
his xd 370,-132      ; his 29 right wall (1m)
his yd 354,-121.9    ; his 30 left roof (1m)
his yd 366,-121.9    ; his 31 right roof (1m)
his yd 359.8,-122.4    ; his 32 mid roof (EDZ 0.5m)
his yd 359.8,-121.9      ; his 33 mid roof (EDZ 1m)
his yd 359.8,-120.9      ; his 34 mid roof (EDZ 2m)
his yd 359.8,-117.9      ; his 35 mid roof (EDZ 5m)
his yd 359.8,-112.9      ; his 36 mid roof (10m)

; 2-BLA
his xd 388,-132        ; his 37 left wall (1m)
his xd 407.5,-132      ; his 38 right wall (1m)
his yd 391,-121.9      ; his 39 left roof (1m)
his yd 404,-121.9      ; his 40 right roof (1m)
his yd 397.7,-122.4    ; his 41 mid roof (EDZ 0.5m)
his yd 397.7,-121.9    ; his 42 mid roof (EDZ 1m)
his yd 397.7,-120.9    ; his 43 mid roof (EDZ 2m)
his yd 397.7,-117.9    ; his 44 mid roof (EDZ 5m)
his yd 397.7,-112.9    ; his 45 mid roof (10m)

; 2-BMA
his xd 233.6,-126    ; his 46 left wall (1m)
his xd 246,-126      ; his 47 right wall (1m)
his yd 237.6,-119.6  ; his 48 left roof (1m)
his yd 252,-119.6    ; his 49 right roof (1m)
his yd 244.8,-120.1  ; his 50 mid roof (EDZ 0.5m)
his yd 244.8,-119.6  ; his 51 mid roof (EDZ 1m)
his yd 244.8,-118.6  ; his 52 mid roof (EDZ 2m)
his yd 244.8,-115.6  ; his 53 mid roof (EDZ 5m)
his yd 244.8,-110.6  ; his 54 mid roof (10m)
his yd 244.8,-105.6  ; his 55 mid roof (15m)
his yd 244.8,-100.6  ; his 56 mid roof (20m)
his yd 244.8,-95.6   ; his 57 mid roof (25m)
;--------------------------------------------------------------------------------

; ---- excavate 1-BRT First ------------------
joint model area jkn 80e9 jks 2e9 jfric 45 jcoh 0.15e6 jt 0.1e6 jdil 5 jperm 80 &
        azero 1e-4 ares 1e-5 range reg 430,-127.5 430,-122 449,-122 449,-127.5
zone model null dens 2700 bu 37e9 sh 24.4e9 range mat 5
step 2500
joint model area jkn 80e9 jks 2e9 jfric 45 jcoh 0.15e6 jt 0.1e6 jdil 5 jperm 80 &
        azero 1e-4 ares 1e-5 range reg 430,-136 430,-122 449,-122 449,-136
zone model null dens 2700 bu 37e9 sh 24.4e9 range mat 4
step 2500
save 05-3a-Excavate-1BRT.sav
```

```
; ---- excavate 2-BLA Second ------------------
joint model area jkn 80e9 jks 2e9 jfric 45 jcoh 0.15e6 jt 0.1e6 jdil 5 jperm 80 &
      azero 1e-4 ares 1e-5 range reg 386.7,-127 386.7,-120.9 408.6,-120.9 408.6,-127
zone model null dens 2700 bu 37e9 sh 24.4e9 &
        range mat 9 above 388.7,-127.1 406.6,-127.1
step 2500
joint model area jkn 80e9 jks 2e9 jfric 45 jcoh 0.15e6 jt 0.1e6 jdil 5 jperm 80 &
      azero 1e-4 ares 1e-5 range reg 386.7,-132 386.7,-120.9 408.6,-120.9 408.6,-132
zone model null dens 2700 bu 37e9 sh 24.4e9 &
        range mat 9 above 388.7,-132 406.6,-132
step 2500
joint model area jkn 80e9 jks 2e9 jfric 45 jcoh 0.15e6 jt 0.1e6 jdil 5 jperm 80 &
      azero 1e-4 ares 1e-5 range reg 386.7,-136 386.7,-120.9 408.6,-120.9 408.6,-136
zone model null dens 2700 bu 37e9 sh 24.4e9 range mat 9
; scaling (to be changed to backfill later)
zone model null dens 2700 bu 37e9 sh 24.4e9 &
        range bl 5325182 5324782 5323982 5323406
step 2500
save 09-3a-Excavate-2BLA.sav

; ---- excavate 3-BLA Third -------------------
joint model area jkn 80e9 jks 2e9 jfric 45 jcoh 0.15e6 jt 0.1e6 jdil 5 jperm 80 &
      azero 1e-4 ares 1e-5 range reg 348.8,-127 348.8,-120.9 370.7,-120.9 370.7,-127
zone model null dens 2700 bu 37e9 sh 24.4e9 &
        range mat 8 above 350.8,-127.1 368.7,-127.1
step 2500
joint model area jkn 80e9 jks 2e9 jfric 45 jcoh 0.15e6 jt 0.1e6 jdil 5 jperm 80 &
      azero 1e-4 ares 1e-5 range reg 348.8,-132 348.8,-120.9 370.7,-120.9 370.7,-132
zone model null dens 2700 bu 37e9 sh 24.4e9 &
        range mat 8 above 350.8,-132 368.7,-132
step 2500
joint model area jkn 80e9 jks 2e9 jfric 45 jcoh 0.15e6 jt 0.1e6 jdil 5 jperm 80 &
      azero 1e-4 ares 1e-5 range reg 348.8,-136 348.8,-120.9 370.7,-120.9 370.7,-136
zone model null dens 2700 bu 37e9 sh 24.4e9 range mat 8
step 2500
save 08-3a-Excavate-3BLA.sav

; ---- excavate 4-BLA Fourth ------------------
joint model area jkn 80e9 jks 2e9 jfric 45 jcoh 0.15e6 jt 0.1e6 jdil 5 jperm 80 &
      azero 1e-4 ares 1e-5 range reg 310.9,-127 310.9,-120.9 332.8,-120.9 332.8,-127
zone model null dens 2700 bu 37e9 sh 24.4e9 &
        range mat 7 above 312.9,-127.1 330.8,-127.1
step 2500
joint model area jkn 80e9 jks 2e9 jfric 45 jcoh 0.15e6 jt 0.1e6 jdil 5 jperm 80 &
      azero 1e-4 ares 1e-5 range reg 310.9,-132 310.9,-120.9 332.8,-120.9 332.8,-132
zone model null dens 2700 bu 37e9 sh 24.4e9 &
        range mat 7 above 312.9,-132 330.8,-132
step 2500
joint model area jkn 80e9 jks 2e9 jfric 45 jcoh 0.15e6 jt 0.1e6 jdil 5 jperm 80 &
      azero 1e-4 ares 1e-5 range reg 310.9,-136 310.9,-120.9 332.8,-120.9 332.8,-136
zone model null dens 2700 bu 37e9 sh 24.4e9 range mat 7
step 2500
save 07-3a-Excavate-4BLA.sav
```

```
; ---- excavate 5-BLA Fifth ------------------
joint model area jkn 80e9 jks 2e9 jfric 45 jcoh 0.15e6 jt 0.1e6 jdil 5 jperm 80 &
       azero 1e-4 ares 1e-5 range reg 273,-127 273,-120.9 294.9,-120.9 294.9,-127
zone model null dens 2700 bu 37e9 sh 24.4e9 &
         range mat 6 above 275,-127.1 292.9,-127.1
step 2500
joint model area jkn 80e9 jks 2e9 jfric 45 jcoh 0.15e6 jt 0.1e6 jdil 5 jperm 80 &
        azero 1e-4 ares 1e-5 range reg 273,-132 273,-120.9 294.9,-120.9 294.9,-132
zone model null dens 2700 bu 37e9 sh 24.4e9 &
         range mat 6 above 275,-132 292.9,-132
step 2500
joint model area jkn 80e9 jks 2e9 jfric 45 jcoh 0.15e6 jt 0.1e6 jdil 5 jperm 80 &
         azero 1e-4 ares 1e-5 range reg 273,-136 273,-120.9 294.9,-120.9 294.9,-136
zone model null dens 2700 bu 37e9 sh 24.4e9 range mat 6
step 2500
save 06-3a-Excavate-5BLA.sav

; ---- excavate 2-BMA Sixth ------------------
joint model area jkn 80e9 jks 2e9 jfric 45 jcoh 0.15e6 jt 0.1e6 jdil 5 jperm 80 &
       azero 1e-4 ares 1e-5 range reg 232.6,-125 232.6,-118.6 257,-118.6 257,-125
zone model null dens 2700 bu 37e9 sh 24.4e9 &
         range mat 11 above 234.6,-125.5 255,-125.5
step 2500
joint model area jkn 80e9 jks 2e9 jfric 45 jcoh 0.15e6 jt 0.1e6 jdil 5 jperm 80 &
       azero 1e-4 ares 1e-5 range reg 232.6,-128 232.6,-118.6 257,-118.6 257,-128
zone model null dens 2700 bu 37e9 sh 24.4e9 &
         range mat 11 above 234.6,-128.2 255,-128.2
step 2500
joint model area jkn 80e9 jks 2e9 jfric 45 jcoh 0.15e6 jt 0.1e6 jdil 5 jperm 80 &
        azero 1e-4 ares 1e-5 range reg 232.6,-136 232.6,-118.6 257,-118.6 257,-128
zone model null dens 2700 bu 37e9 sh 24.4e9 range mat 10 11
step 17500
save 10-3a-Excavate-2BMA.sav

;---------------------------------------------------------------------
; Backfilling after repository closure

; Concrete (model as elastic w/ properties from Table 2-7 in R-13-53)
; E = 17 GPa, v = 0.15
zone model elastic dens 2400 bu 8.1e9 sh 7.4e9 range mat 4 10

; Macadam (model as elastic w/ properties)
; E = 300 MPa, v = 0.3
zone model elastic dens 1900 bu 250e6 sh 115e6 range mat 5 11

; Backfill pressures
his sxx 433.6,-125  ; his 58 (1-BRT backfill)
his syy 433.6,-125  ; his 59 (1-BRT backfill)
his sxx 433.6,-130  ; his 60 (1-BRT concrete)
his syy 433.6,-130  ; his 61 (1-BRT concrete)

his sxx 245,-125  ; his 62 (2-BMA backfill)
his syy 245,-125  ; his 63 (2-BMA backfill)
his sxx 245,-130  ; his 64 (2-BMA concrete)
```

```
his syy 245,-130  ; his 65 (2-BMA concrete)

step 40000
save 11-3a-Backfill.sav
```

## Time-Dependent Strength Degradation FISH Functions – Fracture Contacts

```
;********** Fracture Contacts **********

def c_strength
    ;dum = out('_time: ' + string(_time))
    _phi_0_c = 40
    _c_0_c   = 0.1e6
    _n_dc = 0 ; number of degraded contacts
    _n_tc = 0 ; total number of contacts
    cid = contact_head                          ; list of contacts
    loop while cid # 0                          ; loop for each single contact
        l_c   = c_length(cid)     ; contact length
        if l_c > 0
            nf_c  = c_nforce(cid)               ; normal force on contact
            sf_c  = c_sforce(cid)               ; shear force on contact
            ns_c  = nf_c / l_c                  ; normal stress on contact
            ss_c  = sf_c / l_c                  ; shear stress on contact
            pss_c  = ns_c * tan(_phi_0_c * degrad) + _c_0_c   ; Peak shear
strength at contact normal stress
            DSR_c = ss_c / pss_c                ; Driving stress ratio
            if DSR_c > 1.0
               DSR_c = 1.0
            endif
            phi_t_c = fmem(c_jex(cid) + $ac_phi)
            c_t_c = fmem(c_jex(cid) + $ac_coh)
            t_t_c = fmem(c_jex(cid) + $ac_ten)
            if _time < 101.0
                ; Look for support influenced joints around vaults
                if c_group(cid) = 'Support'
                    phi_t_c = phi_t_c - 5
                    fmem(c_jex(cid) + $ac_phi) = phi_t_c
                    c_t_c = c_t_c - 0.05e6
                    fmem(c_jex(cid) + $ac_coh) = c_t_c
                    t_t_c = 0
                    fmem(c_jex(cid) + $ac_ten) = 0
                    endif
                endif
                if ns_c < 0
                    fmem(c_jex(cid) + $ac_coh) = 0
                    fmem(c_jex(cid) + $ac_ten) = 0
                endif
                if c_t_c < 0
                    c_t_c=0
                    fmem(c_jex(cid) + $ac_coh) = 0
                endif
                if DSR_c > 0.3
```

```
        A_c = 30.0 * exp(0.1 * (ns_c / 1e6))
        B_c = 1.0 + A_c * (1.0 - DSR_c)
        D_t_c = max(((log(_time*365*24*60*60)- B_c)/(-B_c)),0.3)
        c_t_c = D_t_c * _c_0_c
        fmem(c_jex(cid) + $ac_coh) = c_t_c
        phi_t_c = D_t_c * _phi_0_c
        fmem(c_jex(cid) + $ac_phi) = phi_t_c
    endif
    ; The support effect until year 100
    if _time < 99.0
        ; Look for support influenced joints around vaults
        if c_group(cid) = 'Support'
            fmem(c_jex(cid) + $ac_phi) = phi_t_c + 5
            fmem(c_jex(cid) + $ac_coh) = c_t_c + 0.05e6
            fmem(c_jex(cid) + $ac_ten) = 0.1e6
        endif
    endif
    ; adding permafrost effect at 20k years:
    ;+10% in pp, +0.5e6MPa in cohesion, +0.25e6 in tensile
    if _time > 19999
        if _time < 20001
            if c_y(cid) > -200
                _d1_c = c_d1(cid)
                _d2_c = c_d2(cid)
                _pp_d1 = d_pp(_d1_c)
                _pp_d2 = d_pp(_d2_c)
                fmem(_d1_c + $kpp) = 1.1 * _pp_d1
                fmem(_d2_c + $kpp) = 1.1 * _pp_d2
            endif
        endif
    endif
    if _time > 20010.0
        if _time < 21010.0
            if c_y(cid) > -200.0
                _d1_c = c_d1(cid)
                _d2_c = c_d2(cid)
                _pp_d1 = d_pp(_d1_c)
                _pp_d2 = d_pp(_d2_c)
                fmem(_d1_c + $kpp) = _pp_d1 / 1.1
                fmem(_d2_c + $kpp) = _pp_d2 / 1.1
                c_t_c = fmem(c_jex(cid) + $ac_coh)
                if c_t_c > 0.5e6
                    fmem(c_jex(cid) + $ac_coh) = c_t_c - 0.5e6
                else
                    fmem(c_jex(cid) + $ac_coh) = 0
                endif
                fmem(c_jex(cid) + $ac_ten) = 0
            endif
        endif
    endif
    if _time > 65010.0
        if _time < 66010.0
            if c_y(cid) > -200.0
                _d1_c = c_d1(cid)
```

```
                                _d2_c = c_d2(cid)
                                _pp_d1 = d_pp(_d1_c)
                                _pp_d2 = d_pp(_d2_c)
                                fmem(_d1_c + $kpp) = _pp_d1 / 1.1
                                fmem(_d2_c + $kpp) = _pp_d2 / 1.1
                                c_t_c = fmem(c_jex(cid) + $ac_coh)
                                if c_t_c > 0.5e6
                                    fmem(c_jex(cid) + $ac_coh) = c_t_c - 0.5e6
                                else
                                    fmem(c_jex(cid) + $ac_coh) = 0
                                endif
                                fmem(c_jex(cid) + $ac_ten) = 0
                            endif
                        endif
                    endif
                endif
                cid = c_next(cid)       ; next contact in list
            endloop
end
```

## Time-Dependent Strength Degradation FISH Functions – Intact Block Zones

```
;********** Intact Block Zones **********

def z_strength
    bid = block_head                        ; list of blocks
    loop while bid # 0                      ; loop for each single block
        if b_mat(bid) = 2 then              ; Intact rock in Near-field except
the deformation zone
            _phi_0_z_2 = 40   ; initial friction angle for intact rock
            _c_0_z_2 = 23.3e6 ;initial cohesion for intact rock
            _t_0_z_2 = 6.8e6   ;initial tensile strength
            zid = b_zone(bid)  ; list of zone in each block
            loop while zid # 0  ; loop for each single zone
                z_s_xx = z_sxx(zid) ; sxx of zone
                z_s_xy = z_sxy(zid)         ; sxy of zone
                z_s_yy = z_syy(zid)         ; syy of zone
                ; major and minor principal stresses in zone
                _ps3_temp = 0.5 * (z_s_xx + z_s_yy)
                _ps3 = _ps3_temp + sqrt(z_s_xy^2 + 0.25 * (z_s_xx - z_s_yy)^2)
                _ps1_temp = 0.5 * (z_s_xx + z_s_yy)
                _ps1 = _ps1_temp - sqrt(z_s_xy^2 + 0.25 * (z_s_xx - z_s_yy)^2)
                ; Calculation of confined strength according to Gen. H-B with
sigci=205 MPa, GSI=90, mi=28
                _m_i = 28.0
                _sigci = 205.0e6
                _GSI = 90.0
                _DF = 0.0
                _sigt_HB = 3.4e6
                _m_b = _m_i * exp((_GSI - 100.0)/(28.0-(14.0*_DF)))
                s_HB = exp((_GSI-100.0)/(9.0-(3.0*_DF)))
                a_HB = 0.5 + (exp(-_GSI/15)+exp(-20.0/3.0))/6
```

```
            ; H-B strength at different confining pressures for DSR calculation
            ; _ps3 multiplied by -1 to reverse the sign
            ; if ps3 > tensile strength, tensile strength is used instead of ps3 in H-B
                if (-_ps3) > (-_sigt_HB)
sig1_HB_z_2 = (-_ps3) + _sigci * ((_m_b*(-_ps3)/_sigci) + s_HB)^a_HB
                else
                    sig1_HB_z_2 = (-_sigt_HB) + _sigci * ((_m_b*(-
_sigt_HB)/_sigci) + s_HB)^a_HB
                endif
                ; Driving stress ratio
                DSR_z_2 = abs((_ps1 - _ps3) / (sig1_HB_z_2 - (-(_ps3))))
                if DSR_z_2 > 1.0
                    DSR_z_2 = 1.0
                endif
                if DSR_z_2 >= 0.4
                    ; parameters named after Marks's strength degradation report
                    A_z_2 = 30.0 * exp(0.1*(-_ps3)/1.0e6)
                    B_z_2 = 1.0 + A_z_2 * (1.0 - DSR_z_2)
                    D_t_z_2 = max(((log(_time*365*24*60*60)-B_z_2)/(-
B_z_2)),0.4)
                    temp_z_2=(_sigci* (1 - sin(_phi_0_z_2 * degrad)))
                    temp_z_2=temp_z_2 / (2 * cos(_phi_0_z_2 * degrad))
                    dum=out(string(temp_z_2))
                    z_prop(zid,'cohesion') = D_t_z_2 * temp_z_2
                    z_prop(zid,'tension') = D_t_z_2 * _t_0_z_2
                endif
                zid = z_next(zid)               ; next zone in list
            endloop
        else
            if b_mat(bid) = 3                   ; Deformation zone
                _c_0_z_3 = 2e6
                _phi_0_z_3 = 51
                _t_0_z_3 = 0.1e6
                _sigci_z_3 = 11.3e6 ; calculated using c and phi
                zid = b_zone(bid)               ; list of zone in each block
                loop while zid # 0              ; loop for each single zone
                    z_s_xx = z_sxx(zid) ; sxx of zone
                    z_s_xy = z_sxy(zid)         ; sxy of zone
                    z_s_yy = z_syy(zid)         ; syy of zone
                    ; major and minor principal stresses in zone
                    _ps3_temp = 0.5 * (z_s_xx + z_s_yy)
                    _ps3 = _ps3_temp + sqrt(z_s_xy^2 + 0.25 * (z_s_xx -
z_s_yy)^2)
                    _ps1_temp = 0.5 * (z_s_xx + z_s_yy)
                    _ps1 = _ps1_temp - sqrt(z_s_xy^2 + 0.25 * (z_s_xx -
z_s_yy)^2)
                   ; if ps3 > tensile strength, tensile strength is used instead of ps3
                    if (-_ps3) > (-_t_0_z_3)
                        t1_z_3 = 2*_c_0_z_3*(cos(_phi_0_z_3*degrad))
                        t2_z_3 = t1_z_3/(1-sin(_phi_0_z_3*degrad))
                        t3_z_3 = (-_ps3)*((1+sin(_phi_0_z_3*degrad)))
                        t4_z_3 = t3_z_3/(1-sin(_phi_0_z_3*degrad))
                        sig1_z_3 = t2_z_3 + t4_z_3
                    else
```

```
                    t1_z_3 = 2*_c_0_z_3*(cos(_phi_0_z_3*degrad))
                    t2_z_3 = t1_z_3/(1-sin(_phi_0_z_3*degrad))
                    t3_z_3 = (-_t_0_z_3)*((1+sin(_phi_0_z_3*degrad)))
                    t4_z_3 = t3_z_3/(1-sin(_phi_0_z_3*degrad))
                    sig1_z_3 = t2_z_3 + t4_z_3
                endif
                ; Driving stress ratio
                DSR_z_3 = abs((_ps1 - _ps3) / (sig1_z_3 - (-(_ps3))))
                if DSR_z_3 > 1.0
                    DSR_z_3 = 1.0
                endif
                if DSR_z_3 >= 0.4
                    ;dum = out('DSR_z_3: ' + string(DSR_z_3))
                    ;dum = out('_ps3: ' + string(_ps3))
                    ; parameters named after Marks's strength degradation
report
                    A_z_3 = 30.0 * exp(0.1*(-_ps3)/1.0e6)
                    B_z_3 = 1.0 + A_z_3 * (1.0 - DSR_z_3)
                    D_t_z_3 = max(((log(_time*365*24*60*60)-B_z_3)/(-
B_z_3)),0.4)
                    temp_z_3=(_sigci_z_3* (1 - sin(_phi_0_z_3 * degrad)))
                    temp_z_3=temp_z_3 / (2 * cos(_phi_0_z_3 * degrad))
                    z_prop(zid,'cohesion') = D_t_z_3 * temp_z_3
                    z_prop(zid,'tension') = D_t_z_3 * _t_0_z_3
                endif
                zid = z_next(zid)           ; next zone in list
            endloop
        endif
    endif
    bid = b_next(bid)                       ; next block in list
endloop
end
```

## Year 10 to Year 66,000 Strength Degradation

Provided here for SFR 1 geometry. Minor differences for SFR 3 relating to geometry differences.

```
restore 09a-Backfill.sav

;**************************************
;--------- Group Supported Joints ---------
group joint Support range reg 237.9,-79.1 237.9,-67.9 257.1,-67.9 257.1,-79.1
group joint Support range reg 272.4,-79.1 272.4,-67.4 291.6,-67.4 291.6,-79.1
group joint Support range reg 306.9,-78.1 306.9,-63.9 326.1,-63.9 326.1,-78.1
group joint Support range reg 341.4,-77.1 341.4,-58.4 365.2,-58.4 365.2,-77.1

;----- Call required FIN / FIS files -----
call boucnr.fin
call contact.fin
call domain.fin
call jmat.fin
call ZSDF.fis
call CSDF.fis
```

```
;----- Degradation at year 10 with support -----
set _time = 10.0
z_strength
c_strength
step 10000
save 10a-Year10.sav
;*****************************************

;*****************************************
;----- Degradation at year 20 with support -----
set _time = 20.0
z_strength
c_strength
step 10000
save 11a-Year20.sav
;*****************************************

;*****************************************
;----- Degradation at year 50 with support -----
set _time = 50.0
z_strength
c_strength
step 10000
save 12a-Year50.sav
;*****************************************

;*****************************************
;----- Degradation at year 100 without support -----
set _time = 100.0
z_strength
c_strength
step 10000
save 13a-Year100.sav
;*****************************************

;*****************************************
;----- Degradation at year 200 without support -----
set _time = 200.0
z_strength
c_strength
step 10000
save 14a-Year200.sav
;*****************************************

;*****************************************
;----- Degradation at year 500 without support -----
set _time = 500.0
z_strength
c_strength
step 10000
save 15a-Year500.sav
;*****************************************
```

```
;*****************************************
;----- Degradation at year 1000 without support -----
set _time = 1000.0
z_strength
c_strength
step 100000
save 16a-Year1000.sav
;*****************************************

;*****************************************
;----- Degradation at year 2000 without support -----
set _time = 2000.0
z_strength
c_strength
step 10000
save 17a-Year2000.sav
;*****************************************

;*****************************************
;----- Degradation at year 5000 without support -----
set _time = 5000.0
z_strength
c_strength
step 10000
save 18a-Year5000.sav
;*****************************************

;*****************************************
;----- Degradation at year 10000 without support -----
set _time = 10000.0
z_strength
c_strength
step 10000
save 19a-Year10000.sav
;*****************************************

;*****************************************
;----- Degradation at year 20000 without support -----
;----- Beginning of the permafrost -----
set _time = 20000.0
z_strength
c_strength
step 10000 ;
save 20a-Year20000.sav
;*****************************************

;*****************************************
;----- Special Case: Degradation at year 21000 without support -----
;----- Permafrost melt -----
set _time = 21000.0
z_strength
c_strength_1
step 10000
save 21a_Year21000.sav
```

```
;**************************************
;----- Degradation at year 50000 without support -----
;----- Horizontal stress decrease and increase before and while glaciation loading  ---
--
rest 20a-Year20000.sav
; geo a- gradient displacement steps from begin:50000 to 10%extension: 67000
; to5MPa compression: 73100
bound xvel -0.01 range -1 1 -301 1
step 43000
save 22a_1mmExten_dcBC.sav
boundary stress 0,0,-20e6 range -1 604 -1 1
bound xvel 0.01 range -1 1 -301 1
step 6000
save 22a_1mmComp_dcBC.sav
bound xvel 0.0 range -1 1 -301 1
step 20000
save 22a_0mmComp_dcBC.sav
;----- Beginning of glaciation -----
set _time = 50000.0
z_strength
c_strength
step 100000 ;
save 23a-Year50000.sav
;----- Beginning of deglaciation -----
boundary stress 0,0,20e6 range -1 604 -1 1
step 100000
save 24a-Deglaciation.sav
set _time = 65000.0
z_strength
c_strength
step 10000
save 24a-Year65000.sav
;----- Final permafrost melt -----
set _time = 66000.0
z_strength
c_strength_1
step 100000
save 25a_Year66000.sav
```

2

**Author:** Biswajit Dasgupta [1)]
[1)]Southwest Research Institute

# Review of the hydraulic conductivity, sorption, and mechanical properties of concrete barriers of SFR

**Activity number:** 3030014-1025
**Registration number:** SSM 2016-4331
**Contact person at SSM:** Flavio Lanaro

# Contents

# 1. Introduction

This report documents an independent review by the Center for Nuclear Waste Regulatory Analyses (CNWRA®) of SKB information supporting the license application for extension of the final repository for low- and intermediate-level waste at Forsmark (SFR). Specifically, the focus of the review is on SKB's treatment of the changes in the hydraulic conductivity, porosity, sorption, and mechanical properties of concrete barrier structures during operations and after closure. The activities and results documented in this report are intended to support the SSM review and assessment of SKB's application.

The CNWRA review focused on potential concrete degradation processes that may affect concrete structures during the operation of the repository before closure and, for the time after closure, assessing the (i) sensitivity of concrete degradation to the magnitude of groundwater flow through the concrete structures; (ii) influence of concrete degradation and porosity evolution in the concrete barrier structures on the mechanical properties of the concrete; (iii) implications of the geometry of the concrete structures, rock cavern backfill, and the direction of groundwater flow on the equivalent hydraulic conductivity and hydraulic conductivity contrast between concrete structures and backfill; (iv) implications of localised groundwater inflow through the backfill (e.g., due to discrete rock fractures and fracture zones) in comparison to homogeneous inflow; (v) implications of the frequency, geometry, and width of the fractures in concrete resulting from shrinkage and mechanical loads for the hydraulic conductivity, sorption, and mechanical properties of the concrete; (vi) influence of concrete degradation on the freezing temperature of pore and fracture water in the concrete structures and the effect of freezing on the mechanical integrity and mechanical properties of the structures; and (vii) influence of chemical dissolution of other concrete structures, waste packages (e.g. chemical effects of sulphate), rock supports, and grouting on the degradation of the concrete structures.

In conducting the review, the CNWRA reviewers focused on parameters such as hydraulic conductivity, sorption, porosity, and mechanical properties that are representative of the degraded status of the concrete structures at 1,000, 10,000, 20,000, and 50,000 years after closure of the repository, and on the processes affecting the bentonite and concrete plugs that will seal the waste vaults. The review also included consideration of possible ranges of groundwater flow, concentrations of leaching chemicals and pH, and mechanical and hydraulic loads that might imply significant deviations from the reference evolution of concrete parameters assumed in SKB's safety analysis. The review effort was limited to the intermediate-level waste vaults 1BMA in the existing SFR 1 and 2BMA in the proposed SFR 3.

Chapter 2 is the central part of this report and includes the specific assessments requested by SSM. Chapter 3 provides a review summary and Appendix 1 includes a list of SKB documents evaluated during this review.

# 2. Review and assessment

## 2.1. The SR-PSU safety assessment

SKB designated its report "Safety Analysis for SFR Long-Term Safety: Main Report for the Safety Assessment SR-PSU" (SKB TR-14-01) to serve as the main document for the assessment of long-term safety of the SFR repository in Forsmark, Sweden. This SKB SR-PSU report (hereafter called Main Report) supports the SKB application to SSM for a license to extend the SFR repository. The extended SFR repository includes two parts: the existing facility, SFR 1, and the proposed extension, SFR 3.

The SKB objective for post-closure safety is based on the principle of preventing, limiting, and delaying release of radionuclides from the repository. Two main safety functions in the long-term performance of SKB's near-field repository systems are low flow in waste vaults and retention of radionuclides in engineered barriers. The assessment of the response of waste form matrix and the engineered barrier systems to mechanical and chemical processes is based on evaluation of

(i) degradation of hydraulic properties that limit groundwater flow and

(ii) reduction of sorption capacity that limits the mobility of radionuclides.

SKB implemented abstractions of processes to analyse scenarios that may lead to radionuclide release and radiological doses.

The Main Report (SKB TR-14-01) provides an overview of the purpose of demonstrating long-term (post-closure) safety of the extended SFR repository; an overview of general prerequisites including regulations; bases for post-closure safety relying on preventing, limiting, and delaying release of radionuclides; and the 10-step safety assessment methodology. SKB concludes that the extended SFR repository meets regulatory criteria with respect to long-term safety. This review focuses on information in the body of the Main Report (SKB TR-14-01) and relevant cited references that is relevant to the evolution of concrete barriers important to the safety assessment.

## 2.2. Description of vaults and safety functions

1BMA and 2BMA are concrete vaults at SFR constructed in large underground rock caverns for disposing intermediate-level radioactive waste. 1BMA is currently operational in the existing part of the repository (SFR 1) and 2BMA will be constructed in the planned expansion area (SFR 3) (SKB TR-14-02).

The 1BMA vault is located about 60 m below the seabed. The excavation is 160 m long, 19.5 m wide, and 16.5 m high, while the concrete vault is approximately 140 m long, 16 m wide, and 8 m high. The 2BMA system, which will be constructed approximately 117–137 m below the seabed, is 275 m long, 19.2 m wide and 16.8 m high, while the concrete vault is approximately 245 m long, 16 m wide, and 8 m high. The vaults in 1BMA consist of concrete walls and floor built like a long box structure divided into several compartments separated by concrete walls, founded on crushed rock and levelled with gravel. The thickness of walls and foundation of 1BMA are 0.4 m and 0.25 m respectively (SKB TR-1-02). 2BMA will have 14 free standing caissons. The 2BMA caissons walls and foundation are 0.5 m thick (SKB TR-1-02). The waste packages consisting of steel and concrete moulds or steel

drums will be placed in the caissons using a remote-controlled overhead crane, and the caissons will be filled with grout. The BMA vaults will be backfilled with crushed crystalline rock without fine particles.

Two plug sections, P2TT and P2BST (SKB TR-14-01, Figure 4-27), are to be installed to seal the waste vaults in SFR 3. Individual plug systems for 2BMA are depicted in Figures 4-10, 4-23, and 4-26 of the Main Report. In general, all plug systems consist of a hydraulically tight bentonite section and a concrete plug to act as a mechanical constraint for the bentonite section. Mechanical stresses can develop in the concrete plugs because of the swelling pressure of the bentonite material, but concrete plugs are designed to withstand the bentonite swelling pressure (SKB TR-14-01).

The primary engineered barriers in 1BMA and 2BMA are the waste package, concrete walls, and backfill. The safety functions of the waste package and concrete walls are to limit radionuclide advective transport and diffusion, and provide radionuclide sorption and mechanical stability. Highly permeable backfill is designed to provide a hydraulic contrast, developing a hydraulic cage around the concrete structure, which functions as a permeability barrier. Backfill also allows mechanical stability of the cavern. Safety functions of concrete barriers may degrade over time because of decreases in pore water pH or increases in hydraulic conductivity and diffusivity.

## 2.3. Review

### 2.3.1. Rationale of the degradation processes of the concrete structures during the operation of the repository

The SKB plan to address degradation processes during the operational phase of the repository is discussed in the Initial State Report for Safety Assessment SR-PSU (TR-14-02) and in Safety Analysis for SFR Long-Term Safety (TR-14-01). The state of degradation of the concrete vaults affects the hydraulic conductivity, diffusivity, and mechanical properties for post-closure performance analyses. SKB cited a closure plan report (SKBdoc 1358612) describing the inspection and controls for both 1BMA and 2BMA during the operating stage until prior to closure. The plan includes inspection and control of concrete structures during construction and emplacement operations before placement of macadam backfill and closure of plugs. 1BMA in SFR 1 has been operational since 1988 (TR 14-01) and consists of a large, concrete box-like structure, 140-m long and with approximately 16-m high walls, divided into 13 compartments. Fractures were observed in the concrete walls and floors during inspections in 2000 and 2011 (R-13-40). Taking into account the fracture frequency and width, SKB estimated corresponding increases in hydraulic conductivity by several orders of magnitude in vault regions of high fracture concentration. SKB stated that “repair and reinforcement measures need to be adopted to achieve desired hydraulic and mechanical properties at closure” (TR-14-01 and TR-14-02). A different design was adopted for 2BMA at SFR 3, where 14 free-standing concrete caissons (16 m × 16 m at the base and approximately 8 m high) will be constructed. The walls and the floor will be constructed in one step to reduce the risk of fracture formation. SKB further described implementation of requirements for suppliers and material, and methods for testing and inspection during construction to achieve required conditions.

The approach to rely on defect detection and defect repair plans to attain a desired initial state for post-closure safety assessments is common in international radioactive waste management programs. Those plans need to be supplemented with an influence matrix or influence database that tracks the dependence of initial conditions for post-closure safety assessments on the implementation and success of defect detection and defect correction plans. Assumptions need to be adopted on the level of success of those plans, which may be verified during a performance monitoring phase. The influence database may be used in case a level of assumed success of the correction/repair plans cannot be achieved. (For example, it may be assumed that all cracks on concrete will be repaired; however, in practice some cracks may go undetected and would be left in the system without repair.) The influence database would facilitate locating the assumed initial conditions that would be affected by the implementation of less effective than anticipated correction/repair plans. Alternatively, the influence database may be used to define goals of a monitoring program and desired level of success of correction/repair plans. If that level of success is not attainable, the analysis of implications for post-closure safety assessments may be efficiently developed starting from the influence database. For example, the U.S. Department of Energy (DOE) identified in its safety analysis report for Yucca Mountain (DOE, 2009) features, events, processes (FEPs) that relate to parameters requiring procedural safety controls or design configuration control to ensure that the performance assessment analysis basis is met (Tables 1.9-9 and 2.2-3 in DOE, 2009). The DOE considered a FEP titled Repository Design (FEP 1.1.07.00.0A) and the controlled design parameters (Table 2.2-3, DOE, 2009) to define the initial state or boundary conditions in the models and the analyses in the post-closure performance assessment. The U.S. Nuclear Regulatory Commission (NRC) considered the referred Table 2.2-3 as an adequate mechanism to track interdependencies and identify FEPs with screening technical bases that would need re-evaluation if some parameters depart from initial design considerations (NRC, 2014). The SKB approach to rely on maintenance and repair plans is consistent with the international practice. However, it is not clear whether SKB is currently tracking all assumptions for post-closure safety assessments that rely on the success of performance monitoring and maintenance and repair plans.

### 2.3.2. Sensitivity of degradation to the magnitude of groundwater flow through the concrete structures

Chemical degradation of concrete barriers is dependent on the characteristics of groundwater in the near-field, such as its chemical composition and local hydraulic head gradients and hydraulic conductivities that control groundwater fluxes. The degradation process is enhanced during inflow of groundwater by leaching of soluble calcium-based components of hydrated cement (SKB R-13-40). Dissolution of calcium hydroxide (portlandite) and calcium silicate hydrated gel (CSH-gel) during leaching increases porosity, which increases the diffusion coefficient and hydraulic conductivity of the concrete barriers. Additionally, loss of calcium reduces the strength and stiffness of the concrete and may lead to development of fractures.

SKB evaluated advection-controlled leaching of portlandite and CSH-gel (with dissolution due to water flow through pores in the concrete) in SKB R-13-40 using simplified models. These models address leaching of portlandite and CSH-gel in a homogeneous porous medium (concrete matrix) and leaching of portlandite in the fractured concrete. The fracture models included dissolution through entire fracture surfaces, in a thin surface layer, and through the concrete matrix, and SKB evaluated

the depth of leaching zones with time for an assumed groundwater flux. SKB estimated a porosity increase in the leached zone of concrete associated with the loss of solid material.

SKB R-13-40 simulated chemical degradation of concrete in 1BMA and 2BMA over a period of 100,000 years. The evolution of the chemistry in the concrete barriers was analysed using two-dimensional (2-D) reactive transport modelling of a cross-section of the vault perpendicular to the long axis. The BMA repository system in the model was simplified by considering a rectangular boundary of the rock excavation, macadam backfill, and concrete barrier containing a grout liner. For flow calculations in these models, the input groundwater flux was obtained from the 3-D repository scale groundwater flow model for 2BMA (SKB TR-13-08) and for 1BMA (SKB R-01-02). The input groundwater flux to the 2-D model is based on the maximum volumetric inflow rate from any of the caissons from the 3-D model repository scale model, and is applied as the groundwater flux on one side of the vertical boundary. The use of total flow in reactive transport modelling as input to the flow analysis is likely to be conservative, as higher flow rates would be expected to increase the concrete chemical degradation rate.

In the 2BMA geochemical model, the groundwater flux ($m^3/m^2$/year) was increased in steps from $6.5\times10^{-5}$ (0–1,000 years) to $5.3\times10^{-3}$ (1,000– 2,000 years) to $6.7\times10^{-3}$ (greater than 3,000 years). For the 1BMA geochemical model, the groundwater flux ($m^3/m^2$/year) was assumed to be $1.95\times10^{-3}$ for 0–2,000 years and $2.5\times10^{-2}$ after 2,000 years. The groundwater flux for 2BMA was generally lower with respect to 1BMA by a factor 4 to 5 beyond 2,000 years. Geochemical modelling results were presented as changes in the volume of individual minerals, permeant pH, and concrete porosity over time. For 2BMA (Case 20 Large) permeant pH in concrete matrix (position GE near the top section of the model) decreased from a highly alkaline value of 13 to about 9 over 100,000 years, and concrete porosity increased from an initial value of 0.11 to about 0.25 over the same period. The changes in the 1BMA system occurred faster than in the 2BMA system due to the higher flow rates in the 1BMA system. For 1BMA Case 10 Large, permeant pH in the concrete matrix (position AE near the bottom section of the model) decreased from a highly alkaline value of 13 to about 10 in the first 10,000 years, and concrete porosity increased from an initial value of 0.11 to about 0.23 over the same period. The changes in permeant pH and concrete porosity are highly correlated with the leaching of calcium hydroxide (portlandite) and CSH-gel.

The sensitivity of chemical degradation to variations of groundwater inflow was not explicitly evaluated in SKB R-13-40. SKB estimated flow rates and fluxes independently assuming values of the hydraulic conductivity of concrete. SKB used those fluxes as input to the geochemical model. SKB did not consider any couplings in the system. For example, porosity increases (due to leaching) would cause increases in the hydraulic conductivity, which would increase water fluxes, which would enhance leaching rates and shorten the concrete lifetime. It appears that SKB overestimated flow rates for the reactive transport model of the 1BMA system. For that system, concrete degradation times are unlikely to shorten if a more detailed and fully coupled model were adopted. On the other hand, for the 2BMA system, it is unclear whether the water fluxes for the reactive transport model were overestimated; and in that case, it is not possible to conclude that the computed concrete lifetimes are adequate for safety assessments. Considering feedback between the porosity and hydraulic conductivity may lead to shorter estimates of the concrete lifetime.

The geochemical model that SKB implemented is reasonable, as well as the approach to independently estimate water fluxes with a water balance model. The geochemical model is in effect a "wash-away" model, in which the concrete is depleted of portlandite and CSH-gel in proportions regulated by the groundwater flux through the concrete and solubility constraints. Assuming concrete porosity increases in proportion to solids lost is also reasonable. The permeant pH tends to equilibrate with groundwater pH as time elapses and portlandite and CSH-gel are lost. The time estimated for permeant pH to equilibrate with that of the groundwater is dependent on the solubility of portlandite and CSH-gel, the corresponding amounts of those materials in the concrete barriers, and permeant fluxes. That thousands of years was estimated as the equilibration time is consistent with similar work performed by CNWRA related to the longevity of reducing conditions of grout in radioactive waste disposal applications (e.g., near-surface facilities at the Savannah River Site and Idaho National Laboratory; Painter and Pabalan, 2009; Pabalan et al., 2009), as well work by others related to the evolution of pore water chemistry in a radioactive waste repository environment (e.g., Berner, 1992). The final concrete porosity approximately equal to 0.25 is justifiable, based on the initial portlandite and CSH-gel content in the concrete.

The adequacy of the concrete lifetime estimates depends on the magnitude of the water fluxes used in the geochemical models. The water fluxes SKB input to the reactive transport model for the 1BMA system may be overestimates of expected fluxes. In that case, the SKB concrete lifetime estimates can be argued to be shorter than if the water flux was explicitly computed as a function of increases in the porosity. On the other hand, the assumptions adopted for the 2BMA system regarding water flows are not clear. Was a degraded concrete state assumed in the derivation of those flow rates? How were the transition times in water flow rates established? Were those transition times selected based on results of the geochemical model? It is not possible to assert that the estimated concrete lifetime for the 2BMA system is a reasonable input to the safety analysis. It is warranted to request SKB to justify water fluxes used as inputs to the geochemical model, as well as the relationship of those water fluxes to the porosity increases computed by the geochemical model. In other words, SKB should justify the sequential approach to compute porosity changes as a function of time (using water fluxes as independent input to the geochemical model), given that the porosity affects the hydraulic conductivity and the water fluxes.

### 2.3.3. Influence of the degradation and evolution of porosity in the concrete barrier structures on the mechanical properties of the concrete

Increase in porosity causes decreases in mechanical strength and stiffness of concrete. SKB evaluated the evolution of porosity of concrete in the context of effects on the hydraulic conductivity. SKB discussed the influence of degradation of concrete on mechanical properties only qualitatively in SKB R-14-40. Loss of calcium hydroxide (portlandite) and CSH-gels in cement increases the porosity and reduces the mechanical strength of concrete. In addition to leaching of the concrete matrix, cracks may develop and propagate into through-wall fractures. Fractures would further increase the equivalent porosity of the concrete barriers. SKB evaluated evolution of the porosity due to chemical degradation (i.e., leaching of portlandite and CSH-gels) using reactive transport modelling of 1BMA and 2BMA. According to the modelling, the porosity would increase from an initial value of 0.11 to approximately 0.3. The values of porosity suggested for SR-PSU for

different time periods are given in Table 10-4 of SKB R-14-40, which also includes hydraulic conductivities. The SKB evaluation of concrete degradation did not include quantification of mechanical properties (and consequences of changes) in relation to the porosity evolution. SKB did, however, estimate the hydraulic conductivity of construction concrete in local flow modelling in SKB R-13-40, assuming fractures in the concrete. The deterioration of concrete over time was based on assuming increased fracture aperture or spacing over time (Table 7-5 for 2BMA and Table 7-7 for 1BMA; SKB R-13-40). SKB stated that the porosity increase due to chemical degradation becomes prominent only after 10,000 years, and the degradation is influenced by physical processes during the first 10,000 years (SKB R-13-40). CNWRA considers the SKB evaluation of mechanical effects as changes in hydraulic conductivity of concrete (changes computed as functions of fracture properties) to be reasonable. Other secondary changes, such as collapse of structures, were not explicitly accounted for by SKB. Laboratory tests conducted on cement mortar by Chen et.al. (2012) showed compressive strength was 44 percent lower and flexure strength was 38 percent lower at a porosity of 0.3 compared to 0.1. Although those changes to the compressive and flexure strengths may be substantial and be associated with collapse of structures, it is not obvious that significantly higher flow rates would ensue and mobilize waste forms more than was computed based solely on extreme values of the hydraulic conductivity (assumed for degraded concrete conditions). The assessment of degraded concrete by SKB is based on the predominance of physical degradation (dry shrinkage and temperature changes) during the early part of the period of analysis (less than 10,000 years) and the predominance of chemical degradation after 10,000 years. However, SKB has yet to demonstrate mechanical stability of the concrete barrier under a range of loads and alternative scenarios (e.g., earthquakes). It is recommended that SKB examine potential early degradation caused by mechanical loading.

### 2.3.4. Implications of the geometry of the concrete structures, rock cavern backfill, and the direction of groundwater flow for the determination of the equivalent hydraulic conductivity and hydraulic contrast

The effects of geometry of the 1BMA and 2BMA engineered systems (concrete structures, backfill, and rock excavation) and the groundwater flow direction (i.e., normal or parallel flow relative to the axis of the repository) controlling the effective hydraulic conductivity of the entire engineered system were not explicitly addressed by SKB. SKB TR-14-05 asserted that groundwater flow may be affected by the repository geometry, because the excavation backfill and surrounding disturbed zones may provide a permeable path through rock and additional connections between fractures. This statement is not substantiated with modelling studies for the SFR 1 and SFR 3 repository sites. Groundwater flows through the BMA vaults were evaluated in SKB R-13-08, SKB R-01-02, and SKB R-13-40. However, these and other reports cited therein did not conduct sensitivity analyses that address effects of changes in geometry of the cavern (e.g., rock fall), concrete structures (e.g., spalling), and backfill material (e.g., compaction or filling of void spaces) on the hydraulic conductivity and hydraulic contrast. These reports analysed the effects of concrete degradation by considering changes in hydraulic and diffusivity parameters. The effect of the direction of groundwater flow through the vaults is not clear in SKB reports. For example, the regional and repository scale groundwater flow models include heterogeneity and anisotropy of rock mass hydraulic properties in a deterministic manner (SKB TR-13-08) and the results show the inflow of

groundwater into the vaults along a preferential path is influenced by the fracture network.

The approach SKB adopted to determine broad flow values (and ignore details related to geometry effects, orientations, and presence or absence of preferential flow features) is common in performance assessments aimed at estimating expected releases and consequences. We consider it unlikely that consideration of detailed effects and features would significantly change the average water flows that would contact the waste forms, and significantly affect release estimates. Although it is possible that localized preferential flow paths may exist, they generally scavenge flow from some other parts of the system. Fast flow paths may lead to early releases of limited quantities of waste, but average releases are less dependent on localized flow effects. Follow-up questions to SKB on this topic are warranted; however, while we consider that answers to those questions would contribute to completion of a thorough analysis, they are unlikely to change the overall conclusion of the safety analysis of the system.

### 2.3.5. Implications of localised groundwater inflow through the backfill compared to homogeneous inflow

The three-dimensional (3-D) groundwater flow simulation for 2BMA consists of regional- and repository-scale hydrogeological models (SKB TR-13-08). For groundwater flow simulations in the repository-scale model (also called the near-field model), the boundary conditions (e.g., hydraulic head and flux), and the material properties (e.g., hydraulic conductivity of the surrounding host rock) are imported from the regional-scale model. The repository-scale model simulates groundwater flow through the backfilled excavation, the concrete vaults, and the volume of the host rock surrounding the excavation(s). Groundwater flow models for both the regional- and repository-scale models are based on a continuum approach. The groundwater flow rates from the repository scale model are used in radionuclide transport modelling (SKB TR-14-09) and BMA concrete degradation analysis (SKB R-13-40).

SFR is hosted by a fractured crystalline rock and groundwater flows through a network of connected open fractures (SKB TR-13-08). The hydraulic heterogeneity and anisotropy of the fracture network are defined deterministically as fracture zones in the model, rather than being represented as discrete rock fractures. The discrete fracture network is first generated and the large fracture zones are mapped onto the continuum representation of the domain. SKB TR-13-08 discusses the major fracture zones that are included in the regional scale model. The anisotropic hydraulic conductivity field defined by the fracture zones in the regional-scale model was input to the host rock domain of the repository-scale model. The repository-scale model for 2BMA consists of waste inside each vault compartment, concrete barriers, and the highly permeable backfill that comprises the hydraulic cage surrounding the waste caissons. The effect of concrete degradation was studied for moderate, severe, and complete degradation of the concrete and compared to the base case, in which there is no degradation of the engineered barriers. The flow analysis results show that flow into the 2BMA vault is highly localized at fracture zones that preferentially transmit flow. Total flow through each of the 2BMA caissons and the backfill at corresponding locations of the 2BMA compartments show interaction between 2BMA and the deformation zones. The peaks in the total flow coincide with where the deformation zones intersect the 2BMA vault. Flow through the backfill is higher than through the waste, demonstrating the hydraulic

cage effects. The maximum volumetric flow rate per caisson predicted by the repository-scale model was used in the reactive transport modelling for concrete degradation in SKB R-13-40.

SKB's approach that treats fracture networks as an equivalent porous continuum system in a regional flow model is standard. The analysis shows that fracture networks may give rise to localized flows larger than those associated with continuum porous media. However, those localized flows may have a limited impact on waste release. In addition to reducing the hydraulic gradient in the vault, the permeable backfill used for the hydraulic cage may redistribute localized inflow, which justifies the use of average, large-scale, groundwater fluxes in performance assessments. We consider the use of average equivalent flows in performance assessments to be reasonable. Follow-up questions to SKB about the effects of fracture flows are warranted; however, it is our opinion that the effect of using localized flows alone is unlikely to change the conclusion of the system safety analysis.

### 2.3.6. Implications for concrete properties of the frequency, geometry, and width of concrete fractures resulting from shrinkage and mechanical loads

Fracture formation processes in concrete considered in SKB R-13-40 include (i) drying shrinkage during construction and operation, (ii) thermal contraction due to groundwater-induced cooling post-closure, and (iii) corrosion of different steel components used as construction elements in concrete barriers.

Inspection of the concrete structure in 1BMA revealed the formation of fractures in the floor and walls (SKB R-13-40 and SKB R-13-51). Some fractures extended through the walls and were visible from inside and outside of the wall. The apertures or widths of these fractures ranged from 0.1 to 1.8 mm. The most likely cause of these fractures was attributed to temperature changes and shrinkage. Although 1BMA concrete walls have several steel bolts, fractures related to corrosion of bolts were not observed.

The modelled hydraulic conductivity of concrete with fully penetrating fractures as a function of width and spacing is given by Equation 6-17 of SKB R-13-40, based on derivations discussed in Sections 6.3 and 6.5 of that report. The hydraulic conductivity of fully penetrating fractures is derived based on flow through two parallel plates with smooth surfaces separated by a given aperture or width. The hydraulic conductivity is modified with a factor to include surface roughness or potential infill material (e.g., precipitates of ettingrite or calcite). The overall hydraulic conductivity given by Equation 6-17 considers the conductivity of intact concrete and the density of fully penetrating fractures with distributed fracture widths, spacings, and lengths. The derivation of overall diffusivity of concrete with fully penetrating fractures is discussed in sections 6.4 and 6.6 of SKB R-13-40. The increase in porosity due to fractures in concrete is estimated from the ratio of fracture width to fracture spacing (Equation 6-60 of SKB R-13-40).

Using the fracture data (i.e., length and width) collected at sections of the 1BMA concrete wall in 2000 and 2011, SKB calculated fractured concrete hydraulic conductivity using Equation 6-17 of SKB R-13-40. Based on data collected during the year 2000, the estimated concrete hydraulic conductivity was $5.2\times10^{-5}$ to $1.1\times10^{-4}$ m/s for the western long side and $1.1\times10^{-4}$ to $2.2\times10^{-4}$ m/s for the eastern

long side, and, more recently, the concrete hydraulic conductivity was $2.6\times10^{-4}$ to $5.3\times10^{-4}$ m/s based on data collected from the entire vault during 2011. Therefore, fractures in the 1BMA wall had a major effect on the concrete hydraulic conductivity compared to the initial state hydraulic conductivity used in the safety analysis ($8.3\times10^{-10}$ m/s). SKB proposed to repair the concrete to achieve the initial state hydraulic conductivity before closure.

SKB used reactive transport modelling to analyse degradation of 2BMA concrete barriers and 1BMA concrete barriers that include repair measures. The data used for reactive transport modelling are given in Table 7-5 for 2BMA and Table 7-7 for 1BMA (SKB R-13-40). The model accounted for the degraded state of the concrete matrix by assuming fracture densities and apertures that increase with time. Hydraulic conductivity calculated based on the assumed fractures was used as input to the flow model as part of reactive transport modelling. SKB used modified Kozeny-Carman relations and the evolution of porosity from reactive transport modelling to evaluate hydraulic conductivity of concrete over time. The evaluated hydraulic conductivity for 2BMA (Figure 9-1, SKB R-13-40) remained steady at approximately $10^{-9}$ m/s up to 10,000 years and then increased sharply up to 100,000 years. Based on the analysis, SKB concludes that the effect of chemical degradation on hydraulic conductivity is more pronounced after 10,000 years. Concrete degradation prior to 10,000 years is caused by fractures developed by physical processes (e.g., shrinkage and temperature changes). SKB accounted for physical degradation by assuming a range of increased hydraulic conductivity of $5.0\times10^{-9}$ m/s to $5.0\times10^{-8}$ m/s for 50–100 years, and $5.0\times10^{-8}$ to $5.0\times10^{-7}$ m/s for 100–10,000 years.

SKB's overall approach for estimating the hydraulic conductivity of degraded concrete is reasonable. However, SKB did not provide a basis for the conductivity values used to represent enhancement due to fractures relating to physical and mechanical processes during the first 10,000 years. Based on observations of fractures in 1BMA, hydraulic conductivity can increase from the initial state by up to five orders of magnitude due to fracturing. Flow rates are directly proportional to the hydraulic conductivity and radionuclide release rates are, in general, proportional to water flow rates contacting waste forms. Thus, it is important for SKB to clarify how fracturing was considered in developing the particular hydraulic conductivity values used for the concrete degradation abstraction in the safety assessment.

### 2.3.7. Influence of concrete degradation on water freezing temperature and the effect of freezing on mechanical properties of the structures

Given the shallow repository depth, permafrost could freeze downward to the repository horizon for SFR 1 and SFR 3 and freeze water contained in the engineered barriers. The SKB study of concrete degradation caused by the freeze-thaw effect is reported in SKB P-13-07 and SKB R-07-60, and the consequence of freezing on the concrete structures was reported in SKB TR-12-13. Concrete contains gel pores, capillary pores, and air voids. When a saturated material possessing a continuous range of pore sizes is subjected to low temperatures, according to thermodynamics, the temperature at which water freezes depends on the size of the pore (Korhonen, 2002). The smaller the pore size, the lower is the freezing temperature of pore water. Freezing point depression as a function of pore size is shown in Figure 3-1 of SKB TR-12-13. SKB P-13-07 discussed laboratory tests conducted on core samples taken from 1BMA in SFR 1 to study the

temperature at which water-saturated concrete will freeze. Based on the test results, the temperature range for freezing of concrete in 1BMA was estimated as −3 °C to −7 °C.

SKB TR-12-13 studied the effects on mechanical and hydraulic properties of freezing concrete in 1BMA. The report assumed the concrete is fully saturated and the groundwater surrounding the concrete structure will be frozen before ice formation in the concrete, constraining any flow of pore fluid. Freezing of pore water in concrete will increase pressure on the unfrozen water and exert stresses on the surrounding solid (hardened cement paste and aggregate). The report estimated the quantity of water in the pore space and employed poroelasticity models to calculate overpressure of unfrozen liquid and induced stress and strain in the porous body. The study determined that freezing of pore water resulted in micro-cracks after freeze and thaw cycles at decreased temperatures and estimated the reductions in compressive and tensile strengths and the increase in hydraulic conductivity. During a thawing cycle, the fluid will migrate inside through the fracture network and increase the fluid volume inside the concrete. Concrete will further degrade by forming more fractures during the next freezing cycle. SKB reports do not address the effect of concrete degradation on the freezing temperature of the pore water. This issue may not be important after the first instance of freeze-related damage because SKB assumed the concrete to be completely fractured thereafter, as can be seen in Tables 4-1, 4-6, and 4-7 of SKB TR-14-09.

For the SKB TR-14-01 performance assessment model, a concrete pore water freezing temperature of −3 °C was used based on the upper limit of the test results of SKB P-13-07. Based on the Climate Report, SKB concluded that periglacial climate conditions in the early periglacial climate case occur by approximately 17,500 AD, and for the global warming climate case by approximately 52,000 AD (SKB TR-14-01). For the early periglacial climate case, the maximum depth of the 0 °C isotherm is forecast to be approximately 150 m. However, bedrock temperature may not fall below −3 °C and cause freezing-related damage to the concrete barriers. For the global warming climate case, bedrock temperatures may fall to −3 °C or less at the repository depth and cause substantial damage to the concrete. In Tables 4-1, 4-6, and 4-7 (SKB TR-14-09), the concrete is considered completely degraded for hydrological modelling after the first episode of permafrost, and flow through barriers was modelled as fracture flow. The approach that SKB implemented to account for freezing of concrete structures is reasonable to conservative. SKB considered the hydraulic conductivity to significantly increase after the first occurrence of permafrost. However, SKB also computed that the temperature of the concrete structures may not necessarily fall below −3 °C; thus, concrete structures may remain intact longer than SKB assumed. As previously stated, ranges of hydraulic conductivity that SKB considered for degraded concrete states are regarded as adequate and even conservative. We regard hydraulic conductivity to be the most important property directly connected to estimates of water flow rates contacting waste forms (and to radionuclide release rate estimates). Other concrete properties may also be affected by freezing, but because hydraulic conductivity may vary by orders of magnitude, changes to it may dominate other effects.

### 2.3.8. Influence of chemical dissolution of other concrete structures, waste packages, rock supports, and grouting on the degradation of the concrete structures

The evolution of chemistry for 1BMA and 2BMA was evaluated in SKB R-13-40. The reactive transport modelling of chemical degradation over time as a function of the initial state of the concrete barrier consisted of groundwater flow simulation and geochemical reaction calculations. The 2-D models used in the analysis are depicted in Figure 7-1 for 2BMA and Figure 7-6 for 1BMA (SKB R-13-40). The 2BMA model consists of macadam backfill surrounding the concrete structure and a 0.1-m thick layer of concrete grout. The space representing the waste is initially filled with concrete pore water in the model. Similarly, the volume representing waste is saturated for the 1BMA model. Thus, in the detailed reactive transport modelling, SKB dismissed any effects of chemical interaction of the waste on the degradation of the concrete structures; similarly, SKB disregarded the effects of rock supports. For the geochemical reaction calculation, SKB analysed the evolution of pore water chemistry at specific locations in the concrete structure. The SKB model did not include any change in the chemistry of water as it flows through the waste and potential effects on the downstream concrete structure. The 1BMA waste contains ion-exchange resins solidified in bitumen or cement, and stabilized scrap metal and refuse, as shown in Figure 3-5 (SKB TR-14-02). Waste is stored in concrete or steel moulds or drums, as shown in Table 3-13 (SKB TR-14-02). The waste stored in 2BMA is similar and the distribution of type of waste, matrices, and packaging is shown in Figure 3-6 (SKB TR-14-02). The chemistry of the water in contact with the waste form and rock supports could alter the degradation rate of the concrete. For example, if the pH were to evolve towards alkalinity, then the leaching rate of concrete constituents would slow down, or expedite if the pH would tend towards acidity. It is difficult to establish *a-priori* and unequivocally whether the evolution would be towards alkalinity or acidity, as the behaviour could depend on unexamined factors such as component degradation rates and relative proportions of bitumen and cement forms. Cronstrand (2014) modelled for SFR 1 the pH evolution of water in contact with various waste forms containing, among other materials, cementitious, bitumenized, and steel components. Cronstrand found that for 1BMA compartments having either cement stabilized or bitumenized waste, pH evolution was dominated by the cementitious components. In other words, the chemical impacts on water chemistry of non-cementitious waste forms and compartment components are likely to be minor and can be neglected. Therefore, the study of Cronstrand (2014) suggests that, in evaluating concrete degradation, it is reasonable to dismiss the chemical interaction of pore water with the waste forms, drum internals, and rock supports.

In an earlier SSM-commissioned expert review of the SR-PSU representation of chemical evolution in the engineered barrier system, Savage (2016, Section 4.2) defined information needs that would clarify the SKB bases for models of interactions between saline water and cementitious materials in SFR. First, Savage noted that the model in R-13-40 did not show a pH increase above 13 that would be expected to result from early Friedel's salt precipitation, citing Honda et al. (2009) as an example study. It is noted that calculations by Honda et al. (and others cited) showed the pH increase, but the Honda et al. experiments with hardened ordinary Portland cement did not. Nevertheless, the current review concurs with the need for clarifying information on the potential for elevated pH from Friedel's salt precipitation. This process could also potentially have an effect if chloride is released from exposed waste forms and reacts with cementitious materials.

Savage (2016) also commented that R-13-40 did not clearly recognize the degradation effects of the lower pH (~10) imposed by brucite precipitation. While it is true that R-13-40 does not explicitly address this effect, the report models the formation of brucite and mentions this as a degradation process. During the first 2,000 years of the modelled period, while the infiltrating water is relatively magnesium-rich seawater, it is apparent that brucite forms in the models but does not control pH. Rather, pH is responsive to the gradual evolution of portlandite and other cementitious phases in this heterogeneous chemical system. Thereafter, dissolved magnesium is lower in the infiltrating fresh water and brucite may not have an effect on pH until most cementitious solids (e.g., portlandite, ettringite, and CSH phases) have been consumed. Additional discussion could clarify how magnesium degradation effects are treated in R-13-40. The current review is not expected to be affected by the response to this Savage (2016) request for clarification, unless potential longer-lived sources of magnesium-rich infiltrating water are identified.

Finally, Savage (2016) questioned the applicability of activity coefficient calculations, based on the Debye-Hückel and Davies equations, used for chemical models in R-13-40. Savage acknowledged that the effects of using these activity models, rather than others more appropriate for high-ionic strength solutions, may be minor for the defined saline groundwater. He added, however, that these models may not be applicable for more saline groundwaters that could plausibly infiltrate SFR concrete structures. The current review concurs with the Savage (2016) request that additional information be provided regarding the selection of activity coefficient models. Additional discussion will help clarify whether processes such as upconing of saline water or salt exclusion could result in higher-ionic strength solutions interacting with the concrete. It does not appear that other components of the disposal system could themselves generate more saline waters on a large scale.

### 2.3.9. Review of the parameters in Tables 9-4, 9-5, and 10-4 of SKB TR-14-10

Table 10-4 in SKB TR 14-10 summarized the data for hydraulic conductivity and porosity of construction concrete and concrete grout in the BMA vaults for use in SR-PSU. The parameter values in this table are provided for construction concrete (walls, bottom slab, and lid), concrete moulds, and concrete grout. The degraded states of hydraulic parameters were evaluated by dividing the performance assessment period into five stages that consist of initial state prior to closure, early stages of groundwater flow and saturation, a period of portlandite leaching that will occur as the flow continues, a period of leaching of CSH-gel and ingrowth of enttrigite, and finally, a severe leaching stage. The basis for the values of the parameters is discussed in SKB R-13-40. The initial value of hydraulic conductivity during the operational phase [i.e., assumed to be 0 to 50 years (Figure 9-1, SKB R-13-40)], is $8.3\times10^{-10}$ m/s for construction concrete and $8.3\times10^{-9}$ m/s for concrete grout. The SKB estimates for the hydraulic conductivity of construction concrete are based on assumptions that hydraulic conductivity of intact concrete is $1\times10^{-11}$ m/s, and that the concrete would be slightly fractured with aperture widths of 10 μm at spacings of 1 m. The analytical process for evaluating hydraulic conductivity with fully penetrating fractures is discussed SKB R-13-40 (Chapter 6). The hydraulic conductivity of concrete grout was assumed to be one order of magnitude higher than that of concrete. SKB stated that grout is not assumed to be a barrier to groundwater flow in the vault, and argued that larger values of the grout hydraulic conductivity could divert the flow around the waste packages. CNWRA finds that

the hydraulic conductivity assumed for grout by SKB is higher than the data available for strong grout in the literature. Based on laboratory experiments using several approaches, Dixon and Phifer (2007) recommended hydraulic conductivity of strong grout as $2.1\times10^{-10}$ m/s, which is approximately the same order of magnitude for concrete and grout assumed by SKB. The initial porosity value for construction concrete, assumed to be 0.11, is based on the composition of the concrete and assumptions about initial fracture characteristics (SKB R-13-40). SKB assumed the initial porosity value for concrete grout to be 0.3, which is higher than the measured strong grout porosity of 0.27 (Dixon and Phifer, 2007). Thus, the porosity estimates are reasonable.

During the early model stages of groundwater flow and saturation (i.e., between 50 and 100 years), the hydraulic conductivities of all concrete components were increased by a factor of 10. SKB addressed concrete degradation by reactive transport modelling of leaching of cementitious material from the concrete barrier. The model was used to evaluate the evolution of the individual mineral volumes and porosity for 1BMA and 2BMA until 100,000 years. Based on reactive transport modelling of the leaching process, SKB estimated evolving values of hydraulic conductivity from changes to porosity using a modified Kozeney-Carmen relation. During the chemical dissolution process, the porosity of construction concrete increases from the initial value of 0.11 to 0.25. Using this model, the hydraulic conductivity of construction concrete (Figure 9-1 of SKB R-13-40) is approximately $10^{-9}$ m/s from 100 to 10,000 years, slightly increases to $3.0\times10^{-9}$ m/s from 10,000 to 20,000 years, and sharply increases to $7.0\times10^{-5}$ m/s from 20,000 to 100,000 years. SKB stated that the hydraulic conductivity during the first 10,000 years will be influenced by a physical degradation process, that is, fracture development caused by shrinkage due to drying and temperature changes. To account for this physical effect, SKB assumed for the safety assessment a hydraulic conductivity range for construction concrete of $5.0\times10^{-8}$ m/s to $5.0\times10^{-7}$ m/s during the period from 100 to 20,000 years—which is about 50 to 500 times higher than obtained from the chemical porosity model discussed above. Construction concrete is assumed to degrade at a faster rate during the period from 20,000 to 50,000 years, resulting in hydraulic conductivities in the range of $5.0\times10^{-7}$ m/s to $5.0\times10^{-6}$ m/s. During the severely degraded state occurring between 50,000 and 100,000 years, the hydraulic conductivity of construction concrete is assumed to increase by an order of magnitude ($5\times10^{-6}$ m/s to $5\times10^{-5}$ m/s). The overall increase in hydraulic conductivity from the initial state is approximately 4 to 5 orders of magnitude. The hydraulic conductivity of concrete grout for all periods is assumed to be 10 times greater than that of construction concrete.

The modelling report on flow through the SFR 1 and SFR 3 repository systems (Table 6-2, SKB TR-13-08) used four sets of hydraulic properties: a base case and moderate, severe, and completely degraded cases. The hydraulic conductivities for these cases, in the same order, are $8.3\times10^{-10}$ m/s, $1\times10^{-7}$ m/s, $1.0\times10^{-5}$ m/s, and $1\times10^{-3}$m/s. The hydraulic properties for the modelled waste system for the above cases are $8.3\times10^{-7}$ m/s, $1\times10^{-4}$ m/s, $1.0\times10^{-3}$ m/s, and $1\times10^{-3}$ m/s, respectively. The macadam backfill conductivity in all cases was assumed to be $10^{-3}$ m/s. The parameters used in flow modelling are comparable to those presented in Table 10-4 (SKB TR-14-10), except that for the completely degraded state, the flow modelling report uses higher conductivity values by almost two orders of magnitude.

We consider the modelling approach that SKB used to predict the hydraulic properties for progressively degraded states based on reactive transport modelling, the modified Kozeney-Carmen relation, and a fully penetrating fracture formulation

to be technically sound. SKB's assumption regarding shrinkage-induced fractures during the first 10,000 years is reasonable. However, parameter values used in these models need realistic assessment. For example, the initial hydraulic conductivity of construction concrete used in all models was estimated to be $8.3\times10^{-10}$ m/s. This estimate is based on the known hydraulic conductivity of intact concrete and assumed fully penetrating fractures. SKB reports (R-13-40, R-13-51, TR-14-01) discussed observed fractures in 1BMA, analysis of the collected data, and a revised estimate of hydraulic conductivity showing increased values influenced by the presence of fractures. SKB's strategy is to repair and reinforce the concrete to the initial stage hydraulic conductivity. The observations, however, provided an opportunity to revise the hydraulic conductivity data for the initial state and conduct a sensitivity analysis to study the impact on the safety assessment. SKB should consider these additional analyses.

Table 9-4 of the Data Report for the Safety Assessment SR-PSU (SKB TR-14-10) provided effective diffusivities in concrete materials that have been suggested for use in the safety assessment calculations for different time periods. SKB stated that the suggested values are based on interpretation of the results of reactive transport modelling of the chemical degradation of 2BMA concrete barriers, in combination with estimates computed using simple mathematical models to assess different physical degradation processes. The chemical degradation of the 2BMA concrete barriers was considered representative of concrete barriers of different parts of SFR because it was assumed that other concrete barriers, such as the 1BMA vault, will be repaired to a state where barrier function is equivalent to that of 2BMA barriers. We consider the assessment of the effect of degradation on diffusion coefficients to be technically adequate. Changes of values of diffusion coefficients are constrained. We consider the process of diffusion to be secondary to advection, in case flow paths contacting waste forms are established in degraded concrete.

### 2.3.10. Review of the progressions of hydrological cases in Tables 4-1, 4-6, and 4-7 of SKB TR-14-09

Table 4-1 of Radionuclide Transport and Dose Calculations for the Safety Assessment SR-PSU (SKB TR-14-09) provides the evolution of hydraulic conductivities for different degradation states of concrete barriers in the near-field for the "global warming" calculation case. These values are (i) $8.3\times10^{-10}$ m/s for intact concrete, (ii) $10^{-7}$ m/s for moderately degraded concrete, (iii) $10^{-5}$ m/s for severely degraded concrete, and (iv) $10^{-3}$ m/s for completely degraded concrete. Consistent with the global warming case, no radionuclide release during the first 1,000 years was assumed. Table 4-1 also refers to hydraulic conductivities for the base case scenario and fracture flow. SKB selected the hydraulic conductivities in Table 4-1 (SKB TR-14-09) based on available models, simulations, calibrations, and literature (SKB TR-13-08; SKB TR-14-10; SKB R-01-14; SKB R-01-02; and SKB R-01-21). Hydraulic conductivity values in Table 4-1 are reasonable for intact concrete because values less than $10^{-8}$ m/s are common for high quality concrete. Hydraulic conductivities on the order of $10^{-3}$ m/s are equivalent to that of coarse sand to gravel aggregate (McWhorter and Sunada, 1977; Domenico and Schwartz, 1990), which provide reasonable upper bounds for highly degraded, leached concrete.

Table 4-6 provides the evolution of near-field hydraulic conductivities for the "timing of the releases" calculation case. SKB considered this case to analyse the effect of assuming releases during the submerged period (i.e., radionuclide release

commences immediately upon closure). This case forms the SKB basis for the calculation of collective doses, which are to be calculated from releases during the first 1,000 years post-closure. The models of the near field, the far field, and the biosphere are handled the same as they were in the global-warming calculation case. The global-warming and timing-of-releases calculation cases comprise the two bounding cases of possible outcomes. The evolution of hydraulic conductivities with concrete degradation is reasonable, including transition times. It is likely that degradation processes will persist over hundreds of years.

Table 4-7 provides the evolution of near-field hydraulic conductivities for the "accelerated concrete degradation" calculation case. This case assesses uncertainties in the concrete degradation process. In this case, it is assumed that the hydraulic conductivity of the concrete increases earlier or to a greater extent than in the global warming calculation case. This assumption yields: (i) earlier or greater increase in the water flow through the waste vaults, (ii) earlier or greater increase in the diffusivities of the concrete barriers, and (iii) earlier or greater increase in the concrete porosity. The transitions between time periods were modelled as a gradual change over 100 years. The handling of the near field, the far field, and the biosphere are identical to the global warming calculation case. We consider transitions taking place in the first 100 years to be fast. Processes affecting the degradation of concrete are controlled by diffusion and slow mass transfer that could span hundreds of years in the absence of kinetically active processes (such as those due to corrosion of steel for reinforcement) (Pabalan et al., 2009).

### 2.3.11. The effects of different uncertainties on the choice of the parameters for the safety analysis and radionuclide transport model

SKB addressed spatial and temporal variability of hydraulic properties in SKB TR-14-10. SKB recognized considerable spatial variability may exist in hydraulic conductivity of concrete barriers because of the primary heterogeneity of concrete and the potential presence of fractures imprinting secondary heterogeneities onto the material property distribution. Although data on fractures at 1BMA were collected and analysed, the data collection was limited to one section of 1BMA and fractures less than 100 μm wide were not recorded. SKB asserted that site-specific data are not sufficient to quantify uncertainty in the hydraulic properties, as applicable to modelling the entire repository. SKB evaluated changes to the hydraulic conductivity and porosity over time, due to chemical and physical degradation processes (Table 10-4, SKB T-14-10). SKB stated that the available data on chemical and physical degradation processes either observed at the repository or recorded in the literature are too constrained to fully support quantification of uncertainties (temporal) via statistical analyses. SKB documented models to quantify changes to the hydraulic conductivity of concrete due to chemical and physical degradation processes, as well as hydraulic conductivity values to be used in the safety analysis in SKB R-13-40.

SKB estimated the hydraulic conductivity of 1BMA on the basis of data collected from fractures observed in the concrete structure. The hydraulic conductivity at specific areas of the 1BMA wall varied between $5.2\times10^{-5}$ and $5.3\times10^{-4}$ m/s (SKB R-13-40) which is about 5 to 6 orders of magnitude higher compared to the initial state hydraulic conductivity ($8.1\times10^{-10}$ m/s) used in the SKB safety analysis. As stated in SKB TR-14-10, SKB plans to repair and reinforce the barrier in 1BMA to achieve the target initial hydraulic conductivity state. The design and construction of the

2BMA vault was revised to minimize development of such fractures. The mitigation strategy that SKB planned for 1BMA and 2BMA needs to be evaluated separately, to ensure that a target (low) hydraulic conductivity is attainable prior to closure. At this time, there is uncertainty about the initial state of concrete and its hydraulic conductivity for post-closure safety analyses. CNWRA recommends performing a sensitivity analysis that varies the initial hydraulic conductivity value to assess the impact of the initial state of concrete, and the relevance of proposed maintenance/repair process.

### 2.3.12. The derivation and significance of the variation of hydraulic conductivity and hydraulic contrast with respect to the backfilling as a function of the concrete barrier porosity and fracture density

For the SKB analysis, the hydraulic contrast is defined as the ratio between the hydraulic conductivities of the concrete barrier and the backfill material. Figure 6-14 of SKB TR-14-01 displays the hydraulic contrast as a function of barrier porosity and fracture density. SKB stated that the contrast was estimated using the Kozeny-Carman equation for the backfill and the concrete barrier, and referred to two supporting reports (SKB R-13-51 and SKB R-13-40) for details on the derivation. SKB R-13-51 discussed evaluation of hydraulic conductivity using the Kozeny-Carman equation for granular backfill material. SKB R-13-40 discussed the use of the modified Kozeny-Carman relation to scale the hydraulic conductivity of intact concrete and a final state after leaching depletion of all cement material, at which point only aggregate ballasts control the hydraulic conductivity. The analysis of the hydraulic contrast between granular backfill and fractured concrete that yielded the results depicted in Figure 6-14 in SKB TR-14-01 was not traceable in the reports that SKB referenced (i.e., reports SKB R-13-51 and SKB R-13-40). In addition, it is not clear how this information was used in the safety analysis. However, this lack of transparency is perceived to be a minor issue. SKB explicitly analysed hydraulic contrast in near-field flow modelling. The repository-scale model of 1BMA and 2BMA included components such as the backfill, the concrete barrier, and the waste block, with three-dimensional geometries and different hydraulic conductivities. SKB considered various degradation scenarios to examine the possibility of flow focusing and enhanced flow paths that could increase radionuclide release estimates.

The hydraulic conductivities for the backfill and concrete barrier were defined in the near-field flow modelling in SKB R-14-14 and SKB TR-13-08 for use in radionuclide transport calculations (SKB TR-14-09). The hydraulic conductivities for the barrier concrete base case and three degraded cases for 1BMA and 2BMA were $8.3\times10^{-10}$ m/s, $10^{-7}$ m/s, $10^{-5}$ m/s, and $10^{-3}$ m/s, while the hydraulic conductivity for the backfill in all cases was $10^{-3}$ m/s. The hydraulic conductivity of waste was varied from $8.3\times10^{-7}$ m/s to $10^{-3}$ m/s. The backfill is designed to create a hydraulic contrast to induce flow through the backfill, forming a hydraulic cage between the backfill and concrete barrier for different stages of concrete degradation. In the limit of complete concrete degradation, the hydraulic conductivity of concrete is assumed identical to the hydraulic conductivity of backfill, the hydraulic contrast disappears, and flow becomes uniform through the system.

CNWRA considers SKB's treatment of hydraulic conductivity contrast and variation with time in the near-field flow modelling to be reasonable. It is reasonable to initially assume a high contrast, allowing the majority of the flow to go through the

backfill. As time elapses and the concrete barriers degrade, flow may become more uniform. SKB does not consider the scenario where the concrete barrier becomes the dominant flow path relative to the backfill. It is difficult to envision that flow through the concrete barriers would predominate over flow through backfill at large spatial scales. Therefore, we agree with excluding the scenario in which hydraulic conductivity of concrete exceeds that of backfill. SKB's analysis of the hydraulic contrast is not entirely transparent because supporting references do not provide details about the computation of the contrast. SKB addressed the main question of consideration of effect of degradation of hydraulic conductivity contrast in the safety analysis.

# 3. Summary

This review found that, in general, SKB made reasonable assumptions and applied technically sound modelling approaches to characterizing concrete degradation effects on radionuclide release and transport in the safety assessment for the SFR extension. A number of recommendations have been made for clarifications or additional analyses. While in our judgment most of these requests concern factors unlikely to significantly affect the results of the safety assessment, two particular items are particularly notable and may be more significant. First, clarification is needed for the choices of flow rates used in the 2BMA chemical degradation model. Second, sensitivity of safety assessment results to the initial concrete hydraulic conductivity state should be evaluated.

# 4. References

Berner, U.R., 1992. Evolution of Pore Water Chemistry During Degradation of Cement in a Radioactive Waste Repository Environment, Waste Management, Vol. 12, pp. 201–219.

Chen, X., S. Wu, and J. Zhou, 2013. Influence of Porosity on Compressive and Tensile Strength of Cement Mortar, Construction and Building Materials, Vol. 40, pp. 869-974.

Cronstrand, P., 2014. Evolution of pH in SFR 1. SKB R-14-01. Stockholm, Sweden: Swedish Nuclear Fuel and Waste Management Company.

Dinwiddie, C.L., D.R. Bannon, M.K. Todt, G.R. Walter, and M.M. Roberts, 2012. Fiscal Year 2012 Meso- and Intermediate-Scale Grout Monolith Test Bed Experiments: Results and Recommendations (Final Report). San Antonio, Texas: Center for Nuclear Waste Regulatory Analyses.

Dixon, K. and M. Phifer, 2007. Hydraulic and Physical Properties of Tank Grouts and Base Mat Surrogate Concrete for FTE Closure, WSRC-STI-2007-00369, Revision 0. Aiken, South Carolina: Savannah River National Laboratory.

DOE, 2009. DOE/RW–0573, "Yucca Mountain Repository License Application." Rev. 1. U.S. NRC electronic library accession number ML090700817. Las Vegas, Nevada: U.S. Department of Energy, Office of Civilian Radioactive Waste Management.

Domenico, P.A. and F.W. Schwartz, 1990. *Physical and Chemical Hydrogeology*. New York, New York: John Wiley & Sons, Inc.

Honda, A., K. Masuda, H. Nakanishi, H. Fujita, and K. Negishi, 2009. Modeling of pH elevation due to the reaction of saline groundwater with hydrated ordinary Portland cement phases, in N.C. Hyatt, D.A. Pickett, and R.B. Rebak (eds.), Scientific Basis for Nuclear Waste Management XXXII. Materials Research Society Symposium Proceedings, Vol. 1124, pp. 365-372.

Korhonen, C, 2002. Effect of High Doses of Chemical Admixtures on the Freeze–Thaw Durability of Portland Cement Concrete. Technical Report, ERDC/CRREL TR-02-5. Cold Region Research and Engineering Laboratory, Engineer Research Development Center, U.S. Army Corps of Engineers.

McWhorter, D.B. and D.K. Sunada, 1977. *Ground-Water Hydrology and Hydraulics*. Highlands Ranch, Colorado: Water Resources Publications.

NRC, 2014. Safety Evaluation Report Related to Disposal of High-Level Radioactive Wastes in a Geologic Repository at Yucca Mountain, Nevada. Volume 3: Repository Safety After Permanent Closure. NUREG-1949, Vol. 3. Washington, DC: U.S. Nuclear Regulatory Commission. U.S. NRC Electronic Library Accession Number ML14288A121.

Ofoegbu, G., R. Fedors, C. Grossman, S. Hsiung, L. Ibarra, C. Manepally, J. Myers, M. Nataraja, O. Pensado, K. Smart, and D. Wyrick, 2007. Summary of Current Understanding of Drift Degradation and Its Effects on Performance at a Potential Yucca Mountain Repository. Rev. 1. CNWRA 2006-02. San Antonio, Texas: Center for Nuclear Waste Regulatory Analyses. U.S. NRC Electronic Library Accession Number ML070650462.

Pabalan, R.T., F.P. Glasser, D.A. Pickett, G.R. Walter, S. Biswas, M.R. Juckett, L.M. Sabido, and J.L. Myers, 2009. Review of Literature and Assessment of Factors Relevant to Performance of Grouted Systems for Radioactive Waste Disposal. San Antonio, Texas: Center for Nuclear Waste Regulatory Analyses. April 2009.

Painter, S.L., R. T. Pabalan, 2009. Estimated Longevity of Reducing Environments in Grouted Systems for Radioactive Waste Disposal. San Antonio, TX, USA: Center for Nuclear Waste Regulatory Analyses. U.S. NRC Electronic Library Accession Number ML101160513.

Savage, D., 2016. Review of chemical evolution in rock and engineered barrier systems in SFR according to the safety assessment SR-PSU. Part 4 of SSM Report 2016:08, SSM's External Experts' Reviews of SKB's Safety Assessment SR-PSU – Hydrogeological and Chemical Aspects. Initial Review Phase. Stockholm, Sweden: Swedish Radiation Safety Authority.

Winterle, J., S. Mohanty, R. Rice, and O. Pensado, 2008. Final: Risks Insights Derived From Analyses of Model Updates in the Total-System Performance Assessment Version 5.1 Code. Rev 2. San Antonio, Texas: Center for Nuclear Waste Regulatory Analyses. U.S. NRC Electronic Library Accession Number ML0802240343.

APPENDIX 1

# Coverage of SKB reports

Following reports have been covered in the review.

**Table A-1: List of reports consulted and evaluated in the task**

| Reviewed report | Reviewed sections | Comments |
|---|---|---|
| SKB TR-14-01, 2015: Safety analysis for SFR, long-term safety: main report for the safety assessment SR-PSU | 4.3, 6.2, 6.3, 6.4.8, 7.4.3 | |
| SKB TR-14-09, 2015: Radionuclide transport and dose calculations for the safety assessment SR-PSU, | 4.1 | |
| SKB TR-14-10, 2014:Data Report for the safety assessment SR-PSU, | Chapters 9 and 10 | |
| SKB R-13-40, 2014: The impact of concrete degradation on the BMA barrier functions | All chapters | |
| SKB R-14-14, 2014; Flow Transport Modelling on the Vault Scale SR-PSU | 3.0, 4.2 | |
| SKB TR-13-08, 2013: Flow Modelling on the Repository Scale for the Safety Assessment SR-PSU | Chapters 2, 3, 7, 8 | |
| SKB R-13-51, 2013: Flow and Transport in Fractures in Concrete Walls in BMA – Problem Formulation and Scoping Calculations | Chapters 2, 3, 6 | |
| SKB TR-14-02, 2014: Initial State Report for Safety Assessment SR-PSU | Chapters 4 and 5 | |
| SKB P-13-07, 2013:: Studier av frysningsegenskaper hos betong från 1 BMA (In Swedish) | All chapters | |

| | |
|---|---|
| SKB R-07-60, 2013: Långtidsstabilitet till följd av frysning och tining av betong och bentonit vid förvaring av låg-och medelaktivt kärnavfall i SFR 1 (In Swedish) | All chapters |

| | |
|---|---|
| SKB TR-12-13: 2013: A study of Consequences of Freezeing of Concrete Structures for Storage of Nuclear Waste due to Permafrost | All chapters |

2017:31

The Swedish Radiation Safety Authority has a comprehensive responsibility to ensure that society is safe from the effects of radiation. The Authority works to achieve radiation safety in a number of areas: nuclear power, medical care as well as commercial products and services. The Authority also works to achieve protection from natural radiation and to increase the level of radiation safety internationally.

The Swedish Radiation Safety Authority works proactively and preventively to protect people and the environment from the harmful effects of radiation, now and in the future. The Authority issues regulations and supervises compliance, while also supporting research, providing training and information, and issuing advice. Often, activities involving radiation require licences issued by the Authority. The Swedish Radiation Safety Authority maintains emergency preparedness around the clock with the aim of limiting the aftermath of radiation accidents and the unintentional spreading of radioactive substances. The Authority participates in international co-operation in order to promote radiation safety and finances projects aiming to raise the level of radiation safety in certain Eastern European countries.

The Authority reports to the Ministry of the Environment and has around 300 employees with competencies in the fields of engineering, natural and behavioural sciences, law, economics and communications. We have received quality, environmental and working environment certification.

**Strålsäkerhetsmyndigheten**
**Swedish Radiation Safety Authority**

SE-171 16 Stockholm
Solna strandväg 96

**Tel:** +46 8 799 40 00
**Fax:** +46 8 799 40 10

**E-mail:** registrator@ssm.se
**Web:** stralsakerhetsmyndigheten.se

Arkitektkopia AB, Bromma, 2017